NBS SPECIAL PUBLICATION **727**

U.S. DEPARTMENT OF COMMERCE/National Bureau of Standards

Laser Induced Damage in Optical Materials: 1984
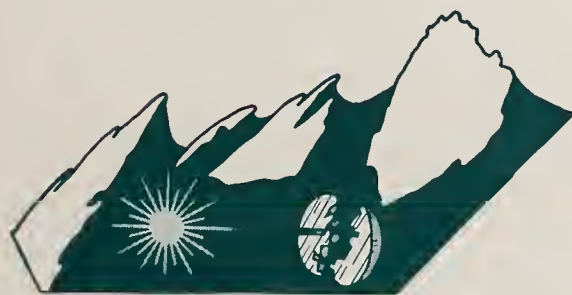
BOULDER DAMAGE SYMPOSIUM

STP 954

*T*he National Bureau of Standards[1] was established by an act of Congress on March 3, 1901. The Bureau's overall goal is to strengthen and advance the nation's science and technology and facilitate their effective application for public benefit. To this end, the Bureau conducts research and provides: (1) a basis for the nation's physical measurement system, (2) scientific and technological services for industry and government, (3) a technical basis for equity in trade, and (4) technical services to promote public safety. The Bureau's technical work is performed by the National Measurement Laboratory, the National Engineering Laboratory, the Institute for Computer Sciences and Technology, and the Institute for Materials Science and Engineering.

The National Measurement Laboratory

Provides the national system of physical and chemical measurement; coordinates the system with measurement systems of other nations and furnishes essential services leading to accurate and uniform physical and chemical measurement throughout the Nation's scientific community, industry, and commerce; provides advisory and research services to other Government agencies; conducts physical and chemical research; develops, produces, and distributes Standard Reference Materials; and provides calibration services. The Laboratory consists of the following centers:

- Basic Standards[2]
- Radiation Research
- Chemical Physics
- Analytical Chemistry

The National Engineering Laboratory

Provides technology and technical services to the public and private sectors to address national needs and to solve national problems; conducts research in engineering and applied science in support of these efforts; builds and maintains competence in the necessary disciplines required to carry out this research and technical service; develops engineering data and measurement capabilities; provides engineering measurement traceability services; develops test methods and proposes engineering standards and code changes; develops and proposes new engineering practices; and develops and improves mechanisms to transfer results of its research to the ultimate user. The Laboratory consists of the following centers:

- Applied Mathematics
- Electronics and Electrical Engineering[2]
- Manufacturing Engineering
- Building Technology
- Fire Research
- Chemical Engineering[2]

The Institute for Computer Sciences and Technology

Conducts research and provides scientific and technical services to aid Federal agencies in the selection, acquisition, application, and use of computer technology to improve effectiveness and economy in Government operations in accordance with Public Law 89-306 (40 U.S.C. 759), relevant Executive Orders, and other directives; carries out this mission by managing the Federal Information Processing Standards Program, developing Federal ADP standards guidelines, and managing Federal participation in ADP voluntary standardization activities; provides scientific and technological advisory services and assistance to Federal agencies; and provides the technical foundation for computer-related policies of the Federal Government. The Institute consists of the following centers:

- Programming Science and Technology
- Computer Systems Engineering

The Institute for Materials Science and Engineering

Conducts research and provides measurements, data, standards, reference materials, quantitative understanding and other technical information fundamental to the processing, structure, properties and performance of materials; addresses the scientific basis for new advanced materials technologies; plans research around cross-country scientific themes such as nondestructive evaluation and phase diagram development; oversees Bureau-wide technical programs in nuclear reactor radiation research and nondestructive evaluation; and broadly disseminates generic technical information resulting from its programs. The Institute consists of the following Divisions:

- Ceramics
- Fracture and Deformation [3]
- Polymers
- Metallurgy
- Reactor Radiation

Laser Induced Damage In Optical Materials: 1984

Proceedings of a Symposium Sponsored by:
National Bureau of Standards
American Society for Testing and Materials
Office of Naval Research
Department of Energy
Defense Advanced Research Project Agency
Air Force Office of Scientific Research

October 15-17, 1984
NBS, Boulder, Colorado 80303

Edited by:

Harold E. Bennett
Naval Weapons Center
China Lake, California 93555

Arthur H. Guenther
Air Force Weapons Laboratory
Kirtland Air Force Base, New Mexico 87117

David Milam
Lawrence Livermore National Laboratory
Livermore, California 94550

Brian E. Newnam
Los Alamos National Laboratory
Los Alamos, New Mexico 87545

BOULDER DAMAGE SYMPOSIUM

The Proceedings contain the papers presented at the Sixteenth Symposium on Optical Materials for High Power Lasers held at the National Bureau of Standards (NBS) in Boulder, Colorado, on October 15-17, 1984. The Symposium was jointly sponsored by the National Bureau of Standards, the American Society for Testing and Materials, the Office of Naval Research, the Defense Advanced Research Projects Agency, the Department of Energy, and the Air Force Office of Scientific Research. The Symposium was attended by approximately 200 scientists from the United States, the United Kingdom, France, West Germany, and the Netherlands. It was divided into sessions devoted to the following topics: Materials and Measurements, Mirrors and Surfaces, Thin Films, and finally Fundamental Mechanisms. The Symposium Co-Chairmen were Dr. Harold E. Bennett of the Naval Weapons Center, Dr. Arthur H. Guenther of the Air Force Weapons Laboratory, Dr. David Milam of the Lawrence Livermore National Laboratory, and Dr. Brian E. Newnam of the Los Alamos National Laboratory. They also served as editors of this report. Dr. Alexander J. Glass of KMS Fusion acts as Conference Treasurer with Aaron A. Sanders of the National Bureau of Standards as the Conference Coordinator.

The editors assume full responsibility for the summary, conclusions, and recommendations contained in the report and for the summaries of discussion found at the end of each paper. The manuscripts of the papers presented at the Symposium have been prepared by the designated authors, and questions pertaining to their content should be addressed to those authors. The interested reader is referred to the bibliography at the end of the summary article for general references to the literature of laser damage studies. The Seventeenth Annual Symposium on this topic will be held in Boulder, Colorado, from October 28-30, 1985. A concerted effort will be made to ensure closer liaison between the practitioners of high peak-power and the high average-power community.

The principal topics to be considered as contributed papers in 1985 do not differ drastically from those enumerated above. We expect to hear more about improved scaling relations as a function of pulse duration, area, and wavelength, and to see a continuing transfer of information from research activities to industrial practice. New sources at shorter wavelengths continue to be developed, and a corresponding shift in emphasis to short wavelength and repetitively pulsed damage problems is anticipated. Fabrication and test procedures will continue to be developed, particularly in the diamond-turned optics and thin-film areas. Comprehensive modeling studies are, as well, anticipated.

The purpose of these symposia is to exchange information about optical materials for high power lasers. The editors will welcome comment and criticism from all interested readers relevant to this purpose, and particularly relative to our plans for the Seventeenth Annual Symposium.

<div style="text-align:right">

H. E. Bennett, A. H. Guenther,

D. Milam, and B. E. Newnam

Co-Chairmen

</div>

DISCLAIMER

Certain papers contributed to this publication have been prepared by non-NBS authors. These papers have not been reviewed or edited by NBS; therefore, the National Bureau of Standards accepts no responsibility for comments or recommendations contained therein.

Certain commercial equipment, instruments, and materials are identified in this publication in order to explain the experimental procedure adequately. Such identification in no way implies approval, recommendation, or endorsement by the National Bureau of Standards, nor does it imply that the equipment, instruments, or materials identified are necessarily the best available for the purpose.

CONTENTS

Materials and Measurements

Mirrors and Surfaces

Thin Films

Fundamental Mechanisms

Symposium Welcome and Perceptions of Future Research

Brian E. Newnam
Los Alamos National Laboratory
Los Alamos, New Mexico 87545

On behalf of the Symposium Steering Committee of Drs. Harold Bennett, Arthur Guenther, David Milam, and myself, I welcome all of you to the 16th Annual Symposium on Optical Materials for High Power Lasers. Having participated in these Symposia since 1971, I recognize among you a number of persistent old timers as well as many new faces. Obviously, these Symposia are still of great interest to a significant number of scientists in the laser community. For the last several years, we have comprised between 180 and 200 participants and between 40 and 60 papers, as revealed by figure 1, a chart of our experience.

In his opening remarks at last year's Boulder Damage Symposium, Art Guenther reviewed the main themes of laser damage research of the previous 15 years. This year I want to describe my percep-tions of the progress needed in the near future. Do you recall the fervor of activity in the late 1960's associated with America's Apollo spacecraft mission? A major concern in those days was the impact of the space environment on the thermal control surfaces such as white reflective paints and second-surface metal mirrors. The potentially dangerous elements of the space environment included solar ultraviolet radiation, electrons and protons in the Van Allen radiation belts, micrometeor-ites, and the vacuum of space. A number of aerospace companies assembled space effects laborato-ries, including high-pressure arc lamps, to simulate the ultraviolet portion of the solar radiation and charged-particle simulation chambers. These environmental simulations produced a large amount of very useful data on radiation resistance. Thus, adequately damage-resistant materials were identified or subsequently developed, and the mission to the moon was a resounding success.

Today, similar attention is beginning to be focused on the effects of machine-produced high-energy radiation environments on the window materials and reflective coatings in lasers driven by electron accelerators. Currently, there is much concern about optical elements in the large e-beam-driven excimer lasers for 248 and 351 nm, in particular. Besides having adequate damage resistance for the primary uv laser wavelength, optical coatings must survive the impact of elec-trons of 100 to >300 kV energies and the resultant x rays. To add further insult, some of the coatings must function in a fluorine gas environment! Laboratory research on coating degradation for e-beam-pumped excimer lasers has been proceeding now for only one or two years.

Recently, another very important accelerator-driven device, the free-electron laser (FEL), has become prominent. Having been associated with the FEL research program at Los Alamos for the last five years, I am very optimistic about its future role in such applications as materials research, industrial chemistry, medical surgery, as well as a potential military tool. Since the first op-eration of an FEL oscillator at 3.4 μm at Stanford University in 1977 [1], there has been a number of FEL oscillator demonstrations extending from the visible through the sub-millimeter range. Table 1 lists the experimental progress. For more information, the interested reader should con-sult the review article of Charles Brau [9].

FELs require electron accelerators with energies ranging from a few MeVs for submillimeter waves to 100 to 200 MeV for visible wavelengths. Upon collision with various materials in the ac-celerator structure, electrons with such energies naturally produce other high-energy radiations, such as x rays, gamma rays, and neutrons. Additionally, the periodic wiggling motion of the elec-trons traveling through the magnetic undulator (gain region) naturally produces harmonics of the fundamental lasing wavelength. For example, for an FEL lasing at 500 nm, there can be significant power in the harmonics in the extreme-ultraviolet range (<100 nm). The optical elements composing the oscillator cavity and the external directing mirrors cannot be allowed to degrade significantly by any of these radiations.

In the first tests with an infrared (10 μm) FEL oscillator at Los Alamos, electrons caused some permanent damage and x rays caused temporary color centers in the NaCl Brewster windows. The presence of transient absorption was also suspected. With the resulting round-trip losses, the FEL could not reach the lasing threshold. To avoid these losses and attain vigorous lasing, it was necessary to remove the Brewster windows, leaving the cavity mirrors in the vacuum [6,8].
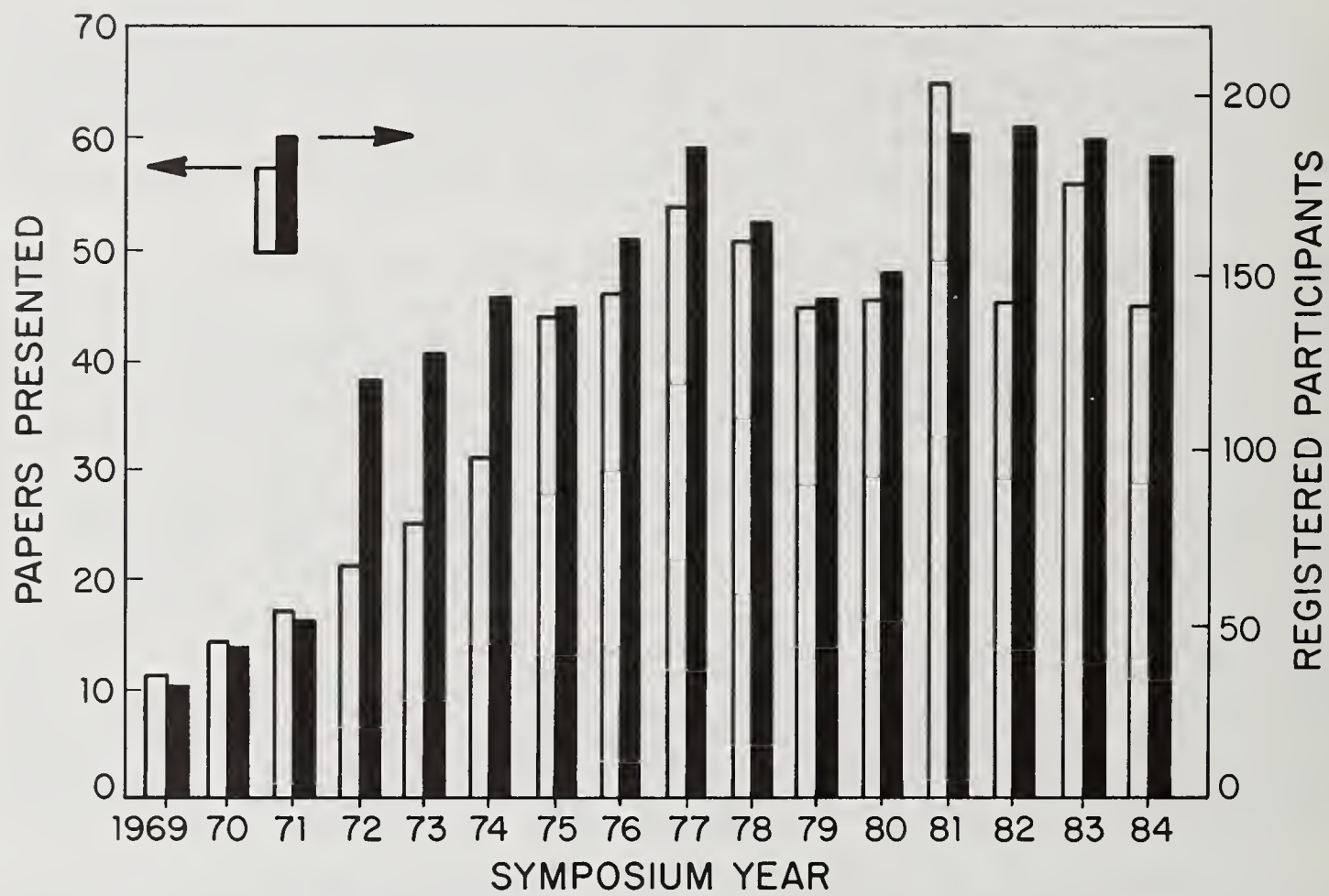
Figure 1. Boulder damage symposium history.

Although radiation-induced degradation of output windows between the laser and atmosphere will still be a concern for powerful, visible-wavelength FELs, the primary future requirement will be for cavity reflectors with reflectances of the order of 99.9% which are not significantly degraded by the multiple environments. We should take note that in the last year FEL researchers at the University of Paris at Orsay have already had to contend with actual degradation of resonator mirror coatings (TiO_2/SiO_2) induced by ~120-nm photons associated with lasing at 640 nm.

The frontier for FELs, as well as for laser oscillators based on harmonic generation and four-wave mixing, is in the VUV and XUV. Attainment of sufficiently high reflectance below 100 nm to permit lasing is a present limitation. However, the recent attainment by Barbee, et al. [10] of over 50% reflectance at near-normal incidence at 17 nm by a Mo/Si multilayer reflector is very encouraging. Such a reflectance over a large enough surface could make an XUV FEL oscillator possible. Who knows? Perhaps one of the topics about which we will hear in future Laser Damage Symposia will be the damage resistance of 100-nm reflectors!

In concluding, I wish to extend our gratitude to the staff of the National Bureau of Standards at Boulder for making these fine facilities available, and for their great assistance in the planning, arrangements, and conduct of our meeting plus their part in preparing the proceedings for publication. These include Dr. Robert Kamper, Chief of NBS-Boulder, Aaron Sanders, Head of the Optical Electronic Metrology Group and the NBS Coordinator of these meetings, and Susie Rivera, Aaron's able administrative assistant who has dealt with almost all facets of these Symposia over the years. Other involved NBS staff are Ann Mannos, Kathy Sherlock, and Shirley Deeg. Pat Whited of the Air Force Weapons Laboratory has also participated in the meeting planning and arrangements.

References

[1]   D. A. G. Deacon, L. R. Elias, J. M. J. Madey, G. J. Ramian, H. A. Schwettman, and T. I. Smith, Phys. Rev. Lett. 38, 892 (1977).

[2]   M. Billardon, P. Elleaume, J. M. Ortega, C. Bazin, M. Bergher, Y. Petroff, M. Velghe, D. A. G. Deacon, K. E. Robinson, and J. M. J. Madey, Phys. Rev. Lett. 51, 1652 (1983).

[3]   J. A. Edighoffer, G. R. Neil, C. E. Hess, T. I. Smith, S. W. Fornaca, and H. A. Schwettman, Phys. Rev. Lett. 52, 344 (1984).

[4]   R. W. Warren, B. E. Newnam, W. E. Stein, J. G. Winston, R. L. Sheffield, M. T. Lynch, J. C. Goldstein, M. C. Whitehead, O. R. Norris, G. Luedemann, T. O. Gibson, and C. M. Humphry, in Proc. of the Int'l. Conf. on Lasers '83, R. C. Powell, Ed. (STS Press, McLean, VA), pp. 316-320, 1983.

[5]   A. Ts. Amatuni, M. L. Petrosian, B. V. Petrosian, N. T. Shahbazian, and K. B. Oganesian, Yerevan Phys. Inst. Rept. 727 (42)-84, Yerevan, USSR 1984.

[6]   B. E. Newnam, R. W. Warren, J. C. Goldstein, R. L. Sheffield, and C. A. Brau, Nucl. Inst. and Methods in Phys. Res. A237, 187 (1985).

[7]   L. R. Elias, J. Hu, and G. Ramian, Nucl. Inst. and Methods in Phys. Res. A237, 203 (1985).

[8]   B. E. Newnam, R. W. Warren, R. L. Sheffield, W. E. Stein, M. T. Lynch, J. S. Fraser, J. C. Goldstein, J. E. Sollid, T. A. Swann, J. M. Watson, and C. A. Brau, IEEE J. Quantum Electron. QE-21, 867 (1985).

[9]   C. A. Brau, IEEE J. Quantum Electron. QE-21, 824 (1985).

[10] T. W. Barbee, Jr., S. Mrowka, and M. C. Hettrick, Appl. Opt. 24, 883 (1985).

Table 1

Summary of Visible and Infrared Free-Electron Laser Oscillators

		Wavelength	Peak Power	Average Power*
1977	Stanford University [1]	3.4 μm	400 kW	5 W
1983 (June)	University of Paris and Stanford University [2]	640 to 655 nm	16 W	5×10^{-4} W
1983 (July)	TRW Inc. and Stanford University [3]	1.6 μm	1.2 MW	80 W
1983 (November)	Los Alamos [4]	9 to 11 μm	700 kW	1000 W
1984	Yerevan Phys. Inst. (Armenia) [5]	~40 μm	~6 kW	10 W
1984 (March)	Los Alamos [6]	9 to 11 μm	5 MW	3000 W
1984 (August)	University of California at Santa Barbara [7]	400 μm	~10 kW (est.)	3000 W
1984 (October)	Los Alamos [8]	9 to 35 μm	10 MW	6000 W

*Average over electron macropulse

Laser-Induced Damage in Optical Materials
Sixteenth ASTM Symposium
October 15-17, 1984

The Sixteenth Annual Symposium on Optical Materials for High Power Lasers (Boulder Damage Symposium) was held at the National Bureau of Standards in Boulder, Colorado, October 15-17, 1984. The Symposium was held under the auspices of ASTM Committee F-1, Subcommittee on Laser Standards, with the joint sponsorship of NBS, the Defense Advanced Research Project Agency, the Department of Energy, the Office of Naval Research, and the Air Force Office of Scientific Research. Approximately 180 scientists attended the Symposium, including representatives from England, France, The Netherlands, Scotland, and West Germany. The Symposium was divided into sessions concerning Materials and Measurements, Mirrors and Surfaces, Thin Films, and Fundamental Mechanisms. As in previous years, the emphasis of the papers presented at the Symposium was directed toward new frontiers and new developments. Particular emphasis was given to materials for high power apparatus. The wavelength range of the prime interest was from 10.6 μm to the uv region. Highlights included surface characterization, thin film-substrate boundaries, and advances in fundamental laser-matter threshold interactions and mechanisms. Harold E. Bennett of the Naval Weapons Center, Arthur H. Guenther of the Air Force Weapons Laboratory, David Milam of the Lawrence Livermore National Laboratory, and Brian E. Newnam of the Los Alamos National Laboratory were co-chairmen of the Symposium. The Seventeenth Annual Symposium is scheduled for October 28-30, 1985, at the National Bureau of Standards, Boulder, Colorado.

Key words: laser damage; laser interaction; optical components; optical fabrication; optical materials and properties; thin film coatings.

1. Introduction

The Sixteenth Annual Symposium on Optical Materials for High Power Lasers (Boulder Damage Symposium) was held, as in previous years, at the National Bureau of Standards in Boulder, Colorado, October 15-17, 1984. The Symposium was held under the auspices of the ASTM Committee F-1, Subcommittee on Laser Standards, with the joint sponsorship of NBS, the Defense Advanced Research Projects Agency, the Department of Energy, the Office of Naval Research, and the Air Force Office of Scientific Research. Approximately 180 scientists attended the Symposium, including representatives from England, France, The Netherlands, Scotland, and West Germany. The Symposium was divided into sessions concerning Materials and Measurements, Mirrors and Surfaces, Thin Films, and finally, Fundamental Mechanisms. In all, approximately 45 technical presentations were made. Harold E. Bennett of the Naval Weapons Center, Arthur H. Guenther of the Air Force Weapons Laboratory, David Milam of the Lawrence Livermore National Laboratory, and Brian E. Newnam of the Los Alamos National Laboratory were co-chairmen of the Symposium. Alexander J. Glass of KMS Fusion is Conference Treasurer and Aaron A. Sanders of the National Bureau of Standards acts as Conference Coordinator.

The purpose of these symposia is to exchange information about optical materials for high power lasers. The authors welcome comments and criticism from all interested readers relevant to this purpose and particularly relative to our plans for the Seventeenth Annual Symposium, scheduled for October 28-30, 1985, at the National Bureau of Standards, Boulder, Colorado.

2. Principal Conclusions

The cataloging of properties and damage thresholds of bulk materials continued to be of interest. Authors at this conference discussed studies of liquid crystals, plastics, cubic zirconia, and a laser host crystal, gallium scandium gadolinium garnet. Of particular interest was the successful fabrication of polarizers from liquid crystals.

Laboratories for studying laser-induced damage have continued to become more sophisticated. Four authors described automated experiments in which computers control the operating parameters of the source laser, the devices used to diagnose the laser pulses, the manipulation of the damage sample, and the determination as to whether damage occurred at a particular site. A multiple-bounce reflectometer usable with intense 248-nm laser pulses, and a variable attenuator for the 248-nm wavelength were also described.

Detection of the defects responsible for damage initiation has been an elusive goal. Low-energy electron diffraction (LEED) was used to study recrystallization of sites on metal surfaces that had been irradiated at fluences below those required to cause apparent damage. A closely

1

related paper described a study by transmission electron microscopy of metal samples that were thinned after having been damaged. Localized damage was found to have occurred at grain boundary sites that frequently contained impurities such as Fe.

It is clear that emphasis has shifted from single-pulse, one-on-one experiments to the much more difficult multipulse laser damage. The exploration of the mechanism of multipulse damage utilizing electron or ion emission from the damaged surface has continued. Apparently, simple probability as evidenced by the 1972 lucky-electron theory of Bass and Barrett will not explain multi-pulse damage, and the cumulative effect of excitations must be considered. Damage levels were related to pulse energy but not to pulse repetition rate and may be related to evaporation at localized hot spots, at least in silicon. A generalized theoretical framework for analyzing multi-pulse thermal events was provided, but the mechanism of initiation remains unknown. In addition, surface-potential measurements were explored as an alternative to charged particle emission. It was demonstrated that the influence of multipulse damage extends far beyond the diameter of the initiating laser beam, at least for small spot sizes. Further exploration of multipulse damage using these tools can be anticipated.

Other, more traditional questions in the field of laser damage were also clarified. Careful work on the theory of two-photon absorption resulted in theoretical values calculated from material parameters which are in good agreement in all cases with experimental values. Eleven semiconductor materials of various types were studied. Several other longstanding problems have been attacked in the same spirit.

Self-focusing was examined utilizing a theory reported at this meeting last year. In cases where sufficient data were available, the experimental results of various authors were recalculated, yielding improved values. It was shown that previous analyses gave results which may be in error by an order of magnitude. Ripples associated with single- and multiple-pulse damage were also investigated, and it was shown that, whereas single-pulse-derived ripples are correctly predicted by present theory, multipulse-generated ripples are not. Finally, multipulse damage measurements using 30-ps pulse lengths at 1.06 μm on ruled and holographic gratings were reported. This data is of immediate importance in optical system design. A theoretical analysis of these results has yet to be reported, but is anticipated shortly.

It is gratifying to note that, along with improved damage ratings, increased resistance to adverse environments is being addressed as well. This is particularly true for corrosive chemicals and electron beams as in excimer lasers as well as to abrasion and humidity as in outdoor applications. However, the true advances have come in improved understanding of the effect of deposition parameters (particularly in the novel techniques of molecular-beam epitaxy, laser evaporation, sputtering, and ion-beam-assisted processes) on film structure such as substrate temperature, photon or particle energy, background-gas composition, and pressure, as well as post-deposition techniques like annealing. This work is leading to denser, more damage-resistant, robust films with lower absorption.

We see as well a correlation of damage susceptibility with residual stress in films and can identify initiating defect types and location by the morphology of damage. Most importantly besides the new processes, materials, and correlations, we are realizing the benefit of diagnostic techniques well-suited to films, e.g., Raman scattering to map structure and time resolve thermal processes. This latter point is most important because we now have the approaches in hand to study the thermophysical properties of thin films, like thermal conductivity, and to determine if they are near bulk values.

An outstanding development in optical coatings has been the process for producing porous-silica antireflection coatings. When properly made, they have exhibited damage thresholds equal to that of bare fused silica surfaces, and their usefulness has been proven from the ultraviolet to the near ultraviolet (0.2 to 1.2 μm).

Not yet understood, however, is the physics behind the wavelength-dependent influence of over-coats. As reported at the last conference and again this year, use of either overcoats of MgF_2 or SiO_2 resulted in a moderate reduction (2 to 20%) in damage threshold at 355 nm. This contrasts with the 50% to 100% average improvements previously demonstrated at 248 and 1064 nm.

One controversial topic of discussion was the theoretical versus actual performance of intracavity, grazing-incidence reflectors, now considered essential for high-average power operation of free-electron lasers (FEL). The optimized designs for multilayer dielectric reflectors for use at grazing-incidence angles, advocated at this meeting, predict large (>100X) increases in damage thresold over that possible at normal incidence. However, careful damage tests at 351 nm, also reported at this conference, revealed a very modest (only 2.5X) increase in threshold at 85°

2

compared to normal incidence. (About double this enhancement was measured in other unpublished tests at 248 nm.) Possible explanations have been suggested, but these results are still not entirely understood. Until future tests with other dielectric mirrors show considerable improvement, metal mirrors must be considered the conservative choice for grazing-incidence applications, particularly in the presence of the other high-energy radiation environments of FEL resonators.

3. Summary of Papers

The subject matter of the Sixteenth Annual Symposium covered four broad areas of interest to the high-power laser community: (1) Materials and Measurements, (2) Mirrors and Surfaces, (3) Thin Films, and (4) Fundamental Mechanisms. These conference proceedings are organized accordingly. In this section, a concise summary of each paper is provided, and closely related papers are discussed together, whenever possible. The interested reader is referred to the complete manuscript of any paper for further details. Our intention here is to provide the reader with an overview of the Symposium and to identify the topics of current interest, the authors, and their organizations. To highlight the presented papers, each topical area is discussed with a brief statement of the under- lying problems and the status of understanding within the area of interest.

3.1 Materials and Measurements

In the category of optical materials and measurement techniques, four general topics received attention this year. These included: (1) liquid crystals whose properties are being exploited for use as polarizers, electro-optical shutters, and modulators, (2) bulk damage resistance of new laser crystals and windows, (3) application of two types of electron microscopy for analysis of metal surfaces to deduce the cause of laser damage, and (4) automation of laser damage facilities in- cluding development of advanced diagnostic measuring devices.

Development of novel materials for laser applications continues to be a major goal of those participating in these annual symposia. Installation of polarizers made from liquid crystals in the high-power glass development laser (GDL) at the University of Rochester was discussed by S. Jacobs, K. Cerqua, T. Kessler, W. Seka, and R. Bahr of the Laboratory for Laser Energetics. The polarizers consisted of an 11-μm-thick layer of a base nematic doped with either left-handed (LH) or right-handed (RH) chiral additive to produce a helical twist structure in the crystal. A cir- cularly polarized beam with wavelength $\lambda_0 = nP$, where n is the average refractive index and P is the pitch dimension of the helix, is diffusely scattered by the crystal if wave rotation is in the same sense as the helix, but is transmitted when the wave rotation and helix are opposed. This property of liquid-crystal polarizers allows them to be used in polarizer/analyzer roles with cir- cularly polarized light. Extinction of ~10^4 for the crossed polarization case was reported. They have been installed in GDL as the crossed polarizers associated with Pockels-cell shutters and as single elements to serve as isolators for waves propagating backward through the chain.

The reported advantages of liquid crystal polarizers over Brewster-angle thin-film polarizers were low cost and easy replacement due to in-house fabrication, insensitivity to tip angles as large as 20° off normal, insensitivity to temperature change (0.35 to 1.4 nm/°C in the position of the central maxima), high transmittance (~98%), and the capability to propagate circularly polarized light over most of the path length in a laser arm. Laser damage thresholds (1054-nm, 1-ns) were 3 J/cm² for the RH units, but <1 J/cm² for LH units, a problem that the authors circumvented by fabricating LH polarizers as RH polarizers on quartz halfwave plates.

Additional data on liquid crystals were presented by S. Wu and L. Hess of Hughes Research Laboratories. They described a study at 10.6 μm of the nonlinearity of the optical rotatory power of a 90° twisted nematic liquid crystal. The crystal (BDH-E7) exhibited the expected dependence of rotatory power on crystal thickness when subjected to low power (<0.3 kW/cm²) irradiation at 10.6 μm. When the intensity was increased, the rotatory power decreased due to alignment of the liquid crystal molecules with the polarization of the laser beam. The incident power required to obtain a given loss of rotatory power depended on the inverse square of the crystal length. The loss of rotatory power was reversible for intensities up to 7.5 kW/cm², at which level a crystal with 52-μm thickness underwent a phase change into an isotropic material. Recovery of the anisotropic state required about 2 min. At a higher intensity, ~8.5 kW/cm² for the 52-μm crystal, permanent damage occurred, but crystals with thicknesses of either 24 μm or 13.5 μm were not altered at that power level. The mechanism for the permanent damage was not known.

Other authors discussed their efforts to produce and characterize improved crystals for use as laser hosts or windows. N. Mansour, M. Soileau, and E. Van Stryland of North Texas State University reported measurements with 45-ps, 1064-nm pulses of the bulk damage thresholds for cubic zirconia crystals stabilized by the addition of 9.4 to 21% of Y_2O_3. The beam diameter at the waist formed by their focusing lens was 7.2 μm (half width at I_0/e). Breakdown thresholds were the same

3

for either linearly or circularly polarized beams, indicating that self-focusing was not a factor, and thresholds were also independent of the Y_2O_3 concentration. When the beam waist was increased in size to 10 μm, self-focusing dominated the experiment. Measurement of the critical power for self-focusing yielded an estimate of the value of n_2 in the stabilized zirconia of 8 x 10^{13} esu. This value is in reasonable agreement with a theoretical estimate made by the authors of 10 x 10^{13} esu, which value is the same as predicted using an empirical equation, derived previously, that relates n_2 to the Abbe number and linear refractive index.

M. Acharekar and D. McCarthy of Litton Systems, and R. Blachman of Material Progress Corporation described damage tests of crystals of gadolinium scandium gallium garnet doped with both chromium and neodymium (Nd:Cr:GSGG), and the performance of lasers using this crystal. Their Q-switched laser equipped with a 5 mm × 65 mm rod provided 135 mJ/pulse at 1061 nm with 2.2 milliradian divergence when pumped with 8-J pulses at 10 Hz. The typical pulsewidth (FWHM) was 17 ns. These 17-ns pulses were used to measure both the bulk and surface damage thresholds for crystals of Nd:Cr:GSGG that had been polished with 0.3-μm alumina powder. Beam sizes used in the test were not specified. The bulk damage threshold for this laser crystal was reported to be greater than that of BK-7 glass but less than that of fused silica. It was also reported that a 10% reduction in Nd concentration led to a 13% increase in bulk damage threshold. The surface damage threshold was 14 J/cm^2.

Methacrylate polymers were studied in a collaborative effort by R. O'Connell and R. Ellis of the University of Missouri at Columbia, A. Romberger of Pennsylvania State University (Berks Campus), T. Deaton, K. Siegenthaler, A. Shaffer and B. Mullins of the USAF Academy, and T. Saito of Lawrence Livermore National Laboratory. These authors prepared samples of polymethylmethacrylate (PMMA), polyethylmethacrylate (PEMA) and polycyclohexylmethacrylate (PCMA), some containing up to 10 wt% of a plasticizer, dibutylpthalate (DBP). The monomers were initially distilled and, in some cases, also passed through filters with pore sizes of 0.40 or 0.22 μm. Both heating (40°C) and ultraviolet light were used to obtain polymerization. The samples were tested with 1064-nm, 8-ns pulses focused to a beam size of 33 μm (radius at I_o/e^2), and tests were conducted to insure that the experiments were not influenced by self-focusing. Thresholds for either single-shot or multiple-shot tests were defined to be the fluence necessary to cause damage at 50% of the sites, a convention that leads to an overestimate of the large-area damage thresholds. Using this convention, the authors found single-shot thresholds of 29, 67, and 86 J/cm^2 for samples of PMMA made from distilled monomer and subjected to, respectively, 7.1, 0.5, and 0.1 particles/mm^3, which correlated well with the thresholds. However, the lowest fluences for which damage occurred in the samples, 12, 28, and 21 J/cm^2, respectively, only partially correlated with dust content, and these minimum fluences are the best indication of how the materials would perform in actual usage.

These authors also reported that single-shot thresholds of UV-polymerized samples were systematically greater than those of thermally polymerized samples, and that multiple-shot (250) thresholds were independent of the technique used for polymerization and much less than single-shot thresholds. Multiple-shot thresholds were also found to be independent of the amount of plasticizer used, although the authors felt this observation was possibly invalid due to unequal dust concentrations in the plasticized samples.

A portion of each preceding conference has been given to discussions of experimental techniques for characterizing materials and measuring damage thresholds. At this conference, A. Helms, C. Cho, and S. Bernasek of Frick Chemical Laboratory at Princeton University described analysis by low energy electron diffraction (LEED) of sites on molybdenum surfaces that had been laser irradiated. They studied two samples (A and B) that had carefully prepared 100-oriented surfaces and a third (C) with similar orientation whose surface had been disordered by Ar$^+$ ion bombardment. The surfaces were initially analyzed by both LEED and by Auger Electron Spectroscopy (AES), and then moved under vacuum into a sample chamber which was used to transport the sample under vacuum to a separate laboratory for laser irradiation. One half of each surface was irradiated by 140-ns, second-harmonic pulses from a Nd:YAG laser operating at 5 kHz. The laser spot size was approximately 25 μm. Area coverage was obtained by a raster motion of the samples. The two crystalline surfaces A and B were irradiated at, respectively, 15 MW/cm^2 and 60 MW/cm^2, intensities that are below and above that necessary to produce cratering. The ion-bombarded surface was irradiated at 75 MW/cm^2. Subsequent LEED evaluation of surfaces A and B indicated that both contained randomly distributed islands of raised 100-oriented material whose edges were oriented with crystalline planes, indicating both the occurrence of damage during irradiation at subthreshold intensities and the regrowth of 100-oriented material from melts produced at higher intensities. Laser annealing of the disoriented surface on Sample C produced a partial recovery of crystallinity.

H. Hurt of the Michelson Laboratory at the Naval Weapons Center described the use of transmission electron microscopy (TEM) to investigate the defects responsible for site-selective damage on copper mirrors. The surfaces studied were on small (3-mm diameter × 0.25-mm thick) samples of

4

either OFHC copper or OFHC copper plated with a UBAC (Ultra-Bright Acid Copper) copper film. These surfaces were diamond turned at NWC using tool rake angles of either -5° or -15°, and then damaged with 100-ns, 10.6-μm CO_2 laser pulses. The damaged areas were thinned from the back and examined by TEM. Sites on a UBAC surface which appeared by Nomarski microscopy to have wavy slip were found to have been melted. One pit at a selective damage site was centered on a grain boundary and contained small particles of iron. In tests of additional 1.5-inch diameter samples "apparent" slip was observed as the limiting damage mechanism and occurred at 8 and 10 J/cm^2 in OFHC copper turned with rake angles of, respectively, -5° and -15°, and at 19 J/cm^2 in UBAC copper.

Several papers discussed automated laser damage experiments or improved apparatus for use in damage studies. J. Franck, S. Seitel, V. Hodgkin, W. Faith, and J. Porteus of the Naval Weapons Center have automated an infrared damage facility equipped with CO_2, HF, and DF lasers. A computer system controls the fluence of the laser pulses and raster scanning of the sample to allow multiple-site irradiation. Their system automatically detects occurrence of damage by detecting a laser-induced alteration of the scattering of light from the beam of a HeNe laser that irradiates the test site. For samples in which damage consisted of micropits, this technique for detecting damage was found to give results equivalent to those obtained by post-irradiation inspection of test sites by Nomarski microscopy. Scattering was a less suitable detector of spatially uniform damage, but a cursory examination of the sample was able to detect whether failure by this mode had influenced the automated damage detection. The stated intent of the group was to speed testing so that 400-800 sites could be tested on each sample, thereby providing an accurate and statistically meaningful large-area threshold.

P. Filbert, J. Guttman, C. Navoda, and B. Watson of the Lockheed Palo Alto Research Center reported use of a computer-automated IR-sensitive camera to record fluence distributions in the beam of a large Nd-glass laser being used in damage tests. A fraction of the beam was directed to a diffusely reflecting screen, and a down-magnified image of this screen was recorded by 100 × 200 pixel silicon-photodiode array. The computer processed image of the beam profile, appropriately scaled in size, was superimposed on an enlarged photograph of the damage site, allowing the damage to be correlated with fluence contours in the beam. The authors indicated that the ability to measure thresholds with large beams of varied profile would allow determination of the importance of material stress gradients in damage.

A high-precision multiple-pass ultraviolet reflectometer was described by L. Jolin and S. Foltyn of Los Alamos National Laboratory. The instrument was based on the White cell and allowed computation of the net loss in a dielectric reflector through measurement of the intensity of a 351-nm laser beam as a function of the number of times (>100) it had interacted with the reflector. To obtain damage resistance, dielectric thin-film reflectors were used as the secondary mirrors needed in a White cell arrangement. Repeated measurements by several operators indicated that the precision in reflectance measurements was ±0.0007. The authors reported 351-nm reflectances ranging from 0.8498 to 0.9976 that were measured on 17 multiple-layer HR coatings.

In another instrument paper from Los Alamos National Laboratory, S. Foltyn, J. Griggs, L. Jolin, J. Roberts, and D. Keaton described a new attenuator for controlling the fluence in the divergent and usually unpolarized beams emitted by excimer lasers. Their device employs two reflectors operated at incidence angles near 40°. The incident beam is deflected by the first reflector onto the second reflector, which is oriented to restore the initial direction of propagation. Because the reflectance of a multilayer dielectric reflector varies with incidence angle, beam attenuation could be accomplished by tuning the incidence angles at the reflectors. The reflectors were mounted in an assembly that allowed angle tuning by stepper motor control. Transmittance at 248 nm was measured as a function of incidence angle for an attenuator equipped with 49-layer Al_2O_3/SiO_2 reflectors designed to be reflective at 248 nm for normally incident beams. Transmittance varied from 99% to 3% as incidence angle was tuned from 34° to 44°, and beam steering was less than 0.5 mr. A transmissive version of the device was also described.

Variable pulsewidth was an important feature of the recently completed CO_2 laser damage test facility at Barr and Stroud, Ltd., as described by D. Gibson and A. Wilson. Through variations in the gas fill, their laser can be made to provide pulses with durations of ~100-ns, either with or without a 2-μs tail. Introducing a locking signal from a small CO_2 laser into the principal CO_2 source laser provided 6-μs pulses. Pulses with tunable duration <90 ns were obtained with a plasma shutter in which the attenuating plasma was induced by irradiation of a dielectric. The laser provided output energies ranging from 10 J at 10 Hz to 15 J at 1 Hz, which allowed deposition of damaging fluences (1 - 100 J/cm^2) over areas about 1 mm in diameter. Their stated intent was to compile a data base suitable for use in laser design applications, and initial test results were reported for a wide range of window materials and optical films.

3.2 Mirrors and Surfaces

Three themes were evident in the contributions concerning the effects of intense laser irradiation of surfaces. The first was a continuation of the experiments to extend our understanding of the physical processes involved at high laser intensities. This included evaluation of surface-potential as a predamage indicator and multiple-pulse accumulation effects in silicon. Two papers treated the topic of laser-induced ripple structure, primarily for semiconductors. Adequate understanding of this phenomenon will undoubtedly lead to practical applications. The third and related topic was picosecond-pulse damage to manufactured diffraction gratings, both ruled and holographic.

Surface-potential modification as a precatastrophic damage indicator was studied by M. Becker of the University of Texas, J. Kardach, of the Air Force Institute of Technology, and A. Stewart and A. Guenther of the Air Force Weapons Laboratory. Two-dimensional surface-potential measurements were made using a vibrating Kelvin probe on OFHC diamond-turned copper mirrors, single-crystal silicon, and MgF_2, HfO_2, and ThF_4 half-wave films on fused SiO_2, oriented MgF_2, and crystalline and amorphous quartz substrates. In damaged areas a positive surface potential was observed for the diamond-turned Cu, while all others gave negative values. Except in the case of one copper sample, no predamage changes in surface potential on irradiated surfaces were detected, and not all damaged areas exhibited changes in surface potential. Although the laser beam had a diameter of only 0.39 mm FWHM, changes in surface potential extended over a 4-6 mm range and small changes could be observed several millimeters beyond that, suggesting care in site spacing for multiple-site damage tests, at least on dielectrics. Decay relaxation times for the modified surface potentials were over an hour for dielectrics and "permanent", i.e. long duration, changes at damage sites were observed.

Y. Jhee, M. Becker and R. Walser of the University of Texas continued to explore the mechanism of multiple-pulse laser damage of silicon using pulse trains of 60-ps, 1.06-μm pulses produced by a cw-modelocked Nd:YAG laser. Initial damage as seen using an SEM was correlated to the onset of electron and ion emission. This emission was subsequently monitored as a damage indicator. They encountered multiple-pulse damage thresholds below the one-on-one damage threshold for crystalline silicon. In addition, the probability of damage for single events at various sites was not the same as that for multiple-shot damage (i.e., temporal and spatial probabilities were unequal). Thus, the 1972 lucky-electron theory of Bass and Barrett could not explain these results. No evidence of slip accumulation as evidenced by an increase in surface roughness as a precursor of damage was found either. They conjectured that a cumulative effect of excitations, not simple probability, is required to explain the results, even though damage does depend on pulse energy but not on pulse repetition frequency. They concluded that a multiphonon process is unlikely and the damage mechanism may have been as simple as thermal evaporation at localized hot spots in Si. The charged particle emission followed an Arrhenius equation, supporting the concept of laser-induced defect sites that then become evaporation sites. The mechanism for formation of these sites and their character was not identified.

N. Mansour, G. Reali, P. Aiello, and M. Soileau all of North Texas State University, examined in detail the ripple structure formed near the onset of laser damage in wide gap dielectrics and the intermediate-gap semiconductors ZnS and ZnSe. For the dielectrics the ripple spacing is consistently (within 5%) equal to the wavelength of incident light in the medium. The ripple direction is normal to the direction of polarization of the incident light for smooth surfaces but can be perturbed by scratches or surface defects. The results can be explained by a simple electrostatic-dipole model but not by the competing surface excitation model. By contrast, results for the intermediate-gap semiconductors are not easily explained by any model. They differ at front and back surfaces, spacings vary by over a factor of 2 at the same surface for ZnSe and the back surface ripples are not oriented perpendicular to the polarization and may be parallel to it. No explanation is offered for these anomalies.

The analysis of laser-induced surface ripples for Si, Ge, GaAs, and Cu in terms of the interference between the incident light and surface waves in the sample was presented by P. Fauchet of Princeton University and A. Siegman of Stanford University. Unfortunately, the authors did not adequately reference previous and alternate explanations of the phenomena. Single-pulse ripples fit the presented theory quite well for materials studied. However, ripples formed by multipulse illumination were not explained by the simple theory. Irradiation levels below which ripples did not form under multipulse illumination were found to be one-third of the single-pulse threshold for crystalline materials and as low as one-tenth the single pulse threshold for amorphous materials. The authors pointed out that two possible hypotheses reported by others are not inconsistent with their data, but they offered no experimental data, such as an increase in surface roughness or small crystallite formation, which would support these hypotheses.

The results of extensive measurements of the laser damage resistance of diffraction gratings were presented for the first time at these symposia. At the Los Alamos National Laboratory, D. Gill and B. Newnam tested holographic and ruled gratings using 30-psec, 1.06-μm wavelength radiation. Holographic gratings had thresholds 1.5 to 5 times higher than ruled gratings and the replicas had higher damage thresholds still, sometimes by over a factor of 2, than did the master holographic grating. S-polarized light had a threshold from 1.5 to 6 times higher than P-polarized light, and first-order gratings had as much as 5 times the damage threshold of more finely ruled gratings used at the same angle in third order. At 1.06-μm gold-coated gratings had 1.4 to 9.7 times higher damage threshold than aluminum-coated gratings. No quantitative theoretical analysis of these results was given.

3.3 Thin Films

Thin films continued to lead the interest at these annual symposia with over 50% of the presented papers addressing various aspects of this complex topic. A full third of these dealt with evaluation of the properties of films produced by new processes and comparing them with those of standard deposition methods. Others examined the possible correlation of laser damage with coating absorption and variations of film stress over small areas. Multiple papers also addressed the requirements for intracavity reflectors for high-average power operation of free-electron lasers. Of special interest was a measurement study of the thermal properties of films, including thermal conductivity and specific heat, and the comparison with bulk properties.

We begin by considering the numerous papers involving development, demonstration, and evaluation of advanced coating deposition methods. K. Lewis, J. Savage, A. Cullis, N. Chew, L. Charlwood, and D. Craig of the Royal Signals and Radar Establishment in Malvern, England, have pioneered the growth of optical thin films by molecular-beam techniques. The films, primarily ZnSe, had negligible values of absorption at 10.6 μm and exhibited very high damage thresholds. The authors attributed the latter, in part, to the high-density character of the films of polycrystalline, columnar morphology whose crystallite size is dependent primarily on the deposition temperature. Also, the films showed no evidence of pinholes and had a very low impurity level.

As an indication of how good these films are, the laser-induced damage threshold of 1-μm-thick ZnSe films on polycrystalline ZnSe substrates was in the range of 60 - 73 J/cm^2 (1/e^2 diameter ∿102 μm) which compared well with 50 - 60 J/cm^2 for the uncoated region of the sample. This observed difference was real and repeatable. For these tests, the temporal pulse from the gain-switched CO_2 laser included an initial spike, 33-ns wide FWHM, followed by a long tail extending to 1.7 μs. For simple pulses of ∿340-ns duration, damage of the films occurred at ∿31-38 J/cm^2 (180 μm diameter). Finally, although no voids could be detected in the films, high densities of micro-twins and stacking faults were evident. Thus, further improvements in damage threshold may be feasible.

Variations of novel deposition techniques and well-regarded procedures continue to be investigated for potential improvements on present-day methods. T. Raj, L. Weaver, S. Tuenge, J. Price, and K. Jungling of the Martin-Marietta Aerospace Company reported on coatings of ZrO_2 produced in ultra-high vacuum (UHV) of 5 x 10^{10} torr using either electron-beam or laser evaporation by a 100-W cw CO_2 laser. Substrates were maintained at either 150°C or 250°C while background O_2 pressures were varied between 0 and 5 x 10^{-5} torr. Coatings were evaluated for stoichiometry and impurities by AES and for refractive index by ellipsometry. Some coatings were damage tested at 351 nm. Results obtained led to the conclusion that the stoichiometry of ZrO_2 films deposited by either technique is not affected by variations in O_2 backfill pressure to 5 x 10^{-5} torr. However, stoichiometry was superior at 150°C than for higher substrate temperatures, and the refractive index was closer to bulk values at this lower temperature. Another observation was that coatings produced under UHV conditions had at least an order-of-magnitude lower contamination level than coatings produced in normal HV chambers. In all cases, free metal and sub-oxides of ZrO_2 were evident. Unfortunately, damage trends were inconclusive. These investigations should be continued with a larger sized sample set.

As we continue progressing in our separation of the controlling variables in the coating process, we can focus on optimization of the variables if they are sufficiently independent. In ion-beam deposition of refractory oxides, one such well-established variable is beam composition. H. Demiryont and J. Sites of Colorado State University have identified a critical level of oxygen necessary in the beam to produce stoichiometric films of TiO_2, Ta_2O_5, and SiO_2 when using both elemental or oxide targets. The threshold was easily seen in the film composition, refractive index, and optical band-gap character. There was strong evidence that an oxide forms on elemental targets and this is subsequently sputtered onto the substrate.

The demand for higher quality thin films has stimulated experimentation with a number of novel coating deposition techniques that offer the possibility of fine control of the film properties. A. Stewart and A. Guenther of the Air Force Weapons Laboratory conducted a limited survey of characteristics of single-layer films of ZrO_2 and Al_2O_3 produced by a number of these processes. Besides the conventional electron beam technique, the other processes evaluated included electron beam in ultrahigh vacuum, electron beam with ion-beam assist, cw laser in ultrahigh vacuum, and an advanced epitaxial technique. Characterization of the film properties included total-integrated scatter, film transmittance near the uv absorption edge, x-ray diffractometry, and multiple-pulse laser damage thresholds varied by only a factor of two for each material. The results of this study will serve as a benchmark for future progress. As the parameters of the newer processes are optimized for maximum damage resistance over the next several years, any relative advantages should become manifest.

Substantial progress in the development of porous silica antireflection coatings for large-scale optics used in high-power laser systems was reported by I. Thomas, J. Wilder, W. Lowdermilk, and M. Staggs of Lawrence Livermore National Laboratory. To maximize laser damage resistance by minimizing the chances of any carbonaceous residue, a highly purified organic silicate, tetraethyl orthosilicate, $Si(OC_2H_5)_4$ was hydrolyzed by a basic catalyst to yield a colloidal suspension of silica particles in anhydrous ethanol. When applied in quarterwave thicknesses to optical components made of fused silica and KDP by a dip or spin process at room temperature, no further treatment was necessary. Damage thresholds measured at 248, 346, and 1064 nm were approximately the same as for the uncoated substrates.

In a second experimental study of porous-silica antireflection coatings, D. Milam, L. Thomas, C. Weinzapfel, and J. Wilder of Lawrence Livermore National Laboratory determined the pulse-duration scaling of laser damage for a series of coatings using pulse durations of 1, 5, and 9 ns. Ten porous-silica antireflection coatings were deposited from both methanol and ethanol solutions containing silica particles with diameters of 10 to 20 nm. The median thresholds measured at the three pulse durations were 11, 26.5, and 38 J/cm^2, respectively. The observed threshold scaling to the 0.56 power of the pulsewidth is, within experimental error, close to the 0.5 power previously measured for both bare, polished glass surfaces and those with graded-index made by etching.

Porous silica coatings can be deposited from alcoholic solutions containing either silica microspheres with diameters of 10-20 nm or smaller, polymer silica molecules. To further develop the versatility of these as antireflection coatings, D. Milam and G. Peterson of Lawrence Livermore National Laboratory studied how a mixture of these two forms could be optimized to maximize the spectral bandwidth of high transmission over the 0.2- to 1.2-μm range. Calculations were made for three single-layer density gradients: (1) homogeneous refractive index, (2) index profiles that increase monotonically with distance into the coating, and (3) index profiles that rise in discrete steps. They determined that the maximum bandwidth occurs for the linear-ramp coating whose index rises linearly from that of air to that of the substrate. In current practice, however, this design can not be realized because a sufficiently porous film at the air-film interface cannot be attained. For currently attainable fractional silica contents, estimated to range from 0.4 to 0.5, the optimum bandwidth results from a coating with a single discrete step in its index profile.

Besides the study of new coating procedures, new coating materials and combinations are being investigated for specific applications as more novel techniques become commonplace. To this end, multilayer AR coatings of AlN_3/Al_2O_3, prepared by reactive sputtering, were characterized for scratch-resistance by L. Koshigoe, L. Johnson, T. Donovan, and C. Marrs of the Michelson Laboratory of the Naval Weapons Center. These materials appeared to have adequate stability. A variety of sputtering techniques were employed from the use of dc magnetrons to ion-beam and rf diodes. An important aspect of this study was a determination of the resistances of these materials and coatings to laser radiation, fluorine, electron-beam irradiation, and humidity, while coating composition and stoichiometry were evaluated by SAM, SEM, EDX, XPS, and Nomarski microscopy. Substrates included fused silica, silicon, and calcium fluoride. The first tests on these films were encouraging. However, considerable work needs to be done to reduce the number of damage-initiating defect sites. It was pointed out that in most cases, the oxide layer should be the outer layer because it is more impervious to environmental degradation.

Raman scattering continues to gain in utility as a routine diagnostic technique for characterizing thin films. Its use to study annealing and phase transformation, such as crystallization, was reported by R. Rujkorakarn, L. Hsu, and C. She of Colorado State University. Two types of low-loss, low-scatter, amorphous sub-micron-thick titania films were thermally annealed in air. The transition to anatase/rutile crystalline phases coincided with a decrease in optical transmission, small changes in refractive indices and energy gap in the film, along with a 100× increase in inelastic scattering.

Raman scattering has also found considerable use as an analytical measurement technique to probe the structure, thickness, and homogeneity of optical thin films. G. Exarhos of Battelle Pacific Northwest Laboratory and P. Morse of the Air Force Weapons Laboratory added a new twist by employing time resolution to investigate laser-induced damage in TiO_2 coatings. The technique involved two lasers which allowed one to follow surface transformation/relaxation phenomena, etc. One laser was used as a Raman probe while another pulsed laser stimulated the disturbance. The authors observed that anatase-phase coatings have lower damage thresholds than those with the rutile phase, and the former failed via an irreversible phase transition to the rutile structure at temperatures below 910°C. On the other hand, rutile-phase coatings apparently accommodate energy in an excited electronic state resulting in "non-equilibrium" phase transformation to an "anatase-like" state.

In support of high power laser development for operation in the near ultraviolet, A. Stewart of the Air Force Weapons Laboratory and D. Gallant of Rocketdyne Division of Rockwell International have assembled a laboratory of instrumentation to characterize low-loss optical surfaces and thin film coatings. These were used to measure scatter, absorption and reflectance at 351 nm of maximum reflectors deposited by commercial vendors on super-polished silicon and fused silica substrates. Ion-beam sputter-deposited reflectors realized the lowest losses and exhibited the highest reflectance of 0.999 on the average. However, laser damage tests on these reflectors, conducted by S. Foltyn's group at Los Alamos National Laboratory, determined that electron-beam-produced coatings are presently more damage resistant by a factor of 2. Since the ion-beam deposition process is in the early phases of optimization for damage resistance, large improvements may well be attained by persistent effort.

As reported at several previous Boulder Damage Symposia, the damage resistance of multilayer-dielectric reflectors is substantially increased by addition of half-wave thick overcoats of low-index material. Experiments at 1064 nm and 248 nm have demonstrated that overcoats result in average improvements of approximately 50% and 100%, respectively. However, at the 1983 Symposium, C. Carniglia and T. Hart of the Optical Coating Laboratory, Inc., and M. Staggs of the Lawrence Livermore National Laboratory reported that halfwave overcoats of SiO_2 on high reflectors containing ZrO_2 amd Ta_2O_5 caused about a 20% reduction in damage thresholds at the intermediate wavelength of 355 nm. This very surprising result prompted these authors to conduct another and even more careful series of coating and damage experiments using a scandia/silica/magnesium fluoride reflector design which had experienced the 100% threshold enhancement with overcoats of both MgF_2 and SiO_2. Again, on the average the overcoated reflectors had slightly lower (2 to 7%) thresholds. The physics behind the wavelength-dependent influence of overcoats is still not understood and offers the coating researcher a challenge.

In a paper of considerable interest to the thin-film damage community, D. Decker, L. Koshigoe, and E. Ashley of the Michelson Laboratory, Naval Weapons Center, reported on measurements of the thermal properties of optical material in thin film form and compared them to tabulated bulk material properties. Materials initially analyzed were the important refractory oxides Al_2O_3 and SiO_2. Measured values of SiO_2 thin-film thermal conductivity were found to be lower by a factor of 5 to 8 when compared to bulk fused silica while the observed decrease for Al_2O_3 was on the order of 80. The large variations were ascribed to the greater disorder present in thin films than in bulk materials. In point of fact, the Al_2O_3 films were quite amorphous suggesting support for the workers' contention. Specific-heat values for the films were quite comparable with bulk values since this property should be largely independent of structural characteristics and density. The conclusions drawn in this work have far-reaching implications when modeling the laser interaction and thermal response in thin film damage experiments. Clearly, more work is needed to corroborate the present results, determine the extent of variation in other materials, such as fluorides, and to address discontinuities between layers and the substrate/film system boundary. We were most pleased to see this work under way and reported.

For many years, scientists have been trying to relate absorption to damage sensitivity. While this has been relatively easy in windows and for some surfaces, no strong correlation has been found for thin films perhaps because all films have been of uniformly poor quality. However, a new attack on this problem was reported this year by D. Ristau, X. Dang, and J. Ebert of the University of Hannover, Federal Republic of Germany. Employing an infrared, scanning-line technique, they measured the temporal and spatial development of surface-temperature increases of coated material irradiated with a cw Nd:YAG laser. In this way, they were able to separate the interface and bulk absorption of single and multiple layers and relate them to laser damage thresholds for 15-ns, 1.064-μm pulses. All oxide samples of Ti, Ta, Hf, Al, and Si were prepared by electron-beam and ion-beam assisted deposition. Thermal conductivities much lower than bulk values were recorded for the oxides of Si and Al, with the e-beam-deposited films exhibiting higher absorption and lower thermal conductivity. Interestingly, absorption was much higher in the bulk of the films than at interfaces between layers.

With the exception of HfO_2 and the co-evaporated TiO_2 layers, there was a "strong correlation" between absorption and damage threshold. Damage morphology affords evidence of inclusions in the bulk while for stacks, interface damage is frequently manifest, probably due to it being a region of high stress. Co-evaporation may help alleviate this problem.

A. Heiney, J. Eastman, and C. Gabel of the Laboratory for Laser Energetics at the University of Rochester attempted a study of the effect of anisotropic stress in thin films on laser-induced damage sensitivity. Use was made of a microscope-based, modulated ellipsometer to determine the directional dependence of the stress in the plane of the film via induced birefringence. Interestingly, areas with negative anisotropic stress were found to have higher damage sensitivities more frequently than regions of positive anisotropic stress. The authors reported that damage thresholds changed from 1.3 to 6.9 J/cm^2 within 100 µm. The width of measured bands in this work ranged form 0.5 to 2.5 J/cm^2. Pulse lengths were 30 ps at 1.06 µm, and the test samples were generally TiO_2/SiO_2 reflectors.

Intracavity grazing-incidence mirrors appear necessary to handle the high-average powers expected in future free-electron laser (FEL) oscillators. With slight curvature of the figure, these mirrors diverge the reflected beam to tolerable intensity levels at the cavity end mirrors. However, these intracavity reflectors now become potentially very susceptible to laser-induced damage and/or thermal distortion. W. Southwell of Rockwell International Science Center evaluated the advantages of multilayer-dielectric reflectors for this purpose and presented an optimized design for the layer thicknesses. With the standard design using quarter-wave layer thicknesses, very high reflectance was predicted for s-polarized radiation with drastically reduced internal standing-wave (SW) electric fields. For a reflector designed for 86° incidence and film-material pairs with refractive indices of 2.0 and 1.38, the calculated peak SW fields-squared were reduced by a factor of 160 relative to normal-incidence reflectors, but only for s-polarization. A design with improved performance for both s- and p-polarizations was also devised, but a smaller field-squared reduction factor of 40 was predicted. Based upon previous correlations of laser damage and the internal SW electric fields, the author predicted that these designs should be much less susceptible to laser damage and thermal distortion.

With FELs still in mind, the theoretical design of intracavity grazing-incidence reflectors using multilayer dielectric coatings was also treated by J. Shellan of W. J. Schafer Associates. His criterion was to maximize the reflectance of the multilayer stack to minimize the power transmitted to an absorbing substrate. With coating absorption assumed negligible compared to that of the substrate, he derived analytical expressions for the thickness of the outermost layer of otherwise all quarter-wave-layer reflectors and benchmarked the predicted reflectance against that generated using numerical methods of nonlinear optimization. For 100% s-polarized light, maximum reflectance requires the outer layer to have quarter-wave optical thickness, whereas it should have half-wave thickness for 100% p-polarization. Shellan's expressions are most helpful for analyzing the most likely configuration where the fraction of p-polarized light is small, but nonzero. Even if only 0.1% of the incident flux is p-polarized, optimization of the top layer thickness will reduce the reflector transmittance, and thereby the substrate absorption, by at least an order of magnitude.

One would expect that the angular dependence of damage to thin film coatings would be something one could calculate in a straight forward, if somewhat involved manner. But as B. Newnam, S. Foltyn, D. Gill, and L. Jolin of Los Alamos National Laboratory showed, first principle calculations and experimental verifications don't always agree! The results of their study was not only surprising but has wide-reaching implications since it was expected that near-grazing angles of incidence could be employed to diverge the tightly focused beams such as are present in free electron lasers and thereby realize a higher intensity throughput. Their work centered on measuring the damage resistance of HfO_2/SiO_2 multilayer reflectors subjected to a 10-ns pulsed 351-nm XeF laser operating at 35 pps. Several angles of incidence between 0° and 85° were employed using an S-polarized beam. Calculations of the expected damage threshold increase with angle of incidence included both areal intensity decrease ($1/cos\theta$) and appropriate electric field variations in the thin film/substrate system. In one case, a multilayer designed and tested at 85° afforded only a 2.5× increase in damage threshold compared to normal-incidence reflectors while one could conceivably expect a factor of 100×. Potential explanations for this discrepancy included: effects due to increased irradiation area at large angles and physically thicker layers, both resulting in the interception of more defects, plus scattered- and trapped-light effects. Obviously, more work needs to be accomplished to shed light on this problem.

It is readily accepted that defects are bad in optical elements used in high-power/high-energy laser systems, so that anything we can learn about them is useful whether it enables us to determine their origin or to model their influence. The powerful use of scanning-electron microscopy was employed by L. Johnson, E. Ashley, T. Donovan, J. Franck, R. Woolever, and R. Dalbey of the

Michelson Laboratory of the Naval Weapons Laboratory to study damage-initiating defects in ZnSe/ThF$_4$ and SiH/SiO$_2$ multilayers.

For ZnSe/ThF$_4$ multilayer mirrors, oblong-shaped damage sites, oriented perpendicular to the laser electric field, were associated with particulates at or near the surface while circular-shaped damage sites were related to those defects below the top layer. A third type of damage was identified as pinholes. Stress-related cracking was frequently observed as well. Frequently, damage related to nodule defects was seen in SiH/SiO$_2$ multilayers. Good correlation was seen between nodule density and damage sensitivity. Excellent micrographs of the different types of damage morphology related to different types of defects were presented.

Laser damage data for pulsewidths longer than a few-hundred nanoseconds are scarce, especially for visible-wavelength or near-infrared lasers. Thus, the results of a multilayer reflector damage survey using 8-µs (FWHM) pulses from an atomic iodine laser at 1.315 µm, presented by T. Deaton of the U.S. Air Force Academy, were especially interesting. Large 2.8-mm spot diameters were used in the single-shot-per-site mode. A number of coating materials combinations and designs from several vendors, each deposited on silicon and molybdenum substrates, were tested. Using the onset of pitting visible by Nomarski microscopy as the damage criterion, threshold fluences ranged widely from 5 J/cm^2 to over 140 J/cm^2, with uncertainties typically about 15%. Titania/silica coatings had some of the highest thresholds, and reflectors incorporating lead fluoride layers had the lowest damage resistance. As might be expected, very little dependence on the substrate material was evident. Hopefully, this survey will be followed by optimization of the best reflector designs.

A contribution from H. Deng, M. Bass, and N. Koumvakalis of the Center for Laser Studies at the University of Southern California concerned the measurement of the 10.6-µm damage resistance of multilayer-dielectric reflectors comprised of ZnSe and ThF$_4$ as a function of substrate material, reflectance, and defect density. Testing was conducted with a CO$_2$ laser restricted to operate in the TEM$_{00}$ mode with a pulse duration of 230 ns. The single-shot-per-site mode of testing with a small-diameter beam (120 µm at 1_0/e level) was used. For these conditions, the average threshold was 90 J/cm^2 with no apparent dependence on substrate material (Si, Ge, and ZnSe), reflectance (ranging from 65% to 100%), or defect density. Antireflection coatings of these two materials on ZnSe had a much lower threshold (40 J/cm^2), which was probably due to laser absorption by embedded impurities at the substrate/coating interface. Additional tests to relate visible-light scatter to damage susceptibility revealed no correlation.

The problem of economical recovery of damaged coated optics for recoating has been awaiting a satisfactory solution. This is especially important when large-diameter substrates, figured to the tolerances necessary to ultraviolet coatings, are involved. J. Asmus and J. Oldenettel of Maxwell Laboratories evaluated the effectiveness of a pulsed xenon flashlamp for removal of a number of dielectric coatings including SiO$_2$, LaF$_3$, MgF$_2$, and HfO$_2$. They found that a train of exposures with 30 J/cm^2 fluence and 600-µs pulsewidth is sufficient to dislodge these coatings without damaging fused silica or Zerodur substrates. The authors suggested that coating removal results from absorption near the ultraviolet bandedge with consequent differential heating and expansion. In some instances, a thin coating residue remained after irradiation indicating the need for further refinement of this technique.

3.4 Fundamental Mechanisms

With the practical problems of thin film coatings drawing so much attention this year, only three papers addressed the fundamental physics questions of importance. These included calculations of the thermal response of thin films under repetitive-pulse irradiation, theoretical analysis and critical review of past work concerning self-focusing in transparent solids, and calculation of two-photon absorption coefficients for semiconductors.

Extending their thermal modeling work for dielectric thin films M. Lange, and J. McIver of the University of New Mexico and A. Guenther of the Air Force Weapons Laboratory solved the thermal diffusion equation for repetitive pulses. The possibility of irreversible changes occurring with each pulse was included in the theory. In this case, the spatial dependence of the absorption from pulse to pulse is a key parameter. The special case of spherical or cylindrical absorption centers was shown to lead to an elegant closed-form solution. Various models of absorption proportional to number of pulses were explored and the basis was laid for further work on multipulse damage analysis.

M. Soileau, W. Williams and E. Van Stryland of North Texas State University continued to address nonlinear electro-optical processes. Theoretical analysis, indicating that the critical parameter of self-focusing is the second critical power P$_2$ (presented in 1983), was applied to

various experimental studies reported in the literature and to measurements made on SiO_2, NaCl, BK-7 glass and CS_2. In cases where sufficient data were available the recalculations were made, yielding improved values. It was shown that some previous analyses yield results which are both logically inconsistent and in error by as much as an order of magnitude.

An analytical relationship for the two-photon absorption coefficient based upon material parameters such as energy gap, linear index of refraction, wavelength, and a parameter f was derived by E. Van Stryland, H. Vanherzeele, M. Woodall, M. Soileau, A. Smirl, S. Guha and T. Boggess of North Texas State University. (The parameter f is a function of the assumed band structure and hence those optical states which are coupled.) Using this relation, the two-photon absorption coefficients of ZnTe, CdTe, CdS/Se mixtures, GaAs, ZnS, ZnSe, CdS, and ZnO were calculated using published parameters and compared against measured pulses. Good agreement was found in all cases, although a dependence on crystal type and single or polycrystalline structure was observed. Calculated values for ZnS, ZnSe, CdS and ZnO were reported for a wavelength of 0.53 μm, and values for the others for a wavelength of 1.06 μm. Data on InSb, reported previously, was shown to fit the theory, also. The nonlinear real part of the index was calculated assuming that it arises from two-photon generated free carriers. An optical limiter made of GaAs, which employs both two-photon absorption and self-defocusing transmitting 33% of the incident light at low intensities, was demonstrated. For energies above 10 μJ the transmitted energy was constant at 10 μJ over an incident energy range of at least 20. In comparison, GaAs melted above an energy of 100 μJ (0.9 J/cm^2), but the device continued to function. Response time was shown to be in the picosecond range.

4. Recommendations

We should retain a commitment to the extensive and lengthy development required to adapt promising new materials to practical applications. The successful and novel use of liquid crystals as polarizers is a significant example of the advantage obtained through concentrated study of a new material. In addition, increased use of surface diagnostic devices, particularly those capable of studying damage precursors, is needed to find the causes of damage. We hasten to add that automation of damage test laboratories will provide a needed increase in the national capability for significant damage testing. However, such labs should use procedures that contain adequate redundancy to insure detection of error due to malfunctions of the apparatus.

The increasing use of diffraction gratings in high-power laser resonators motivates more laser damage testing for a wide range of laser pulsewidths. Based on the results reported at this conference, an especially valuable achievement would be development of a process for fabricating large-size, blazed holographic gratings directly on high-conductance substrates such as silicon, silicon carbide, or molybdenum. Elimination of the photoresist or epoxy layer used in current fabrication would greatly increase the damage threshold for long-pulse and cw laser applications.

While it was gratifying to note the many correlations between deposition process variables and film structure on one hand and optical properties on the other, insufficient attention was paid to correlating damage resistance with these process-dependent characteristics. We all agree that lower absorption, denser, less-stressed films are good goals. However, there are some conflicting, or at least not readily consistent, results regarding the magnitude of the stress dependence of damage. This should be pursued with attention given to stress compensation in multilayers. Continued development of new processes, materials, and new diagnostics is warranted. UHV and multiple-beam epitaxy look promising as does ion-beam-assisted deposition; too little is known about laser evaporation as yet, but laser-induced desorption or substrate modification appear promising. The most advantageous of the diagnostics is Raman scattering, particularly when time-resolved, and surface emission as an indicator of surface cleanliness or pre-catastrophic damage. But most importantly, we must resolve the issue of thin-film thermophysical properties. The early results seem to say that thermal conductivities are on one hand of similar magnitude as those of bulk materials while on the other hand they are orders-of-magnitude lower. These statements have not been applied to the same materials. Quality measurements, those in which the community can have confidence, are most important in modeling thermal failure, material selection, and film design. They must certainly be structure dependent.

Finally, two unexplained results concerning the damage resistance of multilayer dielectric reflectors, described at the beginning of this review, should be pursued vigorously with careful experimentation and analysis. These are the wavelength-dependent influence of overcoat layers and the angular dependence, especially at angles beyond 60°.

5. Acknowledgments

their interest, support, and untiring efforts in the professional operation of the symposium. Particular thanks to to Ms. Susie Rivera for her part in the preparation and publication of the proceedings and to Ms. Pat Whited of the Air Force Weapons Laboratory for conference coordination.

6. References

[1]   Glass, A. J.; Guenther, A. H., eds. Damage in Laser Glass, ASTM Spec. Tech. Publ. 469, ASTM, Philadelphia. PA; 1969.

[2]   Glass, A. J.; Guenther, A. H., eds. Damage in Laser Materials, Nat. Bur. Stand. (U.S.) Spec. Publ. 341; 1970.

[3]   Bloembergen, N. Fundamentals of Damage in Laser Glass, National Materials Advisory Board Publ. NMAB-271, National Academy of Sciences; 1970.

[4]   Glass, A. J.; Guenther, A. H., eds. Damage in Laser Materials: 1971, Nat. Bur. Stand. (U.S.) Spec. Publ. 356; 1971.

[5]   Bloembergen, N. High Power Infrared Laser Windows. National Materials Advisory Board Publ. NMAB-356; 1971.

[6]   Glass, A. J.; Guenther, A. H., eds. Laser Induced Damage in Optical Materials: 1972, Nat. Bur. Stand. (U.S.) Spec. Publ. 372; 1972.

[7]   Glass, A. J.; Guenther, A. H., eds. Laser Induced Damage in Optical Materials: 1973, Nat. Bur. Stand. (U.S.) Spec. Publ. 387; 1973.

[8]   Glass, A. J.; Guenther, A. H. Laser Induced Damage in Optical Materials, 1973: A Conference Report. Appl. Opt. 13 (1): 74-88; 1974.

[9]   Glass, A. J.; Guenther, A. H., eds. Laser Induced Damage in Optical Materials; 1974, Nat. Bur. Stand. (U.S.) Spec. Publ. 414; 1974.

[10]   Glass, A. J.; Guenther, A. H. Laser Induced Damage in Optical Materials: 6th ASTM Symposium. Appl. Opt. 14 (3): 698-715; 1975.

[11]   Glass, A. J.; Guenther, A. H., eds. Laser Induced Damage in Optical Materials: 1975, Nat. Bur. Stand. (U.S.) Spec. Publ. 435; 1975.

[12]   Glass, A. J.; Guenther, A. H. Laser Induced Damage in Optical Materials: 7th ASTM Symposium.   Appl. Opt. 15(6): 1510-1529; 1976.

[13]   Glass, A. J.; Guenther, A. H., eds. Laser Induced Damage in Optical Materials: 1976. Nat. Bur. Stand. (U.S.) Spec. Publ. 462; 1976.

[14]   Glass, A. J.; Guenther, A. H. Laser Induced Damage in Optical Materials: 8th ASTM Symposium, Appl. Opt. 16(5): 1214-1231; 1977.

[15]   Glass, A. J.; Guenther, A. H., eds. Laser Induced Damage in Optical Materials: 1977, Nat. Bur. Stand. (U.S.) Spec. Publ. 509; 1977.

[16]   Glass, A. J.; Guenther, A. H. Laser Induced Damage in Optical Materials: 9th ASTM Symposium, Appl. Opt. 17(15): 2386-2411; 1978.

[17]   Glass, A. J.; Guenther, A. H. Laser Induced Damage in Optical Materials: 1978, Nat. Bur. Stand. (U.S.) Spec. Publ. 541; 1978.

[18]   Glass, A. J.; Guenther, A. H., eds. Laser Induced Damage in Optical Materials; 10th ASTM Symposium, Appl. Opt. 18(13): 2212-2229; 1979.

[19]   Bennett, H. E.; Glass, A. J.; Guenther, A. H.; Newnam, B. E. Laser Induced Damage in Optical Materials: 1979, Nat. Bur. Stand. (U.S.) Spec. Publ. 568; 1979.

[20]   Bennett, H. E.; Glass, A. J.; Guenther, A. H.; Newnam, B. E. Laser Induced Damage in Optical Materials: 11th ASTM Symposium, Appl. Opt. 19(14): 2375-2397; 1980.

[21]   Bennett, H. E.; Glass, A. J.; Guenther, A. H.; Newnam, B. E. Laser Induced Damage in Optical
       Materials: 1980, Nat. Bur. Stand. (U.S.) Spec. Publ. 620; 1981.

[22]   Bennett, H. E.; Glass, A. J.; Guenther, A. H.; Newnam, B. E. Laser Induced Damage in Optical
       Materials: 12th ATSM Symposium, Appl. Opt. 20(17): 3003-3019; 1981.

[23]   Bennett, H. E.; Guenther, A. H.; Milam, D.; Newnam, B. E. Laser Induced Damage in Optical
       Materials: 1981, Nat. Bur. Stand (U.S.) Spec. Publ. 638; 1983.

[24]   Bennett, H. E.; Guenther, A. H.; Milam, D.; Newnam, B. E. Laser Induced Damage in Optical
       Materials: 13th ASTM Symposium, Appl. Opt. 22(20): 3276-3296; 1983.

[25]   Bennett, H. E.; Guenther, A. H.; Milam, D.; Newnam, B. E. Laser Induced Damage in Optical
       Materials: 1982, Nat. Bur. Stand. (U.S.) Spec. Publ. 669; 1984.

[26]   Bennett, H. E.; Guenther, A. H.; Milam, D.; Newnam, B. E. Laser Induced Damage in Optical
       Materials: 14th ASTM Symposium, Appl. Opt. 23(21): 3782-3795; 1984.

[27]   Bennett, H. E.; Guenther, A. H.; Milam, D.; Newnam, B. E. Laser Induced Damage in Optical
       Materials: 1983, Nat. Bur. STand. (U.S.) Spec. Publ. 688; 1985.

[28]   Bennett, H. E.; Guenther, A. H.; Milam, D.; Newnam, B. E. Laser Induced Damage in Optical
       Materials: 15th ASTM Symposium, Appl. Opt. 25(2): 258-275; 1986.

Retrofit of a High Power Nd:Glass Laser System with Liquid Crystal Polarizers

S. D. Jacobs, K. A. Cerqua, T. J. Kessler, W. Seka, R. Bahr

Laboratory for Laser Energetics
University of Rochester
250 East River Road
Rochester, New York 14623

The glass development laser (GDL), has been operating at the Laboratory for Laser Energetics since 1978. This Nd:phosphate glass system produces high peak power optical radiation at $\lambda = 1054$ nm or $\lambda = 351$ nm for use in studying the interaction physics of intense laser beams with matter. The amplifier staging incorporates the propagation of linearly and circularly polarized light in rod amplifiers which vary in diameter from 16 mm to 90 mm. Numerous quartz or mica quarter waveplates and Brewster angle dielectric thin film polarizers are required to limit accumulated phase retardation between amplification stages, and to accommodate interstage Pockels' cell isolation switches.

We have recently replaced most of the waveplate-dielectric polarizer combinations in GDL with liquid crystal polarizers. Comprised of 11 μm thick cholesteric fluids sandwiched between optical quality glass plates, liquid crystal polarizers provide excellent polarization properties, low insertion loss, angular insensitivity, and laser damage resistance at $\lambda = 1054$ nm.

The design, fabrication and performance of left-handed and right-handed circular polarizers will be discussed.

Key words: cholesterics; circular polarizers; liquid crystals; Nd:glass laser; optical isolators; polarizers; selective reflection.

1. Introduction

Brewster angle linear polarizers composed of alternating high and low index, thin film layers which have been deposited on glass substrates have been utilized in the glass development laser (GDL) system at LLE since it was first constructed [1]. Produced by standard e-gun deposition technology in apertures ranging from 2 cm to 20 cm, these optical elements routinely achieve polarization levels of 200 to 500:1 at 1054 nm with good laser damage resistance. They are essential to the operation of electro-optic switching devices such as Pockels' cells. Three disadvantages to Brewster angle polarizers include environmental instability, tendency to displace the laser system beamline, and physical space requirements.

We have recently replaced six Brewster angle linear polarizers in GDL with liquid crystal (LC) polarizers, varying in clear aperture from 38 mm to 100 mm. Figure 1 shows the locations of the liquid crystal cells in the system, which has been reconfigured to drive active mirror amplifiers [2].
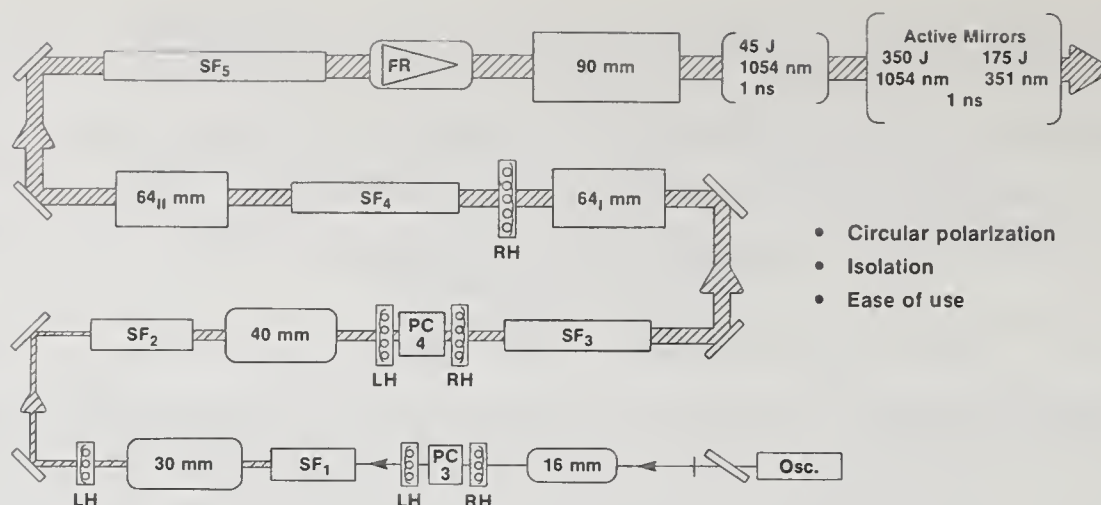
G1465

Figure 1. GDL Nd:glass laser system with liquid crystal polarizers.
The 3 left-handed (LH) and 3 right-handed (RH) circular
polarizers vary in clear aperture from 38 mm to 100 mm and
permit the propagation of circularly polarized laser
radiation through most of the beamline.

Liquid crystal polarizers have none of the disadvantages associated with Brewster angle polar-
izers, and offer additional features not available with any other polarizer technology. Figure 2
shows how, in addition to serving as polarization elements for electro-optic switches, liquid crys-
tal cells can provide optical isolation or back reflection protection.
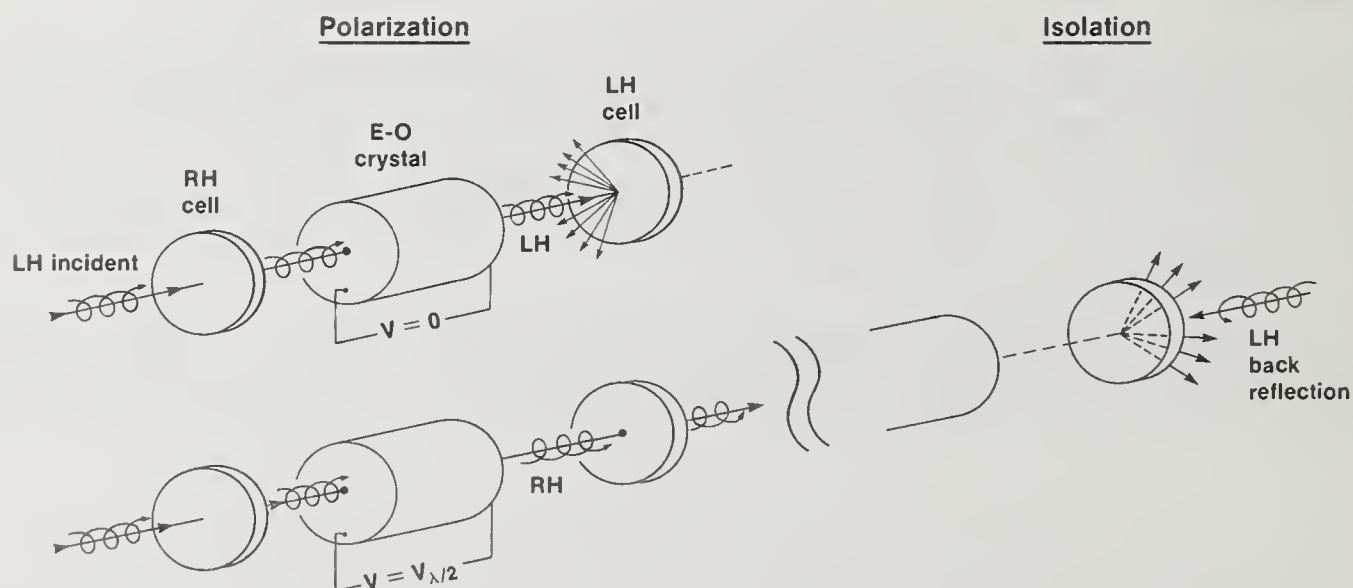
G1466

Figure 2. Dual function of liquid crystal polarizers. Left-handed (LH) and right-handed
(RH) circular polarizer elements may be fabricated and installed to perform
traditional polarizer/analyzer functions in electro-optic switch-out devices.
In addition, they act as optical isolators to prevent beamline component damage
due to specular back-reflections from fusion targets or ghosts.

16

This versatility has permitted us to incorporate the following changes in reconfiguring the GDL system:

1. propagation of circularly polarized laser radiation through the entire front end, minimizing stress-birefringence induced by the laser rods,

2. relocation of the Faraday rotator toward the output end of the system, providing for better protection against system back reflection,

3. reduced concern with back reflected ghosts, due to the isolation properties of the LC polarizers,

4. improved throttle adjustment at the oscillator input to the beamline with the use of circular polarization, and

5. ease of installation and alignment.

In this article we describe the in-house design, fabrication, installation, and testing of liquid crystal polarizers on GDL.

2. Selective Reflection in Cholesterics

The use of selective reflection in liquid crystals for high power laser applications has been discussed in the literature [3,4,5]. Briefly reviewed, selective reflection occurs in organic liquid crystal compounds when LH or RH chiral additives are mixed into base nematics so that a helical twist structure results.

Figure 3 shows how, if the pitch, P, characteristic of this twisted structure, satisfies the equation

$$\lambda_0 = \bar{n}P \tag{1}$$

where $\bar{n}$ is the average refractive index of the liquid, then incident laser radiation at wavelength, λ_0, experiences Bragg-like interference and diffuse reflection for that circularly polarized component which rotates in the same sense as the helical structure.

Molecular planes order in RH helix

3 Å

Unpolarized incident

P

Case A: $\lambda \neq \lambda_0$
- No interaction
- Complete transmission

RH helix

LH

RH

Case B: $\lambda = \boxed{\lambda_0 = \bar{n}P}$
- Strong interaction for one chirality
  - selective (diffuse) reflection
- No interaction for opposite chirality
  - complete transmission

λ, laser wavelength
λ_0, wavelength of selective reflection
$\bar{n}$, average refractive index for liquid crystal
P, pitch of structure

G1469

Figure 3. Selective reflection and Bragg-like interference. The chiral structure of liquid crystals will selectively reflect incident laser radiation if the laser's sense of circular polarization and wavelength equal the product of helical pitch times average liquid refractive index. Otherwise, no interaction occurs.

17

By using two cells in tandem, each filled with a fluid layer whose pitch and refractive index are tuned by compound blending to satisfy eq (1) but with _opposite_ chirality, laser radiation of any arbitrary polarization state can be polarized and rejected by the cells. They act as a pair of crossed, circular polarizers at λ_0. Figure 4 shows spectral absorptance in unpolarized light for LH and RH cells tuned to 1064 nm. Scanned separately, each fluid exhibits a selective reflection peak with few other features between 300 nm and 2000 nm. When scanned together the composite exhibits strong extinction near 1064 nm.
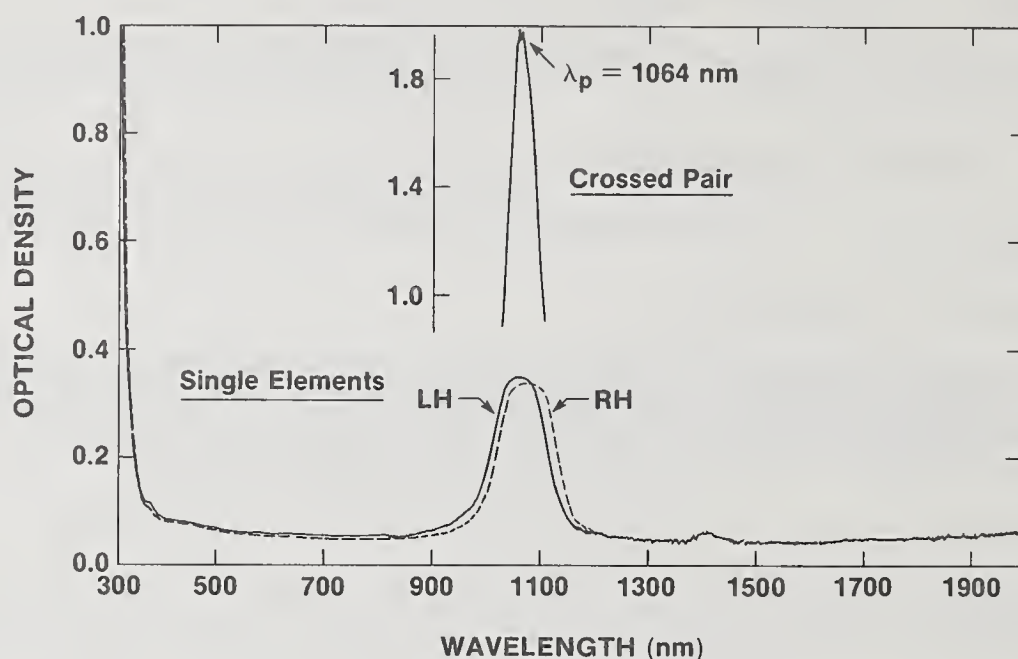
Figure 4. Spectral transmission through liquid crystal polarizers. Single LH and RH element scans indicate that, apart from regions of increased optical density due to selective reflection, the spectral transmission of liquid crystal polarizers is featureless. Crossed polarizers exhibit blocking extinction at any desired wavelength, which is determined by tuning liquid crystal pitch with composition mixing.

3. Cell Fabrication

Cell fabrication begins with selection of the compound. Table 1 lists the pure, base nematics which we have selected from commercial sources. They represent eutectic mixtures of long, rod-like molecules whose terminal and bridging groups are chosen to optimize properties such as melting and clearing points, viscosity, birefringence, optical transmittance, and environmental stability. The base nematics are all liquids at room temperature. The LH and RH chiral additives listed in table 1 may be solids (wax or powder) or liquids. The quantity of additive required for pitch tuning depends upon the intrinsic pitch of the substance (150 nm for CB15, 800 nm for C15), but it is usually on the order of 10-20 wt.%. Compound mixing is performed at elevated temperatures near 70°C to promote dissolution of the chiral additive.

Table 1. Base Nematics and Chiral Additives

Nematics		**LH Additives**

$X - \hexagon - A - B - \hexagon - Y$

X, Y	A–B
Cyano-CN	Schiff-CH = N-
Alkyl-$CH_3(CH_2)_n$	Azoxy-N = N(O)-
Alkoxy-$CH_3(CH_2)_nO$	Ester-COO-

LH Additives

COC ⎫
ZLI-811 ⎬ wax

C15 ⎫
CN ⎬ powder

$CH_3(CH_2)_7COOC_{27}H_{45}$

Merck: Licristal V, ZLI1646
BDH: E7, E8, ... E44
Roche: TN-403, TN701

RH Additives

CAA ⎫
S1082 ⎬ solid
CE1, 2, . . . 7 ⎭

CB15   fluid

$CH_3CH_2\overset{*}{C}HCH_2 - \hexagon - \hexagon - CN$
$\quad\quad\ |$
$\quad\quad CH_3$

The recipe for circular polarizer fabrication is as follows:

1.   choose supporting substrate type (usually BK-7) and diameter (20 mm to 100 mm for present work)

2.   unidirectionally buff inner substrate surfaces with 1/10 micron diamond paste to create a preferred alignment direction and to provide wall anchoring for the liquid crystal molecules

3.   heat substrates and tuned liquid crystal compound to ∿ 70°C, apply 12 μm thick "Mylar" spacer tabs, and form an air-gap sandwich

4.   fill air-gap with heated fluid using capillary action

5.   quench cell to room temperature and shear one substrate with respect to the other by 1/2 mm to orient the pitch structure along the beam propagation direction (see fig. 5)

6.   adjust cell for zero wedge in an interferometer and seal the fluid edge with epoxy.
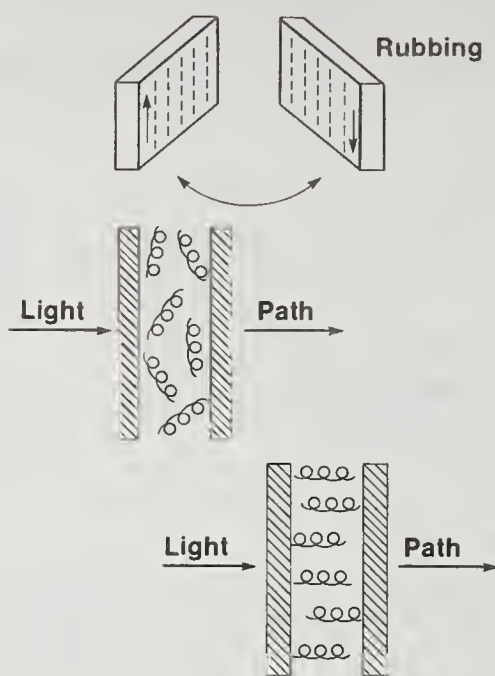
Figure 5. Liquid crystal polarizer fabrication. Substrate
inner surface rubbing helps to orient the rod-
like liquid crystal molecules which contact the
cell boundaries. A mechanical shear after cell
assembly tips molecular helices normal to the
laser beam propagation direction, thereby minimiz-
ing scatter losses for the preserved polarization
and maximizing rejection for the rejected polariz-
ation.

4. Performance

We have determined that fluid paths of 11 to 18 microns provide optimum polarization for the
1000 nm wavelength regime. The uniformity of fluid thickness across the polarizer clear aperture
does not affect performance, as long as the layer exceeds a minimum of 10 pitch lengths. Transmis-
sion for the preserved polarization through a single element approaches 98%. Blocking extinction
through crossed polarizers approaches 10^4.

The angular sensitivity of liquid crystal polarizers can be minimized by using base nematics
whose birefringence, Δn, is large. Composition detuning to the long wavelength side of the laser
wavelength may also be employed to create polarizer elements whose angular performance resembles
that shown in fig. 6. Extinction from 0 to ± 20° off normal in excess of 10^3 has been demonstrated.

Figure 6. Blocking extinction and angular sensitivity.
Liquid fluid paths of between 11 and 18 μm are
adequate to provide crossed polarizer blocking
extinction levels of 10^4. The use of highly
birefringent base nematics promotes selective
reflection bandwidth in excess of 150 nm
(FWHM). This in turn enables liquid crystal
polarizers to be relatively insensitive to
angle of incidence effects.

    We have found that the temperature sensitivity of liquid crystal polarizers depends upon the
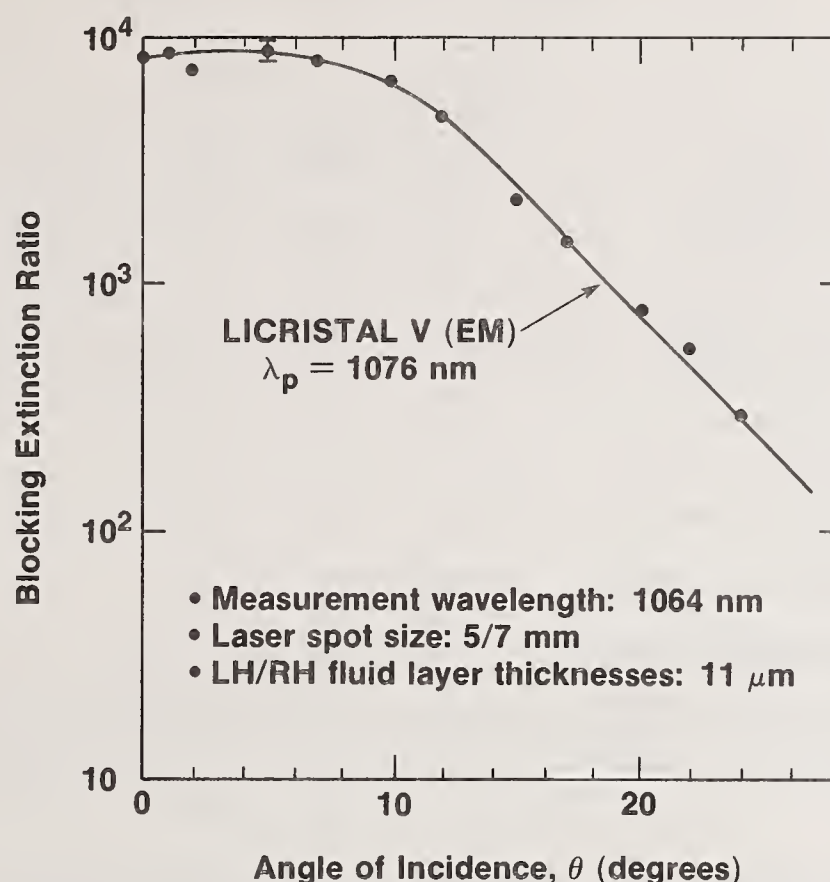type of base nematic and the type and quantity of chiral additive. Center wavelength temperature
shifts from 0.35 to 1.4 nm per °C have been measured. This level of sensitivity presents no problem
to the use of these devices in our laboratory, where temperature is controlled to ± 3°C.

    A series of on-line laser damage tests was performed on 50-100 mm diameter cells using the
1054 nm output of the GDL system. The RH combination of CB-15 in nematic E7 was found to be damage
resistant to average fluences of 3 J/cm^2 (1 nsec). LH polarizer cells failed at substantially lower
fluences of less than 0.2 J/cm^2. Failure is determined by polariscopic observation of bubble growth
in irradiated cells. We suspect that the primary reason for low damage thresholds in LH fluids is
the lack of a room temperature, liquid chiral additive, or inadequate dissolution of the LH solid
during fluid composition tuning. Our interim solution to this problem has been to employ RH element/
half waveplate combinations to simulate the three LH elements indicated in fig. 1.

5. High Power Polarizer Technologies

    A comparison of liquid crystal polarizers with other polarizer technologies is given in table 2.
Liquid crystals offer the advantages of high optical quality at large apertures, high contrast with
angular insensitivity, high transmission for the preserved polarization, and environmental stability.
They represent the only polarizer technology which, by itself, can provide back-reflection protection
during standard use. Work is presently being conducted to understand and solve the LH element laser
damage problem.

Table 2. Comparison of Polarizer Technologies

Attribute	Crystal Prism	Brewster Thin Film	Dielectric Cube	Dyed Plastic	Liquid Crystal
• Optical quality at large apertures	no	yes	no	no	yes
• High contrast with angular insensitivity	no	no	no	yes	yes
• High transmission for passed polarization	yes	?	yes	no	yes
• Environmental stability	yes	no	yes	yes	yes
• Laser-damage resistance	some	yes	some	no	adequate
• Back-reflection protection	no	no	no	no	yes

6. References

[1] Seka, W., et al., "High-power phosphate-glass laser system: design and performance characteristics", Appl. Opt. 19; 409-419; 1 February 1980.

[2] Abate, J. A., et al., "Active mirror: a large-aperture medium-repetition rate Nd:glass amplifier", Appl. Opt. 20; 351-361; 15 January 1981.

[3] Jacobs, S. D., "Liquid Crystals for Laser Applications", in CRC Handbook Series of Laser Science and Technology; III; M. J. Weber, Ed.; in press.

[4] Jacobs, S. D., "Liquid Crystals as Large Aperture Waveplates and Circular Polarizers", SPIE 307; 98-105; 28 August 1981.

[5] Jacobs, S. D., Abate, J. A., Bauer, K. A., Bossert, R. P., and Rinefierd, J. M., "Liquid Crystal Isolator for Fusion Lasers", Technical Digest - CLEOS/ICF '80; 128-129; 26 February 1980.

Is the liquid crystal polarizer temperature dependent? The author stated that there is no significant dependence between -20C and +50C. The uniformity of the polarizer film is also not important provided that the film thickness is 10 of more pitch lengths. The rejected light is reflected diffusely, not specularly, an important advantage in device applications. Finally it was suggested that stacked plate polarizers should be added to the list of possible polarizing methods. Extinction ratios as high as 40,000 to 1 have been obtained with these in the infrared.

NONLINEAR ROTATORY POWER
OF 90° TWISTED NEMATIC LIQUID CRYSTALS

Shin-Tson Wu and LaVerne D. Hess

Hughes Research Laboratories
3011 Malibu Canyon Road
Malibu, California 90265

The optical rotatory power of 90° twisted nematic liquid crystal cells was measured with a CW CO_2 laser and found to be intensity dependent for intensities > 1 kW/cm². We found that the rotatory power can either decrease monotonically or increase first and then decrease as the laser intensity increases; this effect depends on the liquid crystal layer thickness. A threshold-like transition was observed and the threshold power was found to be linearly proportional to the inverse square of the liquid crystal layer thickness. These results provide evidence that optical field induced molecular reorientation and thermal effect are responsible for the observed nonlinear optical effect. Self-defocusing, self-phase modulation and laser-induced damage were also observed with the use of a HeNe laser probe beam.

Key words: CO_2 laser; diffractions; dynamic recovery; liquid crystals; nonlinear rotatory power; phase transition.

1. Introduction

The optical rotatory power of liquid crystals (LCs) is a measure of the capability of a liquid crystal layer with a twisted molecular orientation to rotate the angle of incident polarized light. It is an important physical quantity for LC devices such as electro-optic shutters or spatial light modulators using the twisted nematic liquid crystal (TNLC) configuration. In particular the contrast ratio of these devices is critically influenced by the rotatory power of the LC cell used. Under the condition of low light intensities, nonlinear effects are absent and the optical rotatory power is a function of LC birefringence, film thickness, twist angle, and wavelength.[1]

In this paper, we report experimental measurements of intensity dependent rotatory power of LC cells having the 90° TNLC configuration. The studies were conducted with a CO_2 laser and with LC cells of different thicknesses. Results indicate that the rotatory power is constant when the incident light intensity is below a threshold value (this threshold-like transition is analogous to the Freedericksz transition [2] which occurs with a magnetic or electric field). Above this threshold, the rotatory power either decreases monotonically or increases first and then decreases depending on the thickness of the LC layer. The threshold intensity was found to be linearly dependent on the inverse square of the LC layer thickness in agreement with theoretical predictions. [3,4] These observations provide direct evidence that a laser-induced Freedericksz transition occurs, and is the physical mechanism responsible for the observed intensity dependent rotatory power of TNLC cells. A HeNe laser beam was used to probe the CO_2 laser/liquid crystal interaction region. Diffraction fringes associated with self-defocusing [5,6,7] of the HeNe probe laser beam were studied at different intensities until CO_2 laser-induced phase transition or damage to the liquid crystal occurred.

2. Experiment

The experimental setup is sketched in Fig. 1. A vertically polarized tunable CO_2 laser operating at 10.59 μm is attenuated by a pair of crossed polarizers and focused onto a LC cell by a 254 mm focal length, NaCl lens. The spot size is 155 μm in diameter at the $1/e^2$ intensity points. The LC director at the front surface of the 90° TNLC cell is aligned parallel to that of the laser polarization axis. Two transmission measurements were made at each laser intensity when the analyzer was (1) perpendicular, and (2) parallel to the polarization axis of the incident beam. Details of the experimental technique and sample preparation process have been reported earlier. [8] In the present study the highly absorbing conductive electrode (indium-tin-oxide) layer was not deposited on the KCl windows in order to minimize thermal effects on the rotatory power measurements. A positive dielectric anisotropic liquid crystal mixture, designated as BDH-E7, was used in this study. The optical absorption coefficient of this material was measured to be 5×10^{-3} μm⁻¹ at 10.59 μm for the ordinary ray, i.e., when the polarization of the laser beam is perpendicular to the liquid crystal director.

The rotatory power represents the basic modulation capability of a polarizer-LC cell-analyzer system, and represents the fraction of incident light intensity whose polarization has been rotated by 90° in passing through the liquid crystal cell. Thus, with a polarizer-TNLC cell-crossed analyzer arrangement, the rotatory power will be proportional to the transmission, $T_\perp$, through the analyzer. The intensity dependent transmission, $T_\perp$ (normalized transmission [8]) of BDH-E7 liquid crystal is shown in Fig. 2 for three LC film thicknesses, 13.5, 24.0 and 52.0 μm. The transmission is constant at low intensities for all three cells. However, when the intensity exceeds particular threshold values, the transmission of the 13.5 μm and 24.0 μm thickness cells decreases monotonically. For the 52.0 μm cell, the transmission first increases to about unity at a power of 300 mW and then decreases to <5% at a power of 2.5 W, corresponding to an intensity of

7.5 kW/cm². Note that this process is reversible as indicated by the two sets of experimental points plotted in the figure.

3. Theory

To understand these intensity dependent phenomena, we first compare transmission data obtained at low intensities with the relevant theoretical expression [1] for optical transmission for our experimental configuration.

$$T_{\perp} = 1 - \frac{\sin^2[\phi\sqrt{1+u^2}]}{1+u^2} \tag{1}$$

where $u = \pi d\Delta n/\lambda\phi$; d is the thickness of the LC layer, Δn is the LC birefringence which has been measured to be 0.205 for BDH-E7 at 10.59 µm,[9] λ is the wavelength, and ϕ is the twist angle of the liquid crystal in the LC cell; for the present case, $\phi = \pi/2$.

As shown by the plot in Fig. 3 there is good agreement between experimental measurements and theoretical calculations. It is readily seen that the first maximum of the transmission appears at a thickness of 44.7 µm. Hence, the transmission of the 52 µm thickness cell is less than unity at low laser intensities (Fig. 2). Once the intensity exceeds a certain threshold (0.3 kW/cm²), however, the liquid crystal molecules tend to line up along the polarization axis of the laser due to an optical field induced torque,[10]

$$\vec{\Gamma} = \frac{\Delta\varepsilon}{4\pi} (\vec{E}\cdot\hat{n}) (E \vec{x} \hat{n}) \tag{2}$$

where $\Delta\varepsilon = \varepsilon_{\parallel} - \varepsilon_{\perp}$ is the dielectric anisotropy of the liquid crystal, $\vec{E}$ is the electric field of the incident light, and $\hat{n}$ is the unit vector of the liquid crystal director. Due to this optical field induced molecular reorientation, the effective LC thickness (dΔn) of the 90° TNLC cell is reduced, which results in an increased transmission as expected from a reduction in effective cell length (Fig. 3), and indeed observed (Fig. 2). When the intensity is increased further, more molecules are aligned along the laser polarization direction, and the effective twisted cell thickness is further decreased leading to decreased transmission at high intensities.

4. Threshold Power

It is also shown by the data plotted in Fig. 2 that the measured threshold power depends on the liquid crystal thickness. The thinner the cell, the higher the threshold. The specific functional dependence of this relationship is illustrated in Fig. 4 where the threshold power is plotted as a function of the inverse square of the LC thickness. The threshold power is defined as the power where the transmission, T begins to deviate from the constant value at low intensities. In our experiments, a 10% accuracy was estimated and is indicated by the error bars shown in the figure. A linear dependence is obtained, and the slope is determined by the dielectric constants and Frank constants of the liquid crystal under study. This linear relationship between the threshold power and inverse square of the LC thickness provides evidence that the observed intensity dependent rotatory power is a consequence of optical field induced molecular reorientation.

5. Diffraction

In addition to the direct measurements of the intensity dependent rotatory power described above, a HeNe laser beam was used to probe the interaction region as shown in Fig. 1. The 4-mm-thick KCl windows are used as beam splitters to reduce the reflection losses at 10.59 µm. The reflected HeNe laser beam from the front surface of the KCl beam splitter was aligned coincident with the CO₂ laser beam. Another reflected HeNe laser beam from the back surface of the beam splitter served as the reference beam as shown in the right hand side of each photograph in Fig. 5. These photographs were taken from a screen which is located 60 cm away from the 52-µm liquid crystal cell. When the incident CO_2 laser power is below threshold (~100mW) no diffraction ring appears (Fig. 5a). As the power exceeds this threshold, diffraction rings associated with the divergence of the HeNe laser beam change drastically as indicated in Fig. 5b, c, and d for the powers of 200 mW, 700 mW, and 2.0 W, respectively. The threshold powers determined by the appearance of the first diffraction ring are also plotted in Fig. 3 (the triangle data points) for three LC film thicknesses. Good agreement is found between these two methods of measurement. Further increase in the incident power may cause a liquid crystal phase transition to occur (due to thermal effects) resulting in formation of the isotropic state. Fig. 5e reveals such a transition at an intensity of 7.5 kW/cm². If the LC cell is irradiated at this intensity for a short time (few seconds), recovery to the original anisotropic state occurs in about 2 minutes after the incident power is turned off; this indicates that the process is reversible.

6. Dynamic Recovery

The dynamic recovery processes are illustrated by the data shown in Fig. 6a, b, and c. These photographs were taken within an interval of 30 seconds after the phase transition (Fig. 5e) occurs (the CO_2 laser beam was turned off immediately after the phase transition was observed). Once the liquid crystal recovers (from Fig. 6c to Fig. 5a), it can withstand about 20% higher optical power without a further phase transition occurring. This observation may be explained as resulting from laser-induced purification of the liquid crystal mixture. Small particulates in the interaction region may be heated by the CO_2 laser beam. This induced temperature change results in a lower viscosity causing the small particulates to preferentially leave the interaction volume. However, if the incident power is further increased, an irreversible process occurs. Fig. 5f shows the diffraction pattern of the HeNe laser beam after the LC cell was irradiated at 8.5 kW/cm² for about one second. This pattern remains unchanged and corresponds to the pinhole diffraction pattern with a pinhole diameter of 100 μm, which is in good agreement with the result measured directly from a microscope. No damage of 24-μm and 13.5-μm cells was detected at this intensity level. This indicates that the damage to the liquid crystal is not due to the breakdown of surface alignment layers deposited on the KCl windows. The detailed mechanism corresponding to the damage to the LC layer is so far not clear, and is still under investigation. Therefore, the thinner cells have not only higher Freedericksz transition thresholds but higher damage thresholds. This fact is particularly important for high power laser applications of liquid crystal devices. In order to know whether the self-defocusing effect occurs in the CO_2 laser beam, knife edge beam scans were performed at a constant location (150 mm from the focal plane) to determine the transmitted beam size. The following conditions were used: (1) the LC cell was removed from the beam path; (2) a 24-μm LC cell was irradiated at 200 mW (which is below the threshold intensity); and (3) same as (2) except for higher power, 1 W (above the threshold intensity). The measured beam sizes were equal within 5% for all three conditions. This indicates that the critical power for self-action effect to occur is higher than the power used in these experiments.

7. Conclusion

In summary, we have studied the intensity dependent rotatory power of 90° twisted nematic liquid crystal cells at a wavelength of 10.59 μm. The rotatory power was found to be constant at intensities below a threshold intensity. Above this threshold, the rotatory power can either increase or decrease as the intensity increases. The threshold intensity is proportional to the inverse square of the LC layer thickness. These observations provide direct evidence that both laser field induced molecular reorientation, analogous to a.c. electric field induced molecular reorientation, and thermal effect are the basic mechanisms of the observed intensity dependent rotatory power. The intensity dependent transmission measurements discussed above represent spatially averaged effects. Diffraction patterns with a HeNe probe laser provide further details about the nonlinear process within the spatial profile of the Gaussian shaped CO_2 laser beam. Damage phenomena resulting from laser interactions with liquid crystal materials were also investigated. It was found that thinner cells have both higher Freedericksz transition thresholds and higher damage thresholds; this is particularly important for high power laser applications of liquid crystal devices.

References

1. Gooch, C. H., and Tarry, H. A., "The optical properties of twisted nematic liquid crystal structures with twist angles ≤90°," J. Phys. D. $\underline{8}$, 1575 (1975).

2. Freedericksz, V., and Zolina, V., Trans. Faraday Soc. $\underline{29}$, 919 (1933).

3. Ya Zel'dovich, B., and Tabiryan, N. V., "Theory of optically induced Freedericksz transition," Sov. Phys. JETP $\underline{55}$, 656 (1982).

4. Barbero, G., Simoni, F., and Aiello, P., "Nonlinear optical reorientation in hybrid aligned nematics," J. Appl. Phys. $\underline{55}$, 304 (1984).

5. Volterra, V., and Wiener-Avnear, E., "CW thermal lens effect in thin layer of nematic liquid crystal," Optics Comm. $\underline{12}$, 194 (1974).

6. Durbin, S. D., Arakelian, S. M., and Shen, Y. R., "Laser-induced diffraction rings from a nematic-liquid-crystal film," Opt. Lett. $\underline{6}$, 411 (1981).

7. Khoo, I. C., "Theory of optically induced molecular reorientations and quantitative experiments on wave mixing and the self-focusing of light," Phys. Rev. A$\underline{25}$, 1636 (1982).

8. Wu, S. T., Efron, U., and Hess, L. D., "Optical rotatory power of 90° twisted nematic liquid crystals," Appl. Phys. Lett. $\underline{44}$, 842 (1984).

9. Wu, S. T., Efron, U., and Hess, L. D., "Infrared birefringence of liquid crystals," Appl. Phys. Lett. $\underline{44}$, 1033 (1984).

10. deGennes, P. G., The Physics of Liquid Crystals (Clarendon Press, Oxford, 1974), p. 96.
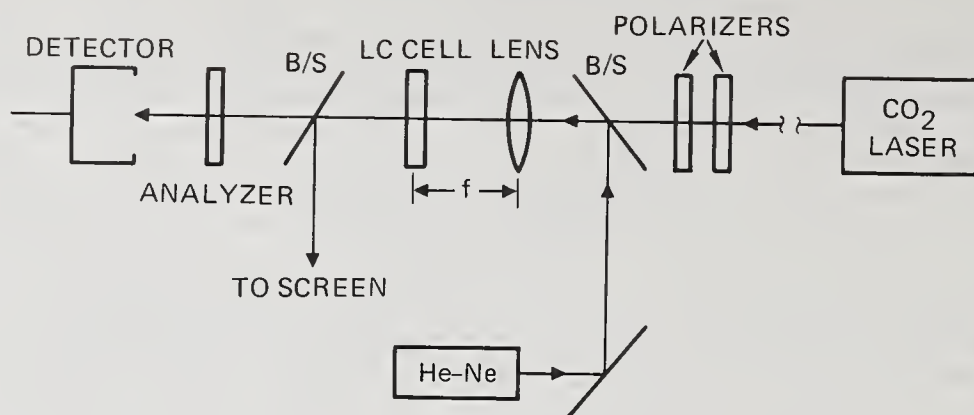
Figure 1. Schematic diagram of the experimental apparatus.
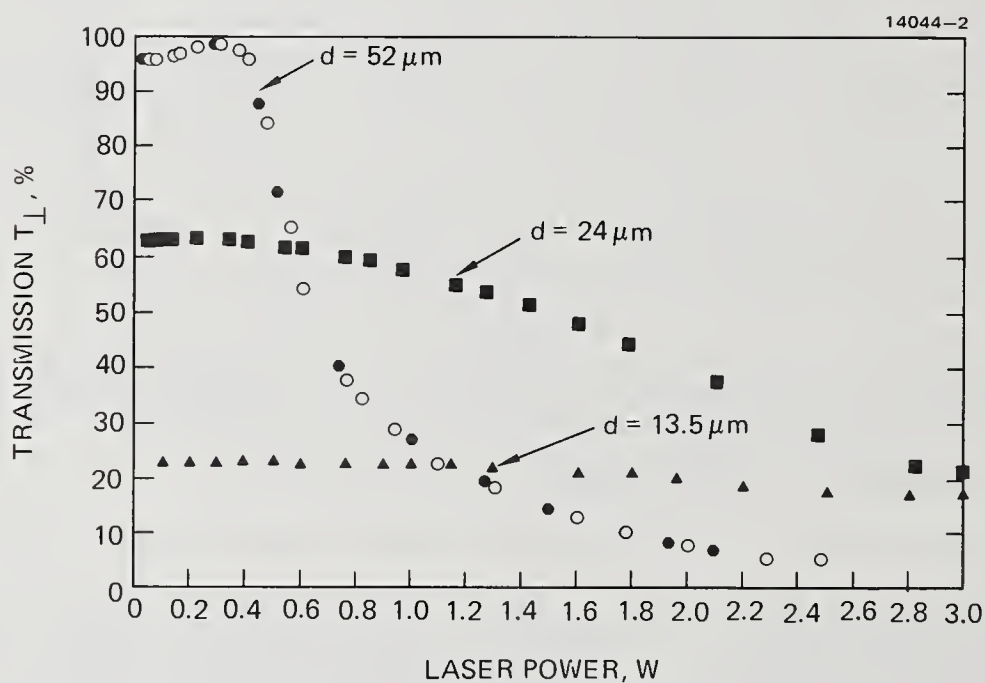
Figure 2. Transmission of the nematic liquid crystal mixture, BDH-E7, as a function of CO_2 laser power for three cell thicknesses having a twist angle of $\pi/2$; the dots represent the reversibility of intensity dependent transmissions of the liquid crystal under study; the laser spot size is 155 µm ($1/e^2$ intensity points); $T = 24°C$.
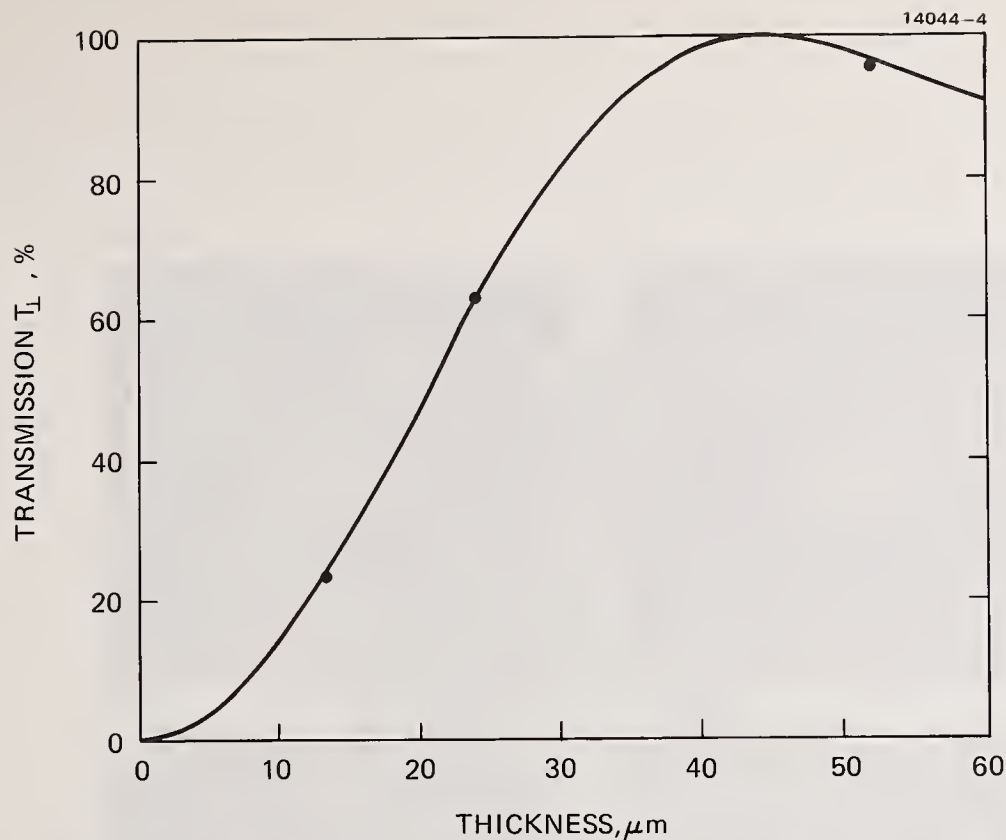
Figure 3. Normalized transmission of BDH–E7 as a function of cell thickness for low CO_2 laser (10.59 μm) intensities; solid curve is theoretical, points are experimental; T = 24°C.
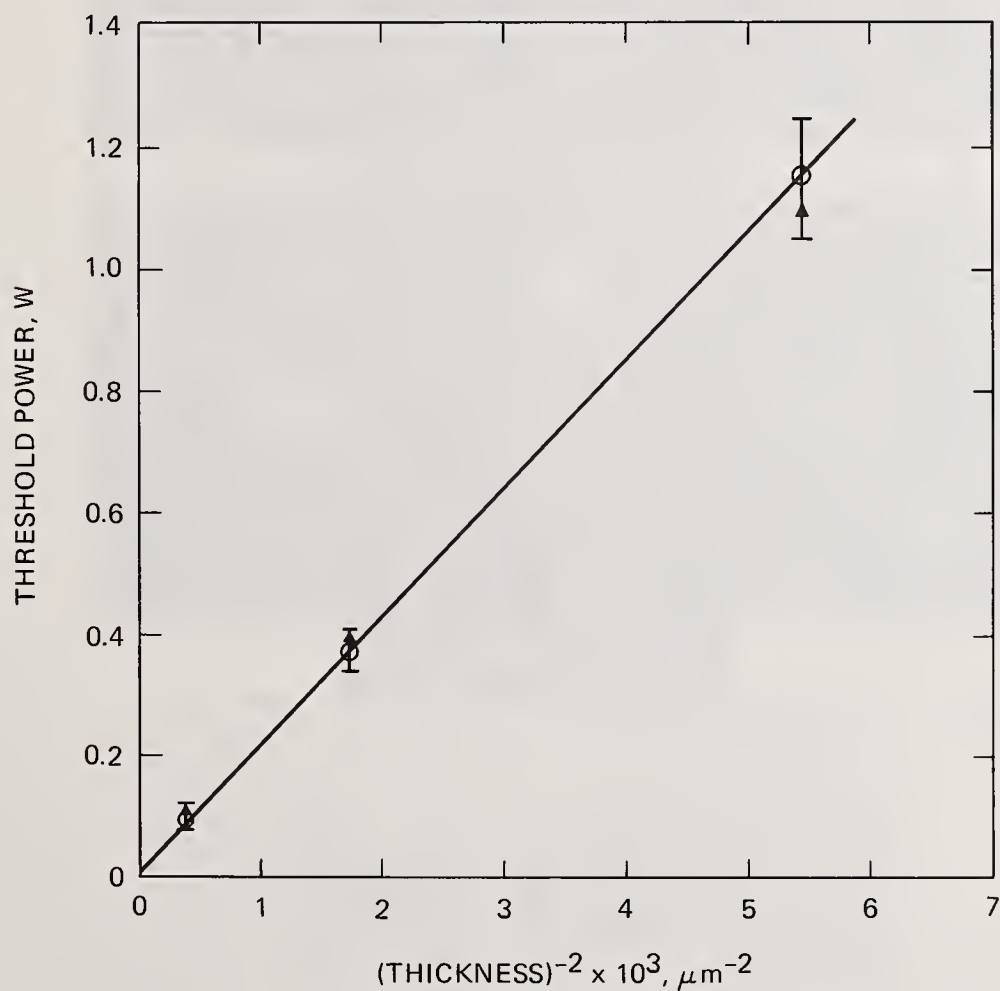
Figure 4. Observed threshold CO_2 laser (10.59 μm) powers for nonlinear transmission of BDH–E7 plotted as a function of $1/d^2$ where d is the cell thickness; Δ represents the threshold power determined by the HeNe laser probe technique; the laser spot size is 155 μm ($1/e^2$ intensity points); T = 24°C.
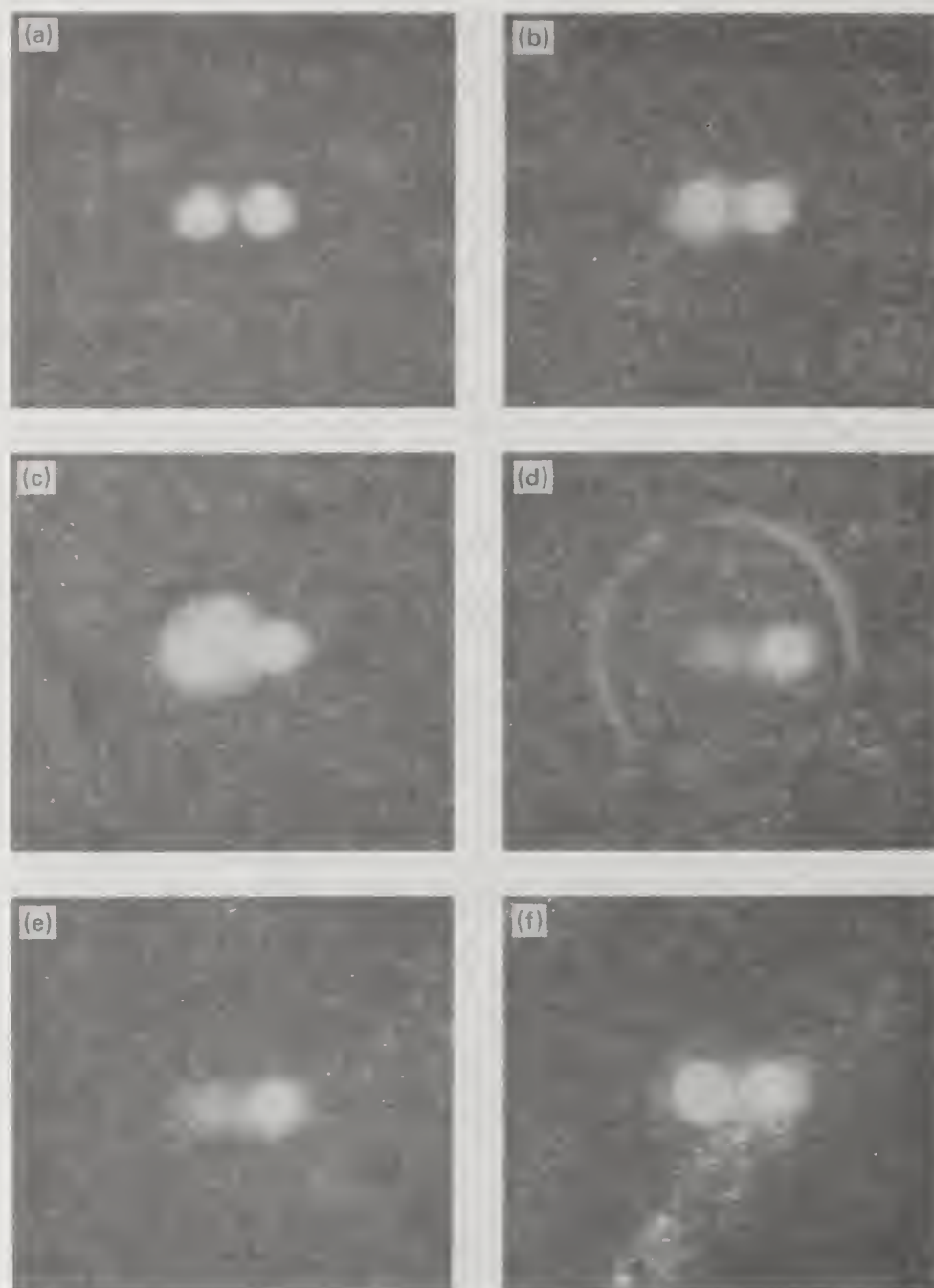
Figure 5. Diffraction patterns observed with a HeNe laser probe beam coincident with the CO_2 laser beam (normal incidence) for five power levels: (a) 50 mW, (b) 200 mW, (c) 700 mW, (d) 2W, and (e) 2.5 W; laser spot sizes are 155 μm and ~10 μm for the CO_2 and HeNe lasers, respectively.   (f) is the diffraction pattern of the HeNe laser beam when a small hole in the liquid crystal cell has been created by the CO_2 laser beam. LC cell thickness = 52 μm, screen is located 60 cm from the cell.
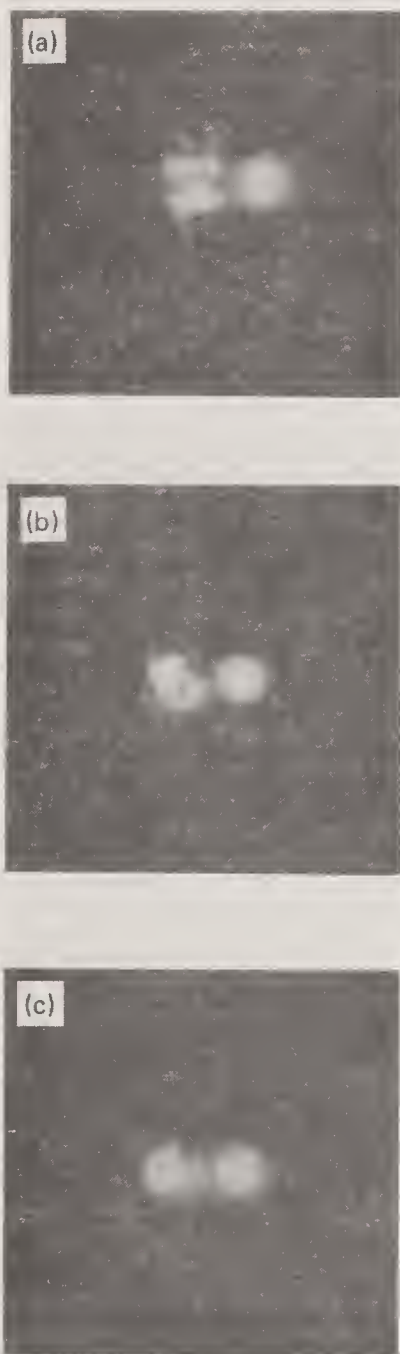
Figure 6. Dynamic recovery of liquid crystal after a
thermal induced phase transition occurs.
Photographs were   taken   at   the   same
conditions as those shown in Fig. 5 with
an interval of 30 seconds from (a) to (c).
The complete recovery is the same as that
shown in Fig. 5a.

The observed absorption coefficient was clarified 5x10^{-3}/micrometer is 50 cm^{-1}. The rational for assigning the observed long relaxation time toreorientational rather than thermal effects was also discussed. The author pointed out that if the effect was thermal, one should see a temperature rise. No phase transition was observed except at much higher temperatures than used here.

Picosecond Damage in Y_2O_3 Stabilized Cubic Zirconia

Nastaran Mansour, M. J. Soileau, and Eric W. Van Stryland

Center for Applied Quantum Electronics
Department of Physics
North Texas State University
Denton, Texas 76203

The hardness, strength, and transparency of cubic zirconia ZrO_2 makes it a good candidate as a laser window material; however, to obtain these qualities a relatively large percentage of Y_2O_3 is added to stabilize the crystals and increase their mechanical strength. As impurities are often regarded as the initiators of laser-induced damage we have performed a study of the damage thresholds of optical quality ZrO_2 stabilized with Y_2O_3. These thresholds have been measured with picosecond 1.06 μm laser pulses in crystals having Y_2O_3 concentrations of 9.4%, 12%, 15%, 18%, and 21%. We found that the addition of Y_2O_3 for increasing the mechanical strength of zirconia does not necessarily lead to a decrease in the damaging irradiance. In addition, the thresholds for ZrO_2 are comparable to those of NaCl.

Key Words: laser damage; picosecond pulses; ZrO_2 stabilized with Y_2O_3; estimation of n_2; 1.06 μm.

1. Introduction

The ideal optical materials for use with high power lasers should be transparent over a broad spectral range, mechanically strong, environmentally stable, and resistant to laser induced damage. Few materials meet all these criteria. For example, NaCl has low absorption from the infrared to the ultraviolet, is resistant to pulsed laser damage but has poor mechanical strength and is hydroscopic. ZnSe has good mechanical properties and broad band transmission but damages easily by pulsed laser irradiation. Fused silica is resistant to pulsed laser damage and has good mechanical properties but has high transparency only in the visible and near infrared spectral region.

Cubic zirconia stabilized with Y_2O_3 is mechanically strong, transparent from the UV to the mid-infrared and is now available in the industrial market. These factors make this material a good candidate for use as a high power laser window. The laser damage thresholds of this material had not previously been measured. In this paper we present measurements of the bulk laser-induced damage threshold of cubic zirconia stabilized with Y_2O_3 having concentrations of 9.4%, 12%, 15%, 18%, and 21%. Measurements were conducted using picosecond pulses at 1.06 μm.

2. Experiment

The laser source used in this study was a passively mode-locked, microprocessor-controlled, neodymium:yttrium aluminum garnet (Nd:YAG) oscillator-amplifier laser system operating at 1.06 μm. A single pulse of measured Gaussian spatial and temporal irradiance distribution was switched from the mode-locked train and amplified. The temporal pulsewidth was 45 psec [full width at half maximum (FWHM)]. The width of each pulse was monitored by measuring the ratio of the square of the energy in the fundamental (1.06 μm) to the energy in the second harmonic, produced in a $LiIO_3$ crystal. The ratio was calibrated by measuring the pulsewidth using an autocorrelation scan. Essential details are described in reference 1.

The laser half-angle beam divergence was 0.18 mrad. The beam divergence and the spatial beam spot size were determined by pinhole scans at several different positions along the propagation direction. A 37 mm focal length lens designed for minimum spherical aberration was used to focus the light into the bulk of the materials. The calculated focal spot radius using this lens is 7.2 μm (HW 1/e M in irradiance). A rotating half-wave plate, polarizer combination was used to vary the irradiance on the sample. The energy incident on the sample was continuously monitored by a sensitive photodiode peak-and-hold detector, and was calibrated with respect to a pyroelectric energy monitor. The incident beam polarization on the sample was changed from

linear to circular by adding a quarter wave plate in front of the focusing lens. Each site was irradiated only once, and damage was defined by the observation of scattered light from a coaxial HeNe laser as viewed through a 10x microscope.

3. Experimental Results and Discussion

Tables 1 and 2 summarize the results of measurements of the laser induced breakdown threshold for ZrO_2 stabilized with Y_2O_3. The ZrO_2 samples having Y_2O_3 concentrations of 9.4%, 12%, 15%, 18%, and 21% were studied for linearly and circularly polarized light at 1.06 µm. The uncertainties listed in the tables of data are the relative errors obtained by the method used in reference 9. For all the data presented in tables 1 and 2 we used 45 picosecond (FWHM) pulses and a calculated 7.2 µm focused spot size (HW 1/e M in irradiance). The values given for the electric field are rms fields corresponding to the peak-on-axis irradiance. As indicated in the tables of data, increasing the percentage of Y_2O_3 does not significantly change the breakdown threshold. The breakdown fields for linearly and circularly polarized light are displayed in figure 2. As clearly represented by bar graphs, the breakdown field remains unchanged (to within ±10%) for Y_2O_3 concentrations ranging from 9.4 to 21%.

In this work, we carried out the same measurements for circularly as well as linearly polarized light in order to determine the effect of self-focusing on laser-induced damaged threshold measurements. For the data listed here, we have done the polarization dependence test (2,6) which insures the absence of self-focusing in bulk damage measurements. Figure 3 is the experimentally determined ratio of breakdown electric field for circular polarized light to that for linearly polarized light. The ratios are constant (within uncertainties of experiment), and approximately equal to 1 for all different concentrations.* This implies that for our experimental conditions self-focusing did not dominate the damage process in these measurements. Note that we carried out the same experiment for a different focused spot size (10 µm). The ratios increased by a factor of 1.2 to 1.5 for all the samples tested. The polarization dependence of self-focusing has already been seen experimentally in a variety of materials. For example, for NaCl the ratio of the critical powers for circular to linear polarization is 1.37 to 1.46 [6]. For various laser glasses this ratio is equal to 1.50 [10]. Therefore, we concluded that for the larger focal spot size self-focusing is controlling the damage process.

The critical power for self-focusing of a focused Gaussian beam within a Rayleigh range, is obtained from numerical solutions of the nonlinear wave equation [4], and is given by

$$P_2 = 3.77c\lambda^2/32\pi^2 n_2$$

where n_2 is the nonlinear refractive index in esu, λ is the laser wavelength, and c is the speed of light in vacuum. If for the 10 µm focused spot size, self-focusing is the dominant process (as seems to be indicated by the polarization dependence), then the measured breakdown power (P_B) should be the same as the critical power P_2. We used the values of the measured breakdown power and the equation above to calculate an estimated value of n_2 for the ZrO_2 samples at 1.06 µm. Using the assumption that $P_B \sim P_2$ we find that $n_2 = 8 \times 10^{-13}$ esu. This value is in agreement with the rough theoretical estimation of n_2 in the next paragraph.

Self-focusing is an induced lensing effect in materials resulting from the changes of the optical dielectric constant when an electric field is applied. In this case, the total dielectric constant can be written as

$$\varepsilon = \varepsilon_0 + \varepsilon_2 \langle E \cdot E \rangle$$

where $\langle E \cdot E \rangle$ is the time average of the square of the optical field. The induced polarization in the medium is

---

*The 15% concentration sample was tested near the samples' edge for circularly polarized light where the optical figure of the front surface was poor. This probably accounts for the slightly greater than unity ratio for this sample shown in figure 3.

$$P = \chi^{(1)}E + \chi^{(3)} \langle E \cdot E \rangle E$$

where

$$\varepsilon_o = 1 + 4\pi\chi^{(1)} \quad \text{and} \quad \varepsilon_2 = 4\pi\chi^{(3)}$$

and the refractive index n is

$$n = \sqrt{\varepsilon} \sim n_o + n_2 \langle E \cdot E \rangle \quad .$$

In solid materials, the n_2 can be roughly estimated by using the argument given in reference 8. There it is assumed that the nonlinear polarization, $\chi^{(3)} \langle E \cdot E \rangle E$, becomes strong when the electrostatic energy of the applied optical field $\varepsilon_o/8\pi \langle E \cdot E \rangle V$ (V is the volume of the atom) is comparable to the electronic transition energy, $\hbar\omega_o$. The nonlinear polarization will then be comparable to the linear polarization so that

$$\frac{\chi^{(3)} \langle E \cdot E \rangle E}{\chi^{(1)} E} \sim \frac{\varepsilon_o/8\pi \langle E \cdot E \rangle V}{\hbar\omega_o} \quad .$$

With $n_2 = 2\pi\chi^{(3)}/n_o$, this gives

$$n_2 \sim \frac{n_o (n_o^2 - 1)}{16\pi\hbar\omega_o N}$$

where n_o is the linear index of refraction and $N = 1/V$ is the number density of atoms. For the ZrO_2 sample with $n_o = 2.12$ [11] and $\omega_o \sim 55 \times 10^{14}$ Hz, we estimate n_2 to be 10×10^{-13} esu which agrees with our experimental estimate of 8×10^{-13} esu. The validity of this estimation procedure can be shown by comparing its predictions for other materials where n_2 has been measured. The estimate of n_2 for NaCl is 1.3×10^{-13} esu and for SiO_2 it is 1.0×10^{-13} esu which compares to experimentally determined n_2's of $(1.37 \pm .15) \times 10^{-13}$ esu and $(.62 \pm .03) \times 10^{-13}$ esu, respectively [7]. Another empirical expression which has accurately given the nonlinear refractive index for a wide variety of transparent insulating materials is

$$n_2 (10^{-13} \text{ esu}) = K \frac{(n_d - 1)(n_d^2 + 2)^2}{\nu[1.517 + (n_d^2 + 2)(n_d + 1) \nu/6n_d]^{1/2}}$$

where ν is the Abbe number, n_d is the helium d line refractive index and $K=68$ [12]. This expression predicts an n_2 for ZrO_2 of 13×10^{-13} esu which again agrees with our estimate.

4. Summary

    Laser induced breakdown was studied at 1.06 μm for cubic zirconia stabilized with Y_2O_3. Samples having concentrations of 9.4%, 12%, 15%, 18%, and 21% were investigated. We find that increasing the percentage of Y_2O_3 to stabilize the zirconia does not decrease the breakdown threshold. The breakdown field is unchanged (to within ±10%) for Y_2O_3 concentration ranging from 9.4% to 21%. The breakdown fields for circular and linear polarized light were found to be approximately the same for the small spot size used. The implication of this is that for these conditions self-focusing did not play a major role in the measurements. Also, we estimate the nonlinear index of refraction n_2 for the ZrO_2 samples. For this estimate we used the breakdown data for which self-focusing was a dominant process. The value for n_2 agrees with theoretical estimates.

5. References

[1] Van Stryland, E. W.; Soileau, M. J.; Smirl, A. L.; Williams, W. E. Pulsewidth and focal-volume dependences of laser-induced breakdown. Phys. Rev. B 23(5): 2144-2151; 1981.

[2] Soileau, M. J.; Williams, W. E.; Van Stryland, E. W.; Boggess, T. F.; Smirl, A. L. Pico-second damage studies at .5 and 1 m. Opt. Eng. 22(4): 424-430; 1983.

[3] Soileau, M. J.; Williams, W. E.; Van Stryland, E. W. Optical power limiter with picosecond response time. IEEE J. Quant. Elect. QE-19(4): 731-735; 1983.

[4] Marburger, J. H. Self-focusing: Theory. Progress in Quantum Electronics, edited by Sanders, J. H.; Stenhold, S. Pergamon. Oxford. 4(1):35-110; 1975.

[5] Williams, W. E.; Soileau, M. J.; Van Stryland, E. W. Optical switching and n_2 measurements in CS_2. Optics Communications. 50(4): 256-260; 1984.

[6] Williams, W. E.; Soileau, M. J.; Van Stryland, E. W. The effect of self-focusing on laser-induced breakdown. Natl. Bur. Stand. (U.S.) Spec. Pub.; 1983.

[7] Williams, W. E.; Soileau, M. J.; Van Stryland, E. W. Simple direct measurements of n_2. Natl. Bur. Stand. (U.S.) Spec. Pub.; 1983.

[8] Yariv, A. Quantum Electronics, 2nd ed. New York; Wiley; 498-507; 1975.

[9] Porteus, J. O.; Jernigan, J. L.; Faith, W. N. Multithreshold measurement and analysis of pulsed laser damage on optical surface. Natl. Bur. Stand. (U.S.) Spec. Pub. 568; 507-515; 1979.

[10] Moran, M. J.; She, C. Y.; Carman, R. L. Interferometric measurements of the nonlinear refractive-index coefficient relative to CS_2 in laser-system-related materials. IEEE J. Quant. Elect. QE-11: 259-263; 1975.

[11] Wood, D. L.; Nassau, K. Refractive index of cubic zirconia stabilized with yttria. Applied Optics. 21(16):2978-2981; 1982.

[12] Milam, D.; Weber, M. J.; Glass, A. J. Nonlinear refractive index of fluoride crystals. Appl. Phys. Lett. 31(12): 822-824; 1977.
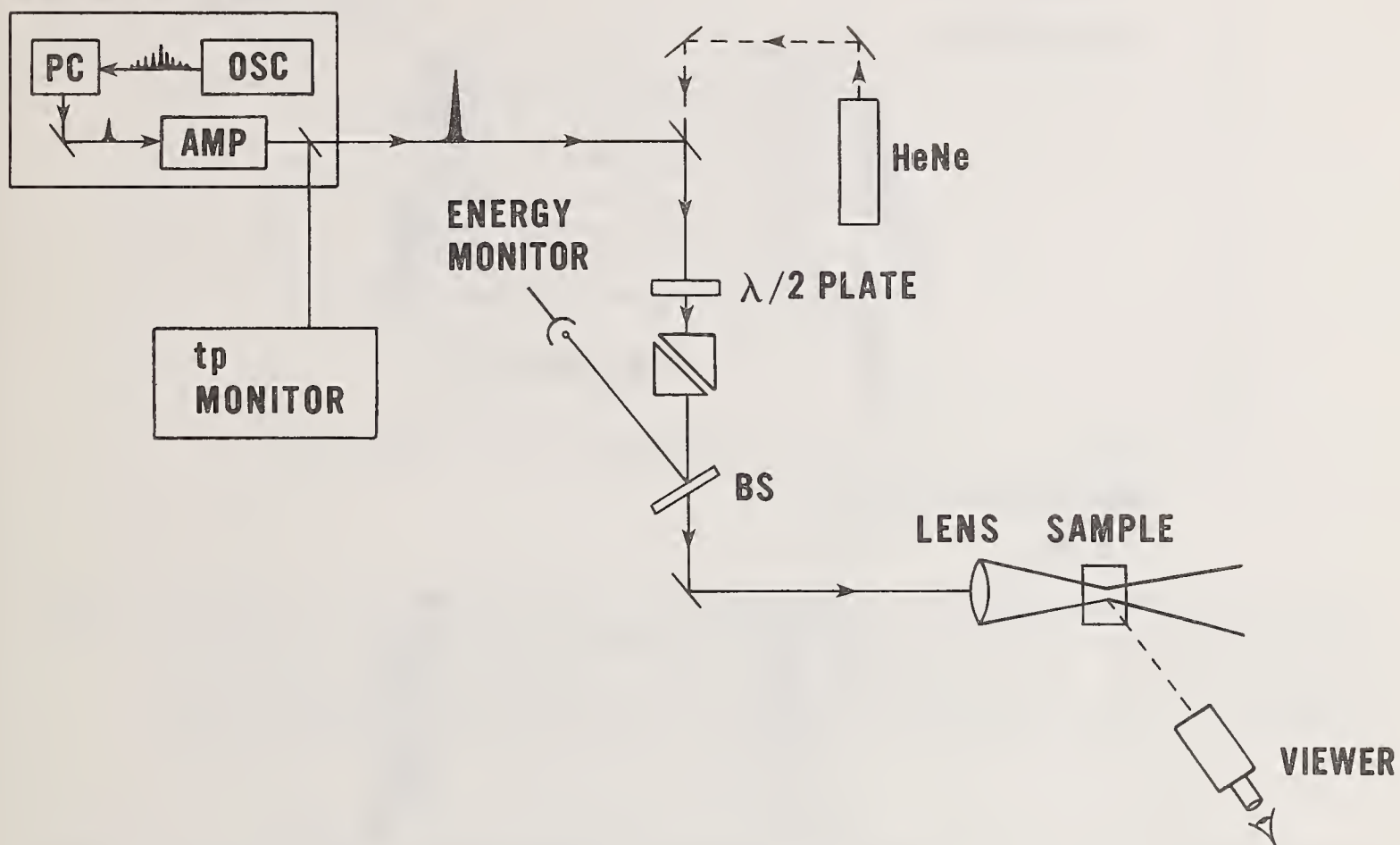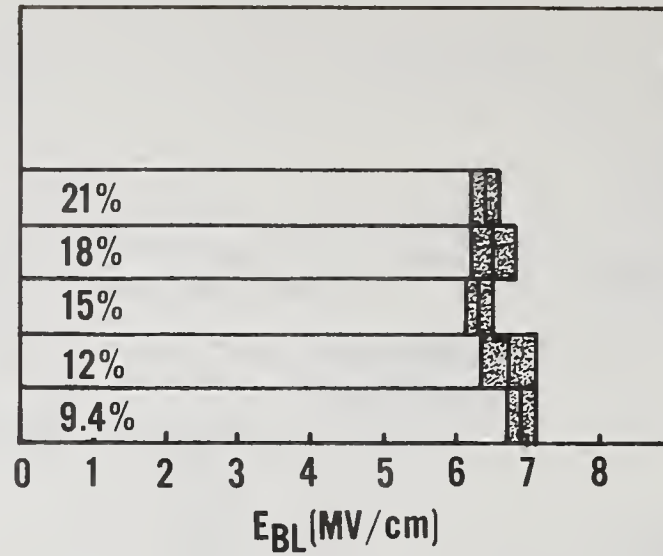
Figure 1.   Experiment.
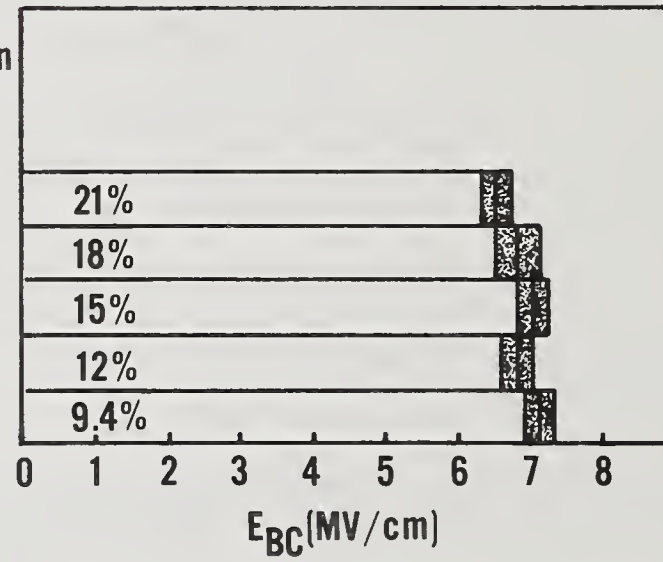
Figure 2. Experimentally determined breakdown electric field for linearly and circularly polarized light, E_{BL} and E_{BC}, for cubic zirconia ZrO_2 stabilized with Y_2O_3 having concentrations of 9.4%, 12%, 15%, 18%, and 21%.
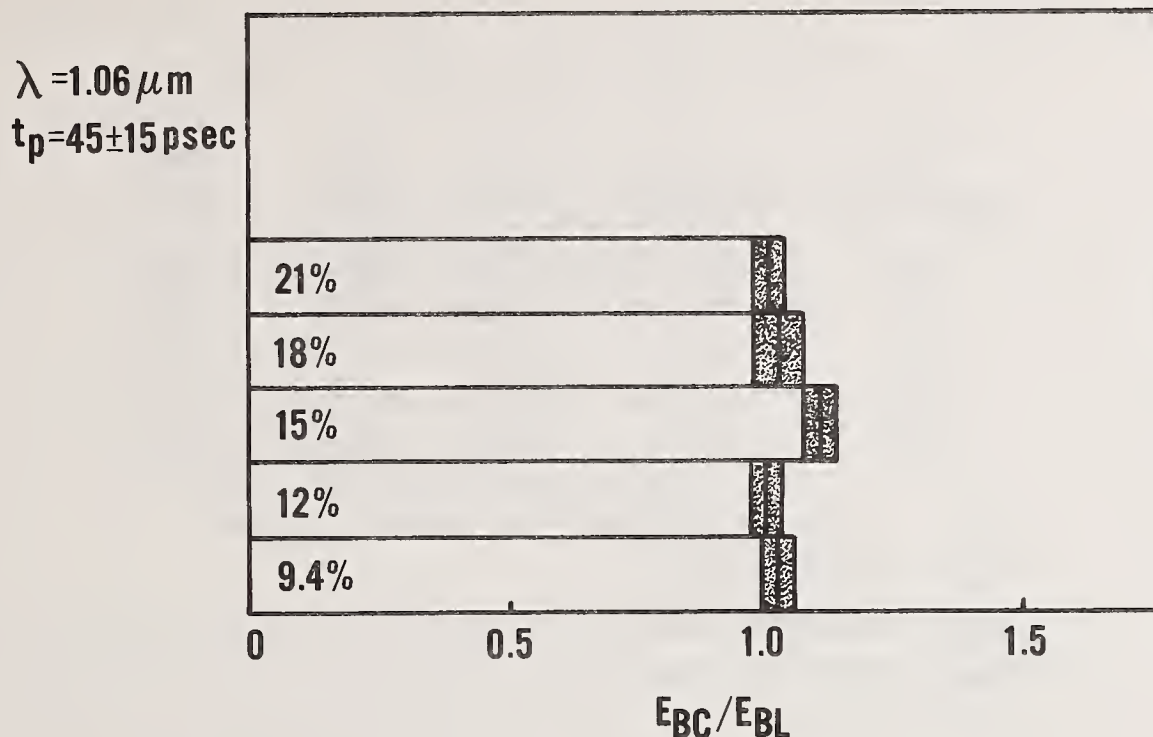
Figure 3. Experimentally determined ratio of breakdown electric field for linearly and circularly polarized light, E_{BC}/E_{BL}, for cubic zirconia stabilized with Y_2O_3 having concentrations of 9.4%, 12%, 15%, 18%, and 21%. (E_{BC} is the breakdown field for circularly polarized light and E_{BL} is the breakdown field for linear polarized light.) Note that $E_{BC} \sim E_{BL}$. The lack of polarization dependence indicates that its breakdown power is significantly less than its critical power for self-focusing.

Table 1. Laser induced damage data for ZrO_2 stabilized with Y_2O_3 at 1.06 μm using linearly polarized light.

Y_2O_3 Concentration	I_{BL} GW/cm^2	E_{BL} MV/cm	P_{BL} KW	F_{BL} J/cm^2
9.4%	$265^{+}_{-}18$	$6.9^{+}_{-}0.2$	$438^{+}_{-}30$	$12.7^{+}_{-}0.9$
12.0%	$257^{+}_{-}30$	$6.7^{+}_{-}0.4$	$423^{+}_{-}49$	$12.3^{+}_{-}1.4$
15.0%	$222^{+}_{-}11$	$6.3^{+}_{-}0.2$	$366^{+}_{-}19$	$10.6^{+}_{-}0.6$
18.0%	$237^{+}_{-}24$	$6.5^{+}_{-}0.3$	$389^{+}_{-}40$	$11.3^{+}_{-}1.2$
21.0%	$230^{+}_{-}17$	$6.4^{+}_{-}0.2$	$380^{+}_{-}28$	$11.0^{+}_{-}0.8$

I_{BL} = breakdown irradiance (peak on-axis irradiance)

E_{BL} = breakdown field

P_{BL} = breakdown power

F_{BL} = breakdown fluence

Table 2.   Laser induced damage data for ZrO_2 stabilized with Y_2O_3 at 1.06 μm using circularly polarized light.

Y_2O_3 Concentration	I_{BC} GW/cm^2	E_{BC} MV/cm	P_{BC} KW	F_{BC} J/cm^2
9.4%	282±17	7.1±0.2	465±27	13.5±0.7
12.0%	260±17	6.8±0.2	430±28	12.4±0.8
15.0%	278±13	7.0±0.1	458±22	13.3±0.6
18.0%	257±25	6.8±0.3	424±42	12.3±1.2
21.0%	238±16	6.5±0.2	393±26	11.4±0.7

I_{BC} = breakdown irradiance (peak on axis irradiance)

E_{BC} = breakdown field

P_{BC} = breakdown power

F_{BC} = breakdown fluence

Pulsed Laser Induced Optical Damage Threshold
In Nd:Cr:GSGG Crystal

M.A. Acharekar and D.P. McCarthy
Litton Systems, Inc.
International Laser Systems Division
3404 N. Orange Blossom Trail
Orlando, FL 32804

and

R. Blachman
Material Progress Corporation
1395 N. Dutton Avenue
Santa Rosa, CA 95401

Gadolinium scandium gallium garnet (GSGG) doubled doped with neodymium (Nd) and chromium (Cr) shows higher efficiency than the commonly used neodymium doped yttrium aluminum garnet (Nd:YAG) laser. The performance characteristics of 6.3 mm diameter by 100 mm long and 5 mm diameter by 65 mm long Nd:Cr:GSGG rods were obtained. A flashlamp pumped Nd:Cr:GSGG laser was operated in both normal and Q-switch modes. The performance data for the material will be presented and compared with Nd:YAG laser rod.

Q-switch output pulses of Nd:Cr:GSGG laser with 17 ns pulse width and 1.061 μm wavelength were used to study surface and bulk damage in coated and uncoated, polished samples of Nd:Cr:GSGG crystal. These optical damage threshold measurements were compared by measuring damage threshold of fused silica and BK-7 glass samples using the same experimental set up. Nd:Cr:GSGG damage threshold was higher than BK-7 glass and slightly lower than fused silica.

Key Words: Nd:Cr:GSGG, Co-doped GSGG, 1.061 μm laser, Laser Damage.

1. Introduction

Neodymium doped yttrium aluminum garnet (Nd:YAG) lasers have found numerous uses in scientific, military, and industrial applications. The typical overall efficiency for Nd:YAG is presently limited to 2-3 percent. The increase in this overall efficiency would be a very desirable improvement for reducing size and output energy of the system. The concept of improving efficiency by co-doping a neodymium (Nd^{3+}) laser crystal with chromium (Cr^{3+}) ions and transferring excitation absorbed by the broad Cr^{3+} absorption bands over to the Nd^{3+} ions is nearly as old as the Nd^{3+} laser itself.[1] No dramatic efficiency improvement was achieved with the host crystal YAG, because all Cr^{3+} excitation was deposited in ^2E level and the spin-forbidden nature of the $^2E \longrightarrow {}^4A_2$ transition resulted in an inefficient transfer process. However, nearly 100 percent transfer efficiency could be achieved in the co-doped gadolinium scandium gallium garnet (GSGG).

Figure 1. shows a schematic energy level diagram of octahedrally
coordinated Cr^{3+} in a configurational coordinate model.[2]

A series of measurements [3],[4] performed indicated that co-doped GSGG
laser rods provide several times higher efficiency under flashlamp pumped
conditions as compared to the more common host, Nd:YAG . In this paper, some
of the performance data collected at International Laser Systems (ILS) for
Nd:Cr:GSGG laser rods will be summarized. The data collected indicates that
Nd:Cr:GSGG crystal can be used in high power applications if the optical
damage threshold for the material is suitable for the applications.
Therefore, pulsed laser induced optical damage threshold for the material was
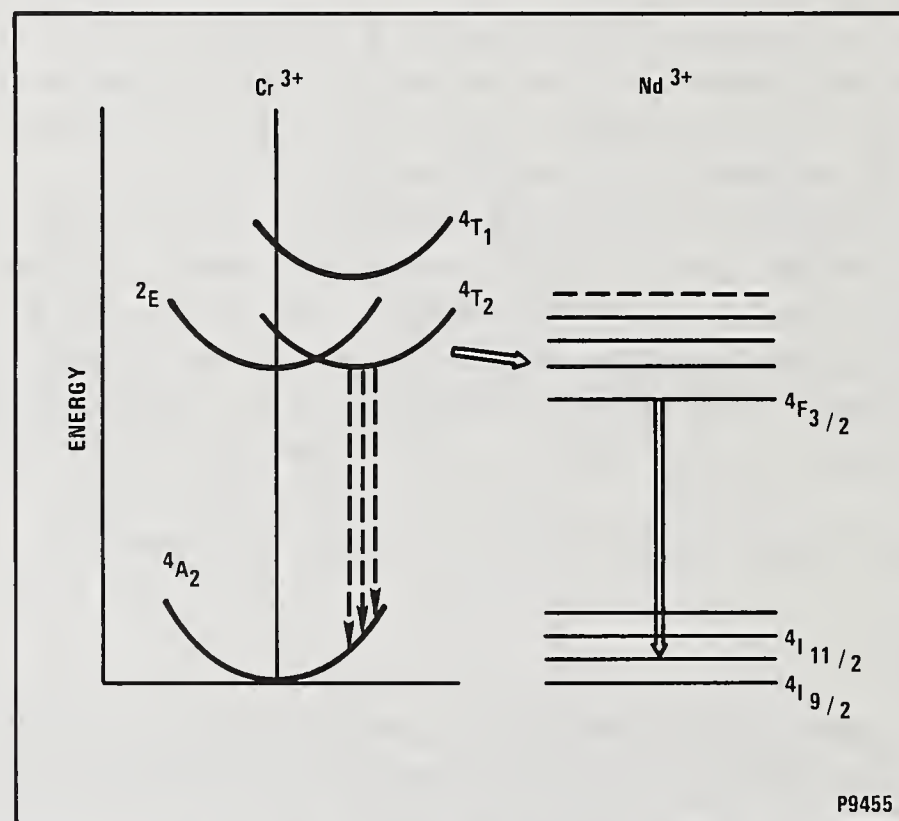measured. These measurements are discussed in the paper.

P9455

Figure 1. Energy Level Diagram of the Donor Cr^{3+}
and Acceptor Nd^{3+} in GSGG System.

2. Spectrophotometric Measurements

The transmission spectra for Nd:Cr:GSGG at room temperature was obtained using Varian model 2390 spectrophotmeter. The sample[5] was 1.58 mm thick with concentrations for Nd^{3+} of $1.5 \pm 0.5 \times 10^{20}$ cm^{-3} and Cr^{3+} of 1×10^{19} cm^{-3}. The transmission spectra clearly shows narrow Nd^{3+} transitions at 810, 800, 750 and 690 nm while the broad absorption observed at 460 and 645 nm is of Cr^{+3} for $^4T_1$, and $^4T_2$ electronic levels.

Fluorescence spectra for Nd:Cr:GSGG was studied also. The spectra comprises a wide band having maximum at 750 nm of Cr^{3+} fluorescence spectrum due to a transition from $^4T_2$ excited state of the Cr^{3+} ion to the $^4A_2$ ground state. The $^4F_{3/2} \longrightarrow ^4I_{11/12}$ transition in Nd^{3+} ions is seen at 1.06μm wavelength range in the fluorescence spectra. Also, the $^4F_{3/2} \longrightarrow ^4I_{9/2}$ transition in Nd^{3+} ions is observed at 946 nm wavelength range. As expected, the efficient $Cr^{3+} \longrightarrow Nd^{3+}$ steady state energy transfer reduces the intensity of the chromium fluorescence at 750 nm in the spectra observed for Nd:Cr:GSGG crystal. Fluorescence spectrum at 300°K for 0.63 cm diameter by 10.16 cm long Nd:YAG and Nd:Cr:GSGG laser rods were obtained by using Xenon gas filled flashlamp to pump the laser rods and a Farrand Optical Company Model 117182 grating monochromator to measure the fluorescence. The data obtained is shown in figure 2. Although, the monochromator resolution was 1.0 nm it appears that only the major fluorescence lines at 1.06 μm and 0.93 μm with high effective cross-section are observed.
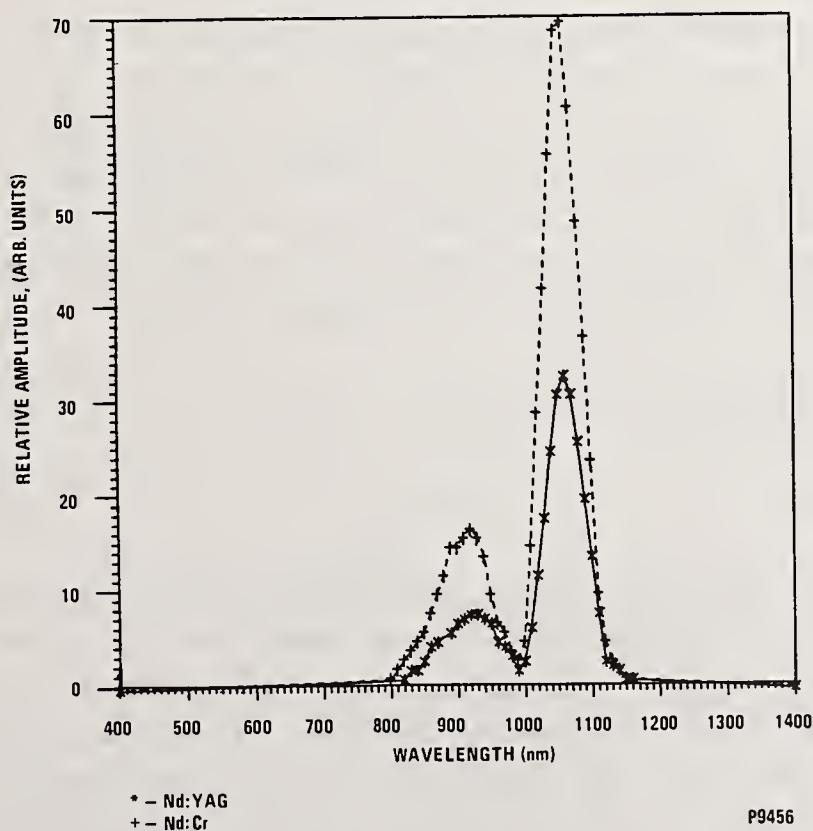

* − Nd:YAG
+ − Nd:Cr

P9456

Figure 2. Fluorescence Spectrum Nd:YAG Vs. Nd:Cr.

3. Lasing Properties of Nd:Cr:GSGG

The lasing properties of Nd:Cr:GSGG were investigated in the free lasing regime in the 1.06 μm wavelength range in the following two modes:

i) Pulsed normal mode operation
ii) Q-switched mode of operation

The experimental data was collected for the pulse normal mode operation using 0.63 cm by 10.16 cm Nd:Cr:GSGG rod. The experimental set up as shown in figure 3. The laser rod was installed in a single elliptical pump cavity. The same pump cavity is used for the Nd:YAG laser systems manufactured by ILS. Thus, the performance characteristics for the pump cavity using 0.63 cm by 10.16 cm Nd:YAG laser rod are known. The pump cavity, laser rod, and flash-lamp were cooled using cooling system that consisted of a heat exchanger, pump, and coolant reservoir. The 50:50 ethylene glycol and water coolant was used with a 1 liter capacity reservoir. The pulse forming network (PFN) of 35.5 μF capacitor and 39 μH inductor was used with a Xenon gas filled at 400 torr pressure in cerium doped fused silica envelope flashlamp. The input-output characteristics for the resonator consisted of 5 meter radius mirror coated for maximum reflectivity spaced 40 cm apart with an output coupling mirror of 40 percent is shown in figure 4. The comparison of Nd:YAG and Nd:Cr:GSGG laser rods of the indentical size in exactly same set-up is shown in figure 5.

The experimental data was collected for Q-switch mode operation using 0.5 cm diameter by 6.50 cm long Nd:Cr:GSGG laser rod. In the resonator a lithium niobate pockel cell with a polarizer was added. Also, the PFN was changed, capacitor 49.6 μF and inductor 29.3 μH was used. Q-switched output energy of 135 mJ was obtained in beam divergence of 2.18 mR with 8 J/P input energy at 10 pps. The pulse width of the Q-switched pulses was measured using EG&G 580 radiometer and Tektronix Model 454A oscilloscope. The typical full width at half aplitude (FWHA) pulse width for the laser was 17.0 ns.

4. Laser Damage Threshold for Nd:Cr:GSGG

4.1 Test Specimens

For measuring damage threshold of Nd:Cr:GSGG two types of samples were prepared. For the bulk damage threshold measurements rods of 0.63 cm diameter by 0.5 cm long were optically polished and single layer magnesium floride antireflection (AR) coated. The samples with two different concentrations of Nd^{3+} dopant were used. For the surface damage threshold measurements optically polished discs of 0.38 cm diameter by 0.1 cm thick were used. It may be noted that all the samples were inspected under cross polarizer to make

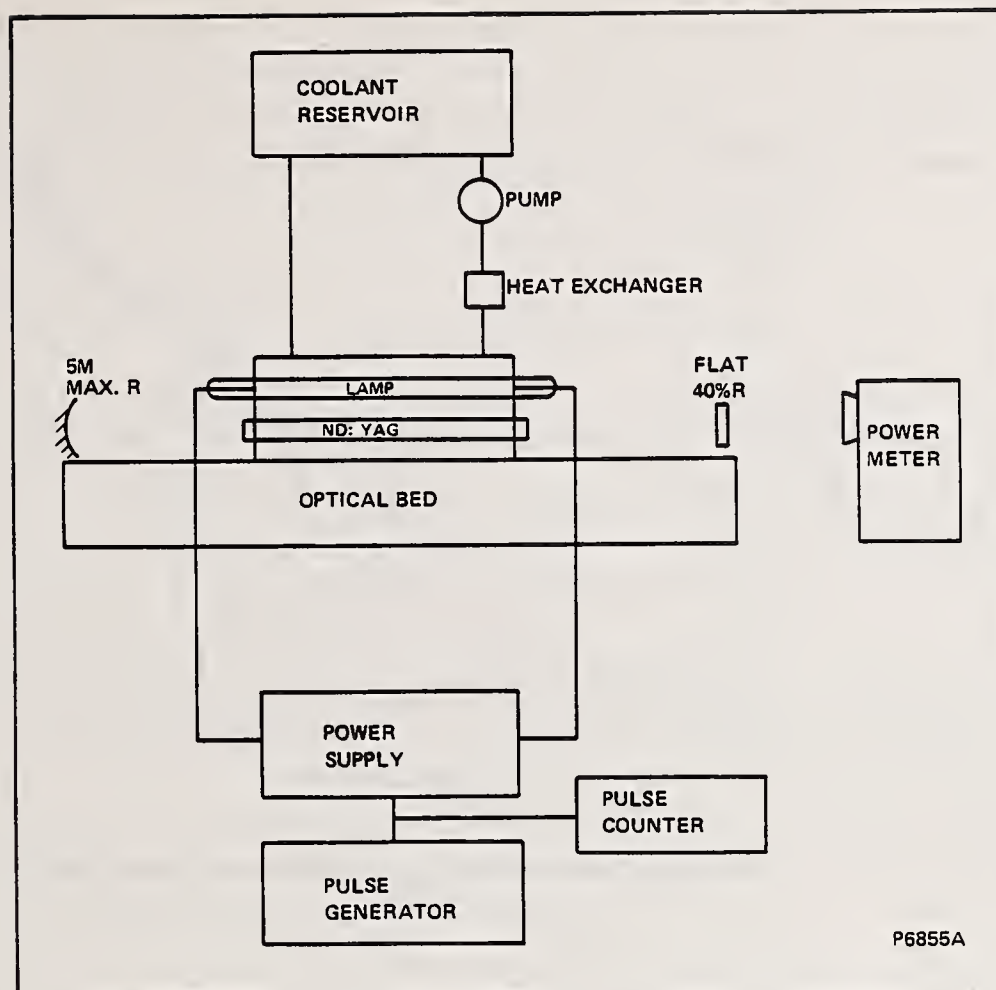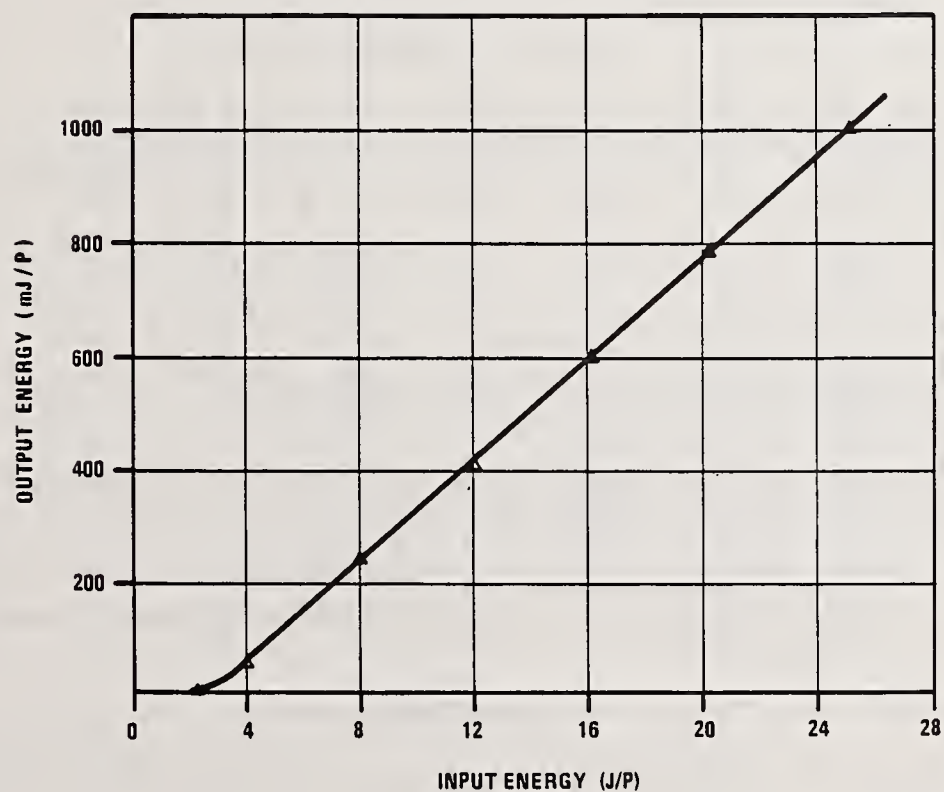Figure 3. Experimental Setup.

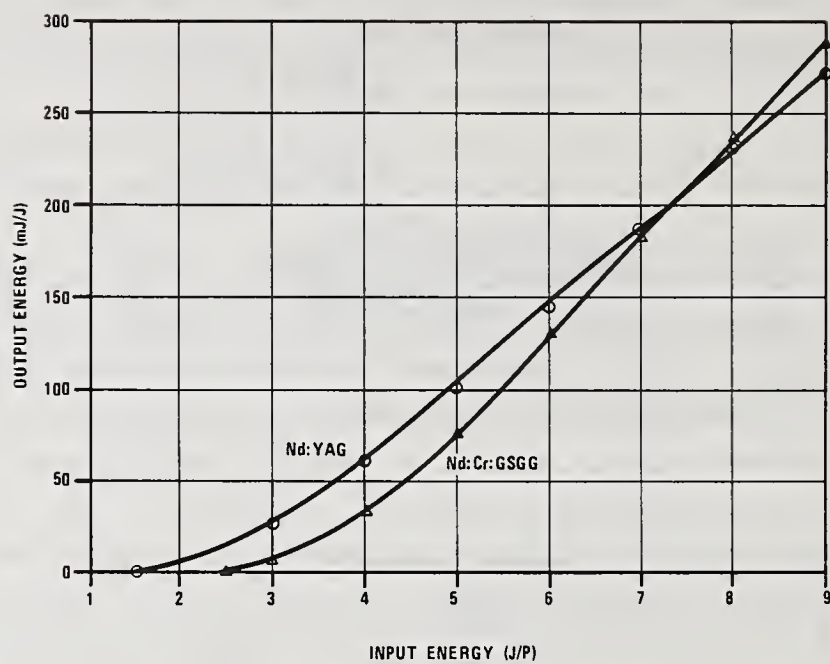
Figure 4. Nd:Cr:GSGG Laser Input-Output Characteristics.

43

P9450

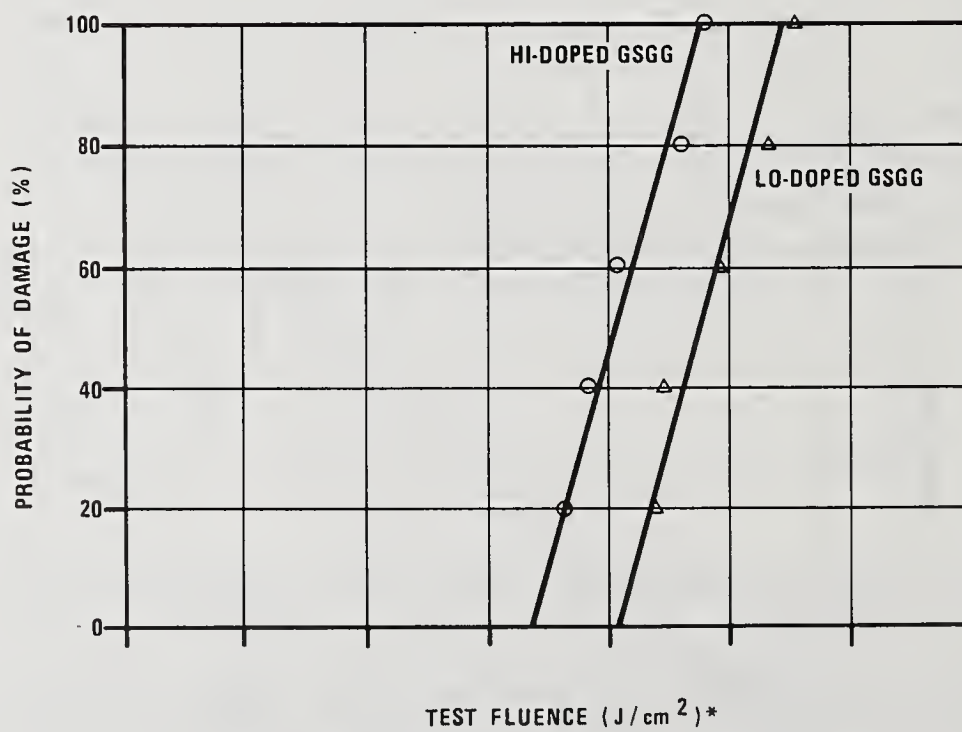Figure 5. Comparison of Nd:Cr:GSGG to Nd:YAG Laser.

Figure 6. Bulk Damage Measurements for Nd:Cr:GSGG. P9451

* DoD has classified the data.

44

sure that they were free of stress and crystal defects. The surfaces polished
were perpendicular to crystal axis of growth, thus the samples were oriented
in the same direction as the laser rod during its operation. The samples were
polished using 0.3 μm size alumina (Al_2O_3) on a pitch polisher and flatness of
$\lambda/2$ was obtained.

4.2 Experimental Techniques

The Q-switched, Nd:Cr:GSGG laser system described above was used. As
mentioned before the laser provided 135 mJ output energy in 17 ns pulse width
at 1.061 μm. The desired power density on the test sample was obtained using
focusing lenses of different focal lengths. The spot size was calculated and
actually measured on a photosensitive film, however, calculated spot size was
used in obtaining the damage threshold.

The surface damage threshold measurements were conducted using single
shot while in the bulk damage threshold measurements multiple shots were used.
In this work "damage" is defined by the appearance of a flash of light and the
attenuation of transmitted pulse through the sample. This definition and
method is widely used in the study of single and multiple shot damage and the
details of the methods can be found in reference [6].

4.3 Experimental Results

Figure 6. represents the results of bulk damage threshold measurements
using multiple shots (average of 4-6 shots) on the samples of Nd:Cr:GSGG. As
seen in the figure, high and low doped GSGG crystal samples were investigated.
Actually, the samples came from two ends of a five inch long Nd:Cr:GSGG
crystal. The chemical analysis of the samples indicated that Cr-dopant was
uniformly distributed within the crystal, however, concentration of Nd showed
10 percent difference in the samples. The damage threshold was 12.5% lower
for the higher Nd-doped crystal.

The surface damage threshold data obtained for Nd:Cr:GSGG samples is
shown in figure 7. All the samples tested for the surface damage were tested
using a single shot. The comparison of the single-shot surface damage
threshold obtain for BK-7 and fused silica is also provided in the figure.
The front surface damage threshold of Nd:Cr:GSGG was observed to 14.0 J/cm^2.
It may be noted that the samples tested for the single-shot surface damage
threshold were low-doped Nd:Cr:GSGG.

FLUENCE (J/cm^2) *

FUSED SILICA   Nd:Cr:GSGG   BK - 7 GLASS
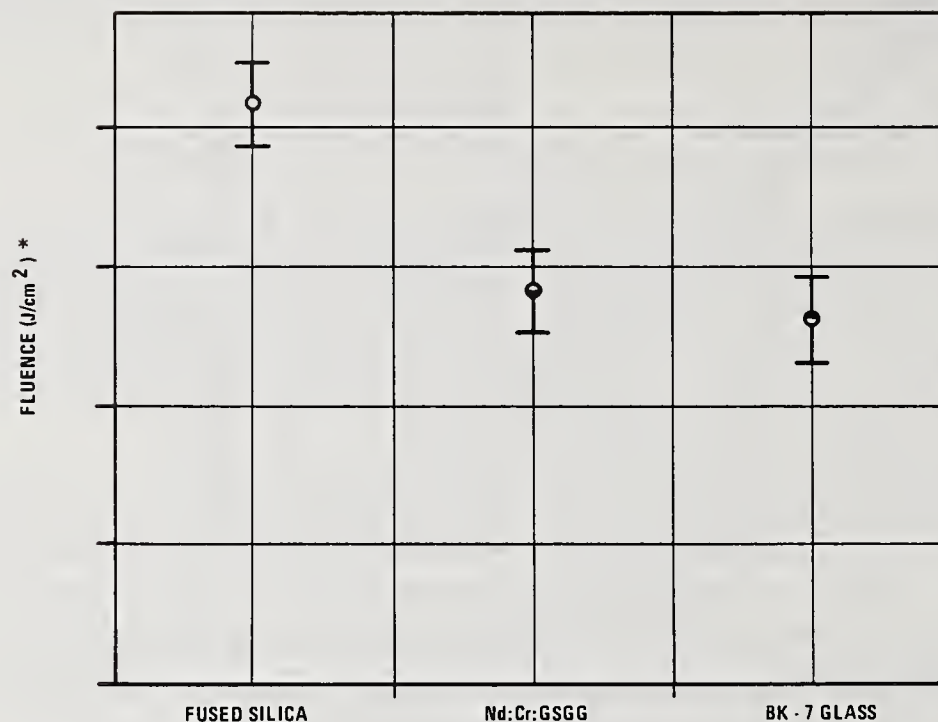
Figure 7. Damage Threshold Comparison Chart.   P9452

* DoD has classified the data.

5. Conclusions

The following conclusions can be drawn based on the data collected for Nd:Cr:GSGG crystal.

1. The spectrophotometric and the fluoremetric data collected show that for 1.5 ± 0.5 X 10^{20} cm^{-3} Nd^{3+} concentration and 1.0 X 10^{19} cm^{-3} Cr^{3+} concentration in GSGG host, almost 100 percent transfer efficiency is observed.

2. The lasing data collected for the Nd:Cr:GSGG laser rod shows 4 percent laser efficiency for the normal mode operation. The experimental data also shows that over 7.5 J/p input energy Nd:Cr:GSGG laser performance was superior to the same size Nd:YAG laser rod.

3. The pockel cell Q-switch used with the 5 mm X 65 mm Nd:Cr:GSGG laser rod provided output energy and beam divergence equal to a typical 6.3 mm X 1016 mm Nd:YAG laser rod.

4. Multiple shot bulk damage threshold for the Co-doped GSGG crystal measured indicates its dependance on the Nd concentration. For 10 percent increase in Nd concentration bulk damage threshold of was decreased by 12 percent.

5. Single-shot surface damage threshold for Nd:Cr:GSGG crystal was measured The damage threshold was compared with fused silica and BK-7 glass. Nd:Cr:GSGG surface damage threshold is slightly higher than BK-7 glass but lower than fused silica.

6. The damage morphology (figure 8) shows the uniform surface damage. This indicates that the polishing technique used for Nd:Cr:GSGG was adequate. Also the excellent energy profile obtained in the Nd:Cr:GSGG laser was used for the damage measurements.

Figure 8. Damage Morphology Near Threshold.

References

[1] Z.J. Kiss and R.C. Duncan, Appl. Phys. Lett. 5, 200 (1964).

[2] D. Pruss, V.V. Laptev, et. al., Appl. Phys. B28, 355 (1982).

[3] P.F. Moulton, Laser Focus 19, 83 (1983).

[4] E.V. Zharikov, V.V. Laptev et. al., SOV. J. Quant. Elec. 13, 82 (1983).

[5] The material was grown by Material Progress Corp, CA.

[6] L.D. Merkle, M. Bass and R.T. Swimm, NBS Spec. Publ. 669, 50 (1982).

Since chromium absorbs strongly in the ultraviolet, one might expect a degraded beam quality. However, the author replied that they were pleasantly surprised with how good the beam quality was. They were not cleared to discuss it further. It was suggested that chromium fluorescence in the ultraviolet would be expected and its absence required an explanation. The author replied that perhaps the concentration of chromium was just optimum to prevent fluorescence. The surface damage was found to be lower than the bulk threshold. The surface was polished by Virgo Optics using 0.3 μm alumina on a pitch lap. The samples were flat to about a half wave.

Laser Damage Studies of Several Methacrylate Polymeric Materials

R.M. O'Connell* and R.V. Ellis

Electrical Engineering Department
University of Missouri-Columbia
Columbia, Missouri 65201

A.B. Romberger

The Pennsylvania State University, Berks Campus
Reading, Pennsylvania 19608

T.F. Deaton and K.E. Siegenthaler

Frank J. Seiler Research Laboratory, USAF Academy
Colorado Springs, Colorado 80840-6528

A.A. Shaffer

Department of Chemistry, USAF Academy
Colorado Springs, Colorado 80840-5791

B.W. Mullins

Department of Physics, USAF Academy
Colorado Springs, Colorado 80840-5821

T.T. Saito

Lawrence Livermore National Laboratory
Livermore, California 94550

The bulk damage resistance of several acrylic polymers was investigated with a 1.06 μm wavelength pulsed Nd:YAG laser having a pulse length of 8-9 ns and a spot size of 33 μm. These materials were synthesized in bulk form using either thermal or ultraviolet initiation after extensive distillation and/or filtration at the monomers with sub-micron porosity membrane filters. Samples of pure poly(methyl)methacrylate, poly(ethyl)methacrylate and poly(cyclohexyl)methacrylate as well as plasticized polymers were studied. Details of synthesis methods and results of the damage measurements are presented, and the influence of synthesis methods on damage properties is discussed. In addition, a simple technique that uses scattered, depolarized helium-neon laser light to quickly estimate the impurity content of these samples is described and its ability to predict simple-shot damage resistance is discussed. Finally, a somewhat different method of analyzing multiple-shot damage data is applied and the results are discussed.

Key Words: bulk laser damage; multiple-shot; single-shot; plastics; polymethylmethacrylate

1. Optical System For Laser Damage Measurements

The bulk laser damage properties of the polymerized samples were measured using the Frank J. Seiler Research Laboratory (FJSRL) laser damage facility[1,2] which is shown schematically in figure 1. Briefly, the facility consists of a 1.06 μm wavelength Q-switched Nd:YAG laser that provides 8 $\pm$ 2 nsec FWHM pulses with up to 300 mj/pulse at a pulse repetition frequency of up to 10 pulses per second (pps). A 25 cm focal length lens L_1 focuses the beam into the test sample S. Careful knife-edge measurements of the focused 1.06 μm beam showed that its spatial profile is reasonable Gaussian in and near the focal plane with a $1/e^2$ radius (spot size) of 33 $\pm$ 1.7 μm and an associated focal volume (in PMMA) of approximately 0.01 mm^3. The spot size was determined by least-squares-fitting a Gaussian profile to the numerically differentiated knife-edge data. The peak fluence level in joules/cm^2 for each pulse was obtained by

normalizing the measured spatial profile to the total pulse energy, which was measured calorimetrically. Based upon uncertainties in the spot size and the power meter P.M. used to monitor pulse energy, a standard deviation of 15% was obtained for these values.

A collinear helium-neon laser probe[3] is used to monitor damage and to help align the 1.06 μm beam optics. Lenses L_2 and L_3 precondition the probe beam's focus to approximately coincide with that of the Nd:YAG beam. The components from the dielectric turning mirror M_3 to the photodiode (PD) monitor damage by measuring the onset of damage-induced probe-beam scatter out of the focal volume.
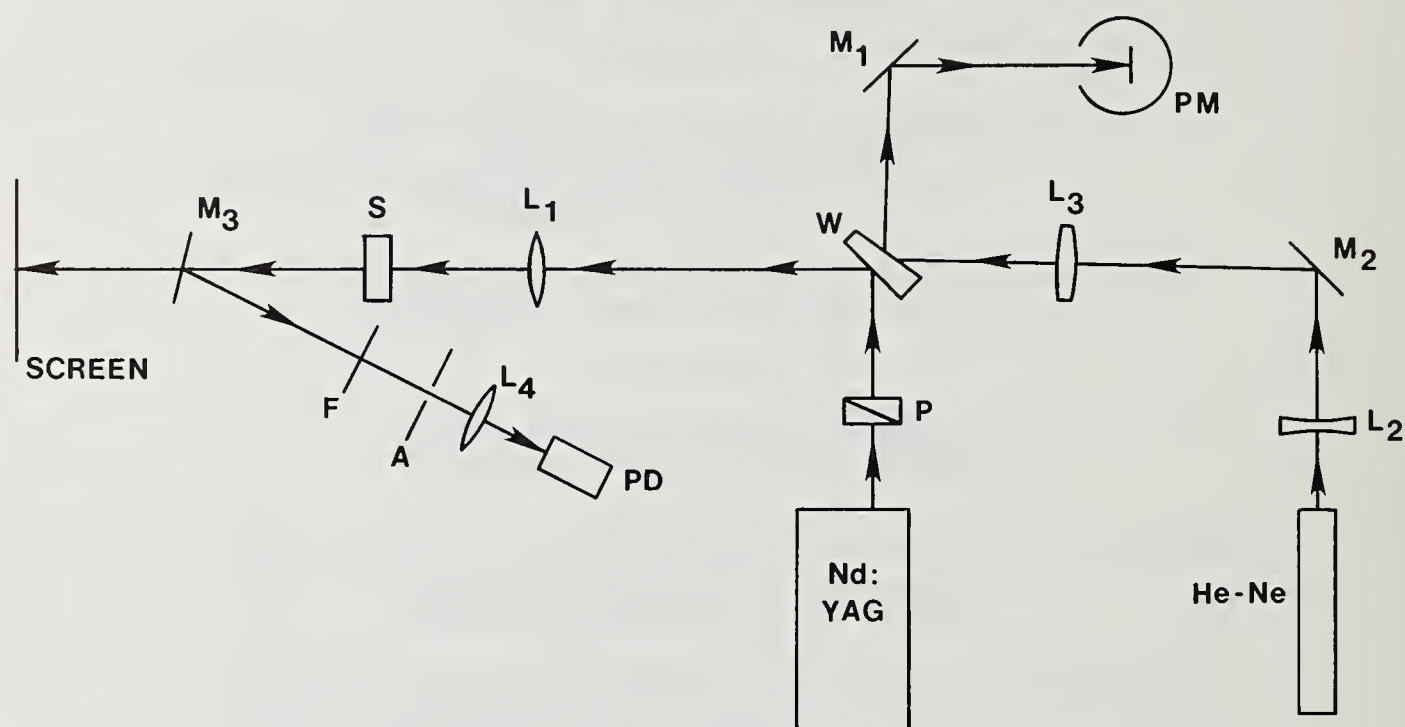
Figure 1. The optical system for laser damage experiments.
M_1,M_2 and M_3 - flat turning mirrors; P - polarizer
attenuator; W - silica wedge beam splitter;
L_1,L_2,L_3,L_4 - lenses, S - sample, A - aperture,
F - attenuating filter;
P.D. - photo diode; P.M. - power meter.

2. Materials and Synthesis Methods

Several polymer samples were prepared from monomer which in some cases included a plasticizer. The polymers prepared for this study included poly(methyl)methacrylate (PMMA), poly(ethyl)methacrylate (PEMA), poly(cyclohexyl)methacrylate (PCHMA) and samples of each with either 5 or 10% by weight dibutylpthalate (DBP) added as a plasticizer. Groups of samples were prepared under identical conditions, and all samples were prepared using very similar procedures.

In order to reduce impurity levels and remove chemical inhibitors (hydroquinone, for example), the materials were all fractionally distilled either under 1 atmosphere of nitrogen (MMA, EMA) or under partial vacuum (MMA, CHMA, DBP). Prior to distillation, some samples were dried with CaH_2 to remove water (table 1). Many samples were filtered with membrane filters of mean porosity of 0.40 μm or 0.22 μm. The prepared monomers, with or without plasticizers, and without any chemical initiators, were then sealed in cylindrical ampoules (typically 6 cm long x 17 mm in diameter) under nitrogen atmosphere or in a vacuum and bulk polymerized either thermally in a temperature controlled bath or by exposure to ultraviolet (UV) light. The thermal bath was held at 40°c and, because no chemical initiators were used, took approximately two weeks to produce fully

solidified samples. UV light (300-400 nm) was provided by either a fluorescent "black light" or a laboratory mercury lamp. These sources produced fully solidified samples in approximately three days.

All of the synthesized PMMA and PEMA samples were hard, odorless, bubble-free, colorless and transparent. The PCHMA samples were hard, odorless, and bubble-free, too, but they turned slightly cloudy upon fully solidifying. The sample with 10 weight percent DBP took the longest time to turn cloudy, which leads us to speculate that the cloudiness was due to partial crystallization, which the plasticizer could delay but not prevent.

Table 1. Summary of synthesis methods

Monomer-plasticizer	Dried	Distillation Method	Filtered	Polymerization method
MMA*	Some samples	N_2 atmosphere or vacuum	Some Not Some with 0.44 μm filter Some with 0.22 μm filter	Thermal or Ultraviolet (UV)
MMA + 5% DBP MMA + 10% DBP	No	N_2(MMA) Vacuum (DBP)	No	UV
EMA EMA + 5% DBP EMA + 10% DBP	Yes (EMA only)	Vacuum	No	UV
CHMA CHMA + 5% DBP CHMA + 10% DBP	No	Vacuum	No	Thermal or UV UV

*one sample of PMMA (R-3) was handled in a sealed vacuum system using a procedure similar to that of reference 4.

3. Dust Content Estimation from Scattered Depolarized Helium-Neon Laser Light

To evaluate the effectiveness of the various distillations and filtrations in removing impurities, as well as to avoid performing unnecessary damage tests on contaminated materials, a method was sought for quickly and easily estimating the dust content of the monomer and polymer samples. The optical arrangement shown in figure 2 was found to be well-suited to the task. The helium-neon laser beam was polarized with a sheet of polaroid, focused into the sample with a 30 cm focal length lens to somewhat concentrate the beam, and observed with a 25X microscope mounted with its observation axis perpendicular to the scatter track and parallel to the electric field vector of the polarized light. This arrangement allowed observation of scattered depolarized light from the micron-sized particles of interest against a minimized background of Rayleigh-scattered light from molecular matter and particles much smaller than those of interest. Thus the dust content of a sample could be estimated simply by counting the relatively bright scattering centers seen with the 25X microscope in the approximately 0.35 mm^3 volume occupied by a 5 mm length of scatter track.

This scheme proved to be most useful when it was used to estimate the relative dust content of two or more samples. For example, in a recent study of the effects of simple monomer purification (i.e., drying and single distillation) on the laser damage properties of PMMA[5], it was found that the purified sample had significantly greater resistance to laser damage than the unpurified sample. To confirm that the purification effort had actually been successful at removing dust, the depolarized scattered light scheme was used to estimate the relative dust content of the two samples. The unpurified material was found to contain approximately six times as many dust particles as the purified material, thereby establishing a direct correlation between dust content and susceptibility to laser damage. Similar results were obtained with the material used in the work of this report, as will be shown later. (See tables 2 and 3.)
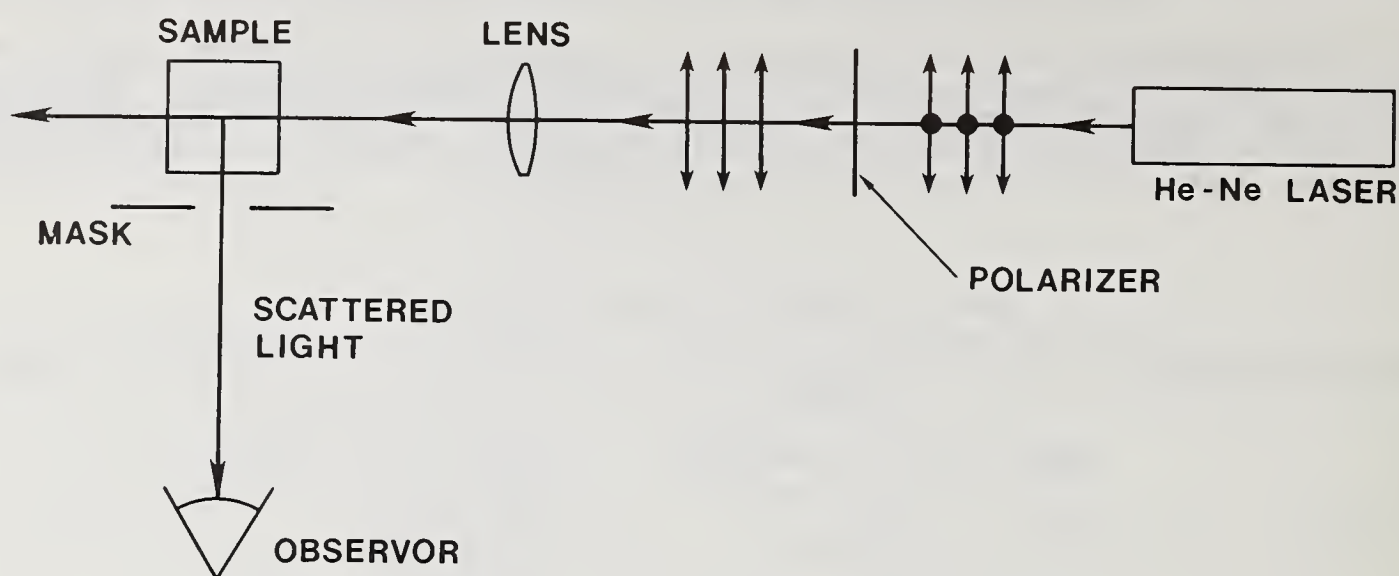
Figure 2. Experimental arrangement for observation of scattered depolarized helium-neon laser light.

4. Investigation for Self-Focusing

The data reported here have not been corrected to account for self-focusing. A check for the possible significance of self-focusing in PMMA at threshold fluence levels was performed by comparing single-shot damage thresholds determined for linearly polarized and circularly polarized laser irradiation, respectively. Circular polarization was obtained by the insertion of a quarter-wave plate just before the focusing lens. The resulting data for a particular PMMA sample are shown in figure 3. There appears to be no significant difference between the damage thresholds for the two polarization conditions, verifying that self-focusing is not a significant factor in this work. This result is as expected because the sign of the thermo-optic coefficient dn/dT for PMMA is negative,[6] and therefore, self-focusing should not occur.[7]
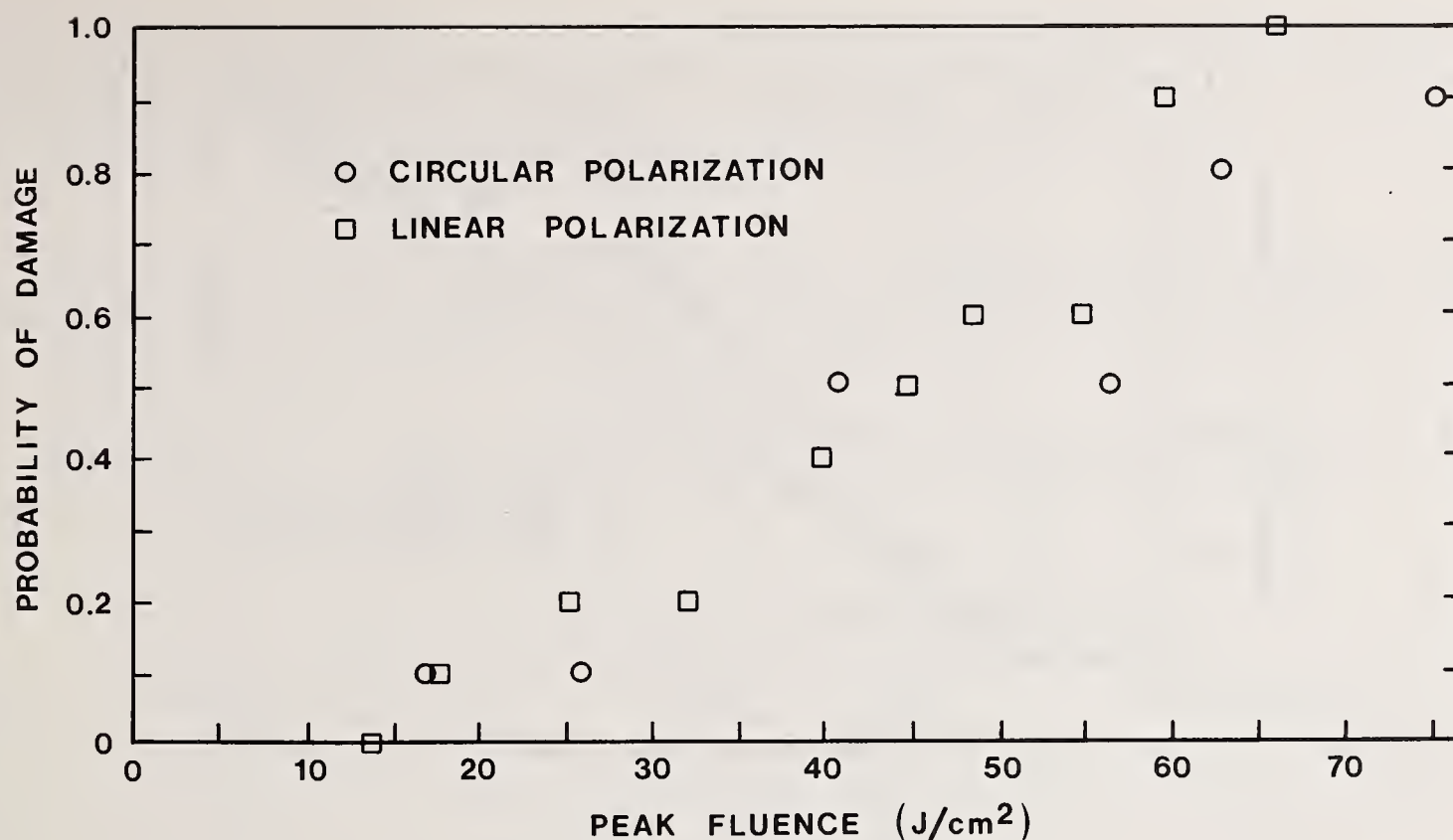
Figure 3. Comparison of damage data for PMMA under irradiation by linearly polarized and circularly polarized single pulses.

5. The Effects of Monomer Filtration on the Single-Shot Damage Thresholds of PMMA

In the above mentioned study of the effects of simple monomer drying and distillation on the laser damage properties of PMMA[5], it was found that both the single- and multiple-shot behavior could be significantly improved. The next step was to determine whether micropore filtration of the monomer prior to polymerization could produce further improvement over distillation. To study this, three PMMA samples were synthesized at the University of Missouri and laser-damage-tested at FJSRL. All three samples were made from carefully distilled monomers which were then passed through a filter apparatus containing either no filter, a 0.40 μm filter, or a 0.22 μm filter, respectively. Polymerization was by UV initiation without any free-radical initiator.

The occurence of laser damage was defined as a large enough permanent change in the material to be detected with the collinear helium-neon laser damage probe described in section 1, which was found to be reliable in detecting damage sites as small as 5-10 μm in diameter. Besides using the laser probe, which suffers from high sensitivity to slight misalignment, the occurrence of damage was also indicated by a spark or flash, and/or by the appearance of one or more bright scattering centers in the beam path after irradiation.

To measure single-shot damage thresholds, defined as laser fluence levels (J/cm^2) with a 50% probability of causing damage in one pulse, approximately 10 sites in each test sample were irradiated with one pulse each at a given fluence level and evaluated as discussed above for the occurrence of damage. This process was repeated at several fluence levels. A plot of the resultant damage statistics is shown in figure 4 along with the results of least-squares-fitting (LSF) straight lines to the data. The statistical nature of the data is caused by the 15% standard deviation in the peak fluence values discussed in section 1; by the subjectivity inherent in deciding whether damage occurred in marginal cases, which introduces no more than a 5% error in the damage probabilities; and by site-to-site variations in the material, as discussed in reference 5. The damage thresholds, obtained from the midpoints of the LSF lines, are given in table 2 along with the dust content of each sample, as determined with the depolarized scattered light scheme. Each dust content number in the table is the average of six readings taken with the scattered light probe.
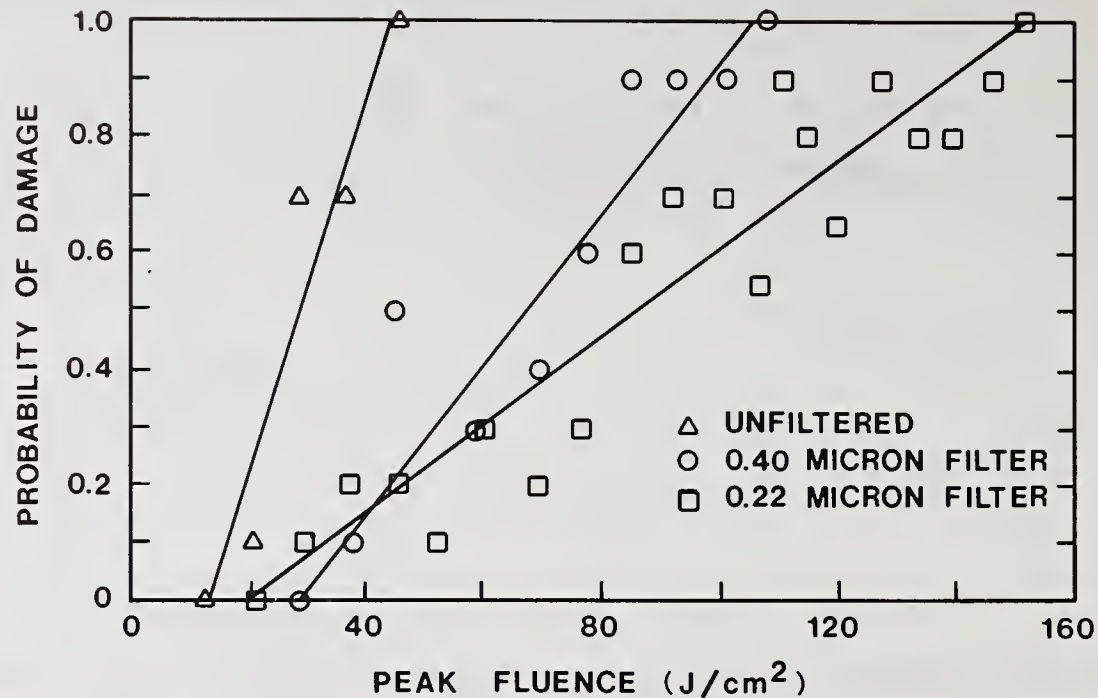
Figure 4. Single-shot damage statistics for PMMA in the monomer-filtration study.

Table 2. Dust Content and Single-Shot Damage Thresholds of PMMA in the Monomer
Filtration Study

Sample	Monomer Description	Dust Content (Particles/mm^3)	Single-Shot Damage Threshold (J/cm^3)
E20	distill only	7.1	29
E22	distill and 0.40 µm filter	0.5	67
E24	distill and 0.22 µm filter	0.1	86

The data in table 2 show a clear correlation between decreasing filter pore-size, significantly decreased dust content, and significantly increased single-shot damage thresholds. When combined with the results of reference 5 that distillation alone can significantly raise the damage threshold of PMMA, these results provide strong evidence that micropore filtration can significantly reduce dust and raise the single-shot damage threshold beyond, i.e., in addition to, the level of improvement possible with distillation alone.

Multiple-shot damage measurements on the three samples of table 2 were begun, too, but an analysis of the data showed that it was insufficient for any firm conclusions to be drawn for inclusion in this report.

6. The Effects of Polymerization Method on Damage Thresholds in PMMA

Table 3 presents a summary of the single- and multiple-shot damage thresholds and dust contents for 9 samples of PMMA. They were chosen for their low and very similar dust contents, and are listed in increasing order of their single-shot damage thresholds. Clearly, the UV-polymerized samples were superior in that regard. To explain this, the samples were carefully

examined with a 100x microscope. The thermally polymerized samples all contained flaws, not seen in any of the UV-polymerized samples, that range in size up to approximately 100 μm. We suspect that these flaws act as the nuclei of damage sites, thereby reducing thresholds. The flaws may be vapor bubbles that become generated and trapped in the viscous mixture of monomer and polymer while the reaction proceeds at the 40°C bath temperature. During UV-polymerization, the medium is much cooler (approximately 30°C) and therefore less likely to bubble.

The multiple-shot damage threshold was defined as the fluence level with a 50% probability of causing damage to a given site within 250 shots. F/F_{TH} is the ratio of the peak fluence for the multiple-shot damage to peak fluence for the single-shot damage threshold. Table 3 contains data for two pulse repetition frequencies, 1 pps and 10 pps. Unlike the single-shot data, the multiple-shot data favor neither of the polymerization methods.

Sample R-3 is unusual in that the multiple-shot damage resistance is very high. R-3 was the only sample prepared in a vacuum using the multiple distillation technique of reference 4. The reasons for its high multiple-shot damage thresholds are unclear and require further study.

Table 3. Comparison of the Damage Resistance of Several PMMA Samples

Sample	Polymerization Method	F_{TH}	F/F_{TH} at 1 pps	F/F_{TH} at 10 pps	Dust Content (Particles (mm^3))
S-47	thermal	44	0.22	0.20	0.6
S-46	thermal	48	-	0.1	0.9
S-43	thermal	49	-	0.5	1.7
E-9	uv	54	-	<0.01	1.1
R-3	uv	57	0.75	0.61	<0.1
E-6	uv	62	-	0.1	0.5
E-22	uv	67	-	-	0.5
E-5	uv	79	-	<0.01	1.4
E-24	uv	86	0.2	0.21	0.1

7. The Effects of Plasticization on the Single-Shot Damage Thresholds of PMMA and PEMA

It has been asserted[8] that plasticization should improve a material's laser damage resistance by allowing the relief of thermoelastic stresses. Supposedly, plasticization should be especially useful in the case of low fluence level, multiple-shot damage, which is very important from an applications point of view. Since no domestic research in this area had been reported to date, the initiation of such was recently established as part of the FJSRL plastics damage program. In this report we present the results of measurements on PMMA and PEMA. Three samples of each were plasticized with 0, 5, and 10 weight percent dibutyl phthalate, respectively, and UV polymerized as described in section 2. The maximum plasticizer content was limited to 10 weight percent because plasticizers are known to reduce glass transition temperatures rather sharply[9], and a material whose glass transition temperature is near room temperature would not have the desirable thermal and mechanical properties mentioned above.

Damage tests on the PMMA and PEMA samples were performed exactly as described in the filtration study of section 5. LSF straight lines were fit to single-shot damage statistics, and damage thresholds were obtained from the midpoints of the LSF lines. Table 3 lists the six samples tested, their single-shot damage thresholds, and their respective dust contents as determined with the depolarized scattered light scheme.

The relatively high dust contents of the samples in table 4 as compared to those in table 2 is probably because the samples in table 4 were not micropore-filtered before polymerization. Despite the high dust contents, the data in table 3 allow an interesting observation to be made. Whereas the plasticized materials all had significantly higher dust contents than their unplasticized counterparts, their thresholds were not significantly lower.

Table 4. Dust Content and Single-Shot Damage Thresholds of PMMA and PEMA in the Plasticization Study

Sample	Description	Dust Content (Particles/mm^3)	Single-Shot Damage Threshold (J/cm^2)
RO-1	PMMA	20.0	32
RO-2	PMMA + 5% DBP	37.1	29
RO-3	PMMA + 10% DBP	31.4	32
RO-8	PEMA	72.9	19
RO-9	PEMA + 5% DBP	96.6	17
RO-10	PEMA + 10% DBP	97.7	17

For example, sample RO-3 contained more than 50% more dust than RO-1, but their single-shot damage thresholds were identical. Using the results from reference 5 and section 5 above that damage thresholds are always inversely correlated with dust content, the results here suggest that plasticization can significantly increase single-shot damage thresholds. Because the dust contents and damage thresholds of unplasticized PMMA and PEMA were so different, no valid comparison of the single-shot behavior of the two materials can be made with the data in table 3.

Preliminary multiple-shot damage measurements were also made on the six samples in table 3. Whereas the PMMA samples showed virtually no plasticizer-dependent multiple-shot behavior, the plasticized PEMA was somewhat more damage resistant than its unplasticized counterpart. No strong conclusion can be drawn, however, because of the differences in dust content. To study the effects of plasticizer alone, both the unplasticized and plasticized samples would have to have identical, or at least similar, dust contents. Table 3 shows that such was not the case here.

8. Multiple-Shot Data Analysis

The multiple-shot threshold measurements were conducted, as described earlier (section 6), in such a way that the shot number at which damage was first detected was recorded. Survival curves were then compiled from that data for the arbitrarily selected values of 10, 20, 30, 50, 100, and 200 shots. A least-squares fit of a straight line through the data for each case yielded the 50% probability point, analogous to the reported single-shot threshold. Sample data for 1 pps irradiation are shown in figures 5 and 6.
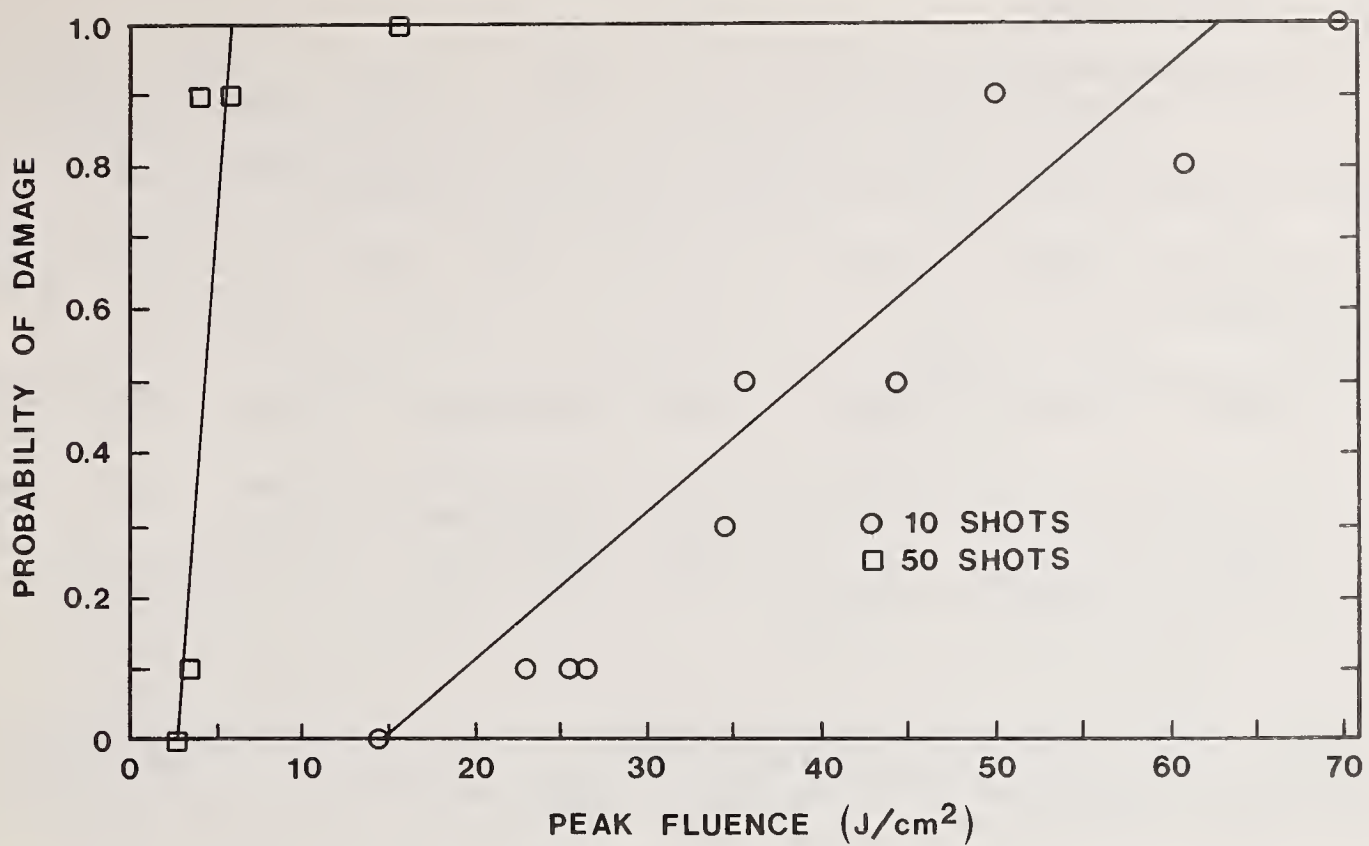
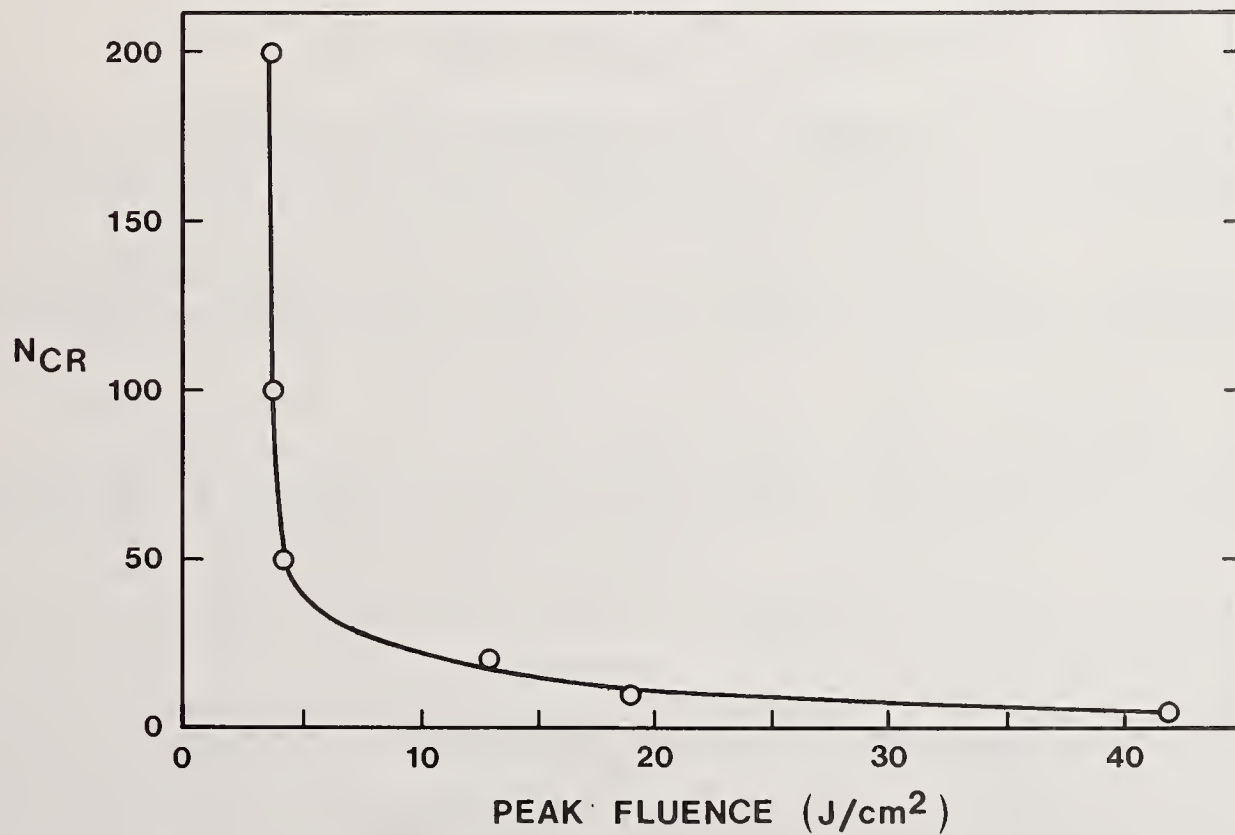Figure 5. Multiple-shot damage data for a typical sample.

Figure 6. Plot of N_{CR} versus peak fluence for the same sample as in figure 5. Fluence plotted for each N_{CR} is that value of peak fluence at which the probability of damage is 0.5.

9. Summary and Conclusions

1. The scattered depolarized helium-neon laser scheme is a simple yet reliable indicator of a sample's micron-sized impurity content and prediction of its single-shot damage resistance.

2. Micropore filtration of distilled monomer before UV-initiated polymerization can improve the single-shot damage threshold beyond the level possible with distillation alone.

3. UV-initiated PMMA is generally more single-shot damage-resistant than thermally polymerized PMMA, presumably due to the presence of fewer thermally generated voids in the UV-initiated material.

4. PEMA samples had good mechanical and optical properties, but relatively large dust content and, consequently, relatively low damage resistance. Further study is needed.

5. Plasticization of PMMA and PEMA with DBP can improve their single-shot damage resistance. This result and the effects on multiple-shot behavior both need further study.

6. Although UV-initiated PCHMA polymerized slightly cloudy, it was hard, odorless and bubble-free, thereby warranting further work.

10. References

[1] O'Connell, R.M., Deaton, T.F. and Saito, T.T., "Single- and Multiple-Shot Laser-Damage Properties of Commercial Grade PMMA," Appl. Opt. 23(5), 682 (1984).

[2] O'Connell, R.M., Saito, T.T., Deaton, T.F., Siegenthaler, K.E., McNally, J.J., and Shaffer, A.A., "Laser Damage in Plastics at the F.J. Seiler Research Laboratory (FJSRL)," in Proceedings of the 15th Annual Symposium on Optical Materials for High Power Lasers, Boulder, CO, 14-16 Nov 83.

[3] Mullins, B.W., and Richert, B.A., "Strehl Ratio Measurements of Laser Damaged Plastics," in Proceedings of the 15th Annual Symposium on Optical Materials for High Power Lasers, Boulder, CO, 14-16 Nov 83.

[4] Aardsma, G. and Stevens, J.R., "Preparation of Clean Polymers for Rayleigh-Brillouin Light Scattering Studies," Appl. Polym. Sci. 23, 2533 (1979).

[5] O'Connell, R.M., Romberger, A.B., Shaffer, A.A., Saito, T.T., Deaton, T.F., and Siegenthaler, K.E., "Improved Laser-Damage-Resistant Polymethylmthacrylate," J. Opt. Soc. Am. B. 1(6), 853 (1984).

[6] Waxler, R.M., Horowitz, D., and Feldman, A., "Optical and Physical Parameters of Plexiglas 55 and Lexan," Appl. Opt. 18(1), 101 (1979).

[7] Akhmanov, S.A., Krindach, D.P., Migulin, A.V., Sukhorokov, A.P., and Khokhlov, R.V., "Thermal Self-Action of Laser Beams," IEEE J. Quantum Electron., QE-4(10), 568 (1968).

[8] Adoshin, M.I., Gerasimov, B.G., Manenkov, A.A., and Nechitailo, V.S., "Decisive Importance of the Viscoelastic Properties of Polymers in their Laser Damage Mechanism," Sov. J. Quantum Electron. 9(9), 1102 (1979).

[9] Bruins, P.F., Plasticizer Technology, Reinhold, New York, 1965.

LEED ANALYSIS OF PULSED LASER DAMAGE TO Mo(100) SURFACES

Aubrey L. Helms, Jr., Chih-Chen Cho, and Steven L. Bernasek

Department of Chemistry, Frick Chemical Laboratory, Princeton University, Princeton, NJ 08544

Low Energy Electron Diffraction (LEED) and Auger Electron Spectroscopy (AES) have been used to investigate the effect of Q-switched, frequency doubled Nd:YAG laser pulses on the surface structure and composition of Mo(100). The experiments were conducted in a special ultra-high vacuum (UHV) chamber which allowed the characterized surfaces to be irradiated in an UHV environment. Good epitaxial regrowth of the Mo(100) surface was observed after laser surface melting as evidenced by LEED. Changes in the spot profiles and their dependence on incident electron energy after irradiation suggest the incorporation of defects and the formation of random islands on the surface. The study included laser fluences both above and below the melt threshold of the surface. Additionally, the annealing action of laser pulses on surfaces that had been heavily damaged by Ar^+ ion bombardment was investigated.

Key Words: dislocations, LEED, molybdenum, pulsed laser damage, Q-switched laser

INTRODUCTION

The demand for better materials for use in high power laser systems has grown dramatically in the past few years. With the development of high power laser systems, one has to consider the damage introduced in the materials used in these systems. This has been the topic of many studies presented in the proceedings of this conference. The peak power attained in such a system depends heavily on the thresholds for different types of damage in the components. (1) Typical responses of metals to pulsed laser irradiation are slip (2), crater formation (3), pitting, dislocation motion and multiplication (4), and increased vacancy concentration (5). The optical properties and response of the metal to laser irradiation are sensitive to the condition of the surface. This study investigated the response of Mo(100) single crystals to pulsed laser irradiation.

The development of spot profile analysis (SPA) applied to LEED has made the use of this technique to study defect structures on surfaces possible (6-10). Careful analysis of the angular profile of the LEED spot in reciprocal space as a function of incident electron energy allows a qualitative determination of the structure of the surface. The technique is very surface sensitive, probing only the top few atomic layers of the surface. It allows the distinction of random point defects, ordered terraces, ordered islands, random islands, and facets (9).

LEED-SPA, AES, Rutherford Backscattering Spectrometry (RBS), and Nomarski Interference Contrast Microscopy have been used to characterize the response of Mo(100) single crystals to pulsed laser irradiation at laser fluences both above and below the visible melt threshold. The use of LEED has been shown to be very sensitive to the introduction of disorder. The results indicate that random islands form on the surface after pulse laser irradiation, even at laser fluences below the melt threshold. These islands coalesce back toward the flat surface after long periods of heating at 1000°C. A sample which had been disordered by Ar^+ ion implantation was annealed by pulsed laser irradiation in a manner similar to the laser annealing of silicon (11). The LEED analysis indicates random island formation in the irradiated region of this sample.

EXPERIMENTAL

The samples were cut from a single crystal boule oriented to within 1° of the (100) face by means of the back reflection Laue method. Standard metallographic techniques were employed to obtain a mirror finish. The crystals were spot welded to thin tantalum foils which were mounted on a special transfer block. The sample was heated by thermal conduction from the tantalum foil which

could be resistively heated. The temperature was monitored using an optical pyrometer focussed on the sample through an 8" viewport at the front of the system. Sample temperatures in excess of 1000°C were routinely used for cleaning and annealing purposes.

The experiments were conducted in a conventional ion pumped UHV chamber with additional pumping supplied by a titanium sublimation pump and liquid nitrogen cryotrap (Fig. 1). The base pressure of the system was less than 2.0×10^{-10} torr. The chamber was equipped with standard 4-grid LEED optics, a cylindrical mirror analyzer (CMA) for AES, a quadrupole mass-spectrometer for residual gas analysis, a 3 KeV ion gun for Ar^+ sputtering and a variable leak valve.
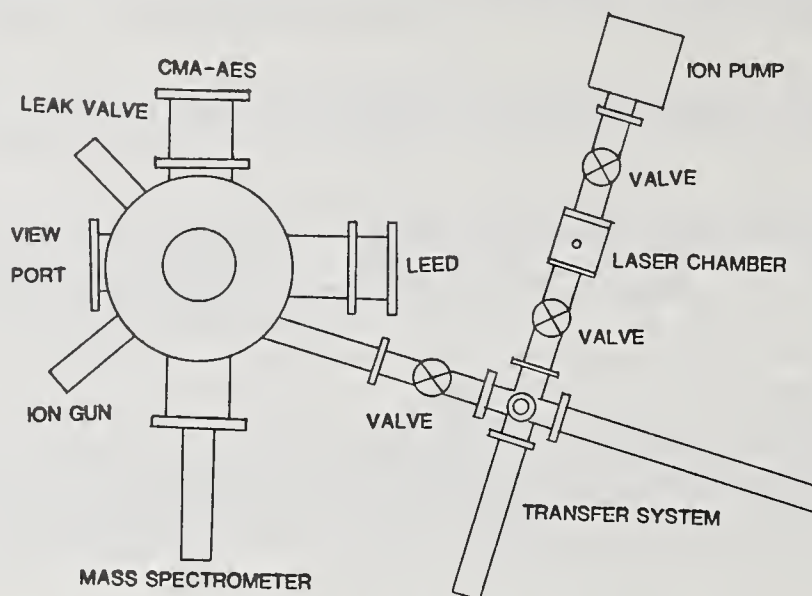

Figure 1. Schematic of the experimental apparatus showing the main chamber, transfer system, and laser chamber.

Attached to the main system was a small UHV laser chamber and associated transfer systems. This chamber could be isolated from the main chamber by means of high vacuum valves. The laser chamber was independently pumped by a 20 l/s ion pump. A detailed description of the design and capabilities of the laser chamber and its associated transfer system will appear elsewhere (12).

Briefly, the samples were cleaned and characterized in the main chamber and then transferred to the laser chamber under UHV conditions. The laser chamber was then detached from the transfer system and transported to AT & T Technologies Engineering Research Center where the samples were pulse laser irradiated. The system was then transported back to Princeton where the sample was transferred back to the main chamber for analysis. UHV conditions were maintained throughout the experiment.

The laser system used for these studies was a Q-switched, frequency doubled Nd:YAG that is part of an ESI laser trimming system. The laser was typically operated at a repetition rate of 5 KHz with a pulse width of 140 nsec. The spot diameter was approximately 25 microns. To ensure complete coverage of the surface, the beam was rastered across the surface by means of computer controlled linear induction motors. Parameters such as raster speed, displacement, and the coordinates of the spot pattern were chosen to guarantee good spot-to-spot overlap. The top half of the crystal was irradiated, leaving the bottom for in situ comparison. To further ensure uniform modification, the process was repeated five times.

Samples were pulsed laser irradiated under three different conditions. One sample was irra-diated at 15 MW/cm^2, which was below the threshold for surface melting as defined by the appearance of a crater. This sample will be designated as 'Sample A' in the following discussion. A second sample was irradiated at 60 MW/cm^2 which was well above the threshold for crater formation. This sample will be designated as 'Sample B'. The third sample was a sample that had been Ar^+ bombarded

at 3 KeV in 1.0×10^{-6} torr Ar for one hour. This bombardment produced a disordered surface as evi-denced by the absence of a LEED pattern. This sample was laser irradiated at a laser fluence of 75 MW/cm^2 and will be designated as 'Sample C'.

The LEED patterns were photographed using a 35 mm camera mounted in front of the 8" viewport. The negatives were then evaluated using a computer interfaced Vidicon camera system described pre-viously (13). The data obtained with this system included the spot profile, spot to spot distance, and relative intensity between the spot and the background. The photographic technique provides a permanent record of the experiment while allowing the collection of a large amount of data in a very

short time. This ensures that the system will change very little in the course of the data collection.

The composition of the surface was monitored using AES. Great care was taken to make certain that the conditions for taking the spectra remained constant. The surface concentrations of carbon, sulfur, and oxygen were calculated by evaluating the ratio of the peak-to-peak heights of these elements to the peak-to-peak height of the Mo-220 eV transition. The ratios could then be compared with literature values to give concentrations in units of monolayers (14). Additional calibrations could be obtained in the case where a clear overlayer structure was observed in the LEED pattern.

The typical procedure involved characterizing the surface using both AES and LEED followed by transfer and laser irradiation. After the sample was returned to the main chamber, AES was used to determine compositional differences in the laser irradiated versus the virgin areas of the crystal. The sample was then heated to 1000°C for two minutes to desorb contamination accumulated during transfer and laser irradiation. Photographic data was taken as a function of incident electron energy for both the laser irradiated and virgin areas. Sequences of heating, AES, and LEED were repeated to a total accumulated heating time of three hours.

The analysis was accomplished by comparing the spot profile and trends with the work of Henzler, Lagally, and others (6-10). By restricting the study to the spot profiles and neglecting the use of integral intensities, they have calculated the expected diffraction profiles for a variety of surface defect structures within the kinematical approximation. Figure 2 summarizes the profiles expected from a variety of defect structures (9). The results to be described in the following section were compared with their calculations, thus indicating the surface structure resulting from pulsed laser irradiation under a variety of experimental conditions.
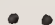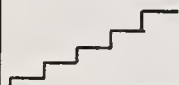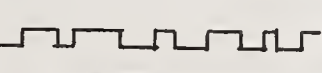
information extracted from LEED spots			
spot shape	spot profile	surface structure	
•		————————————	ideal surface
• •	O		regular steps
●	FWHM		random steps
◉	R		regular size islands or regular distance
●	FWHM		random size and distance islands

Figure 2. Table from Gronwald and Henzler (9) summarizing the information available from LEED-SPA.

RESULTS

The results for samples A and B were similar and can be described simultaneously. The levels of carbon and oxygen were observed to increase on both the virgin and laser irradiated surfaces as evidenced by AES. The level of these contaminants were higher on the virgin area indicating that the process of laser induced desorption was active in the laser irradiated region. The levels of contamination on both surfaces dropped to the pre-irradiated values after heating the sample to 1000°C for two minutes.

A distinct LEED pattern was observed in both the virgin and laser irradiated regions of both samples. The geometry of the pattern was consistent with the expected (100) orientation. The pattern for the virgin surfaces were visually sharper with a lower background and higher spot intensities than the pattern observed for the irradiated regions. The appearance of the LEED pattern on the irradiated region of sample B indicates that the melt puddle regrew epitaxially on the (100) substrate.

Photographic analysis of the data indicated that in each case, the half-width of the the angular profiles for the irradiated regions were greater than that for the virgin areas (Fig. 3) indicating the incorporation of surface disorder in the irradiated regions.

61
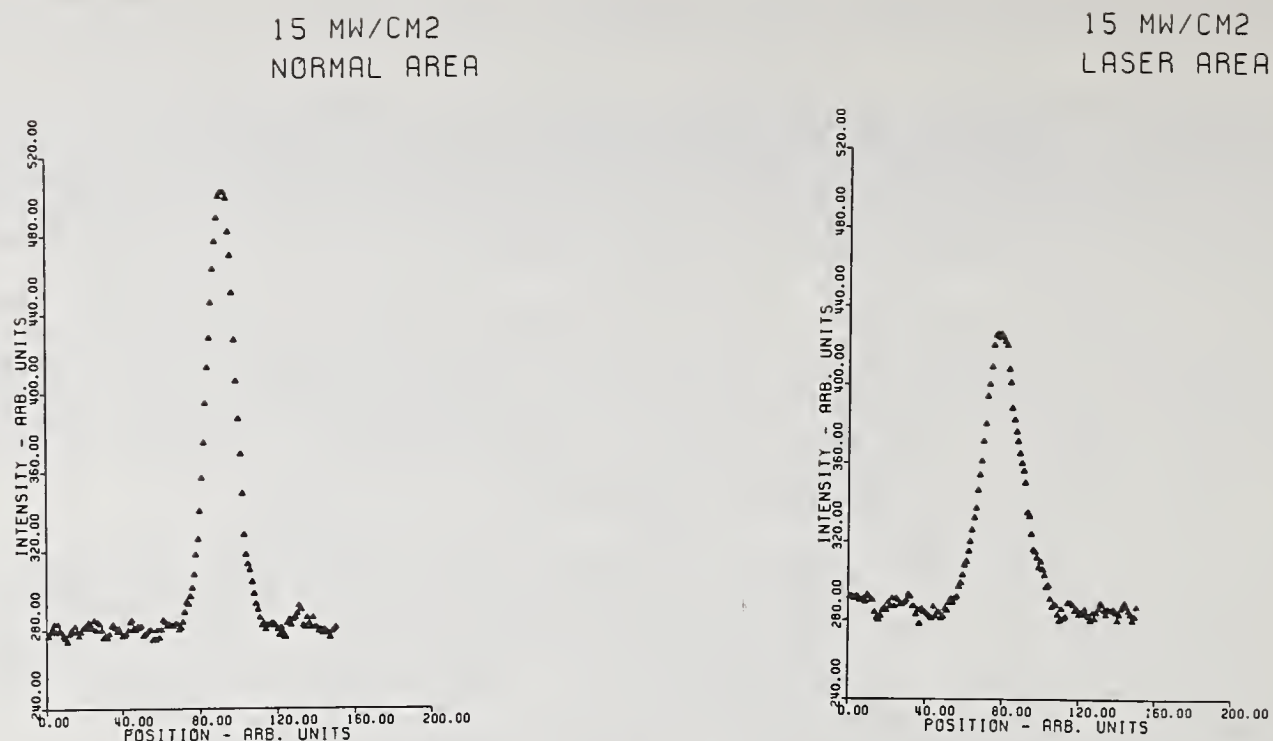
Figure 3. A plot of intensity versus position for typical spot profiles from both the virgin and irradiated regions of sample A.

A plot of relative half-width versus incident electron energy for first-order spots in the irradiated regions showed an oscillatory behavior indicating the formation of stepped structures on the surfaces (9) (Fig 4).
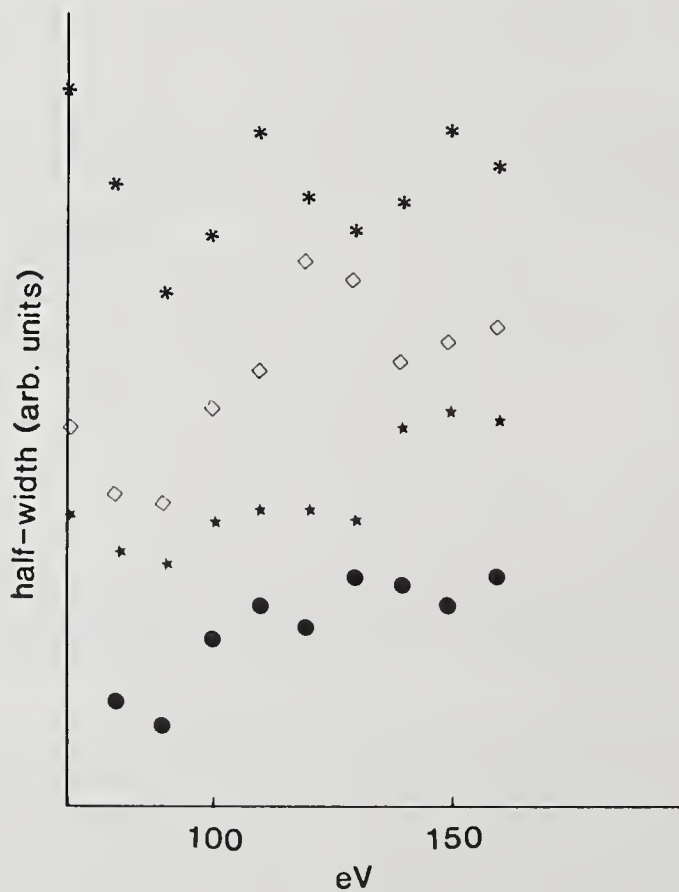
Figure 4. A plot of relative half-width (half-width divided by the intensity) versus incident electron energy for several heating times. (✳) 5 minutes, (◇) 20 minutes, (★) 35 minutes, (●) 80 minutes.

The amplitude and frequency of the oscillations decreased as a function of heating time as the defect structures coalesced into a flat surface.

Careful analysis of the shape of the spots indicated that the spots in the irradiated regions contained 'shoulders' which were aligned along the <010> and <001> directions indicating the orientation of terrace edges along the major crystallographic directions (Fig. 5).
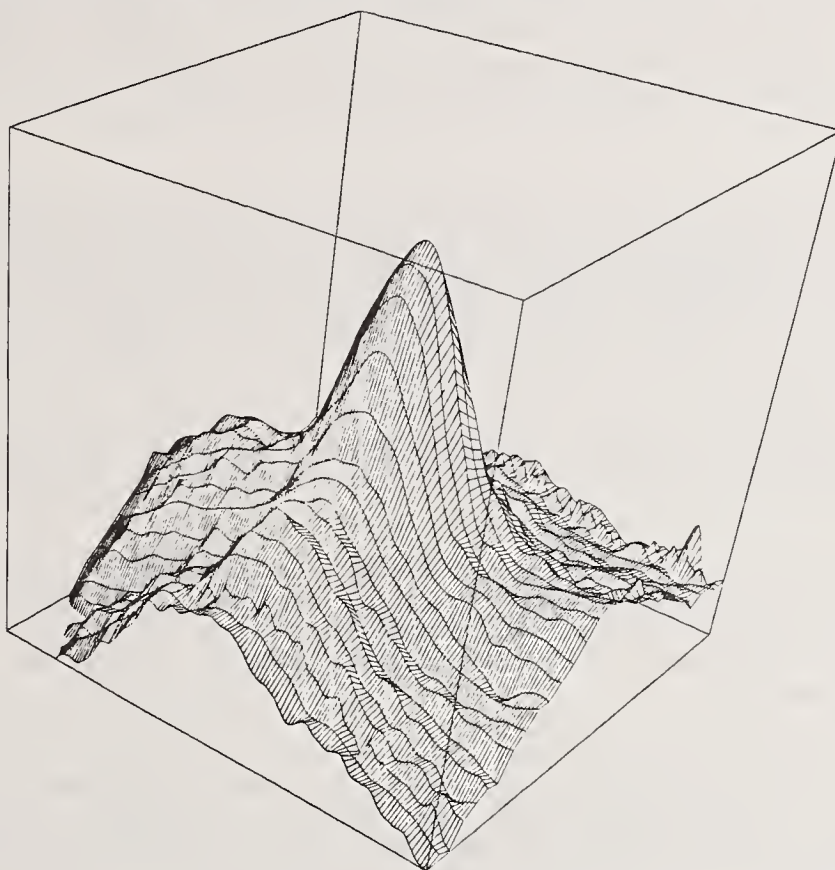
Figure 5. A plot of intensity versus position for a spot in the irradiated region of sample B.

Both the half-width and the prominence of the shoulders were observed to decrease as a function of heating time, again, an indication of the annealing of the surface defect structures.

The LEED patterns in the laser irradiated regions were slightly expanded relative to the patterns for the virgin areas as evidenced by an increase in the spot-to-spot distance. The expansion was 3.4% for sample A and 7.7% for sample B. The expansion was isotropic and was determined not to be an experimental artifact due to sample positioning or errors in incident electron energy. The difference in the patterns indicates that the irradiated surfaces are slightly contracted parallel to the surface in real space relative to the normal regions.

The carbon and oxygen contamination levels for sample C followed the same trends observed for the other two samples. A LEED pattern was observed in the irradiated region and not observed for the virgin area. This indicates that the melted region extended beyond the damage range and then underwent liquid phase epitaxial regrowth. A very poor LEED pattern was observed for the virgin area after a heating time of seven minutes and remained more diffuse than the pattern for the irradiated area throughout the experiment. The half-widths of the LEED spots from the irradiated region were smaller than the half-widths of the LEED for spots in the virgin region indicating that the

laser had annealed some of the disorder introduced by the ion bombardment. The irradiated region was still damaged relative to the well annealed single crystal before Ar^+ implantation. The half-width of the spots in both regions decreased as a function of heating time.

DISCUSSION

The increase in the levels of carbon and oxygen on the sample after the transfer and laser irradiation is due to the adsorption of residual gases on the surface. The conductance of the valve that separates the 20 1/s ion pump from the laser chamber is very small. The base pressure in this chamber is on the order of 1.0×10^{-8} torr. At these pressures many monolayers of gas will be incident on the surface in the time required for the experiment. The lower levels observed on the irra-

63

diated region indicate that the surface was cleaned by laser induced desorption. The features observed in the LEED pattern cannot be attributed to this difference in absorbate concentrations because the carbon and oxygen levels in both regions decreased to values equal to the pre-irradiated surface after a short heating to 1000°C.

The craters observed on samples B and C with Nomarski Interference Contrast Microscopy are clear indications that the surface has melted. The appearance of a LEED pattern for the irradiated regions of these two surfaces implies that epitaxial regrowth took place during the solidification phase. The geometry of the pattern is consistent with that of the (100) substrate. The epitaxial regrowth is further evidenced by the low backscattered yield observed in the channeling spectra. Nomarski Interference Contrast Microscopy showed that the irradiated surface of sample A was visually identical to the virgin region indicating that the surface had not melted.

By carefully applying the principles of LEED-SPA, it is possible to derive information about the morphology and defect structure of the surface from the shape and energy dependence of the LEED spots. The technique is very sensitive and allows the investigation of the defect structure introduced at laser fluences well below the melt threshold of the surface. The increased half-width and decrease in intensity of the spots from the irradiated region of samples A and B is an indication of an increase in disorder (8). The half-width oscillated as a function of incident electron energy which indicates the formation of steps on the surface. The spot profiles show sharp central spikes with broad shoulders. This profile is typical of that expected for a surface with a random distribution of randomly sized islands. These shoulders are aligned along the major crystallographic directions, implying that the edges of the islands are aligned along the major crystallographic directions.

The half-width of a first-order spot was followed as a function of heating time. The half-width decreased as a function of heating time which is consistent with the coalescence of these multi-tiered islands into a flat surface. The trends observed in samples A and B were similar implying that the features observed in the LEED patterns were not simply due to the macroscopic roughness of the melted surface.

The appearance of a LEED pattern for the irradiated region of sample C indicates that the surface melted to a depth below the disordered region to the good single crystal below. As the melt solidified, liquid phase epitaxial regrowth was nucleated on the single crystal substrate and resulted in an annealing of the surface. Although the crystalline quality was better than the disordered, implanted region, the irradiated region still contained many defects and damage relative to the well annealed surface prior to implantation. The spot profiles were similar to those observed for samples A and B indicating the formation of random islands. The profiles differed in the fact that the shoulders were not aligned in the crystallographic directions, but were circularly symmetric. The symmetry of the shoulders implies that the preferential orientation of the edges of the islands formed on this sample is not as strong as in the other two samples.

It has been shown previously that the damage introduced in metals after pulsed laser melting is in the form of dislocation networks and vacancies (15). The damage is introduced by thermal stresses introduced by the temperature gradients created by the absorbtion of the laser pulse. When these stresses exceed the yield point for plastic deformation, the sample is irreversibly damaged. It has been shown for the case of copper that this yield point can be reached for very small temperature excursions at the surface, on the order of 20°C (16). The deformation occurs through a mechanism involving dislocation motion and multiplication which sometimes results in the formation of slip lines on the surface.

The disorder and island formation in sample A may be due to the motion of dislocations caused by the stress introduced when the hot surface under the laser beam expands against the cold bulk material. The movement of a dislocation to the surface results in the formation of a ledge. The slip systems in body centered cubic metals are not as well defined as in face centered cubic systems which may explain the lack of slip lines on the surface and the formation of randomly sized islands.

The disorder and island formation in samples B and C must be due to stresses introduced during the solidification of the melt puddle because the liquid cannot support shear or tensile stresses. These two samples probably also contain a large number of vacancies. The mechanism for island formation on these samples is the same as for sample A. The magnitude of the damage is greater because the temperatures are higher and the introduced stresses greater.

CONCLUSIONS

The method of LEED-SPA has been successfully applied in the investigation of the response of Mo(100) to pulsed laser irradiation. It has been shown that this method is sensitive to surface disorder introduced by laser fluences ranging from below the melt threshold to fluences where deep

cratering of the surface is observed. The behavior of the half-width as a function of incident electron energy and the profile of the spots after irradiation indicate the formation of multi-tiered, randomly sized, randomly distributed islands on the surface with their edges aligned along the major crystallographic axes. The appearance of a sharp LEED pattern in the irradiated region of a sample which had been previously disordered by 3 KeV Ar^+ ion bombardment indicates that the melt extended beyond the disordered region and underwent liquid phase epitaxial regrowth resulting in an ordered surface. The expansion of the LEED pattern is an indication of a contraction parallel to the surface of the laser irradiated surface in real space.

REFERENCES

1. J.O. Porteus, D.L. Decker, J.L. Jernigan, W.N. Faith, and M. Bass, IEEE J. of Quantum Electronics, QE-14, 776 (1978).
2. J.O. Porteus, M.J. Soileau, and C.W. Fountain, Appl. Phys. Lett., 29, 156 (1976).
3. M.K. Chun, and K. Rose, J. of Appl. Phys., 41, 614 (1970).
4. F. Haessner, and W. Seitz, J. of Mat. Sci., 6, 16 (1971).
5. S.A. Metz, and F.A. Smidt, Jr., Appl. Phys. Lett., 19, 207 (1971).

6. M. Henzler, Appl. Surf. Sci., 11/12, 450 (1982).
7. M. Lagally, Appl. Surf. Sci., 13, 260 (1982).
8. M. Henzler in ELECTRON SPECTROSCOPY FOR SURFACE ANALYSIS, Ibach ed., (Springer, Berlin, 1977), ch. 4.
9. K.D. Gronwald, and M. Henzler, Surf. Sci., 117, 180 (1982).
10. J.F. Houston, and R.L. Park, Surf. Sci., 21, 209 (1970).
11. G. Foti, and E. Rimini in LASER ANNEALING OF SEMICONDUCTORS, Poate, and Mayer eds., (Academic, New York, 1982), ch. 7.
12. A.L. Helms, Jr., W.A. Schiedt, B.M. Biwer, and S.L. Bernasek, to be published.
13. T.N. Tommet, G.B. Olszewski, P.A. Chadwick, and S.L. Bernasek, Rev. Sci. Instrum., 50, 147 (1979).
14. M. Salmeron, G.A. Somorjai, and R.R. Chianelli, Surf. Sci., 127, 526 (1983).
15. L. Buene, E.N. Kaufmann, C.M. Preece, and C.W. Draper in LASER AND ELECTRON-BEAM SOLID INTERACTIONS AND MATERIALS PROCESSING, Gibbons, Hess, and Sigmon eds., (Elsevier North Holland, New York, 1981), pp. 591.
16. H.M. Musal, Jr., Symp. on Optical Materials for High Power Lasers, Boulder, (1979).

The Effect of Defects on the Laser Damage Performance of Metal Mirror Surfaces*

H. H. Hurt

Michelson Laboratory, Physics Division
Naval Weapons Center, China Lake, California 93555-6001

From a laser damage standpoint, the optical surface is not isotropic as evidenced by the selected area damage phenomenon. This is because the modern processes that generate specular surfaces and coatings inherently introduce defects and damage into the bulk material. These defects then act as preferential sites for the onset of laser damage, and the distribution of these defects appears to affect almost all laser damage parameters. This paper presents the development of high resolution electron microscopy methods to identify deleterious imperfections in typical metal-mirror surfaces. Pulsed-laser damage testing of identical surfaces shows systematic changes in the damage resistance of the material that can be correlated directly to defects in the near-surface region. By this method, it is possible to identify trace impurities that are deleterious to high fluence optical components. In addition, one can now specify process parameters that will control not only surface roughness and figure, but will also control laser damage resistance.

Key words: defects; diamond turning; laser damage; optical materials.

Introduction

The study of the optical properties of metal-mirror surfaces has been extensive [1].[1] From these studies it has been apparent that the surface finishing method changes both the reflectance of the surface and its laser damage resistance. Copper mirrors that are diamond turned, for example, have higher reflectance and damage thresholds than conventionally polished copper surfaces [2]. It is also known that changing the machining conditions of the diamond-turning process changes the laser damage resistance. The selected area damage phenomenon is also related to the process parameters. These empirical data suggest that the performance of these optical surfaces is directly tied to the state of the mirror material in the near-surface region that "sees" the incident radiation.

Through the process of generating the mirror surface, damage and disorder have been introduced into the starting material. The amount and type of damage are dependent on the mechanical/chemical finishing conditions and are caused by the forces exerted on the surface, heat generated, and chemical reactions with the fresh surface. Trace impurities in the mirror base material can also be a problem as they tend to collect at sinks such as grain boundaries so that concentrations are sufficient to act as nucleation sites for laser damage.

Consider that an optical component is designed to meet a wide range of environmental, structural, and optical requirements in addition to laser damage resistance. Except for electronic materials, defects are not necessarily bad. Defects can give strength, fatigue resistance, corrosion resistance, and other desirable properties. The control and manipulation of defects in engineering materials has been important since ancient times and is the basis for many modern manufacturing processes. Science has unraveled the secret behind the medieval swordmaker who forged a blade that had both great strength and good impact resistance. It was not a piece of single-crystal iron, but had a very high point defect concentration. In this investigation, the role of defects in optical materials is explored to reach the same type of goal: higher laser damage threshold.

Small-Spot Laser Damage Testing of Diamond-Turned Surfaces

Copper mirror surfaces were fabricated on the Naval Weapons Center's (NWC) advanced diamond-turning machine under highly controlled conditions to ensure correlation of data as the machining conditions were altered to change the surface structure. The mirror blanks were 1.5-in.-diameter OFHC copper.

Several of the blanks were overplated with fine grained UBAC copper that was subsequently diamond machined. The UBAC copper machines better than the softer OFHC copper, and it is popular as a diamond-machinable cladding for heat exchanger structures. The machining conditions are those that are known to produce the best optical surfaces. Previous studies have shown a large difference in the IR reflectance and the microstructure of the diamond-turned surface as the tool rake angle is made more negative [1,3]. Therefore, the OFHC surfaces were machined at two different rake settings.

The laser damage behavior of the metal-mirror surfaces was then determined using the NWC automated pulsed-laser damage facility. Details on the design and function of this facility are included in another paper in these proceedings [4]. A 10.6 μm CO_2 TEA laser with a pulse length of 100 ns was employed. The $1/e^2$ spot size on the sample was 250 μm. A nominal vacuum of 250 microns was achieved using a roughing pump on the sample chamber. Several hundred irradiation sites were needed per sample to generate valid statistical data for the the plotting of damage-probability curves. The use of a HeNe scatter probe to detect which irradiation sites had failed was successful in detecting melt and selective damage. Unfortunately, the surface roughening caused by microslip was below the detection level of the scatter probe device. This necessitated the laborious inspection of each irradiation site with a Nomarski phase interference microscope.

The other part of this investigation involved looking at the laser damage with electron microscopy methods. To do this, specialized 3-mm-diameter by 0.010-in.-thick copper disks were prepared from the mirror base materials. These small disks were then diamond machined in a manner identical to the larger laser damage test mirrors. The small mirror disks were loaded into a holder in the laser damage test chamber and then irradiated at fluence levels to cause damage. By carefully electropolishing the disks from the backside, electron transparent regions of 500 to 1000 Å thickness could be produced in the damage areas. Since the surface was untouched by the thinning operation, microtopography changes that accompany the microstructural changes caused by the laser damage were easily correlated in the electron microscope.

The electron microscopy was performed on a Phillips EM 420T located at the University of Southern California, Center for Electron Microscopy and Microanalysis. The capabilities of the instrument utilized in this investigation included transmission electron microscopy (TEM), scanning electron microscopy (SEM), and energy dispersive X-ray analysis (EDX).

Laser Damage Test Results

A plot for the melt thresholds for the diamond-turned copper surfaces is shown in figure 1. The two characteristics in this plot are the steep rise in damage frequency that characterizes the bulk damage threshold and the low-damage frequency "tail" that extends to very low fluences. These two parts of the curve correspond to two different damage types. The bulk damage is characterized by a large melt pool, while the salient characteristics of melt damage at the lower fluences are small melt pits that do not correspond to the intensity maximum of the laser beam. What this means is that the defects that fail at the lower fluences are widely distributed in comparison to the 250-m spot size. What is important is the realization that if this test was scaled up to large spot size, the optic would always damage at a very low fluence.

As demonstrated in an earlier study, the -15-deg rake surface has a much higher bulk damage threshold than the -5-deg surface [1]. The electroplated UBAC coating falls approximately in the middle. Strangely, the -5-deg rake surface showed no selective damage behavior. As will be shown, this selective damage phenomenon is linked with impurities in the base material and the -5-deg machined mirror may have come from different parent material.

Microslip is the other damage characteristic of metal-mirror surfaces and is displayed in figure 2. Slip is visually defined as a roughening of the surface that is not characterized by surface tension delineations that accompany melting. At higher fluences, slip is very evident. At the lower fluences, the detection of slip in the Nomarski microscope is very subjective. It is best accomplished by rotating the sample so that the periodic structure of the diamond-machining grooves disappears. It can be seen from the graph that the onset of slip is very steep but shows some slope. This is caused by the fact that the yield strength of copper is very anisotropic, and the orientation of the grains with relation to the surface determines the resistance of slip.

The data in figure 2 shows that the fine grain size of the electroplated UBAC copper results in a more slip-resistant surface. Surprisingly, the OFHC surfaces do not follow the inverse relationship between slip and melt. This relationship was determined in earlier testing of a variety of copper surfaces and showed that a surface that had a higher melt threshold necessarily had a lower slip threshold [1]. The highest melt threshold surface -- an electropolished single crystal -- was so soft that its yield stress was low; therefore, the slip threshold was at very low fluence. A diamond-turned surface, by comparison, was much more slip resistant because of its harder, deformed surface. The results of this study do not agree with the earlier observations. The -15-deg rake surface is superior in both melt and slip performance to the -5-deg rake surface. This is not an artifact of the

testing procedure but is the result of surface microstructure modification when machining at high negative rake angles.

Electron Microscopy of the Laser Damage Sites

In the electron microscopy study, the main concern was identifying the causes of the selective damage. The bulk structure of the diamond-turned surfaces has been investigated and reported on in last year's conference [3]. The study showed that the -5-deg rake surface was highly deformed in the near-surface region. The -15-deg rake surface structure was very interesting, as the top surface layer had recrystallized during machining. The resulting structure then had a low defect, high reflectance outermost layer backed by a strong, highly deformed base. The surface microstructure can explain the bulk melting behavior of these surfaces as will be described.

As for the selected damage initiators, the defects were widely dispersed and would be almost impossible to find with the electron microscopy methods. And if one did find a defect, is it a type that leads to catastrophic laser damage? The answer was to let the laser "find" the defects at a fluence high enough to initiate damage but not to let the damage sites grow appreciably. Hopefully, there would be enough information in the postmortem analysis to reconstruct the nature of the initiating defect. As indicated previously, the microscopy test samples were laser damaged and prepared for electron microscopy. Figure 3 shows the selective damage on a macroscopic scale with a Nomarski microscope. The figure on the left is what has been described as "wavy slip" and is from the fine grain UBAC sample. The right figure is an OFHC surface and shows selective damage pits aligned on the grain boundaries. Figure 4 is a TEM micrograph of the "slip" damage in the UBAC. It is evident that what looks like slip in the Nomarski is actually laser melting and solidification as the grain size has increased a hundredfold, and there are few defects. The rest of this discussion will concern itself with the selective damage pits in the OFHC surface.

Figure 5 is a SEM micrograph of one of the selective damage pits. The grain boundary can clearly be seen as a line bisecting the pit in the horizontal. Whatever initiated the laser damage must have been located at the grain boundary. Rings of blast debri are evident around the pit. At higher magnification (fig. 6), the bottom of the crater contains melted material and particles. TEM analysis showed the melted material to be amorphous and almost all copper. An analysis of the particles, however, showed the interesting result that they are predominantly iron. The EDX analysis of this particle is shown in figure 7. In addition to iron, significant amounts of zinc and phosphorous are present.

Discussion

The direct correlation of the laser damage test data and the microscopy data has allowed the following statements to be made about the laser damage behavior of metal mirror surfaces:

Diamond turning or, for that matter, any surface finishing operation inherently imparts energy in the form of deformation and heat into the mirror surface. When machining at a certain condition (-5-deg rake angle), the surface is highly deformed and the dislocation density is high. The resulting material is stronger and therefore more laser-slip resistant. However, the dislocations also act as scattering sites for the "free" electrons in the metal and cause increased Drude absorption even at room temperature [1]. This means that the melting threshold of a deformed material is lower than if the material were defect-free. Compounding this effect is the released stored energy of the dislocations that will tend to drive the melting or recrystallization event once initiated.

From this it would appear that for a given material one is faced with equal trade-offs between slip and melt performance. That is, improvements in one are paid for by degradation in the other. There are, however, ways around the problem. The simplest is to use the known slip resistance of a fine grained material such as electroplated UBAC copper. The laser damage test data confirm this as the UBAC has very high slip resistance and good melt thresholds. Another more subtle way is to impart enough deformation and heat into the surface during machining to recrystallize the surface layer. The low defect recrystallized layer has low absorption and high melt behavior and is backed by the strong, deformed underlayer that resists slip.

It looks like what appears to be slip in the Nomarski can actually be melting, as shown in figure 4. This is illustrative of the need for more than one method for characterizing the type of laser damage. For thin films on metal substrates, the number of types of failure are much greater than for the simple bare metal case. Hopefully, the microscopy methods described can be extended to provide a better understanding of thin-film damage.

The selective damage in the large-grained OFHC copper is caused by the impurities that have collected at the grain boundaries. It is obvious now that even a 99.99% pure substance is inadequate as an optical material if the impurities can collect in sufficient concentrations and are highly absorbing. For mirrors and transmissive optics that are crystalline, the problem of grain boundary

segregation will continue. However, knowledge of which impurities are deleterious and those which are benign will be of great use.

The main lesson to be learned is the fact that controlled processes that produce laser optics can produce components with known and repeatable optical and laser damage properties. From the design standpoint, the optic can be irradiated at higher fluences because of more confidence in the actual damage threshold. Also, control of the materials properties allows one the possibility to specify the type of laser damage resistance desired in an optic: melt, slip, pulsed or CW, etc.

Conclusions

The electron microscopy methods illustrated here can completely characterize the state of the surface of the copper mirrors. The pulsed laser damage testing on identical surfaces has allowed a direct correlation of damage test data with known microscopic defects in the material. This is the first attempt to define and improve the laser damage performance of optical materials by a nonempirical method. This methodology can and is being extended to look at optical thin films and window materials.

Acknowledgments

The author would like to acknowledge the input of J. B. Franck in performing the pulsed-laser damage testing at the Naval Weapons Center.

References

[1] Decker, D. L.; Hurt, H. H.; Porteus, J. O.; Grandjean, D. L. "Optical properties of diamond machined metal surfaces and their relationship to physical and chemical surface perfection," in Proceeding of the 15th annual symposium on optical materials for high power lasers, Bennett, H. E.; Guenther, A. H.; Milam, D.; Newnam, B. E., ed. 1983 November 14-16; Boulder, CO. Nat. Bur. Stand. (U.S.) Spec. Publ. 688; 1985 November. Pp. 147-56.

[2] Porteus, J. O.; Fountain, C. W.; Jernigan, J. L.; Faith, W. N.; Bennett, H. E. "Pulsed-laser stress phenomena on highly reflecting metal and alloy surfaces," in Proceedings of the 9th annual symposium on optical materials for high power lasers, Glass, A. J.; Guenther, A. H., ed. 1977 October 4-6; Boulder, CO. Nat. Bur. Stand. (U.S.) Spec. Publ. 509; 1977 December. Pp. 204-14.

[3] Hurt, H. H.; Decker, D. L. "Inherent mechanical damage in diamond machine optical surfaces," in Proceedings of the 15th annual symposium on optical materials for high power lasers, Bennett, H. E.; Guenther, A. H.; Milam, D.; Newnam, B. E., ed. 1983 November 14-16; Boulder, CO. Nat. Bur. Stand. (U.S.) Spec. Publ. 688; 1985 November. Pp. 140-46.

[4] Franck, J. B.; Seitel, S. C.; Hodgkin, V. A.; Faith, W. N.; Porteus, J. O. "Automated pulse testing using a scatter-probe damage monitor," these proceedings.
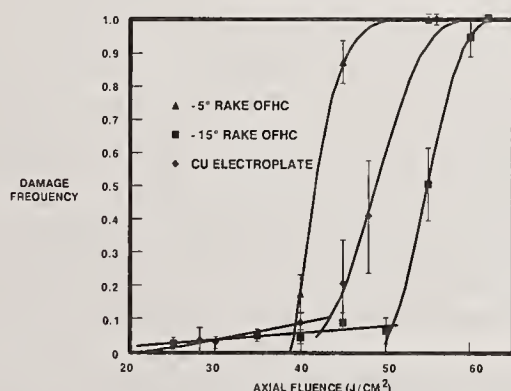
Figure 1. Melt threshold laser damage performance for diamond-turned copper.
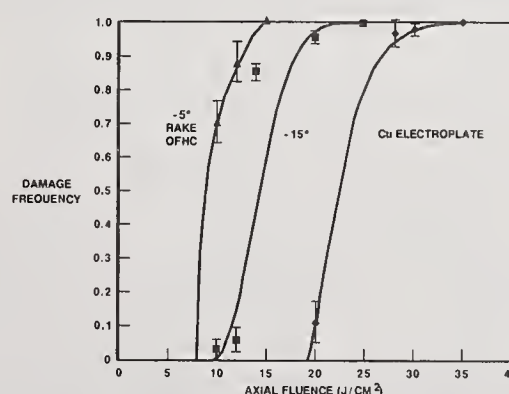
Figure 2. Slip threshold laser damage performance for diamond-turned copper.
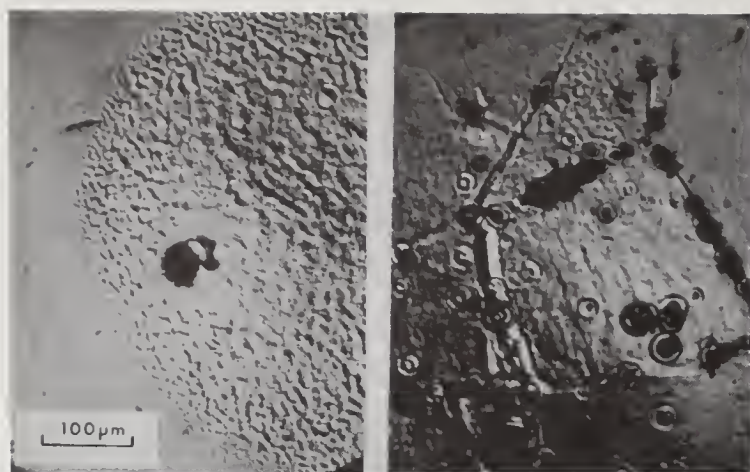
Figure 3. Nomarski micrograph showing low frequency damage in electroplated UBAC (right) and OFHC copper (left). Note the damage pits aligned along the grain boundary.

Figure 4. TEM micrograph showing the recrystallized and low defect microstructure of the laser-damaged UBAC for figure 3.
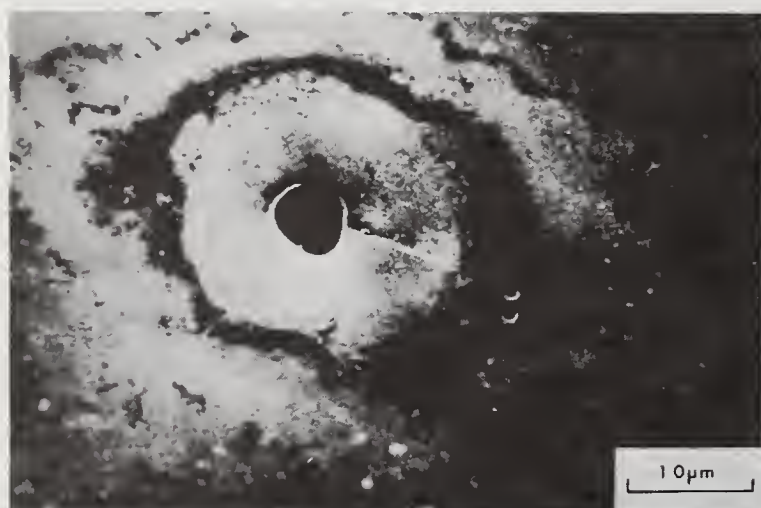
Figure 5. SEM micrograph of a selective damage pit aligned along a grain boundary.
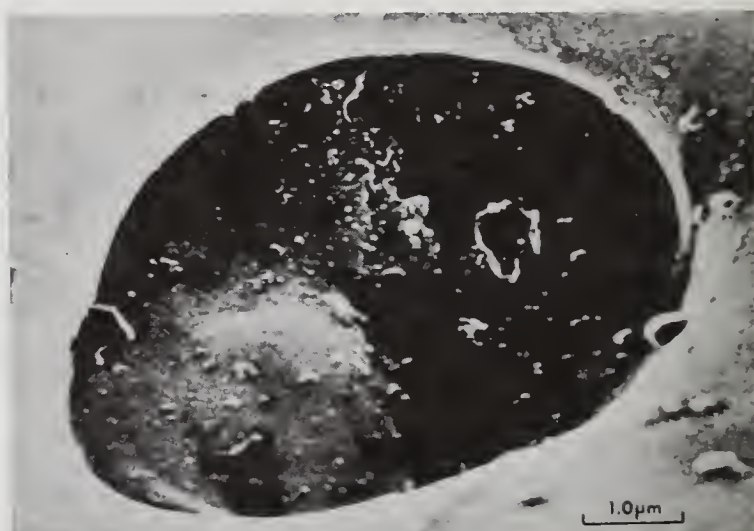
Figure 6. SEM micrograph of the bottom of the pit showing melted material and small particles.

PARTICLE IN MELT PIT

Figure 7. EDX spectra of one of the particles in figure 6 showing a high concentration of iron and trace amounts of phosphorus and zinc.

70

Automated Pulsed Testing Using a Scatter-Probe Damage Monitor*

J. B. Franck, S. C. Seitel, V. A. Hodgkin, W. N. Faith, and J. O. Porteus

Michelson Laboratory, Physics Division
Naval Weapons Center, China Lake, California 93555

This paper describes automated pulsed testing of infrared mirrors based on scatter-probe detection of laser damage. Advantages of our approach are (1) ability to monitor minute changes in surface condition without an observer, (2) rapid sampling of a large matrix of test fluences and test positions on the mirror, (3) automatic selection of test fluences, (4) automatic control of laser intensity drift, and (5) compatibility with a vacuum test environment.

Automated determination of damage frequencies and relative damage onsets will be described for single-layer-coated and uncoated metal and semiconductor mirrors. Tests were performed at 2.7 and 10.6 μm with $1/e^2$ focal spot diameters of 150 and 240 μm, respectively, using a nominal 100-ns pulse length in all cases. Results obtained with the scatter probe will be compared with those obtained from Nomarski postdamage analysis.

Key words: automation; CO_2; DF; HeNe scatter; HF; laser; laser-induced damage; multilayer dielectric coating; onset; scatter probe.

Introduction

Scattered radiation has been used in the past [1-3],[1] to detect laser-induced, low-level damage to test-sample surfaces. Specifically, an auxiliary helium-neon (HeNe) laser was used to produce visible scatter from damaged areas. In this paper, we discuss an improved HeNe laser scatter probe recently developed at the Naval Weapons Center (NWC) for automated damage detection. The device has been used in one-on-one tests performed in vacuum at wavelengths of 2.7 and 10.6 μm, with Gaussian spatial profiles having 150 and 240 μm $1/e^2$ diameters, respectively. Data taken in the automated arrangement were analyzed using an algorithm developed at NWC [4,5] to determine the onset of laser damage. Moreover, a direct correlation was found between the scatter probe data and observation of selective damage using Nomarski microscopy after testing. Damage onsets derived from the scatter probe are thus in excellent agreement with those obtained via the much more laborious method of microscopic postdamage analysis. Further, low-level damage assessment can be performed in real time, which aids in the selection of optimum laser test fluences during a test run. Such automation is almost mandatory when the sample area to be tested greatly exceeds the area of the spatial profile.

Background

The development of an automated laser-damage test facility was driven by the need to increase the sample throughput for tests at NWC where large numbers of samples were to be tested. For manual systems, speed and accuracy are limited by the individuals performing the testing, including the time required for visual damage monitoring. Fatigue becomes an increasingly important factor when testing for several hours unabated. "Off-the-shelf" hardware for computer-controlled sample positioning has been available for several years, and computer monitoring and control of the fluence levels delivered to a sample are also relatively straightforward. The fact that our system was to be built around an existing test facility was a major constraint. This required that the sample-positioning hardware fit into an existing lucite vacuum chamber, since avoidance of air breakdown was desired. Again, off-the-shelf and easily obtained hardware (1) meets the dimensional requirements, (2) has adequate positioning accuracy, and (3) is vacuum compatible. The more severe requirement of damage-assessment automation was fulfilled by the development of the scatter probe.

Shown schematically in figure 1 is the scatter probe ray diagram. The pulsed laser source is directed into the evacuated chamber through a NaCl window at Brewsters angle and is focused onto the surface of sample S by lens L3. For positioning adjustment, a HeNe laser is directed into the chamber by a periscope and is focused onto a small beam block (negative pinhole) by a combination of lens L1, mirror M1, and the surface of sample S. By a simple translation of lens L1 and mirror M1, the $1/e^2$ diameter of the HeNe probe beam can be made to match approximately that of the test beam. Tilt adjustment of mirror M1 allows both beams to be coincident on the sample surface. Thus, by adjusting

---

[1]Numbers in brackets indicate the literature references at the end of the paper.

tilt and translation, the probe beam can reflect off the same region as the testing beam. The specularly reflected HeNe beam is blocked by the negative pinhole. The scattered component, however, is distributed over 2π steradians with the intensity maximum in the specular direction. A portion of the scattered radiation which is not blocked by the negative pinhole is collected and focused by lens L2 onto a photodetector via mirror M_2. The operating principle is shown in figure 2, where a small damage pit is represented on the sample surface, the result of laser irradiation by the test beam. The probe beam is reflected off the sample surface, and the focused beam is blocked by the negative pinhole. The shaded area represents the scattered light from the pit, while the unshaded area represents the scattered radiation collected by the lens and focused onto a detector. Note the shadow of the negative pinhole.

The Automated System

Shown in figure 3 is a schematic diagram of the laser beam line. The test laser sources are a CO_2 laser [6] or an HF/DF laser [7] operating at 10.6 and 2.7/3.8 μm, respectively. The energy output from the laser source is controlled by a computer-driven attenuator consisting of a set of Ge plates at Brewsters angle in a polarizer/analyzer arrangement. The polarizer plate A_1 is mounted in a rotatable periscope which directs the output beam along a fixed axis. The analyzer plate A_2 is fixed and gives a plane-polarized output. An alignment HeNe laser beam is made coaxial with the test laser beam after the attenuator. A portion of the test beam, which is reflected off of a wedged NaCl beamsplitter B, is sent to detector D_1 which is calibrated against a standard calorimeter. The remainder of the beam is sent to the experiment test station. Figure 4 is a block diagram of the automated test facility. The computer is shown (1) monitoring and controlling the laser energy delivered to the sample, (2) keeping the distance from the lens to the front surface of the sample constant while testing nonplanar samples, (3) translating the sample in the x- and/or y-direction to expose fresh test sites, and (4) monitoring the scattered light signal from the scatter-probe detector prior to and after test irradiation. Damage is recorded when the change in scatter exceeds a predetermined value entered into the computer.

The scatter level change corresponding to damage is determined for a family of samples by irradiating a matrix of sites at varying known fluences on a sample typical of the family. The sites are then inspected under Nomarski microscopy to compare scatter-probe signal to damage morphology. In general, certain types of morphology (i.e., pitting, erosion, substrate slip) produce specific ranges of scatter-probe signals. While there may be some overlapping from one range to another, a lower bound for the limiting type of damage can be chosen. Some subsequent microscopy is generally required to validate the selected lower bound. The software controlling the measurement sequencing is designed to generate damage frequency data used to obtain the onset of laser damage [4]. If desired by the operator, this software has the ability to predict appropriate fluence values for the damage frequency curve from evolving data trends. Typically, to develop an adequate damage frequency curve, 400 to 1200 sites must be sampled depending on the mean defect separation relative to the focal spot size and on the uniformity of the sample tested. This provides from 8 to 14 points on the curve.

Experiment

Reflective coatings were tested at 2.7 and 10.6 μm in vacuum at normal incidence. For all tests reported here, each site was irradiated once only at one of several fixed (±20%) pulse energies. Shown in figure 5 is a plot of damage frequency versus fixed energy density at the peak of the Gaussian spatial profile, i.e., axial fluence, in arbitrary units. The sample is a single-layer Al_2O_3 coating on diamond-turned, plated Cu irradiated at 2.7 μm. The shaded circles represent an increase in scatter as seen by the scatter probe, while the darkened squares represent visible damage as seen by Nomarski microscopy. Both techniques show agreement for lower values of axial fluence, but the curves diverge for upper levels of axial fluence. The reason for this divergence can be seen in figure 6 where damage frequencies for different types of visible damage are plotted. The crosses here represent an increase in scatter as seen by the scatter probe. The visible damage of figure 5, as seen by Nomarski microscopy, has been separated into uniform erosion (dark squares) and selective pitting related to defects (shaded circles). The increase in scatter correlates closely with the pitting but begins to diverge once uniform erosion occurs. This occurs because the scatter probe is relatively insensitive to uniform erosion until fully developed. An analysis of the data of figures 5 and 6 for the onset of damage is shown in figure 7. The solid and shaded curves indicate the results of least-squares modeling of the pitting and increased scatter data, respectively. To minimize distortion of the results by the uniform erosion damage mechanism, only the four lowest fluence data points in each case have been used in the analysis. As indicated in the figure, the damage onset based on the scatter probe agrees closely with that based on Nomarski microscopy.

Damage frequencies from a sample exhibiting predominantly selective damage (pitting) are shown in figure 8, where the results of modeling the Nomarski and scatter-probe damage data are again compared. The sample in this case consists of a single layer each of Cu, Au, and Al_2O_3 deposited on a polished Mo substrate. Damage testing was performed at 2.7 μm. Increased scatter as seen by the scatter probe is represented by the shaded circles and damage visible in Nomarski microscopy by the dark squares. Reasonably good agreement is obtained, as indicated.

For the two examples just discussed, damage generally produced an increase in local scatter. If the sample contains strongly scattering defects, the local scatter can decrease when damage occurs. The damage frequencies shown in figure 9 exhibit both effects. The sample represented here is an enhanced reflective coating on Si tested at 10.6 μm. The damage frequencies based on scatter change (shaded circles) (i.e. representing either an increase or decrease) provide a better representation of visible damage than those based on increased scatter alone (shaded squares). All three frequency distributions provide virtually the same damage onset when analyzed by the method of reference 4.

The automated laser damage facility was developed primarily for determining the damage onset of multilayer dielectric mirror coatings. Figure 10 shows damage frequencies from such a sample using both Nomarski and the scatter probe. The sample is a ThF_4/ZnSe paired multilayer on a polished and Au-coated Mo substrate. For this sample, visible damage as seen by Nomarski microscopy exactly matches the increase in scatter signal as seen by the scatter probe. Selective pitting was the only type of damage exhibited by this sample. The onset of damage, of course, is the same for both methods of damage determination.

Shown in figure 11 for the same multilayer sample is a plot of damage frequency versus initial, i.e., predamage local scatter. Squares represent damage frequencies averaged over half-unit scatter increments. The data shown were taken at a constant fluence of 3.5 times the damage onset level indicated in figure 10. This correlation between initial scatter and damage frequency may be expected to hold for coatings where defects that scatter strongly fail at fluences below the damage levels of other defects or of the intrinsic material.

Conclusion

This study has validated the utility of an automated scatter probe for determining damage frequencies used to determine the onset of laser-induced damage in mirror coatings. The following conderations apply.

(1) The scatter probe is very useful for monitoring defect-initiated selective damage, i.e., pitting, which is ordinarily the limiting failure mode of dielectric coatings.

(2) While available improvements in signal processing indicate that sensitivity of the scatter probe for uniform damage can be greatly improved, this sensitivity is inherently less than that for selective damage. Apparently, the uniform damage observed here represents subtle surface modification, possibly including recrystallization [8] that only slightly affects the surface microscatter as seen by the scatter probe.

(3) Care must be taken to correlate the amplitude and sign of the scatter signal to the damage morphology which limits the operational viability of the optical surface under test.

(4) While the scatter probe may be useful in predicting damage via initial scatter, this may apply only to a limited class of samples.

When using the scatter probe to obtain damage frequency data in the automated system, four times as many samples can be tested with improved statistics as compared to manual testing.

References

[1] Newnam, B. E. "Damage resistance of dielectric reflectors for picosecond pulses." Glass, A. J.; Guenther, A. H., ed. Proceedings of the 6th annual symposium on optical materials for high power lasers; 1974 May 22-23; Boulder, CO. Nat. Bur. Stand. (U.S.) Spec. Publ. 414; 1974 December. 39-47.

[2] Saito, T. T.; Milam, D; Baker, P.; Murphy, G. "1.06 μm 150 psec laser damage study of diamond turned, diamond turned/polished and polished metal mirrors." Glass, A. J.; Guenther, A. H., ed. Proceedings of the 7th annual symposium on optical materials for high power lasers; 1975 July 29-31; Boulder, CO. Nat. Bur. Stand. (U.S.) Spec. Publ. 435; 1976 April. 29-40.

[3] Newnam, B. E.; Gill, D. H.; Faulkner, G. "Influence of standing-wave fields on the laser damage resistance of dielectric films." Glass, A. J.; Guenther, A. H., ed. Proceedings of the 7th annual symposium on optical materials for high power lasers; 1975 July 29-31; Boulder, CO. Nat. Bur. Stand. (U.S.) Spec. Publ. 435; 1976 April. 254-271.

[4] Porteus, J. O.; Seitel, S. C. "Absolute onset of optical surface damage using distributed defect ensembles." Appl. Opt. 23; 3796-3805; 1984 November.

[5] Porteus, J. O.; Franck, J. B.; Seitel, S. C.; Allen, S. D. "Defect characteristics of optical surfaces using pulsed laser damage methods." Proceedings of SPIE's 1985 L. A. symposium on optical and electro-optical engineering; 1985 January 20-25; Los Angeles, CA (in process).

[6] Porteus, J. O.; Decker, D. L.; Jernigan, J. L.; Faith, W. N.; Bass, M. "Evaluation of metal mirrors for high power applications by multithreshold damage analysis," IEEE J. Quantum Electron. QE-14; 776-782; 1978.

[7] Porteus, J. O.; Donovan, T. M.; Jernigan, J. L.; Faith, W. N. "Multithreshold evaluation of 100-nsec pulsed laser damage to coating materials at 2.7- and 3.8-μm wavelengths." Glass, A. J.; Guenther, A. H., ed. Proceedings of the 10th annual symposium on optical materials for high power lasers; 1978 September 12-14; Boulder, CO. Nat. Bur. Stand. (U.S.) Spec. Publ. 541; 1978 December. 202-211.

[8] Hurt, H. H.; Franck, J. B. "High resolution electron microscopy of defects in optical materials." Proceedings of the 16th annual symposium on optical materials for high power lasers; 1984 October 15-17; Boulder, CO (in process).
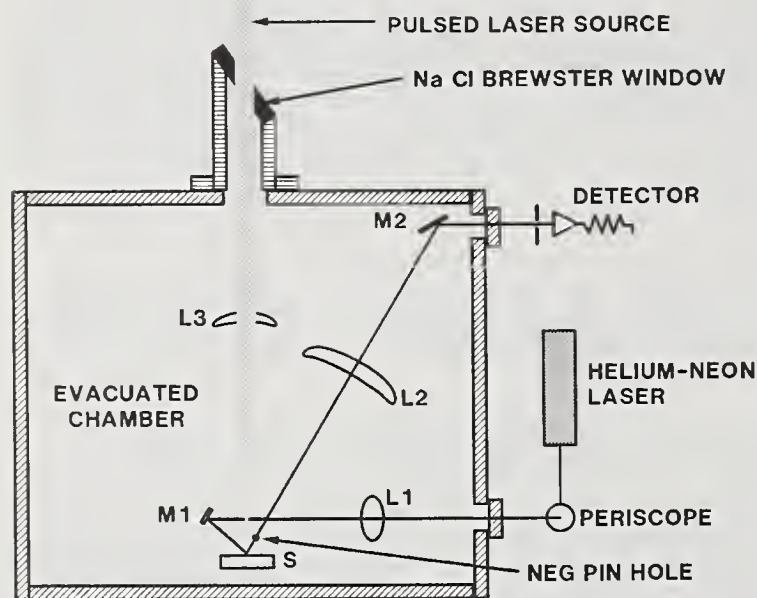
Figure 1. Block diagram of test chamber showing laser-damaging source focused by lens L3 and HeNe laser scatter-probe arrangement consisting of the HeNe laser, periscope, optical train (L1-M2), and apertured detector.
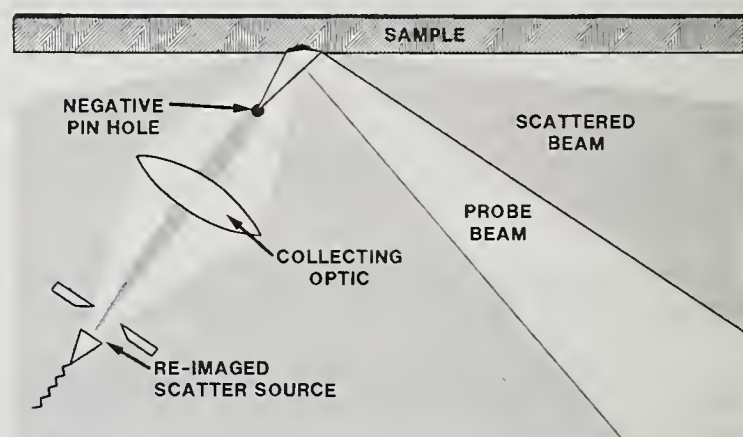
Figure 2. Close-up schematic diagram of the scatter-probe arrangement. The focused specular beam is blocked by the negative pinhole, and the light scattered by the laser-induced pit is collected by a lens system. The collected beam is spatially filtered and sent to a photodiode detector.
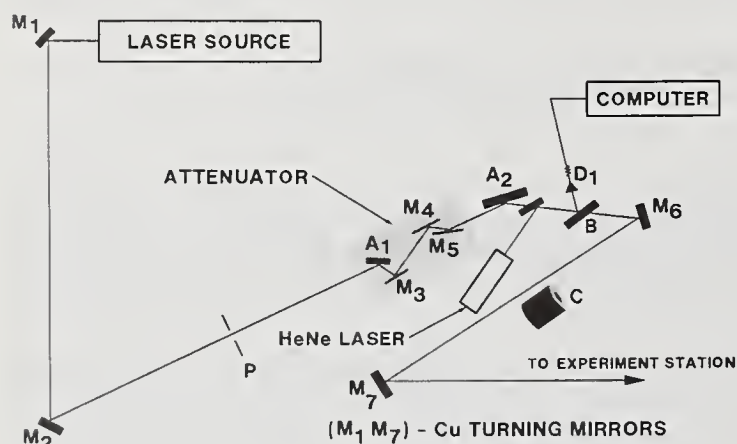
Figure 3. Schematic diagram of the laser system. The laser source can be either the HF/DF or the CO_2 laser. Also shown is the continuously variable attenuator with a constant polarization output off the germanium plate (A_2) at Brewster's angle. The energy during the experiment is monitored by detector D_1 and calibrated versus an isoparabolic calorimeter C.
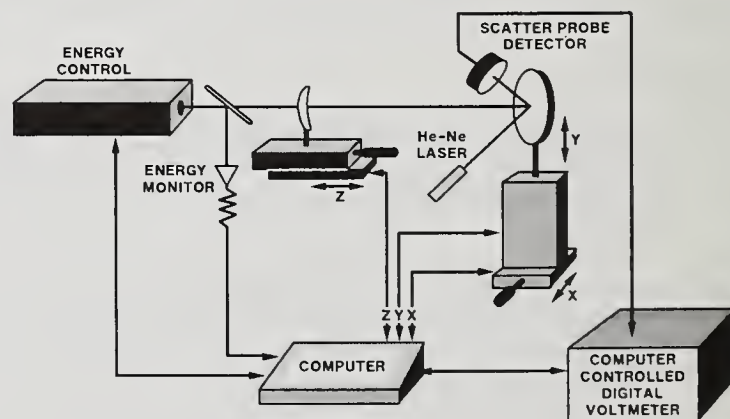
Figure 4. Block diagram of the automated test station. The computer monitors and maintains a required energy level based on an ongoing ten-shot average. The computer translates the test sample and maintains focal distance of the lens (z-axis) to the sample if nonplanar samples are to be tested. On-line damage assessment is determined from changes seen by the scatter probe from the irradiated surface.

74
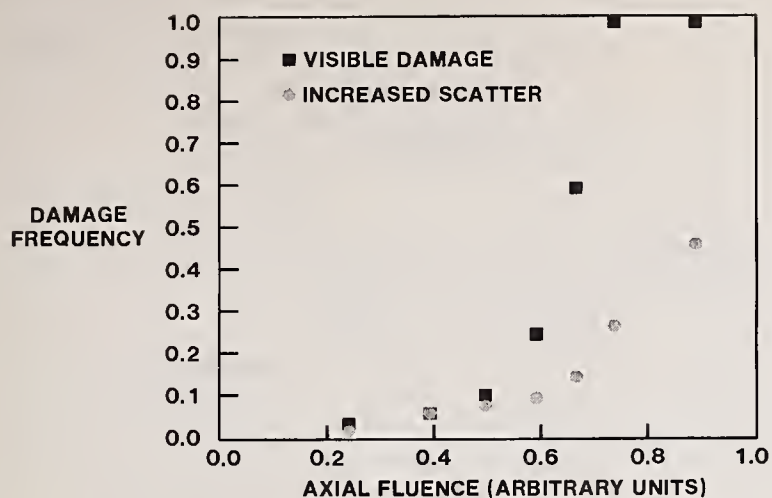
Figure 5. Damage frequencies determined by the scatter probe compared with those determined from Nomarski microscopy. The sample is a single-layer Al_2O_3 coating on plated and diamond-turned Cu tested at 2.7 μm.
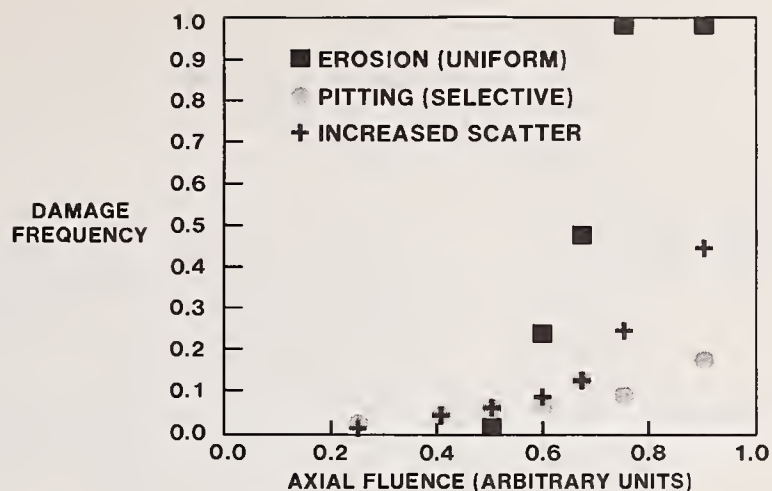
Figure 6. Data of figure 5 where the visible damage determined by Nomarski has been resolved into the two different morphological types observed on this sample. Since the scatter probe is more sensitive to pitting, it provides a better representation of the frequency of this type of damage.
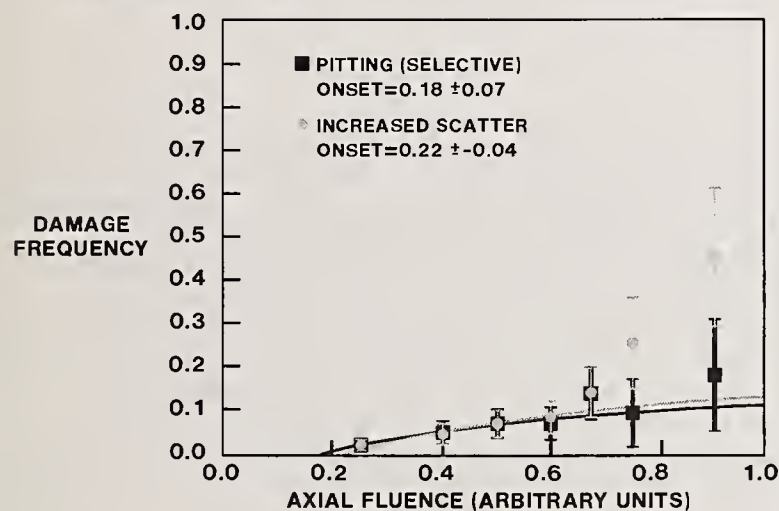
Figure 7. Data of figure 6 analyzed for the onset of laser damage using the model described in ref. [4]. Results of applying the analysis to pitting damage determined by Nomarski and damage detected by the scatter probe are compared. The uncertainties in the onsets are model dependent.
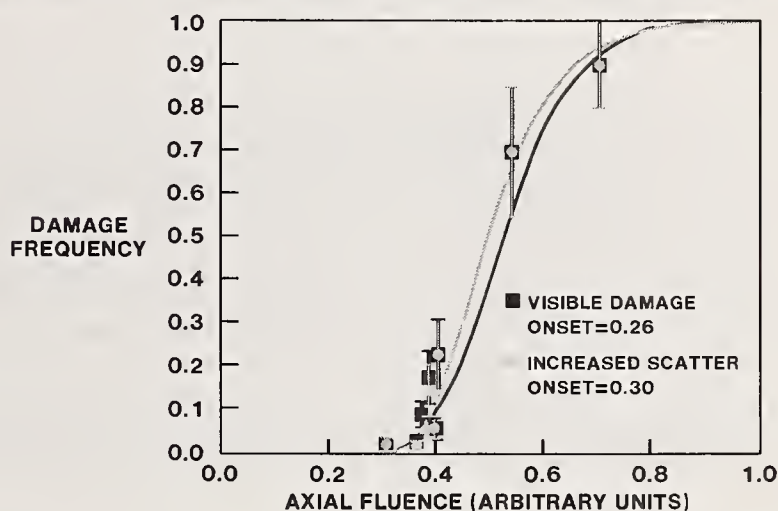
Figure 8. Comparison of damage frequencies obtained from Nomarski with those obtained from the scatter probe on a sample where pitting predominates. The measured damage frequencies were analyzed by the method of ref. [4].
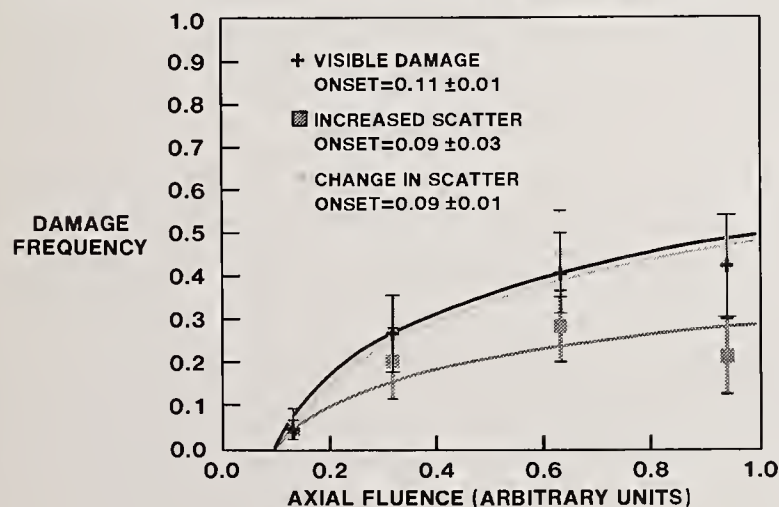
Figure 9. Damage frequencies with onset analyses based on Nomarski and on scatter-probe measurements from a sample which exhibited either positive or negative scatter changes with damage. Inclusion of scatter decrease as an indication of damage (change in scatter) provides a better representation of visible damage than increased scatter alone.
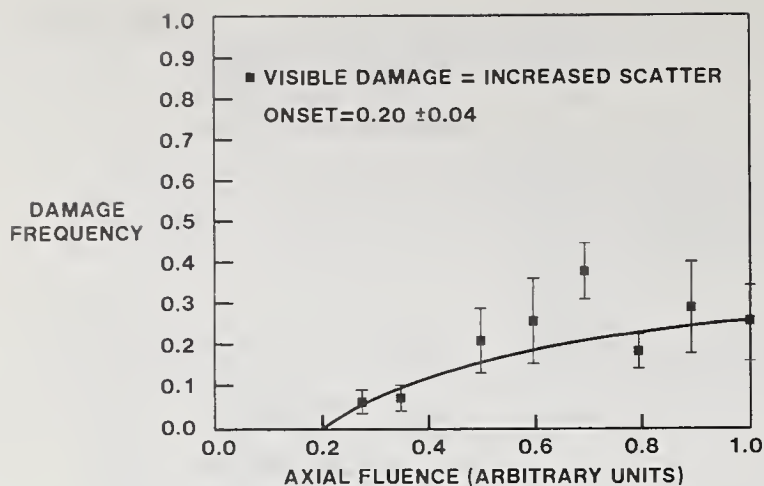
Figure 10. Identical damage frequencies with onset analysis obtained via Nomarski and the scatter probe from a multilayer dielectric mirror at 2.7 μm. The uncertainty in the onset is model dependent [4].
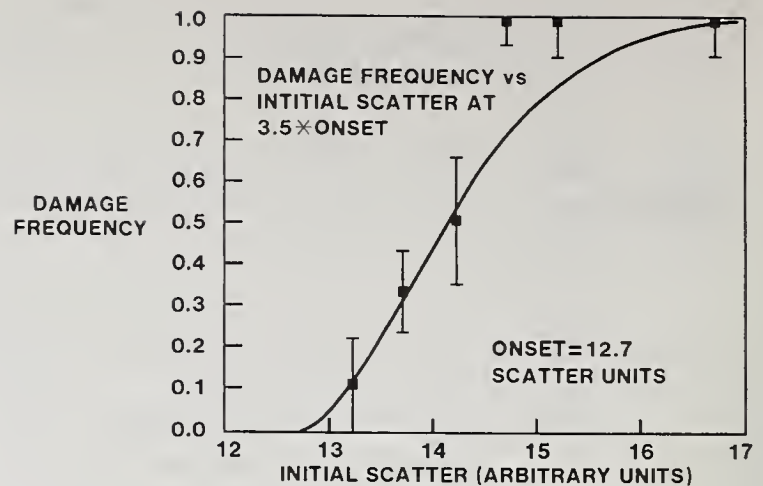
Figure 11. Damage frequency versus local scatter before damage as measured by the scatter probe. The curve represents the damage onset model of ref. [4], which has been applied arbitrarily to indicate the data trend.

Was the range of total integrated scatter from the sample measured before the damage measurement? No. The onset model was used to determine the threshold using least squares fits. In all but one case the model was degenerate and all the defects failed at once. The onset model uses a three parameter fit. If the wavelength were changed the damage threshold might well change. In response to another question the speaker replied that the system had been running for about 4-6 months and 30 or more samples had been tested. The main point of the paper was that agreement was found in these tests between the scatter probe results and previous microscopy. A questioner pointed out that Newnam in the period 1972-74 presented work with 6943 A 10 ns pulses and 1.06 μm 30 ps pulses in which the correlation of damage threshold with scatter was only slight. Initial scatter of the sample was thus not a reliable monitor. Was sample dependence or wavelength dependence the cause of the discrepancy? The author did not know but pointed out that in their setup they were looking among the specular direction at the scatter, which might give better correlation than at an angle.

Application of a Computer-Automated IR Sensitive Camera
To the Determination of Pulsed Laser Surface Damage Thresholds

P. C. Filbert, J. L. Guttman, C. L. Navoda, and B. A. Watson

Lockheed Palo Alto Research Laboratory
3251 Hanover Street
Palo Alto, California 94304

An inexpensive, easily constructed infrared-sensitive camera system which as an active electronic readout is described in detail and examples of its utility in the determination of surface damage thresholds are presented. A small fraction of the pulsed 1.06 μm laser beam incident on the sample is split off and directed to a screen. The beam spatial profile of each shot is then imaged onto a 100 x 100 photodiode array whose output is digitized and stored by a PDP 11/23 computer-controlled data acquisition system. Further processing of the image data by a VAX 11/780 computer yields a high resolution fluence contour map of the laser beam incident on the sample. This map is especially useful when irradiating areas of several cm^2 during material testing experiments. The map, showing the variation of beam fluence over its cross-section, can be superposed over the damaged sample providing an accurate value for the surface damage threshold for the material or coating. Examples will be presented and additional advantages of large area irradiation discussed.

Key words: beam profiling; data acquisition; large area irradiation; pulsed laser damage; surface damage thresholds.

1. Introduction

Recent materials testing at the Lockheed Palo Alto Research Laboratory requires the irradiation of numerous samples with pulsed 1.06 μm laser light over an area of several cm^2 to approximately 10 cm^2. In order to deduce surface damage thresholds over such a large spot size, an accurate spatial intensity map of the incident laser beam is needed. To this end, an infrared-sensitive camera with a 100 x 100 photodiode array at the focal plane is used to image the beam on a shot by shot basis. The image data is acquired and processed under computer control and a fluence contour map generated.

This paper will first describe the experimental configuration used in the materials testing experiments. Second, a detailed description of the camera and data acquisition system is given. The third section describes the procedure to reduce the image intensity data to absolute fluence values which are input to a contour plotting routine. Fourth, the application to the determination of surface damage thresholds is demonstrated. Last, the additional advantages of large area irradiation testing will be discussed.

2. Experimental Configuration

Figure 1 is a schematic of the target chamber and the laser beam diagnostics used to perform pulsed laser testing. The Nd glass laser system used in consists of an oscillator and 5 amplifiers. The system can be operated in one of three modes. First is the relaxation-oscillation mode which produces a 200 μs pulse train composed of approximately 100 μs pulses spaced 2 μs apart. The maximum energy available in this mode is 400 Joules. Second is a Q-switched mode which produces a

single 20 ns pulse with a maximum energy of roughly 175 Joules. Third is a pulse-sliced mode which provides a 3 ns pulse with $\sim$ 100 Joules maximum energy.

The temporal profile of the beam is monitored by an S1 response photodiode, the beam energy is measured by a total energy calorimeter and the beam spatial profile is obtained by the camera. The data from these diagnostics are fed into computer controlled data acquistion system.

For testing, samples are placed into the center of the vacuum chamber which is then evacuated to 2×10^{-5} Torr. The ports at 45° can be used to field varous target diagnostics as the testing requires.

3. The Camera System

The camera system described here is similar to that described in reference [1]. A small fraction of the laser beam is deflected by a glass pickoff onto a screen which is then focussed by a 50 mm camera lens onto a 100 x 100 silicon photodiode array manufactured by E.G.&G. Reticon. The array is square with an inter-diode spacing of 60 μm in the x and y directions. The array is self-scanning with the integration time of each diode beginning upon diode readout. The required wave-form and clocking to drive the array are supplied by a readout circuit board which is also available from Reticon (model RC502A).

Figure 2 shows a block diagram of the array and data aquisition system used. The output of the RC502A readout board is fed into a LeCroy 8212/4 Fast Data Logger which digitizes the video signals to 12-bit accuracy at a maximum rate of 10^5 Hz. The clock pulse from the RC502A is used to initiate the A to D conversion. After conversion, the data are stored in a LeCroy model 8800A/12 memory module which can store up to 32768 12-bit words of data. The Data Logger uses a stop-trigger signal which is generated by the firing of the laser to select the desired frame of video data to containing the beam profile.

The data is read from the memory module into a Kinetic System LSI-11/23 microprocessor based computer system run under the RT-11 operating system. Communication between the computer and the data modules is accomplished by a Kinetic Systems model 1510 power crate and model 2923 crate controller. The crate provides all power and communication busses for the modules placed in it while the controller provides the interface between the modules and the computer system. The entire data acquisition system conforms to the international CAMAC (Computer Automated Measurement And Control) Standards which specify the basic bus structure and the form of the commands at the byte level used to control the instrumentation.

The LSI-11/23 computer provides master control of the data acquisition, storage of the data onto floppy disk, and preliminary image processing. A Tektronix 4025 graphics terminal is used as the keyboard and image display device while a tektronix 4632 Video Hardcopy unit is used to obtain a permanant record of images displayed on the terminal screen.

An Ethernet data link allows communication between the LSI 11/23 and a VAX 11/780 computer which is used to generate equal fluence contours from the image data. A licensed commercial graphics package (DISSPLA^{TM}) is used which derives the contours from the image data and performs the plotting. However, the LSI 11/23, or other minicomputers (e.g. HP 9000 series) could be used for the contouring depending on the availability of the appropriate software.

All the components of the camera system are available "off the shelf" and are made to be compatable owing to the conformance to the CAMAC standards. Similar components can be obtained from other vendors and the selection is up to the individual user. In addition it should be mentioned that the system as described is quite versatile and is far more than a dedicated camera system. The total cost of the system is less than 18,000 dollars (without the VAX of course), and could be

less depending on the features selected.

4.   Data Processing

Two forms of image presentation are routinely employed, both of which are illustrated in figure 3. The bottom portion is a 3-D plot of the relative pixel response in an 80 x 80 subset of the array. This particular spatial profile is of the 200 μs pulse train. For this shot the beam was focussed to a 0.75 inch diameter. Using the procedure described below, the pixel response can be converted to a fluence value in the target plane which is used to label the vertical axis in the figure.

Directly above the 3-D plot is a fluence contours derived from the 3-D data. The contours are labelled by the fluence in the target plane. The multi-spatial mode of the beam is quite apparent from these images.

To calculate the fluences in the target plane the following steps are followed. First, normalize the area under the 3-D image to the measured beam energy. This gives the fraction of energy represented by each pixel response (E_{ij}). Second, the magnification of the camera is measured. This determines the area represented by a pixel on the screen, (A_s). Third, the linear magnification (M) of the focussing lens is known and so the area in the target plane represented by a pixel (A_t) can be obtained by:

$$A_t = M^2 A_s$$

Last, the fluence in the target plane is then:

$$F_{ij} = E_{ij}/A_t.$$

The array F_{ij} is then used as the input of the routine used to generate the fluence contour.

5.   Application

The application of the fluence contour map in the determination of surface damage thresholds is straightforward as figure 4 illustrates. Here, the appropriately scaled map is superposed onto an enlarged photo of a damaged sample. By correlating the visible surface damage with the nearest contour permits the damage threshold to be rapidly determined. The example shown here is of an aluminum alloy (7075) clad with 98% pure aluminum which has been electropolished. The 200 μsec pulse train was used to irradiate the sample with a total energy of 80 Joules over an area of 1.7 cm^2.

Although the sample is not of optical quality, the application to optical surfaces and for shorter laser pulses is obvious.

6.   Discussion

The technique described here was prompted by the requirement that large target areas of at least several square centimeters be irradiated and that surface damage thresholds be obtained. Currently materials testing is often done with small lasers which are focussed to a spot diameter of ≈ 100 μm or so. Because the beams usually have gaussian spatial profiles, the intensity gradient across the spot is relatively large. (For a gaussian spot, δI/I is approximately 1 over the spot diamter). The use of larger area irradiation allows a more gradual intensity profile to be obtained across the sample thus reducing the complication of thermally induced mechanical stresses in damage threshold determination. In fact, by the proper tuning and apodizing of the incident beam the intensity gradient can be varied systematically enabling the quantitative study of the intensity gradient effects. In addition, large area irradiation also allows the study of surface and coating uniformity

79

and how it relates to the failure of optical components. The use of the beam imaging system described here is an indispensable and necessary tool for these studies.

7.   References

[1] Knudson, J. Thomas; Ratzlaff, Kenneth L. Laser beam profile analysis using a two dimensional photodiode array. Rev. Sci. Instrum. 54(7), July 1983.
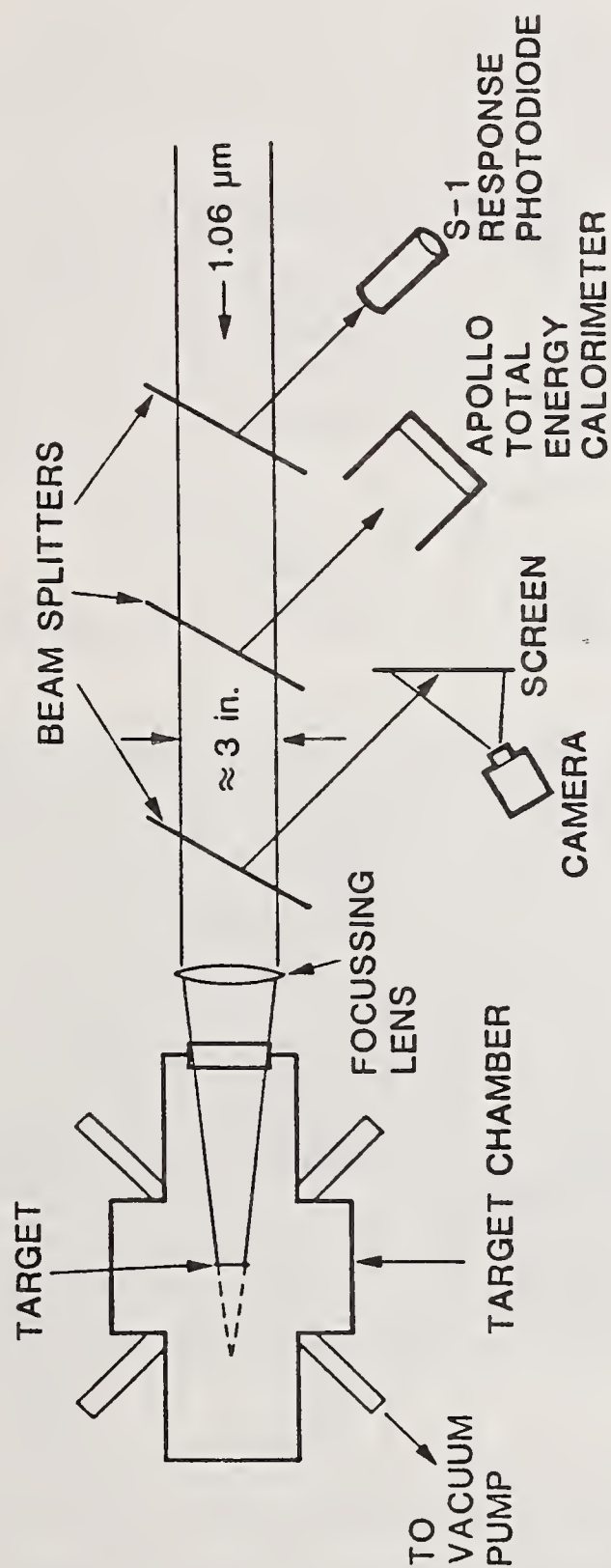
Figure 1. Schematic showing the target chamber used for pulsed laser testing and the placement of the laser beam diagnostics.

81
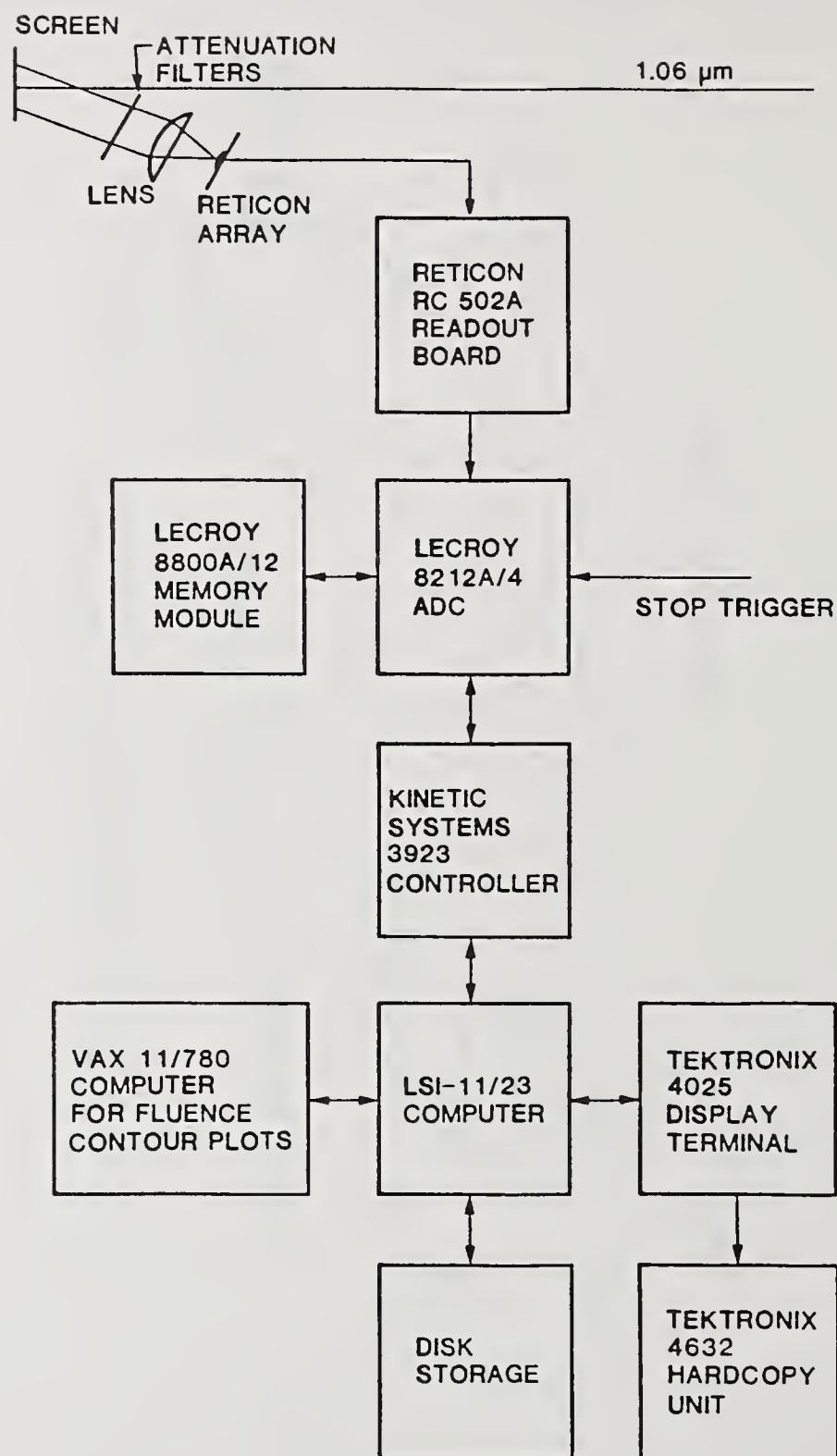
Figure 2. Block diagram showing the details of the data acquisition system used to record, store and process the image data.
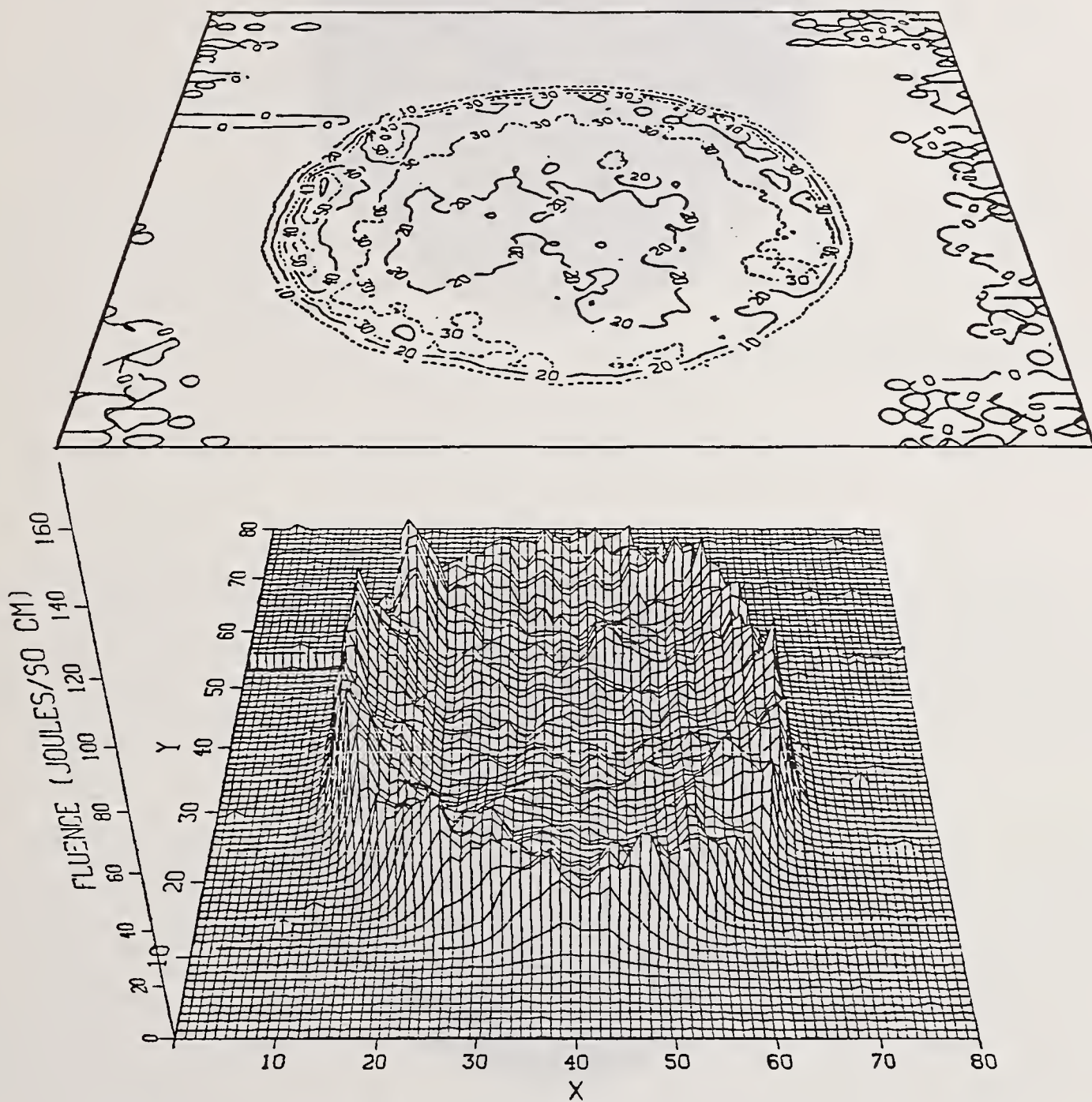
Figure 3. A computer-generated illustration of the two types of display used to characterize the laser beam spatial profile.

83
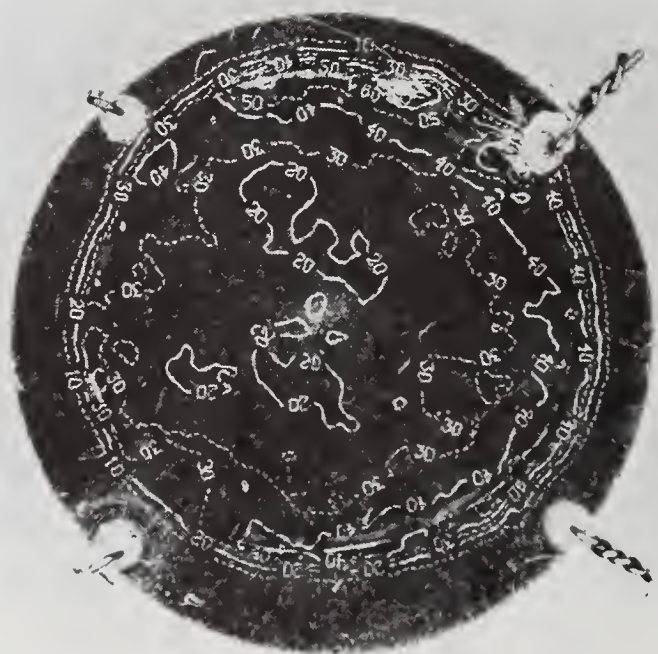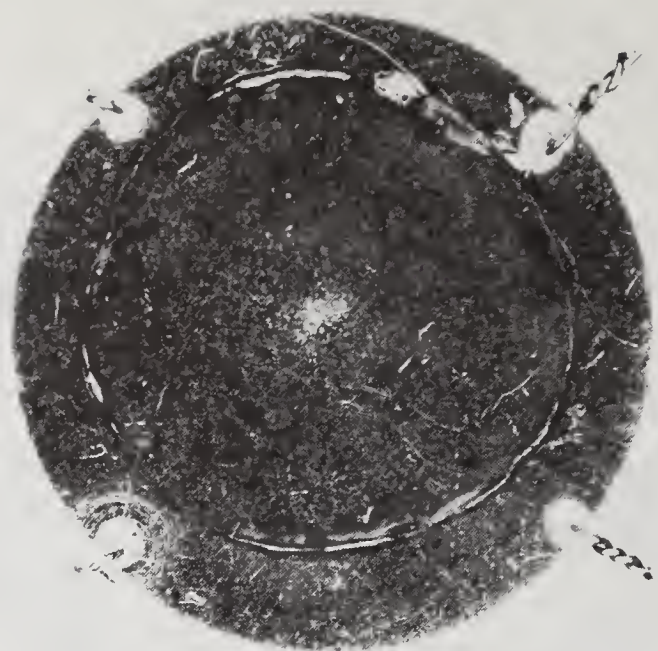
Figure 4. Illustration of the application of the contours to the deter-
mination of surface damage thresholds. Top is a photo of a
damaged sample; note the damage in the ring produced by the
pulse in figure 3. Bottom is the same photo with the contour
overlay.

High-Precision Damage-Resistant Multiple-Pass Ultraviolet Reflectometer

L. John Jolin and S. R. Foltyn

University of California, Los Alamos National Laboratory, Los Alamos, NM 87545

A multiple-pass cell was reported by John White in 1942 [1]. Since then, it has been adapted for use as a high-precision reflectometer. The multiple-pass reflectometer has been studied and reported by Arnon and Baumeister [2].

Here, a reflectometer which is similar is described. It utilizes a uv laser operating at λ = 351 nm as the source and the White-cell mirrors are high-reflection dielectric coatings designed for that wavelength. Because of the low-loss reflectors used in the cell, a high number of traversals, reflections, can be achieved; $R \geq 239$. The use of dielectric mirrors also improves the damage resistance of the apparatus which is important when a uv laser beam is used.

The results of reflectance measurements performed on several ultraviolet high reflectors are also reported. These include conventional dielectric coatings as well as a hybrid coating consisting of Al_2O_3, HfO_2, and SiO_2 layers.

Key words: dielectric coatings; high reflectance; multiple-pass reflectometer; White cell.

1. Introduction

The Los Alamos optical damage laboratory has observed and defined several types of laser-induced damage to optical materials [4]. In the case of high reflection, multi-layer, dielectric coatings, damage may be defined as any change in the coating layers or at the substrate interface which causes a measurable change in reflectance at its design wavelength. Since most dielectric high reflectors have reflectances approaching unity, and a change caused by laser irradiation can be minute, a precise method for measuring high reflectance must be utilized. A multiple-pass reflectometer based on the White cell was selected because of its demonstrated precision and high accuracy. It utilizes a laser as the source for reasons described later.

2. Reflectometer

2.1. The reflectometer configuration is similar to that described by Edwards and Baumeister [3] with the exceptions of dimensions, number of traversals, and light source. Figure 1 shows the optical layout for the reflectometer described here. Although figure 1 shows both a folded and an unfolded cavity about M2, the reflectometer discussed here is only used in the folded configuration. The cell mirrors are M3, M5, M2, and M4 and have a radius of curvature of 50 cm, with the exception of M2 which is flat. All four of these mirrors are dielectrics designed for 351 nm which is the laser wavelength. They were all coated in a single run and all have the same reflectance. In practice, M3 and M5 are positioned directly above and in close proximity to M4 (figs. 2 and 3). This allows for near normal angle of incidence on M2 which is the location of the mirror under test, and alternately, the calibration mirror. M6 is positioned so that it intercepts the output laser energy and directs it toward the output detector. M1 is the injection mirror and has a radius of curvature of 25 cm which mode matches the collimated laser beam to the cell modes.

The laser used for this apparatus is a Lumonics excimer laser, Model 861, operating at 35 Hz, with a 10-ns pulse duration. As is typical with excimer lasers, the output decreases slightly with increasing age of the static fill gas so a small portion of the beam is diverted to detector B as a reference. The detectors are Laser Precision, Model RjP 734 and Model RjP 735 for A and B, respectively. The detector outputs are compared by a ratiometer, also Laser Precision, Model Rj 7200.

2.2. General Considerations

As discussed in much detail by Arnon and Baumeister, and Edwards and Baumeister, the multipass reflectometer relies on the ability to vary the number of reflections on an unknown and to achieve a high number of reflections. To this end, high-reflection dielectric coatings are utilized in this cell to not only minimize losses but also to withstand the higher energy of the laser.

There are several advantages to using a laser as the source. These include an increased signal-to-noise ratio, an increased number of traversals within the reflectometer, and relatively easy mode matching of the source to the cell. The higher energy of the laser also allows for measurements to be performed under room light conditions.

2.3. Reflectance Measurements

The key to operation of the reflectometer is to keep track of the number of reflections, or traversals, within the cell at any given time. Each traversal consists of eight reflections--one on each of mirrors M3 and M5, two on M4, and four on M2. This is true for all traversals except the last since the energy will escape one bounce on M4 and proceed to the output detector via M6. Thus, the last traversal will have only seven reflections. This reflectometer routinely utilizes up to 30 traversals (239 reflections), so keeping track of them can seem a formidable task. In reality, however, all that is necessary is to align for one traversal and from then on keep track of each additional traversal. Successive traversals can be achieved by horizontal adjustment of M3, and counted as they swing into position on the output detector.

To perform a reflectance measurement on an unknown, the reflectance of the cell mirrors must first be determined. To accomplish this a cell mirror is used in position M2. The output is recorded for each set of traversals from 1 to 30. The number of traversals is converted to number of reflections, (N), and the negative log of the ratio of B to A is plotted vs N. Using a linear-regression fit, a straight line is fit to the data. The average reflectance of all of the mirrors within the cell is related to the slope of this line. Since all reflectances are equal, the equation for the cell mirror reflectance is:

$$R = \log^{-1} m \quad , \tag{1}$$

where: m is the slope.

Now that the cell mirror R has been determined, M2 can be replaced by an unknown and measurements are performed in the same manner as for the cell. Now, however, there will be a change in slope caused by the different R value of the unknown.

Since the laser energy enters and exits from M2, there is always one more reflection on M2 than all three cell mirrors combined. This can be seen in a simplified layout for one traversal, figure 4. A and B are detectors. R_c represents the three cell mirrors, and R_u represents the unknown (M2).

If the extra bounce on the unknown mirror in the reflectometer is ignored there is, of course, an equal number of reflections on the cell mirrors as on the unknown. If the total number of reflections within the cell is N then the reflections on M2 = the reflections on the cell mirrors = N/2. The following equation can be generated:

$$-\log \frac{\phi_B}{\phi_A} = N \left(\frac{\log R_c}{2} + \frac{\log R_u}{2} \right) + \log k \quad , \tag{2}$$

where, ϕ_A = energy at detector A

ϕ_B = energy at detector B ,

and $K = \frac{\phi_{in}}{\phi_B}$.

It can be seen that this is an equation to a straight line with

$$\frac{\log R_c}{2} + \frac{\log R_u}{2} \tag{3}$$

as the slope, (m). Minor manipulation of eq (3) and insertion into eq (1) yields the equation for the unknown reflectance value.

$$R_u = \frac{\log^{-1} 2m}{R_c} \tag{4}$$

where: R_u = the reflectance of the unknown
and: R_c is the reflectance of the cell mirrors.

To disregard the extra reflection on the test sample causes no significant error since the number of bounces is in N in eq (2) and not in the slope.

3. Results and Conclusions

Figure 5 shows data plots and fits for several reflectors tested. Notice that reflectors with higher R's than the cell itself can be measured. The measured R for a number of reflectors available for test is shown in table 1. (The coating materials are listed for reference only and not intended to indicate general ranking of these materials.) Repeated measurements and multiple users yielded a precision for this reflectometer of ±0.0007.

Table 1. Measured Reflectance of Various Mirrors

R	COATING MATERIALS	SUBSTRATE
0.9976±0.0007	Ta_2O_5/SiO_2	F.S.
0.9948	HFO_2/SiO_2	DYN1000
0.9948	HFO_2/SiO_2	S.C. Si
0.9938	Al_2O_3/SiO_2	PC. Si
0.9938	HFO_2/SiO_2	DYN1000
0.9934	ZrO_2/SiO_2	S.C. Si
0.9933	Al_2O_3/SiO_2	PC. Si
0.9924	$10(HFO_2/SiO_2)\ 7(Al_2O_3/SiO_2)$	DYN1000
0.9906	UNAVAILABLE	--
0.9906	UNAVAILABLE	--
0.9902	Al_2O_3/SiO_2	S.C. Si
0.9898	$(ZrO_2/SiO_2)(Al_2O_3/SiO_2)$	S.C. Si
0.9875	UNAVAILABLE	--
0.9863	Al_2O_3/SiO_2	F.S.
0.9844	UNAVAILABLE	--
0.8859	Al_2O_3/SiO_2	S.C. Si
0.8498	Al_2O_3/SiO_2	S.C Si
0.8095	ALUMINUM MIRROR WITH MgF_2 O.C.	(NRC MIRROR)

The alignment necessary to achieve the number of reflections reported here was relatively easy. With care, more traversals could be obtained; however, it is easy enough now that an inexperienced operator can learn to operate it within minutes and obtain results within the reported precision.

The reflectometer will probably prove most useful in a range from about 0.9990 down to 0.8000. From figure 5 it can be seen that for a reflector of 0.8498 the attenuation was so high that only 23 reflections were possible. The laser energy could have been increased but mirror damage would have been possible. The cell mirrors have damage thresholds much below state of the art so this could be improved with better coatings.

4. References

[1] White, John U. Long optical paths of large aperture. J. Opt. Soc. Am. Vol 32, No. 285; 1942.

[2] Arnon, O.; Baumeister, P. Versatile high-precision multiple-pass reflectometer. Appl. Opt. Vol. 17, No. 18; 1978.

[3] Edwards, David F.; Baumeister, Philip. High-precision multipass reflectometer, SPIE Vol. 288, Los Alamos Conf. on Opt.; 1981.

[4] Foltyn, S. R.; Jolin, John. Catastrophic versus microscopic damage: applicability of laboratory measurements to real systems, Nat. Bur. Stand., Boulder Damage Symposium; 1983. (To be published)
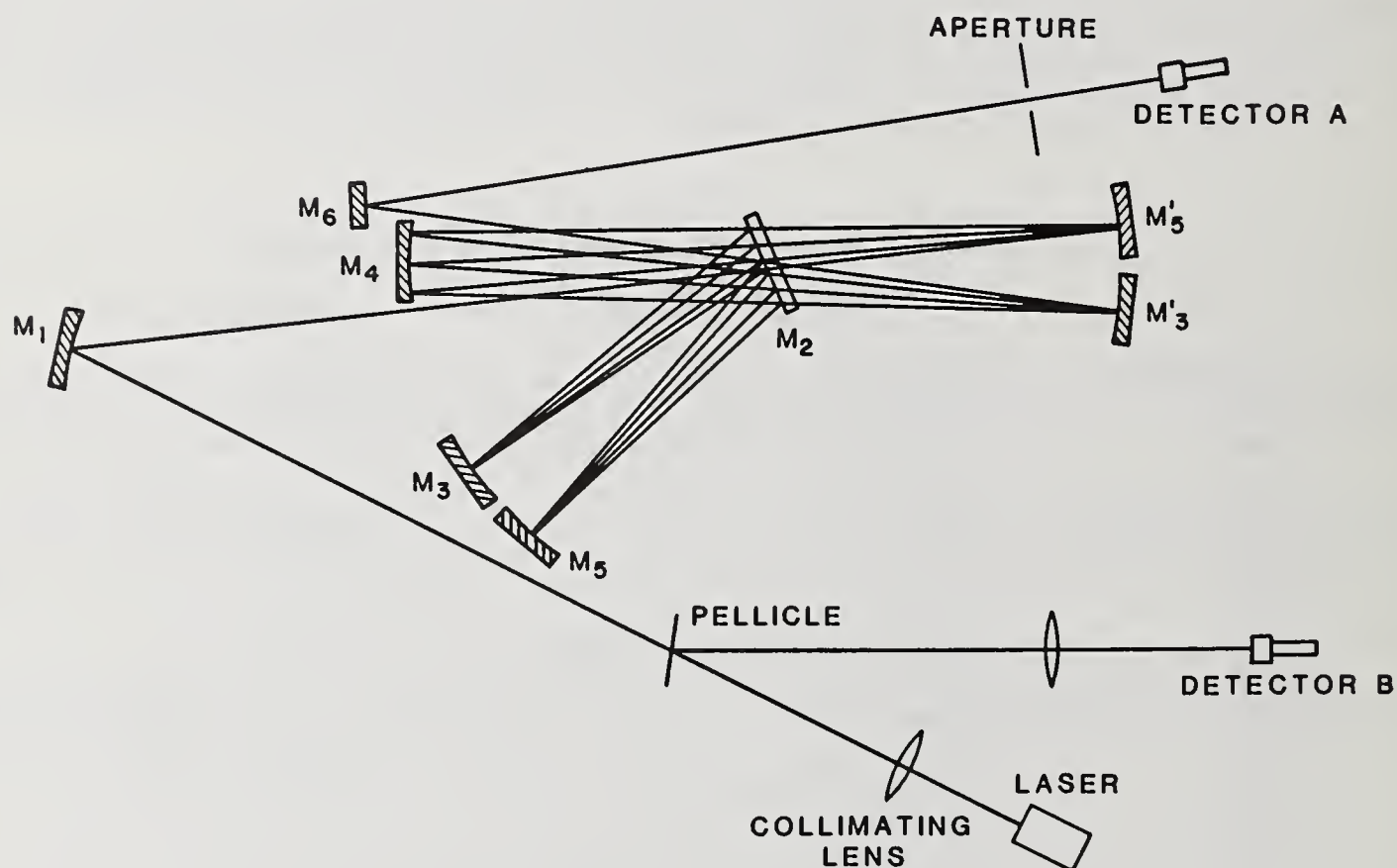
Figure 1. Reflectometer optical layout. Here, 15 reflections (2 traversals), is illustrated. This reflectometer utilizes only the folded cavity as represented by M_4, M_2, M_3, and M_5. M_2 is the position of the unknown.
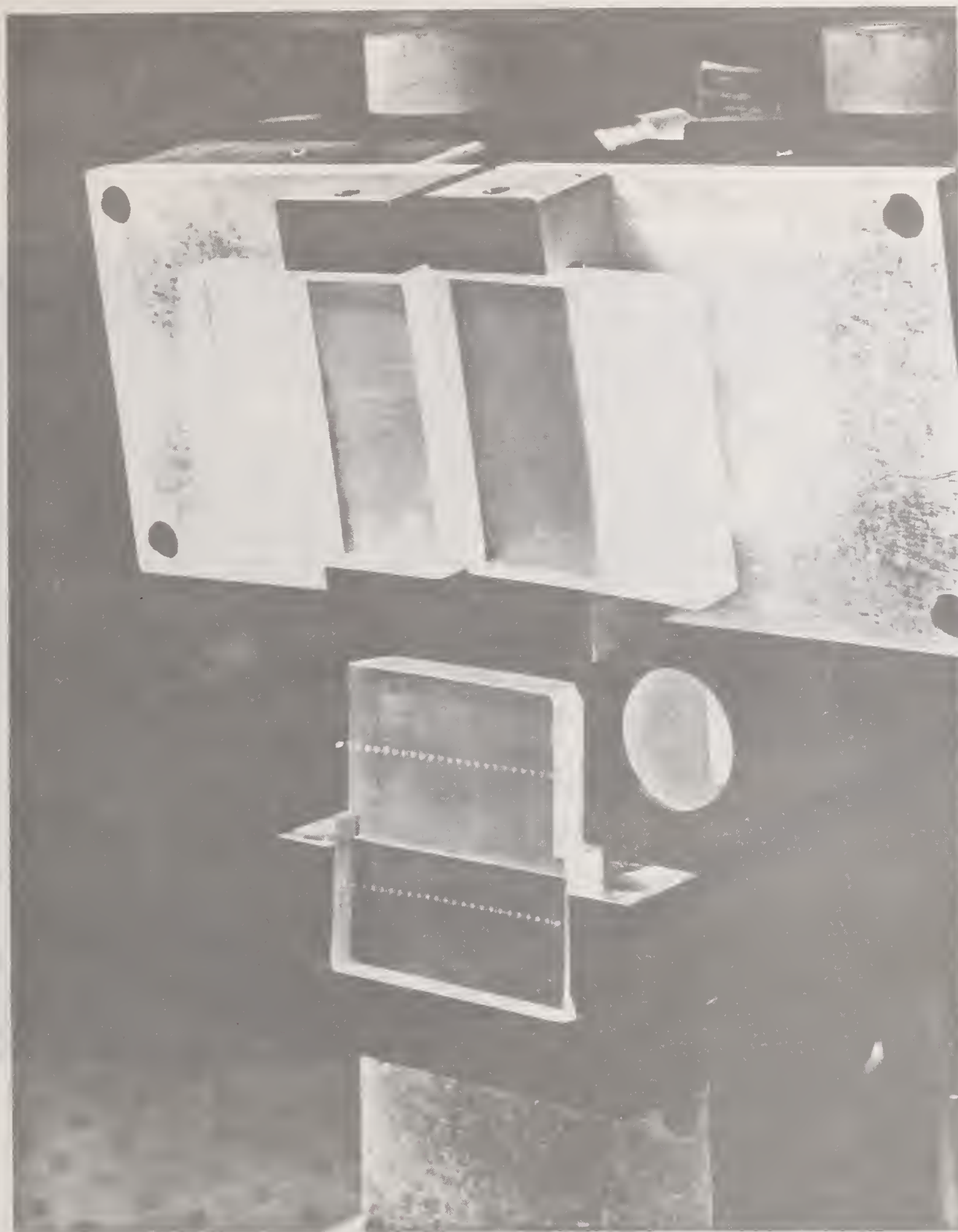
Figure 2. M_3, M_5 (top), and M_4 (bottom) are shown. The separation of the irradiated areas in the vertical direction limits the angle of incidence at which one can test. Here, it is 7 degrees.

89
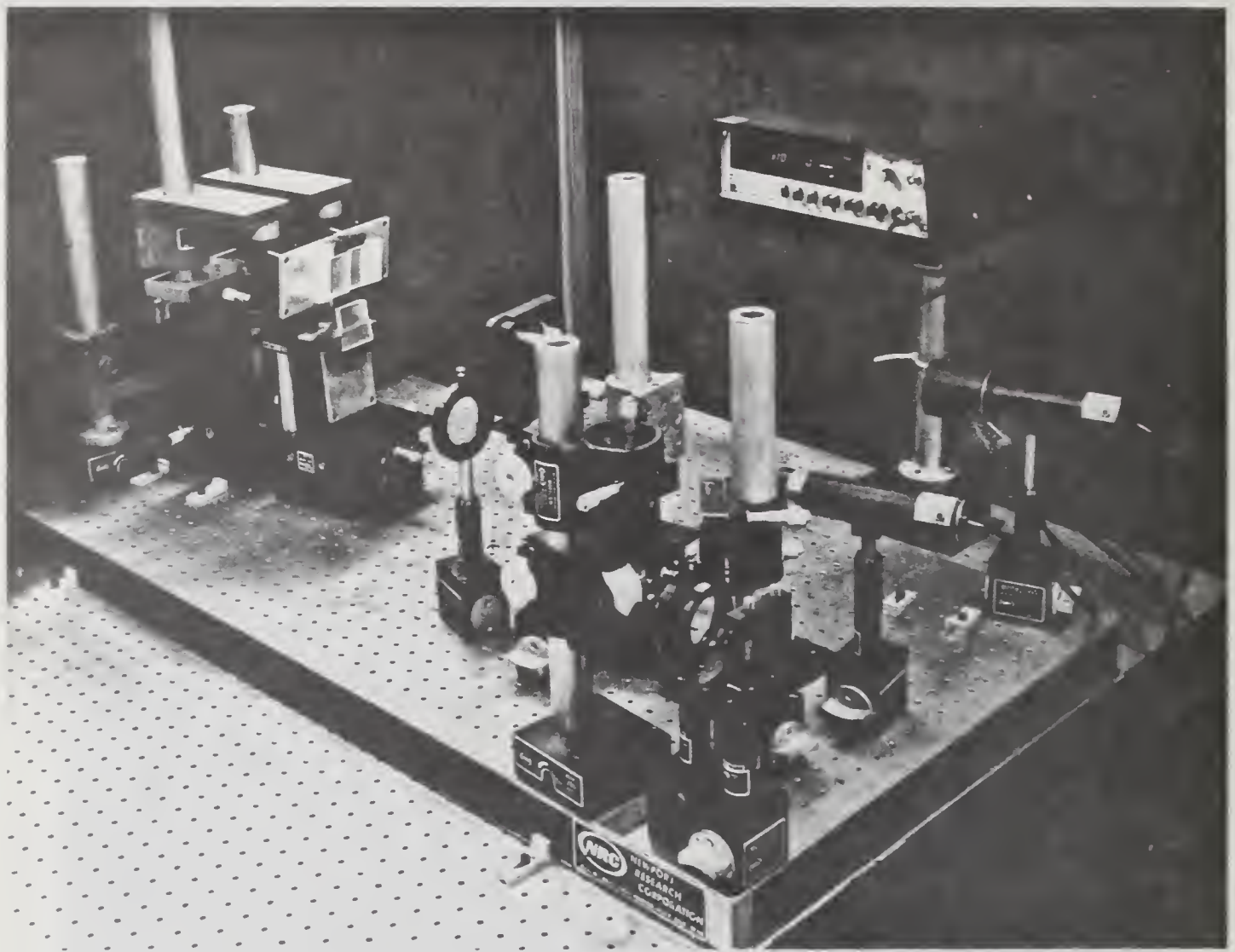
Figure 3. Overall layout of the multiple-pass reflectometer.

90

Figure 4. Simplified schematic for a reflectometer. R_c represents the cell mirrors; R_u represents the unknown reflector. n can assume values of 3,7,11,...for the reflectometer described.
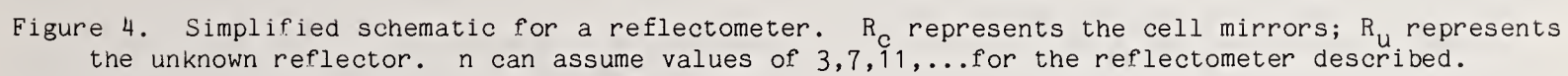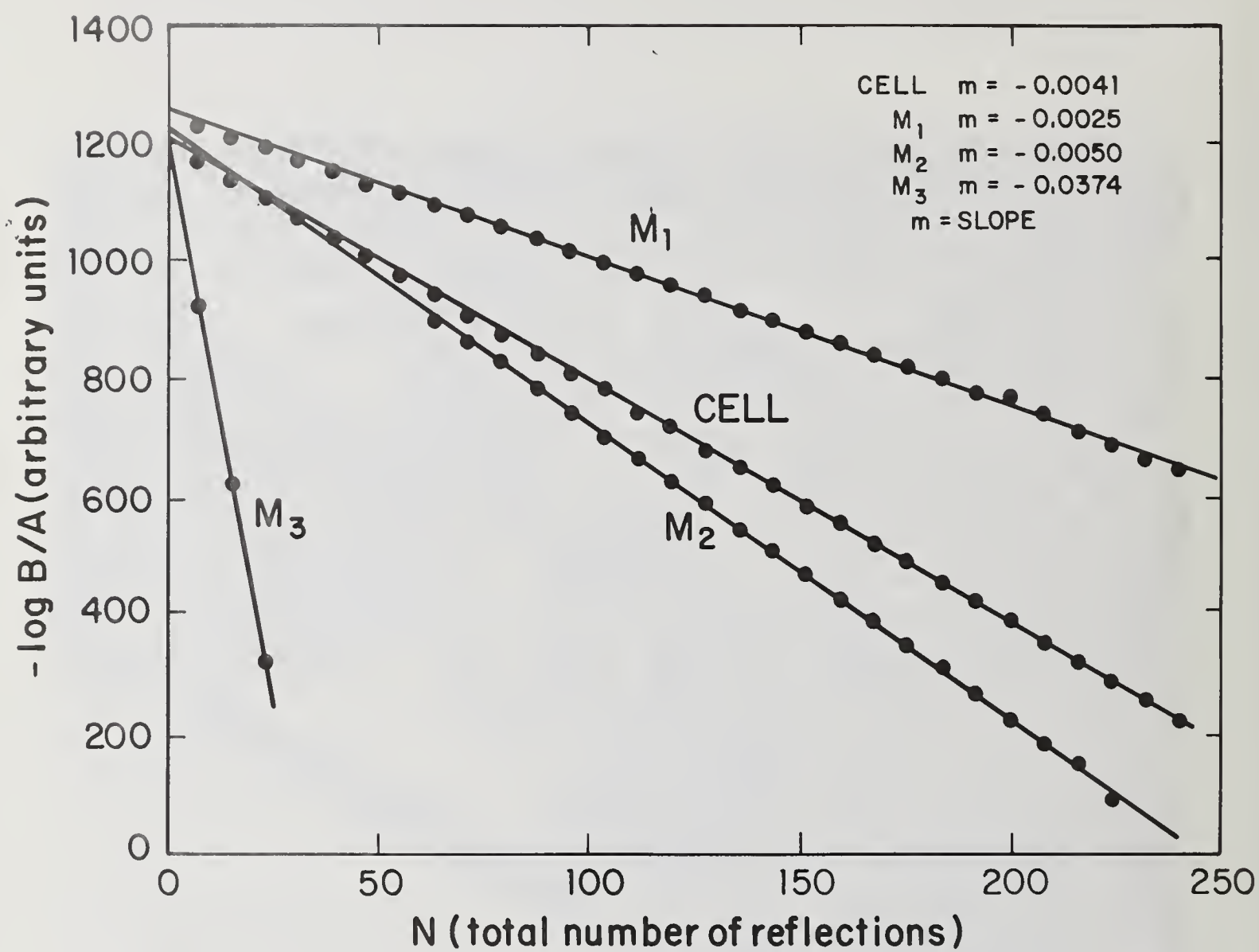
Figure 5. Data plot for several reflectors and the cell, itself, are shown. The reflectances are: $M_3 = 0.8484$, $M_2 = 0.9863$, $M_1 = 0.9976$, and the cell mirror = 0.9906.

A Low Loss, High Power Variable Laser Attenuator

S. R. Foltyn, J. E. Griggs, L. J. Jolin,
J. H. Roberts, and D. Keaton

Los Alamos National Laboratory
Los Alamos, NM 87545

The need for improved means of beam attenuation in uv optical damage experiments has led to the development of a new reflective attenuator using conventional multilayer dielectric optics. The device has low insertion loss even for unpolarized beams, high damage resistance, continuously variable attenuation, and a large clear aperture. Also discussed is a transmissive version of this device which uses standard reflectors or edge filters. Either version lends itself well to computer automation.

Key words: angle tuning; excimer lasers; laser attenuation; optical interference filters

1. Introduction

A perennial problem faced in most experiments using lasers is intensity control, this being typically accomplished by attenuation of the output beam. The problem of laser attenuation is especially important in measurement of optical damage thresholds where repeated variations of fluence are an integral part of the testing. In response to specific needs of the ultraviolet damage projects at Los Alamos, a simple and effective beam attenuator that is particularly useful with high power unpolarized lasers (eg. commercial excimer devices) has been developed. Attenuation is derived from angle tuning of multilayer dielectric interference filters.

2. Existing Attenuation Schemes

The two most commonly used elements for attenuating beams are polarizers and neutral density filters. A third type of attenuator involves Fresnel reflection losses from a set of wedged plates. While each type provides effective attenuation under certain conditions, none was found to be especially well suited for use in excimer-based optical damage experiments. A brief description of these attenuation schemes – and why yet another approach was needed – follows.

Polarizers – Polarizers are available in a variety of configurations and provide, by rotation with respect to the linear input polarization, a simple and efficient means of attenuation. Problems arise however for excimer lasers, which usually produce unpolarized and highly divergent output beams; collimating adequately for small polarizer acceptance angles can be problematic, and producing polarized excimer output can reduce its energy by half.

Neutral-Density Filters – These elements, typically inconel coated glass or fused silica, do not require polarized or collimated beams and are also available in a variety of configurations. However, because they operate by absorbing part of the incident radiation (part is reflected), they have very low ultraviolet damage resistance: 248nm and 351nm damage thresholds of less than 0.05 J/cm^2 have been measured [1]. Furthermore, at even lower fluence levels, metallic filters are subject to changing density values during long exposures.

Wedged-Plate Attenuator – As an alternative to these conventional methods, Bennett and Byer [2, 3] developed a novel attenuator using two pairs of counterrotating quartz wedges. While offering numerous advantages over polarizers and filters, this design is somewhat lossy for unpolarized light and has a limited clear aperture even for long wedges. In addition, there is some beam expansion in the plane of incidence that may be unacceptable, for example, in optical damage testing.

3. Attenuation with Interference Filters

3.1. Principle of Operation

The spectral response of an interference filter is a function of angle of incidence and polarization of the input radiation. For example, as a normal-incidence reflector is tilted, the reflectance band shifts toward shorter wavelengths and transmittance at the design wavelength increases, first for p-and then for s-polarization. This is shown graphically in figure 1 for a reflector of narrow bandwidth - in this case a uv design employing 49 quarterwave layers of Al_2O_3 and SiO_2. For polarized input and ideal non-absorbing films, transmittance at fixed wavelength varies from essentially 100% to 0% over a 12° angular range. Figure 2 shows the result for an unpolarized incident beam: The reflectance (approximately 1-T) varies from 100% at 20° to less than 20% at 33°. This variable reflectance is the basis for laser attenuation.

The use of a narrow bandwidth coating is important. Figures 3 and 4 show that a reflector of moderate bandwidth (23 layers of Sc_2O_3 and MgF_2) exhibits problems such as a large angular tuning range and strong oscillatory behavior. If an attenuator is to be computer driven via an active feedback loop, oscillations at the band edge - artifacts of polarization splitting and reflector sideband structure - are unacceptable. Fortunately, actual Al_2O_3/SiO_2 reflectors were found to give a relatively smooth, monotonic functional response as shown in the next section.

The above discussion pertains to the use of standard quarterwave dielectric reflectors as attenuating elements. It should be noted that improved performance can be achieved with different filter designs such as long- or short-pass filters, or non-polarizing edge filters. An example is presented in a later section.

3.2. Reflective Attenuator

Figure 5 is a photograph of a reflective attenuator showing the beam path for an incident angle of 26°. Each mirror rides on a carriage that allows translation in the input/output beam direction. The carriage fixtures also allow mirror rotation about an axis perpendicular to the plane of incidence.

Simultaneous translation of the mirror carriages in opposite directions is accomplished by a double rack and pinion driven by a stepper motor. A cam, visible at center, provides coordinated rotation of the reflectors. The cam faces were contoured on a numerically-controlled milling machine to provide the following relationship between angle of incidence θ, and the translational distance x:

$$x = D/(2\tan 2\theta),$$

where D is the distance between translational axes and $x \equiv 0$ when the beam segment between mirrors is vertical ($\theta = 45°$). The design shown is operable for incident angles from 25° to 50°.

One problem with the prototype shown in figure 5 - and a key concern for tunable attenuators in general - is beam deviation. The design is particularly sensitive to contour errors in the cam and tracking errors in the carriages. Nonetheless, this initial version of a reflective attenuator exhibited less than 0.5 mrad of angular beam deviation and no measureable beam displacement. A more robust version with linear bearings and a precision cam has been fabricated but has not yet been evaluated. Also, computer-coordinated translational and rotational hardware could eliminate entirely the need for a cam, but this variation has not yet been pursued. To date, no simple linkage arrangement has been found that can provide the required mirror motion.

Optical performance of the reflective attenuator at 248nm is shown in figure 6 - a plot of transmitted energy fraction versus incident angle. The reflectors were well-centered at 248nm and employed 49 layers of Al_2O_3 and SiO_2 giving a FWHM bandwidth of only 24nm. Energy throughput could be varied from approximately 99% to 3% over a 10° tuning range. The small ripples in the response function for these off-the-shelf reflectors are not problematic in most applications; however, as will be shown in the next section, they can be eliminated by use of an alternate coating design. The small difference between the results of figure 6 and the prediction of figure 2 is a result of using, for the calculations of figures 1 and 2, a value of 1.70 for the index of Al_2O_3 instead of the more realistic value of 1.65. Also, the use of two reflectors in the actual attenuator effectively squares the response function of a single element.

3.3. Transmissive Attenuator

Figure 7 is a photograph of an attenuator for which the output is the transmitted beam fraction. Two elements are used to compensate for beam displacement. The fixture is much less complicated than a cam-based reflective attenuator, and has been further simplified by elimination of the orthogonal adjustments on each optic holder. The same reflectors described in the previous section can be used; however, maximum throughput for two reflective surfaces is limited to about 70%.

Improved response is obtained by using edge filters as shown in figure 8. Here, attenuator throughput is calculated for two identical elements, each with a filter on one side and a matched AR coating on the other [4]. Actual transmitted energy for such filters was found to be variable from 0.3% to 88% over a 28° tuning range.

4. Discussion

Thus far, several advantages and disadvantages of this type of attenuator have been presented; these are summarized in table 1.

<p align="center">Table 1. Advantages and Disadvantages of Tunable Filter Attenuators</p>

<p align="center">Advantages</p>

* High Damage Resistance[a]

* Low Loss Even for Unpolarized Beams

* Large Clear Aperture (Typically 70% of Component Diameter)

* Continuously Variable Attenuation

* Suitable for Automation via Active Feedback

Disadvantages

* Output Polarization Varies if Input is Unpolarized[a]

* Attenuator Coatings Must Be Designed for a Specific Wavelength

* Stray Reflections Must Be Blocked

[a]See discussion below

Damage resistance of optical coatings depends strongly on both the coating materials and the vendor who deposits them. In addition, run-to-run variations can be quite large, especially for non-sequential coating runs. What can be said, however, is that both detuned reflectors and edge filters have damage thresholds that are comparable to those for standard reflectors using the same materials. Based on this argument, thresholds of up to 4 J/cm^2 (248nm) and 8 J/cm^2 (351nm) can be obtained at 10-20 ns pulselengths for an appropriate choice of materials and vendor.

Regarding the output polarization, potential users should be cautioned that, in some cases (eg. when conventional reflectors are used), the output polarization state varies as the attenuator is tuned. This can be alleviated to a large extent by the use of non-polarizing edge filters. If, however, the attenuator optics are illuminated by s- or p-polarized light, then input polarization will be preserved at the attenuator output.

5. Conclusions

A new type of variable laser attenuator has been presented. While several implementations of this attenuator have been constructed and described, all are based on angle-tuning to produce a change in reflectance (or transmittance) of multilayer dielectric filters. The achieved ranges of attenuation are useful for most applications and can be further extended by use of additional filter elements. Several features of this design make it particularly well-suited for use with high-power, unpolarized excimer lasers.

6. References

[1] L.J. Jolin, S.R. Foltyn, Damage Thresholds of Ultraviolet Neutral Density Filters, Los Alamos Memorandum CHM-5-83:119 (1983).

[2] K. Bennett, R.L. Byer, Computer-Controllable Wedged-Plate Optical Variable Attenuator, Appl. Opt. 19(14), 2408 (1980).

[3] K. Bennett, R.L. Byer, Variable Laser Attenuators - Old and New, Laser Focus, April, 1983.

[4] Filter design data courtesy J. Latore, Airtron, Morris Plains, New Jersey.
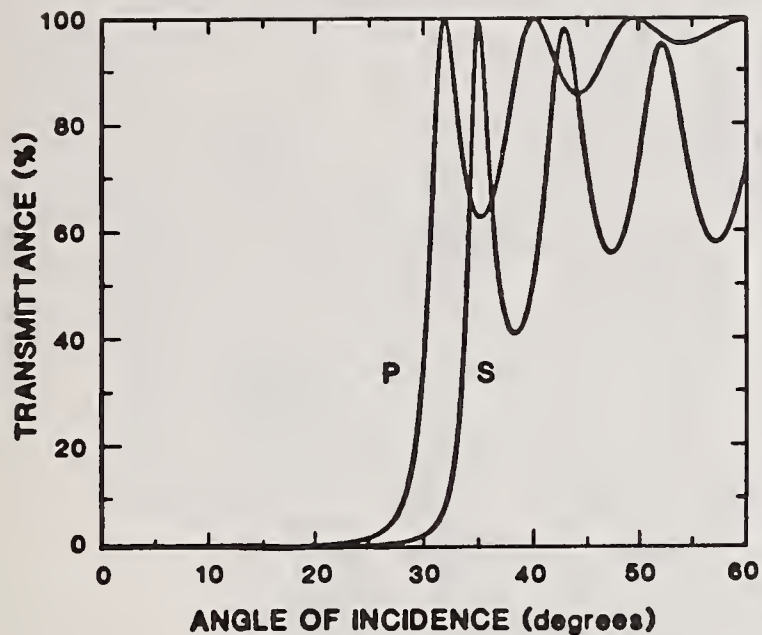
Figure 1. Calculated change in transmittance versus incident angle for either p- or s-polarized irradiation of a narrow band reflector. In this and the next three figures, reflectors are designed for use at normal incidence and the wavelength is fixed.
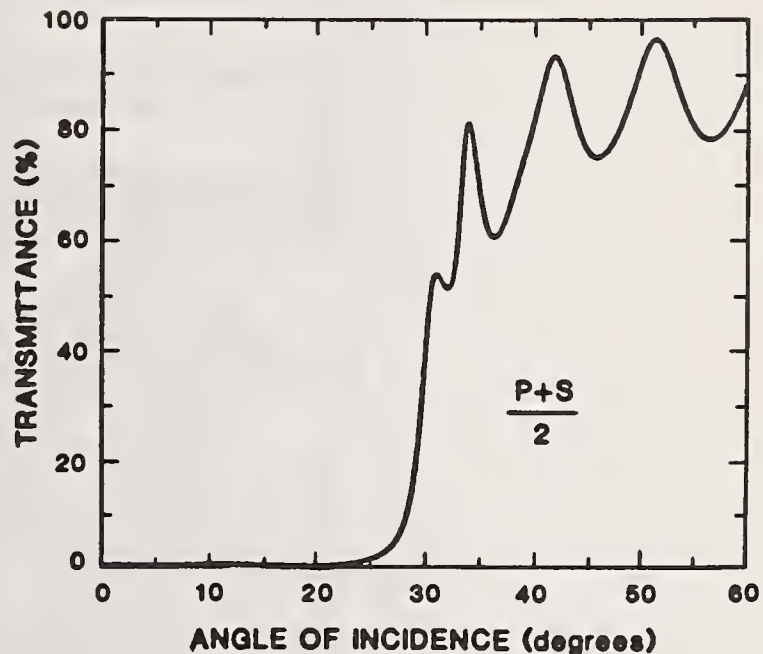
Figure. 2. Response of the Fig. 1 reflector to unpolarized light. The small oscillation on the edge of the reflectance band is problematic and was not observed experimentally (see text).
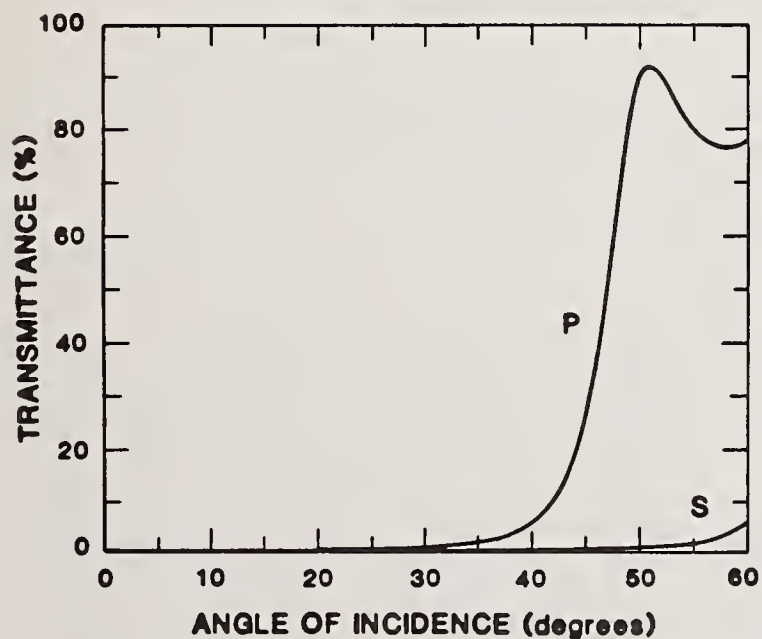
Figure 3. Calculated response for a reflector of moderate bandwidth showing alarger angular range and a greater degree of polarization splitting.
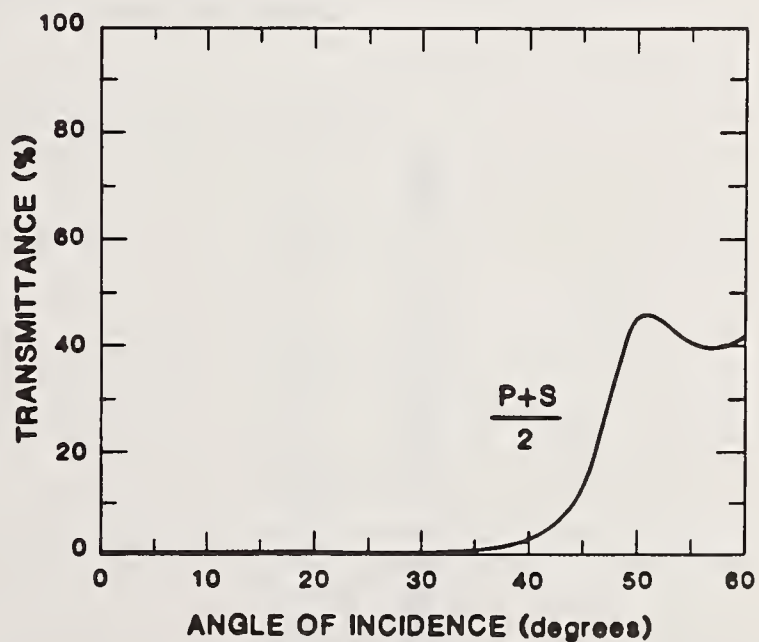
Figure 4. For the moderate-bandwidth case with an unpolarized incident beam, the range of attenuation values is limited and response is strongly oscillatory.

97
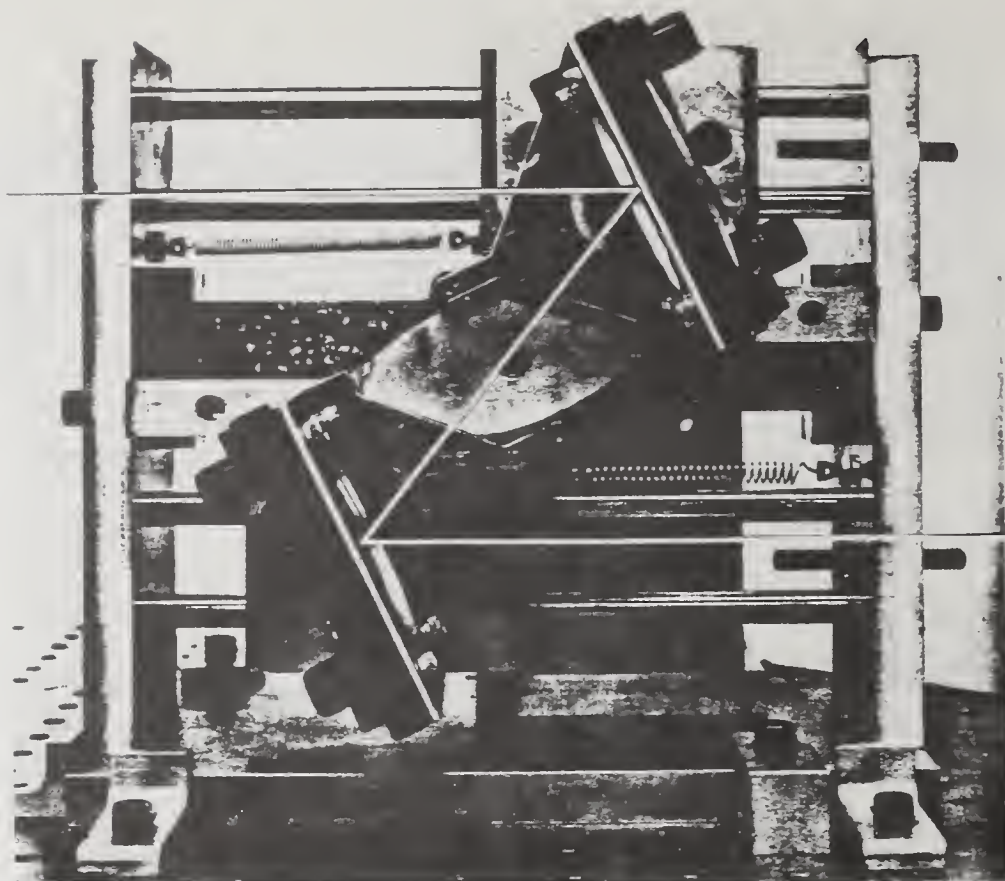
Figure 5. Reflective attenuator prototype.
Mirror rotation is coordinated with trans-
lation by the camvisible at center; this allows
incident angle to be continuously varied from
25° to 50° without deviation in the output beam.
Beam path for an incident angle of 26° is shown.
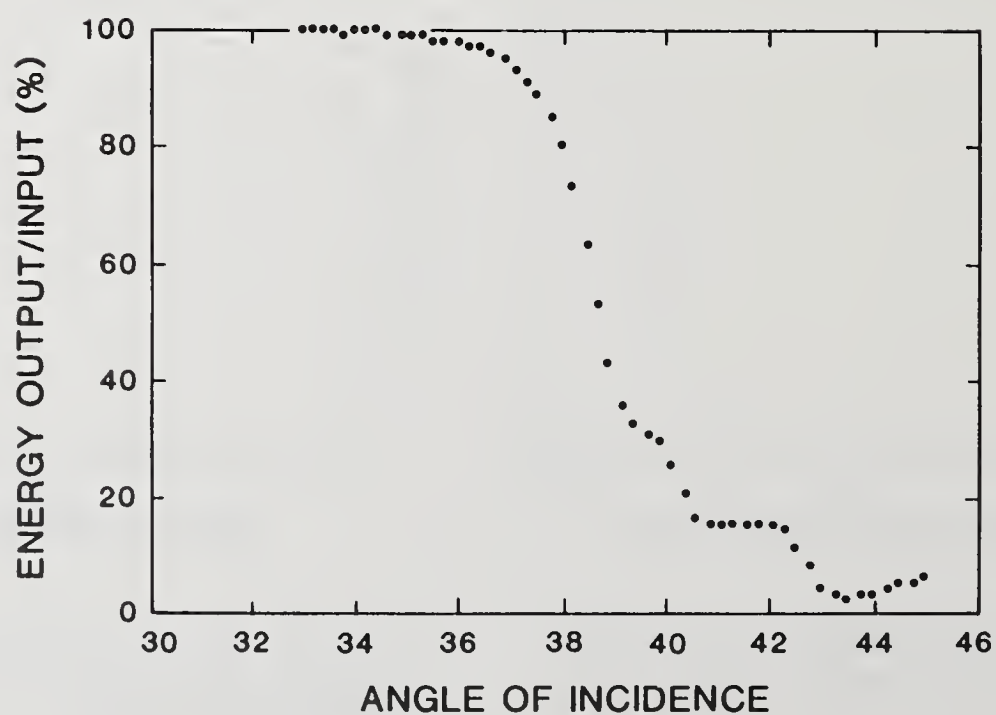
Figure 6. Measured throughput of the reflective
attenuator for unpolarized illumination at 248 nm.
A 10° change in incident angle gave a monotonic
decrease in output energy fraction from over
98% to 3%.
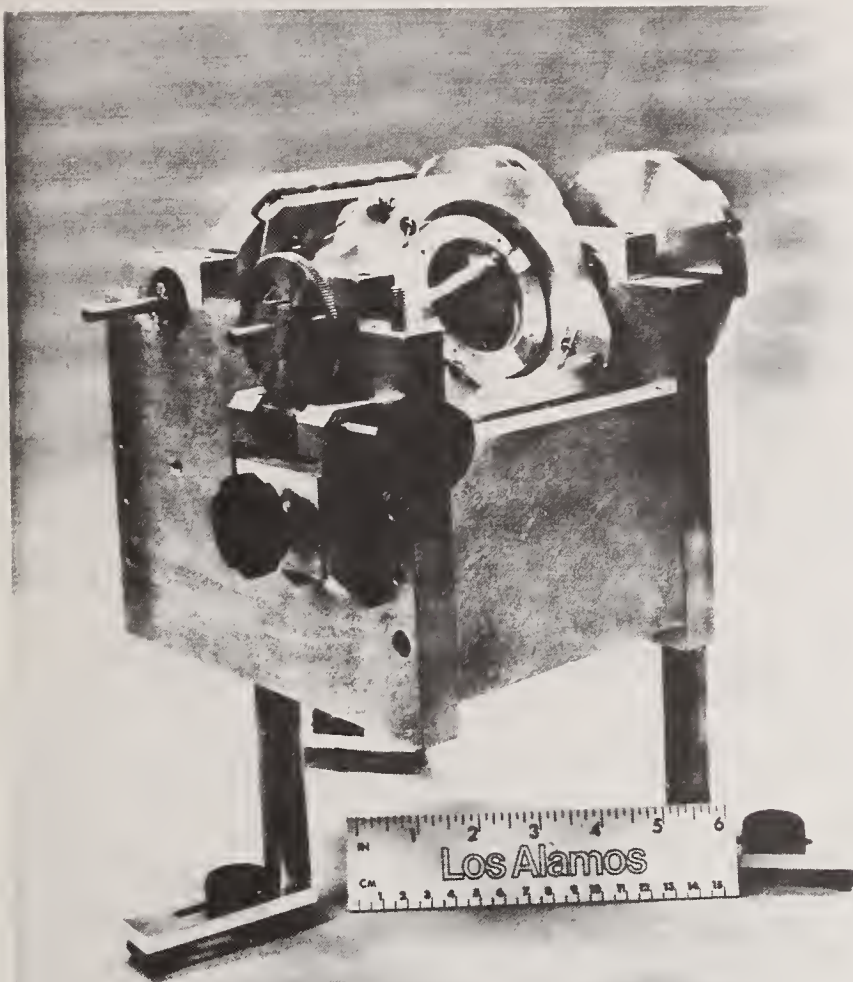
Figure 7. Transmissive attenuator employing two counterrotating elements. Interference filters can be used on from one to four surfaces depending upon the required attenuation range. Nonactive surfaces must be antireflection coated to minimize losses.
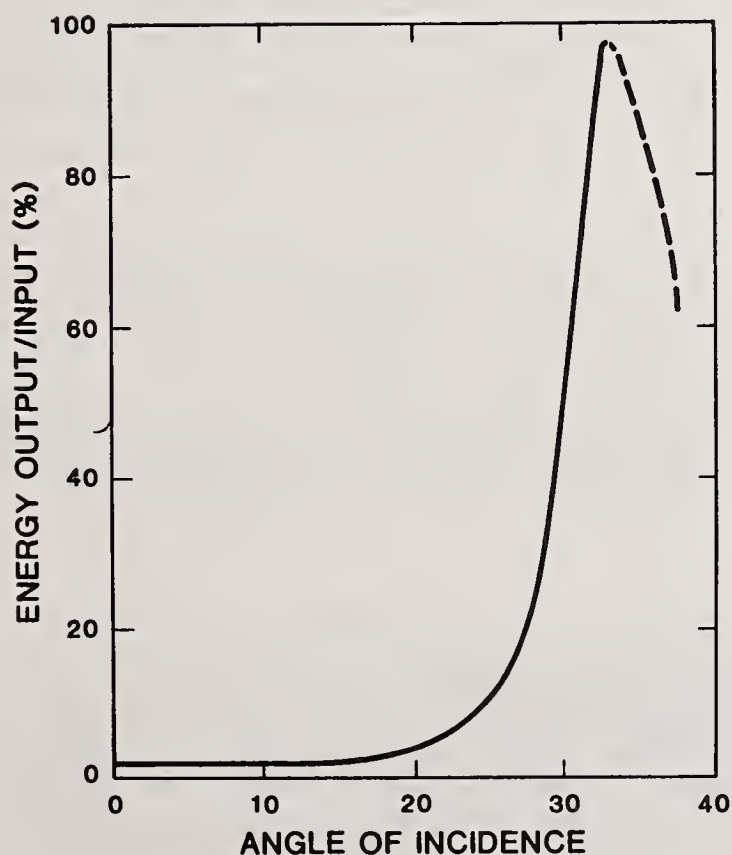
Figure 8. Calculated response of a transmissive attenuator at 351 nm (unpolarized) using two Al_2O_3/SiO_2 edge filters with AR-coated back surfaces. (Edge filter data courtesy J. Latore, Airtron).

STUDIES OF CO_2 LASER INDUCED DAMAGE TO INFRARED OPTICAL MATERIALS AND COATINGS

D.R. Gibson and A.D. Wilson

Barr & Stroud Limited
Physics Department
Caxton Street, Anniesland
Glasgow G13 1HZ, U.K.

A new versatile CO_2 laser damage facility which uses a TEA laser giving a single mode output of up to 15 Joules per pulse is described. The temporal characteristics of the pulse can be readily varied. A method of producing pulses with durations less than that of the gain switched spike using plasma-based temporal attenuators is described. Data is presented on a range of infrared optical materials as well as commercial and experimental AR coatings and dielectric reflectors. Detailed examination of the damage morphologies coupled with the dependence of the damage threshold on pulse length is used to determine the mechanisms of laser induced damage.

KEY WORDS: CO_2 Laser Damage; Coatings; IR Materials; Plasma; Pulse-Length Variation.

1. INTRODUCTION

The interaction of CO_2 laser radiation with optical materials and thin films continues to be of considerable technological and scientific importance to those engaged in the design of optical systems for handling high energy laser pulses.

Inspection of literature data on transmissive components reveals that a wide range of laser damage threshold (LDT) values have been reported for any given material. This is not too surprising in view of the reported LDT dependence on spot size [1, 2], pulse length [3, 4], method of surface preparation [5], sample purity [6], and the type of coating [7, 8]. It is also noted that little data is available on the performance of the commercial coatings which most system designers are constrained to use. Consequently, we have initiated a study programme which will examine the interaction of CO_2 TEA laser pulses with substrate materials and commercial and experimental coatings as a function of the laser parameters (pulse temporal profile, spot size, pulse repetition rate, etc.) and the methods of preparation of components (substrate polishing, cleaning, film deposition conditions, film materials, etc.). The aim is to provide a comprehensive and consistent data base which can be used by system designers.

In this initial paper we describe the CO_2 TEA laser damage facility including methods of varying the pulse temporal characteristics to allow the pulse length dependence of the LDT to be investigated. This aspect is not only of practical interest to the system designer, but, as will be demonstrated, can also provide useful insights into the mechanism of the damage process.

The laser damage characteristics of a range of infrared optical materials (Ge, ZnS, ZnSe, KCl, and chalcogenide glasses) as well as commercial and experimental antireflection coatings and multilayer dielectric reflectors are presented. Data on damage morphology and the pulse length dependence of the LDT are used to comment on damage mechanisms in certain materials and coatings.

2. THE CO_2 LASER DAMAGE FACILITY

The CO_2 single transverse mode TEA laser (Laser Applications, Hull, U.K.) is housed in a large enclosed optical table assembly, as shown in figure 1. The TEA cavity has an unstable resonator configuration, the output pulse being extracted using a scraper mirror. A 3W cw rf waveguide, wavelength tunable CO_2 laser can be used to injection lock the output of the TEA cavity to the normally dominant 10P20 transition (10.591μm). Cavity tuning both the TEA and injection lasers enables operation in a single longitudinal mode [9] thereby eliminating mode beating. The maximum energy output is 15J for single shot operation, 10J at 5Hz repetition rate and is reproducible to $\pm$ 5%.

As a consequence of the TEA cavity configuration, the output beam is annular (50mm o.d., 25mm i.d.). This is reshaped using an axicon to minimise the central obscuration (28mm o.d., 3mm i.d.) before being focussed by an AR coated Ge lens to give the effective far field profile shown in figure 2a. Use of a beam profiling detector array during set-up eliminates significant alignment errors and thus beam irregularities which would be undetectable by examination of burn marks.

The temporal profile can be varied by changing the TEA cavity gas composition. Normal operation ($CO_2/N_2/He$ = 1/1/8) gives an initial gain switched spike of FWHM $\simeq$ 100ns followed by a 2µs relaxation tail, figure 2b. Increasing the N_2 content allows the tail to be extended to $\simeq$ 4µs which is on the limit for a system with an effective output reflectivity of $\simeq$ 50% [10]. The tail can be extended to $\simeq$ 6µs by injection locking on the 10P16 transition (10.551µm). It is likely that the 10P16 transition predominates during the initial part of the pulse but that the higher gain 10P20 transition predominates during the later stages. The small change in wavelength (0.04µm) is not considered important for damage work. Running without N_2 gives a high intensity spike of FWHM $\simeq$ 90ns (injection locking used) without a relaxation tail, figure 2b.

Pulses with durations less than that of the gain switched spike are produced using a plasma-based temporal attenuator. Using the arrangement sketched in figure 3a, pulse durations as short as 20ns FWHM can be reliably obtained, figure 3b. (The incident pulse had the normal spike and tail form).

The use of a plasma to attenuate a CO_2 laser beam is well established [11-14]. In all cases the beam is tightly focussed in order to cause electric field induced breakdown in a gas. With air breakdown, we find the spatial profile of the transmitted pulse is poor, with very pronounced side-lobes, figure 4a, and is also highly variable making accurate damage studies impossible. Air breakdown is initiated at random dust particles which provide the initial electrons for avalanche[12]. The ensuing plasma, which is irreproducible and of non-uniform density, acts as a lens of spatially variable power deflecting radiation out of the direct beam. It is also well established [15-19] that surface plasma formation at transparent solids leads to pulse truncation. We have examined a number of materials (KCl, Ge, AR coated Ge) and find that the spatial profile of the transmitted pulse is regular and without significant side-lobes, figure 4b, reflecting the near uniform plasma density formed at high incident/damage threshold fluence ratios: typically > 20 in this work. A fresh area of the solid is exposed on each shot. The superimposed spatial profiles from three consecutive shots, figure 4c, show that the reproducibility of the transmitted pulse is excellent, and thus a surface plasma pulse truncator can be used for laser damage work.

Two further advantages accrue from the use of a surface plasma initiator: (i) The energy density required for pulse truncation (100Jcm^{-2} for AR coated Ge) is lower than that required using air breakdown 2000Jcm^{-2}); (ii) The transmitted pulse length (20-90ns) can be altered by varying the incident fluence. It can be shown that the broadening of the spatial profile of surface plasma truncated pulses (cf. figures 2a and 4b) is due to the reduced attenuation experienced by the beam wings. This effect is eliminated from damage threshold evaluations by 2D spatial integration to obtain the peak energy density.

The optical elements and the beam diagnostic equipment, figure 5, are housed in a laminar flow cabinet to minimise dust contamination. Pulse energy is monitored using calibrated volume and surface calorimeters (Scientech). The temporal profile of the pulse is measured using Ge photon drag detectors (Rofin). The spatial profile of the beam is measured using a 64 element pyroelectric array (Spiricon). In all measurements reported herein, the spot size is > 0.9mm and is defined as the 1/e^2 diameter of an equivalent Gaussian fitted to the beam profile. The onset of damage is assessed by viewing, with a x 6 telescope, the scatter from a HeNe beam co-incident with the area irradiated by the high energy pulse. The damage thresholds are single shot values and are reported as the peak energy density at which an increase in scatter is first observed from either the front or back sample surfaces.

3. RESULTS AND DISCUSSION

3.1 IR Substrate Materials

Figure 6 summarises the damage threshold, measured with a spike + 2µs tail pulse, and absorption coefficient data for a range of ir substrate materials. Clearly there is no correlation between LDT and absorption coefficient. This is not surprising since the materials also exhibit a wide range of thermal behaviour and, as we shall discuss, are subject to various damage mechanisms.

The two samples of n-type Ge have very similar damage thresholds. The Barr and Stroud material is a standard ir grade, polished using alumina. The Laser Power Optics material is designated laser

quality. Both samples have similar surface roughnesses (around 20Å RMS) but the LPO material has fewer residual polishing defects, such as scratches and digs, as determined by Nomarski microscopy.

Both samples show very similar damage morphologies comprising localised sites distributed within the irradiated area and occurring on the entrance face only, figure 7. Since the dimensions of these sites are generally in the range 25 to 100μm with an inter-site separation of up to 200μm, studies carried out with small diameter beams (< 200μm) will measure a wide range of LDT values depending on whether a defect is within the irradiated area. In the present work, use of a large diameter beam (> 0.9mm) allows examination of the distribution and frequency of the damage sites and gives the defect dominated damage threshold which should be independent of spot size [20]. Most often the damage sites are located along residual polishing scratches but are also found to follow a smooth locus which does not correspond to a surface feature (see top photograph in figure 7). Individual damage sites show signs of melting. This is most clearly demonstrated by surface profiling which reveals a central raised peak and a raised rim, figure 7. This morphology is consistent with the melting/resolidification process described in detail by Willis and Emmony [21]. At the periphery of the damage site there is a ripple pattern which may be due to interference of the incident radiation with a defect scattered wave as suggested for many other materials [22, 23]. We suggest that damage occurs at absorbing regions (probably polishing debris or physical damage) which are located in surface or sub-surface defects (scratches or grain boundaries). The obvious surface scratches have sub-micron widths and thus are in the regime where enhanced field and absorption effects are most likely for 10.6μm radiation [24].

In a preliminary study of ion beam planing of conventionally polished Ge we have observed significant increases in LDT (up to 30%). The ion planing process removes some of the layer of physical damage produced by conventional polishing, widens and reduces the slope of surface scratches and also reduces the surface roughness at low spatial wavelengths, i.e. below 50μm. Each effect is expected to increase the LDT value. This work is continuing.

In a high refractive index material, such as Ge, exit surface damage should predominate [28]. However, as will be discussed in a further paper [25], the non-linear nature of the defect induced thermal damage mechanism modifies the back surface field distribution and only front surface damage is incurred.

The infrared glasses (As_2S_3, As_2Se_3 and GeAsSe) show very low damage thresholds. The damage morphology of GeAsSe glass consists of localised sites occurring primarily on the exit face but also occasionally on the entrance face. Unlike Ge, the damage sites are not particularly associated with obvious surface defects. Profilometry reveals that these sites are pits, figure 8. In view of the relative softness of this class of material it is likely that localised defects will be produced during the polishing process. The existence of a defect surface is supported by laser calorimetry data for a range of sample thicknesses which show the bulk absorption coefficient to be $\simeq$ 0.015cm^{-1} with a typical surface contribution of $\simeq$ 0.06% per surface. Such defects are most probably located in a sub-surface layer. The low damage thresholds may be understood by noting that for impurity dominated damage [26] the LDT is independent of the thermal properties of the impurity but scales as $T_{Dh}\sqrt{k_h}$, where T_{Dh} is the damage temperature and k_h is the thermal conductivity of the host material. The very low value of k_h for GeAsSe (2.5mW cm^{-1}K^{-1} [27] cf. 600mW cm^{-1}K^{-1} for Ge) coupled with its low "melt" temperature would combine to give a low LDT value. That pitting damage occurs preferentially on the exit face is consistent with the enhanced electric field near that surface leading to preferential heating of exit surface defects.

Although having absorption coefficients which differ by an order of magnitude, ZnS and ZnSe, both produced by chemical vapour deposition, have very similar damage thresholds and morphologies. Damage occurs at the exit face often having the form of a single deep pit, as in the lower surface profile of figure 9, and is always accompanied by intense plasma formation. This suggests an electron avalanche ionisation mechanism. The upper photomicrographs of figure 9 illustrate a damage site in which material removal has not occurred. Rather a large area, sub-surface damage event has fractured the sample surface. The profile obtained normal to the fracture shows the surface has been displaced upwards by $\propto$ 1μm. This is a fortuitous "snapshot" of the first stage in the damage event. If slightly more energy had been input the deformed surface would have been further stressed and the more normally observed pit would have formed. The lower photograph of figure 9 shows an instance where only part of the surface has been lost. The clear evidence of sub-surface initiation, confirming the prediction of Boling et.al.[28] that standing wave patterns should be largest just inside the exit face, is further evidence for field induced avalanche ionisation.

KCl also shows damage at and near the exit face with extensive fracturing occurring just within the sample. This is again consistent with an avalanche ionisation mechanism.

3.2   Coatings on Ge : Location and Nature of Damage Sites

An examination of laser damage sites on coated Ge, using Nomarski microscopy, reveals a variety of morphologies which can be broadly classified into two groups:

 (i) damage primarily in the film with secondary effect on the substrate;

(ii) damage primarily on the substrate with secondary effect on the film.

Examples of both types are shown in figure 10. A typical $\lambda/4$ layer of ZnS (LDT $\simeq$ 0.5 × LDT of uncoated Ge) shows film damage in the form of localised pitting. With a $\lambda/4$ layer of ThF_4 (LDT $\simeq$ 0.2 × LDT of uncoated Ge) the damage sites are located on the substrate and appear similar to those found on uncoated Ge. Note especially the peripheral ripple pattern which is characteristic of the Ge melt-damage event, see figure 7, and is not observed with film dominated damage. The ThF_4/Ge and uncoated Ge surface profiles are also similar exhibiting a raised hump in each case. A "substrate-like" damage morphology is also observed, figure 11, for a Ge/(LH)^n reflector with n = 1, where L = ThF_4 and H = ZnS, (LDT $\simeq$ 0.75 × LDT of uncoated Ge). When n is increased to 4, virtually no radiation reaches the Ge surface and the damage sites are clearly located in the films (LDT $\simeq$ 1.25 × LDT of uncoated Ge). It is noted that "substrate-like" damage only occurs when ThF_4 films are contiguous to the Ge substrate and never with ZnS films.

At this stage we offer a tentative explanation of these observations and attempt to determine whether these particular systems are limited by the films or by the substrate.

In comparing samples containing ThF_4 contiguous to the Ge which show "substrate-like" damage, the effect of differences in fluence at the substrate-film interface can be examined by normalising the laser damage threshold, LDT, with respect to the interface transmittance, T_i, i.e. with respect to the square of the electric field in the substrate. The product LDT × T_i is similar for the single layer and the Ge/(LH) partial reflector but significantly lower than obtained for uncoated Ge. This suggests that in addition to the fluence at the film-substrate interface an additional factor operates to control the damage threshold.

It is well known that the substrate-film interface can show anomalously high absorption [29, 30]. In the present case, CO_2 laser calorimetry has revealed absorption coefficients of $\simeq$ 12cm^{-1} for $\lambda/4$ ZnS and $\simeq$ 40cm^{-1} for $\lambda/4$ ThF_4 films when deposited onto Ge. The average absorption coefficient of a (ThF_4-ZnS) LH-pair within a Ge/(LH)^4 reflector is estimated from laser calorimetric data, as $\simeq$ 6cm^{-1}. Since the absorption in the Ge/(LH)^4 reflector is dominated by the top two (LH) periods appreciable substrate-film interface absorption is present in our samples. This enhanced absorption is most likely associated with localised defects. When these defects are heated by absorption of radiation both the substrate and film are expected to damage and the damage morphology would be expected to mimic uncoated substrate damage since the new interface defects and the "intrinsic" substrate defects are both located close to the substrate-film interface. As can be seen in figure 10 the damage sites in ThF_4/Ge are often located at substrate scratches where the field enhancement effect [24] will still be significant since ThF_4 has a low refractive index, n $\simeq$ 1.35.

Thus we conclude that, in the cases examined, defects introduced during film deposition are responsible for damage in coated Ge optics.

3.3   Diamond-like Carbon AR Coatings on Ge

Diamond-like carbon (DLC), made by plasma assisted decomposition of hydrocarbons, has received considerable attention due to its extreme hardness and physical/chemical durability [31-36]. The description "diamond-like carbon" is a misnomer since the films consist of crystalline regions in a matrix of amorphous hydrogenated carbon [31]. By varying the composition and structure through processing parameters [33] the refractive index can be varied between $\simeq$ 1.8 and 2.3 and thus DLC is suitable for use as an antireflection coating for high index substrate materials. An absorption minimum between 10 and 11 microns has led to its suggested use as an AR coating for Ge in CO_2 laser systems [34].

We have measured the absorption and damage characteristics at 10.6μm of Ge substrates coated on both faces with DLC AR coatings produced at Barr and Stroud using rf plasma assisted decomposition of butane. The production version of this coating is marketed as ARG4 [35]. A sample produced by STC (UK) using a similar process has also been studied. The data are presented as a plot of LDT (spike + 2μs tail pulse) against the reciprocal of the single film absorptance, figure 12, and show the proportionality expected for film dominated damage. The range of absorptance values is much wider than would be found in commercially available coatings. The lowest absorptance films (3.2% per film) produced for this study are comparable to the best reported elsewhere [36] and define the minimum

absorption coefficient (250cm^{-1}) obtainable for DLC films with n $\simeq$ 2. Normal production runs typically produce films with between 4% and 6% absorption and are represented by two points in figure 12. The STC sample also corresponds to this case. The typical LDT values of $\simeq$ 6Jcm^{-2} are within a factor of two of the values reported by Dischler et.al.[36] for films prepared from benzene and measured using a smaller spot size.

At or just above the LDT, the damage morphology consists of a region of film ablation at the centre of the irradiated area and occurs on both exit and entrance faces. This has an irregular "petal-like" boundary which may indicate that damage is initiated at a series of closely spaced defects.

3.4   High Efficiency AR Coatings on Ge

A number of commercial and experimental high efficiency AR coatings on Ge have also been investigated. These include:

  (i) ARG3 produced by Barr and Stroud [37],

  (ii) the Infralin series (211, 213, 214/216) produced by Balzers [38],

(iii) MLAR coatings on Ge (6040001, 6040008) produced by OCLI [39],

 (iv) a "laser durable" coating produced by STC (Ge0023N) [40],

  (v) single layer ARCs of ZnS and ZnSe.

Measurements were made with the coatings on both faces of the Ge substrates. Transmission spectra, figure 13, reveal the differences between these coatings. ARG3 is a broadband coating for the 8-12μm region. The Balzers and OCLI coatings are similar to ARG3. The STC coating has a V-type character-istic with a transmission region just slightly narrower than for a single layer ARC of ZnS and is specifically designed for use at 10.6μm. The 10.6μm reflectance of most of the commercial coatings is low being typically 0.1%. The ZnS coating has a reflectance of $\simeq$ 1.5%.

A plot of LDT (spike + 2μs tail pulse) against reciprocal film absorptance, figure 14, shows that even for this disparate set of coatings which vary in design, thickness and film materials the trend of increasing damage threshold with lower absorptance is followed. In particular the three examples of the ARG3 design produced with different absorptances emphasise the need to minimise the coating absorptance. That the broadband coatings show higher absorptances and have lower damage thresholds than either the single films or V-type coating is not surprising since, in addition to relatively non-absorbing ZnS and metal fluoride layers, they may contain Ge and thin layers of metal oxides. The STC V-coat, specifically designed for use at 10.6μm, has a slightly lower damage thres-hold than a single layer ARC of ZnS but has the advantage of a minimised reflectance which may be relevant if feedback to a laser cavity must be avoided.

The damage morphologies of all of these coatings show signs of localised damage,most often resembling the sites shown in figure 10 for ZnS films. This again suggests defect controlled damage with the defects, perhaps, occurring in clusters. The ratio of the LDT of ZnS coated and uncoated Ge is $\simeq$ 0.6 for the best coatings examined. This value is close to the ratio of interface transmitt-ances ($\simeq$ 0.65) and suggests that damage may be influenced by the substrate as well as the film defects. For all other films and coatings the ratio is less than 0.5 indicating that film damage predominates.

3.5   Dependence of LDT on Pulse Temporal Characteristics

For selected materials and coatings the LDT has been measured for a range of pulse temporal characteristics. Both variation of the relaxation tail, in which the pulse shape changes, and also pulses with durations less than or equal to that of the gain switched spike, in which the pulse shape is similar, have been used. To test the validity of using plasma attenuated pulses for laser damage studies, a pulse of 90ns was generated from a spike and tail input pulse and used to damage uncoated Ge. The peak fluence LDT was 22Jcm^{-2} which is within 10% of the LDT measured using a 90ns pulse produced by running with no nitrogen in the TEA cavity (LDT = 20.2Jcm^{-2}). A further check was carried out using freshly diamond fly-cut OFHC copper which being a surface absorber should show a $t^{\frac{1}{2}}$ depend-ence [41]. The peak fluence LDT values determined at 50ns and 90ns were 69Jcm^{-2} and 95Jcm^{-2} respectively which do indeed conform to a $t^{\frac{1}{2}}$ law within the measurement accuracy. These data demonstrate the validity of the use of plasma attenuated pulses.

Damage thresholds are shown in figure 15 for materials and figure 16 for AR coatings on Ge. The data are also plotted against pulse length in figure 17 for the pulses of similar shape i.e. 20, 50 and 90 ns FWHM. These latter plots can be used to provide further information on the mechanism of damage. We note that impurity dominated damage leads to a dependence on the square root of the pulse

length [26, 42]. The time dependence of avalanche ionisation is more complex. At short pulse lengths the energy density must exceed a critical value for creation of electrons whereas at longer pulse lengths there is sufficient energy for electron creation but the intensity (i.e. the rate of energy input) must exceed a critical value to overcome electron energy losses. Consequently the damaging fluence is expected to be independent of pulse length at short pulses and approximately proportional to pulse length for longer pulses [42-45]. The transition between these dependencies may occur in the nanosecond regime [44].

The present data have been fitted to $E = At^n$ where n is equal to either $\frac{1}{2}$ (defect) or 1 (breakdown). For Ge and GeAsSe glass substrates and for the AR coatings on Ge the data can be fitted adequately by using $n = \frac{1}{2}$, confirming a defect mechanism. Using 1.15ns and 70ns CO_2 pulses, a near $t^{\frac{1}{2}}$ relationship was observed by Newnam and Gill [3] for both coated and uncoated Ge. For ZnS, ZnSe and KCl the data are adequately fitted using $n = 1$ suggesting an electron avalanche mechanism. Newnam et.al. [46], using pulses of 1.15ns and 65ns duration, observed a $t^{\frac{1}{3}}$ dependence for damaging fluence which apparently contradicts the present data. A possible explanation of this discrepancy may involve the time dependence argument noted previously. Thus we conclude that the measured temporal dependencies corroborate our previous assertions regarding damage mechanisms.

Perhaps of more practical importance to the systems designer is the variation of LDT with changes in the extent of the relaxation tail. The materials which damage through avalanche ionisation exhibit a damage threshold fluence independent (or nearly so) of the tail extent: a result we are, as yet, unable to explain. The defect dominated materials, Ge and GeAsSe glass, and the coatings show a pronounced dependence with the LDT fluence increasing as the tail is extended. An analysis of this effect using a thermal defect model is presently underway. These data confirm the importance of adequately characterising the pulse temporal profile including, the tail duration, in CO_2 damage experiments.

For all substrate materials and coatings investigated the damage morphology was found to be invariant over the range of pulse temporal characteristics used.

4.   SUMMARY AND CONCLUSIONS

A technique of producing pulses with durations less than that of the gain switched spike has been demonstrated and used successfully in CO_2 laser damage studies of materials and coatings. Coupled with detailed morphological examination of samples damaged with a large diameter beam (> 0.9mm) the time dependence of the LDT allows a ready identification of the mechanisms of laser damage.

High purity samples of ZnS, ZnSe and KCl exhibit an electron avalanche breakdown process characterised by an LDT varying linearly with pulse length. GeAsSe glass and n-type Ge substrates show evidence of an impurity damage mechanism with the characteristic dependence of LDT on the square root of the pulse length.

Analysis of coated Ge indicates that substrate-film interface and/or film defects introduced during deposition are predominantly responsible for damage. The measured time dependence for these coatings conforms to LDT = $At^{\frac{1}{2}}$ which is consistent with defect dominated damage. In both the "absorbing" films (diamond-like carbon) and the "less" absorbing coatings (ZnS, commercial ARCs, etc) the LDT increases with decreasing film absorption. This emphasises the importance of minimising the absorption in coated optics.

With diamond-like carbon (largely hydrogenated carbon), which has use as an AR coating on external surfaces, the scope for reducing the absorption is limited by the material's intrinsic absorption due to C-C stretching vibrations. The best films have an absorption coefficient of 250cm^{-1} at 10.6µm and, for spike + 2µs tail CO_2 TEA pulses, peak fluence damage thresholds of $\simeq$ 6Jcm^{-2}. Standard production coatings will probably show higher absorption and hence a slightly lower damage threshold.

Many commercial AR coatings are designed for broadband use in the 8-12µm region and often contain relatively absorbing materials, e.g. metal oxides, to optimise mechanical and/or spectral properties. Clearly there may be scope to improve the CO_2 laser damage characteristics of such coatings by re-design and selection of less absorbing materials. It should not be assumed, however, that use of metal oxide films will necessarily lead to a lower LDT. For example we have recently studied some single films of refractory metal oxides on Ge which show similar absorption to typical DLC films but which have LDT values increased by a factor of two. Clearly this relates to the temperature excursion which a material can tolerate i.e. the material's damage temperature, T_D: the implication

being that these oxide layers have a higher T_D than DLC. Similarly DLC has a higher T_D than ZnS, ThF_4, etc. as judged by examining the product of LDT and film absorptance. In a multilayer stack with contiguous low and high T_D materials, enhanced absorption in the high T_D layer may be insufficient to cause damage to that layer but may lead to damage in the adjacent low T_D layers. In this respect the effect is similar to damage to a matrix by heating of a defect.

For the single layer coatings of ZnS and ZnSe the damage morphology indicates a film dominated defect mechanism. Defects within the substrate surface may contribute to the damage process in certain cases e.g. the best ZnS films. These films have absorption coefficients of $\simeq 10 cm^{-1}$ part of which may be due to an enhanced contribution from the substrate-film interface. These values are orders of magnitude higher than the bulk absorption coefficients but are similar to values quoted for conventional thin films by other workers [47, 48]. Most of the absorption is due to defects. A significant change in absorption coefficient will only be obtained by use of either UHV/MBE growth [49] to eliminate defects formed by contamination (e.g. oxide inclusions in the ZnS, etc.) or energy assisted deposition [50] which promotes adatom mobility in the growing film and thus minimises physical defect structures. Recently ZnSe films with an absorption coefficient $< 1 cm^{-1}$ have been reported [51]. Such films are expected to lead to improvements in damage threshold and may produce optics in which performance is limited by the substrate. At present, damage is mainly film dominated and thus most effort should be applied to improving film quality. The substrate surface may also influence the initial growth of the films and thus may affect the substrate-film interface absorption but as far as we are aware this aspect has not received significant attention.

REFERENCES

1) L.G. DeShazer, B.E. Newnam and K.M. Leung, Appl. Phys. Lett., 23, 607 (1973).

2) K.M. Dyumaev, A.A. Manenkov, A.P. Maslyukov, G.A. Matushin, V.S. Nechitalio and A.M. Prokhorov, NBS Spec. Publ., 638, (1981).

3) B.E. Newnam and D.H. Gill, NBS Spec. Publ., 509, 298 (1977).

4) B.E. Newnam, A.V. Nowak and D.H. Gill, NBS Spec. Publ., 568, 209 (1979).

5) R.A. House, J.R. Bettis and A.H. Guenther, IEEE J. Quantum Electron., QE-5, 361 (1977).

6) H.J. Posen, J. Bruce and D. Milam, NBS Spec. Publ., 414, 85 (1974).

7) R.M. Wood, S.K. Sharma and P. Waite, GEC J. Sci. Technol., 48, 141 (1982).

8) A.D. Baer, T.M. Donovan, A.K. Green and G. Turner, NBS Spec. Publ., 462, 214 (1976).

9) H. Tashiro, T. Shimada, K. Toyoda and S. Namba, IEEE J. Quantum Electron., QE-20, 159 (1984).

10) A. Girad and A.J. Beaulieu, IEEE J. Quantum Electron., QE-10, 521, (1974).

11) G. McLelland and S.D. Smith, Optics Comm., 27, 101 (1978).

12) H.S. Kwok and E. Yablonovitch, Appl. Phys. Lett., 27, 583 (1975).

13) S.J. Czuchlewski and F.J. Figueira, Appl. Phys. Lett., 38, 325 (1981).

14) T.A. Znotins, S.R. Byron, S.E. Moody, R.K. Brimacombe and J. Ried, Rev. Sci. Instrums., 55, 869 (1984).

15) E. Vablonovitch, Appl. Phys. Lett., 19, 495 (1971).

16) H. Dupont, A. Donzel and J. Ernest, Appl. Phys. Lett., 11, 271 (1967).

17) L.D. Merkle, M. Bass and R.T. Swimm, Opt. Eng., 22, 405 (1983).

18) M.J. Solieau, M. Bass and P.H. Klein, NBS Spec. Publ., 568, 497 (1979).

19) T.W. Sheheen et.al., J. Appl. Phys., 53, 4652 (1982).

20) S.R. Foltyn, NBS Spec. Publ., 669, 368 (1982).

21) L.J. Willis and D.C. Emmony, Opt. Laser Technol., 7, 222 (1975).

22) P.A. Temple and M.J. Solieau, IEEE J. Quantum Electron., QE-17, 2067 (1981).

23) P.A. Temple and M.J. Soileau, NBS Spec. Publ., 462, 331 (1976).

24) N. Bloembergen, Appl. Opt., 12, 661 (1973).

25) A.D. Wilson and D.R. Gibson, to be published.

26) M.R. Lange, J.K. McIver, A.H. Guenther and T.W. Walker, NBS Spec. Publ., 669, 380 (1982).

27) "Chalcogenide Glass Type 1", Barr and Stroud, Information Sheet 2060 (1983).

28) N.L. Boling, M.D. Crisp and G. Dube, Appl. Opt., 12, 650 (1973).

29) P.A. Temple, Opt. Eng., 23, 326 (1984).

30) P.A. Temple, Appl. Phys. Lett., 34, 667 (1979).

31) T. Mori and Y. Namba, J. Appl. Phys., 55, 3276 (1984).

32) U.S. Patent No. 4,444,805 (24.4.84) "Optical Coating" by Barr and Stroud Limited.

33) "Summary of the Workshop on Diamond-Like Carbon Coatings", Alberquerque N.M., B. Bendow Ed., April 1982.

34) A. Bubenzer, B. Dischler, G. Brandt and P. Koidl, Opt. Eng., 23, 153 (1984).

35) "ARG4 Ultra-Hard Anti-Reflection Coating for Germanium", Barr and Stroud, Information Sheet 0379 (1979).

36) B. Dischler, A. Bubenzer, P. Koidl, G. Brandt and O.F. Schirmer, NBS Spec. Publ., 669, 249 (1982).

37) "Anti-Reflection Coatings for Germanium Optics", Barr and Stroud Information Sheet 1501 (1982).

38) "Infralin. Anti-Reflection Coatings on Germanium", Balzers, Data Sheet BD800 011 NE(8304),(1982).

39) "Infrared Stock Filter Catalogue", OCLI (1982).

40) "Infrared Coatings and Filters", STC Components, Data Sheets, (1984).

41) J.F. Ready, J. Appl. Phys., 36, 462 (1965).

42) T.W. Walker, A.H. Guenther and P. Nielsen, IEEE J. Quantum Electron., QE-17, 2053 (1981).

43) A.S. Epifanov, A.A. Manenkov and A.M. Prokhorov, Sov. Phys. - JETP, 43, 377 (1976).

44) E.S. Bliss, D. Milam and R.A. Bradbury, Appl. Opt., 12, 677 (1973).

45) A.G. Molchanov, Sov. Phys. - Sol. St., 12, 749 (1970).

46) B.E. Newnam, A.V. Nowak and D.H. Gill, NBS Spec. Publ., 568, 209 (1979).

47) W.E.K. Gibbs and A.W. Butterfield, Appl. Opt., 14, 3043 (1975).

48) A.M. Leger, Appl. Opt., 18, 2979 (1979).

49) M. Rona and P.W. Sullivan, NBS Spec. Publ., 669, 234 (1982).

50) P.J. Martin, H.A. Macleod, R.P. Netterfield, C.G. Pacey and W.G. Saintly, Appl. Opt., 22, 178 (1983).

51) K.L. Lewis and J.A. Savage, Private Communication.

CM, cavity mirror.   BW, KCl Brewster window.
SM, scraper mirror.   G, grating.   P, piezo-positioner.
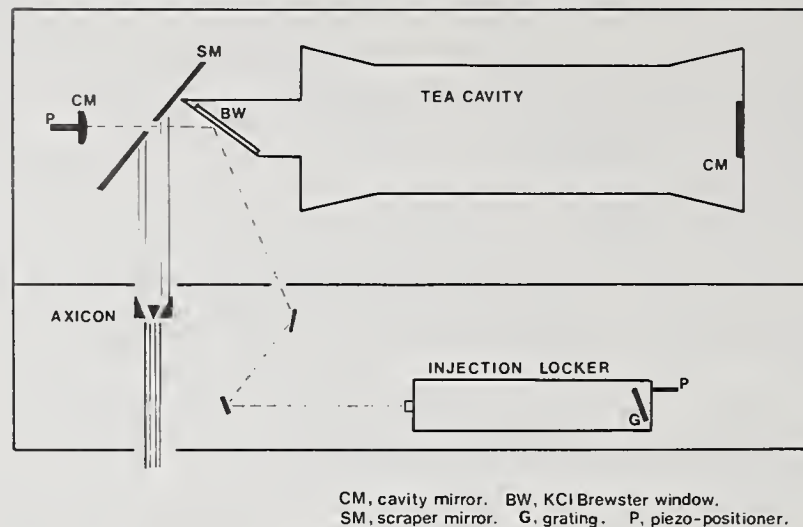
Fig.I   SCHEMATIC OF CARBON DIOXIDE TEA LASER

Fig.2   SPATIAL &
         TEMPORAL
         PROFILES
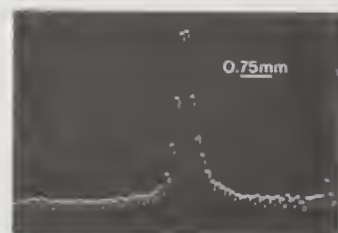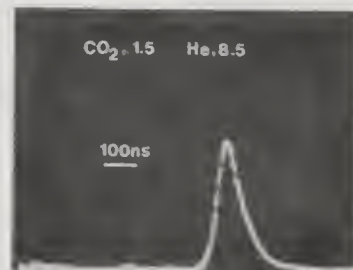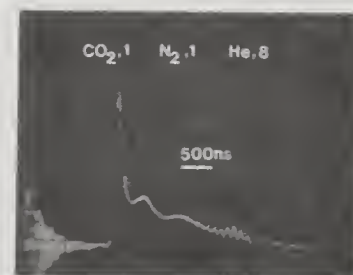
a- SPATIAL PROFILE   b- TEMPORAL PROFILES

a- Experimental Arrangement

AR coated Ge lenses

input beam

location of sample
under test

location of surface
plasma initiator

a- Air Breakdown

0.75 mm

b- Temporal Profiles

50ns

20ns
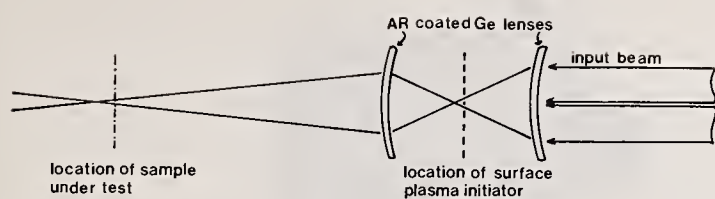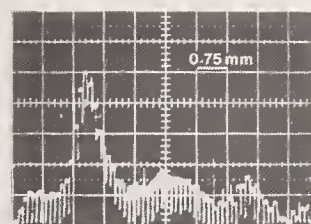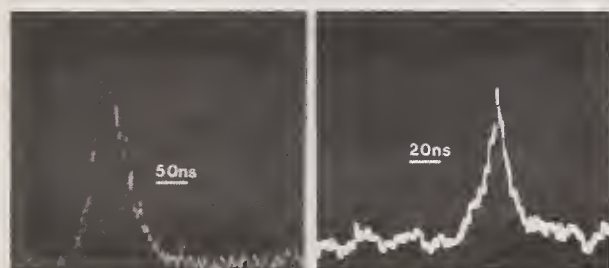
Fig.3 PRODUCTION OF SHORTENED TEA PULSES
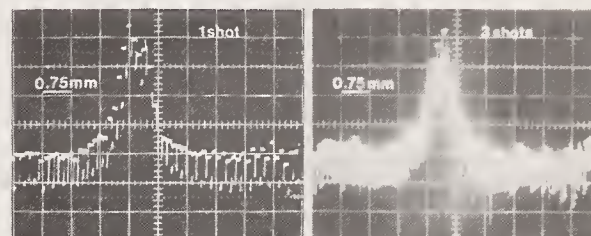
b- Surface Induced Plasma

1shot

3 shots

0.75 mm

0.75 mm

Fig.4 SPATIAL PROFILES OF SHORTENED PULSES

HeNe
laser

to
fast
scope

Ge PDD

PA

to
storage
scope

Energy
Meter

to
fast
scope

Ge PDD

beam
stop

K

S

K

Ge lens

K

CO₂ Laser
Pulse

visual
assessment
of damage
induced
scatter

beam
stop

attenuator (gas cell &/or
variable polariser)

PA = pyroelectric array
GePDD = Ge photon drag detector
K = KCl beamsplitter
S = sample under test
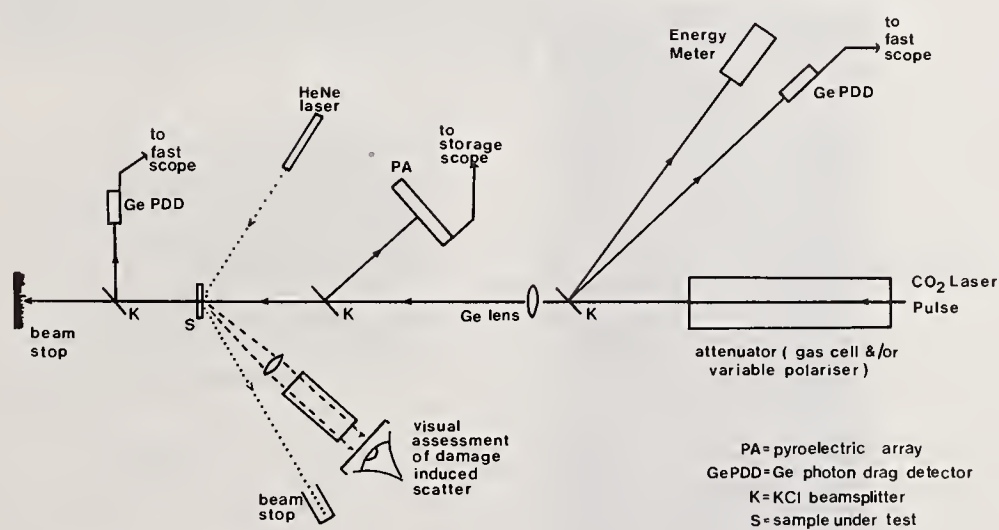
Fig.5 SCHEMATIC OF CO₂ LASER DAMAGE MEASUREMENT FACILITY
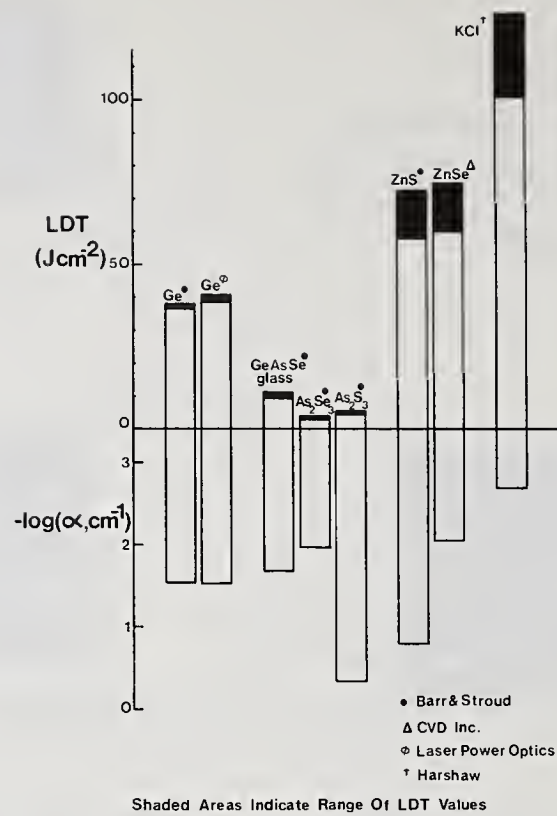
Fig.6 LDTs AND ABSORPTION COEFICIENTS OF INFRA-RED MATERIALS

Nomarski Micrographs
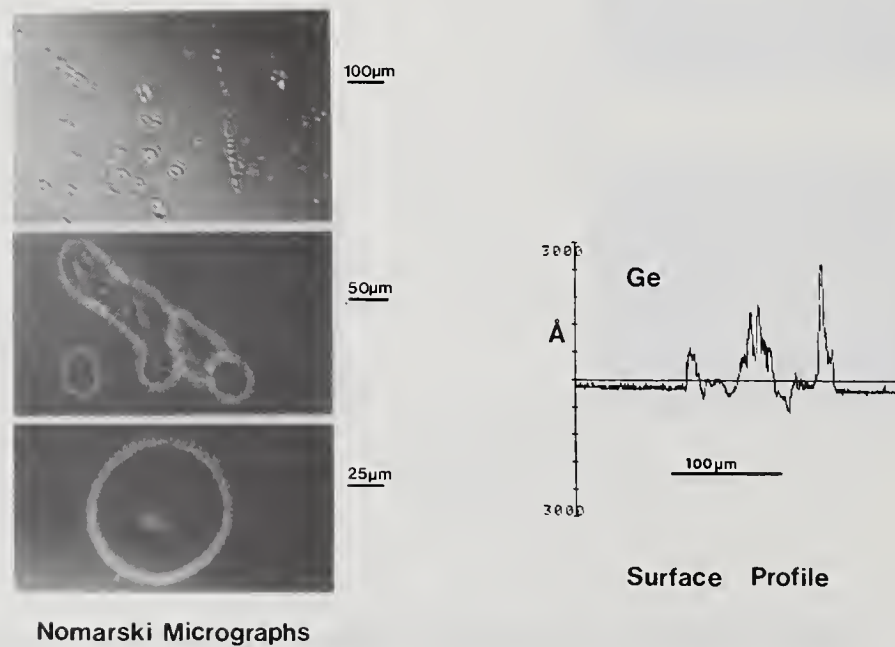
Surface Profile

Fig.7 DAMAGE MORPHOLOGY ON GERMANIUM: ENTRANCE FACE

110
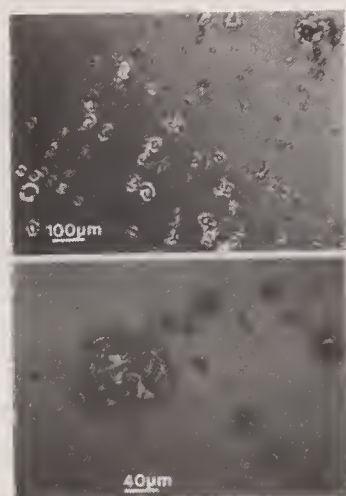
Nomarski Micrographs
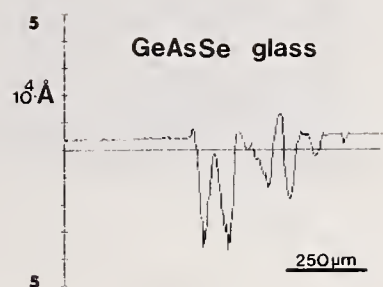
Surface Profile

Fig.8 DAMAGE MORPHOLOGY OF GeAsSe GLASS:EXIT FACE
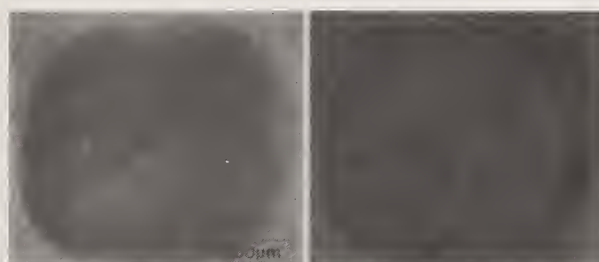
surface   sub-surface
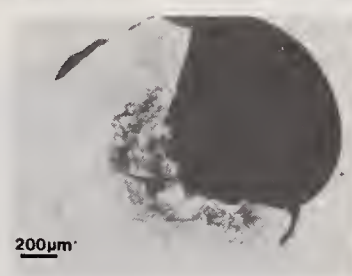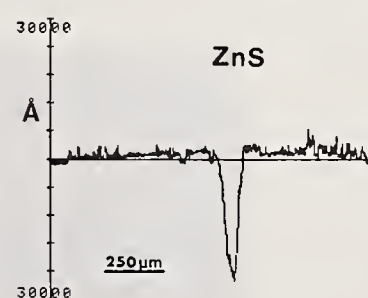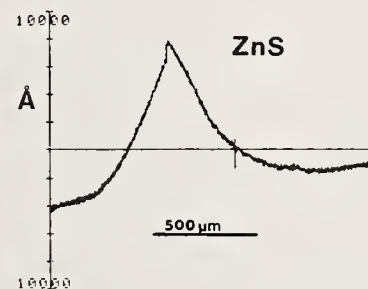
Nomarski Micrographs   Surface Profiles

Fig.9 DAMAGE MORPHOLOGY IN ZINC SULPHIDE: EXIT FACE

ThF$_4$ Ge

unetched   film part-removed   unetched
               by etching
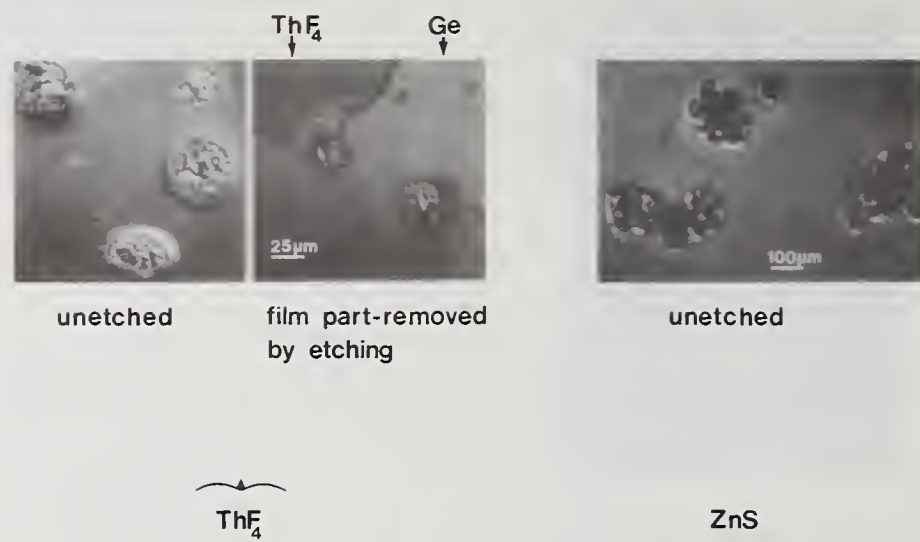
ThF$_4$ ZnS

Fig.10 DAMAGE MORPHOLOGY OF GERMANIUM COATED WITH SINGLE
FILMS OF ThF$_4$ & ZnS

n=1   n=4
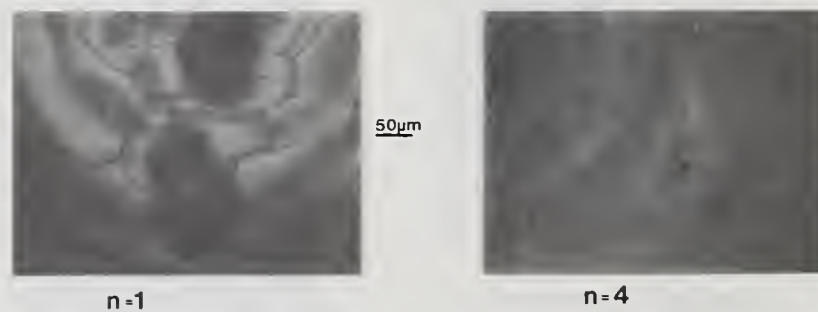
Fig.11 DAMAGE MORPHOLOGY OF REFLECTORS

Ge/(LH)^n L=ThF$_4$ H=ZnS

112

Fig.12 DIAMOND-LIKE CARBON AR COATINGS ON Ge

R(10.6μm)

1 Barr & Stroud ARG 3 .1 %
2 STC (Ge0023N) .1 %
3 ZnS 1.5 %
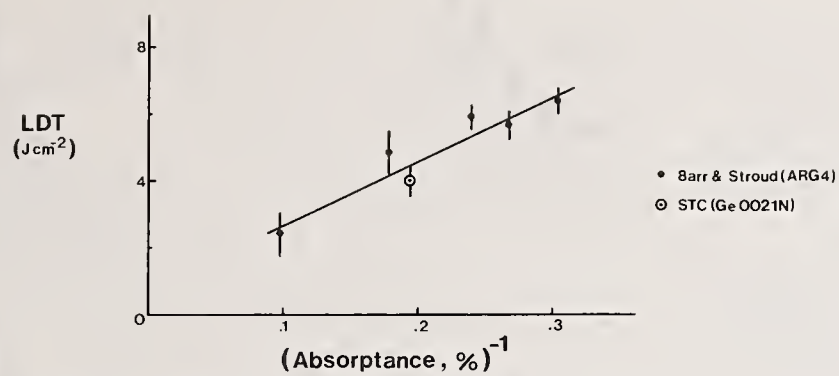
Fig.13 AR COATINGS ON Ge : BOTH FACES COATED
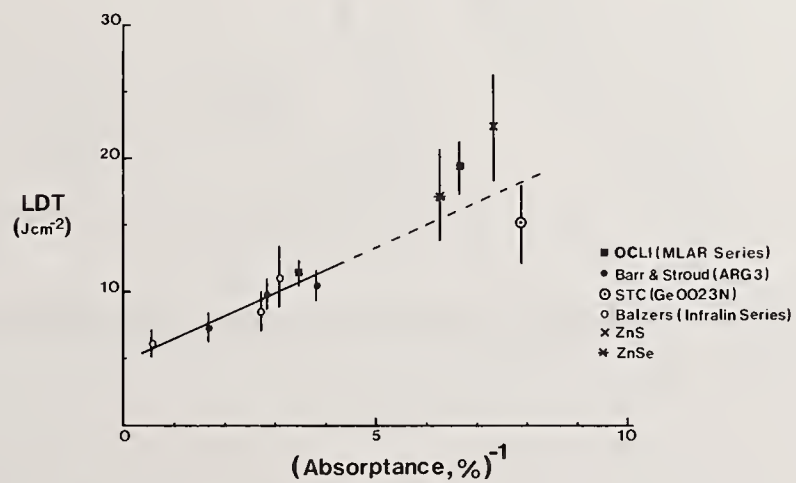
Fig.14 AR COATINGS ON Ge
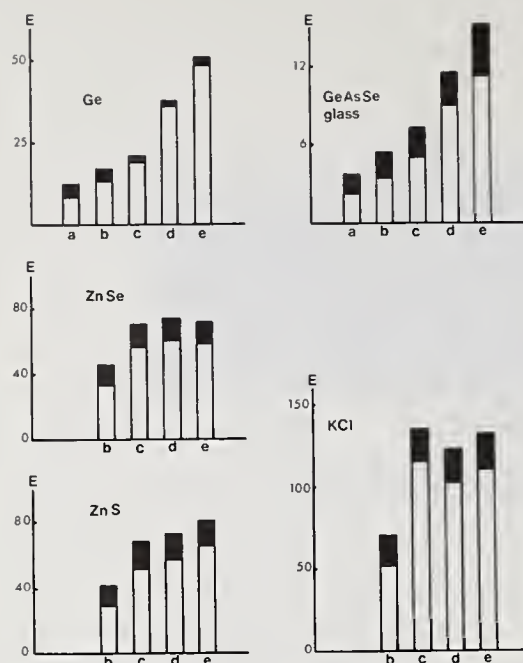
113

Pulse Characteristics: a, 20ns. b, 50ns. c, 90ns. spike only
d, spike + 2 μs tail. e, spike + 5μs tail

Shaded Areas Indicate Range Of LDT Values

Fig.15 DEPENDENCE OF LDT(E,Jcm⁻²) ON LASER
PULSE CHARACTERISTICS : SUBSTRATES

Pulse Characteristics: a, 20ns. b, 50ns. c, 90ns. spike only
d, spike + 2 μs tail. e, spike + 5μs tail

Shaded Areas Indicate Range Of LDT Values

Fig.16 DEPENDENCE OF LDT(E,Jcm⁻²) ON LASER
PULSE CHARACTERISTICS : COATINGS ON Ge

Fig.17 DEPENDENCE OF LDT(E,Jcm⁻²) ON LASER PULSE LENGTH(t,ns).

114

Pulse Characteristics: a, 20ns. b, 50ns. c, 90ns. spike only
d, spike + 2 μs tail. e, spike + 5μs tail

Shaded Areas Indicate Range Of LDT Values

Fig.15 DEPENDENCE OF LDT(E, Jcm^{-2}) ON LASER
PULSE CHARACTERISTICS : SUBSTRATES

Pulse Characteristics: a, 20ns. b, 50ns. c, 90ns. spike only
d, spike + 2 μs tail. e, spike + 5μs tail

Shaded Areas Indicate Range Of LDT Values

Fig.16 DEPENDENCE OF LDT(E, Jcm^{-2}) ON LASER
PULSE CHARACTERISTICS : COATINGS ON Ge

Fig.17 DEPENDENCE OF LDT(E, Jcm^{-2}) ON LASER PULSE LENGTH(t, ns).

114
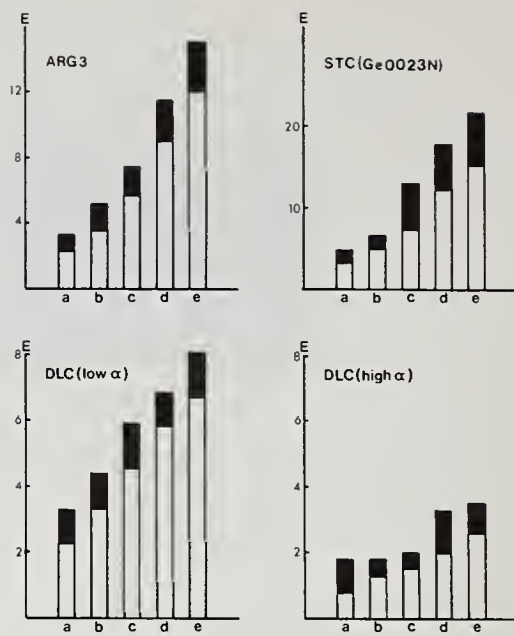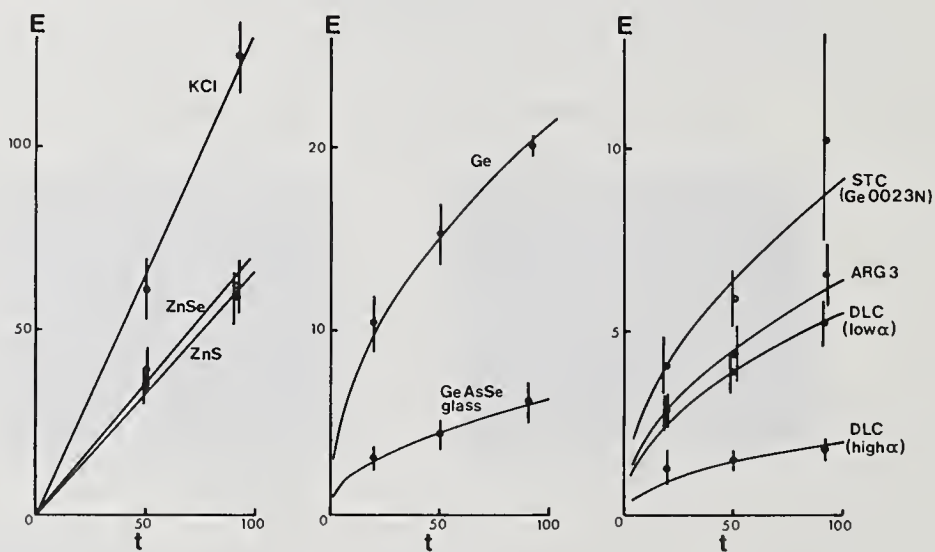
A questioner pointed out that tests reported at this conference in 1977 on damage thresholds of antireflection coatings on germanium showed no correlation between coating absorption and the damage threshold. It depended entirely on the surface of the germanium substrate. Coatings from 13 different vendors and various surface treatments were tested. The speaker replied that the damage thresholds reported in the 1977 paper were somewhat lower than those reported in this paper, which would lead one to infer that perhaps the germanium surface was better in the later work. In response to the surprise expressed about the linear pulse length dependence reported, since the pulse length dependence is often 1/3 and never greater than 1/2, the speaker replied that Bass, as he recalled, reported pulse length dependences as high as zero. The author had checked his plasma chopping by chopping up a spike and tail teapot to give a 90 ns FWHM pulse and compared that to the 90 ns gain switched spike running without nitrogen. They were within about 10%. Also, copper has been checked and found to be about $t^{\frac{1}{2}}$ at 50 ns and 90 ns. The author feels that the data he reports is OK. Another questioner reported that they had been making diamondlike carbon films and had found that the properties of the films depend strongly on how they are made. The optical gap of the films, for example, can range from 1 eV to 3 eV. How are the films reported here made? The author replied that his films are made by rf plasma assisted deposition from butane. Butane, propane, benzene or an unsaturated hydrocarbon give the same results. The refractive index is exactly 2 and reflectances are 0.1% or less. Absorption and damage thresholds may vary considerably in production films. The films damage may be defect dominated, but the author feels that they have reached the practical limit of about 3% per quarter wave or 250 cm^{-1} absorption coefficient. There they are seeing about 7 J/cm axial flux, which is probably as well as one can do. A member of the audience commented that if one believed the impurity dominated damage mechanism, one can get pulse length dependence anywhere from 1/2 to linear depending on the distribution of the particles, their properties and the variables in the experiment.

Surface Potential as a Laser Damage Diagnostic

M. F. Becker

Electrical and Computer Engineering Department
The University of Texas
Austin, TX 78712

J. A. Kardach, A. F. Stewart, and A. H. Guenther

Air Force Weapons Laboratory
Kirtland, NM 87117

We investigated the relationship between surface potential changes and N-on-1 laser surface damage on a wide range of materials. The surface potential or work function difference was measured as a function of position by a small non-contacting Kelvin type probe. This design and operation of the probe is described. Using this probe, the change in surface potential due to laser irradiation was mapped with a ~1 mm resolution. Although no consistent pre-damage changes in potential were observed, all larger damage features had surface potential changes associated with them. The insulating materials studied, fluoride and oxide thin films, bare fused silica and magnesium fluoride substrates, all showed the accumulation of negative charge in areas more than ten times larger in diameter than the laser beam spot or damage area. This initial charge was observed to decay on the time scale of hours to a lower fixed value of potential associated with permanent damage to the surface.

Key words: laser damage, N-on-1 damage, surface potential, contact potential, work function, surface charge, charge decay.

1. Introduction

This is the first reported study of the relationship between surface potential and laser induced damage of insulating and semiconducting optical materials, and the first such study for metals damaged at wavelengths shorter than 10.6 microns [1]. By surface potential we simply mean the difference in work functions or the contact potential between two materials. Usually one material is employed as a reference; stainless steel was used in this study. Surface potential is related to a number of material surface properties which may be of interest in the study of laser damage. For metals and semiconductors, surface potential is sensitive to band bending at the surface which can be related to surface preparation procedures, fixed surface states, or adsorbates. For dielectric materials, surface potential is sensitive to these same effects as well as to fixed charge either in the form of surface or volume charge distributions or even permanent electric dipole states.

Our interest in surface potential was aroused by our previous experiments utilizing charge emission into vacuum as a diagnostic for the onset of laser damage or more importantly as a precursor to laser induced damage [2-4]. Although no charge emission was observed prior to damage in N-on-1 tests for silicon and ThF$_4$ thin films in these earlier experiments, all other materials, including copper mirrors and several types of oxide thin films, showed charge emission at fluences as low as 1/20 of the 1-on-1 damage threshold. The copper mirrors exhibited a reduction of emission for repeated shots to the same site (N-on-1) as one would expect in a conditioning or cleaning effect. To further complicate the situation, all of these materials showed either accumulation or hardening in N-on-1 tests. The idea of a non-contacting charge sensitive technique which could measure changes in the surface state of a sample appeared an attractive method to study these N-on-1 effects.

Previously, Porteus, et al. [1] used Auger electron imaging as a qualitative measure of laser induced changes in work function. In our experiments we have applied a different technique which is capable of giving spatially resolved quantitative maps of surface potential over the region in and around the laser interaction area. This technique utilizes what is known as a Kelvin probe or the Kelvin method to measure surface potential without making physical contact with the surface, and as such is also non-intrusive.

In this paper we first describe the Kelvin probe apparatus used in our experiments as well as the other diagnostics. The sample set was chosen to include a wide variety of optical material classes, including copper mirrors, silicon crystals, dielectric thin films and bare dielectric

substrates. After the experimental samples and cleaning procedures are described, data taken by the Kelvin probe from a series of N-on-1 experiments will be presented. Finally, the implications of these measurements for the understanding of laser induced damage will be discussed.

2. Experimental

2.1 Kelvin Probe

The Kelvin method for measuring surface potential is essentially one of adjusting the dc voltage on the test capacitor formed by the sample surface and the reference electrode so as to null out ac variations in the capacitor voltage caused by physically dithering the reference electrode. In these experiments, we used a feedback technique which would adjust the dc voltage for an ac null automatically [5,6]. The probe assembly is shown in figure 1. The probe electrode tip is 1 mm in diameter and is on a carrier which may be positioned over the laser beam axis and adjusted in spacing from the sample or may be withdrawn when laser irradiation takes place. The sample location is also mechanically controlled in order to position it to new irradiation sites and to scan the sample under the probe in a raster pattern for measuring surface potential contours. Typical raster scans were squares of either 5 mm or 10 mm on a side. Data points were taken at 0.25 mm intervals on each row while the scan rows were separated by 0.25 mm for the small squares and 0.5mm for the large squares. The scan rate of the stepper motors was the chief factor limiting data acquisition speed. A magnetic drive is used to dither the probe at 88 Hz with a peak-to-peak amplitude of 0.1 mm. It requires a drive signal at 44 Hz of about 5 W.

In operation, the probe tip is placed so that its closest approach to the sample surface is about 25 μm as viewed by a long working distance Questar microscope with a CCTV system. This view is shown in figure 2. Since the capacitance between the probe and a grounded sample is about 0.1 pF and the capacitance with a dielectric sample 9.5 mm thick backed by a ground plane is considerably less, eliminating stray capacitance was crucial [7,8]. To do this we mounted a low input capacitance electrometer op-amp directly to the end of the probe arm. Other metallic objects were kept as far away as possible from the oscillating probe tip. As a result, the probe sensitivity to surface potential changes was less than 10 mV. This level is also of the same order as the noise level and the reproducibility of the measurements.

The feedback circuit used to automatically adjust the probe dc voltage to be equal to the surface potential is shown in figure 3. The preamp has an ac voltage gain of 11 while the lock-in amplifier is adjusted for the maximum gain possible without oscillation with a 0.3 sec damping time. The dc output of the lock-in is fed back through a high impedance path to supply the surface potential to the probe. The dc output is also read by a digital voltmeter which was interfaced to the laboratory mini-computer used for automatic data reduction. Only the critical adjustment of setting the probe height above the sample surface was done manually. The probe was always scanned over the unirradiated site to obtain a background potential map which was later subtracted from the data to obtain the laser produced change in surface potential. The probe was next removed, the sample irradiated, and the probe returned to scan for the data. Sequences of scans over time could also be programmed in order to monitor the time decay of laser induced effects. The time needed to scan a 10 mm square was 16 minutes, and about half that for the 5 mm square.

2.2 Diagnostics

The optical and diagnostic layout is shown in figure 4. The fundamental 1.06 μm wavelength of a Molectron Q-switched Nd:YAG laser was used at a rep rate of 10 Hz. It was focused on the sample with a 2 m focal length lens. Time and space profiles were checked regularly. The pulse length was 18 ns FWHM, and the focused spot was typically 0.39 mm in diameter at the $1/e^2$ points. The beam was scanned in both the vertical and horizontal directions with a narrow slit at the focal plane. An electromechanical shutter was used by the computer to control the irradiations. Pulse energy for every shot was recorded and statistics were computed. The standard deviation in pulse energies for 10 to 100 pulses was typically 1% or less and never greater than 3%.

After a sequence of sites had been tested on a sample it was examined under a Nomarski microscope to determine the corresponding damage morphology. Although exact damage thresholds were not measured, data was generally taken at fluences between 1/2 and 2 times threshold with an exposure of 10 or more pulses in order to attempt to observe pre-threshold as well as permanent damaging effects.

2.3 Samples

The sample set consisted of OFHC diamond turned copper mirrors, single crystal [111] silicon substrates, MgF_2 half wave (at 1.06 μm) thin films on fused silica, HfO_2 half wave thin films on fused silica, ThF_4 half wave thin films on fused silica, bare oriented crystalline MgF_2 substrates, crystalline quartz and bare fused silica substrates. The silicon and fused silica substrates used

in this study were fabricated using the controlled grinding technique. Total integrated scattering (TIS) measurements on witness samples indicated an average surface roughness of 5±2 Å RMS for both substrate types. TIS measurements were repeated on fused silica witness substrates after film deposition. The measured surface roughness of half wave HfO_2 films on fused silica was found to be 5±1.5 Å RMS. In contrast, half wave MgF_2 films on fused silica were found to have an average roughness of 10±1.5 Å RMS. In subsequent examination of these samples under the Nomarski microscope, only the MgF_2 films were observed to have a definite microstructure and a "parquet tiled" appearance resulting presumably from columnar growth.

The cleaning procedure did not require touching the sample surfaces with any solid object. The samples were cleaned in a photoresist spinner with deionized water and high purity acetone and blown off with dry nitrogen. The dielectric samples were pre-cleaned by spinning on a collodion layer and subsequently lifting it off to remove any tenaciously held particulates.

3. Experimental Data

In this section, we present a selection of typical data obtained by the Kelvin probe and correlations with microscopically observed damage morphology.

3.1 Dielectric thin films

Figures 5 and 6 illustrate the two graphic formats we used for data presentation. Figure 5 is a three dimensional projection plot of the potential change with a small, unscaled contour plot below, and figure 6 is a full size contour plot. The large contour plots and the raw data arrays were used to extract all numerical data since small changes in surface potential were readily apparent. However, the three dimensional projections are more easily viewed, especially when the change in potential is in an upward direction. For this reason, we show only projection plots in the remainder of this paper with their potential axis polarities oriented such that the change in potential at the damage site is always upwards.

The data in figures 5 and 6 is for an MgF_2 thin film irradiated with 10 pulses at 69 J/cm^2. It is representative of all the thin films studied in these experiments. Note that the observed potential change is negative for this sample. Subsequent microscopic examination showed large scale damage covering the entire beam footprint. The profile of the change in surface potential was 4 to 6 mm in diameter with a magnitude of nearly half a volt. This diameter is distinctly larger than both the laser spot and the resolution of the Kelvin probe. In addition, all large scale damaging events were detected by a similar potential change. No potential changes were detected when laser damage was not observed. In these N-on-1 experiments, small damage pits were observed only on the HfO_2 film. About 50% of these small damage sites were detected by the Kelvin probe as small changes in surface potential, while the remaining sites resulted in no observable change. The surface potential change on these thin film samples was observed to decay with time. This effect and its relation to surface charge will be discussed in a later section.

3.2 Conductors

The surface potential changes on damaged silicon and copper, although similar to each other in diameter and magnitude, were opposite in polarity. In fact, copper was the only material that showed a positive surface potential change when damaged. (Bare MgF_2 substrates also showed a positive potential change but only when bulk cracking was created by exit surface damage.) A typical surface potential plot for single crystal silicon is shown in figure 7. The object to the left in the field is the adjacent, previous damage site.

For silicon, not all microscopically observed surface damage could be detected by the Kelvin probe. When pits were formed, indicating a more severe degree of damage, the potential changed as shown in figure 7. However, when only melting and resolidification occurred with the accompanying formation of ripples or ridges, no change in surface potential could be observed. No pre-damage changes in surface potential were ever detected.

The OFHC diamond turned copper was always observed to damage by melt pit formation, and these pits were detected by their accompanying changes in surface potential. As for the silicon, the observed diameter was limited by the 1 mm resolution of the Kelvin probe tip. One case of pre-damage change in the surface potential was observed for copper. In three other cases near the threshold fluence where no observable surface damage occurred, no surface potential change could be detected.

The surface potential change for the conductive samples was found to be constant and reproducable over time. In this case, no decaying component was observed as was for the dielectric samples.

3.2 Bare dielectric substrates

The bare dielectric substrates seemed to be more unpredictable in their behavior. Experimental difficulty was experienced due to their tendency to damage on the exit surface. In N-on-1 experiments for large enough N, damage would propagate from the rear to the front surface before surface damage was initiated on the front surface. Experiments were thus limited to less than 10-20 pulses per site.

A typical potential contour plot for bare SiO_2 is shown in figure 8. Both fused silica and the polycrystalline MgF_2 substrates showed similar behavior. The surface potential change was 4 to 6 mm in diameter but smaller in magnitude than for the thin films. The Kelvin probe noise level seemed to increase in the vicinity of the damage sites.

Microscopy of the damage sites on the bare substrates showed less distinct damage features which resembled surface erosion. Larger diameter surface damage sites were detected by the Kelvin probe while several smaller diameter damage sites and all undamaged sites showed no surface potential change. These surface potential changes were observed to decay with time just like those for the thin film samples, and will be discussed later.

The MgF_2 substrates showed unusual behavior when a crack from the rear surface propagated to the front. The arrival of the crack at the front surface would be accompanied by a sudden strong positive change in the surface potential. This change may be associated with the piezoelectric properties of the material or with the exoemission of electrons from the crack which leaves the substrate positively charged [9].

4. Discussion

4.1 Surface charge density

One of the most interesting and unexpected findings in these experiments was the significance of surface charge effects on the dielectric samples. First it will be necessary to relate the surface potential measurements to surface charge density. In measuring contact potential as between two conducting samples, the Kelvin probe separation from the surface does not affect the potential difference so long as the increase in distance can be compensated for by an increase in the gain in the feedback loop. The case of free charge on the surface of a dielectric material is entirely different. It resembles very closely the case of fixed charge in a Shottky or MOS device. The potential required to place an equal and opposite charge on the probe tip is now dependent on the tip to surface distance. The surface potential is related to the surface charge density (ignoring fringing field effects) by the parallel plate capacitor formula:

$$Q_S/A = \varepsilon_0 V/d \qquad (1)$$

where Q_S is the total surface charge under the probe, V is the surface potential, and d is the mean probe height over the surface. Typically, d was 70 μm so that a charge density of 1.26×10^{-11} C/cm^2 per volt of potential change was measured in these experiments. As an example, a spot 4 mm in diameter with a potential change of 0.1 V would represent about 1.3×10^6 negative charges. A rather large amount of charge is spread from the 1/3 mm diameter laser damage site to a distance of several mm.

Closer analysis of the surface potential contour maps reveals that the effect is even more widespread. The shape of the potential change peak is flat topped with a sharp drop at a diameter of 4 to 6 mm. The drop is not to zero however, since there is about 10% remaining change in surface potential which decreases slowly with distance for another several mm. This might lead an investigator to rethink the problem of site spacing for laser damage experiments on dielectric samples. The charge related effects of a damaging event extend across the sample surface much further than would be expected from either the observed damage morphology or even the incident beam diameter.

4.2 Charge decay

Detailed measurements of the surface potential decay as a function of time were made on the HfO_2 thin film and on the MgF_2 bare substrate. The results for the two were similar and the thin film data will be presented in detail.

Figures 9a-c show selected surface potential maps of the damage site at t=0, 1 hour, and 2 hours respectively. Note that each scan took about 16 min so that there was an initial delay of 8 min to scan to the beam center. Subsequent scans of the center were spaced by intervals equal to the scan time plus a programmed inter-scan delay time.

In figure 9, the potential change is observed to decay without significant migration of the charge. Presumably recombination, not diffusion, is responsible for the decay. It is not certain whether the recombination charge comes from the air or the material; however, these sites could be discharged artificially with airborne charge by using a static charge gun or by creating another charge cloud from a nearby laser damage site.

The decay of the surface potential peak values obtained from the scans shown in figure 9 is plotted in figure 10. From the simple linear graph, we infer a single exponential decay process with a time constant of 62 min. The decay asymptote is not zero potential change. There is permanent damage, and some fixed change is expected. In this case the fixed part of the potential change is -25 mV as compared to the initial peak of -100 mV. As indicated previously, similar data was obtained for the MgF_2 bare substrate for which a 30 min time constant was observed.

4.3 Conductors

Obviously no such free charge effects will be observed for conductive samples. An earlier study using Auger analysis of damage sites on OFHC copper surfaces demonstrated the effects of surface shape changes (pit formation) on the work function [1]. We also observed these effects on copper with 1.06 μm illumination. There is no way of telling if the sign of the change observed by the authors of reference [1] matches that measured by the Kelvin probe since they used a different method which measured only qualitative potential changes. Similar potential changes were observed at damage pits on silicon but of opposite polarity. There is no obvious reason why such a polarity difference should exist.

4.4 Pre-damage effects

One of the objectives for undertaking these experiments was to observe sub-damage threshold changes in the surface potential on those materials which emitted charge at 1/10 to 1/20 of the threshold fluence, or showed accumulation or cleaning effects. In this respect we were unsuccessful. One possible pre-threshold event was observed for copper out of four total observations. If a sub-threshold surface potential effect exists, it is not large.

5. Conclusions

We observed distinct surface potential signatures associated with laser damage. For conductors, silicon and OFHC copper, small diameter surface potential changes were detected in conjunction with pit formation. No surface potential change was seen on silicon when only surface ripples or ridges formed. Copper differed from silicon and all other materials in that the sign of the surface potential change was positive.

All of the insulating materials showed surprisingly large diameter surface potential changes around the laser damage spots. These potential changes were observed to extend over an area 4 to 6 mm in diameter as compared to the 1 mm diameter Kelvin probe resolution and the 1/3 mm laser beam spot diameter. These charged areas contained as many as 10^7 negative charges. In light of this large diameter charging effect, the spacing of adjacent sites in laser damage experiments on insulating substates and thin films should be carefully reexamined.

The charge on the insulators' surfaces was observed to decay with time constants on the order of an hour to a constant level whose value is 1/4 or less of the initial value. We associated this change with recombination, and the fixed change in potential with the effect of surface geometry and damage morphology on surface potential.

No consistant pre-damage potential changes were observed indicating that the charge emission and surface cleaning observed in previous experiments do not have a significant effect on surface potential. Evidently these effects are not appropriate for study by surface potential methods.

---

6. References

[1] J.O. Porteus, D.L. Decker, D.J. Grandjean, S.C. Seitel, and W.N. Faith, "Defect-Damage Resistant Copper Mirrors," in 11th ASTM Symposium on Optical Materials for High Power Lasers, NBS Special Publication #568, Boulder CO (1979).

[2] M.F. Becker, F.E. Domann, A.F. Stewart, and A.H. Guenther, "Charge Emission and Related Precursor Events Associated with Laser Damage," 15th ASTM Symposium on Materials for High Power Lasers, NBS Special Publication, Boulder CO (1984).

[3] J.K. Jhee, M.F. Becker, and R.M. Walser, "Charge Emission and Accumulation in Multiple-Pulse Damage of Silicon," 16th ASTM Symposium on Materials for High Power Lasers (elsewhere in these proceedings), NBS Special Publication, Boulder CO (1985).

[4] M.F. Becker, Y.K. Jhee, M. Bordelon, and R.M. Walser, "Charged Particle Exoemission from Silicon During Multi-Pulse Laser Induced Damage," 14th ASTM Symposium on Optical Materials for High Energy Lasers, NBS Special Publication #669, Boulder CO (1983).

[5] Y. Petit-Clerc and J.D. Carette, "New Feedback Kelvin Probe," Rev. Sci. Inst. 39, 933 (1968).

[6] J.C. Campuzano and R.G. Greenler, "Instrument for Combining Reflection-Absorption Infrared Spectroscopy with other Surface-Sensitive Techniques," Rev. Sci. Inst. 52, 678 (1981).

[7] R.J. D'Arcy and N.A. Surplice, "The Effects of Stray Capacitance on the Kelvin Method for Measuring Contact Potential Difference," J. Phys. D: Appl. Phys. 3, 482 (1970).

[8] N.A. Surplice and R.J. D'Arcy, "A Critique of the Kelvin Method of Measuring Work Functions," J. Phys. E: Sci. Inst. 3, 477 (1970).

[9] P. Braunlich, "Exoelectron Emission from Optical Surfaces," 2nd ASTM Symposium: Damage in Laser Materials, NBS Special Publication #341, Washington, D.C. (1970).
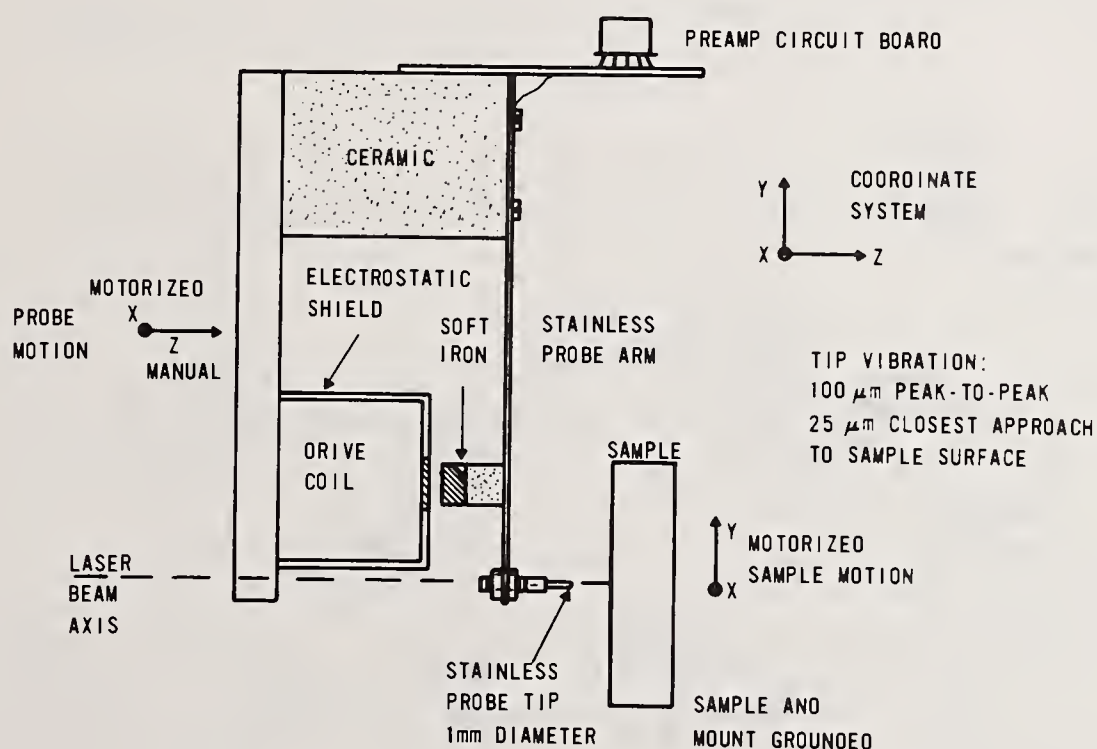
Figure 1. Mechanical diagram of the Kelvin probe.
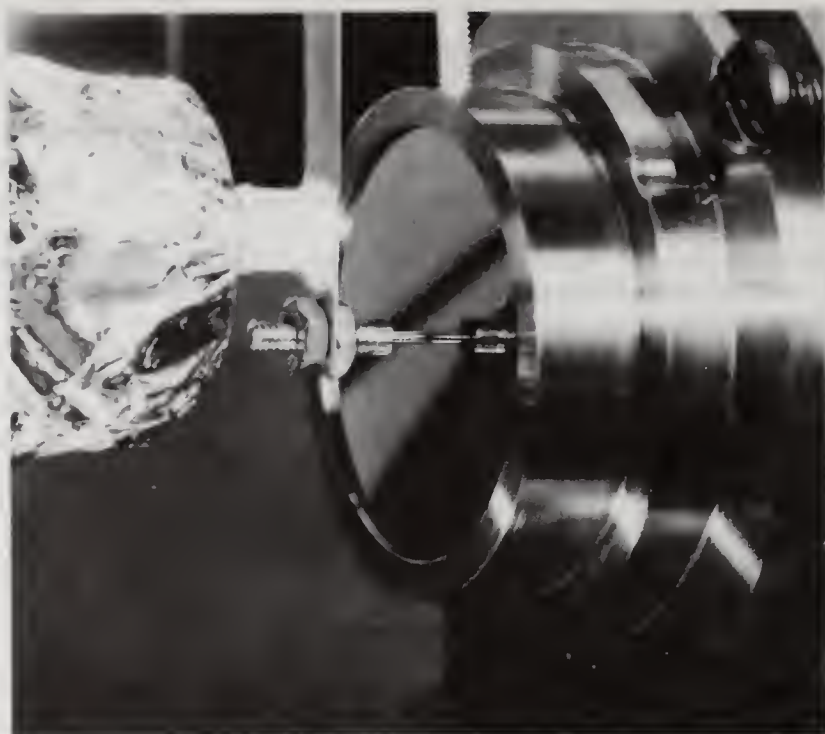
Figure 2. Photograph of the Kelvin probe over a silicon sample. The probe is higher than its usual operating distance above the sample surface.
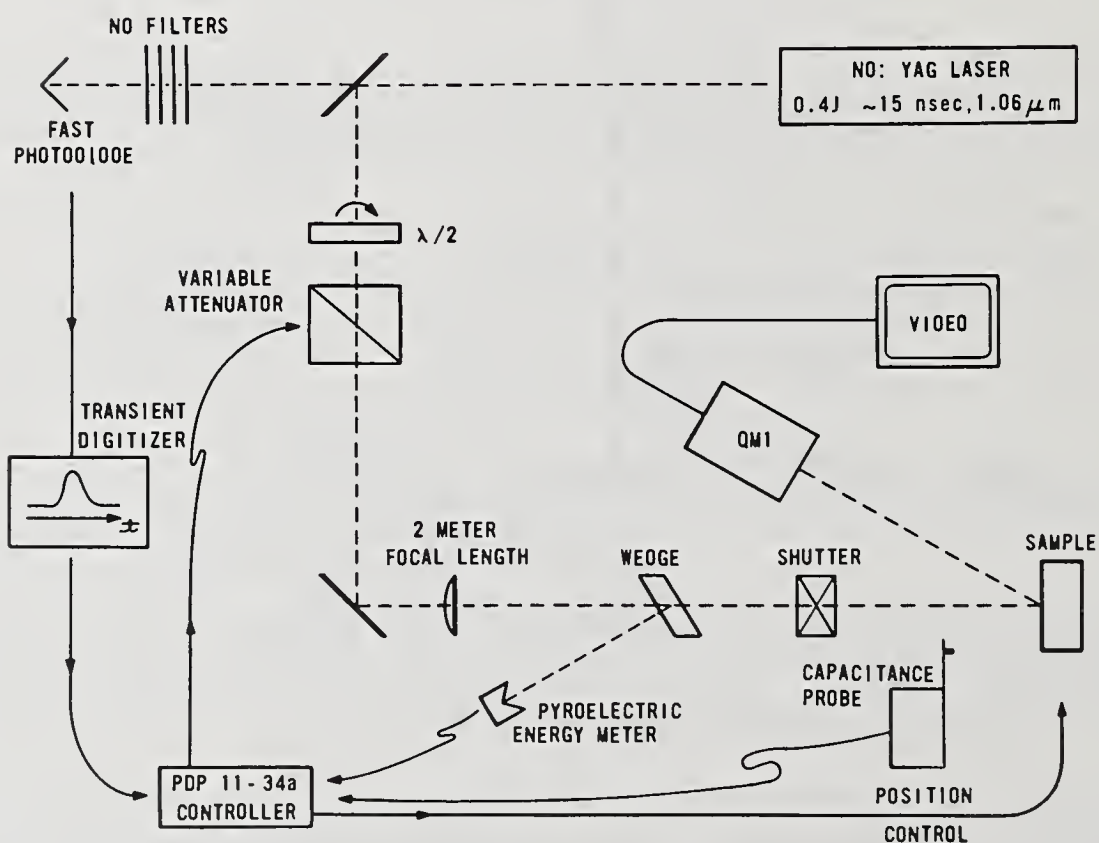
Figure 4. Optical layout and laser diagnostics.
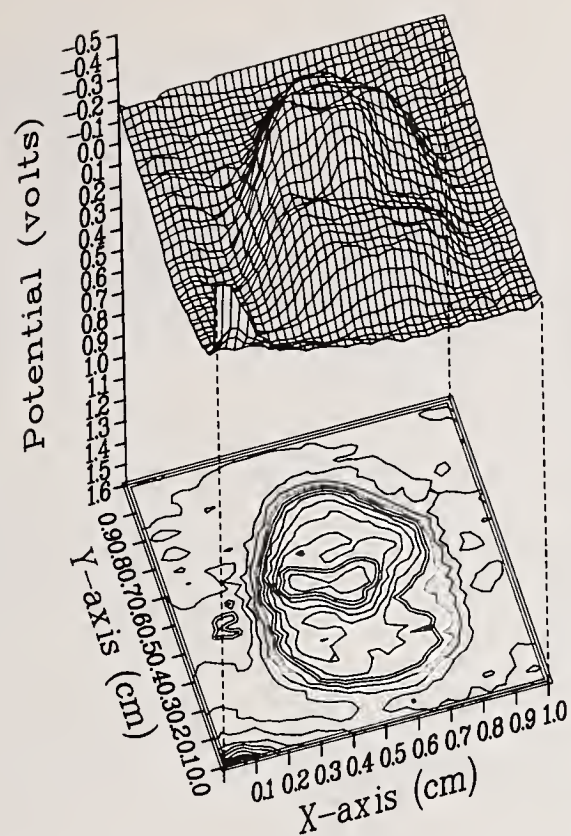
Figure 5. Surface potential change contour plot for the MgF$_2$ thin film irradiated by 10 pulses at 69 J/cm^2. The format is discussed further in the text.

CONTOUR PLOT
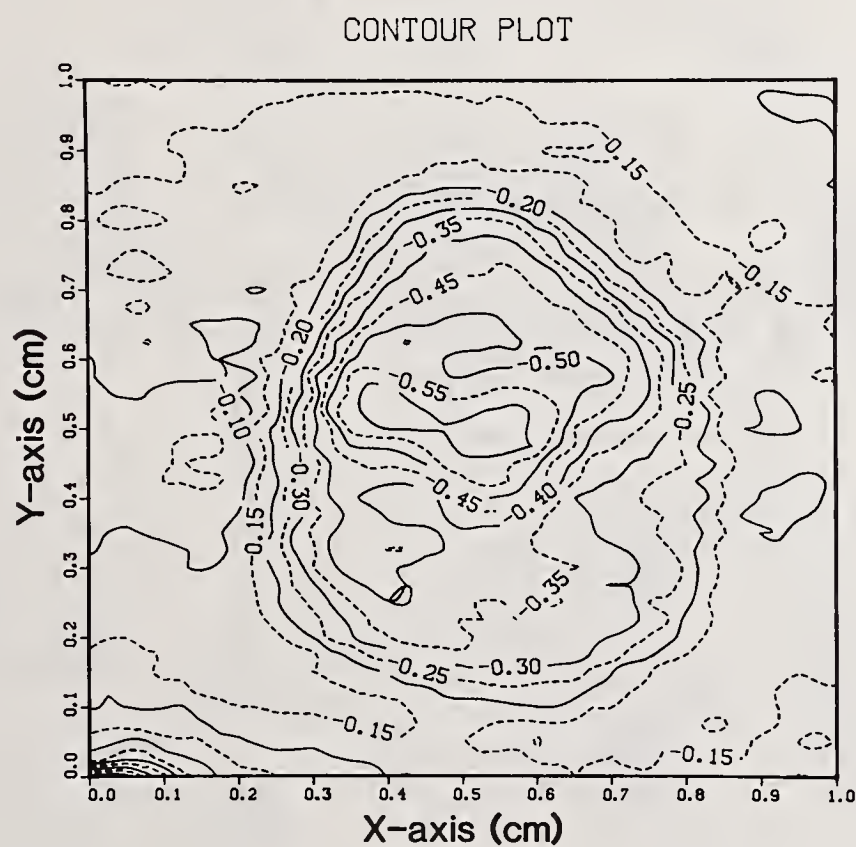
Figure 6. Same subject as figure 5, but plotted in a different format (see text).

123

KELVIN PROBE INSTRUMENTATION
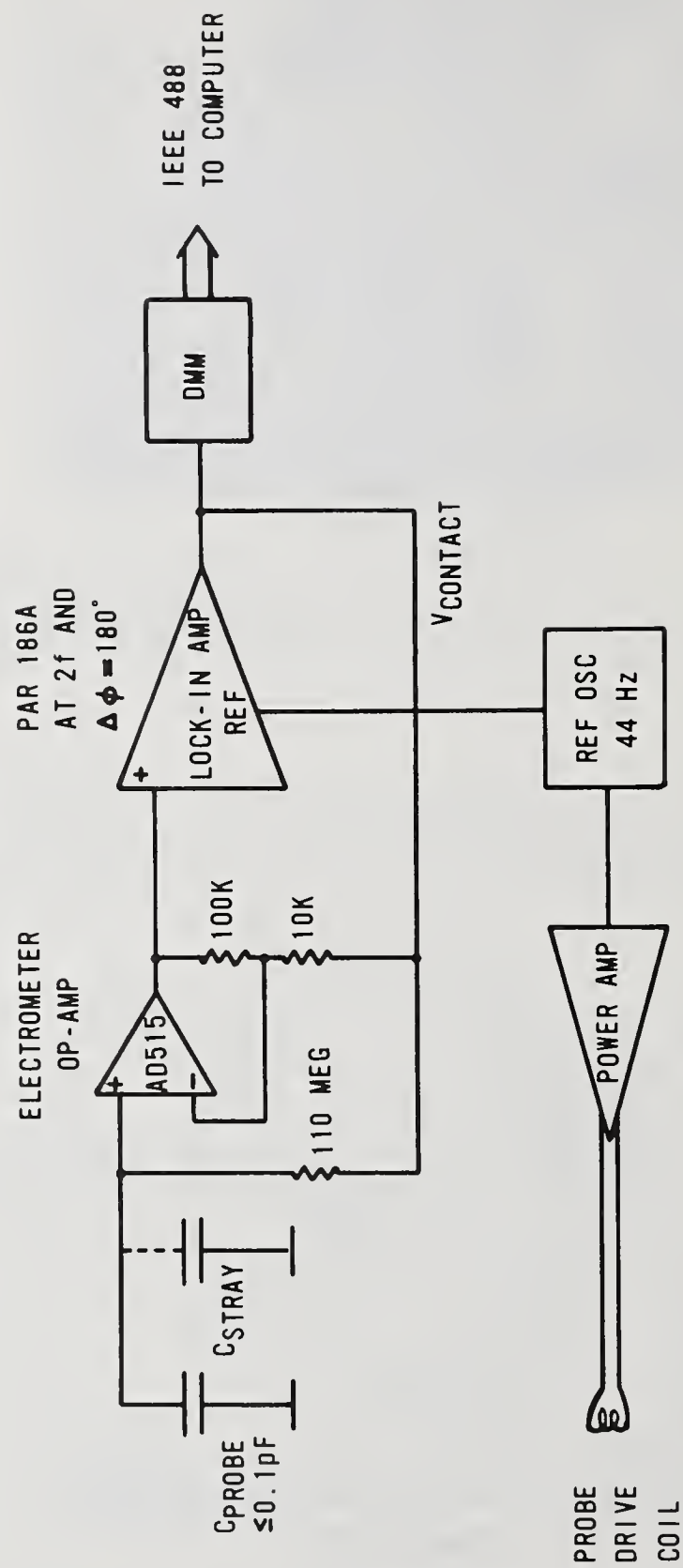
Figure 3. Schematic diagram of the Kelvin probe instrumentation.
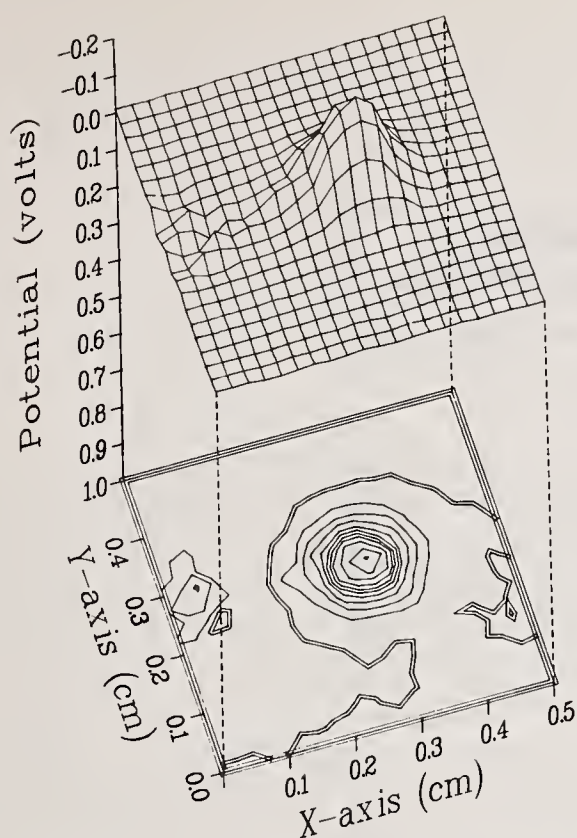
Figure 7. Surface potential change map for single crystal silicon irradiated by 1 pulse at 3.7 J/cm^2. The feature at the left is the adjacent previous damage site.
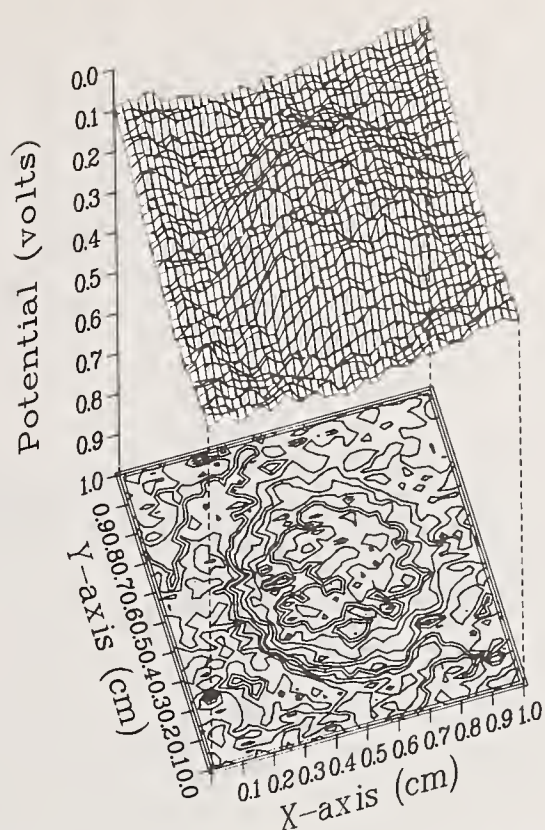
Figure 8. Surface potential change map for bare fused silica irradiated by 10 pulses at 140 J/cm^2.

a.

b.

c.
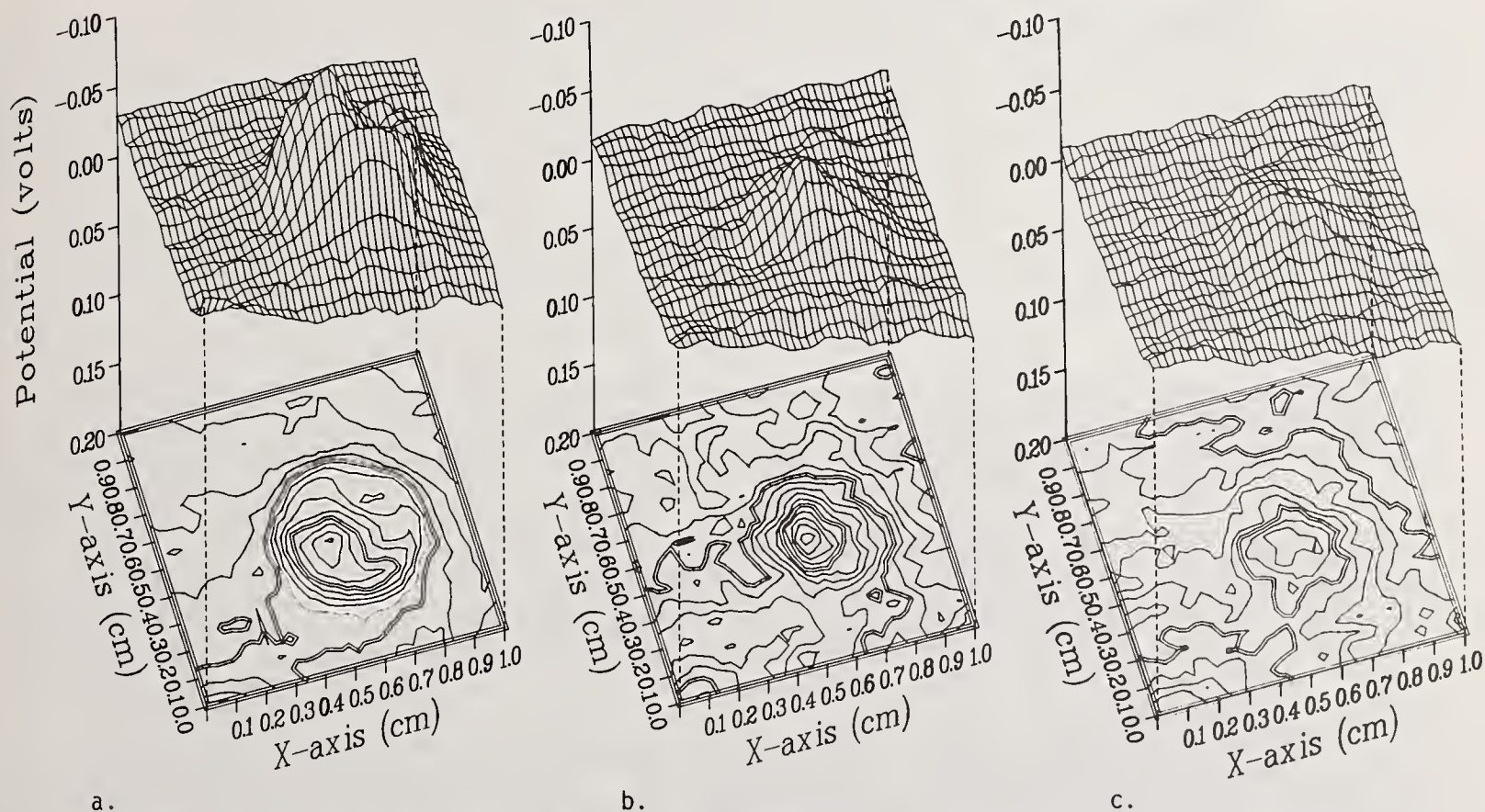
Figure 9. Surface potential maps for the HfO$_2$ thin film irradiated by 10 pulses at 50 J/cm^2 showing the peak decay at times; a. t =0; b. t=1 hour; c. t=2 hours; (left to right).

125
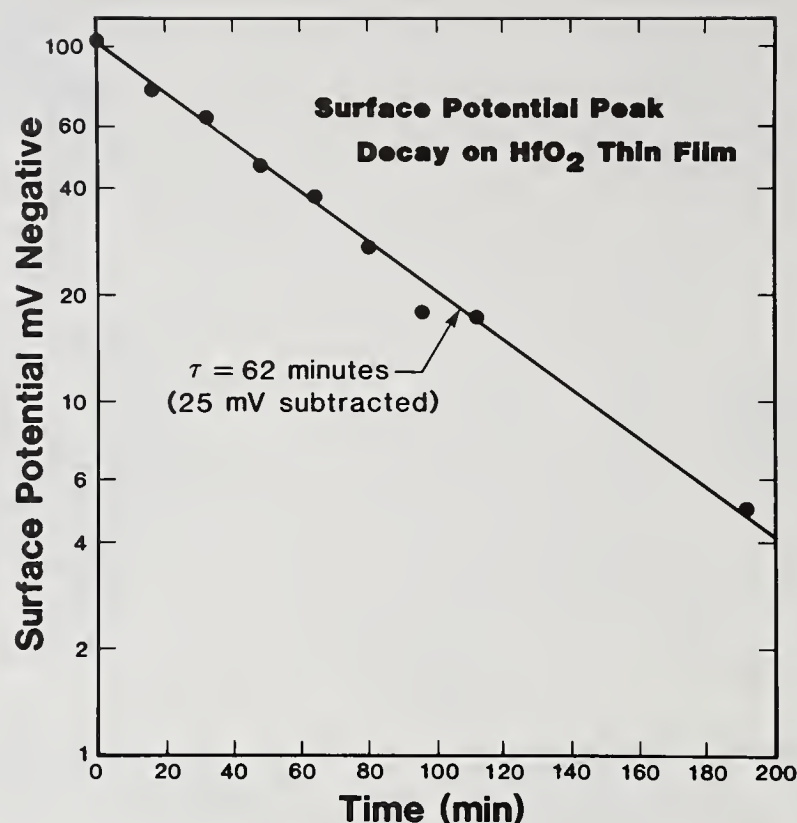
Figure 10. Surface potential peak height versus time for the same site on HfO$_2$ as Figure 9. The constant -25mV has been subtracted since it is the asymptotic value for the exponential decay.

One question was what effect the surface potential developed might have on scanning electron microscope examinations done after the tests. The author replied that he could speculate only since although he had had considerable experience with metallic and semiconducting substrates but not on dielectrics. He would expect that charging would affect electron microscopy for several hours after the tests were done. With SEM one would be charging the sample anyway, which makes use of this technique difficult. In reply to the question of where the charging comes from in the case of laser damage, the author pointed out that when laser damage occurs, both neutrals and charged particles are emitted. Presumably the electrical imbalance created by this process is the origin of the observed charging. Another questioner pointed out that about 10 years ago the Russians put some electronegative gas on the surface of a material they were trying to damage and saw no effect. Why? The author pointed out that the charge occurs after damage. The electronegative gas would affect the decay time and what is seen after damage, but would not be expected to affect damage initiation. Another question was why an effect would be seen in a good conductor such as copper. The author replied that in good conductors he did not believe that they were seeing surface charge but rather the effect of band bending near the surface and changes in the band structure. Effects were only seen in connection with melt pits for silicon and copper.

Charge Emission and Accumulation in Multiple-Pulse Damage of Silicon

Y.K. Jhee, M.F. Becker, and R.M. Walser

Electronics Research Center and Electrical and Computer Engineering Department
The University of Texas at Austin
Austin, Texas 78712

To contribute to further understanding of damage mechanisms of silicon surfaces induced by picosecond Nd:YAG 1.06 µm laser pulses, damage at laser intensities below the 1-on-1 damage threshold has been studied. By using a biased charge collector or an electron multiplier tube, one can detect the charge emitted during small pit formation which may be considered as the initial damage morphology. The investigation of the accumulation period has been conducted by observing the first charge emission which indicates its termination. This accumulation time is analogous to the lifetime of the solids subject to a repeated mechanical load and is characterized by processes that are irreversible for at least 3 seconds. This suggests that the damage precursors are long-lived excitations or an accumulation of permanent states. The heterogeneous nature of the nucleation of damage suggests that these precursor states act as nucleation seeds to the laser induced damage. Charge emission after the incubation period was also studied. Positive and negative particles are emitted equally after damage initiation, probably due to thermal evaporation of silicon from small regions. The charge emission follows the Arrhenius relation. Experimentally, this result was independent of pulse repetition period up to at least 10 seconds.

Key Words: accumulation; charge emission; N-on-1 damage; silicon.

1. Introduction

There have been several reports of undesirable laser-induced surface damage observed during the illumination of semiconductors by intense laser pulses. The nature of this damage has been established [1-3] by studying the nucleation and growth of damage near threshold intensities where the heterogeneous nature of nucleation was confirmed. Furthermore, charge emission from a silicon surface induced by picosecond laser pulses at 532 nm has been studied [4-6], but the energy transfer mechanism from the radiation field to the semiconductor in the multi-pulse damage regime is not well understood.

Single crystal silicon, a covalent material, was chosen because it has an absence of polar optical coupling, well characterized properties, high crystalline quality, and is technically important. Furthermore, Nd:YAG laser light (1.17eV) is ideally matched to the band gap of silicon (1.11 eV at room temperature). Near band gap excitation limits the heating of the sample by fast phonon decay of hot electrons so that damage at fluences below the uniform melt threshold may be studied.

The objective of this study is to contribute to the understanding of the damage mechanism below the 1-on-1 damage threshold on silicon surfaces induced by picosecond Nd:YAG laser pulses at 1.06 µm. Studies of "subthreshold" formation and evolution of damage under the action of laser irradiation may be of considerable importance in understanding the energy transfer mechanism.

In this study, the detection of charged particle emission was used to investigate laser damage on crystalline silicon surfaces at fluences below the 1-on-1 damage threshold. We describe the results of using this method to observe the accumulation period and dynamics of charge emission following the accumulation period. The pulse repetition frequency dependence of these phenomena is also examined.

2. Experimental Method

Figure 1 shows the experimental arrangement. TEM_{00} mode pulses were obtained by the use of a passively mode locked 1.06 µm Nd:YAG laser. The pulses had an average FWHM duration of 60 psec, determined by the use of an autocorrelation system utilizing sum frequency generation in KDP. From the train of pulses, a single pulse was selected by an electrooptic cell which was positioned between the output of the laser (with vertical polarization) and an output polarizer, and was activated by the laser triggered spark gap.

A photodiode, PD-1, was used to trigger the microcomputer. For calibration, the R_j-7100 energy meter from Laser Precision Corp. measured each pulse energy while the output of photodiode, PD-2, was

127

recorded by the microcomputer. These two quantities have a linear relationship for our experimental
energy range. Thus the carefully calibrated photodiode, PD-2, measured the energy incident on the
silicon sample. The standard deviation of the pulse-to-pulse laser energy stability was < 20%. Data
obtained with relatively stable sequences of pulses were selected and averaged. A 330 μm thick, high
resistivity, [100] silicon sample was place 8 mm behind the focus of 172 mm focal length lens where
the beam spot diameter was approximately 100 μm. The spot size at the sample was measured by scanning
with a narrow slit. Experiments were conducted on silicon samples cleaned chemically just prior to
their introduction into a chamber with a vacuum maintained < 10^{-5} torr. The cleaned silicon sample
was used as one electrode while a spiral wire placed 2mm before the sample served as the other electrode.
A ±1300 V bias was applied between two electrodes. This potential was suficient to collect all emitted
charge and was above the saturation point of the collected charge vs. potential curve. At its highest
sensitivity, the detection limit of the charge collector was 10^{-13}C. We also used an electron multiplier
tube, which magnified the charge signal ∿ 10^5 times, to investigate charge emission before damage initia-
tion. The electron multiplier gave results identical to the wire charge collector.

3. The Accumulation Period

     In this set of experiments, we investigated the behavior of silicon before damage was initiated.
The duration of the accumulation period at various pulse rates was studied as well as the absorption
properties of the material for laser fluences below the 1-on-1 damage threshold.

3.1 Nonlinear Absorption

     The absorption coefficient prior to damage initiation was determined from transmission measurements.
The result is plotted in figure 2, where the dots represent averaged values within a small interval
of laser energy. This data was adjusted for sample reflectivity before it was plotted, so intensity
is given within the silicon. The inverse energy transmission coefficient T^{-1} for a Gaussian beam is
given by [7]:

$$T^{-1} = \frac{\beta \sqrt{\pi} \; I_m \, (1-e^{-\alpha L})}{2\alpha e^{-\alpha L} \int_0^\infty \ln[1 + \frac{\alpha}{\beta}(1-e^{-\alpha L})I_m \, e^{-x^2}] \, dx} \tag{1}$$

where L is the thickness of sample, α is the one photon absorption coefficient, and β is the two photon
absorption coefficient. Equation (1) is used to derive β from the experimental results of Figure 2.
A good least squares error fit is obtained with a value of α = 7.25 cm^{-1} and β = 7cm/GW. We find from
this experiment that two photon absorption dominates during the incubation period. Direct two-photon
transitions and two-photon stepwise transitions may both be present in this experiment conducted at
room temperature. Since pure two-photon absorption is small for this laser wavelength, two-photon
stepwise absorption, or free carrier absorption, presumably dominates in this case.

     Though the silicon band gap is well matched with the photon energy of Nd:YAG laser, we cannot
neglect heating of the sample by fast phonon decay of hot electrons generated by free carrier absorption
during the accumulation period. We discuss this temperature rise in a later section. No anomalous
behavior or evidence of accumulation was observed in the nonlinear absorption measurements.

3.2 Intensity-Dependent Accumulation

     In this section we describe measurements of the accumulation period dependence on laser fluence.
Though the conventional methods for defining damage have been applied widely, we used the method of
recording the first observable negative or positive charge emission. This emission was always observed
coincident with the first observable surface damage pits as seen by SEM. Many nondamaging experiments
were carried out to verify this fact. We note that a recent report of multiphoton photoemission from
silicon at 1.06 μm [6] may be used to calculate the photoemission electron fluence expected for our
geometry. The resulting maximum charge is two orders of magnitude below our reported detection limit.

     In figure 3 we plot the number of laser pulses needed to initiate the first charged particle emis-
sion versus laser fluence at 1.06 μm. The experimental points were obtained by observing the first
positive charge emission or negative charge emission. Within experimental error, negative charge emis-
sion and positive charge emission gave identical results as shown in figure 3. The solid curve obtained

by the least squares fit of the given data can be represented by

$$\frac{1}{N} \propto (F-F_o) \qquad (2)$$

where F_0 is the hypothetical multiple-pulse damage threshold fluence, or fatigue limit. Several thousand shots were applied without observation of any charged particle emission at a fluence at or below 0.32 J/cm^2. It is possible that no damage occurs even for $N \rightarrow \infty$ below this energy. This means that there exists a multiple-pulse damage threshold or fatigue limit below which crystalline silicon is undamaged. The sample surface did not undergo visible structural change during the incubation period as seen by SEM or Nomarski microscopy. Surface changes were always observed coincident with negative and positive charge emission even when we used an electron multiplier tube to magnify the charge emission signal 10^5 times. The first visible damage morphology was composed of small pits, about 0.3 μm in diameter or larger.[8,9]

Experimentally, the 1-on-1 damage probability P, determined by applying a single pulse to a number of different sites, is not equal to the N-on-1 damage probability P', determined by applying a series of pulses with the same intensity to a given damage site. That is, "spatial" statistics do not agree with "temporal" statistics. This indicates that a purely random model does not adequately explain the behavior in this case, and that the damage threshold decreases with an increasing number of laser pulses. This suggests the irreversible accumulation of permanent material changes, or the reversible accumulation of long-lived states.

The lucky electron model [10,11] of Bass and Barrett, which is an extension to the optical regime of Shockley's experiments on dc breakdown in semiconductors, does not account for our experimental results. In this model, the damage probability depends on the optical electric field but is independent of the number of pulses. This conclusion leads to the concept of an accumulation of irreversible, or perhaps, reversible changes that create the prerequisites for damage at subthreshold fluences.

To further determine the nature of the incubation period, the relation between the logarithm of the laser fluence and the logarithm of the number of pulses needed to initiate damage was plotted in figure 4. This plot was motivated by the work of Lee, Koumvakalis, and Bass [12] on the N-on-1 damage of metal surfaces. The plot in figure 4 is the analog of a log(strain) vs. log(N) curve for mechanical fatigue testing of materials. Although the two slope behavior resembles that of many metals and alloys, there is no evidence for silicon that slip is accumulating as evidenced by changes in surface roughness. No such changes were ever observed during the accumulation period for silicon.

Recognizing that the one-shot damage threshold is dependent on beam spot size, the experimental threshold fluence can range widely for different focusing conditions. Some earlier experiments conducted with large laser beam areas [13] reveal that the temperature rise at the end of the laser pulse is only about several tens of degrees. The experiment reported here was done with a smaller beam area and measured correspondingly higher laser damage fluences. This result suggests that excitations are accumulated due to laser irradiation in conjunction with the energy of local thermal fluctuations near the peak thermal excursion, rather than due to the average temperature during the incubation period. This result is based on the condition that the average temperature during the incubation period is proportional to laser energy; but is very small in all cases, since the thermal relaxation time is much shorter than the period between laser pulses.

These experiments conclusively establish that the number of pulses needed to initiate the first visible damage on the silicon surface depends on the laser pulse energy. Reduced damage thresholds due to repeated pulses must be explained by the cumulative nature of excitations rather than by probabilistic arguments devoid of time dependent correlation.

3.3 PRF Independent Incubation Period

To examine the cumulative damage effect more extensively, we measured the accumulation period as a function of pulse repetition frequency (PRF). The same experimental configuration as in figure 1 was used. The laser beam was modulated by a mechanical shutter. Damage initiation was determined by recording the positively charged particle emission which was coincident with it. The experimental results are plotted in figure 5. Within experimental error, the accumulation period was independent of pulse repetition frequency. This result rules out the possibility that a thermal accumulation of absorbed energy occurred during the incubation period. It is possible, however, that there is a reversible process whose lifetime is over 3 seconds. The accumulation of long-lived excitations [14] or perma-

nent states caused by repeated laser irradiation is, therefore, a strong candidate. These states may absorb more energy from the field like absorbing inclusions of small diameter in transparent materials.

The experimental temperature dependence of damage to silicon was reported by Sheng [13]. According to his results, the total damage area was reduced as the temperature of the sample was increased. The 38 picosecond laser pulse length was much shorter than the 0.2 sec interval between laser pulses. Some long-lived excitations may have decayed more rapidly during the interval between laser pulses due to the elevated sample temperature. On the average then, fewer nuclei would have sufficient time to reach a critical concentration prior to damage.

It is reasonable to assume that the accumulated long-lived or permanent states preferentially absorb energy from the incident field, and act as nucleation seeds for damage initiation. This accumulation process is heterogeneous, and its heterogeneous nature is revealed by observing the surface damage morphology as explained in Refs. [1-3].

4. Charged Particle Emission and Damage

In this section we report on our measurements of charged particle emission after damage initiation. A dependence on laser intensity, but not on pulse repetition frequency was observed.

4.1 Intensity Dependent Charged Particle Emission

After the accumulation period, for which no visible damage was observed, positive and negative charges were emitted equally from the silicon surface. The variation of such emission was so dispersive at the early stages of damage evolution that it was very difficult to get information from each datum of charge emission. However, when the data was averaged over small energy intervals, a reproducible relationship between the laser pulse energy and total emitted charge was obtained. Negative and positive charges gave the same information.

In a log-log plot the slope of the data fits a fifth power law quite well except in the higher energy range where the slope is higher. This result suggests that five-photon processes might be responsible for initiating the emission of silicon ions. To investigate this possibility, we collected the emitted particles on a microscope cover glass with the aid of a bias accelerating voltage. The collection pattern consisted of clearly visible spherical debris, similar to those seen near the surface damage sites [8,9]. Individual particles were spherical in shape and might be re-solidified droplets of silicon. The thickness of the ejected material on the microscope cover glass could be clearly seen with the naked eye as a darkening. The energy required to remove droplets composed of many atoms is certainly higher than the energy of five-photons. Furthermore, the energy of the fastest particles, as measured by time of flight, is much larger than the energy of five-photons. Thus lattice constituent emission, due to multiple-photon process is unlikely, unless a larger energy release is triggered by a five-photon process.

We show this charge emission data on a semilog scale (see fig. 6) with the log of the average charge emitted on the y-axis and the inverse laser fluence on the x-axis. This plot shows a linear relation between the two quantities. This result suggests that the emission may be due to thermal evaporation of silicon where the temperature of the emission site is linearly proportional to laser pulse energy. In this case the emitted charge, N, follows an Arrhenius relation [5],

$$N = N_0 \exp{\frac{-U_0}{RT}} = N_0 \exp{\frac{-U_0}{k'F}} \tag{3}$$

where F is the laser fluence, N_0 and k' are constants, and U_0 is the energy of activation. This result indicates that the laser energy, absorbed first by free carriers, is transferred eventually to the lattice and localized. The local temperature is raised high enough to evaporate silicon, and some of the evaporated material becomes ionized. Thus charge emission would depend on local temperature and follow an Arrhenius equation. Observations of the corresponding surface damage morphology [8,9] show one or more pits of fairly uniform 0.3 micron diameter. Furthermore, the pits constitute a very small percentage of the laser beam area at the initiation of damage.

For N-on-1 damage, we observed visible light emission coincident with surface damage initiation. That no visible radiation is observed before damage is initiated confirms that the temperature at the sample is much lower. When the vaporization temperature is reached locally and a plasma forms, there will be considerable thermal radiation. These experimental results indicate that the final damage

event induced by a series of laser pulses is the result of local heating of the material at what are now highly absorbing, submicron regions.

4.2 PRF Independent Charged Particle Emission

We discussed charged particle emission after the accumulation period in the previous section. To find how the pulse repetition frequency affects this emission, we interrupted the incident beam in the manner described previously.

The experimental results are shown in figure 7. This figure is a plot of positive charge emission versus fluence for different PRFs. This experiment was conducted over a small range of energies near the multiple-pulse damage threshold. Experimentally we could find little difference in charge emission in spite of the large difference in PRFs. Furthermore, charge emission occurred at the expected pulse number after a five minute interruption of the illumination.

This experiment leads to the conclusion that cumulative thermal effects, that result from stepwise ratcheting increases of the temperature, are not the cause of this charge emission. Charge emission is independent of PRF within the experimental error limit (laser energy fluctuations < 20%). Damage, after the incubation period, is independent of the PRF and is apparently due to irreversible processes or states having a lifetime of more than 10 sec.

4.3 Charge Emission Development

The iso-intensity variation of positive charge emission at 0.45 J/cm^2 and 1.25 J/cm^2 is plotted in figure 8. These fluences are just above the multi-pulse threshold and just below the 1-on-1 threshold, respectively. Note that the vertical scale on the lower curve has been magnified 10 times. Charge emission varied rapidly for a small number of pulses in the early stage of damage evolution. At later times, the charge emission became stabilized.

At higher fluence, the incubation period was very short and was followed by a rapid evolution of damage. The initial damage morphology consisted of a few randomly distributed pit chains. After the first emission event, charge emission increased very rapidly as seen in figure 8. A maximum emission occurred approximately when the beam area was covered with a ripple pattern. This kind of large ripple pattern is often observed for a wide variety of materials including semiconductors, metals, and dielectrics; and is well described by various authors. Our experiments revealed that this large ripple pattern becomes well formed near the 1-on-1 damage threshold. This is not the case for lower fluences near the multiple-pulse damage threshold, because the center of the ripple pattern is destroyed before the edges are fully formed.

5. Conclusions

An investigation of the accumulation period in the laser damage of silicon has been conducted by observing the first charge emission event which indicates the termination of accumulation, and by measuring optical transmission during this period. Negative and positive charges are emitted at the same time and give equivalent information. Nonlinear absorption is dominant before damage is initiated, and it may be attributed mainly to two-photon stepwise absorption (free carrier absorption) rather than simultaneous two-photon absorption. Thus carrier absorption may have an important role during this period. No anomalous behavior was observed in the absorption measurements to indicate an accumulation mechanism. This accumulation effect in laser damage can be compared to the lifetime of solids subject to a repeated mechanical load. Unlike the case of metal mirrors, no accumulating slip or surface roughness was observed on silicon.

Our data suggests that long-lived excitations or permanent states may be accumulated due to laser irradiation. The accumulation period was independent of the pulse repetition frequency and characterized by irreversible processes for at least 3 seconds. This suggests that the precursors to laser damage involve either long-lived excitations or permanent state accumulation. The heterogeneous nature of the nucleation of damage suggests that these precursors may act as the nucleation seeds to laser induced damage.

Positive and negative charge was emitted after the accumulation period in equal amounts. This emission was probably due to thermal evaporation of silicon. The local temperature at the damage sites appeared to increase linearly with laser energy, and the charge emission followed an Arrhenius relation. Visible light was observed coincidently with the occurrence of surface damage and may be considered evidence of high temperature thermal radiation. Experimentally these results were independent of pulse repetition frequency and entirely exclude the possibility that thermal accumualtion occurred. Charge emission increased as the damage extended to fill most of the beam area.

6. References

[1] D.Y. Sheng, R.M. Walser, M.F. Becker, and J.G. Ambrose, Appl. Phys. Lett. 39, 99 (1981).

[2] R.M. Walser, M.F. Becker, D.Y. Sheng, and J.G. Ambrose, "Heterogeneous Nucleation of Spatially Coherent Damage Structures in Crystalline Silicon with Picosecond 1.06 μm and 0.533 μm Laser Pulses," in Laser and Electron-Beam Solid Interactions and Materials Processing, T.J. Gibbons, W. Hess, and T. Sigmon, eds. (Elsevier, New York, 1981) p. 177.

[3] M.F. Becker, R.M. Walser, Y.K. Jhee, and D.Y. Sheng, "Picosecond Laser Damage Mechanism at Semiconductor Surfaces," in Picosecond Lasers and Applications, January 1982, Los Angeles, CA, SPIE Vol. 322, p. 93.

[4] J.M. Liu, R. Yen, H. Kurz, and N. Boembergen, Appl. Phys. Lett. 39, 755 (1981).

[5] J.A. van Vechten, J. Appl. Phys. 53, 9202 (1982).

[6] T.L.F. Leung and H.M. van Driel, Appl. Phys. Lett. 45, 683 (1984).

[7] J.H. Bechtel and W.L. Smith, Phys. Rev. B13, 3515 (1976).

[8] R.M. Walser, M.F. Becker and D.Y. Sheng, "Laser Damage of Crystalline Silicon by Multiple 1.06 μm Picosecond Pulses," in 13th ASTM Symposium on Optical Materials for High Power Lasers, NBS Special Publication #638, Boulder, CO, 1982.

[9] M.F. Becker, Y-K. Jhee, M. Bordelon, and R.M. Walser, "Charged Particle Exoemission from Silicon During Multi-Pulse Laser Induced Damage," in 14th ASTM Symposium on Optical Materials for High Power Lasers, NBS Special Publication #669, Boulder CO, 1983.

[10] M. Bass and H.H. Barrett, Appl. Opt. 12, 690 (1973).

[11] M. Bass and H.H. Barrett, IEEE J. of Quant. Electron. QE-8, 338 (1972).

[12] C.S. Lee, N. Koumvakalis, and M. Bass, J. Appl. Phys. 54, 5727 (1983).

[13] D.Y. Sheng, Ph.D. Dissertation (The University of Texas at Austin, 1981).

[14] M. Bordelon, R.M. Walser, M.F. Becker, and Y.K. Jhee, "A Study of the PRF Dependence of the Accumulation Effect in Multiple Pulse Laser Damage of Silicon," in Proceedings of the 14th ASTM Symposium on Optical Materials for High Power Lasers, NBS Special Publication NBS, Boulder CO, 1984.
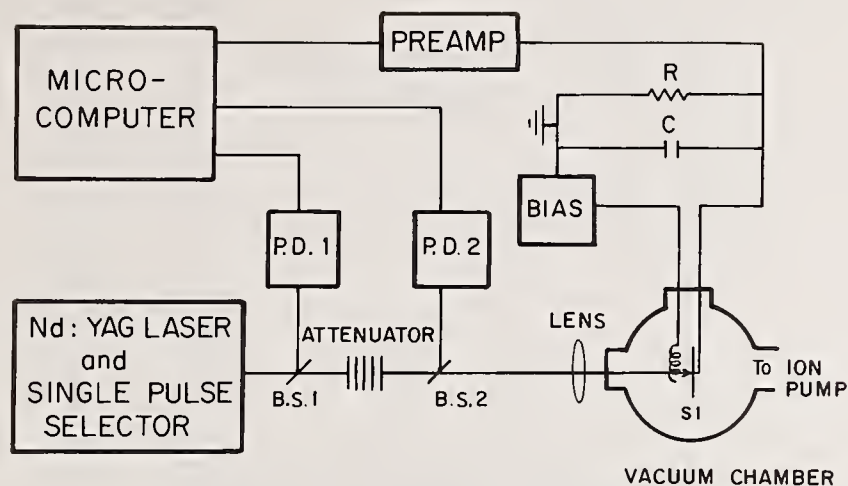
Figure 1.   Schematic of the experimental arrangement.   The laser produced 60 ps, 250 μJ.
             pulses at a PRF of 13 Hz.   The laser spot diameter was 100 μm, and the charge
             detection limit was 10^{-13}C.
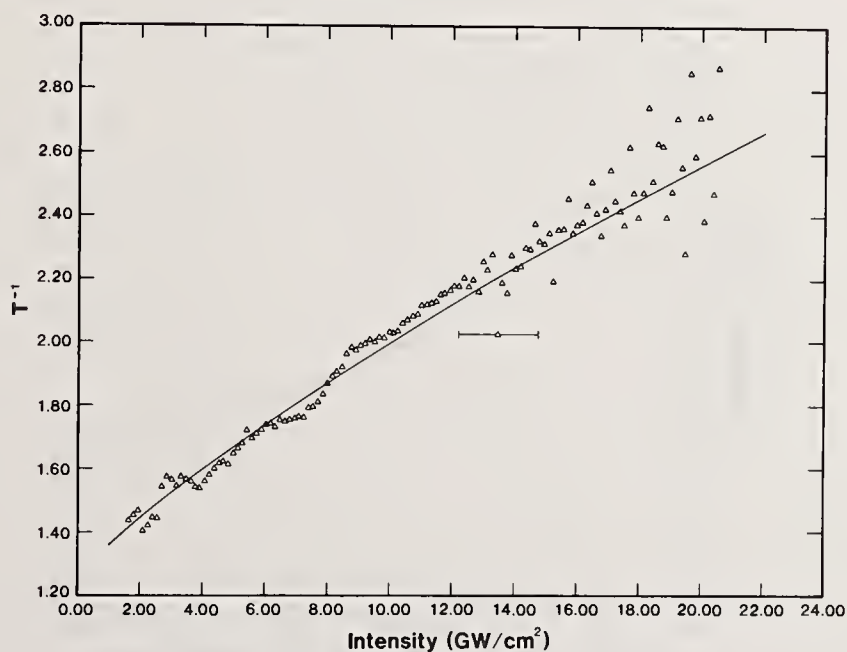
Figure 2.   Dependence of the inverse of transmission upon incident 1.06 μm laser flux for
             [100] Si.   The sample was 300 μm thick and the transmission has been adjusted
             for reflection.   Error bars show standard deviation of laser energy fluctuations.
             (Pulse length = 60 psec.)

133
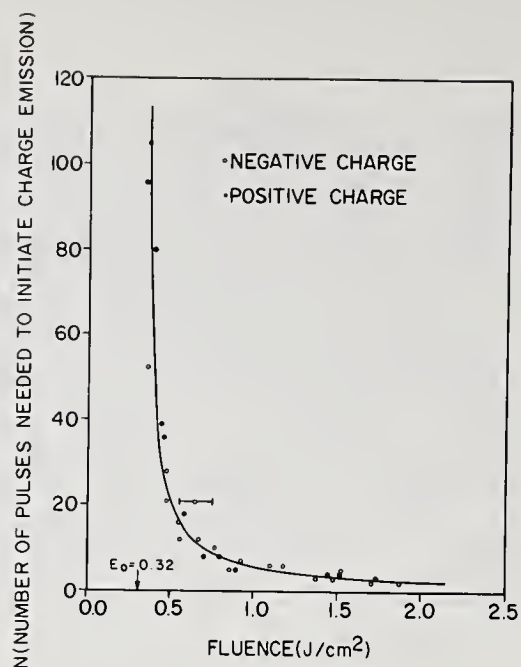
Figure 3. Number of pulses to initiate exoemission and damage versus laser fluence. The solid curve is inversely proportional to laser fluence. The curve diverges at the multi-pulse damage threshold of 0.32 J/cm^2.
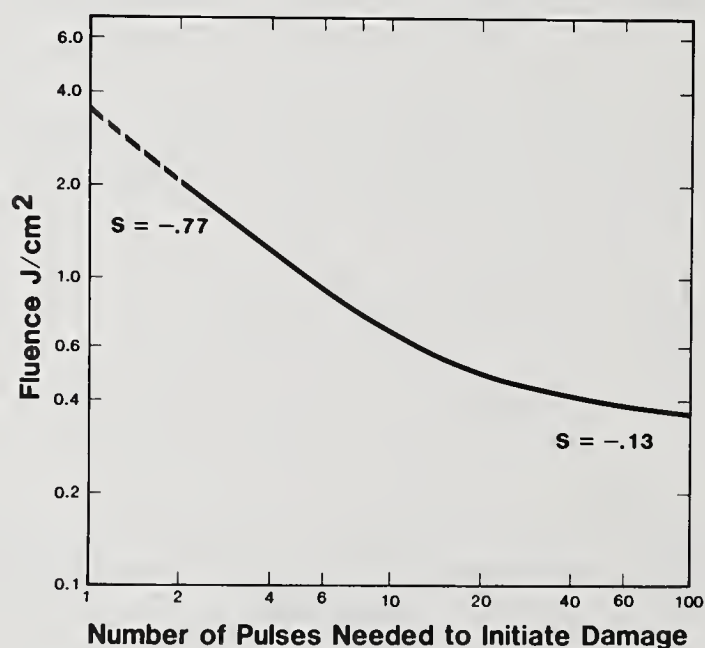
Figure 4. Damage fluence versus number of pulses to damage in log-log format of a strain vs. N curve. Slope S gives power law dependence for each segment of the curve.

134
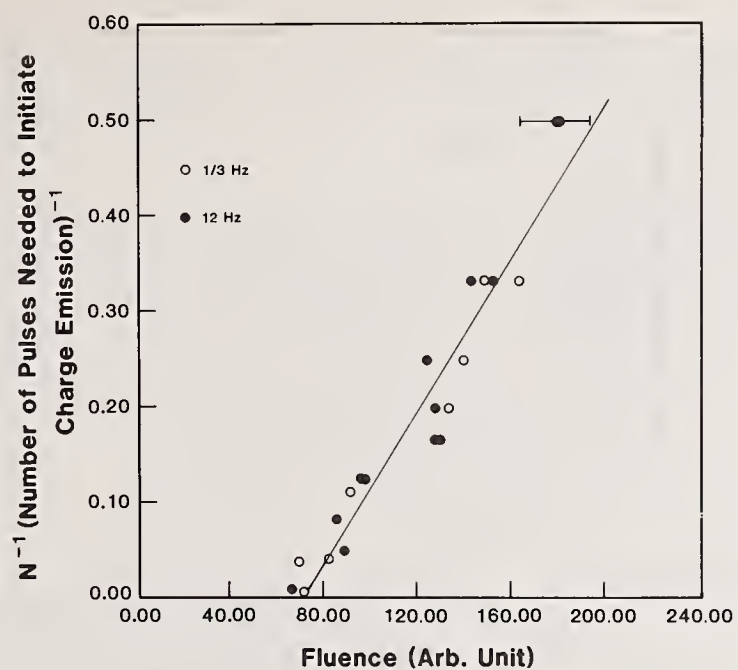
Figure 5. Accumulation period at pulse repetition frequencies 1/3 Hz and 12 Hz. The line is a least squares fit to the data.
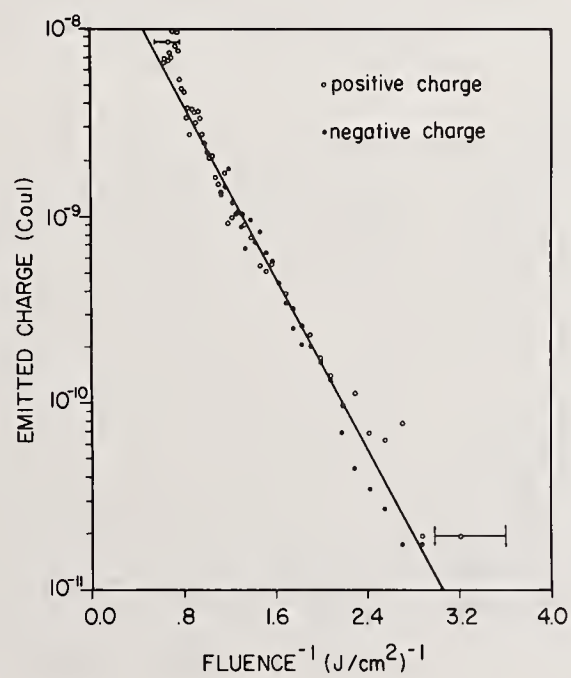
Figure 6. Charge emission versus the inverse of laser fluence for N-on-1 damage. The line is a least squares fit to the data.
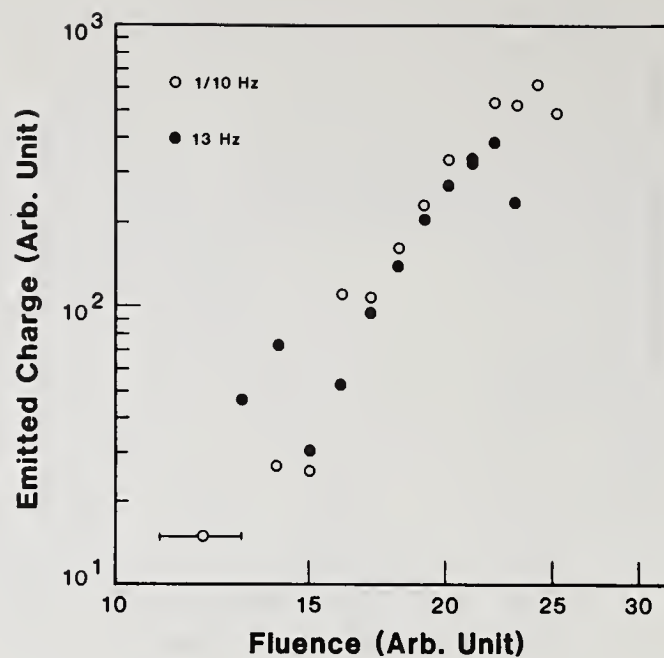
Figure 7.   PRF independent positive charge emission after damage at 13 Hz and 1/10 Hz.
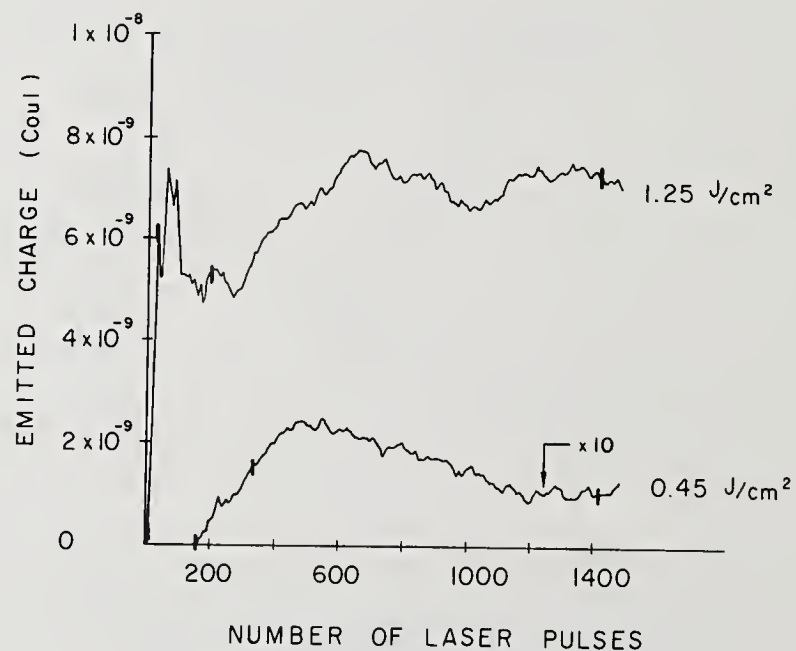
Figure 8.   Positive charge emission versus number of laser pulses at the same site (or vs. time, at a 13 Hz PRF). The upper curve is for an energy density just below the 1-on-1 damage threshold, and the lower curve is at an energy density just above the multi-pulse damage threshold (vertical scale 10x).

136

Laser Generated Ripple Patterns on Dielectrics and
Intermediate Band Gap Semiconductors

Nastaran Mansour, Giancarlo Reali, Patrizia Aiello, and M. J. Soileau

Center for Applied Quantum Electronics
Department of Physics
North Texas State University
Denton, Texas 76203

In this paper we report the results of studies of laser generated ripple patterns on intermediate band gap semiconductors (e.g., ZnS, ZnSe) and dielectrics of various indices of refraction by 10.6 μm laser pulses. The results confirm, only on a coarse scale, the scenario of the formation of coherent structures on the front or rear surface of damaged materials. In particular, for a variety of transparent dielectrics, we carefully determined the ripple spacing through microscopic observation and by diffraction pattern measurements. The ripple spacing and direction are consistent with prior observation by other workers. Similar measurements on front and rear surfaces of ZnS and ZnSe were also carried out revealing the presence of domains of regularly spaced ripple formations and fine structures superimposed parallel to the main pattern. Such fine structures are also present in the damaged dielectric samples, although they are perpendicular to ripple direction. Furthermore a "wrong" orientation, i.e., parallel to the incident field, of the induced gratings was observed. This points toward a less naive interpretation of laser induced ripples than has been described in the literature thus far.

Key words: laser-induced surface damage, dielectric materials, intermediate band gap semiconductors, exit surface damage, ripple structures.

1. Introduction

Laser generated ripple patterns have been studied extensively for dielectrics [1-11], narrow band gap semiconductors [12-22], and metals [3-5,20,22-28]. For the most part these results are explained qualitatively by one or more of the models proposed for the generation of these features [2,9,30,31,32]. Most of the research reported over the past two decades led to an explanation of ripple spacing and direction independent of the dynamics of pattern growth [29]. Laser generated ripple patterns observed in wide band gap dielectrics, small band gap semiconductors and metals are very similar in that they run normal to applied optical field, but they differ in the ripple spacing for a given optical frequency. It has been observed that for small band gap semiconductors and metals the ripple spacing is equal to the optical wavelength in vacuum (λ_o), while for wide band gap dielectrics the ripple spacing is approximately equal to the optical wavelength in the material (λ_o/n). The different behavior of small band gap semiconductors and metals, and wide band gap dielectrics led us to investigate intermediate band gap materials, such as ZnS and ZnSe. In addition we started a more detailed experimental study of a variety of dielectric materials. All the results reported here are for 10.6 μm laser induced surface structures. The experimental setup will be described in Section 2. The results of the laser induced surface structures in dielectrics and ZnS and ZnSe will be presented in Section 3. A summary of the results is contained in Section 4.

2. Experimental Setup

The laser source used in this study was a linearly polarized TEA CO_2 pulsed laser operated in the TEM_{00} spatial mode at 10.6 μm. A cw, inside-the-cavity injection locking section provided single longitudinal mode operation. The resulting pulses had a smooth Gaussian spatial distribution and a smooth temporal profile as shown in Fig. 1. The temporal pulsewidth was approximately 150 nanoseconds [full width at half maximum (FWHM)], as monitored by a photon drag detector and a fast 7834 Tektronix oscilloscope (500 MHz bandwidth). A 5 inch focal length lens was used to produce a focal spot of radius approximately equal to 100 μm (HW 1/e M of the irradiance) on the surface of the samples. A rotating Brewster angle polarizer - wire grid polarizer combination was used to vary the irradiance on targets while keeping the polarization at the samples

constant. Shot-to-shot energy variation was continuously monitored by pyroelectric detector which was calibrated with respect to a GenTec ED-200 energy monitor. A HeNe laser beam (632.8 nm) was used to illuminate the irradiated site in order to provide a diffraction pattern of the damaged regions. A Nomarski microscope with a maximum magnification of 1100x allowed the surfaces to be viewed in real space.

3. Experimental Results

Figs. 2-10 are Nomarski micrographs of laser generated ripple patterns on surface of various dielectrics (SrF_2, BaF_2, KCl, NaCl, KBr) and intermediate band gap semiconductors (ZnS, ZnSe). The laser irradiation for all the samples was linearly polarized and normally incident on the surfaces. The arrows show the direction of the applied electric field. The results of the measurements of ripple spacings are summarized in Table 1. The refractive indices are all at room temperature.

Previous studies of laser-induced ripple patterns on dielectric surfaces showed that the spacing of the ripples produced in such a material is approximately λ_0/n, and they have been consistently interpreted by a simple electrostatic dipole model [2].

An alternative model, assuming surface excitations-laser coupling, has been suggested by other authors [9,28]. This model requires that, during its thermodynamical evolution, the exposed material acquires a negative refractive index to satisfy momentum conservation between incident light and surface excitations.

We have found that the spacing of the ripples, produced by single shot irradiation, is λ_0/n on the exit surface of all the tested dielectric materials. This result was also confirmed by diffraction pattern measurements. In the case of dielectric materials the ripples run perpendicular to the applied electric field. In the presence of defects (e.g., scratches, digs, etc.) the ripple growth is in the privileged direction of the normal to the symmetry axis of the defect. This clearly indicates the relevance of seeds in starting the coherent process [3]. We notice that the characteristics of the ripple formation in SrF_2, BaF_2, KCl, NaCl and KBr are very similar, and that the maximum uncertainty in the λ_0/n-ripple spacing is at most of 5%, as deduced by the statistical analysis of the determinations of the spacings over several sample pictures.

These results are in agreement with the model of Temple and Soileau [2] as well as with a more sophisticated analysis by Sipe et al. [30]. Instead, the surface excitations-model [9,28] seems to be excluded by the fact that 10.6 μm radiation is very unlikely able to match surface polariton dispersion relation of any of the 5 dielectrics examined. [For the dielectrics tested the Reststrahl frequencies vary from 0.35×10^{14}Hz (KBr) to 1.13×10^{14}Hz (SrF_2]. Figure 7 shows laser generated ripple patterns on the front surface of ZnS. The ripples are formed perpendicular to incident field with spacing near to λ_0 (Table 1). On the exit surface of ZnS we found ripple spacing of approximately λ_0/n and also periodic surface structures with variably spaced ripples and wrong direction (parallel to applied electric field). In this sample, ripple structures are generated by multiple shots near the surface damage threshold. The larger uncertainties in the measured spacing in this material and in ZnSe are due to the fact that the ripple structures are not as well coordinated or as sharply defined as those observed for the dielectrics.

Figures 8 and 9 are Nomarski micrographs of ripple patterns on the front surface of ZnSe which are induced by multiple shots just above surface damage threshold of this material. In Fig. 9 we moved the target parallel to direction of applied field. The ripples were formed by multiple shots in the neighborhood of previously formed ripples. We have observed ripple spacings at near λ_0 and λ_0/n on the front surface of ZnSe with direction perpendicular to laser electric field. Similar damaged sites on the exit surface of ZnSe were also produced [Fig. 10]. The resulting ripples on the rear surface are in the "wrong" direction, i.e., parallel to the applied optical field and have spacing of $2\lambda_0/(n+1)$. The appearance of the surfaces of ZnS and ZnSe as viewed by a Nomarski microscope suggest that the process of growth and formation of ripples is quite different from that which produced the ripple in the dielectric materials. The geometry of the peaks and valleys of the ripples, and the general appearance of the ripples on these semiconductors are clearly different than that observed in the dielectrics. The periodicity of patterns are disturbed in some regions of the irradiated site and finer structure is superimposed on the main pattern.

4. Summary

We have presented results of a study of laser induced ripple formation at 10.6 μm on dielec-

trics of various index of refraction (SrF_2, BaF_2, KCl, NaCl, KBr) and intermediate band gap semiconductors (ZnS, ZnSe). Ripple patterns with spacing of λ_0/n were formed on the exit surfaces of the dielectric materials perpendicular to direction of applied field. We observed λ_0 spaced ripples on front surface and ripple patterns with spacing of approximately λ_0/n on exit surface of ZnS. We found ripple spacings of approximately λ_0 and λ_0/n on the front surface of ZnSe. These ripples occurred perpendicular to the laser electric field at both surfaces of ZnS and ZnSe. However, on the exit surface of ZnSe we observed periodic structure with "wrong" orientation (ripples parallel to the applied electric field) having spacing of $2\lambda_0/(n+1)$. Furthermore, we observed wrong direction, variably spaced ripples on the exit surface of ZnS and ZnSe. All these observations taken together cannot be completely described by existing models in the literature so far.

---

5. References

[1] P. A. Temple and M. J. Soileau, Nat. Bureau of Standards, Boulder, Colorado, Rep. 462, pp. 371-378, 1976.

[2] P. A. Temple and M. J. Soileau, IEEE J. Quantum Electronics, Vol. QE-17, No. 10, 1981.

[3] M. J. Soileau and E. W. Van Stryland, Nat. Bureau of Standards, Boulder, Colorado, Rep. 669, pp. 406-414, 1982.

[4] M. J. Soileau and E. W. Van Stryland, J. Opt. Soc. Amer., Vol. 72, p. 1756, 1982.

[5] M. J. Soileau, IEEE J. Quantum Electronics, Vol. QE-20, No. 5, pp. 464-467, 1984.

[6] M. J. Soileau, J. M. Bennett, J. O. Porteus, W. Faith, J. Jernigan, and T. T. Saito, Nat. Bureau of Standards, Boulder, Colorado, Rep. 462, pp. 149-157, 1976.

[7] M. Bass, K. M. Leung, C. Tang, and M. J. Soileau, Nat. Bureau of Standards, Boulder, Colorado, Rep. 462, pp. 136-144, 1976.

[8] M. J. Soileau, J. O. Porteus, and D. L. Decker, Appl. Opt., Vol. 19, pp. 3043-3044, 1980.

[9] F. Keilmann and Y. H. Bai, Appl. Phys. A, Vol. 28, pp. 1-10, 1982.

[10] C. T. Walters, Appl. Phys. Lett., Vol. 25, pp. 696-698, 1974.

[11] M. Siegrist, G. Kaech, and F. K. Kneubuhl, Appl. Phys., Vol. 2, pp. 45-46, 1973.

[12] M. Birnbaum, J. Appl. Phys., Vol. 36, pp. 3688-3689,

[13] D. C. Emmony, R. P. Howson, and L. J. Willis, Appl. Phys. Lett., Vol. 23, pp. 598-600, 1973.

[14] G. N. Maracus, G. L. Harris, C. A. Lo, and R. A. McFarlane, Appl. Phys. Lett., Vol. 33, pp. 453-455, 1978.

[15] H. J. Leamy, G. A. Rozzonyi, T. T. Sheng, and G. K. Celler, Appl. Phys. Lett., Vol. 32, pp. 535-537, 1978.

[16] M. Oron and G. Sorensen, Appl. Phys. Lett., Vol. 35, pp. 782-784, 1979.

[17] P. M. Fauchet and A. E. Siegman, Appl. Phys. Lett., Vol. 40, pp. 824-826, 1982.

[18] J. F. Young, J. E. Sipe, J. S. Preston, and H. M. van Driel, Appl. Phys. Lett., Vol. 41, pp. 261-264, 1981.

[19] J. F. Young, J. E. Sipe, and H. M. van Driel, Phys. Rev. B, Vol. 30, pp. 2001-2015, 1984.

[20] J. F. Fiqueria and S. J. Thomas, Appl. Phys. B, Vol. 28, p. 267, 1982.

[21] N. Tsakada, S. Sugata, and Y. Mita, Appl. Phys. Lett., Vol. 42, pp. 424-426, 1983.

[22] J. F. Young, J. S. Preston, H. M. van Driel, and J. E. Sipe, Phys. Rev. B, Vol. 27, pp. 1155-1172, 1983.

[23] M. A. Cutter, P. Y. Key, and V. I. Little, Appl. Opt., Vol. 13, pp. 1399-1404, 1974.

[24] J. C. Koo and R. E. Dusker, Appl. Phys. Lett., Vol. 28, pp. 614-616, 1976.

[25] N. R. Isenor, Appl. Phys. Lett., Vol. 31, pp. 148-150, 1977.

[26] R. K. Jain, V. N. Kulkarmi, D. K. Lood, and J. S. Uppal, J. Appl. Phys., Vol. 52, pp. 4882-4884, 1981.

[27] S. J. Thomas, R. F. Harrison, and J. F. Figueira, Appl. Phys. Lett., Vol. 40, pp. 200-202, 1982.

[28] S. R. J. Brueck and D. J. Ehrlich, Phys. Rev. Lett., Vol. 48, pp. 1678-1681, 1982.

[29] H. M. van Driel, Laser Focus, Vol. 19, p. 12, 1983.

[30] J. E. Sipe, J. F. Young, J. S. Preston, and H. M. van Driel, Phys. Rev. B, Vol. 27, pp. 1141-1154, 1983.

[31] Z. Guosheng, P. M. Fauchet, and A. E. Siegman, Phys. Rev. B, Vol. 26, pp. 5366-5381, 1982.

[32] R. Ritchie, Surface Sci., Vol. 34, pp. 1-19, 1973.

Material	Index of Refraction n	λ_o/n (um)	Ripple Spacing on Back Surface (um)	Ripple Spacing on Front Surface (um)
SrF_2	1.36	7.79	*$7.76^+_-0.13$	
BaF_2	1.39	7.62	$7.60^+_-0.08$	
KCl	1.45	7.31	$6.98^+_-0.06$	
NaCl	1.49	7.11	*$7.09^+_-0.06$	
KBr	1.52	6.95	*$6.77^+_-0.14$	
ZnS	2.20	4.82	$5.22^+_-0.28$	$9.52^+_-0.46$
ZnSe	2.40	4.42	**$6.24^+_-0.1$ **$7.73^+_-0.1$ **$9.29^+_-0.1$	$4.27^+_-0.30$ $9.50^+_-0.39$

* Checked by diffraction pattern measurements.

**Ripples not perpendicular to the incident field.

Note that $2\lambda_o/(n+1) = 6.24$ um

Table 1.
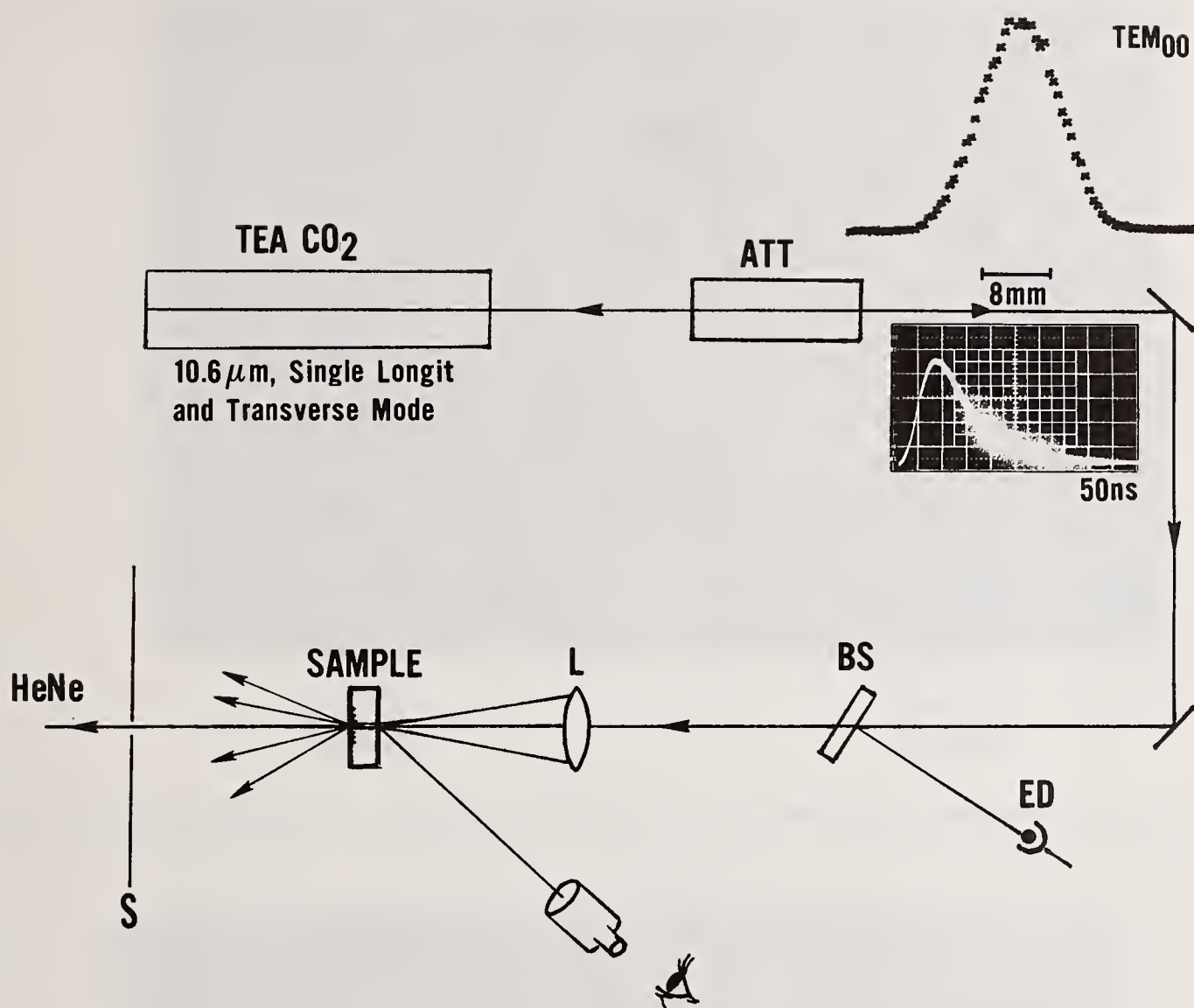
Figure 1. Experiment.
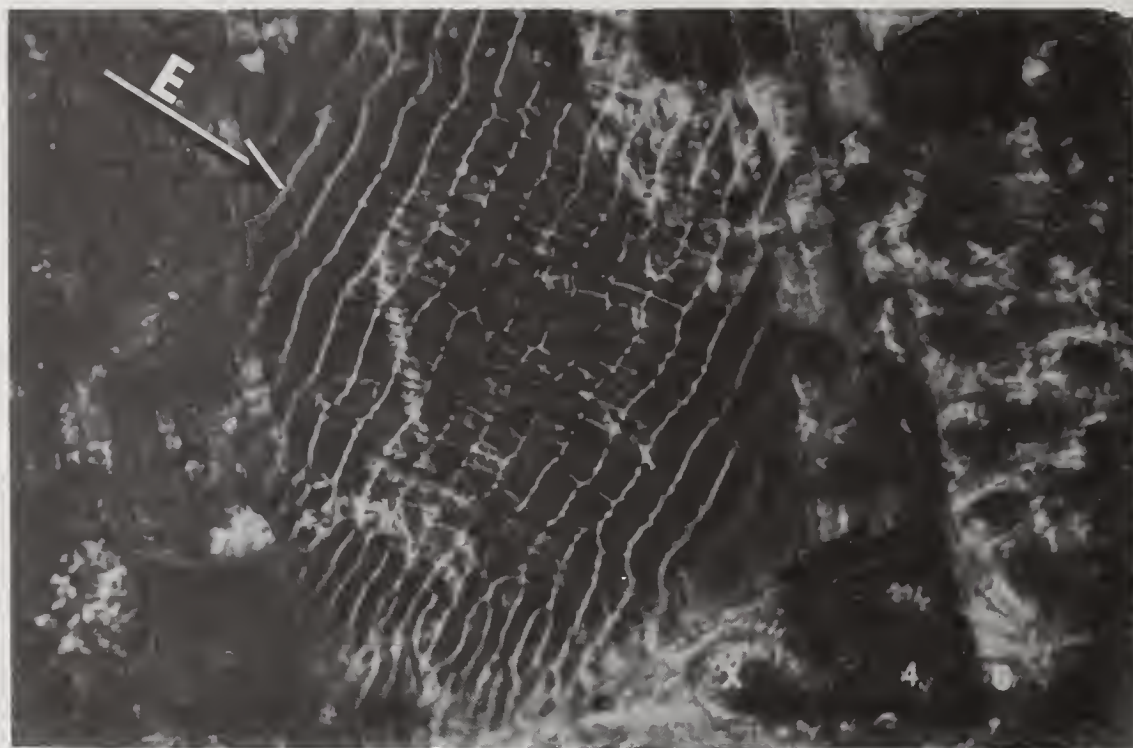
Figure 2.   Laser generated ripple patterns on the exit surface of SrF_2 at 10.6 μm.   The arrow
shows the direction of the applied optical field.   The ripple spacing is
7.76 ± .13 μm.   Note that λ_0/n=7.79 μm.
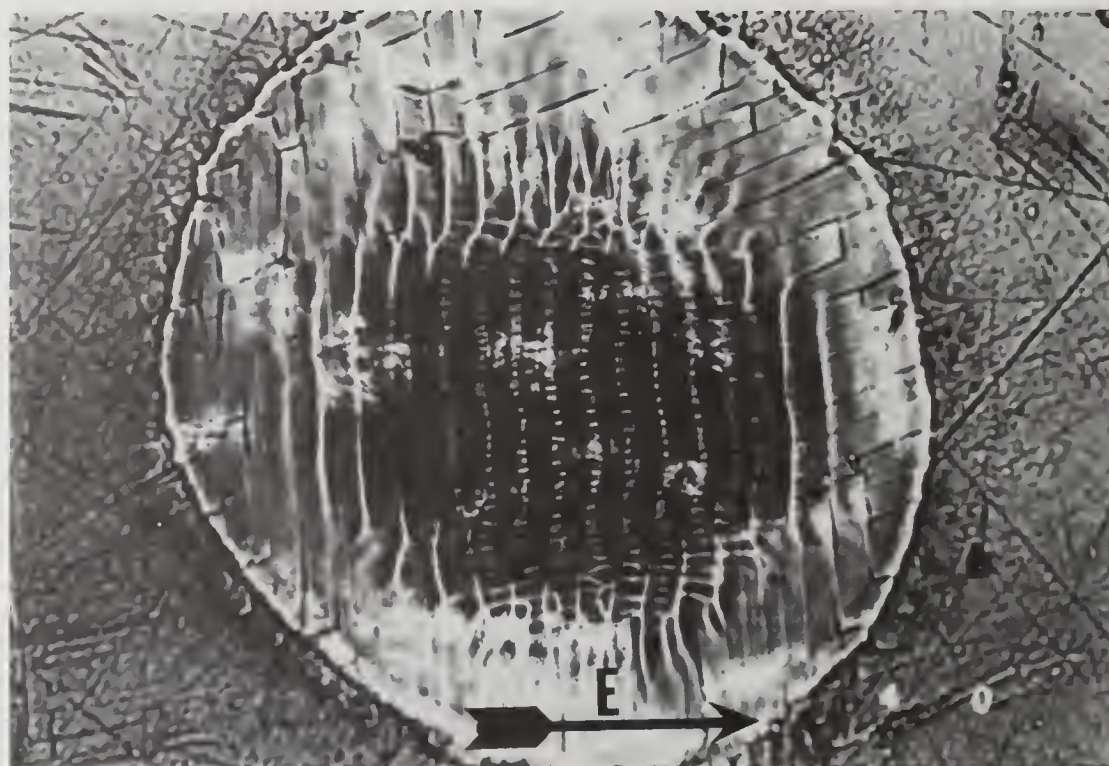
Figure 3.   Laser generated ripple patterns on exit surface of BaF_2 at 10.6 μm.   The laser was
linearly polarized in the direction indicated by the arrow.   The ripple spacing is
7.60 ± .08 μm.   Note that λ_0/n=7.62 μm.
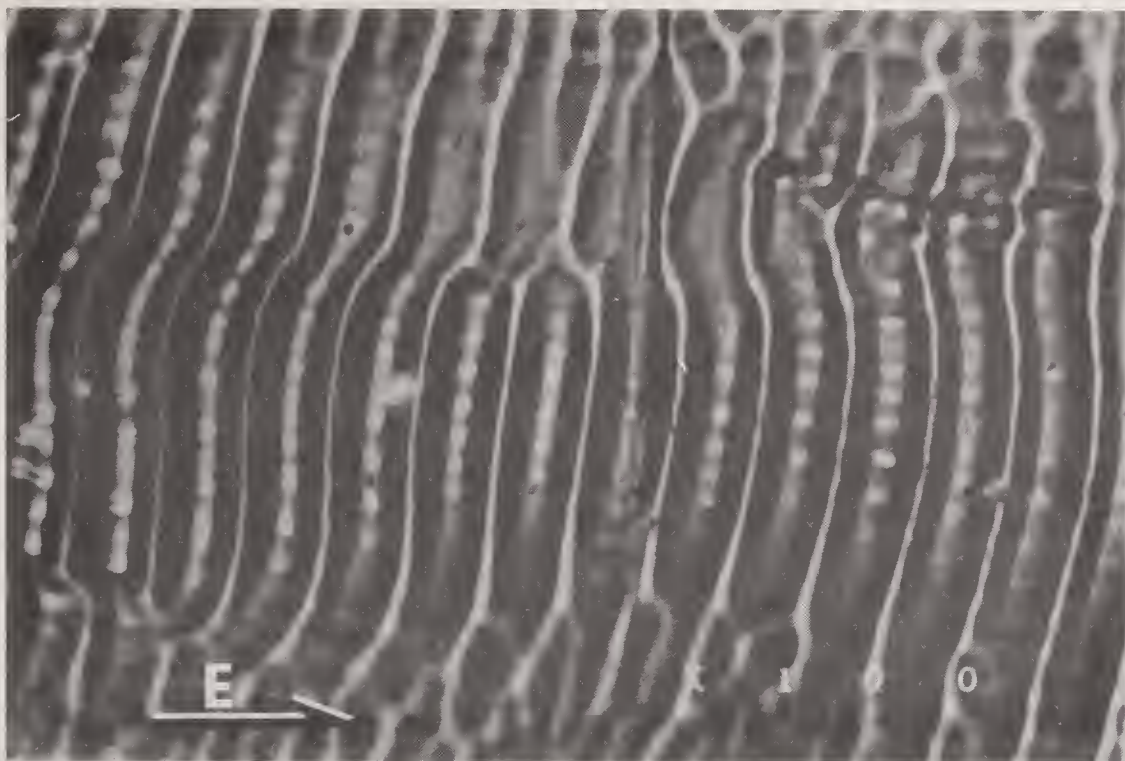
Figure 4.   Laser generated ripple patterns on the exit surface of KCl at 10.6 μm.   The arrow shows the direction of applied electric field.   The ripple spacing is 6.98 ± .06 μm.
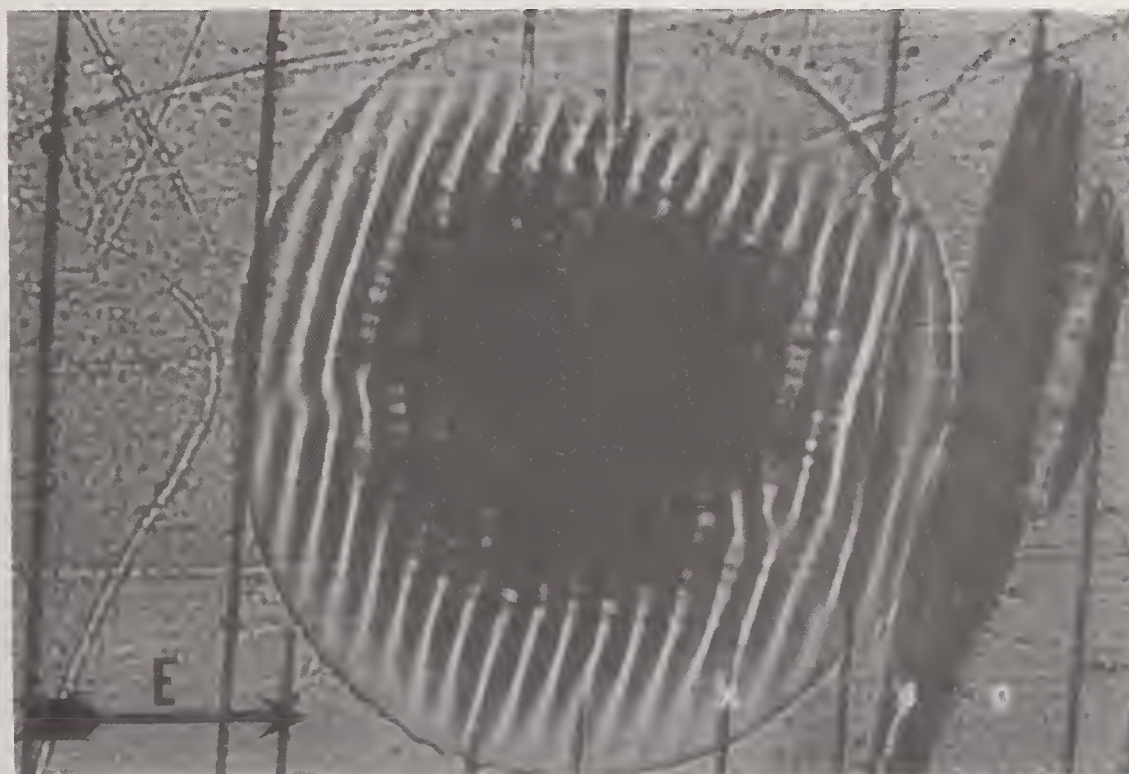
Figure 5.   Laser generated ripple patterns on exit surface of NaCl at 10.6 μm.   Note that ripples formed parallel to existing scratch on the surface.   The ripple spacing is 7.09 ± .06 μm and $\lambda_0/n = 7.11$ μm.

143
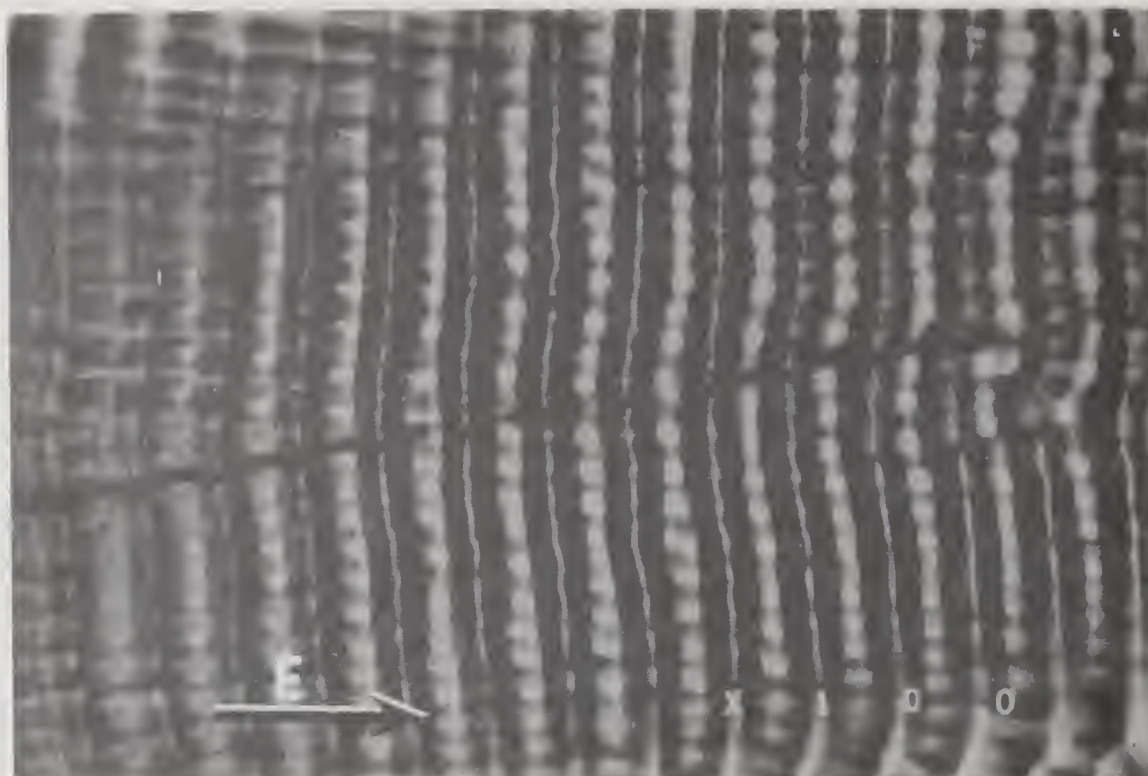
Figure 6. Laser generated ripple patterns on the exit surface of KBr at 10.6 μm. The arrow shows the direction of the applied optical field. The ripple spacing is 6.77 ± .14 μm.
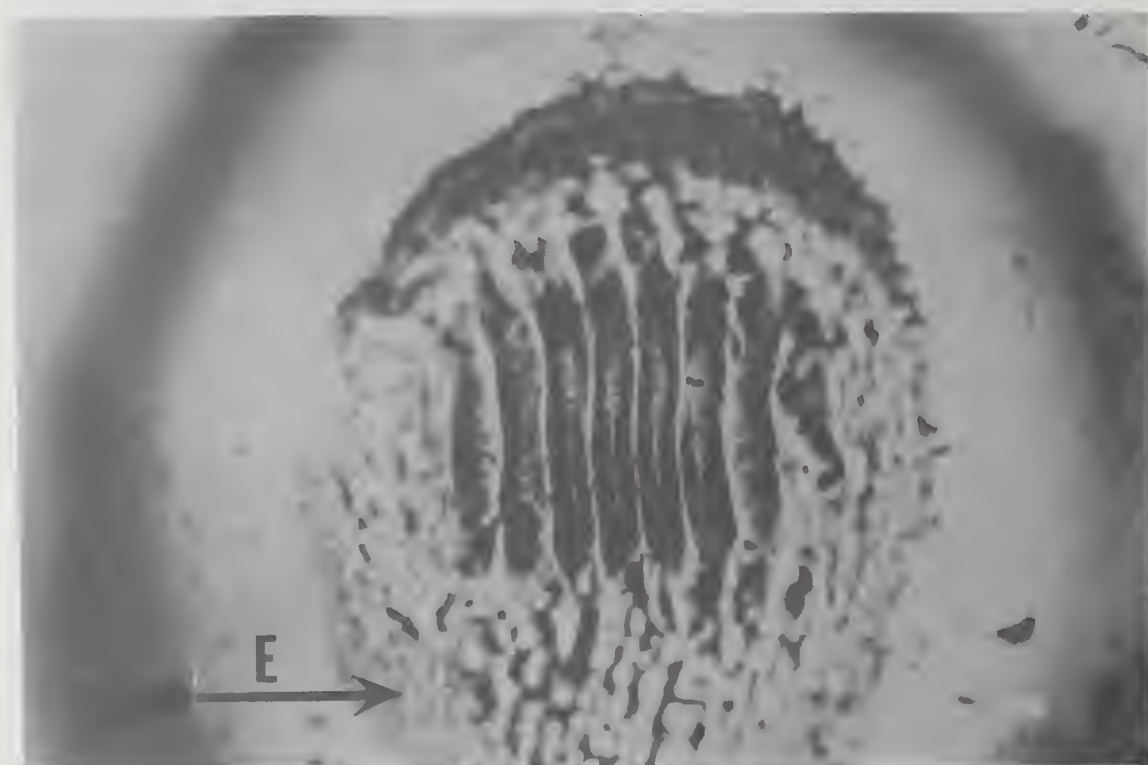
Figure 7. Laser generated ripple patterns on front surface of ZnS at 10.6 μm. The arrow shows the direction of the applied optical field. The ripple spacing is 9.52 ± .46 μm.

Figure 8.   Laser generated ripple patterns on front surface of ZnSe at 10.6 μm.   The ripple spacing is 9.50 ± .39 μm.
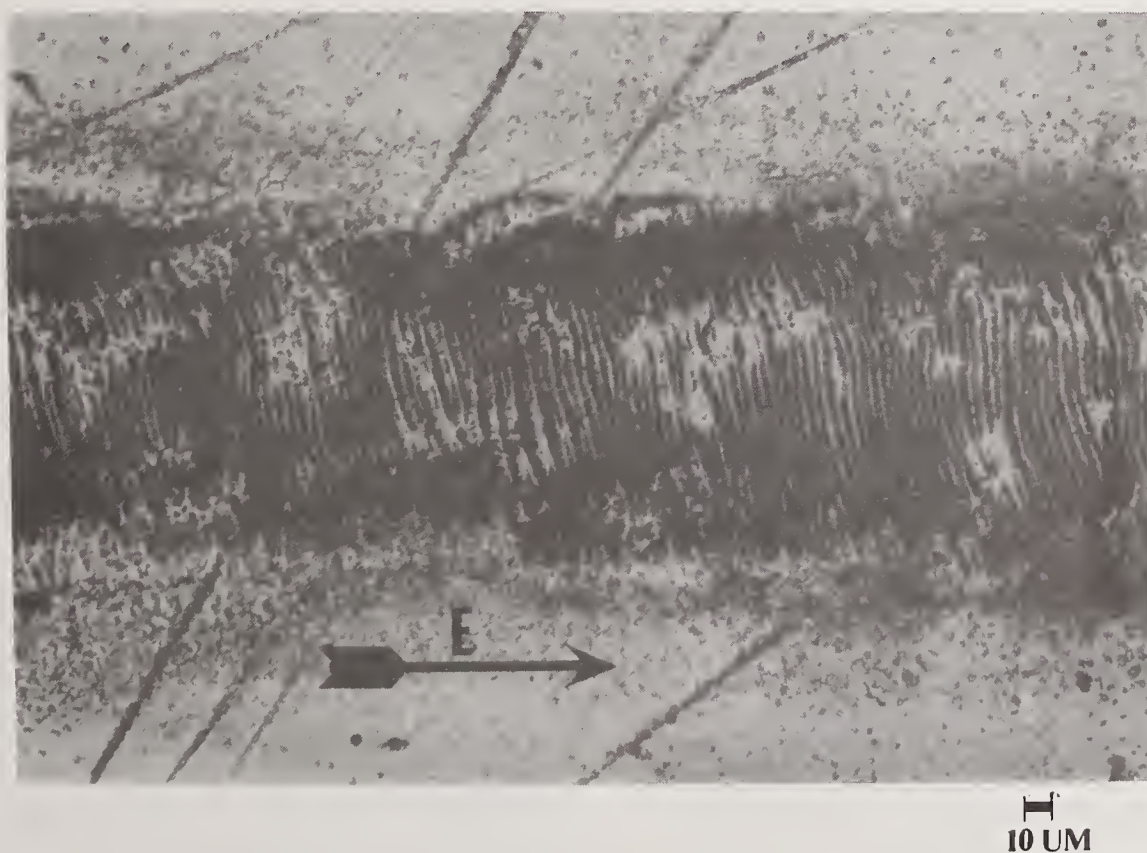
Figure 9.   Laser generated ripple patterns on the front surface of ZnSe at 10.6 μm.   The ripple spacing is 4.27 ± .30 μm.
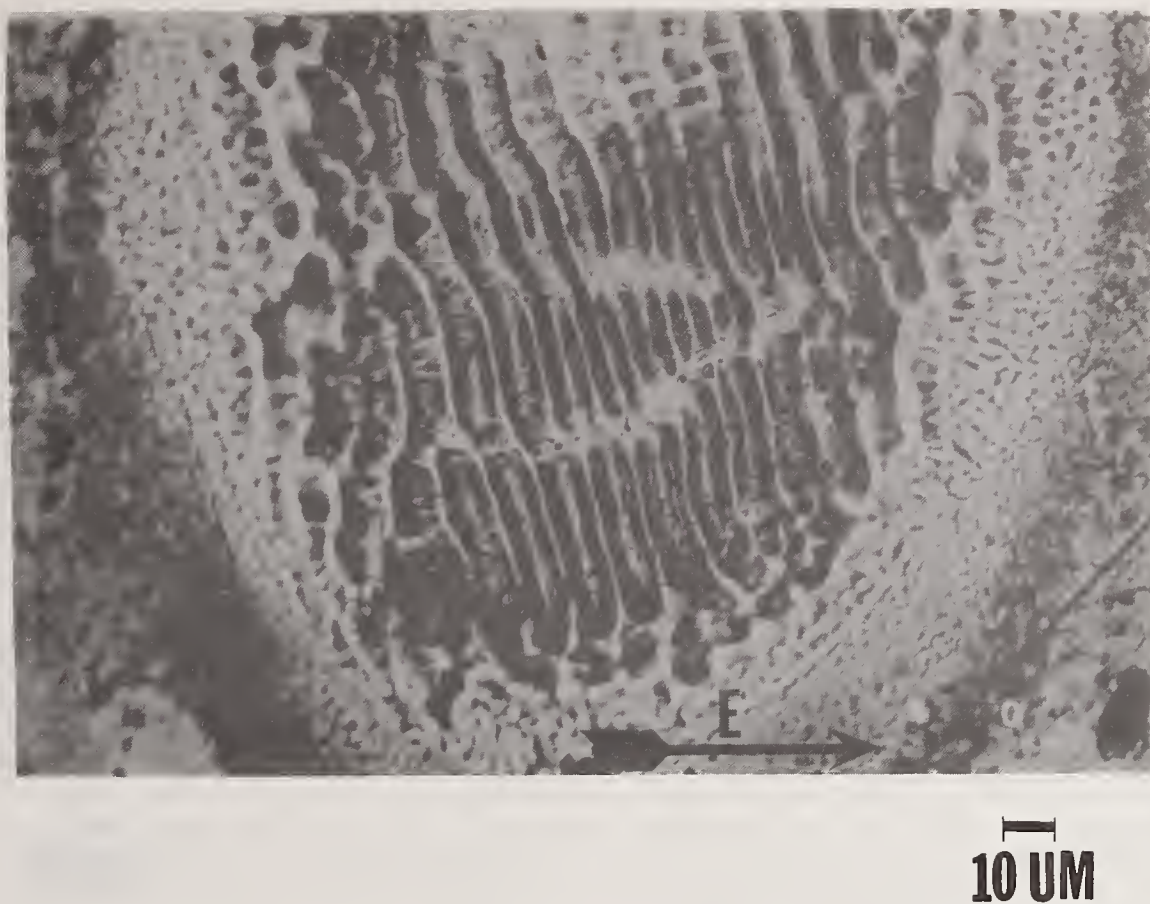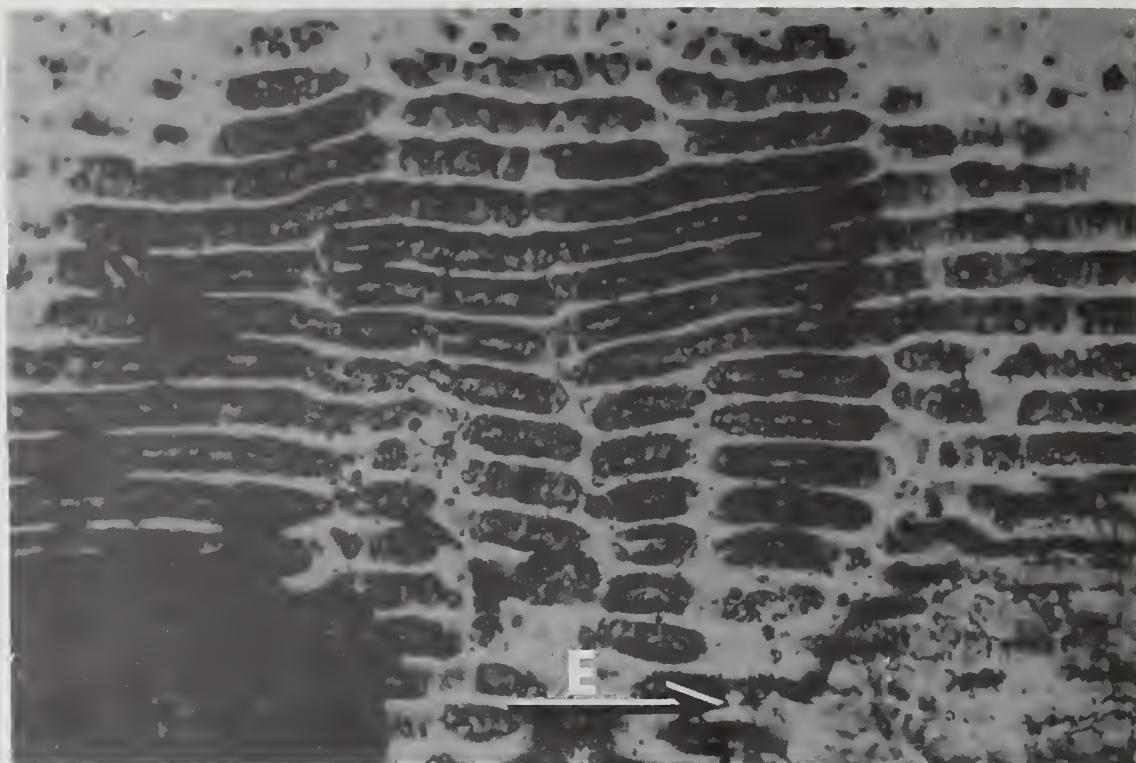
Figure 10. Laser generated ripple pattern on the exit surface of ZnSe at 10.6 μm. The ripple formed is the "wrong" direction, i.e., ripple parallel to the applied optical field as indicated in the above micrograph.

Surface Damage Mechanisms in Nontransparent Media

P.M. Fauchet* and A.E. Siegman[†]

*Department of Electrical Engineering and Computer Science, Princeton University
[†]Edward L. Ginzton Laboratory, Stanford University

Abstract

We review our experimental and theoretical work on surface transformations produced on amorphous and crystalline semiconductors and metals by single or multiple ultrashort laser pulses. In addition to melting and vaporization, two phenomena have attracted our attention: the formation of surface ripples and transformations due to repetitive subthreshold illumination.

A detailed theoretical model that explains successfully the formation and the major properties of the surface ripples has been developed and we illustrate the agreement by many examples. However, we also present experimental results which suggest that to describe the interaction between the incident beam and the surface diffracted waves, a perturbative approach is not always sufficient. A phenomenological explanation is presented for these non-standard ripples.

Repetitive subthreshold illumination can produce the same surface transformations as single pulse illumination above threshold. We present universal growth curves and determine a safe level for multiple shot exposure in various materials. Our results are compared to several models, including accumulation of plastic deformation, creation of microcrystallites, and the early stages of ripple formation.

1. Introduction

We have performed our experimental work exclusively in nontransparent media. Although transparent media are often of more interest to the high power laser community, experimental results obtained on semiconductors or metals can be compared to theory and, at least for single shot experiments, the agreement is quite good. The reason for this is that the index of refraction n has an intrinsic nonzero imaginary component ($n = n + jk$). The intrinsic absorption coefficient $\alpha = \dfrac{4\pi}{\lambda} k$ is therefore finite and the penetration depth $\delta = 1/\alpha$ is small. In most of the experiments reported here, $\delta \simeq 1\,\mu$m, but in principle δ may vary from ~ 1 mm (photon energy at the bandgap) to $\sim 100\text{Å}$ (for metals).

In semiconductors, $n \sim 3\text{-}4$ and the reflection coefficient $R = \left| n - 1/n + 1 \right|^2 \simeq 0.3$; while for most metals, $R > 0.9$. Thus, defects or impurities may play a significant role in laser-induced damage of metallic surface, by locally increasing the absorptance $A = 1 - R$. Semiconductors on the other hand are "perfect" materials. First, they can be made very pure and defect-free. Second, their intrinsic absorptance is quite large and not likely to be altered by any remaining imperfections. We can also predict that intrinsic thermal effects are likely to be important.

Our experiments were performed on amorphous (a-) or crystalline (c-) Si, Ge, GaAs and Cu in bulk or thin film form. The laser pulses were provided by modelocked Nd:YAG laser systems ($\lambda = 1.06\,\mu$m or 532 nm) or by a Q-switched Nd:YAG laser ($\lambda = 1.06\,\mu$m).

2. Single Pulse Damage

2.1 Melting and Vaporization

The simplest form of damage is melting or vaporization. It has been known for years that intense laser pulses can melt and/or vaporize semiconductors. In some cases (e.g., laser annealing of disordered layers), the laser action is beneficial. Picosecond laser pulses have now been shown to produce similar transformations. In fact, picosecond laser-induced transformations include crystalline to amorphous, amorphous to crystalline and crystalline to crystalline (through a molten period) transitions [1].

A reliable theoretical description of these phenomena is now available. Models have been developed to account for the temporal and spatial evolution of the lattice temperature and the electron temperature and density. For example, the melting threshold, the electron temperature (that may be much greater than 2000°K) and carrier density (that may exceed $10^{21}/\text{cm}^3$) predicted by theory agrees with the experimental observations [2]. In fact, we have been able to use this successful theory to predict some electronic properties of highly excited disordered semiconductors [3].

The experimental set-up is described in figure 1. A delay is introduced between two synchronized picosecond pulses. The visible pulse (532 nm) creates a dense ($> 10^{20}/\text{cm}^3$) electron-hole plasma at the surface of the semiconductor. This plasma then absorbs the infrared pulse (1.06 μm) by free carrier absorption (FCA). In the absence of visible pulse, its intrinsic absorption of the sample in very low ($\hbar\omega \sim E_{\text{gap}}$ for Si, two-photon absorption for GaAs). In the presence of the plasma, the coupling of the infrared pulse to the solid is greatly enhanced. The plasma, heated by the infrared light cools down in a few picoseconds, thus transferring energy to the lattice in the form of phonons. Figure 2 shows some computer simulations for a-Si. For negative delays (infrared before visible), heating occurs through the intrinsic absorption; for small positive delays, FCA dominates; for larger delays, the plasma density has decreased when the infrared pulse arrives, thereby decreasing its coupling. Note that the

electron-hole plasma density is maximum for the largest temperature rise: this is attributed to the increase of α with temperature.

We have applied this idea to disordered Si and GaAs (as well as c-Si). Some of our results are shown in figure 3. They are in good qualitative agreement with the model outlined above. In fact, a quantitative agreement can be obtained for small delays if one assumes a 0.1 ps relaxation time for hot electrons, a 10 ps recombination time and a cross-section for free carrier absorption equal to $10^{-17}(T/300)\text{cm}^2$. A more complete discussion of these and other results can be found elsewhere [4]. We want to stress here that it is possible to have a very good description of single-shot melting of semiconductors.

2.2 Surface Ripples

Another common damage mechanism involves the formation of ordered surface structures, commonly called surface ripples [5]. In this section, we concentrate on standard ripples produced by single-shot illumination.

It is now well known that relatively intense c.w. or pulsed laser beams can produce ordered surface structures on most materials. Although such laser-induced surface ripples had been observed for fifteen years, activity in the field started to peak up in the early 80's, when various groups published a detailed theoretical modelling of the electromagnetic interactions that lead to ripple's formation. We now describe and compare briefly the main features of some models and list their successes.

Experimentally, surface ripples are produced during laser damage, laser annealing, laser-assisted deposition or etching, etc. They almost always appear close to the melting or damage threshold and they appear in all materials illuminated with light pulses at various wavelengths (from 10 μm to the U.V.) and of various durations (from ps to c.w.).

In all existing models, ripples result from interference between the incident beam and surface waves. Although it is believed that minute surface irregularities (of dimensions smaller than λ) are necessary for the production of the surface waves, there is a controversy on the exact nature of these waves. Among the candidates are surface polaritons [6] and radiation remnants [7]. In our theoretical work [8], we have described the interaction of the incident beam with surface diffracted waves on a corrugated surface (with a sinusoidal profile) or on a flat surface (where the dielectric function ϵ has a periodic sinusoidal variation).

The nature of the surface wave is revealed by applying the appropriate boundary conditions. After solving Maxwell's equations by first-order perturbation theory, we predict ripples with a periodicity identical to that given by the surface polariton model, if $\text{Re}(\epsilon) = \epsilon_R$ is negative [1]. For $\epsilon_R > 0$, however, we find that ripples can grow with a spacing Λ well described by $\lambda = \Lambda/n(1 \pm \sin\nu)$, where n is the refractive index of the incident medium ($= 1$ if air or vacuum) and ν is the angle of incidence. The ripple growth coefficient is then smaller than for metallic-like surfaces [1].

In all models, first-order perturbation theory describes the interaction (e.g., $h/\Lambda \ll 1$, where h is the height of the corrugation) and the properties of the substrate (e.g.,

crystalline orientation) play an insignificant role. Furthermore, theory has not combined the periodic variation of ϵ during illumination with the effect of surface corrugation. This periodic variation of ϵ is especially striking in the formation of aligned, coexisting liquid and solid lamellae during c.w. illumination [9]. Recently, permanent variations of ϵ have also been observed after U.V. illumination of metal films [10].

Thus, although we do not have a complete theoretical description for the creation of surface ripples with single-shot illumination, we find a rather good agreement between theory and experiments.

3. Multipulse Damage

3.1 Above Threshold

Repeated illumination with identical pulses of intensity above single pulse threshold leads to fascinating but poorly understood nonlinear surface electromagnetic interactions. What is observed is the formation of non-standard ripples, which cannot readily be explained by any model. Although several recent reports are concerned with such ripples, we concentrate on our results.

During a multipulse sequence, the amplitude of the surface corrugation increases (probably due to repeated localized vaporization), so that the ripple's depth h becomes a fraction of its period Λ. Once the aspect ratio ($= h/\Lambda$) of standard ripples becomes comparable to unity, additional illumination may lead to the formation of perpendicular ripples (running at 90° to the standard ripples). Figure 4 shows typical results after repeated illumination of Ge above threshold for ripple formation. Here, the periodicity appears equal for the two types of ripples and the surface looks like a checkerboard. Often, the two spacings are different [12]. In some cases, instead of a regular pattern, we have observed [5] perpendicular stripes with a periodicity that is not very sharp and appears to vary with the intensity. Figure 5 shows such ripples on GaAs. In another experiment, we have observed [11] that repeated pulsed illumination of <111> Ge by normal-incident, circularly-polarized 1.06 μm light produced hexagonal patterns, reminiscent of the crystal orientation, as shown in Figure 6. Note that similar nonstandard ripples have been observed by others [13].

It is quite clear that existing theories must fail for large aspect ratios. Our calculations indicate that the modulation of absorbed power due to surface corrugation reaches 100% before $h/\Lambda = 1$. Then regions where the power flow is maximum alternate with regions where the power flow is zero. Consequently, interactions between different surface diffracted waves has to be considered. Furthermore, the dielectric function is also expected to vary strongly. Theory will break down where the magnitude of the surface wave becomes comparable to that of the incident beam as in the case of illumination of a surface having deep ripples. Since we have shown that the ripple's growth coefficient is larger for metallic-like surfaces ($\epsilon_R < 0$), nonstandard ripples will also be produced more easily during U.V. laser-assisted growth of metal films. We have not developed our model beyond first-order perturbation theory, but we have recently considered various mechanisms and attempted a phenomenological description

of the surface interactions [14]. For example, we have been able to recover the observed diffraction pattern of the surface illuminated by a visible probe beam by considering appropriate mixing among various surface diffracted waves. This approach unfortunately does not give us much insight in the nature of the surface interactions. New surface waves can exist at a nonlinear interface [15]. As we discuss elsewhere [14], it is plausible that by considering the complete nonlinear, inhomogeneous dielectric function of the solid surface, we can predict the observed nonstandard ripples. However, this problem is very difficult and it is not at all certain that a satisfactory solution can be reached.

We thus see a first example for the failure of single-pulse models when we try to use them to explain multipulse effects.

3.2 Below Threshold

It is well known that repeated pulsed laser illumination of solids with identical pulses of intensity below single pulse threshold may eventually produce irreversible transformations including pitting, melting and cracking. Experiments have now been performed on insulators, semiconductors and metals, with very similar results. We review our experimental finding and then discuss the various models that have been proposed.

For these experiments, we have used an actively modelocked, repetitively Q-switched Nd:YAG laser. Prelasing improved the energy stability. Histograms of the pulse energy were obtained after selection of a single pulse. Approximately 95% of the shots have an energy within 7% of the mean energy; the remaining 5% have lower energy and correspond to mistriggering of the Pockels cell. The transverse beam profile is checked with a standard Reticon array and the spot size is known accurately by varying the beam energy and recording the damaged spot size. Figure 7 shows how the spot size and the single-shot threshold can be simultaneously measured. In all cases, the samples were simply cleaned and held at room temperature in air. To determine the onset of damage in a multipulse sequence, we used optical microscopy (Nomarski), scanning electron microscopy, and, occasionally, the probe beam scatter technique or electrical measurements. Nomarski microscopy proved to be the most reliable method.

Figure 8 illustrates some typical results [16]. We plot the damaged or transformed area (as measured by optical microscopy) versus number of laser shots. The single-shot threshold is $\sim$ 2.2 GW/cm^2 for c-Si illuminated with 80 ps pulses at 532 nm. Repeated illumination with pulses having one-third of this intensity produces visible damage after $\sim$ 300 pulses. Repeated illumination with pulses having one-fifth of the single-shot threshold intensity produces no visible damage even after 6000 shots. The optical fatigue of the material is also clearly illustrated by the inset of figure 8. The threshold for damage deduced from these curves decreases with increasing number of pulses and appears to tend asymptotically towards a safe level.

This particular experiment was performed at 100 Hz repetition rate. However, we find no repetition rate dependence of these curves within the experimental uncertainty of the measurement [16]. To further illustrate this, we plot in figure 9, the reduction of the damage threshold of ion-implanted GaAs with increasing number of shots. These data represent an average of seven runs at three different repetition rates (5, 10, and 40 Hz). We note that these curves are in qualitative agreement with those obtained on other materials by other workers [17,18].

In addition, we note that our results are deterministic: two multipulse sequences lead to similar optical fatigue curves. We observe no striking spot size dependence, although the limited output energy of our laser did not allow us to vary this parameter over a wide range. Finally, for crystalline materials, we usually find that the safe level for multipulse exposure was limited to one-third of the single pulse threshold; while in amorphous materials, the safe level could become as low as one-tenth of the single pulse threshold.

In the light of these remarks, we have rejected the hypothesis of a slow temperature increase of the surface during the sequence. Two hypotheses are not inconsistent with our findings.

Musal has proposed that cumulative plastic deformations produced by repeated thermal cycling can explain the eventual failure of Cu mirrors under repeated illumination [19]. The small amount of light absorbed by the metal target produces a temperature increase and thus strain near the surface. If the resulting stress exceeds the yield stress of the metal, plastic strain occurs. This plastic strain accumulates during each thermal cycle (heating due to the laser followed by cooling due to thermal diffusivity), leading to slip bands in Cu. Once the surface becomes rough, absorption increases and a thermal runaway eventually occurs. Musal has obtained analytical expressions for uniform irradiation assuming a linear elastic/perfectly plastic stress-strain diagram for Cu. Bass and coworkers have refined the analysis, including the finite laser beam spot size [20]. Various observations, including those by Bass et al., seem to support this interpretation. No attempt has been made so far to adapt this model to nonmetals, especially semiconductors, which usually absorb at the wavelength of interest. At low substrate temperature (e.g., 300 °K) crystalline silicon does not yield but rather fractures. At elevated temperature however, tetrahedral semiconductors do yield. Since the coupling of visible or infrared light to semiconductors is at least one order of magnitude larger than to most metals, the maximum temperature rise during each pulse can easily be as large as a few hundred degrees °C. This is very favorable for plastic yield in Si (and other semiconductors) and after suitable refinements Musal's model may be a very good candidate for explaining the damage precursors.

Vitali's experimental results imply the formation and growth of very small microcrystalline regions in an amorphous material during repeated subthreshold illumination [21]. Once several of these microcrystallites are present, the effective recrystallization threshold may be lowered under the action of strong band bending at these sites (enhancing locally the electron-hole plasma density by confinement) or of concentration of stresses and strains at the interface. The effects due to the formation of microcrystallites and to the accumulation of plastic strain will effectively be additive. This is consistent with, but not proven by, our observation that the safe level for multipulse laser-induced transformation is lower in disordered

than in crystalline materials. In Vitali's model, the formation of the first microcrystalline region is somewhat mysterious. It may be due to the inhomogeneity, on a microscopic scale, of disordered materials, or it could come from micro-plastic deformations produced by a local plastic strain.

These two models are also consistent with the production of surface ripples during a multipulse illumination sequence with pulses below melting threshold. Local melting or recrystallization is possible in these models and it would occur preferentially where the power flow is maximum. However, nothing is known of the possible changes that occur prior to damage during the illumination sequence. A variety of probes have been used to detect such changes; they include SEM, TEM, RHEED, particle emission, Kelvin microprobe, calorimetry, electrical measurements, probe beam scatter and optical microscopy. To our knowledge, no correlation between the measurements of these probes and structural changes prior to damage has been obtained. No conclusive evidence in favor of or against these models exists and multipulse effects remain misunderstood.

4. Conclusions

In nontransparent media, we can explain successfully our single-pulse damage results. Multipulse effects however, remain unexplained and mysterious, due to the failure of standard single-pulse models. We have presented experimental and theoretical results for single-pulse effects. The agreement is very good. We then have shown selected multipulse experimental results and we have outlined some models that may help explain our findings.

Acknowledgments

References

1. P.M. Fauchet, Zhou Guosheng and A.E. Siegman, in Laser-Solid Interactions and Transient Thermal Processing of Materials, Narayan et al. editors, North-Holland (1983), pp. 205-210.

2. A. Lietoila and J.F. Gibbons, Appl. Phys. Lett. **40**, 624 (1982).

3. P.M. Fauchet and A.E. Siegman, Appl. Phys. Lett. **43**, 1043 (1983).

4. P.M. Fauchet and A.E. Siegman, "Picosecond dynamics of electron-hole plasmas close to the melting phase transition in silicon and gallium arsenide," to be published in the Proceedings of the International Conference on Lasers '83 (1984); and "Ultrafast spectroscopy of very dense and hot electron hole plasmas in crystalline and amorphized semiconductors," to be published in the Proceedings of the 17th International Conference on the Physics of Semiconductors.

5. P.M. Fauchet and A.E. Siegman, Appl. Phys. Lett. **40**, 824 (1982).

6. S.R.J. Brueck and D.J. Ehrlich, Phys. Rev. Lett. **48**, 1678 (1982).

7. J.E. Sipe, J.F. Young, J.S. Preston and H.M. van Driel, Phys. Rev. B **27**, 1141 (1983).

8. Zhou Guosheng, P.M. Fauchet and A.E. Siegman, Phys. Rev. B **26**, 5366 (1982).

9. R.J. Nemanich, D.K. Biegelsen and W.G. Hawkins, Phys. Rev. B **27**, 7817 (1983).

10. R. Wilson, F.A. Houle and C.R. Jones, Materials Research Society meeting, Symposium B, paper B4.5 (Boston, 1984).

11. P.M. Fauchet and A.E. Siegman, Appl. Phys. A **32**, 135 (1983).

12. R.M. Osgood, Jr. and D.J. Ehrlich, Optics Lett. **7**, 385 (1982).

13. A.M. Prokhorov, V.A. Sychugov, A.V. Tishchenko and A.A. Khakimov, Sov. Tech. Phys. Lett. **9**, 28 (1983).

14. P.M. Fauchet and A.E. Siegman, "Laser-induced surface ripples: what is understood and what is not," to be published in the Proceedings of the 1984 Materials Research Society Meeting Symposium A (1985).

15. W.J. Tomlinson, Optics Lett. **5**, 323 (1980).

16. P.M. Fauchet, Phys. Lett. A **93**, 155 (1983).

17. N. Koumvakalis, C.S. Lee and M. Bass, Opt. Engin. **22**, 419 (1983).

18. D.Y. Sheng, R.M. Walser, M.F. Becker and J.G. Ambrose, Appl. Phys. Lett. **39**, 99 (1981).

19. H.M. Musal, in NBS Special Publication **568**, 1979, pp. 159-173.

20. C.S. Lee, N. Koumvakalis and M. Bass, J. Appl. Phys. **54**, 5727 (1983).

21. G. Vitali, Phys. Lett. **78A**, 387 (1980).
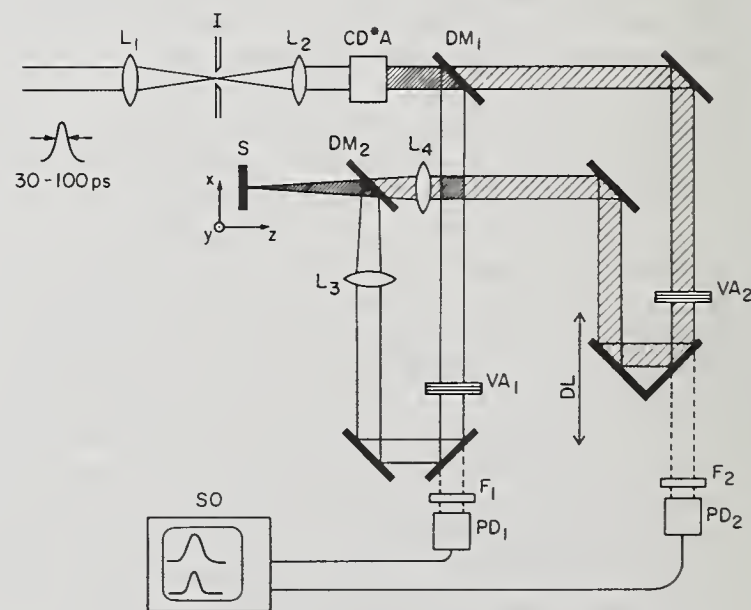
Fig. 1   Experimental set-up for picosecond laser-solid interactions. The 532 nm beam goes into a variable delay line (DL) and the 1064 and 532 nm beams are focussed onto the sample. A storage oscilloscope (SO) monitors the energy in each beam (VA = variable attenuator; F = filter; PD = photodiode).
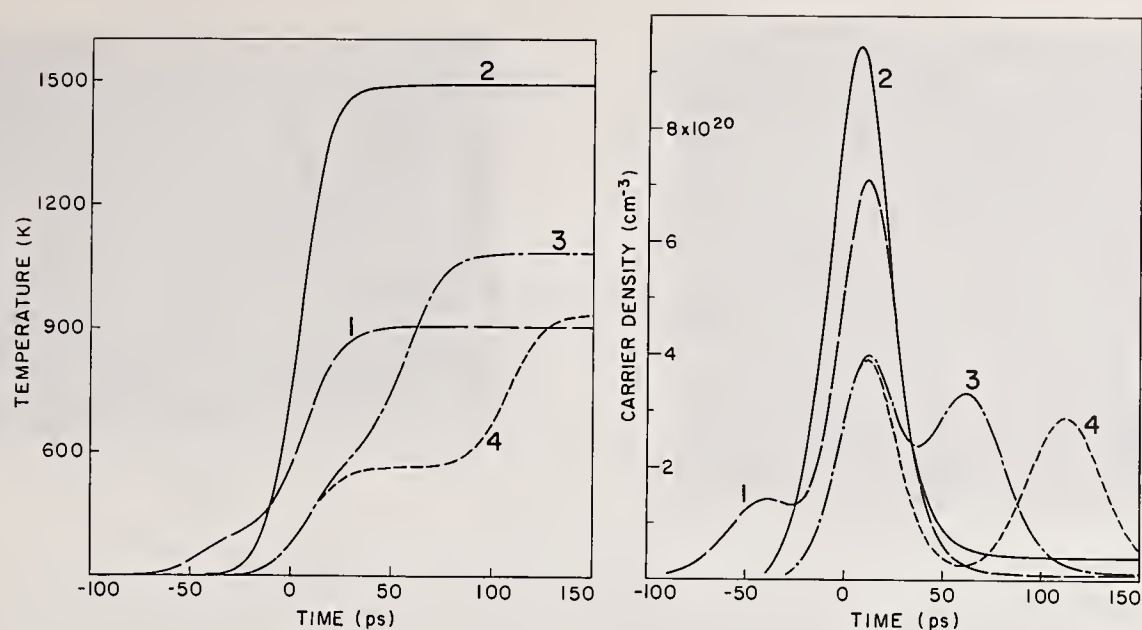
Fig. 2   Computer simulation of the lattice temperature and plasma density as a function of time in amorphized silicon. The time delay of the infrared pulse (0.3 J/cm², 42 ps) with respect to the visible pulse (54 mJ/cm², 30 ps) is -50 ps (1), 0 ps (2), 50 ps (3) and 100 ps (4).
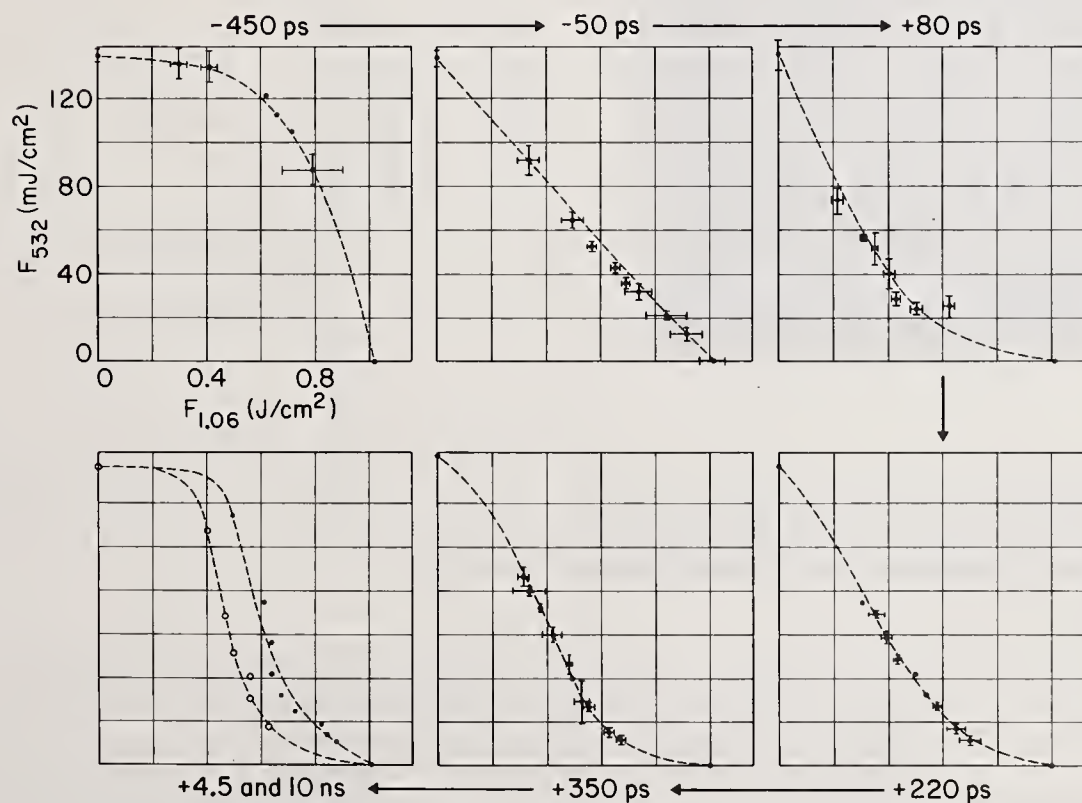
Fig. 3   Combined energy densities just required to melt the surface of a-Si, for various time delays. Further details can be found in references 3 and 4.
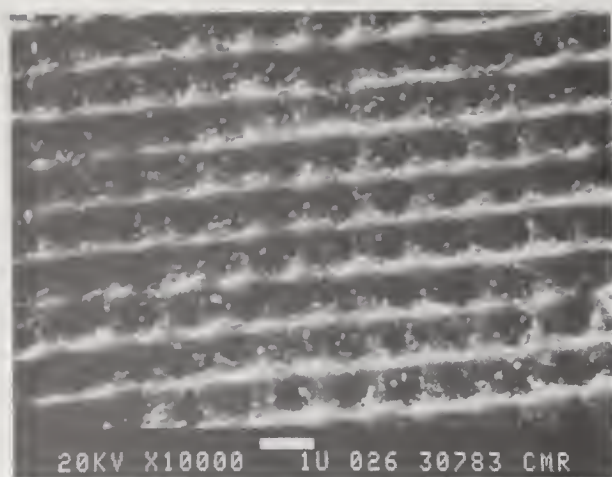
Fig. 4   SEM microphotograph of a Ge surface after repeated illumination above threshold ($\lambda = 1064$ nm). The electric field of the normal-incident beam was perpendicular to the most prominent ripple's direction.
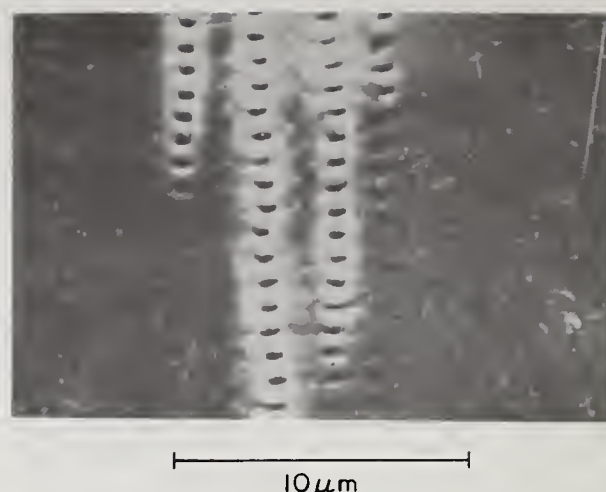
Fig. 5   Microphotograph of GaAs after repeated illumination above threshold ($\lambda = 1064$ nm). The electric field of the normal-incident beam was vertical.
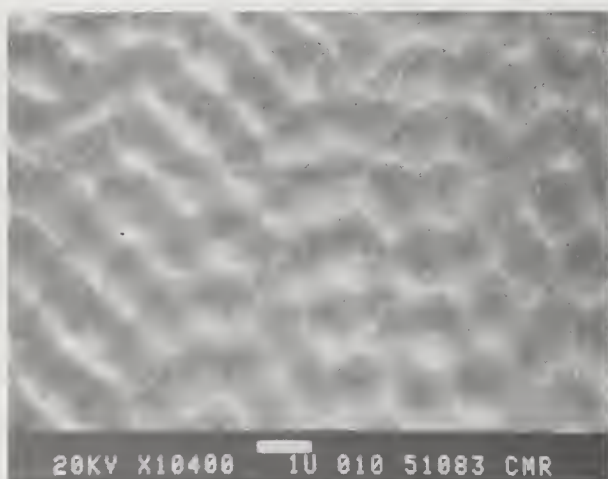
Fig. 6   SEM microphotograph of a $<111>$ Ge surface after repeated illumination above threshold ($\lambda = 1064$ nm) with normal-incident, circularly polarized light.
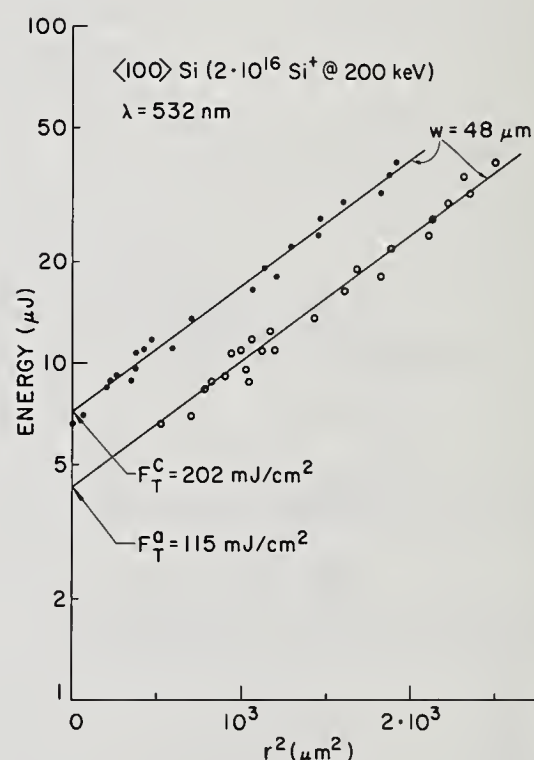
Fig. 7   For a Gaussian beam, $F(r) = (2E/\pi w^2) \exp(-2r^2/w^2)$, where F is the fluence and r is the radius of the melted spot. By varying the energy E and recording r, a simultaneous measurement of the laser spot size (w) and the melting threshold (F_T) is possible. Here, one threshold is for the formation of amorphous material, the other is for crystalline regrowth.

152
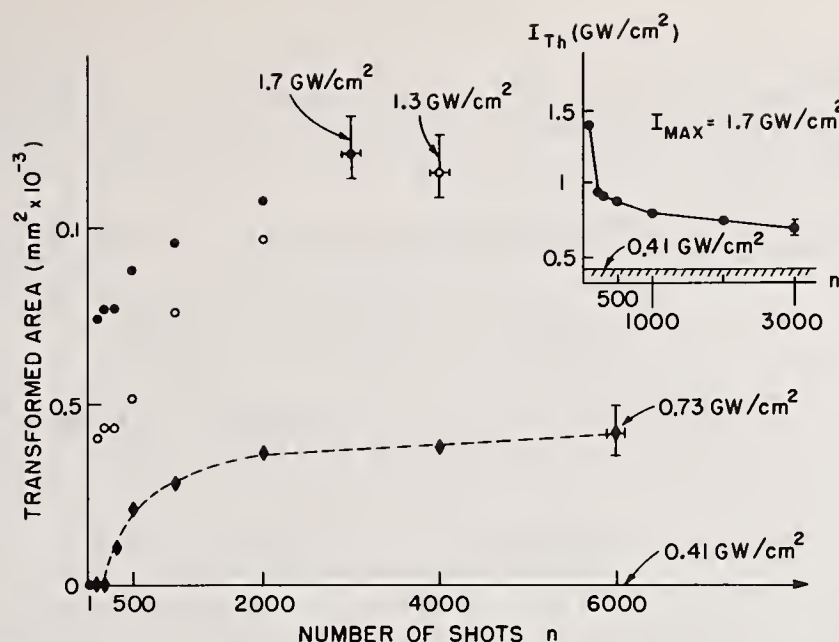
Fig. 8   As the number of identical laser shots increases, damage occurs, which corresponds to a decrease in the damage threshold. For c-Si illuminated with 80 ps pulses at 532 nm, the safe level is $\sim$ 40 mJ/cm^2.
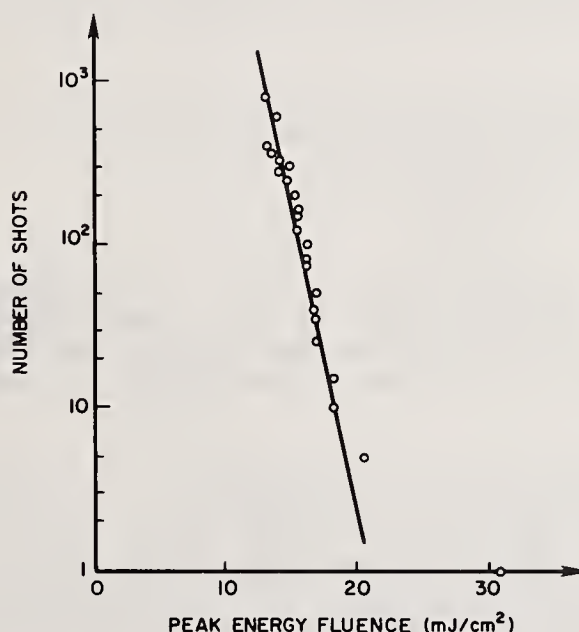
Fig. 9   Results obtained at different repetition rates appear indistinguishable in this experiment performed on a-GaAs. Similar results have been obtained for the other materials under investigation here.

In the sixfold symmetry pattern gotten from the nonlinear mixing case, is there any connection between the sixfold symmetry and the crystal lattice structure of the sample being looked at? The author replied that there was. The direction in which one sees the effect corresponds within 5 deg to one of the crystallographic axes. For surfaces which do not show sixfold symmetry one does not see the correlation. The authors have made no experiments as yet on transparent materials.

153

Picosecond-Pulse Damage Studies of Diffraction Gratings

Dennis H. Gill and Brian E. Newnam

University of California, Los Alamos National Laboratory
Los Alamos, NM 87545

Diffraction gratings are frequently used in dye-laser cavities as wavelength-tuning elements. These gratings often limit the maximum laser output energy because of their low damage thresholds. We have measured the damage characteristics of both ruled and holographically produced gratings, under a variety of conditions. Using the single-shot-per-site mode, the samples were irradiated by 30-ps, 1.064-μm pulses having a spot size of 0.5-mm radius.

It was found that holographic gratings have damage thresholds from 1.5 to 5.0 times higher than similar ruled gratings. Thresholds for S-polarized light (E parallel to grooves) were higher by factors of 1.5 to 6. For the same type grating, gold coatings yielded higher thresholds than aluminum, although this is wavelength dependent. For holographic gratings, replicas have slightly higher thresholds than masters. Dependence upon groove spacing was weak.

Data are presented to show a variety of comparisons between different types of gratings, including two different manufacturers and usage at higher orders of incidence.

Key words: laser-induced damage; holographic gratings; ruled gratings; picosecond pulses; 1064 nm; polarization effect; metallic overcoat.

1.   Introduction

Diffraction gratings are frequently used in laser systems, e.g., dye-laser cavities, as wavelength-tuning elements. These gratings usually have the lowest damage threshold of any component in the system and thus determine or limit the maximum energy output available from the laser. It is therefore important to understand the damage characteristics of gratings and how they can be improved.

Damage-threshold characteristics have been measured for both conventionally ruled (replica) gratings and for the newer holographically produced gratings. A comparison between aluminum and gold as the surface coating has been made, and the effect of the number of lines per millimeter on the damage threshold has been determined. Grating damage thresholds were measured for both S- and P-polarizations. The effect of using ruled gratings in higher orders was investigated. Comparisons were made between master and replica holographic gratings and between replica ruled gratings from two different manufacturers.

For these tests the gratings were mounted in Littrow condition, first order, as is common for their use as tuning elements in dye lasers. Using the single-shot-per-site mode, the samples were irradiated by 30-ps, 1064-nm pulses having a spot size of 0.5-mm radius.

It was found that holographic gratings have damage thresholds from 1.5 to 5 times higher than similar ruled gratings. For all but one of the gratings tested, thresholds for S-polarized light were substantially higher than for P-polarization, by factors ranging from 1.5 to 6.

For the same type grating, gold is a much better overcoat than aluminum at 1064-nm, as would be expected. Thresholds for gold-coated gratings were approximately 1.5 to 10 times higher than the threshold for aluminum-coated gratings.

2.   Experimental Setup

    The laser damage threshold measurements were made using a Nd:YAG oscillator-amplifier configuration. The laser was mode-locked, and a single 30-ps pulse was extracted from the mode-locked train. Care was used throughout the system to maintain a single transverse spatial mode.

    This beam then entered the interaction area shown in figure 1. A 2-m focal-length lens focused the beam at a point beyond the sample (grating) so that the spot size radius at the sample was 0.5 mm (Gaussian parameter w). The spot size was measured on every shot using a Reticon linear-diode array.

    Damage was detected in three ways: (1) visual observation during the shot; (2) photomultiplier observation of spark; and (3) comparative observation of the scattering of a He-Ne laser before and after the shot. The interaction room was completely darkened during the tests and an observer watched the sample through glasses highly shielded for the 1064-nm radiation. The observer saw a spark if substantial damage occurred, and was also able to detect very slight changes in the scattering from a coincident He-Ne beam. The primary damage detection was the signal from a photomultiplier viewing the spark at the interaction point. The photomultiplier was heavily filtered so that it could only see a narrow range of wavelengths centered at 4200 Å.

    After each shot the sample was translated so that no site was irradiated more than once. An average of about 40 shots was used to establish the damage threshold for each test.

    The gratings were mounted in Littrow condition, first order. Therefore gratings having different groove spacings were irradiated at different angles of incidence relative to the plane of the gratings. A half-wave plate was used to change the polarization of the incident laser beam. In order to avoid confusion over the terms S-plane and P-plane, we will explicitly refer to the electric vector parallel to the grooves, $E_{||}$, and the electric vector perpendicular to the grooves, $E_{\perp}$.
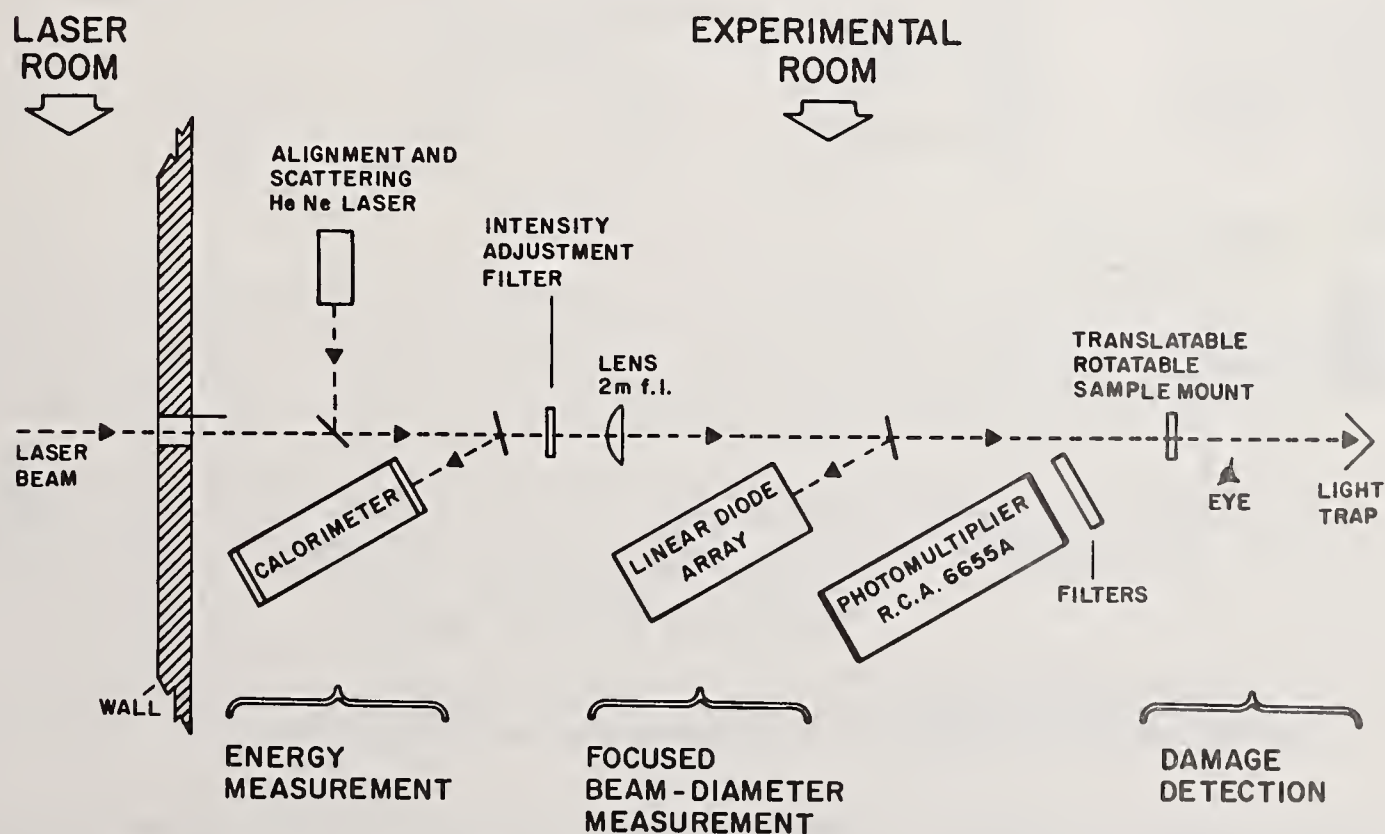
Figure 1. Experimental setup used to measure laser-induced damage thresholds.

3. Metallic Coatings

Four pairs of gratings were obtained such that, within a pair, the gratings were identical except for coating. One grating of each pair was coated with aluminum and one with gold. The damage threshold results are shown in table 1. In every case, the gold coated gratings had higher thresholds by a substantial ratio.

Table 1. Damage thresholds of gold and aluminum-coated gratings used at 1.06 microns.

| | | Damage Threshold (J/cm²) | | | | Threshold Ratio (Gold/Alum.) | |
| | | E//Grooves | | E⊥Grooves | | | |
Type	Grooves/mm	Gold	Alum.	Gold	Alum.	E//Grooves	E⊥Grooves
Holog.	1800	2.6	0.32	1.2	0.14	8.1	8.6
Holog.	1800	1.0	0.28	0.87	0.09	3.6	9.7
Ruled	600	1.1	0.19	0.44	0.07	5.8	6.3
Ruled	300	0.49	0.32	0.07	0.05	1.5	1.4

This is reasonable at 1064 nm, since the reflectivity of gold is higher than that of aluminum, as shown in figure 2. Below 600 nm, however, the situation is reversed and one would expect that aluminum coatings would have higher damage thresholds than gold. Thresholds for both materials would be lower at 600 nm than those thresholds reported here, due to the increased absorption at shorter wavelengths.
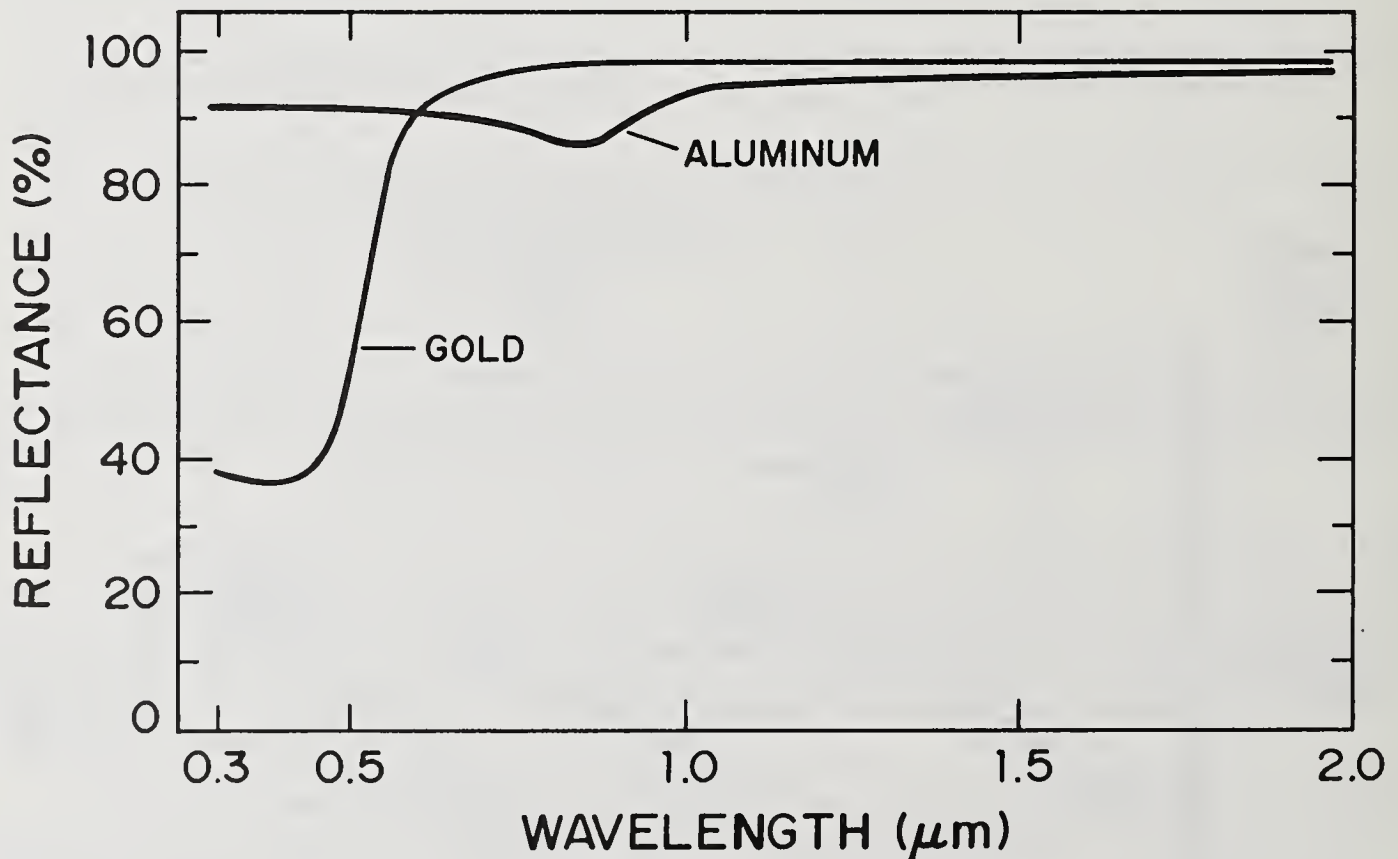
Figure 2. Reflectance as a function of wavelength for aluminum and gold [1].

One might expect a relationship between the minimum coatings thickness that should be used and the laser pulse length (in time). For replica gratings, both ruled and holographic, the layer underneath the outer metallic layer is some form of epoxy (fig. 3). For master holographic gratings, the layer underneath the outer metallic layer is a photoresist material. These materials are thermal barriers, because of their low thermal conductivity, thus keeping most of the heat in the metallic layer. Since all of the absorption occurs in a thin (~200-300 Å) layer at the surface, increasing

the thickness of the coating decreases the maximum temperature attained by the coating. This is only true up to a point, however, since the heat must have time to diffuse into the metal. Once the laser pulse has turned off, further heat diffusion cannot reduce the (already attained) maximum temperature. Although they were not tested in this experiment, ruled masters may have some advantage for long pulse lengths in that they do not have the insulating epoxy layer. The use of metallic substrates could also help for high average power applications. The substrates used here were glass.
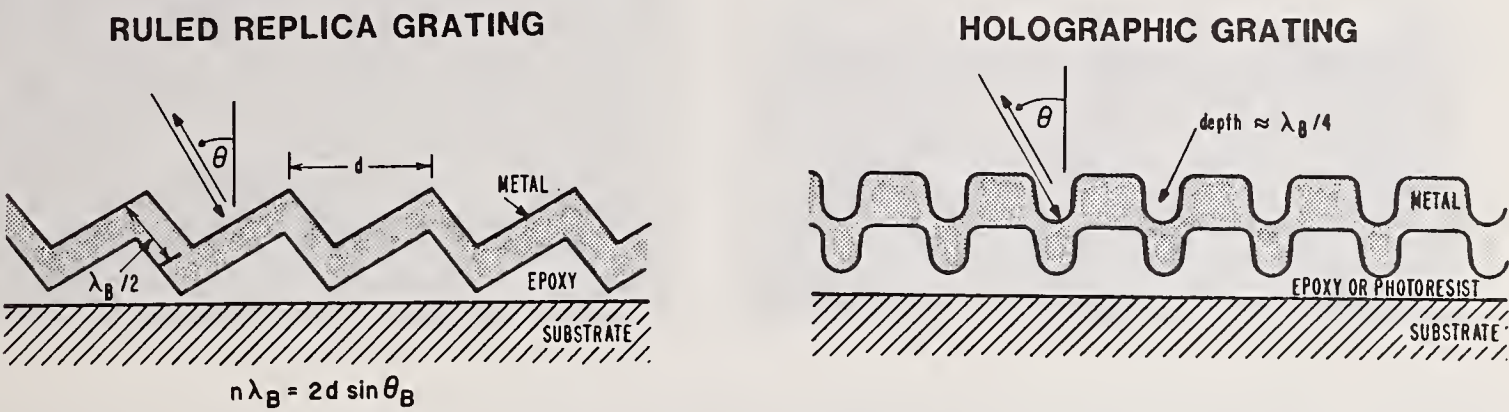
Figure 3. Cross-sectional view of ruled replica and holographic gratings showing metal deposited on epoxy or photoresist material.

4. Ruled Versus Holographic Gratings

Table 2 compares the damage thresholds of machine ruled and holographic gratings (both replicas). It can be seen that holographic gratings hold a clear and substantial advantage over ruled gratings.

Table 2. Damage thresholds of ruled and holographic gratings.

| Grooves/mm | Coating | Damage Threshold (J/cm²) | | | | Threshold Ratio (Holog./Ruled) | |
| | | E//Grooves | | E⊥Grooves | | | |
		Ruled	Holog.	Ruled	Holog.	E//Grooves	E⊥Grooves
1800	Gold	0.47	2.6	0.24	1.2	5.5	5.0
600	Gold	1.1	1.7	0.44	1.0	1.5	2.2

One possible explanation of the difference is the sharpness of the respective groove shapes, as demonstrated in figure 3. Ruled gratings are actually cut into the metal layer with a diamond tool, producing sharp corners and whiskers of metal. Electric-field enhancement at these sharp corners could account for lower thresholds. The ruled gratings used in these tests were actually replicas rather than masters, but it is presumed that the sharp features replicate faithfully.

Holographic gratings are made by irradiating a photosensitive surface with an optical interference pattern. The pattern etched into the surface is some truncated form of a sinusoid and is, therefore, smoother in shape than a ruled pattern. Figure 4 shows photomicrographs of two different holographic gratings. The reflective metal layer is deposited on top of the exposed and developed photoresist material.

All of the gratings in table 2 were tested in first order except the ruled 600 groove/mm grating, which was tested in second order. As will be seen in the next section, this may have had an adverse effect on the results. However, the results for the 1800 groove/mm gratings are clear and valid.

Figure 4.   Photomicrographs of two holographic gratings illustrating groove profiles.   Groove spacing on the left is 1800 ℓ/mm and on the right is 1200 ℓ/mm.

5.   Higher Orders

One possible advantage of ruled gratings is their ability to go to higher orders efficiently. From a laser damage threshold viewpoint, however, using higher orders is not advantageous, as can be seen in table 3.   Here, a holographic grating in first order is compared to ruled gratings in second and fourth orders.   The groove spacing and order number are such that the Littrow angle is constant for the three cases.   Each of the ruled gratings was blazed for use in the order listed in table 3 at 1064 nm.   The use of higher orders reduces the damage threshold.

Table 3.   Damage thresholds of holographic gratings used in first order compared to ruled gratings blazed for higher orders.

| Type | Coating | Grooves/mm | Order | Damage Threshold (J/cm^2) | |
				E//Grooves	E⊥Grooves
Holog.	Gold	1200	1	1.9	1.4
Ruled	Gold	600	2	1.1	0.44
Ruled	Gold	300	4	0.49	0.07

6.   Effects of Polarization

Polarization of the incident beam had a substantial effect on the damage threshold of a grating, as seen in table 4.   For all but one of the gratings tested, the threshold was higher for the electric vector E parallel to the grooves than for E perpendicular to the grooves.   It is well known that the efficiency of diffraction gratings is different for the two different polarizations, and that the curves of efficiency versus wavelength vary from one grating to another [2].   This would imply that the details of the electric field distribution at the surface of the grating differ, perhaps accounting for the different damage thresholds.   Typical grating efficiency curves are shown in figure 5.   A simplistic approach of correlating the efficiency of a grating with its damage threshold for the two polarizations does not work at all.   We have not attempted a detailed analysis of this area, but it can be seen from figure 6 that simple metal absorption theory would predict higher damage thresholds for S polarization (E parallel to grooves), in qualitative agreement with the data.   Specifying the angle of incidence is more difficult, however, because of the angles involved in the grooves themselves.   It is apparent that the higher efficiency configuration (E perpendicular to grooves) has the lower damage threshold.

158

Table 4. Effect of polarization on damage thresholds of gratings.

| Type | Coating | Grooves/mm | Damage Threshold (J/cm²) | | Threshold Ratio |
			E//Grooves	E⊥Grooves	E// /E⊥
Holog.	Gold	1800	2.6	1.2	2.2
Holog.	Alum.	1800	0.32	0.14	2.3
Holog.	Gold	600	1.7	1.0	1.7
Ruled	Gold	1800	0.47	0.24	2.0
Ruled	Alum.	830	0.26	0.35	0.7
Ruled	Alum.	300	0.32	0.05	6.4
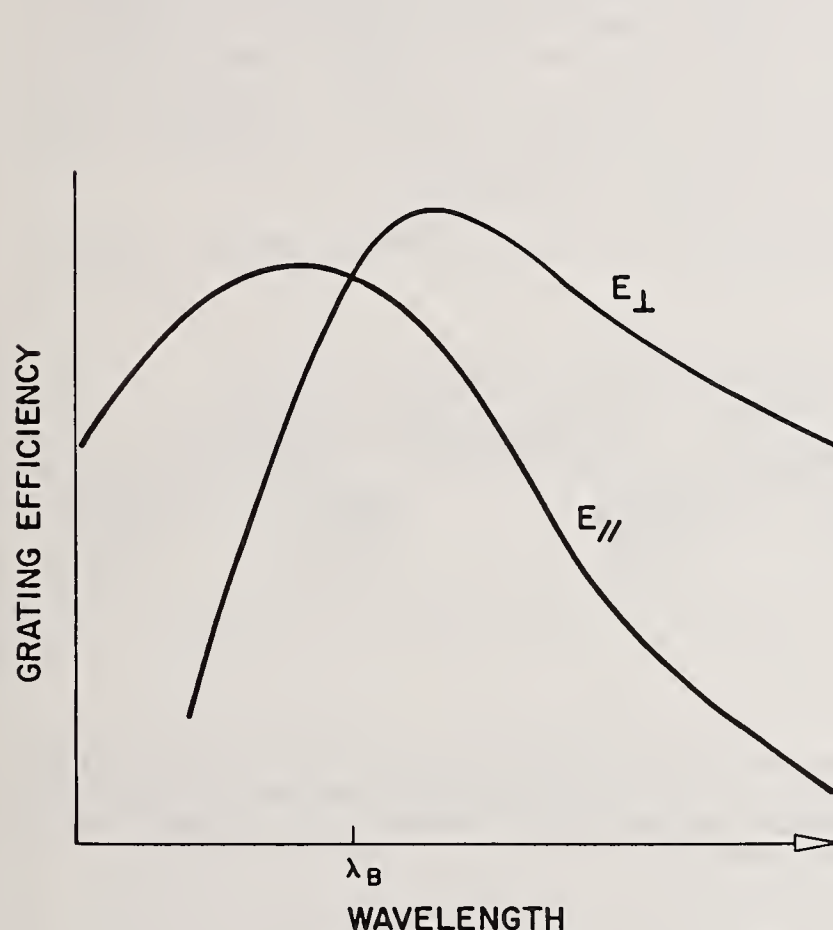
Figure 5. Typical grating efficiency curves. Actual curves vary widely from one grating to another.
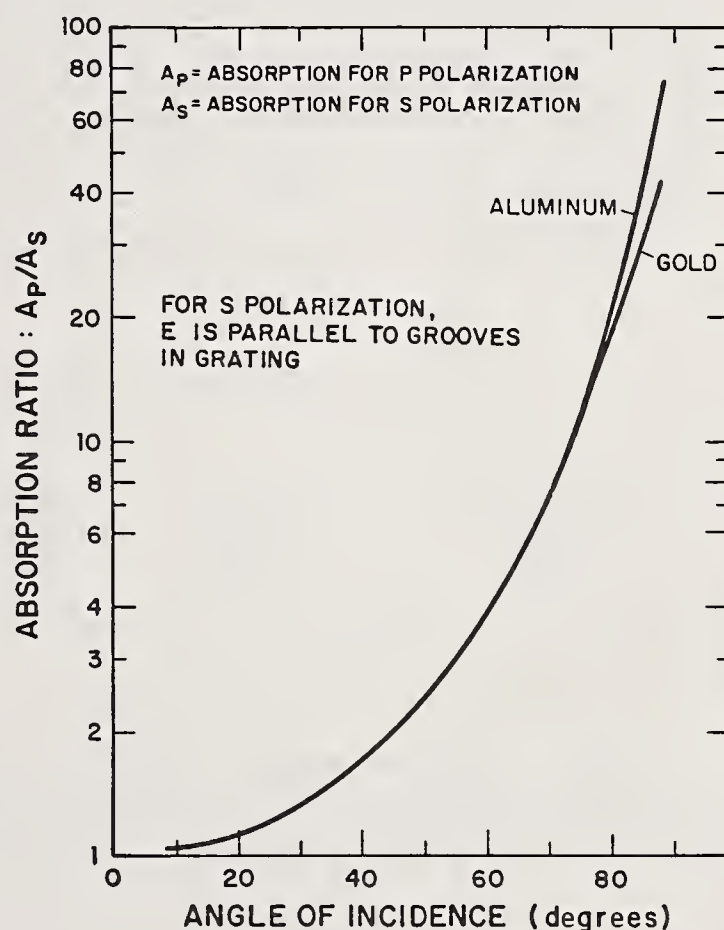
Figure 6. Ratio of absorptions for the two polarizations for Al and Au as a function of angle of incidence.

7. Groove Spacing

The dependence of damage threshold on groove spacing is not clear. In table 5, for holographic gratings and E parallel to the grooves, the threshold increases with the number of grooves per milli-meter. However, for the same gratings and E perpendicular to the grooves, threshold increases from 600 to 1200 grooves/mm, then decreases from 1200 to 1800 grooves/mm. For the ruled gratings shown, the two different polarizations have opposite dependence on groove spacing. One can only conclude that other factors appear to be more important than groove spacing.

Table 5. Damage thresholds of gratings as a function of groove spacing (tested in first order).

Type	Coating	Grooves/mm	Damage Threshold (J/cm²)	
			E//Grooves	E⊥Grooves
Holog.	Gold	1800	2.6	1.2
Holog.	Gold	1200	1.9	1.4
Holog.	Gold	600	1.7	1.0
Ruled	Alum.	830	0.26	0.35
Ruled	Alum.	300	0.32	0.05

8. Master versus Replica Gratings

Two master-replica pairs of holographic gratings were tested for relative damage thresholds. For both aluminum and gold coatings and for both polarizations the replica gratings had higher thresholds than the master gratings, as shown in table 6. One possible explanation is the different types of material layers used under the reflective coating, as discussed in Section 3. Holographic masters use a photoresist material so that the initial pattern can be "recorded." Replicas have no such requirement since they are merely taking the physical shape of the master by impression in an epoxy layer. Another possible explanation is that sharp points and corners may not replicate faithfully, but may come out more rounded. It should be noted that these replicas are actually second-generation or "positive" replicas so as to have the same phase as the master.

Similar tests on ruled gratings were not performed due to the considerable cost of ruled masters.

Table 6. Damage thresholds for master and replica holographic gratings.

Grooves/mm	Coating	Damage Threshold (J/cm²)			
		E//Grooves		E⊥Grooves	
		Master	Replica	Master	Replica
1800	Alum.	0.28	0.32	0.90	0.14
1800	Gold	1.0	2.6	0.87	1.2

9. Two Manufacturers of Ruled Gratings

Table 7 gives the damage thresholds for two ruled gratings made by two different manufacturers but otherwise identical. Since the relative positions of the gratings changed between the two polarizations and the thresholds are close to one another, neither grating appears to be better than the other. This test was not performed on holographic gratings.

Table 7. Damage thresholds of ruled gratings from two manufacturers.

Manufacturer	Type	Coating	Grooves/mm	Damage Threshold*(J/cm²)		Blaze λ
				E//Grooves	E⊥Grooves	
JY	Ruled	Alum.	600	0.19	0.07	2 μm, 1st order
B&L	Ruled	Alum.	600	0.18	0.12	2.5 μm, 1st order

*Damage thresholds for 1.06 μm irradiation, 2nd order

160

10. Conclusions

The thresholds for laser-induced damage to holographic and ruled gratings have been measured and compared for 30-ps pulses of 1.064 µm radiation. For these conditions, holographic gratings have higher damage thresholds than ruled (replica) gratings. Ruled master gratings were not tested. For both holographic and ruled gratings, gold coatings have higher damage thresholds than aluminum coatings, as would be expected at this wavelength. In general, the damage threshold was highest for the electric vector parallel to the grooves, by a substantial factor. Unfortunately, this orientation normally produces lower efficiency. Operating in lower orders gives the best damage resistance, where that is practical. Ruling density does not appear to have a clear effect on damage threshold. The holographic replica gratings tested in this series had higher damage thresholds than holographic master gratings. This is not fully understood. No significant difference was found between ruled replicas from two different vendors.

11. References

[1] Jobin Yvon Optical Systems, Laser Grating Handbook.

[2] Loewen, Erwin G., Maystre, Daniel, McPhedran, Ross C., and Wilson, Ian. Correlations between efficiency of diffraction gratings and theoretical calculations over a wide range. Japan. J. Appl. Phys. 14 (1975) Suppl. 141: 143-152.

Assessment of Optical Coatings Prepared by Molecular Beam Techniques

K.L. Lewis, J.A. Savage, A.G. Cullis, N.G. Chew, L. Charlwood and D.W. Craig

Royal Signals and Radar Establishment
Malvern, Worcestershire
England WR14 3PS

Thin films of ZnSe and other materials have been produced by molecular beam techniques in an ultra-high vacuum facility dedicated to the examination of fundamental aspects of thin film technology as applied to optical coatings. The ZnSe films have negligible values of absorptance at 10.6 μm and have laser damage thresholds in the range 35-38J/cm^2, a significantly higher energy density than hitherto reported for ZnSe films. Examination of the films in cross section by high resolution transmission electron microscopy has revealed a polycrystalline columnar morphology, with the crystallite size dependent on deposition temperature. A complete absence of intergranular voids is noted which renders the film impervious to the ingress of water and other impurities when exposed to the atmosphere. This feature, together with the inherently high purity of the film is believed to be the factor responsible for the enhancement in laser damage threshold.

The electron micrographs do however reveal sub-grain structure in the form of stacking faults and twin planes which are potential sinks for residual impurities in the material. Further improvements in damage threshold may be possible by elimination of this sub-grain structure.

1. Introduction

The case for a fundamental approach to the solution of the problem of susceptibility of thin film structures to laser induced damage was made at the 1983 Boulder Conference [1]. Here, the potential afforded by molecular beam techniques was explored for the deposition of improved optical coatings. The molecular beam technique allows a high degree of control over the deposition process and in situ assessment techniques, such as Auger and X-ray photoelectron spectroscopy allow the characterisation of the surfaces produced. By combining Knudsen evaporation with RF sputtering processes in a dedicated UHV facility, it is possible to fabricate coating structures containing a wide range of different materials including sulphides, selenides, tellurides, arsenides, phosphides, fluorides, chlorides, oxides and nitrides without necessarily having to break vacuum and risk the creation of contaminated interfaces. Application of the equipment was described with reference to the production of ZnSe coatings of up to 3 μm in thickness which had negligible values of absorptance at 10.6 μm.

The achievement of low absorption per se is not a necessary criterion for the realisation of a high damage threshold, although it may play an important role particularly at longer pulse lengths (200 nsec +) where the rate of heat generation by virtue of absorption is greater than its rate of transport to surrounding areas. At short pulses (100 nsec or less) coatings fail either as a result of heating microscopic coating defects or by electron avalanche processes in the coating material itself. It may be argued that the most serious coating defects are voids, from the point of view that they cannot be controlled by attention to cleanliness, dust control etc. The presence of open porosity results in a high susceptibility to water ingress and inevitably a lower damage threshold. Ultra high vacuum conditions create an excellent environment for reducing particulate inclusion during coating deposition. This is especially so for the Knudsen source where the configuration of the oven avoids the ejection or spattering of discrete particles of evaporant.

It is likely that the morphology of thin films plays an important part in determining resistance to laser induced damage. Films prepared by conventional evaporation techniques exhibit a polycrystalline morphology with a characteristic columnar structure [2]. It has long been asserted that void formation is enhanced at grain boundaries in thin films and that diffusion of impurities especially water readily proceeds along such paths. The presence of heterogeneous impurities at such grain boundaries also results in the generation of compressive stresses in the film [3,4]. Lack of control of the deposition process - changing deposition rate, improvements to the vacuum environment as a result of gettering processes potentially lead to gradation of stress levels within a film, increasing the likelihood of poor adherence. An immediate solution would appear to be to avoid producing films with polycrystalline columnar morphology, and to deposit single crystal films with an epitaxial relationship to the substrate. Unfortunately this requires a close match of the crystallographic parameters of the film and substrate and it

may be too much to hope that this can be achieved with simultaneous satisfaction of refractive index criteria in any one film/substrate combination. The requirements of high interface perfection to ensure good epitaxy cannot be met in other than a UHV system employing ion beam cleaning and annealing/surface reconstruction techniques, or in chemical vapour deposition equipment where high substrate temperatures/ gaseous etchants can be employed.

The alternative solution, the adoption of amorphous morphologies may offer some potential since the coating need not be lattice matched to the substrate. The behaviour of materials such as As_2S_3 has already been explored and their ability to withstand moderate levels of laser power demonstrated [5]. Variation of refractive index can be effected by controlled deposition of amorphous alloys typified by the chalcogenide system [6].

As a preliminary stage of our fundamental studies, we have examined the limits to which coatings with columnar polycrystalline morphology may be taken. ZnSe and ZnS are two examples of such thin film materials and are commonly used in various designs of multilayer coatings. The present work assesses the microstructure of films produced by molecular beam techniques and the susceptibility of the coatings to laser induced damage.

2. Experimental

The equipment used for film deposition has been described in a previous publication [1]. The 3-chambered facility, manufactured by Vacuum Generators Ltd., comprises a growth chamber (pumped by ion and titanium sublimation pumps) which contains a molecular beam sampling mass spectrometer and Auger elec- tron spectrometer. A preparation chamber immediately adjacent allows cleaning using a raster scanning ion gun. Specimens are transferred between the separately gated chambers using a rack and pinion manipulator system. A load-lock system is provided allowing rapid entry into the ultra high vacuum (10^{-11} mbar) environment. The loading chamber is UHV cryopumped and contains a small (2" diameter) RF plasma source for the deposition of refractory materials (eg oxides, nitrides). Three Knudsen cells are available for simultaneous use in the growth chamber and for this work were charged with broken lumps of ZnSe (for stoichiometric beams of Zn and Se_2), ZnS (for beams of Zn and S_2) and Ag_2S (for S_2 alone). Substrates for coating (ZnSe, GaAs, Si, Ge) were carefully cleaned with trichloroethane and acetone before loading into the equipment, and following evacuation to 5×10^{-7} mbar were further cleaned by Ar^+ beam bombardment for 10 minutes at a density of approximately 200 $\mu A/cm^2$. Coated specimens were examined by Nomarski inter- ference microscopy, infra-red spectroscopy (Perkin Elmer model 983G) and adiabatic laser calorimetry. The morphology of the coatings was examined in detail by cross-sectional transmission electron microscopy (XTEM). Specimens were prepared in cross-sectional configuration by sequential mechanical polishing/low voltage Ar^+ ion milling, and were examined by direct imaging in a Jeol 120C instrument at 120 kV. The milling beams were generated in saddle-field ion guns and were collimated with a cross-sectional area of about 3 mm^2. The ion energy was usually 5 kV and the ion current 20 μA.

Laser damage thresholds were determined using the equipment shown in figure 1. Two separate TEA CO_2 lasers were used to examine the dependence of damage threshold on pulse length. A short cavity laser [7] was used for short pulse work. Its output consisted of a 33 nsec FWHM gain switched spike followed by a tail extending to 1700 nsec. The energy in this pulse could be approximated by a square pulse of width 120 nsec and a height equal to the intensity of the gain-switched spike. Longer pulse lengths were achieved using a grating tuned hybrid laser (Edinburgh Instruments type 222) operating with its CW section below threshold. The pulse length, comprising solely of a single, slightly skewed gaussian peak (no tail) was 340 nsec FWHM. Temporal profiles were recorded using Labimex model R005 uncooled CMT detectors (rise time 1 nsec) coupled to Tektronics 7912AD transient digitisers. Energy measurements were effected using a calibrated Gentec detector (Joulemeter ED200). Spot widths were varied by choice of focussing lens and measured using a 25 μm scanning aperture. Groups of measurements were made for constant spot widths at varying incident energies by interposing various combinations of ZnSe and CaF_2 attenuators in the incident beam.

3. Coating Morphology

The molecular beam produced coatings were mirror smooth and essentially replicated the topography of the substrate used. In the case of ZnSe substrates a slight degree of surface relief was evident comple- menting that of the polycrystalline substrate. This is largely a result of preferred etching of the different oriented crystallites during ion beam cleaning. Some inclusions were evident in coating Ge windows, but these were also present in uncoated regions of the samples and were attributed to polishing debris.

Examples of XTEM micrographs are presented in figures 2-5. Figure 2 shows a 0.7 μm thick ZnSe grown on GaAs at 50°C. The polygrained morphology is clearly evident with the columnar grains running through- out the thickness of the film. The mean grain width is approximately 250Å. The crystalline structure within the material is highly defective with a high density of stacking faults each running perpendicular

to the direction of growth. X-ray diffraction measurements taken on the film surface show that the material is highly ordered with cubic (111) planes lying parallel to the surface. The fault orientation is as expected since twinned regions in the zinc blende structure usually have a [111] twin axis and composition surface parallel to (111). A few instances of Moire fringe contrast is also found in the micrographs. This arises from interference effects between surface grains and others lying immediately beneath them.

Careful examination (figure 3) of the grain boundary regions reveals the complete absence of any voids within the scale of resolution available (20Å). This is clearly the case since voids are easily distinguished in the TEM, providing contrast which alternates between light and dark when imaging conditions are changed from under to over-focus.

Examination of the interface region at higher magnification (figure 4) reveals a transition region some 1500Å in height above the substrate, where growth of the columnar grains is clearly unstable and new grains are being nucleated. Also evident is the narrow (60Å) amorphous region at the surface of the substrate resulting from ion beam damage during wafer cleaning. This amorphous region would require re-crystallisation in a high temperature anneal (500^{0}C) before epitaxial growth could occur.

The morphology of a ZnSe film produced at 192^{0}C on GaAs is essentially similar to that of the low temperature case with the exception of a greatly increased grain size of 1000Å (figure 5). The grain boundaries are less well defined than in the film produced at 50^{0}C and stacking faults in one grain tend to merge into those of neighbouring grains. No voids were detected.

4.   Damage Assessment and Discussion

4.1 Zinc Selenide Films

Molecular beam grown ZnSe films were assessed as 1 µm thick layers on polycrystalline ZnSe substrates. Typical deposition conditions were as follows - ZnSe source temperature 950^{0}C, substrate temperature 175^{0}C, growth rate 1.2 µm/h, $p(H_2O)$ 2 x 10^{-10} mbar, $p(CO)$ 2 x 10^{-10} mbar. Film absorptances were too small to be measured with the laser calorimeter system available. The laser induced damage threshold (LIDT) of the films for short pulses was in the range 60-73 J/cm^2 (1/e^2 diameter 102 µm). This was in excess of the value of 50-60 J/cm^2 measured on uncoated regions of the same sample. Although the difference between the two values was slight, repeated measurements showed it to be real, with the uncoated sample always damaging at a lower incident energy. This was attributed to the presence of residual surface impurities on the substrate which had been removed in the coated region by the pre-deposition ion beam cleaning procedure. At longer pulse lengths (340 nsec), the LIDT value for the ZnSe coating was determined to be 31-38 J/cm^2 (1/e^2 diameter 180 µm). Micrographs of the coating (figure 6) clearly show that damage was initiated at discrete microscopic inclusions resulting in craters some 10 µm in diameter. The uncoated rear surface of the substrate always damaged at these energy densities.

Although no direct comparison with other measurements is possible, damage thresholds are significantly in excess of those previously reported for ZnSe films on other substrates. For example, Golubovic et al [8] report a value of 20 J/cm^2 (100 nsec FWHM 180 µm spot size) for sputtered ZnSe on KC1 substrates. The high thresholds achieved in this work are attributed to the near theoretical density of the film. Since the films have been fabricated on ZnSe substrates, transmission measurements can be used as a sensitive indication of whether the refractive index of the coating is significantly different from that of the substrate. An example of an expanded transmission spectrum is presented in figure 7. It is difficult to assert whether any of the features suggest interference effects since there are clearly absorption bands present, the most notable being those due to OH at 3420 cm^{-1} and ZnH at 1620 cm^{-1}. From the remaining spectral regions, we suggest that some optical resonance may be apparent but it represents at the most the reflectivity change associated with a $\lambda/4$ film of ZnSe with refractive index some 0.4% different from that of the bulk ZnSe. This is a significant improvement on for example sputtered ZnSe [9] where refractive index variations of up to 15% (albeit at 0.6328 µm) have been reported.

These improvements have been obtained in films that exhibit a polycrystalline columnar morphology. However as the TEM evidence indicates, the structure of each crystallite is highly imperfect with stacking faults and twins running perpendicular to the direction of growth. Since these crystal faults are essentially interruptions in the elementary stacking sequence of planes in the zinc blende lattice they are able to give rise to strain and refractive index inhomogeneity on the atomistic scale particularly when impurity species are present. This may perhaps lead to a reduction in laser damage threshold compared with that achievable in an ideally structured film.

4.2 Zinc Sulphide Films

The molecular beam facility has also been used to study the deposition of ZnS films. The problems of film stoichiometry were considered to be an additional problem in this case since the sticking coefficient

of sulphur from an S_2 flux is likely to be less than that of Zn. Experiments have therefore been carried out to assess the importance of this effect by supplying additional sulphur (specifically S_2) from a second source. This was conveniently provided by a Knudsen oven containing silver sulphide which dissociates to produce S_2 and Ag with partial pressures in the ratio of about 10^4. Provided that this source is purely used as a 'top up' measure, significant contamination of the ZnS with Ag is likely to be negligible.

Most ZnS films have so far been deposited at $\lambda/4$ thicknesses on germanium substrates at $50^\circ C$ and have damage thresholds in the range 15-16 J/cm^2 (33 nsec 200 μm FWHM). This value is slightly lower than the thresholds reported by Gibbs and Wood [10] for clear regions of single-layer AR ZnS/Ge of 16.8-24 J/cm^2 (60 nsec 140 μm spot size). Examination of the samples revealed that the surfaces of the germanium substrates contained a great deal of polishing debris and other visible defects and themselves had low damage thresholds of the order of 25 J/cm^2. The results for the ZnS films cannot therefore be considered as representative of what can be achieved and further parametric studies are underway using different substrates and substrate materials.

Some important factors have however emerged. A direct comparison of film deposition in conventional vacuum environments and UHV has been carried out in the same equipment using otherwise identical coating conditions (deposition rate, temperature, film thickness etc). A conventional coating plant environment was simulated by opening the gate valves between the growth and loading chambers, switching off the growth chamber pumps, running with all cryopanneling at room temperature and arranging for the whole system to be pumped using a small (80 l/sec) diffusion pump. By ensuring that the loading chamber had had a recent exposure to air, it was possible to arrange satisfactory 'dirty' conditions with total pressure of 4×10^{-6} mbar. Residual gas analysis revealed that the dominant species present had partial pressures as follows: $p(H_2O)$ 2.5 $\times 10^{-6}$ mbar, $p(H_2)$ 7 $\times 10^{-7}$ mbar, p (CO) 3 $\times 10^{-7}$ mbar and $p(H_2S)$ 4 $\times 10^{-7}$ mbar. The presence of H_2S was unique to this particular experiment and clearly arises from reaction between H_2O and S_2 in the growth chamber. Residual species for the UHV experiment were as for ZnSe above.

Figure 8 shows a comparison of the damage morphology of the ZnS/Ge samples produced in the two experiments. Although the damage threshold was the same in each case (16 J/cm^2) due to the poor finish and presence of inclusions on the substrate surfaces, there are clearly significant differences in the way that the coatings have responded to the laser pulses. The film produced at 4 $\times 10^{-6}$ mbar has delaminated in a wide region around the central damage zone. In comparison, the UHV produced film strongly adheres to the substrate. Debris from the damage spot is clearly visible well away from the irradiation zone. Infrared spectral analysis (figure 9) clearly shows the presence of OH species in the film produced in poor vacuum whilst the UHV-grown ZnS is essentially free from such impurities.

5. Conclusions

It has been demonstrated that the molecular beam technique is capable of producing optical coatings of near theoretical density which have the potential of high resistance to laser induced damage. This resistance has been demonstrated for ZnS films which have higher damage thresholds than bare ZnSe surfaces. The films have been examined by cross-sectional transmission electron miscroscopy and have polycrystalline columnar morphology. No voids can be detected. A high density of microtwins and stacking faults is evident however, suggesting that further improvements in damage threshold may be feasible.

References

[1] Lewis, K.L. and Savage, J.A.: Proc. 1983 Boulder Damage Symposium.

[2] Guenther, K.H. and Pulker, H.K.: Appl. Optics 15, 2992 (1976).

[3] Pulker, H.K.: Thin Solid Films, 58, 371 (1979).

[4] Pulker, H.K.: Proc. SPIE 325, 84 (1982).

[5] Braunstein, A.I.; Wang, V; Braunstein, M.; Rudisill, J.E. and Wada, J.: Proc. Boulder Damage Symposium 151 (1973).

[6] McLachlan, A.D. and Gibbs, W.E.K.: Boulder Damage Symposium 222 (1977).

[7] Hollings, R.C. and Jordan, D.L.: J.Phys.D.Appl.Phys. 15, 1881 (1982).

[8] Golubovic, A.; Fitzgerald, J.; Berman, I; Bruce, J.; Bradbury, R.; Comer, J.J.; Ewing, W.S. and Lipson, H.G.: Proc. Boulder Damage Symposium 271 (1976).

[9] Walsh, D.A. and Detrio, J.A.: Proc. Boulder Damage Symposium 253 (1976).

[10] Gibbs, R and Wood, R.M.: Proc. Boulder Damage Symposium 181 (1976).
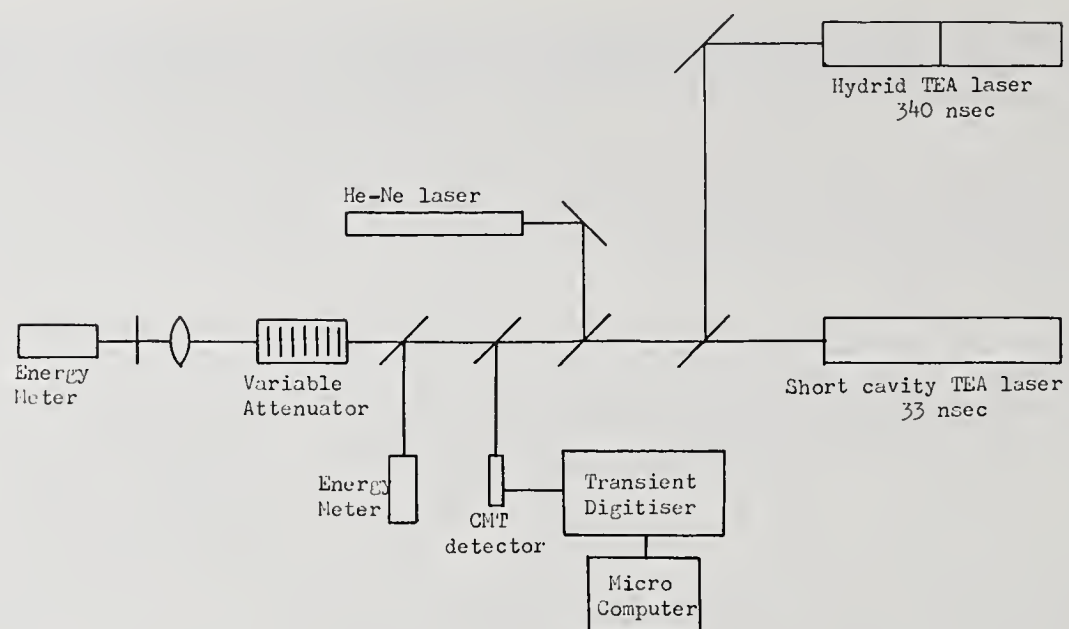
Figure 1   Schematic layout of laser damage facility.
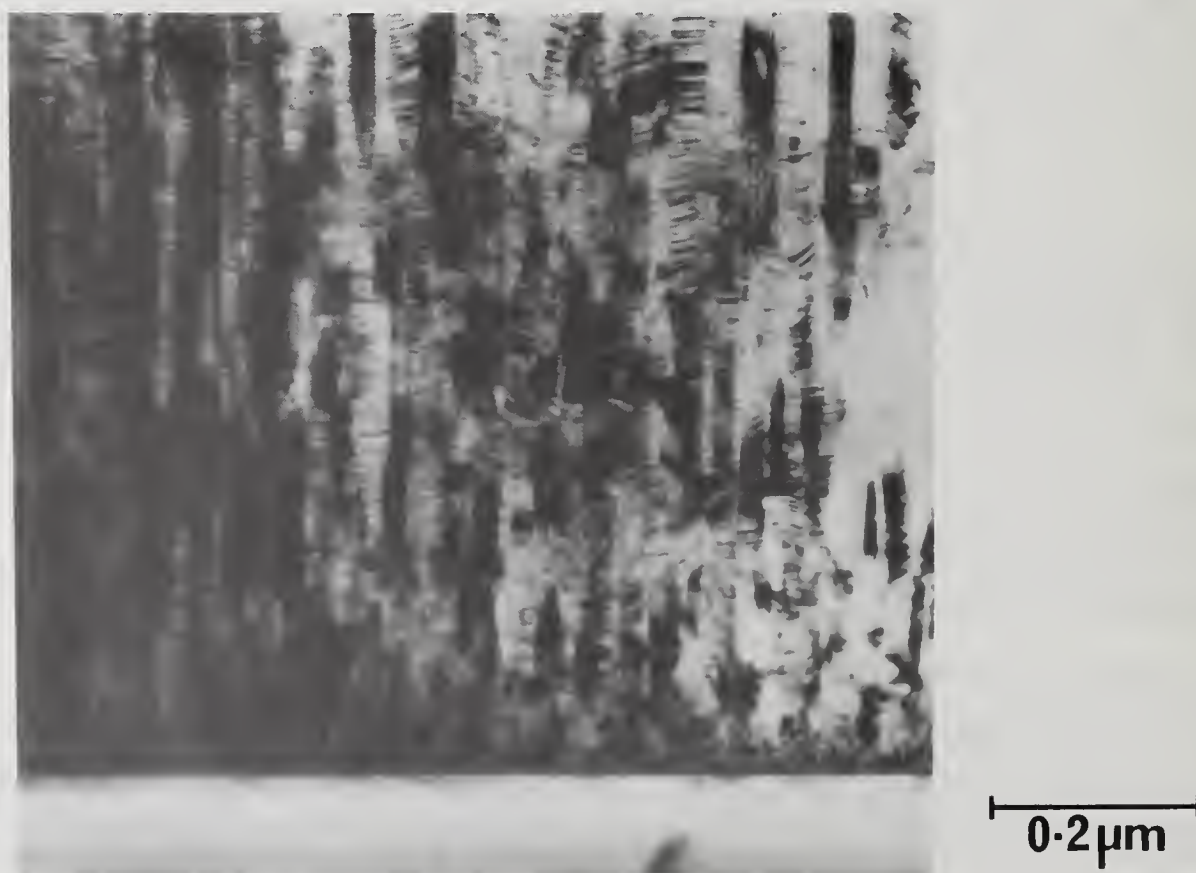
Figure 2   Cross sectional TEM image of ZnSe film grown on GaAs at 50°C.

Figure 3   Detail of 50°C ZnSe film at higher magnification with particular reference to grain boundary regions.

Figure 4   Detail of interface region of figure (2).
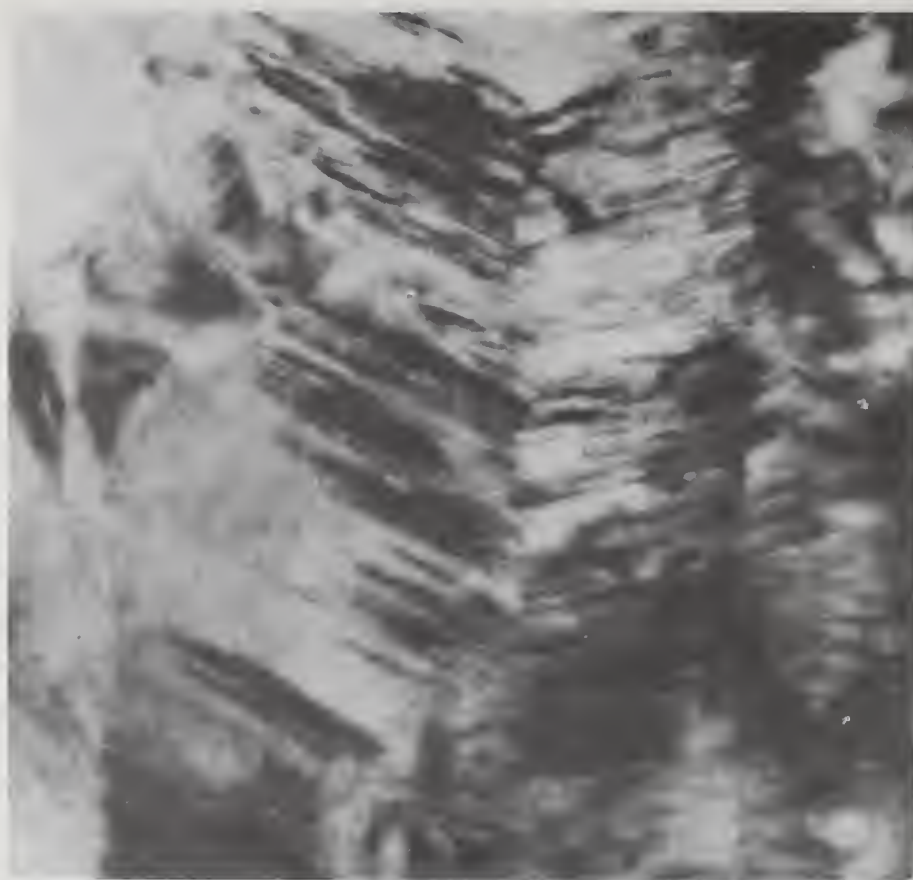
$T_S = 192^{\circ}C$

0·1 μm

Figure 5   Detail of ZnSe film grown on GaAs at 192°C. Magnification is
             as figure (3).

50 μm

Figure 6   Damage morphology in ZnSe film on ZnSe substrate produced by
             340 nsec TEA laser pulse. Spot size 180 μm.

168
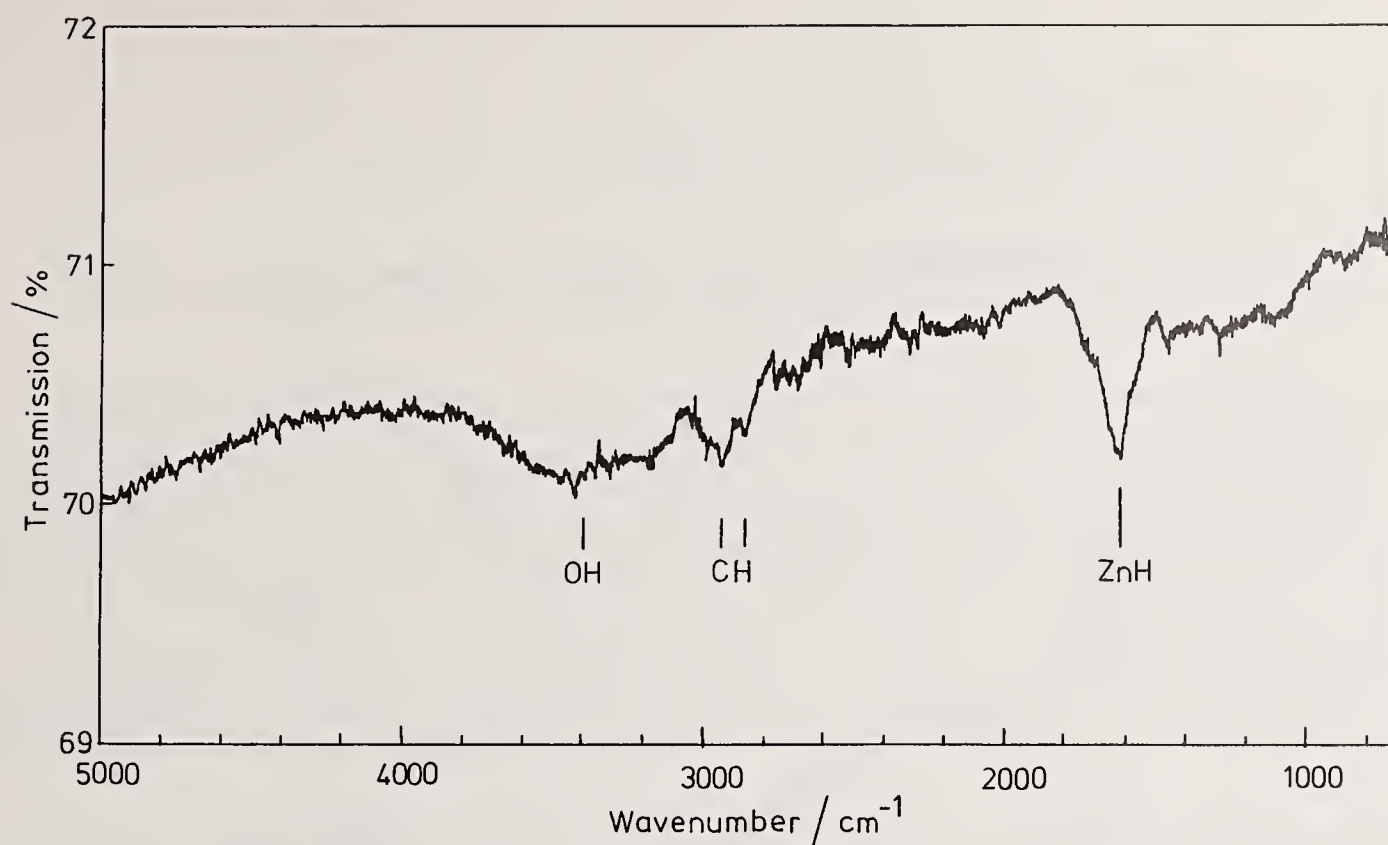
Figure 7   Expanded transmission spectrum of 1 μm ZnSe film on ZnSe substrate.

a

b

250 μm
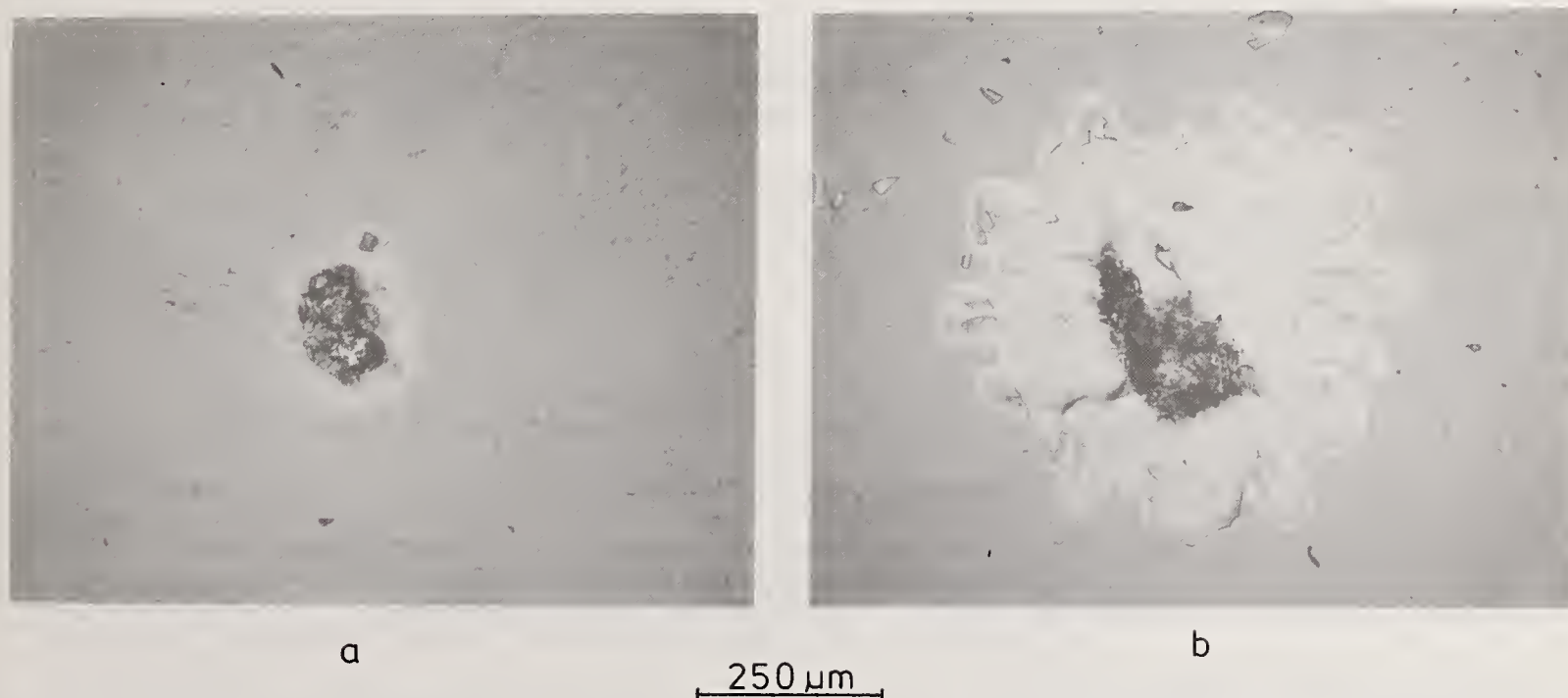
Figure 8   Comparison of damage morphology in ZnS film on Ge substrate
produced by 33 nsec TEA laser pulse.   Spot size 200 μm.

(a) Film produced under UHV conditions.

(b) Film produced under high vacuum 4×10^{-6} mbar.
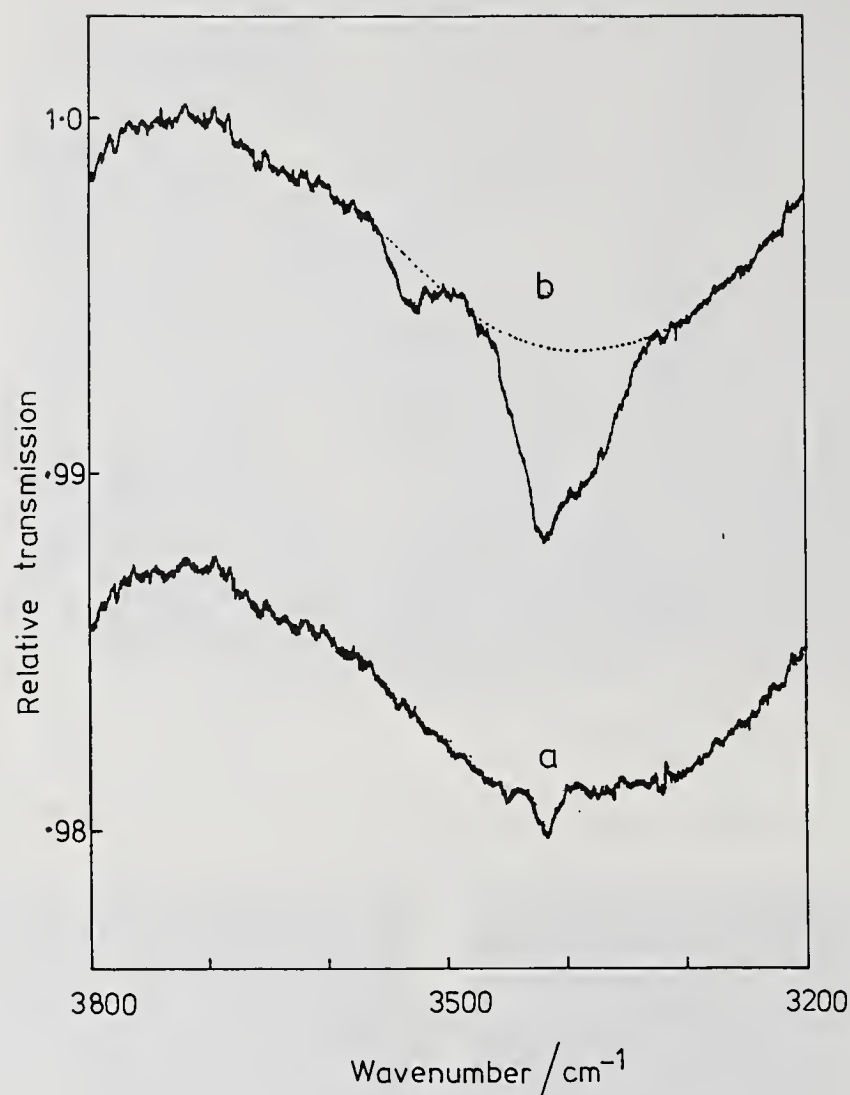
Figure 9   Comparison of infra-red absorption spectra of ZnS films on Ge

(a)   Film produced under UHV conditions.

(b)   Film produced under high vacuum 4 x 10^{-6} mbar. Some interference fringing remains in both traces following the computer flattening and expansion routines. Expansion of X30 in each case.

In response to a question the author pointed out that he couldn't tell if his MBE coatings of ZnS were as low as the bulk ZnS because the absorption of the coatings was too low to measure. The coated windows showed higher damage resistance than the bulk. Possibly the damage on the uncoated surface was caused by polishing defects, which were covered over by the film. Their samples were 1" diameter, but MBE systems are being planned which can take 11" samples. In their system they can have 3 different materials to evaporate. Some systems go as high as 8. Growth rates are comparable to those obtained using normal coating methods. Another questioner pointed out that a less restrictive term than twins would be stacking fault defects. The speaker agreed. He stated that they would do about 8 sites per sample and quoted the lowest fluence at which they got damage at the damage threshold.

Some Recent Observations on the Properties of UHV-Deposited ZrO_2

T. Raj, L. D. Weaver, S. R. Tuenge, J. S. Price and K. C. Jungling

Martin Marietta Aerospace, Albuquerque, New Mexico 87119
(Present affiliation of K. C. Jungling: University of New Mexico, Albuquerque, NM)

Single-layer ZrO_2 coatings were deposited in an ultrahigh vacuum system by two techniques: laser evaporation (utilizing a 100-W, continuous wave, CO_2 laser) and electron-beam evaporation. Substrate temperatures were maintained at either 150°C or 250°C with backfill oxygen pressures between 0 and 5×10^{-5} torr. The coatings were analyzed by Auger Electron Spectroscopy to determine stoichiometry and to provide information on the nature and level of impurities. The refractive indices for the coatings were determined by ellipsometry at 6328 Å. Selected coatings were damage tested at 531 nm.

This report discusses the influence of backfill pressure, substrate temperature and evaporation technique on thin film properties and compares the results obtained by Auger and ellipsometric analyses. Also presented is a comparison between films prepared under high vacuum and ultrahigh vacuum conditions.

Key Words: damage threshold; impurities; optical thin films; refractive index; stoichiometry; ultrahigh vacuum; ZrO_2.

1. Introduction

This paper describes some of the preliminary results of experiments conducted during early phases of the coating development program at the Air Force Weapons Laboratory's (AFWL) Developmental Optics Facility (DOF). Also discussed is Martin Marietta's approach to advancing the science of deposition technology.

The overall approach of the DOF to deposition technology is to first develop the technology required to produce superior single-layer coatings. This is a necessary step before multi-layer designs, having much-improved damage thresholds, can be achieved. Therefore, a long-term objective of this program is to characterize the effects on the optical and mechanical properties of optical thin films (both single-and multi-layer) of what are considered the "controllable deposition parameters". This approach emphasizes the need for control over the following principal film parameters: impurities, stoichiometry and microstructure. Other desirable optical and mechanical properties of thin films (e.g., low absorption, low scatter, good adhesion, low intrinsic stress, hardness and high damage threshold) are products of these controllable parameters. In this context, absorption is related to the stoichiometry, microstructure and purity of the deposited layers; while scatter, internal stress and hardness are functions of microstructure and impurities. Likewise, adhesion is a function of chamber and substrate cleanliness, substrate temperature, method of deposition and choice of material. Finally, the property of laser damage threshold could be related to stoichiometry, microstructure and choice of materials, as well as to defects (including impurities, voids, particulates, etc.).

In order to minimize impurities in the coatings, an ultrahigh vacuum (UHV) system with a typical background pressure of 5×10^{-10} torr was employed for the depositions. Furthermore, the source materials, as well as the substrate, were handled with a UHV-type procedure rather than the usual high-vacuum (HV) procedure of handling.

Two techniques of evaporation were employed for these depositions; continuous wave (CW) laser and electron beam (E-beam). CW-laser evaporation was carried out with two objectives in mind: (1) to reduce the contamination arising from the source container and (2) to determine if CW-laser evaporated coatings were closer than E-beam evaporated coatings to the bulk in stoichiometry.

Oxygen backfill pressure was varied to determine its effect on the stoichiometry of coatings. Finally, different substrate temperatures were employed to determine if a substrate temperature (of approx. 150°C) lower than that commonly used (approx. 250°C) could produce coatings with good mechanical properties. This latter consideration is desirable for several engineering aspects.

Refractory (high melting point) oxides have been selected as the top-priority class of materials to investigate. Most oxides have a spectral transmittance range spanning the ultraviolet to the near-infrared, and this is the wavelength range of interest. Refractory oxides have such desirable characteristics as: (1) being thermally, chemically, and thermodynamically stable materials (i.e., the most environmentally durable), (2) being the best diffusion barriers (i.e., providing the highest resistance to diffusion at interfaces), and (3) having been more thoroughly studied and more understandable than any other compounds of interest.

2. Experimental and Analytical Procedures

2.1. Deposition Procedures

A UHV system (assembled by this laboratory), with a typical base pressure of less than 5×10^{-10} torr, was chosen as the coating chamber for this portion of the program. The evaporation techniques were: (1) laser evaporation with a 100-watt, CW, CO_2 laser (designed and constructed by the DOF) and (2) E-beam evaporation with a UHV-compatible AirCo/Temeseal E-gun.

Three refractory oxides were chosen for this study: ZrO_2, SiO_2 and Al_2O_3. During the initial phase of this program, only ZrO_2 was used. The ZrO_2 deposition rates for CW laser evaporation were restricted to about 0.5 Å/sec due to limited laser output. The E-beam deposition rates of ZrO_2 were kept to the same level in order to compare the two techniques. The substrates chosen for most of the depositions were 5-cm semiconductor-grade silicon wafers. The substrate temperature during deposition was maintained at either 150°C or 250°C, while the backfill oxygen pressure was varied from 0 to 5×10^{-5} torr. The coating thickness was kept below 1000 Å for most of the depositions.

To monitor the progress associated with UHV conditions in general, some ZrO_2 coatings were E-beam deposited in an oil diffusion pumped HV system. The parameters chosen for the HV depositions were, to a considerable degree, influenced by the findings from the UHV depositions, and represented a departure from the usual industry practice.

2.2. Analytical Procedures

The contaminant levels and the stoichiometry of the coatings were determined by Auger Electron Spectroscopy (AES) with a Physical Electronics Spectrometer, Auger 590/ESCA 548/SIMS 2500.

The refractive indices of the coatings were determined by the method of ellipsometery using a Gaertner L117 Null Ellipsometer operating at 6328 Å. The analyses were performed using a computer program developed for the DOF by the University of Dayton Research Institute. The accuracy of the measurements is estimated to be in the range of 1 to 1-1/2 percent.

A few coatings were deposited on superpolished fused silica substrates and were subjected to damage threshold measurements by AFWL personnel.

3. Results and Interpretations

The analytical techniques used to evaluate the quality of the coatings included abrasion resistance, AES, ellipsometry and laser damage threshold; each being discussed below.

3.1. Abrasion Resistance

Representative coatings from each vacuum system were tested for abrasion resistance according to the standards of MIL-C-675. All coatings passed the abrasion test regardless of method of evaporation, substrate temperature or O_2 backfill pressure.

3.2.   AES Analysis

Although AES techniques are not generally suitable for quantitative analysis of dielectric materials, procedures were established to minimize the effects of surface charging, O_2 desorption by the probe electron beam and Argon sputtering. The two primary objectives of AES analysis were the determination of the impurity level and of the chemical composition of the coatings.

The AES peak-to-peak ratio of oxygen to metal of the source material was determined to be 4.8 ± 0.2. AES data for UHV deposited coatings are summarized in tables 1 and 2. The fifth column of each table shows the O:Zr ratio measured at the surface of the coatings. The surface was sputter-cleaned for a few minutes, and the O:Zr ratio was again measured. This near-surface O:Zr ratio is shown in column six. The seventh column indicates an average O:Zr ratio for the depth profile (inside the coating). The comments section indicates whether or not the coating was contaminated. The coating is considered to be contaminated if the carbon peak can be detected unambiguously. It should be pointed out that the carbon sensitivity of the present analysis scheme is about two to three atomic percent.

Table 1.   O:Zr Peak-to-Peak Ratios for Laser Evaporated Coatings

Coating Run *	Substrate Temperature	O_2 Pressure	Thickness (in Å)	O:Zr P-P Ratios			Comments
				Surface	Near Surface	Coating Profile	
LC 29	140°–160°C	3×10^{-5}	845	4.0	4.2	3.6 ± 0.1	
LC 30	140°–160°C	2×10^{-5}	822	4.6	4.1	4.1	
LC 31	140°–160°C	5×10^{-5}	901	4.5	4.3	4.2	
LC 32	140°–160°C	–	781	4.2	–	3.9	
LC 33	140°–160°C	1×10^{-5}	825	–	3.9	3.9	
LC 34	140°–160°C	0	784	4.5	4.4	3.8	
LC 45	240°–260°C	5×10^{-5}	386	4.3	3.8	–	Contaminated
LC 48	240°–260°C	–	550	4.4	3.5	3.5 ± 0.1	Contaminated
LC 49	240°–260°C	5×10^{-5}	551	3.8	3.4	3.2 ± 0.1	Contaminated
LC 51	240°–260°C	–	591	4.3	3.7	3.8 ± 0.1	
LC 52	140°–160°C	–	533	4.4	4.2	4.2	
LC 53	240°–260°C	5×10^{-5}	573	4.5	3.8	3.7 ± 0.1	
LC 56	140°–160°C	–	532	–	4.03	4.4 ± 0.1	
LC 57	240°–260°C	–	534	4.2	3.5	3.4 ± 0.1	
LC 58	240°–260°C	–	687	4.5	3.6	3.6	
LC 59	140°–160°C	–	564	4.7	–	4.2 ± 0.1	

*   LC - laser evaporated coatings.

Table 2. O:Zr Peak-to-Peak Ratios for E-Beam Evaporated Coatings

| Coating Run * | Substrate Temperature | O₂ Pressure | Thickness (in Å) | O:Zr P-P Ratios | | | Comments |
				Surface	Near Surface	Coating Profile	
EC 5	140°-160°C	–	1182	3.5	3.5	3.2	
EC 9	140°-160°C	–	741	3.8	3.4	3.3	High deposition rate (10-12 Å/s)
EC 14	140°-160°C	5×10^{-5}	564	4.5	3.7	3.7	
EC 17	140°-160°C	–	546	4.8	3.8	3.8	
EC 18	240°-260°C	5×10^{-5}	561	–	3.4	3.4	Contaminated
EC 21	240°-260°C	–	573	4.5	3.8	3.9	
EC 22	140°-160°C	5×10^{-5}	604	4.3	3.3	3.4	Contaminated
EC 25	140°-160°C	–	558	4.5	3.6	3.7	

* EC – E-beam evaporated coatings.

Analysis of the ZrO_2 coatings revealed several factors which were common to the majority of UHV coated samples. These factors were:

1. A large number of the coatings contained insignificantly small amounts of carbon. This implies that the UHV coatings were cleaner than similar coatings produced in conventional HV systems.

·2. The O:Zr ratio for every UHV coating was compared with the ratio associated with the ZrO_2 source. In every case, the ratio for the coating was found to be lower than that for the source.

3. The O:Zr ratio inside the coating was lower than the ratio at the surface. This result simply confirms that free Zr at the surface of the coating combines with oxygen.

4. Figures 1 and 2 illustrate the main Zr peak, MNN, of the Auger spectrum of a coating at the surface and near-surface. The MNN Auger peak of Zr (the lowest negative excursion near 140 eV in the survey spectrum) had a different shape and energy peak position at the surface than that inside the coating. This was true even if only 15-20 Å of the coating were removed. The location of the Zr peak in the spectra indicates whether the Zr detected is in chemical combination with other elements or not; the Zr peak observed indicated that some of the Zr within the coating existed in the form of a free metal.

A survey of the data presented in tables 1 and 2 reveals correlations of the stoichiometric properties of the deposited films with both the deposition techniques and the deposition conditions. These correlations are summarized below.

3.2.1. CW Laser UHV Coatings

The O:Zr ratio for a high-temperature deposition is lower than that for a low-temperature deposition in coatings deposited with the same O_2 backfill pressure. This indicates that there is more oxygen loss from coatings at elevated temperatures than at low temperatures.

Among those coatings deposited at the same temperature, there was no systematic dependence between the O:Zr ratio and the O_2 backfill pressure. This implies that molecular oxygen does not combine significantly with the oxygen-deficient oxide during the deposition process.
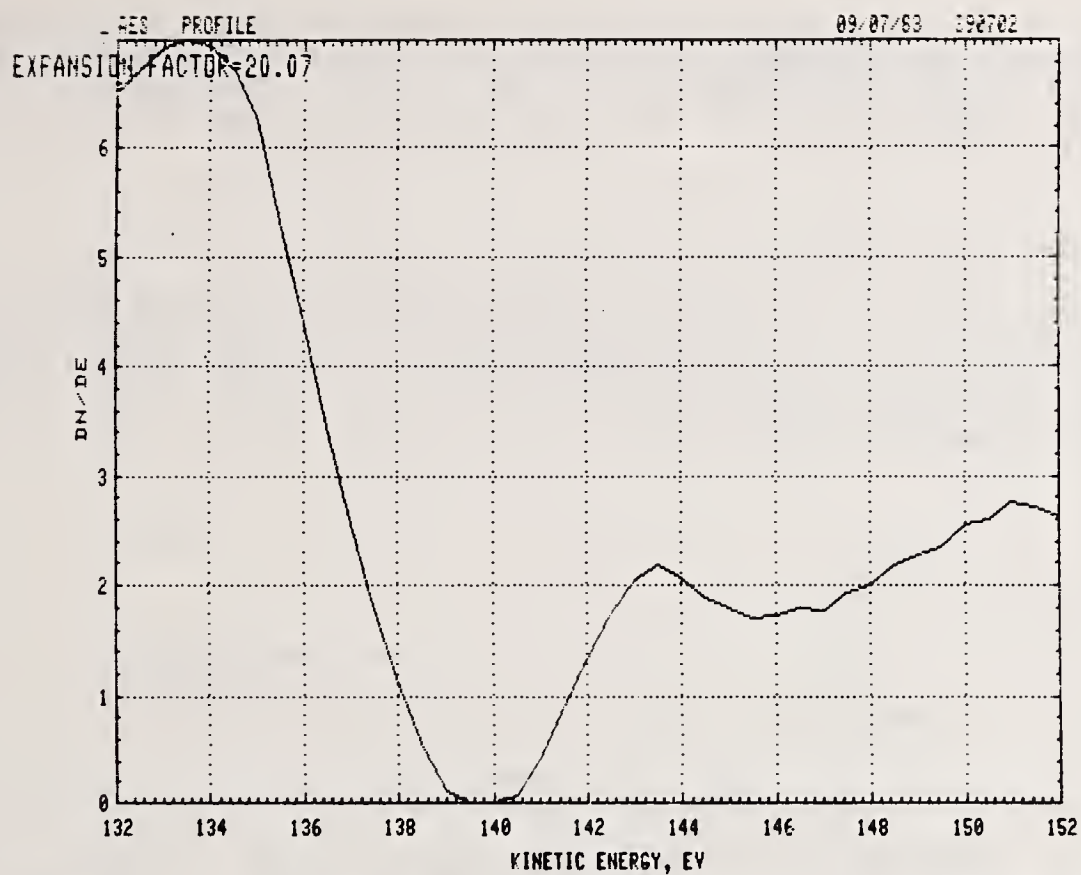
Figure 1.   Zr MNN Auger Peak from a ZrO_2 Coating prior to Sputtering
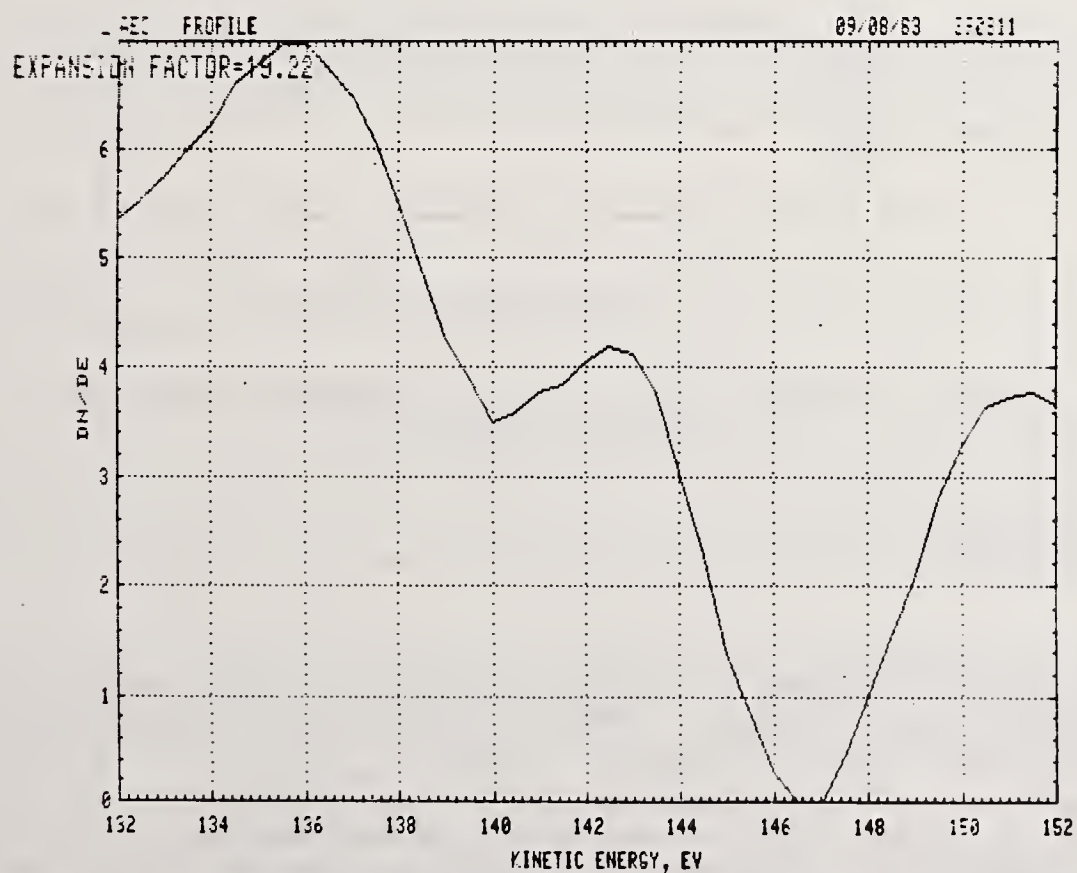
Figure 2.   Zr MNN Auger Peak from a ZrO_2 Coating after Sputtering

3.2.2. E-Beam UHV Coatings

The influences of temperature and O_2 backfill pressure on the film stoichiometry were not pronounced. However, two statements can be made with respect to the data collected: (1) the E-beam evaporated coatings have lower O:Zr ratios than the ratios measured for the CW laser coatings; and (2) a larger fraction of the E-beam coatings have been found to be contaminated as compared to the CW laser coatings.

3.3. Refractive Index Analysis

The refractive indices of all the ZrO_2 coatings deposited in the UHV during this phase were determined from ellipsometric analysis at 6328 Å. Figure 3 shows the refractive index dependence on O_2 backfill pressure for CW-laser-evaporated coatings at both low and high substrate temperatures. The data presented represent the average of several coating runs. Figure 4 shows the results for E-beam-evaporated coatings.
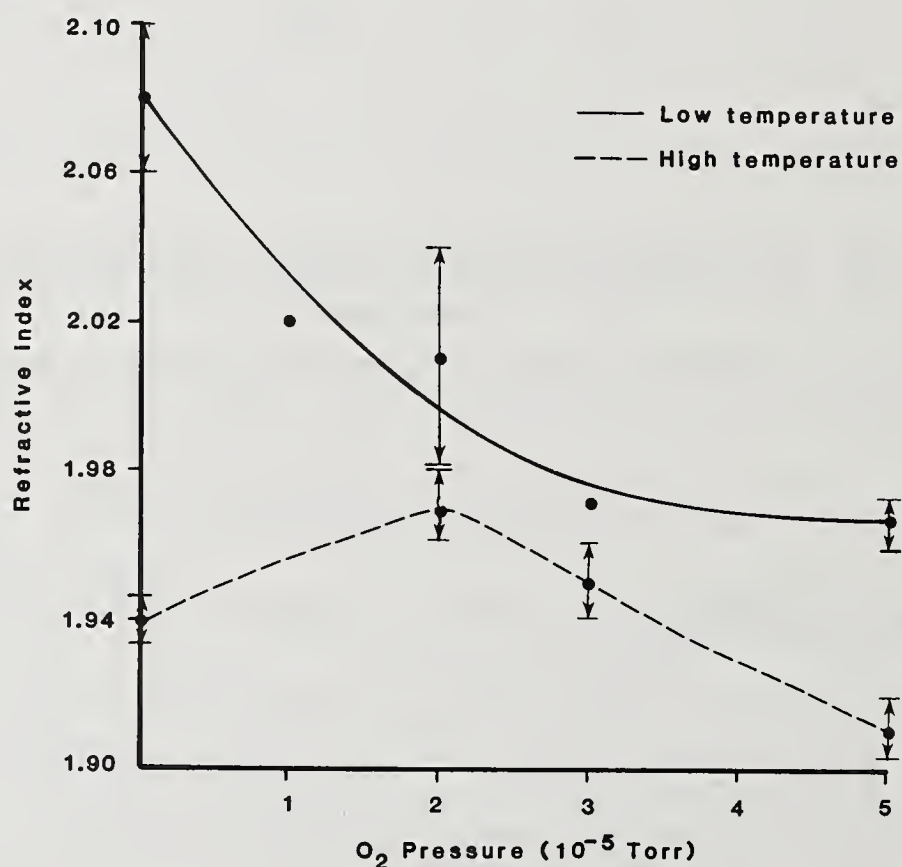
Figure 3. Refractive Index of CW Laser Deposited Coatings vs O_2 Backfill Pressure

3.3.1 Laser Evaporation

Three distinct features are observed in the refractive indices of the laser-evaporated ZrO_2 coatings. These are: (1) a monotonic decrease in the refractive index (away from the bulk index) with increasing O_2 backfill pressure, (2) lower values for the refractive index at high substrate temperatures, and (3) the abnormally low refractive index (1.94) on high-temperature substrates without oxygen backfill. Three film properties could be responsible for this behavior: stoichiometry, structure and purity. It has been pointed out that the O:Zr ratio is independent of O_2 backfill pressure at a given substrate temperature. For low temperatures, the monotonic behavior was observed on clean coatings. By process of elimination, it may be concluded that this monotonic decrease in refractive index is due to the entrapment of molecular oxygen in the coating which, in turn, results in reduced film density.

176
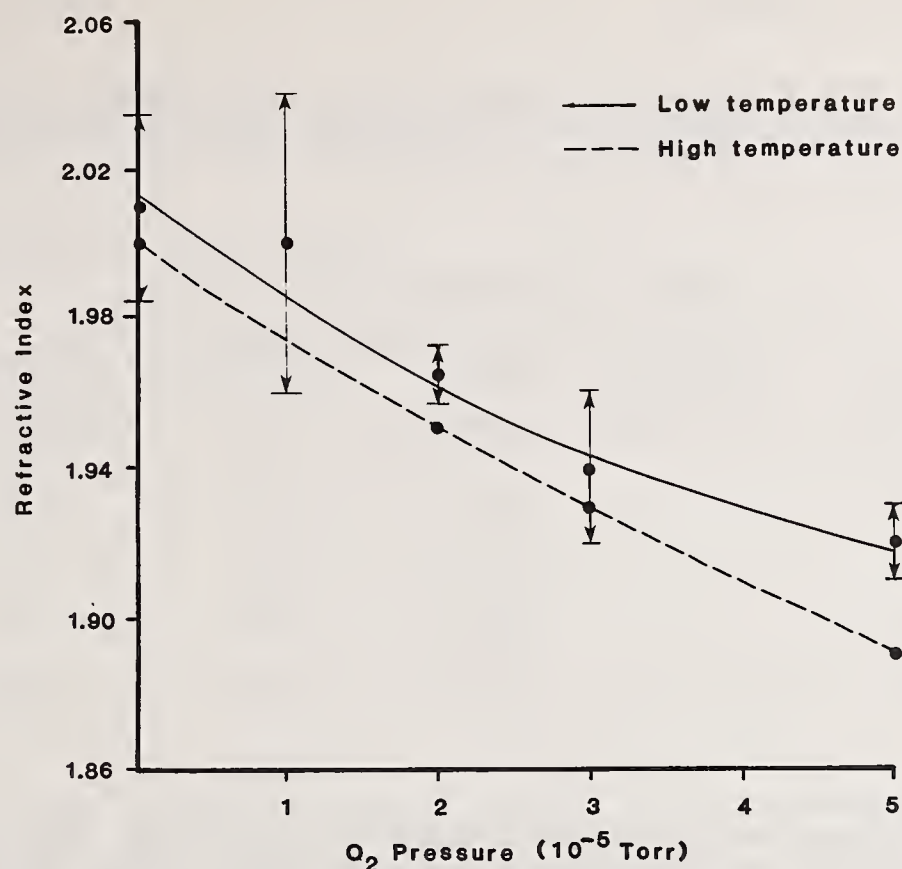
Figure 4. Refractive Index of E-Beam Deposited Coatings vs
O_2 Backfill Pressure

AES analysis indicated that the high-temperature coatings exhibited an even lower $O:Zr$ ratio than the low-temperature coatings. This observation is in agreement with the observation that the high-temperature coatings have a lower refractive index.

The abnormally low refractive index value observed at high substrate temperatures without back-fill oxygen does not appear to be an anomaly since several coating runs yielded similar results. Also it would not seem to be associated with contamination, since most of the coatings made under these conditions were relatively clean. We offer no explanation for this behavior.

3.3.2. E-Beam Evaporation

For E-beam coatings, there is a general trend for the refractive index to decrease with increased O_2 backfill pressure.

The distinction between high- and low-temperature E-beam depositions, although real, is rela-tively minor. This lack of a significant distinction could be due to variations in the deposition rates, to fluctuations in the O_2 pressure, or to the level of contamination (AES analysis in-dicated that these coatings generally had a higher level of contamination than CW-laser-evaporated coatings). Of more significance is the fact that AES analysis indicated that the stoichiometry was about the same for both high- and low-temperature coatings. This would account for the lack of dis-tinction between the refractive indices.

Another observation associated with E-beam coatings is that the presence of an O_2 backfill does not result in a change in film stoichiometry. Thus, the monotonic decrease of refractive index with an increase in O_2 pressure is structure related. Like the CW-laser-evaporated coatings, this is probably due to the entrapment of molecular oxygen, which causes a decrease in the density of the film.

An important final observation is that the indices of refraction of the CW laser coatings are greater than those of the E-beam coatings. This is consistent with AES analyses which indicated lower $O:Zr$ ratio in the E-beam coatings than in the CW laser coatings.

177

3.4.   Miscellaneous UHV Coatings

Table 3 below lists the properties of several ZrO_2 coatings which have characteristics different from those summarized above, but which were deposited during the course of these investigations.

Table 3. Miscellaneous UHV Coatings

Coating Run	Substrate Temperature	O_2 Pressure (10^{-5} torr)	Coating Thickness	Refractive Index	O:Zr Peak to Peak Ratio Surface	O:Zr Peak to Peak Ratio Coating Profile
LC 27	140°–160°C	9	222Å	1.95	4.8	4.9 ± 0.1
LC 28	140°–160°C	5	167Å	1.97	4.8	5.0 ± 0.1
LC 35	140°–160°C	2	343Å	2.03	4.5	4.1 ± 0.1
LC 30	140°–160°C	2	822Å	1.99	4.6	4.1 ± 0.1

For very thin coatings, LC27 and LC28 (thickness less than 250 Å), the O:Zr ratio, at the surface as well as within the coating, approaches the bulk value. However, the refractive indices for these coatings (1.95 and 1.97, respectively) are lower than that of the bulk index. This implies that stoichiometry alone is not the only factor in determining the refractive index; the structure of the coating must also play an important role. It is perhaps of significance that these very thin coatings were deposited at a high O_2 backfill pressure.

Coating LC35 was deposited at an O_2 backfill pressure of 2×10^{-5} torr. At the end of the deposition, the substrate temperature was raised from 150°C to 235°C; the substrates were subjected to a thermal soak in a 2×10^{-5} torr O_2 atmosphere for one hour. Subsequent AES analysis revealed that the O:Zr ratio was the same for this coating as for another coating (LC30) which was not thermally soaked. However, the refractive index had increased from 1.99 (LC30) to 2.03 (LC35). Thus, the thermal soak in the presence of O_2 would seem to produce a rearrangment of O_2 within the ZrO_2 matrix and a corresponding change in refractive index.

3.5.   HV Coatings

A coating deposited by E-beam evaporation in the HV system was analyzed using AES surface and profile techniques. The deposition parameters and conditions were similar to those in the UHV system. The carbon level was found to be ten atomic percent (ten atomic percent means there is one carbon atom for every ten zirconium dioxide molecules). The coating represented one of the highest quality HV coatings produced in the DOF. However, the level of carbon indicates clearly that HV coatings generally exhibit a higher degree of contamination than UHV coatings, a result which is to be expected.

Ellipsometric methods reveal that the indices of refraction for HV coatings are lower than those for coatings deposited in the UHV system (both laser coatings and E-beam coatings). It was also evident that the the repeatability of refractive indices of the HV coatings was not as good as it was for coatings produced in the UHV system.

Also of note is the comparative homogeneity of HV and UHV coatings; the HV coatings being less homogeneous than the UHV coatings. Coatings from the HV system that did exhibit good structure, as evidenced by good homogeneity, had very low indices of refraction, typical values ranging from 1.82 to 1.85.

3.6. Damage Test Results

Coating samples for damage testing were prepared by depositing one-half wave of ZrO_2 on superpolished fused silica substrates. The coatings were deposited in the UHV system by both CW laser and E-beam evaporation and in the HV system by E-beam evaporation.

The samples were damage tested by the AFWL at a wavelength of 531 nm. The damage thresholds (0% probability) are summarized in table 4 below.

Table 4. Damage Threshold of ZrO_2 Coatings at 531 nm

UHV Laser	UHV E-beam	HV E-beam
4.3 J/cm^2	4.3 J/cm^2	4.1 J/cm^2
4.5 J/cm^2	1.3-4.4 J/cm^2	6.8 J/cm^2
2.75 J/cm^2	6.5 J/cm^2	3.8 J/cm^2

Although the damage thresholds of the HV coatings are about the same as those for the UHV coatings, the results are inconclusive. This is probably due to the fact that only a limited number of samples were tested, resulting in a large statistical spread in the measurements. Furthermore, the UHV laser coatings were deposited under unfavorable conditions (deposition rates were far below the rates normally used and the substrate temperature was much higher than planned). Further work is planned under improved conditions.

4. Summary and Conclusions

Many aspects of this investigation are yet to be completed. In particular, extensive work will be required to establish a correlation between the controllable deposition parameters and damage threshold. However, from the work conducted to date the following conclusions may be drawn:

1. The stoichiometry of ZrO_2 films deposited via electron beam or laser evaporation is not directly influenced by molecular oxygen at backfill pressures up to 5×10^{-5} torr.

2. The stoichiometry of ZrO_2 films deposited on substrates at 150°C is superior to that obtained at higher substrate temperatures. Also, the refractive indices obtained at the lower substrate temperature are closer to that of the bulk material as compared to the refractive indices obtained at higher substrate temperatures.

3. The optical isotropy of ZrO_2 coatings deposited by either electron beam or laser evaporation methods in a UHV environment is superior to the isotropy of coatings deposited in a HV environment.

4. The existence of free metal and/or suboxides of ZrO_2 has been established in all coatings irrespective of the method of evaporation or vacuum environment.

5. The contamination level of ZrO_2 coatings deposited in a UHV environment is at least an order of magnitude less than the level found in coatings produced in a HV environment.

Oxygen Threshold for Ion-Bean Sputter Deposited Oxide Coatings

H. Demiryont and J. R. Sites

Physics Department, Colorado State University
Fort Collins, CO 80523

Reactive ion-beam sputter deposition, using a mixed argon-oxygen beam, has been demonstrated to be an effective technique for fabrication of dense, amorphous TiO_2, Ta_2O_5, and SiO_2 coatings. For both elemental and oxide targets there is a critical level of oxygen in the beam necessary to produce stoichiometric films. This threshold is seen in the films' composition, refractive index, and optical band gap. With elemental targets there is a major reduction in deposition rate at the oxygen threshold, strongly implying that an oxide layer is formed on the target, and is subsequently sputtered onto the substrate.

Key words: amorphous; ion beam; optical band gap; optical coatings; reactive sputtering; refractive index; silicon oxide; tantalum oxide; titanium oxide.

1. Introduction

Thin oxide films for optical coating applications can be produced by bombarding a target of the desired material with a beam of argon, or other inert gas, ions. In general, however, the oxygen content of the deposited film is somewhat lower than that of the target. Stoichiometry can be maintained by adding a small amount of oxygen to the bombardment beam, or by adding a second ion-beam directing oxygen at the deposition substrate. In fact it may be preferable from impurity considerations to use an elemental target, such as very pure titanium metal, and add sufficient oxygen to the system to produce stoichiometric TiO_2 [1]. The practical question then becomes how much oxygen is required, and what factors affect that amount.

2. Experimental

Films of silicon, tantalum, and titanium oxides were sputter deposited using a 5 cm diameter bombardment beam from a Kaufman-type ion source [2]. The beam was a mixture of argon and oxygen with ion energy 1100 eV and ion flux typically 1 mA/cm^2. To minimize beam divergence and target charging effects electrons were added to the beam with a hot wire filament. Films were deposited on glass, quartz, or silicon depending on the analysis to be done. Film thickness, as well as refractive index and extinction coefficient as a function of wavelength, were extracted from optical transmission data [3,4]. Thicknesses were generally 200-300 nm, and all films were dense and nearly amorphous.

Optical bandgap was deduced using amorphous semiconductor theory [5] from the extrapolated intercept of $(\alpha h\nu)^{1/2}$ vs. $h\nu$, where α is the absorption coefficient and $h\nu$ the photon energy. Composition was determined from x-ray photoelectron spectroscopy (XPS) by measuring the fraction of Si, Ta, or Ti in each observed bonding state [6,7]. The composition parameter x is defined to be 1 under stoichiometric conditions, and in general the ratio of oxygen atoms present compared to the number needed for stoichiometry. The XPS determination was in all cases consistent with the composition estimate made from the optical constants.

3. Results

Dispersion curves for tantalum oxide films are shown in figure 1. In each case a pure tantalum target was used, the total background pressure in the deposition chamber was 8×10^{-5} torr [1×10^{-2} Pa], and the beam current density was 1.0 mA/cm^2. As the oxygen fraction of the ion-beam, and hence the background partial pressure is raised, the films approach stoichiometric Ta_2O_5. The visible and infrared absorption becomes very small, the absorption edge converges to an optical bandgap of 4.3 eV, and the refractive index at longer wavelengths goes to 2.1. The critical background pressure to produce a stoichiometric film is 40-50%.
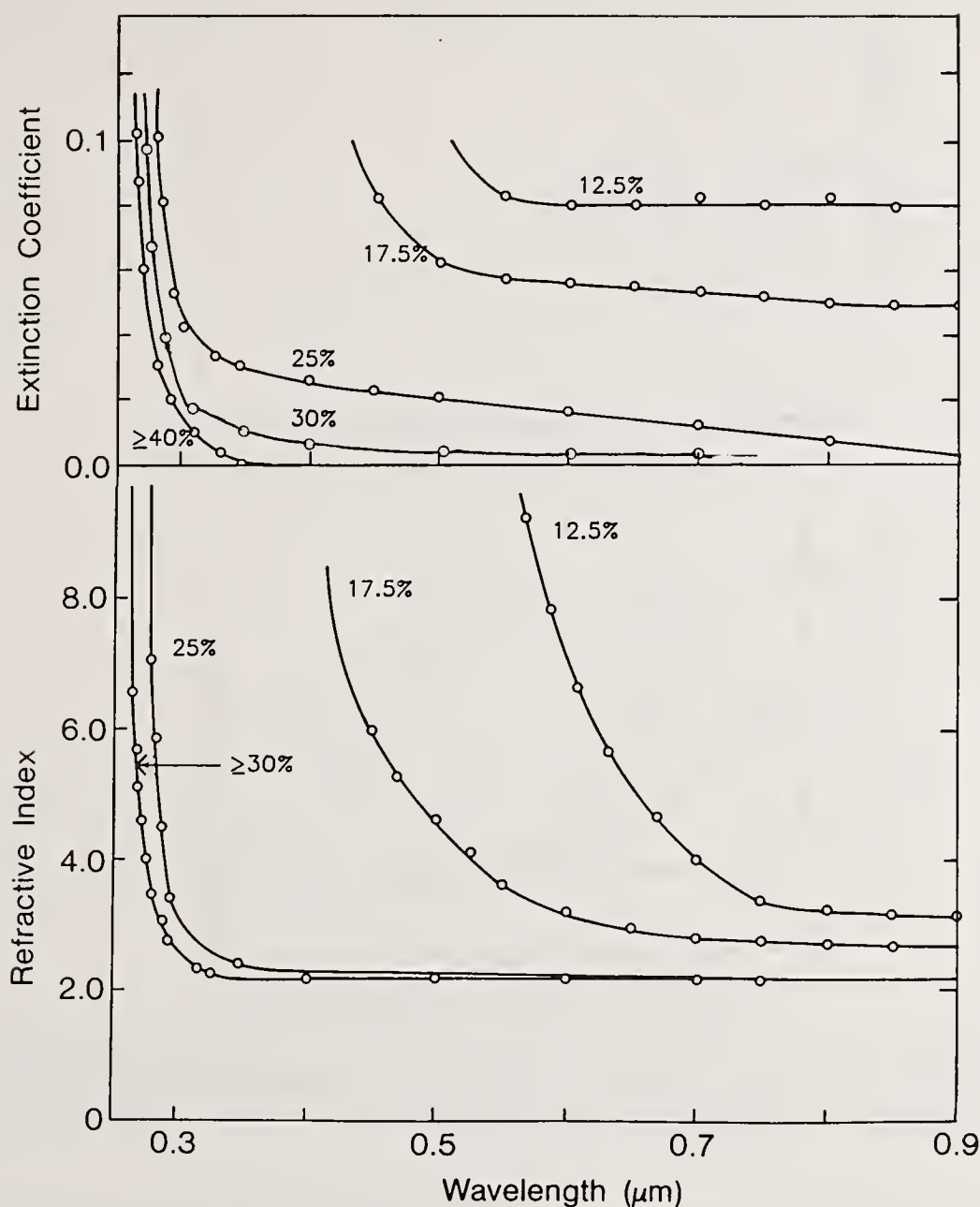
Figure 1. Dispersion curves for tantalum oxide films ion-beam sputter deposited with varying amounts of oxygen in the primary beam. Percentages refer to the fractional amount of oxygen background pressure.

A similar convergence of dispersion curves is found for oxides sputtered from elemental titanium and silicon targets. The critical oxygen background pressure for stoichiometric TiO_2 is somewhat less than for Ta_2O_5; for SiO_2, it is greater. Figure 2a shows the degree of stoichiometry as a function of oxygen background. As can be seen the silicon oxide did not become stoichiometric SiO_2 at the highest oxygen fraction used. In contrast, a SiO_2 target will yield an SiO_2 film with only a small amount of oxygen in the chamber.

There is a strong correlation between the composition of a sputtered film and deposition rate, shown in fig. 2b. The drop in deposition rate with oxygen background corresponds to the difference between a high sputter rate for an elemental target and a slower one for an oxide target. The silicon target rate in fact approaches that of our SiO_2 target in the limit of large oxygen background. The strong implication is that background oxygen is oxidizing the target. if the oxidation rate is faster than the sputter rate, a stoichiometric oxide is sputtered. If it is less, than target oxidation is not complete and an oxygen deficient film is sputtered. The model we suggest is very similar to that of Castellano [8] with slight differences noted below.

181
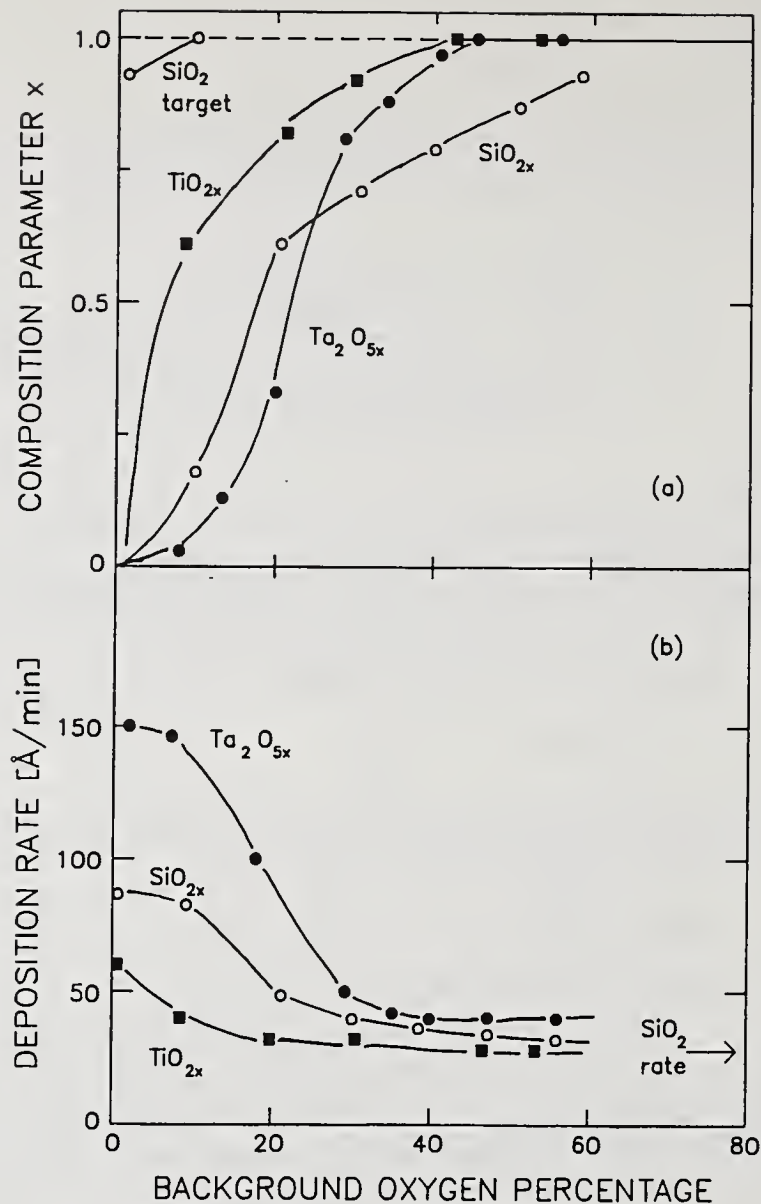
Figure 2. Composition and deposition rates of ion-beam sputter deposited oxides as a function of oxygen background. Total background pressure was 8×10^{-5} torr. Ion beam flux was 1.0 mA/cm^2.

There is (fig. 3a) a dramatic change in the optical band gap of the deposited layers with oxygen background. However, as is suggested in fig. 1a, the convergence of the band gap is less sensitive to the degree of stoichiometry than the longer wavelength absorption, known as the Urbach tail [9]. Furthermore, it is this longer wavelength absorption which is important to minimize in practical optical coating applications. This point is illustrated for silicon oxides in fig. 3b where the absorption, particularly in the 2-4 eV region, increases dramatically with oxygen deficiency.

4.   Model

Returning now to the oxidized target model of deposition, the target should look like the sketch in fig. 4 when a stoichiometric oxide is being sputter deposited. The oxide thickness z must of course be greater than the maximum depth from which material is sputtered. The graph shows the competition between oxidation rate R_{ox} and target sputter rate R_s. In this case sufficient oxygen is available to form a 60 Å thick oxide layer, and for sputtering purposes one has an oxide target. However, if one lowers the oxygen availability or raises the sputter rate, the curves will either cross at a very low oxide thickness or not at all. In either case the target material sputtered will be deficient in oxygen.

182
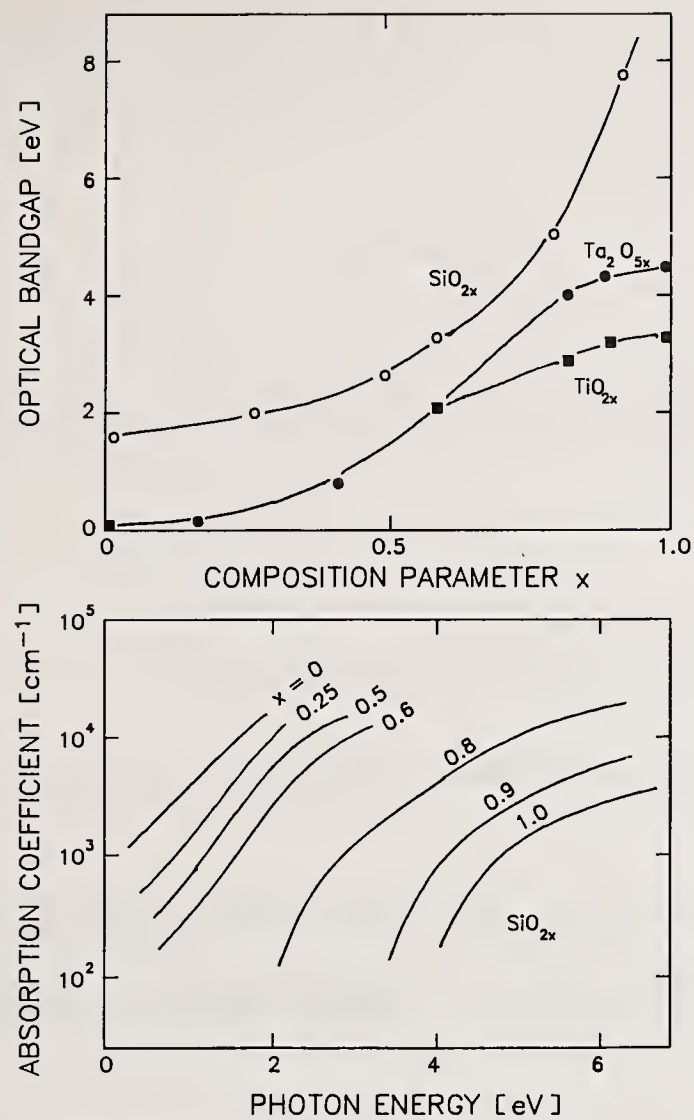
Figure 3. (a) Optical bandgap as a function of composition for silicon, tantalum, and titantium oxides. (b) Optical absorption curves for silicon oxides of varying composition.
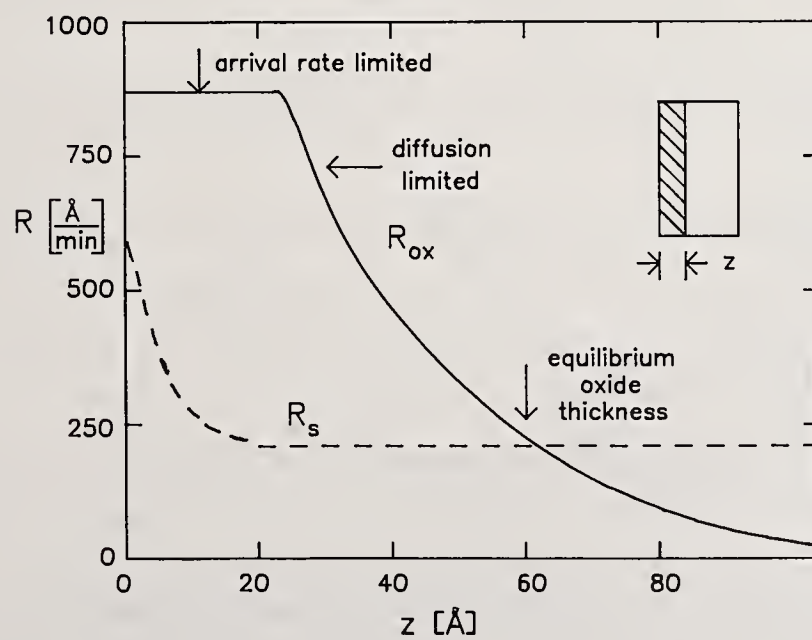
Figure 4. Possible oxidation and sputter rates for an elemental target as a function of the oxide thickness z.

The critical pressure for stoichiometry occurs when the solid and dashed curves intercept at zero. Changes in target temperature will alter the diffusion limited part of the solid curve, but should have little effect on the critical pressure. The only difference in Castellano's model [8] is that he assumes that only a monolayer of oxygen coverage is necessary to create an oxide-like target. From either viewpoint, Castellano's prediction of the critical oxygen pressure

$$P_{ox} = 3 \times 10^{-5} \frac{R_{SM}}{\Delta G_o} \text{ torr} \tag{1}$$

should be valid. R_{SM} is the sputter rate of the metal, and ΔG_o is the free energey of formation. Using our values of sputter rates (approximately 4 times our deposition rates) and published free energies [10], we find

$$P_{ox}[TiO_2] \approx 3.5 \times 10^5 \text{ torr} \tag{2a}$$

$$P_{ox}[Ta_2O_5] \approx 4 \times 10^5 \text{ torr} \tag{2b}$$

$$P_{ox}[SiO_2] \approx 5 \times 10^5 \text{ torr} \tag{2c}$$

With a total argon-oxygen pressures of 8×10^{-5}, these values correspond to oxygen percentages of 44%, 50%, and 63% respectively, in rough agreement with the data shown in figs. 1 and 2.

Equation (1) further predicts that if the sputter rate R_{SM} is increased, the critical oxygen pressure will be proportionally increased. Figure 5 illustrates the point by showing the changes
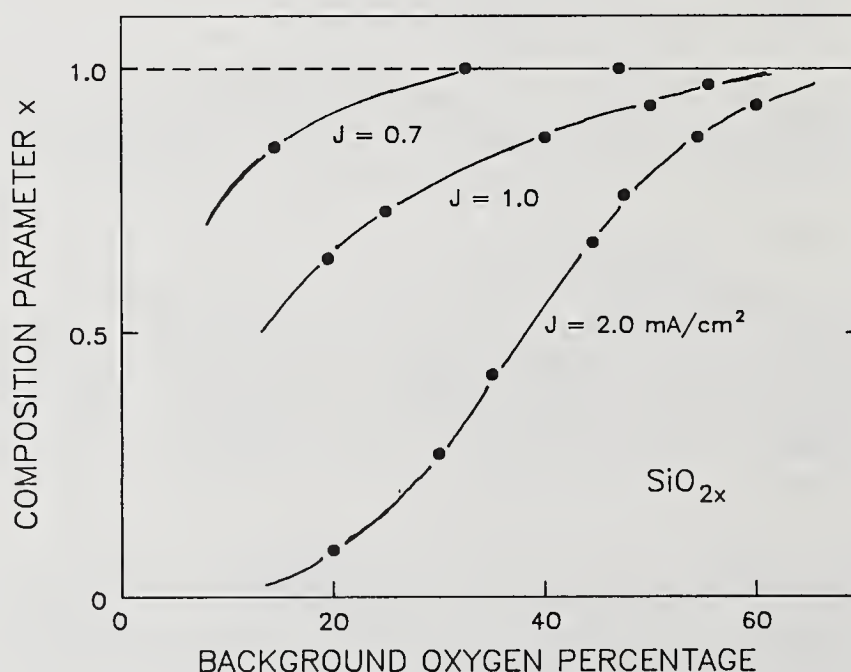
Figure 5. Effect of sputter rate on the increase in composition parameter with background oxygen.

in stoichiometry for silicon oxide films when the ion-beam current density, and hence the sputter rate, is decreased by 30% and increased by a factor of two. The roughly proportional shift in background oxygen needed to maintain constant composition confirms that it is the oxygen background, not the oxygen in the sputter beam, that controls the sputter rate. Thus, one may with some confidence construct the critical oxygen pressure vs. beam density curves of fig. 6. Use of the other elemental targets will require different slopes, which may be related to one of these oxides through the relative ratios of R_{SM} to ΔG_o.

184
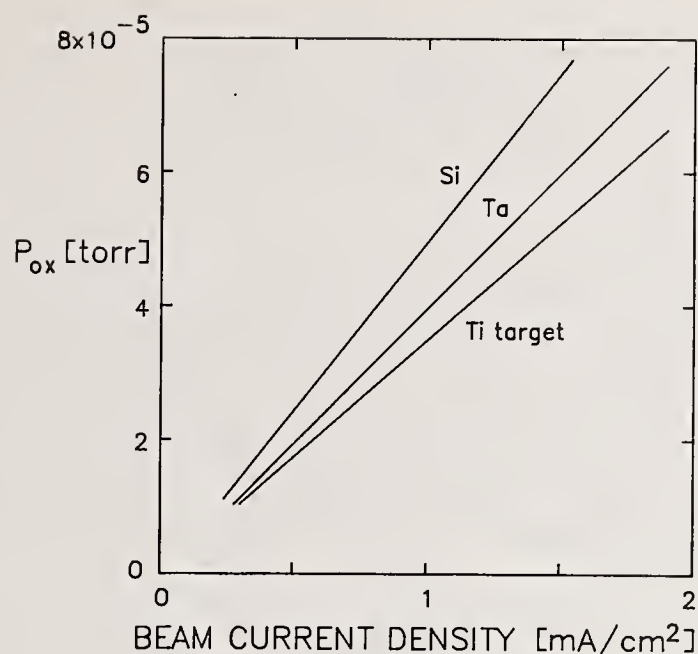
Figure 6. Critical oxygen background pressure P_{ox} to produce stoichiometric oxides by ion-beam sputter deposition of elemental targets.

5. References

[1] Sites, J. R.; Gilstrap, P.; Rujkorakarn, R. Ion beam sputter deposition of optical coatings. Optical Engr. 22(4): 447-449; 1983 July/August.

[2] Kaufman, H. R.; Cuomo, J. J.; Harper, J. M. E. Technology and applications of broad-beam ion sources used in sputtering. Part I. Ion source technology. J. Vac. Sci. Technol. 21(3): 725-736; 1982 September/October.

[3] Manifacier, J. C.; Gasiot, J.; Filland, J. P. A simple method for the determination of the optical constants n, k and the thickness of a weakly absorbing thin film. J. Phys. E: Sci. Instrum. 9: 1002-1004; 1976.

[4] Demiryont, H.; Kerwin, D. B.; Sites, J. R. Optical properties of ion-beam sputtered TiO_2 films. NBS Special Publication, 1983 Boulder Damage Symposium, to be published.

[5] Tauc, J. Amorphous and liquid semiconductors. New York: Plenum; 1974.

[6] Demiryont, H.; Sites, J. R. Effects of oxygen in ion-beam sputter deposition of titanium oxides. J. Vac. Sci. Technol. A2(4): 1457-1460; 1984 October-December.

[7] Demiryont, H.; Sites, J. R.; Gieb, K. Effects of oxygen content on the optical properties of tantalum oxide films deposited by ion-beam sputtering. Appl. Opt. 24(4): 490-495; 1985 February 15.

[8] Castellano, R. N. The metal-dielectric transition pressure in reactive sputtering. Proceedings of the 7th international vacuum conference and 3rd international conference on solid surfaces; 1977; Vienna; 1449-1452.

[9] Dow, J. D. Optical properties of highly transparent solids, S. S. Mitra and B. Bendov, ed. New York: Plenum; 1979. 131-150.

[10] Handbook of chemistry and physics, 51st edition, R. C. Weast, ed. Cleveland: The Chemical Rubber Company; 1971. D69-D71.

One questioner wondered if the oxygen pressure had an effect on the physical properties such as viid density as well as on stoichiometry. The author stated that there were not many voids for films prepared in this way and effect on film phusical properties was slight. The XPS values shown were taken on the surface. After sputter etching the bulk of the film is reduced a little bit. They have tried to approach the limit of low energies for sputter etching but one is still not convinced that the bulk values are being obrained in XPS. On the other hand, these materials are chemically active so an oxide film will form on the surface and just a little sputter etch may be optimum. Another question concerned the reflective medium approximation used. Since only amorphous silicon data was used, were the films assumed to be amorphous? The author replied that the films were amorphous with a band gap at 1.75 eV. Approximately 1% off stoichiometry could be detected. The ion beams penetrated about 2 nm into the surface. If there is sufficient oxygen, the oxide layer is much thicker than 2 nm; otherwise it may be thinner than 2 nm. In response to a question of the perceived advantages of ion beam sputtering over conventional reactive sputtering, the author named three: (1) more nearly amorphous films of $SiOx$ and $TaOx$, (2) better process control and (3) higher density films because more energetic atoms strike the substrate. The main contaminant from the ion gun which gets into the film is carbon. Using XPS they have looked for contaminants, partricularly carbon and iron (because the chamber is stainless steel). They have found no iron. There is a small amount of carbon, which apprears mainly on the surface of the films. The interior of the films has a carbon level below 0.5% to 0.7%, the limit of detection using this technique. How much absorption arises from impurities is not known, but it does not appear to be a major drawback to the technique.

TOMORROWS COATINGS TODAY - THEY NEED HELP

Alan F. Stewart
Arthur H. Guenther
Air Force Weapons Laboratory
Kirtland AFB, NM 87117

A representative set of dielectric coatings prepared using novel deposition techniques have been evaluated. Single layer coatings of ZrO_2 and Al_2O_3 were deposited on super polished fused silica substrates by conventional electron beam, electron beam in UHV, electron beam with ion beam assist, CW laser in UHV, and an advanced epitaxial technique. Characterization included total integrated scatter, spectrophotometry, x-ray diffractometry and pulsed laser damage testing at 532 nm. Our results indicate that considerable additional work will be required to optimize the optical performance of coatings produced by these novel deposition methods, let alone understand the relationship between deposition process, structure, optical characteristics and durability.

Key Words: Electron beam; epitaxial; ion assisted; laser damage; laser deposition; novel deposition techniques; scattering; structure; thin film coatings; ultrahigh vacuum.

1. Introduction

In response to the growing requirement for higher quality optical coatings, thin film process development has undergone a dramatic surge in the past decade, primarily as a result of the stringent demands relating to many laser applications. In most instances, novel deposition techniques offer greater control over the coating growth process than was possible in earlier conventional thermal evaporation systems. More control over film deposition along with carefully planned and controlled experiments should be leading to a higher level of understanding and performance with proponents of each technique promising higher purity films, more stoichiometric films approaching bulk material packing densities, either completely amorphous or epitaxial films and higher laser damage thresholds than heretofore. However, as the complexity of a deposition process increases, the number of control parameters expands and it takes more time to optimize the procedure in a trial or parametric manner. This may explain why the anticipated impressive breakthroughs in thin film performance have not been evidenced to date.

The objective of this small study was to evaluate current performance levels for films produced by several novel deposition techniques. In some cases, the films tested as part of this survey were the first of their kind to reach this laboratory. No attempt has been made yet to optimize coating performance by an iterative process. Data produced thus far will serve as a benchmark to gauge against future improvements.

Refractory oxide films of ZrO_2 and Al_2O_3 were deposited on super polished fused silica substrates. These coatings were characterized using total integrated scatter (TIS), spectrophotometry, x-ray diffractometry and pulsed laser damage testing at 532 nm. Nomarski microscopy was used to study film structure and damage morphology. Overall, test results were encouraging. These films were comparable to coatings deposited by more conventional and practical techniques in most respects presaging an improvement in the future as these new processes evolve.

2. Sample Fabrication

Thin film coatings deposited at five facilities were tested in this survey. Only single layer coatings were tested. Each had an optical thickness of 1λ at 532 nm. All of the coatings tested were deposited on super polished Suprasil T22 fused silica produced by the controlled grinding technique. [1] Two substrates, SN 303 and 304, were polished and coated by one commerical vendor. The remaining 23 substrates were supplied by a second vendor after they deposited coatings on samples SN 37, 38, 84 and 85. All substrates were smooth with total integrated scatter data indicating an average surface roughness for the entire set of 5.5 ± .7 Å Rms. In addition, the Bidirectional Reflectance Distribution Function (BRDF) of these bare substrates was

measured using a variable angle scatterometer. The average scattering level for these super polished substrates was 0.265 PPM/steradian. [2] Both the TIS and BRDF data indicate that these surfaces were of good but not superior quality. Approximately half of the substrates coated in this survey were supplied with a centered sputtered molybdenum dot for film scattering measurements.

Various deposition techniques were used to fabricate these single layer coatings. The deposition methods and cleaning procedures used for each sample tested are summarized in table 1. For samples with ion beam assisted and the epitaxial coatings it was clear from normal visual observation that the substrate cleaning procedures employed were inadequate. Cleaning procedures can certainly be improved. Each deposition method is more thoroughly described in the following paragraphs.

At the Developmental Optics Facility (DOF) at AFWL, ZrO_2 films were deposited in an ultrahigh vacuum chamber (UHV) using either a standard electron beam source or a CW CO_2 laser to heat the coating material. The coating chamber base pressure was typically 5×10^{-10} Torr following a 24 hour pumpdown and bakeout cycle. During deposition, substrates in the chamber were heated to 200^0 C using Quartzline lamps and the system pressure was raised to 2×10^{-5} Torr as oxygen was bled into the chamber. The deposition rate using the electron beam source was 1 Å/sec. With an incident beam power of 70 to 100 watts, the CO_2 laser deposition rate was comparable at 0.5 Å/sec. At all times a residual gas analyzer was used to monitor the chamber environment.

An additional set of ZrO_2 coatings were fabricated at the DOF in a conventional diffusion pumped vacuum chamber outfitted with an LN_2 cold trap. The system base pressure prior to deposition was 2×10^{-6} Torr. During deposition, oxygen was bled into the chamber and the system pressure rose to 3×10^{-5} Torr. The film growth rate during this coating run was 5 Å/sec.

Ion beam assisted electron beam deposition was used to fabricate some Al_2O_3 films, in addition to a fourth set of ZrO_2 thin film coatings. During electron beam deposition an ion beam of either 600 ev O_2^+ or 100 ev Ar^+ ions bombarded the growing film. The O_2^+ ion current density was 60 µ amp/cm^2 . For the ZrO_2 films, the deposition rate was 3.5 Å/sec. The rate was slightly higher for the Al_2O_3 films at 13 Å/sec.

An advanced epitaxial film deposition process was used to fabricate Al_2O_3 and TiO_2 coatings. Details of the deposition process were not available. However these films were baked at 500°C for 10 hours after deposition.

Conventionally deposited commerical coatings of ZrO_2, Al_2O_3 and HfO_2 were included in this survey to provide baseline data. Electron beam deposition was used for each of these coating materials.

Table 1
Sample Preparation and Deposition Parameters

	Deposition Method/Parameters	Cleaning Procedure Prior to Coating
ZrO_2 Films		
SN 97, 99, 110	C.W. CO_2 laser, 70 - 100 watts UHV system, base pressure $5x10^{-10}$ Torr, Deposition pressure, $2x10^{-5}$ Torr with oxygen bleed 0.5 Å/sec deposition rate	cheese cloth rub with isopropanol, isopropanol rinse followed by isopropanol/freon vapor degreasing
SN 98, 101, 111	E beam, UHV system as above Deposition pressure, $2x10^{-5}$ Torr with oxygen bleed 1 Å/sec deposition rate	cheese cloth rub with isopropanol, isopropanol rinse followed by isopropanol/freon vapor degreasing
SN 102, 107, 108	E beam, vacuum system base pressure $2x10^{-6}$ Torr, Deposition pressure $3x10^{-5}$ Torr with oxygen bleed 5 Å/sec deposition rate	cheese cloth rub with isopropanol, isopropanol rinse followed by isopropanol/freon vapor degreasing
SN 25, 52	Ion beam assist, 600 ev O_2^+ ions, ion current density 60 μ amp/cm^2 3.5 Å/sec deposition rate	Spin cleaner with isopropyl alcohol
SN 26, 54	Ion beam assist, 100 ev Ar^+ ions, 3.5 Å/sec deposition rate	uncleaned
SN 303, 304	E beam Deposition pressure $6.5x10^{-5}$ Torr with oxygen bleed	liquid detergent followed by deionized water rinse
Al_2O_3 Films		
SN 30	Ion beam assist, 600 ev O_2^+ ions, ion current density 60 μ amp/cm^2, 13 Å/sec deposition rate	Spin cleaner with isopropyl alcohol
SN 21, 49	Epitaxial followed by baking at 500°C for 10 hrs	lens tissue and ethanol
SN 84, 85	E beam	proprietary
TiO_2 Films		
SN 22, 50	Epitaxial followed by baking at 500°C for 10 hours	lens tissue and ethanol
HfO_2 Films		
SN 37, 38	E beam	proprietary

3. Film Characterization

Coatings deposited by each technique were subjected to extensive characterization. The transmission characteristics of these films near the UV cutoff was studied using a spectrophotometer.[a] Total integrated scatter measurements provided data on the amount of apparent surface roughness induced by the coating. X-ray diffractometry was used in an attempt to study film structure. Pulsed laser damage testing was performed at 532 nm. After damage testing, the surface and damage site morphology was examined using a Nomarski microscope.

Examination of spectrophotometer curves for these films showed that the optical thickness varied considerably from sample to sample. Each thin film coating was nominally half wave at 1.06 microns. However, samples produced by the DOF had thicknesses varying from half wave at 0.89 to 1.39 microns. In addition, there were apparent differences between samples coated in the same run at DOF. These two problems were caused by the lack of calibration of a crystal thickness monitor and no planetary drive. It is not known what problems were experienced at the other facilities although the other coatings tested were generally closer to the design goal.

The transmission characteristics of these films near the UV cutoff were also compared. One ZrO_2 film, SN 25, produced by ion beam assisted electron beam deposition showed lower overall transmission, a shallower approach towards cutoff indicating higher absorption and a longer wavelength UV cutoff. The spectrophotometer curves for SN 25 and a conventional electron beam deposited ZrO_2 film, SN 303, are compared in figure 1. Similar observations hold for an Al_2O_3 film, SN 30, produced by the same technique. All other films of each type had transmission curves which, except for thickness variations, were indistinguishable.

(a) Cary 2300

190

Table 2

Damage Threshold and TIS Results

	Deposition Method	ΔTIS (Film roughness in Å RMS)	532 nm Damage Threshold (J/cm^2) ± 22%
ZrO$_2$ Films			
SN 97	CW laser, UHV		4.3
99	CW laser, UHV		4.5
110	CW laser, UHV	8.5 ± 5.8	2.8
SN 98	E beam, UHV		4.3
101	E beam, UHV		1.3 - 4.4
111	E beam, UHV	7.4 ± 3.3	6.5
SN 102	E beam, HV		4.1
107	E beam, HV		6.8
108	E beam, HV	10.8 ± 1.8	3.8
SN 25	Ion beam assist (600 ev O$_2^+$)		0.8
52	"	6.4 ± 1.8	-
26	Ion beam assist (100 ev Ar$^+$)		3.1
54	"	15.8 ± 2.4	-
SN 303	E beam	14.5 ± 1.3	2.0
304		7.3 ± 0.9	3.7
Al$_2$O$_3$ Films			
SN 30	Ion beam assist (600 ev O$_2^+$)	18.6 ± 2.5	4.0
21	Epitaxial		1.3
49	Epitaxial	37.1 ± 4.9	2.0
SN 84	E beam	10.1 ± 1.2	4.8
85	E beam	6.6 ± 0.8	2.5
TiO$_2$ Films			
SN 22	Epitaxial		< 0.5
50	Epitaxial	28.1 ± 2.1	
HfO$_2$ Films			
SN 37	E beam	5.5 ± 0.7	6.8
38	E beam	5.8 ± 0.7	6.0
SiO$_2$ Bare Surface			
SN 80	None	5.8 ± 0.8 (on Moly dot)	13.1

Total integrated scattering measurements were performed at AFWL using instruments operating at 632 and 514 nm wavelengths. Both instruments track closely with data from other laboratories as demonstrated in round robin testing.[3] Surface roughness calculations based on TIS measurements are summarized in table 2. Total integrated scatter on samples SN 97-111 were inferred from data on witness samples. In each case, the roughness quoted is the difference between measurements performed on the coated and on the uncoated substrate. Overall, the smoothest films evaluated in this study were those fabricated by a commercial vendor using electron beam deposition. Coatings produced at the DOF using electron beam and laser deposition were comparable to those commercially available. Films produced using ion beam assisted electron beam deposition were generally rougher with the exception of SN 52 which was very smooth. The advanced epitaxial technique produced films with consistently high scatter or roughness levels. Unless single crystal films can be grown using this technique, higher scattering losses may prove to be a serious penalty. It should be noted however, that these films were grown in a commercial facility for nonoptical thin film applications.

A Siemen's x-ray diffractometer was used to study the structure of a limited number of thin film coatings. This instrument is equipped with computer enhanced signal processing which provides greater sensitivity to the inherently weak diffraction maxima produced by thin film coatings. The majority of the films tested had a crystalline structure and were not amorphous as had been anticipated. Equally surprising was the fact that the observed structure varied significantly and in a reproducible fashion as the deposition process was altered between coating runs. This is observed particularly in data obtained on zirconia coatings deposited at the DOF. Coatings from each of the three deposition processes used at the DOF were measured and these diffractometer scans appear in figure 2. All three curves exhibit a large broadened peak centered at 21.5 degrees which originates from the fused silica substrate. The lower curve is representative of coatings deposited by DOF using an electron beam in a conventional diffusion pumped vacuum system. Only one very small peak occurs at 34 degrees corresponding to a lattice spacing of 2.57 Angstroms in the tetragonal form of zirconia. The middle curve is representative of coatings produced again by electron beam deposition but this time in a UHV chamber. In sharp contrast to the lower curve, these coatings exhibited many peaks corresponding to the tetragonal structure at 2.94, 2.57 and 1.80 Angstroms. The monoclinic structure was also in evidence with a small peak at 2.84 Angstroms. The monoclinic structure is again absent in the upper curve which is representative of zirconia films produced in the same UHV chamber but using CW laser deposition. Very strong peaks at 2.94, 2.62, 2.54, 1.81 and 1.53 Angstroms all relate to various orientations of the tetragonal structure.

In figure 3, additional data from zirconia films produced by ion beam assisted electron beam deposition is plotted. The lower curve from sample SN 26 (100 ev Ar^+ ions) shows no identifiable peaks other than that due to the substrate. The upper curve from sample SN 25 (600 ev O_2^+ ions) shows a strong peak at 2.84 Angstroms from the monoclinic structure and secondary peaks at 2.94 and 2.61 Angstroms from the tetragonal structure.

The x-ray diffractometer data from the majority of these zirconia films demonstrates that condensation of atoms or molecules from the vapor phase did not occur under equilibrium conditions. The monoclinic structure is the only stable phase of pure zirconia at room temperature. The tetragonal and cubic phases occur only at temperatures above 1,020°C but can be stabilized at lower temperatures by mixing with a few weight percent of alumina or yttria. However, these stabilizing agents are not present in measurable amounts in the zirconia films tested in this survey. The tetragonal form is clearly a metastable phase. It should also be clear that an amorphous zirconia film is also a metastable form. By analyzing films and relating this data back to conditions present during the deposition we may learn how a film grows.

The presence of metastable phases in thin film coatings may have serious implications. When zirconia undergoes a phase transition from monoclinic to tetragonal, the bulk density decreases by about 1.5%. However, optical properties such as refractive index have not been measured for the high temperature phase. Large differences in optical absorption and scattering have been measured between the rutile and anatase phases of titania in thin films. Recent work using Raman spectroscopy to monitor the film structure has demonstrated that phase changes in titania and zirconia films occur while annealing the films at temperatures substantially below the transition temperature for the bulk material. [4] Phase transformations may also be induced by localized heating following the absorption of laser radiation. Laser processing or annealing of thin films might prove to be of considerable benefit by producing uniform films of a stable phase as opposed to the unintentional catastrophic changes that occur during laser damage.

An alumina coating, SN 21, produced by an advanced epitaxial technique was also tested on the x-ray diffractometer. There was no apparent structure in the film. This was very suprising since even if the film had been deposited as amorphous, the long period of baking at elevated temperature might have caused conversion from the metastable amorphous phase into the crystalline phase. Titania films produced by this epitiaxial process have not been tested. However, even if these films did exhibit crystalline structure it would not be clear whether the film nucleated and grew in that form or if the film structure changed radically during the baking cycle.

Examination of both bare fused silica substrates and each coated substrate under a high contrast Nomarski microscope demonstrated a frequently observed phenomenon. The physical structure of some of the thin film coatings, as determined visually, appeared to correlate well with the surface structure of the uncoated substrates. Surfaces coated with zirconia by the DOF at AFWL appeared to be covered with a fine web of scratches as is shown in figure 4. The zirconia films deposited by three different procedures at the DOF all have similar appearances under the microscope. Total integrated scatter measurements on these coatings (table 2) indicated an average roughness of about 8 Angstroms which is excellent for the deposition methods represented in this study. However, these films have very different crystalline structures as is evidenced by the x-ray diffraction data. It is apparent that the nucleation of the coating material on these substrates and hence to some extent their scattering characteristics and physical appearance is largely dependent on the substrate surface and how it was prepared. In contrast, the crystalline structure of the film seems to be solely dependent on the deposition process used.

Thin film coatings produced by ion beam assisted electron beam deposition exhibited a different appearance under the microscope. Unlike the coatings produced at the DOF, these coatings did not appear to replicate the structure of the substrate surface. The coated surfaces appeared to be covered with randomly distributed small diameter (~ 1 μm) pits. This deposition process involves bombarding the surface with energetic and even reactive ions throughout the coating run. This type of process continuously changes the growth surface through kinetic energy transfer and sputtering with higher ion energies and it is thus logical that substrate characteristics would be less influential in the final film topography - at least at the visually observable level. The appearance of surface pitting is almost certainly related to sputtering by the incident ion beam.

Under the microscope, aluminia and titania coatings produced by an advanced epitaxial technique looked like a step backwards. These films were covered with scattering defects, perhaps crystallites, which scattered considerably in the field of view. These observations confirmed the TIS data which showed excessively high scattering levels. The overall roughness of these coatings completely dominated any contribution from the substrate. It should be noted again that these films were part of a production run for a nonoptical thin film application.

A frequency doubled Nd:YAG laser operating at 10 hz was used in damage testing. The laser was extremely stable with shot-to-shot energy fluctuations in the 1 or 2% range. The experiment configuration is detailed in figure 5. Samples were tested in the focal plane of a 2 meter focal length lens. The beam spatial profile was measured in the focal plane using the beam scan technique with a 40 micron wide slit and a sensitive pyroelectric detector. In this way the beam profile was measured to have an ellipticity which ranged from 14 to 27% over the course of these measurements. A representative beam scan appears in figure 6a. The average beam diameter ($1/e^2$ in intensity) was 520 microns. The temporal profile of the laser pulse was measured with a fast vacuum photodiode and a transient digitizer. As shown in figure 6b the waveform is three humped with a central maximum. By adjusting the oscillator pump energy, the side lobes were made to be of comparable height. The pulse duration is therefore not easily defined but was on the order of 15 nsec FWHM.

Damage testing was performed in the N-on-1 mode. The laser was used to irradiate each site with up to 100 consecutive shots. Twelve equally spaced fluence levels were used with 10 sites irradiated at each fluence level. During each irradiation sequence, the sample surface was observed with a long working distance microscope. With the onset of visually observable damage a shutter was closed to prevent splattering on nearby sites. After testing, each site was observed under a Nomarski microscope to provide an absolute determination as to whether permanent damage had occured.

The damage threshold for each sample is listed in table 2. Data was plotted up as shown in figure 7 after reference [5]. The damage threshold was defined as the maximum energy fluence for which there is zero probability of damage occuring. In some instances, the probability would rise to say 20%, fall back again to zero and then increase sharply at still higher fluences. This is

an indication that not enough sites were tested at each fluence to sample a large enough area of the coating.

Some distinct trends were observable in the data. The probability curves obtained on samples SN 25 and SN 26 appear in figure 8. Both zirconia films were produced using ion beam assisted electron beam deposition but with different ion species and different ion energies. The zero probability onset levels are quite different and the slope of the data obtained on sample SN 26 is very shallow by comparison to the steep onset of data from SN 25.

A shallow slope in the probability curve has been attributed to a defect dominated damage process [5] [6]. Sample SN 26 and each of the coatings produced at the DOF appear to have similar defects or impurities which damage at about the same fluence level. However, the density of these defects may be process dependent to some extent. The probability curve measured on coatings produced at the DOF in the UHV chamber generally exhibited shallower slopes as for SN 26 indicating a lower surface density of defects. It should be pointed out that if a larger beam diameter had been used in the test sequence those apparent differences might not have been observed. A larger beam diameter increases the probability of hitting a defect with each shot. Thus the measurement becomes more deterministic and the slope of the probability curve becomes infinite. Using a smaller diameter beam does make the measurement of an absolute threshold more difficult since more sites must be irradiated to generate a smooth curve. However, our qualitative observation of shallower slopes in the data may be an indication that coatings produced in the UHV chamber and using O_2^+ bombardment are a step in the right direction.

The damage morphology of these films was quite different from that observed in previous 1-on-1 testing at this laboratory. Instead of the isolated pits observed previously, much larger area features evolve in N-on-1 testing. The irradiation sequence of 100 shots was halted by the operator only if damage or an increase in light scattering was observed through the telescope. Even under ideal conditions the damage morphology observed after testing is a result of 2 or 3 consecutive destructive shots. However, some general statements can be made. A distinctive feature of damage sites in the zirconia films produced at the DOF appears in figure 9a. Damage sites such as this are about 50 microns in diameter and are surrounded by ejected material. In marked contrast, a damage site on zirconia produced by ion beam assisted electron beam deposition appears in figure 9b. These sites have a much "softer" appearance as the film looks as if it bubbled up on the surface. During irradiation, these coatings were not observed to eject large p-lasma plumes and there was no audible indication of a violent breakdown. The only observed change was a slow increase in the scatter levels at a site. Epitaxial coatings fall somewhere in between as is shown in figure 9c. The damage process appeared to result in a more radical or violent change than that observed in the ion assisted coatings. Although much lower fluences were required to produce damage, a pronounced halo surrounded each damage site. Normally, such a halo is associated with plasma formation. However, the overall features of these sites cannot be clearly studied since they scatter so much. This suggests that in figure 9c the disrupted material inside the halo has undergone a phase change and is the rutile phase of the titania. The observed damage morphology in the epitaxial films may then be the result of a completely different damage process.

The morphology of laser damage sites in alumina films was quite different from that observed in zirconia. As shown in figure 10a, alumina films fracture with the onset of damage. This site on sample SN 84, which is a commercial electron beam coating, shows a large damage site with a thermal or plasma halo and extensive radial fracturing. Films produced by either ion beam assisted electron beam or the epitaxial process exhibited a much different damage morphology. The fracturing, cracking or selective etching tended to pattern itself after what might have been the substrate surface structure as is shown in figure 10b. This site is from sample SN 21, an epitaxial coating with low damage threshold. The fractures are not radially oriented but seem to follow what can only be patterns of polishing scratches on the substrate surface. As stated previously, films produced by these deposition procedures do not appear to replicate the substrate surface. However, the onset of damage nearby may provide the thermal "trigger" for rapid crystallization of the amorphous or metastable film. Another possible mechanism involves the interaction of the damage site plasma with the surrounding surface. Plasmas were not observed to form with the onset of damage in these films.

4. Conclusions

The data collected after extensive film characterization has been summarized for each novel film deposition technique in table 3. The performance levels of the films evaluated in this limited survey in terms of film scattering and laser induced damage thresholds compare well with conventionally deposited films. Thus we have produced an encouraging base line upon which deposition improvements or perfection of these novel methods can ensue. The one exception was the films produced using the advanced epitaxial technique. However, even films produced by this method may perform much better if adequate cleaning procedures are utilized. Each of the deposition procedures sampled by this survey is relatively new to the scene and much work needs to be done to optimize the resultant films. The analysis and characterization work reported here is only an initialization.

The study of film structure using x-ray diffraction or other techniques provides perhaps our most important insight as to how a film grows so we can relate it to how the film damages. The presence of the metastable tetragonal phase of zirconia in laser deposited thin films does indicate that the film formed under nonequilibrium conditions. Comparison of film structure with laser damage thresholds while varying substrate temperature during deposition or in a post deposition annealing treatment is the next logical step. The sensitivity of the film structure to temperature variation is a critical unknown in itself and is currently under study. [4]

There are several inconsistencies which are yet to be resolved. For example, the damage morphology observed in films deposited by ion sputtering has been attributed to uniform film absorption because the damage site appears to replicate the beam footprint. Similiar morphology was observed in this study on thin films produced by ion assisted deposition. Yet it seems contradictory that thin films produced by the ion sputtering technique routinely demonstrate extremely low losses due to scattering or absorption. Certainly these properties are dependent on the type of film defects and impurities and their distribution. The most likely mechanism for damage in these films as in conventionally deposited films is impurity absorption. But the difference lies in that the heated impurity in the ion sputtered or ion assisted film most probably causes the surrounding material to undergo a phase change either from amorphous to crystalline or from one crystalline phase to another. This type of laser induced damage may be more prevalent in conventionally deposited films than was previously thought.

The objectives of this study have been met in that films produced by novel deposition techniques have been evaluated and compared with commerically available coatings. Even though no optimization has occured yet to maximize laser induced damage thresholds or minimize film scattering, the performance levels observed to date are encouraging. Certainly, parameterization of these deposition processes is in order followed by even more extensive film characterization. It is important to realize that a film may perform at a very high level for one application, low scatter films for laser gyros for instance, whereas these same films may not be damage resistant in HEL use. Both performance levels may be attributable to one variable - the film structure - or there may be other "hidden" variables that as yet remain unrecognized. The interrelation of film performance levels is difficult to study because there are so many variables that must be controlled. Once the salient characteristics of a film have been identified and the deposition processes completely parameterized we may reach a positon where the most suitable film can be fabricated for a given application.

Table 3

Summary of Observations/Characteristics

CW Laser, UHV

Film scattering levels, < 10 Å RMS for ZrO_2 .

Crystalline structure of metastable tetragonal phase of ZrO_2.

Film surface replicates substrate surface topography.

Medium level damage thresholds.

Slopes of damage probability curves indicate lower defect densities than found in conventional films.

Electron Beam, UHV

Film scattering levels, < 10 Å RMS for ZrO_2 .

Crystalline structure of metastable tetragonal and stable monoclinic phases of ZrO_2.

Film surface replicates substrate surface topography.

Medium to high damage thresholds.

Slopes of damage probability curves indicate lower defect densities than found in conventional films.

Ion Beam Assist

Low (~ 6 Å RMS) scattering levels are possible with O_2^+ bombardment but with lower damage thresholds.

Crystalline structure of stable monoclinic phase or amorphous in ZrO_2 and Al_2O_3.

Exterior film surface does not replicate substrate surface morphology, but internal film structure may.

Medium level damage thresholds.

Slopes of damage probability curves indicate lower defect densities with O_2^+ bombardment compared with Ar^+ bombardment.

Advanced Epitaxial

Very high scattering levels (> 20 Å RMS).

Low level damage thresholds (< 2 J/cm^2).

A member of the audience commented that he believed that ion assisted deposition should be done with ion beam potentials lower than 100 eV to avoid damage to the growing film. 600 eV potentials are too high. The author made the point that what is needed is a parametric study of deposition conditions vs. damage threshold to settle such questions. Such a study is of particular importance now since new deposition conditions are being used.

5. References

[1] House, R.A.; Bettis, J.R.; Guenther, A.H.; "Correlation of Laser-Induced Damage with Surface Structure and Preparation Techniques of Several Optical Glasses at 1.06 μm", Nat Bur. Stand. (U.S.) Spec Publ. 435, 1975, pp. 305-320.

[2] Silva, Robert M.; Orazio Jr, Fred D.; Stowell, W. Kent; "Scatter Evaluation of Supersmooth Surfaces," Musikant, Solomon, ed. Proceedings of SPIE Vol 362: Scattering in Optical Materials; 1982 Aug 25-27; San Diego, CA pp. 71-76.

[3] Bennett, Jean M; Stowell, W. Kent; "Round-Robin Testing of Low Scatter Optics", Nat. Bur. Stand. (U.S.) Spec. Publ. 688, 1983, to be published.

[4] Rujkorakarn, R.; Hsu, L.S.; She, C.Y.; "Crystallization of Titania Films by Thermal Annealing", Nat. Bur. Stand. (U.S.) Spec. Publ. (1984) to be published.

[5] Folytn, S.R.; "Spotsize Effects in Laser Damage Testing", Nat. Bur. Stand. (U.S.) Spec. Publ. 669; 1982, pp. 368-379.

[6] Seitel, S.C.; Porteus, J.O.; "Toward Improved Accuracy in Limited Scale Pulsed Laser Damage Testing via the Onset Method", Nat. Bur. Stand. (U.S.) Spec. Publ. 688, 1983, to be published.

6. Figure Captions

1) Comparison of spectrophotometer transmission curves of electron beam and ion assisted electron beam deposited ZrO_2 films.

2) X-ray diffractometer scans obtained on ZrO_2 films fabricated using laser and electron beam deposition. Films deposited in an ultrahigh vacuum system exhibit the crystalline structure of the tetragonal phase.

3) X-ray diffractometer scans obtained on ZrO_2 films fabricated using ion beam assisted electron beam deposition. Films deposited using oxygen ion bombardment exhibit the crystalline structure of the monoclinic phase.

4) Nomarski micrograph of ZrO_2 film surface texture showing replication of the substrate surface.

5) Experimental layout used in 532 mm N-on-1 laser damage testing.

6) Representative beam a) spatial and b) temporal profiles.

7) Laser damage probability curve obtained on ZrO_2 film SN 111.

8) Laser damage probability curves obtained on ion assisted ZrO_2 films.

9) Representative laser damage site morphology on a) UHV electron beam deposited ZrO_2 films; b) ion beam assisted electron beam deposited ZrO_2 films; c) advanced epitaxial process ZrO_2 films.

10) Representative laser damage site morphology on a) electron beam deposited Al_2O_3 films and b) ion beam assisted electron beam deposited Al_2O_3 films.
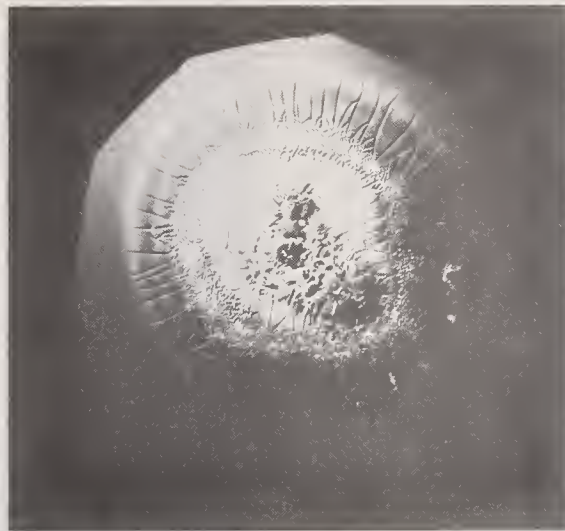
**Al₂ O₃ 532 nm DAMAGE
E BEAM**

200 μm
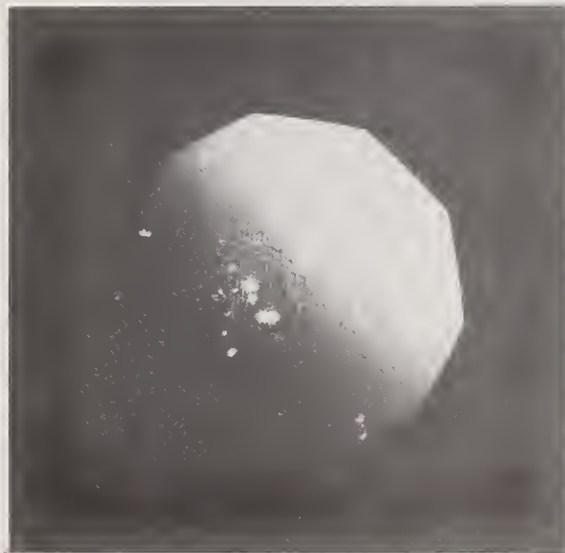
Al₂O₃ ION BEAM ASSISTED

200 μm

Figure 10: Representative laser damage site morphology on
(a) electron beam deposited Al_2O_3 films and
(b) ion beam assisted electron beam deposited
Al_2O_3 films.
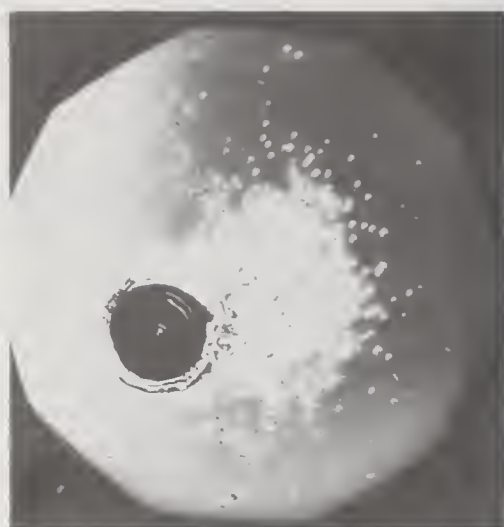
ZrO₂ 532 nm DAMAGE
E BEAM, UHV   100 μm   (a)
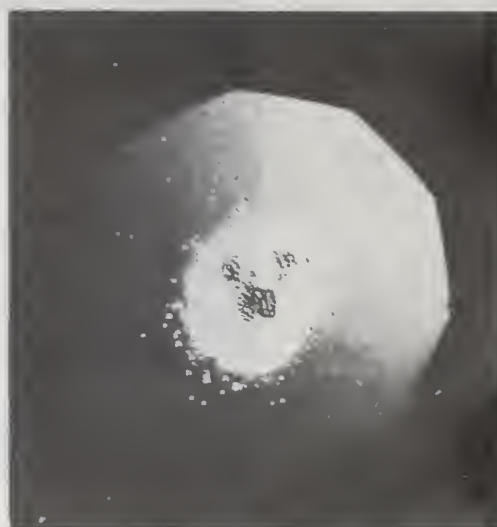
ZrO₂ 532 nm DAMAGE
ION ASSISTED, E BEAM (600 ev O₂⁺)   200 μm   (b)

TiO₂ 532 nm DAMAGE
ADVANCED EPITAXIAL TECHNIQUE   100 μm

Figure 9: Representative laser damage site morphology on
(a) UHV electron beam deposited ZrO₂ films
(b) ion beam assisted electron beam deposited ZrO₂ films
(c) advanced epitaxial process ZrO₂ films.
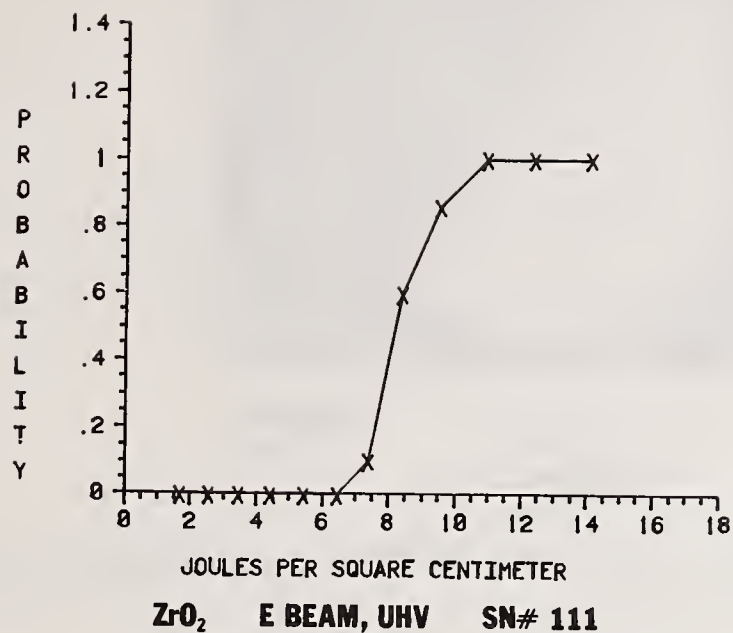
Figure 7: Laser damage probability curve obtained on ZrO_2 film SN 111.
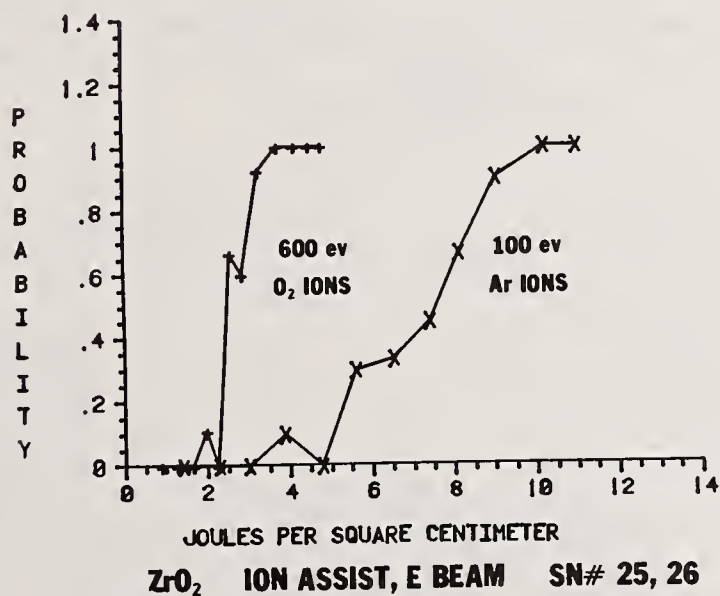
Figure 8: Laser damage probability curves obtained on ion assisted ZrO_2 films.

ZrO₂
E BEAM, UHV

200 μm

Figure 4: Nomarski micrograph of ZrO$_2$ film surface texture showing replication of the substrate surface.
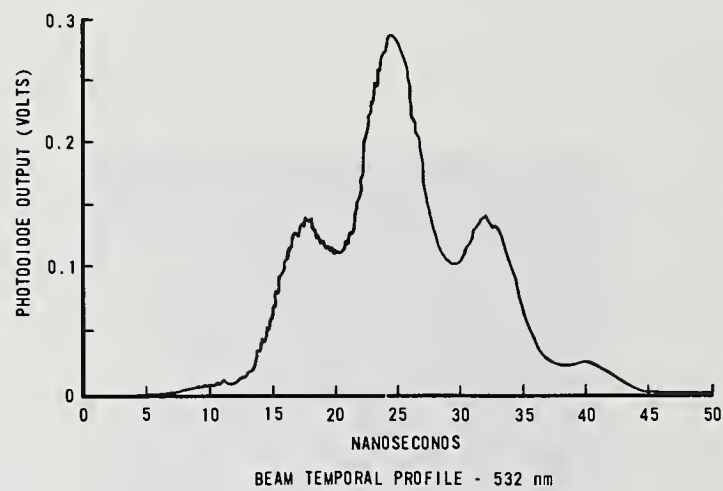
(a)
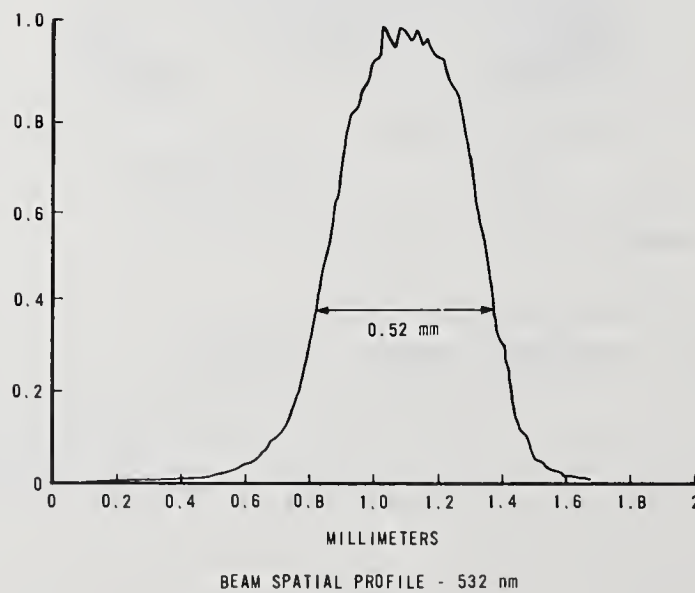
(b)

Figure 6: Representative beam
(a) spatial and (b) temporal profiles.

X-RAY DIFFRACTOMETER DATA
ZrO₂ FILMS - ION ASSIST
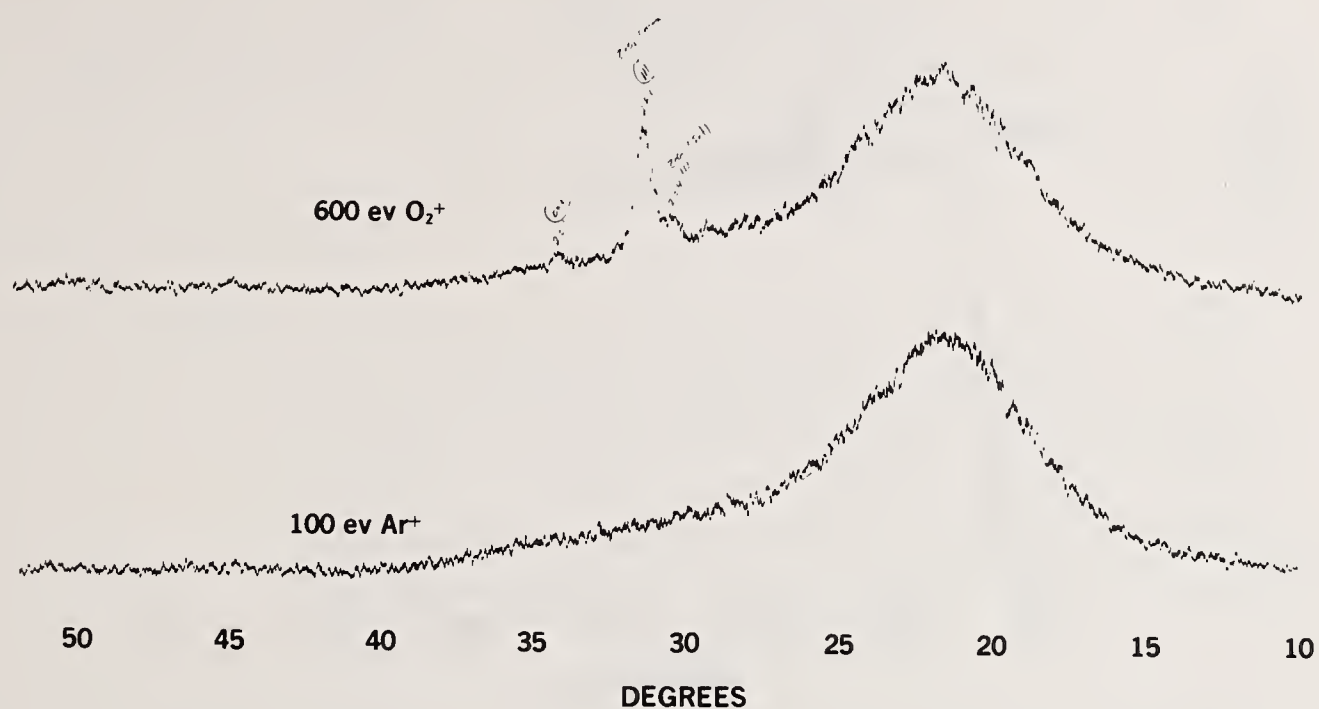
Figure 3: X-ray defractometer scans obtained on ZrO_2 films fabricated using ion beam assisted electron beam deposition. Films deposited using oxygen ion bombardment exhibit the crystalline structure of the monoclinic phase.
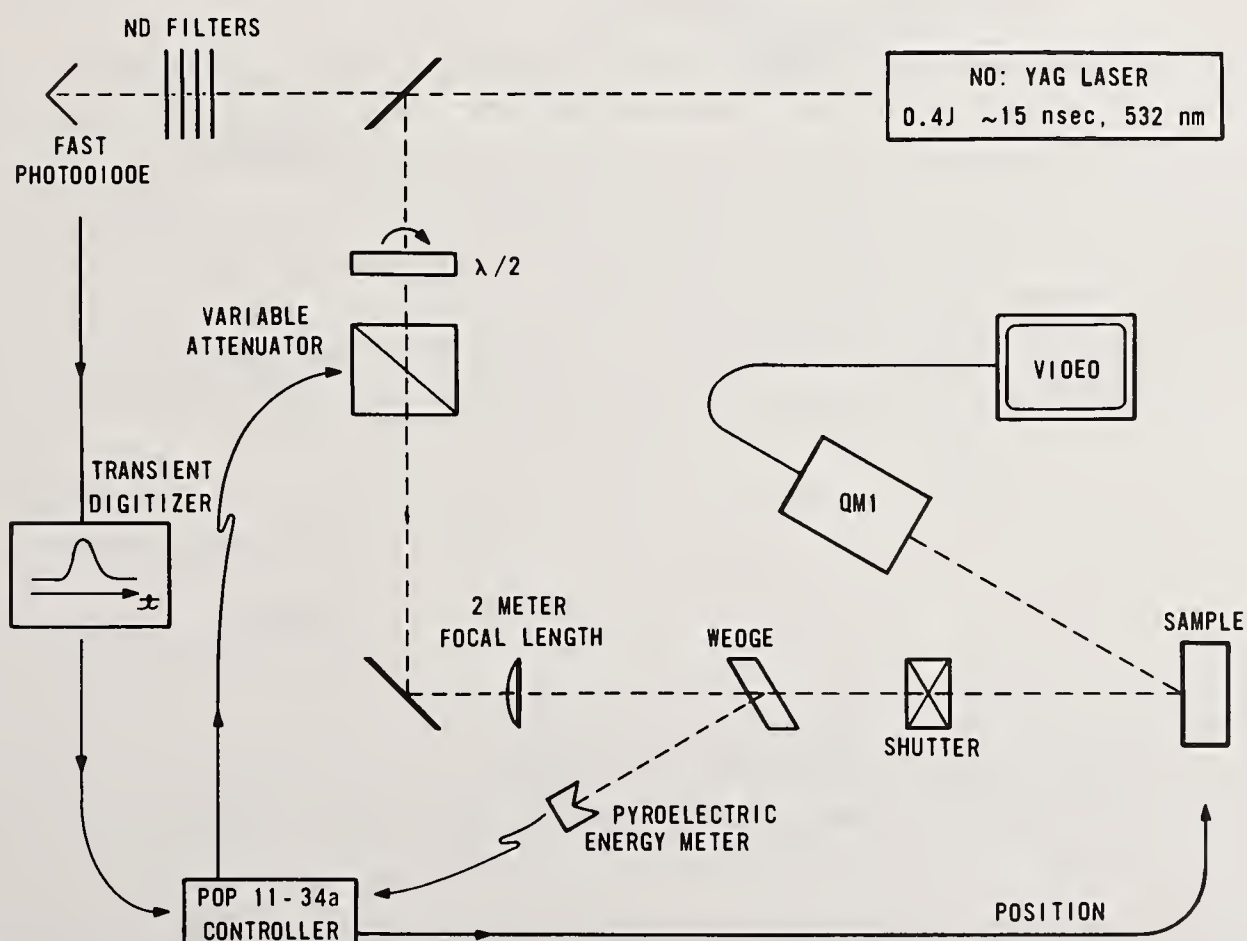
Figure 5: Experimental layout used in 532 mm N-on-1 laser damage testing.
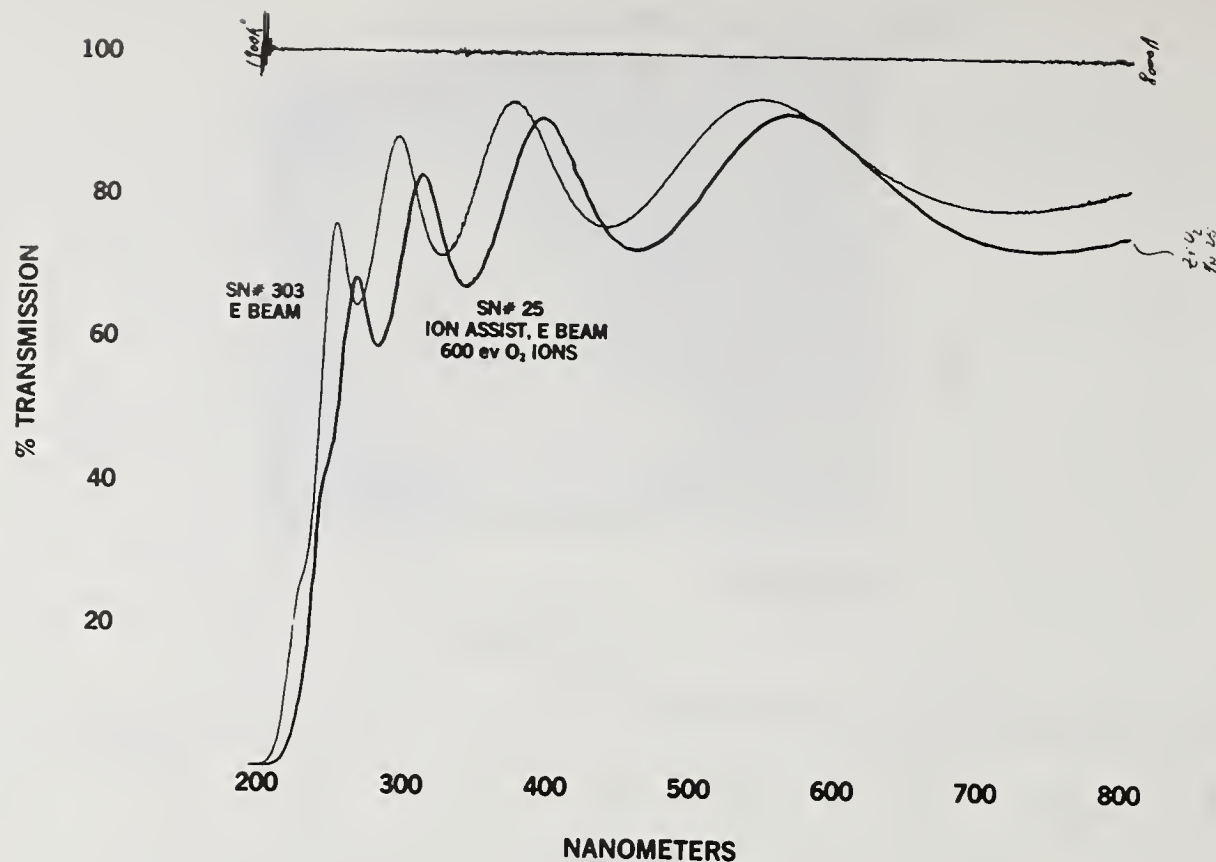
Figure 1: Comparison of spectrophotometer transmission curves of electron beam and ion assisted electron beam deposited ZrO_2 films.
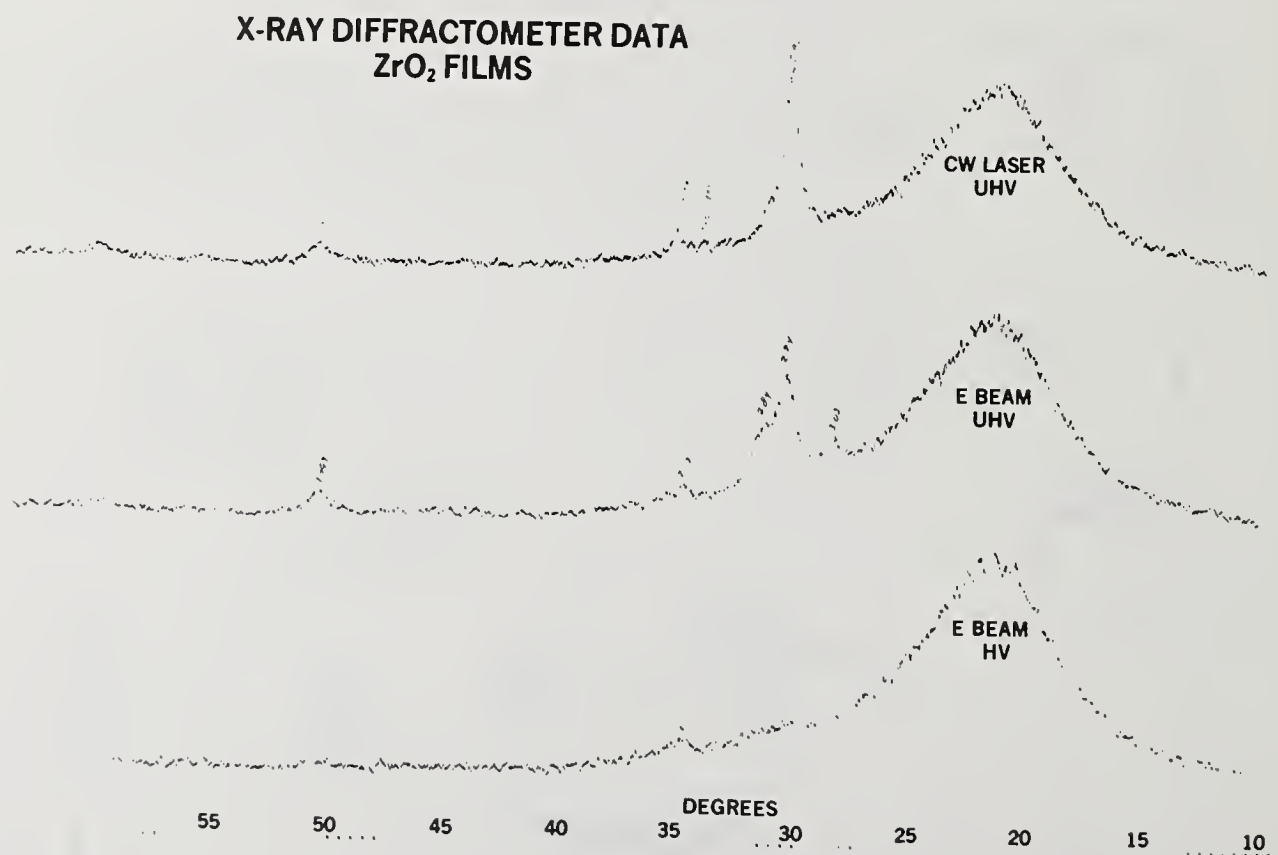
Figure 2: X-ray defractometer scans obtained on ZrO_2 films fabricated using laser and electron beam deposition. Films deposited in an ultrahigh vacuum system exhibit the crystalline structure of the tetragonal phase.

HIGH DAMAGE THRESHOLD POROUS SILICA
ANTIREFLECTIVE COATING*

I. M. Thomas, J. G. Wilder, W. H. Lowdermilk,
and M. C. Staggs

Lawrence Livermore National Laboratory
Livermore, California

A quarterwave-thick, narrow-bandwidth, antireflective coating
for fused silica optical components and KDP crystals has been
developed. The coating consists of porous silica prepared from
a silica sol in ethanol. It is applied by dip or spin from a
solution at room temperature and requires no further treatment.
The damage threshold levels are about equal to the surface damage
thresholds of the uncoated substrates.

Key Words: antireflection coatings, laser damage, tetraethyl
orthosilicate, silica sols, fused silica, potassium dihydrogen phosphate

1. Introduction

For some time we have been investigating the use of porous silica as an antireflective (AR)
coating for high power laser optics. The use of porous silica as an AR coating is well known;
acid leaching, well summarized by Cook and Mader (1), acid neutralized sodium silicate (2), and
silica sols (3) have all been used on glass substrates to produce films of varying degree of
effectiveness. All of these are aqueous systems and use commercially available materials. Some
work has also involved the use of organic silicates in organic solvents as the silica source (4,
5). These materials are readily hydrolyzed to silica and have been applied as acid-catalyzed,
partially hydrolyzed products in organic solution to give porous coatings after exposure to water
and heat:

$$Si(OR)_4 + 2H_2O \rightarrow SiO_2 + 4ROH$$
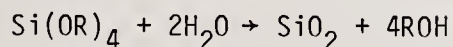
where R represents CH_3 or C_2H_5.

Because of the special nature of coatings required for laser applications, particularly damage
resistance, our investigation has involved the use of organic silicates, specifically tetraethyl
orthosilicate, $Si(OC_2H_5)_4$, as the silica source. This material is a volatile liquid and can
readily be purified by fractional distillation; the silica obtained by hydrolysis retains the high
purity level and thus laser damage due to impurities is minimized.

The hydrolysis of tetraethyl silicate requires either an acidic or basic catalyst and the intermediate products are quite different in each case. The reactions are shown in Figure 1. With an acid catalyst a soluble poly-ethoxysiloxane is first formed; at this stage it can be applied to a substrate and subsequent heat treatment to 450 C, to decompose organic entities, followed by a mild HF etch gives a porous silica coating. When a base catalyst is used, a colloidal suspension of silica particles, completely free of organic entities, is formed and when this is applied to a substrate a porous silica coating of layers of silica particles is obtained with no further treatment.

$$Si(OC_2H_5)_4 + H_2O$$

$$(C_2H_5O)_3 \, SiOH + C_2H_5OH$$

acid

base

$$(C_2H_5O)_2 \, Si(OH)_2$$

$$(C_2H_5O)_3 - Si - O - Si(OC_2H_5)_3$$

80°C

R.T.

$$\left[\begin{array}{c} OC_2H_5 \\ | \\ Si \!-\! O \\ | \\ OC_2H_5 \end{array} \right]_n$$

$$Si(OH)_4$$

R.T.

450°C

$$SiO_2$$

$$SiO_2$$
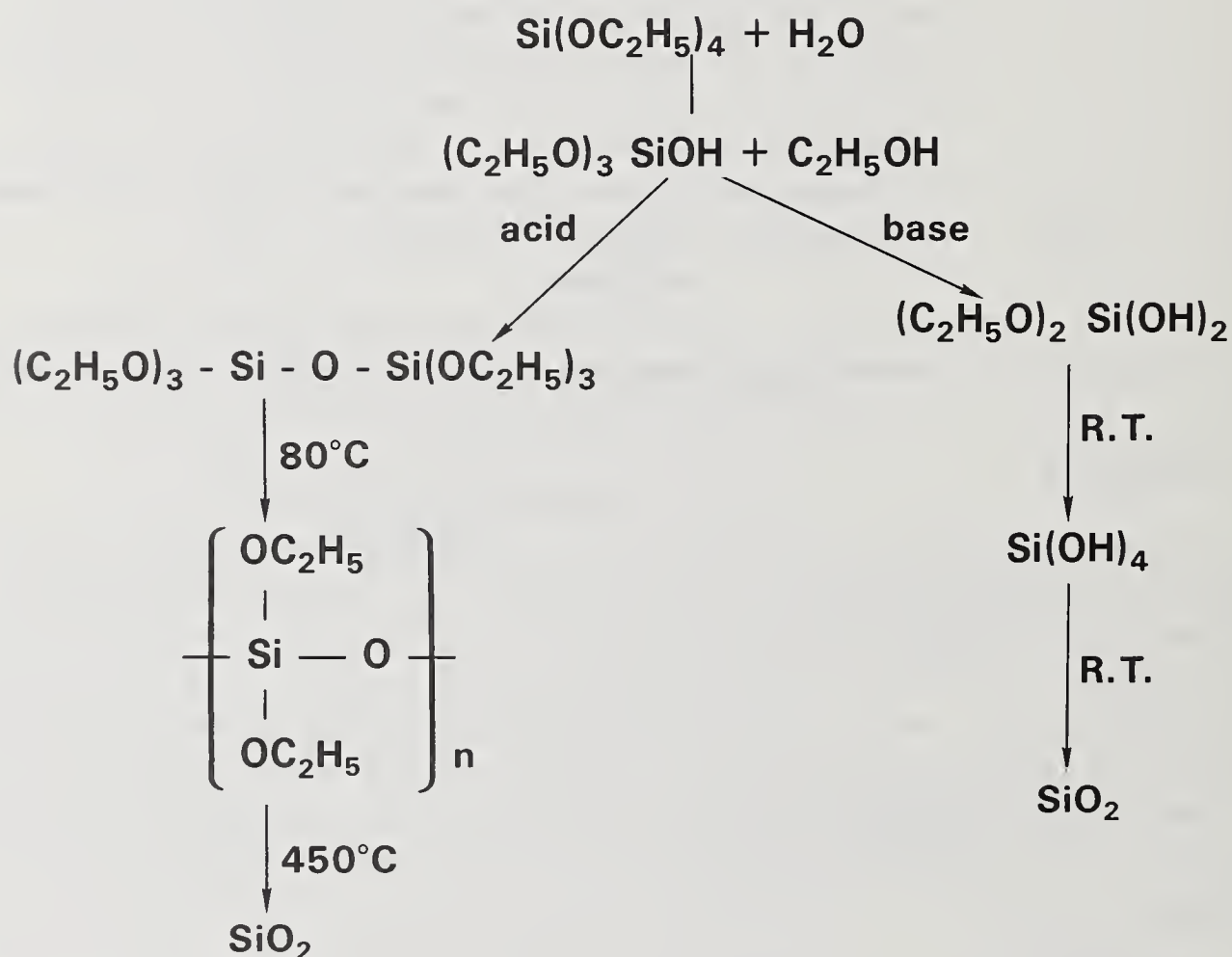
Fig. 1 Hydrolysis of tetraethyl silicate.

Initially, we investigated the acid-catalyzed system, but had problems in some cases with the laser damage threshold being low, even though the AR properties were quite satisfactory. This laser damage was thought to be due to carbonaceous residues left in the coating from incomplete removal of organic material during the heat treatment. We then turned our attention to the base-catalyzed system, and this has given high damage thresholds and quite satisfactory optical performance. In addition, the coatings are much simpler to prepare and apply.

Fused silica focussing lenses of 80 cm diameter and 27 cm square potassium dihydrogen phosphate (KDP) crystals are now coated routinely with the coating solution described below.

2. Experimental

Tetraethyl orthosilicate was fractionally distilled using a 120 cm vacuum jacketed and silvered Vigreux glass column fitted with an infinitely variable distillation head. The fraction boiling at 166-167 C was collected for subsequent use.

The coating sol was prepared by the base catalyzed hydrolysis of the distilled product by a method similar to that described by Stober (6) as follows. Concentrated ammonium hydroxide solution (57% analytical reagent, 9.6 g) was added to a solution of tetraethyl silicate (31.2 g) in anhydrous ethyl alcohol (259 g) with stirring at room temperature. The reaction mixture was then allowed to stand at room temperature for three days to allow hydrolysis and sol formation to be completed. The final product consisted of a colloidal suspension of SiO_2 particles in substantially anhydrous ethanol at a concentration of 3.0%. Transmission electron microscopy indicated the silica particles were approximately spherical with a diameter of about 20 nm.

Coating was carried out either by a spin or dip process. Samples were coated at room temperature and then air dried; no further treatment was required. For AR coatings optimized for 350 nm wave length light, a withdrawal rate of 5 cm/min was suitable for the dip process. Spinning was carried out at 350 rpm and required ethanol dilution of the coating sol to 0.75% silica. Thicker coatings for longer wavelength light were obtained by multidip or spin with air drying in between.

The results described in the next section were obtained on 5 cm diameter by 1 cm thick polished fused silica substrates and on 5 cm x 5 cm x 1.75 cm KDP crystals with diamond turned surfaces. Larger samples are now routinely coated and their performance is similar to that reported for the smaller samples.

3. Discussion of Results

Transmission spectra of our coatings on fused silica and KDP substrates are shown in Figures 2 and 3. These spectra are characteristic of quarterwave AR coatings of refractive index corresponding to the relationship $n_c = \sqrt{n_1 n_2}$ where n_c is the index of the coating, n_1 is the index of air, and n_2 is the index of substrate. Appropriate substitution indicates that the index of the coating is approximately 1.22. Further calculation then shows that the silica particles must be stacked to give an average porosity of about 50%.

It is interesting to note that the densest possible packing of uniform spheres gives a porosity of only 26%. We must therefore conclude that the slight variations in particles size and shape and also possible particle porosity contribute to the increased porosity of coatings obtained from them.

The effect of multicoats on fused silica substrates is also illustrated in Figure 2. The transmission maximum of the first coat is masked by absorption of the substrate; the second and third coats however show that thickness is additive, and in this case calculations indicate that each coat is approximately 39 nm thick (46 nm optical thickness). As the particle size is only about 20 nm, each coat is only two particle layers thick.

We have found that thicker coatings can also be obtained by increasing the silica content in the coating sol, as might have been expected.

Figure 4 gives laser damage thresholds measured at three different laser wavelengths and pulse durations for the sol coatings on fused silica substrates, and that measured at one laser wavelength for the coatings on KDP substrates. The 248-nm threshold was measured by Foltyn at Los Alamos National Laboratory. These thresholds were measured on coatings whose thicknesses were arranged such that maximum transmission occurred at the measurement wavelengths. The thresholds obtained approximate to the thresholds measured for the uncoated substrate surfaces.

4. Summary

A method has been developed to prepare porous silica AR coatings on silica or KDP substrates. This involves the preparation of a silica sol in ethanol from a high purity organic silicate starting material and application of this sol, by spin or dip, to substrates at room temperature followed by an air dry. No further processing is required and coatings with high laser damage thresholds and excellent optical performance are obtained.
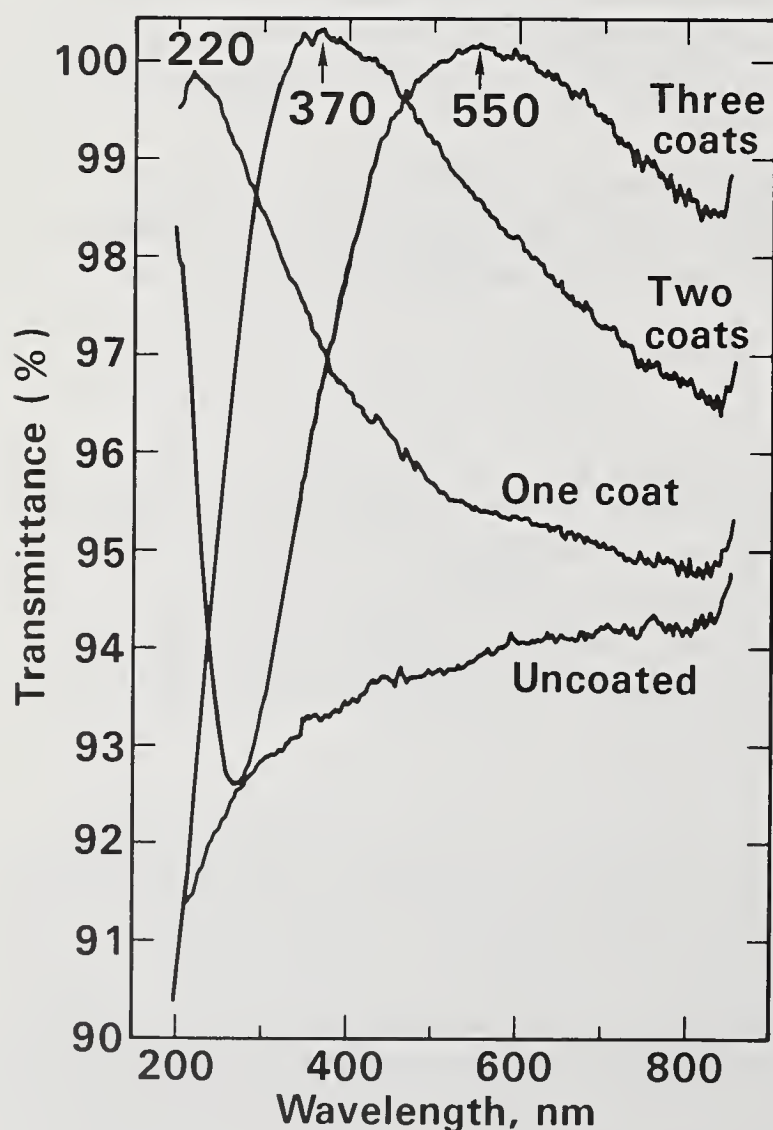
Fig. 2 Transmittance of coatings
on fused silica substrates.
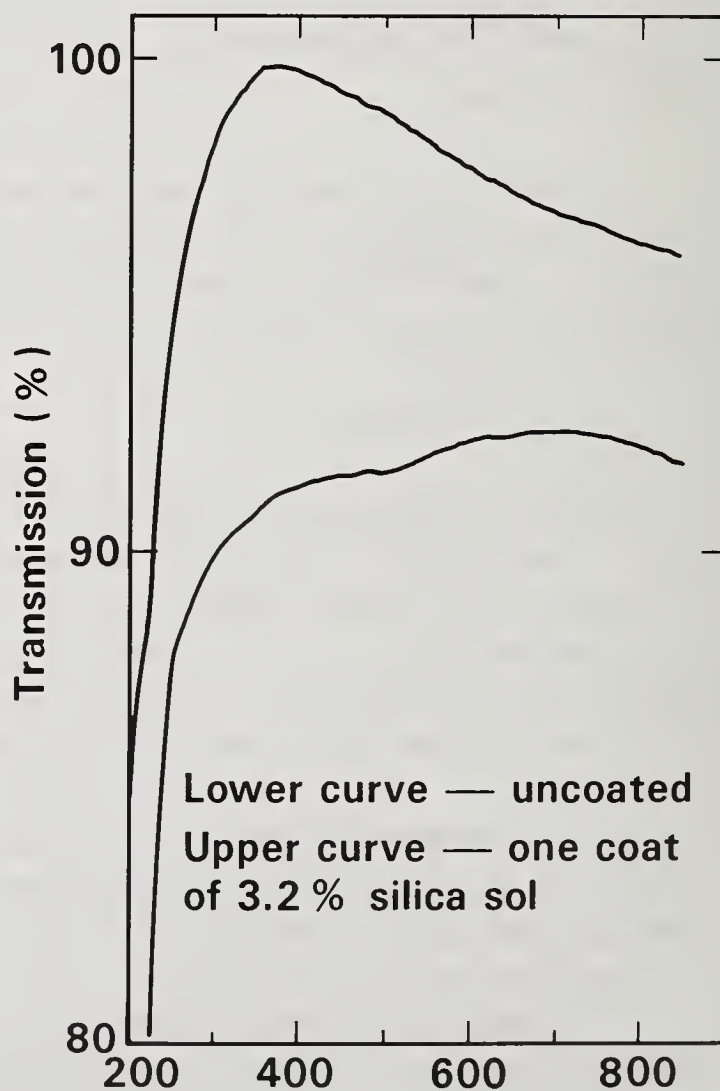
Fig. 3 Transmittance of coatings on
diamond-turned KDP substrates.

5. References

(1)   L. M. Cook and K. H. Mader, Optical Engineering, 21(1), SR-008, 1982.

(2)   E. M. Pastirik and M. C. Keeling, 13th IEEE Protov. Spec. Conf., Washington D.C., 5-8 June (1978).

(3)   H. R. Moulton, U.S. 2601123 (1952).

(4)   H. R. Moulton, U.S. 2474061 (1949).

(5)   B. Yoldas and D. P. Partlow, "Wide spectrum antireflective coatings for fused silica and other glasses. Appl. Opt., 23, 1418 (1984), also
B. Yoldas, and D. P. Partlow, Formation of Broad Band Antireflective Coatings on Fused Silica for High Power Laser Applications, Thin Solid Films, (to be published).

(6)   W. Stober, A. Fink, and E. Bohn. J. Colloid and Inter. Sci. 26, 62 (1968).

Laser	SiO$_2$ substrate	KDP substrate
248 nm, 15 ns pulse	4 - 5 J/cm^2	
346 nm, 0.6 ns pulse	8.5 - 10 J/cm^2	$>$ 4 - 5 J/cm^2
1064 nm, 1.0 ns pulse	10 - 14 J/cm^2	

Fig. 4 Laser damage thresholds.

A questioner wanted to know if these silica gel coatings could be used for calcium fluoride substrates. The author had not tried it but was confident that they could be. The durability of these coatings has not ben studied, but coatings have been used for several months in air with no problems. There is certainly a water layer on the silica, but it has not caused a problem. Also, sol gel coatings are notorious for leaving residual carbon. However, these coatings, which are not heated, are OK. For acid hydrolized systems, which must be heated to 450 C, it was impossible to eliminate carbon residues, which caused very low damage thresholds, and that process was abandoned. Work is just starting on depositing multilayer coatings by using organometallic layers and decomposing to get the oxides. Nothing yet to report on this process.

Pulse Duration Dependence of 1064-nm Laser
Damage Thresholds of Porous Silica Antireflection
Coatings on Fused Silica Substrates

D. Milam, I. M. Thomas, C. Weinzapfel, and J. G. Wilder

Lawrence Livermore National Laboratory
Livermore, CA 94550

We used 1064-nm pulses with durations of 1, 5, 9 ns to measure
laser-damage thresholds of 10 porous silica antireflection coatings
deposited from both methanol and ethanol solutions containing silica
particles with diameters of 10-20 nm. The median thresholds measured
at the three pulse durations, 10.8 J/cm^2, 26.5 J/cm^2, and 38 J/cm^2,
scaled as pulse duration to the 0.56 power.

Key words: laser damage, antireflection coatings, pulse duration
scaling, porous silica.

1. Introduction

Porous silica coatings were developed at Livermore in response to the need for damage
resistant antireflection films for use at ultraviolet wavelengths, primarily 248 nm and 351 nm.
Because these coatings performed well in the ultraviolet, and because techniques had been
developed for applying such films to optical elements with diameters up to 1 meter, it was
interesting to evaluate their potential for use at 1064 nm.

2. Fabrication of Test Coatings

The coatings were deposited from both ethanol and methanol solutions containing 3 weight
percent of colloidal silica particles 10-20 nm in diameter[1]. A substrate was lowered vertically
into the solution and then withdrawn at 4.0 cm/min. Build-up of coating thickness was
accomplished by use of three depositions. The substrates were 2-inch diameter disks of Corning
7940 high purity fused silica that had been polished by Zygo, Inc. Immediately prior to
application of the coating solution, the surfaces of these samples were cleaned with lens tissue
and ethanol. Four of the substrates were also etched in dilute HF prior to being coated:
additional comments on this etching are given below.

The two-surface transmittance spectrum for a silica substrate bearing three-layer sol-gel
coatings is given in Fig. 1. The measured transmittance was .994 at 1064 nm, .996 at the spectral
maximum near 1000 nm, and equal to that of the bare substrate at the minimum near 500 nm. Using
the values of these transmittances and the positions of the spectral extrema, we estimate that the
coatings were homogeneous layers with optical thickness of 250 nm, refractive index $\sim$ 1.26, and
silica content of 56%. The homogeniety of the coating suggests that dried porous material from an

initial deposition was not filled during a subsequent deposition, and that the optical thickness was increased by about 83 nm during each application of the coating. A loss believed to be scattering caused transmittance at wavelengths below 250 nm to be less than expected.

3. Measurement of Laser Damage Thresholds

Damage tests were made with 1064-nm pulses in a weakly convergent beam that was about 2 mm in diameter at the sample surface. For each pulse used, the pulse energy and the energy distribution in the beam were measured, and the peak on-axis fluence was computed to within ± 7%.

Duration of the laser pulses was controlled by using a Pockels cell shutter to slice them from a Gaussian waveform pulse with duration of 150 ns. At the minimum pulse duration, 1 ns, the pulse waveform was governed by the rise and fall times for the shutter and was approximately Gaussian. Pulses with duration 5.5 and 9 ns had rise and fall times identical to those of the 1-ns pulses. These longer pulses were sliced from the leading edges of the 150-ns pulses and had waveforms that were trapezoidal with a slight upramp. Gain saturation in the laser amplifier reshaped the pulses into trapezoids with trailing edges as much as 30% below the leading edges, the saturation and reshaping being most significant in the pulses with greatest energy.

During test of a sample, each test site was irradiated only once. To detect damage, we observed for laser-induced light emission during a shot, visually inspected the test site under intense white light illumination after the shot, and also used dark field microscopy to record 100 times magnified photographs of the center of the test site before and after the site was irradiated. Damage was defined to be a permanent alteration of the sample detectable by these examinations. The threshold-level damage usually consisted of very small volumes visible in the
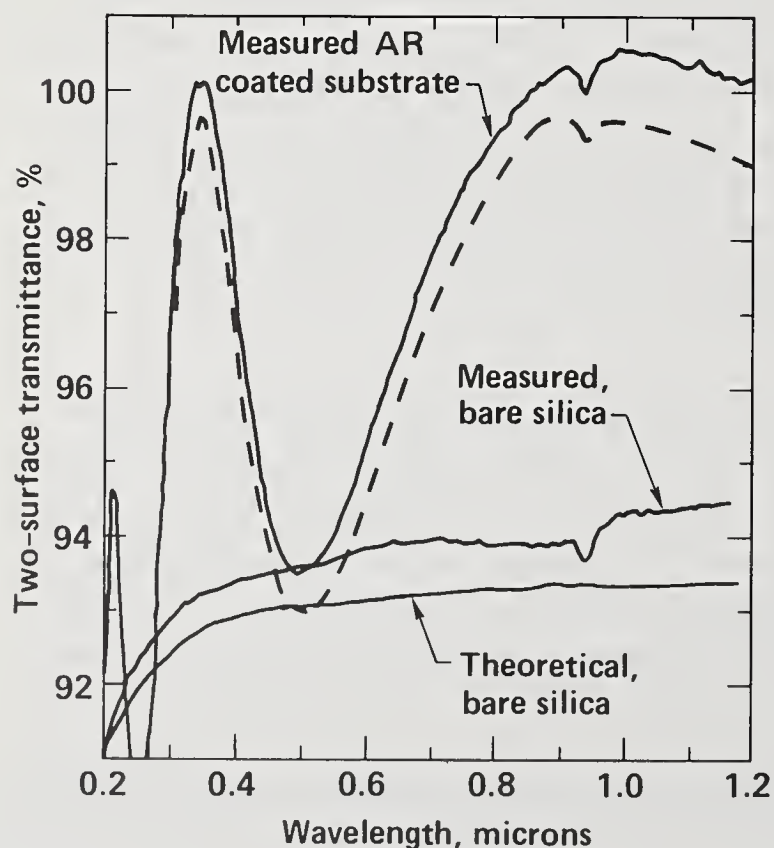
Fig. 1. Two-surface transmittance for a silica window with sol-gel AR coatings on both surfaces. Dsahed curve is the spectrum corrected for small measurement errors.

The scaling of median thresholds as $\tau^{0.56}$ is within error comparable to the $\tau^{.5}$ scaling that has been observed in similar 1064-nm tests with bare polished glass surfaces[2] and with graded-index surfaces made by etching[3]. However, since the rule $\tau^{.5}$ can be attributed to a wide class of physical effects, it does not uniquely identify the mechanism for damage.

These coatings will be useful at a few places in the Nova amplifier chains. Lenses and windows that transmitted only the 1064-nm beams in Nova were made of BK-7 glass and had antireflective surfaces made by neutral solution processing (NSP)[4]. During initial operation of the Novette laser, transmittance of large diameter beams of high-intensity through optical elements made of BK-7 glass revealed the presence of a low volume density of platinum inclusions with damage thresholds of 4-7 J/cm^2 (1-ns, 1064-nm). Therefore, high purity fused silica may be more suitable than BK-7 glass for fabrication of a few elements in NOVA that receive the greatest fluence loading. In Fig. 3, we compare the 1-ns 1064-nm thresholds reported here for sol-gel AR films with thresholds previously measured on NSP surfaces on Bk-7 glass. Thresholds for films made by the two process are comparable, so if we are required to use fused silica for some 1064-nm components in Nova, the sol-gel coatings should adequately serve as damage resistant AR films.
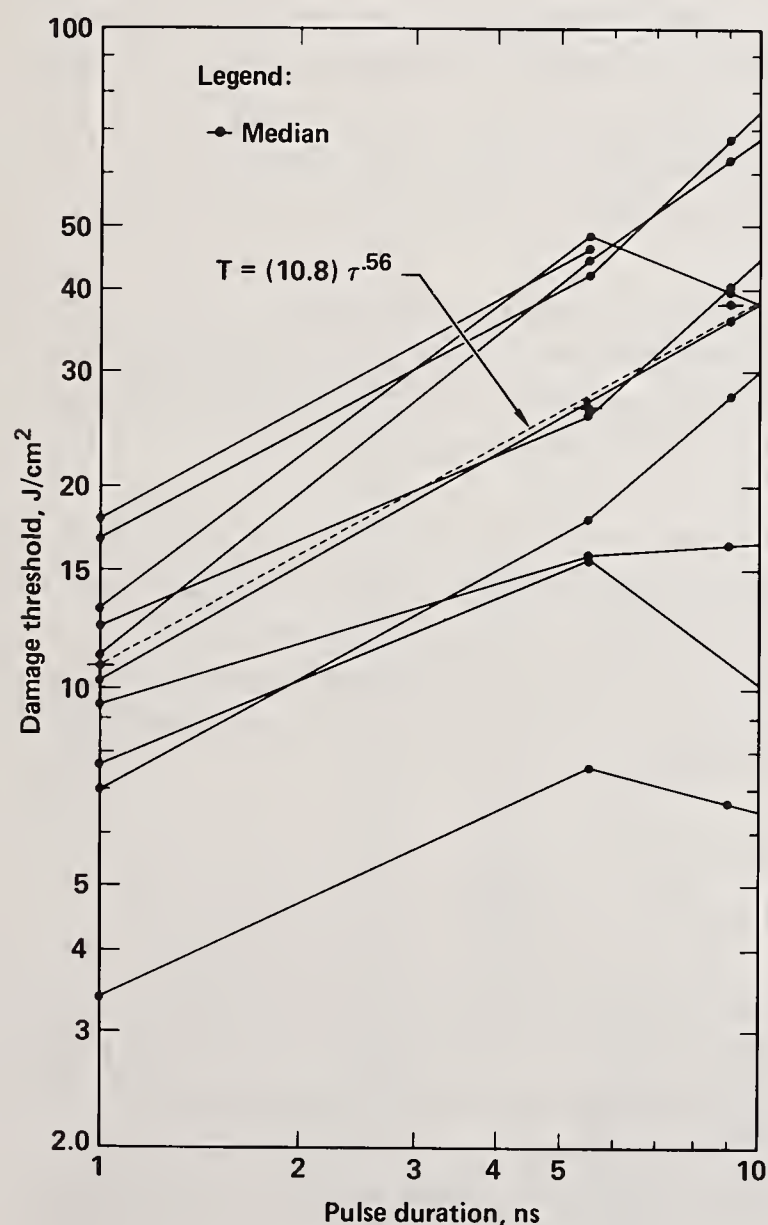
Fig. 2. 1064-nm damage thresholds of sol-gel AR coatings as a function of laser pulse duration. Dashed line is the curve $T = 10.8\ \tau^{0.56}$ which describes scaling of the median thresholds.

dark field presentation of the microscope. Except for the least damages, these areas were usually seen in the simple visual inspection of the test site, but were not always apparent in inspection by either white-light or Nomarski microscopy. Therefore we assume the damages were small localized fractures in the coating that were most apparent by their ability to scatter light.

Laser-induced emission of light was observed on some samples, particularly those with the greatest thresholds, during shots at fluences below those which caused permanent damage detectable by the inspections described above. At these subthreshold-fluences, the light emission did not occur as a bright spark. Instead, it appeared as a weakly luminous disk on the sample surface, had the size and shape of the laser beam, and sometimes abated when a site was repeatedly irradiated. It has not been determined whether this emission of light signals the existence of a plasma with density sufficient to cause a serious perturbation of a beam.

4. Experimental Results

Measured thresholds are given in Table 1. For coatings in the first two preparation groups, thresholds for those made from an ethanol solution were systematically above thresholds of those made from a methanol solution, and thresholds of the methanol-solution coatings were almost independent of pulse duration. This was difficult to understand. Coatings made from the ethanol solution consist of layers of silica spheres having diameters of about 20 nm, whereas those made from the methanol solution consist of smaller spheres with diameters of 6-10 nm. Since the sizes of the spheres are all very small relative to the 1064 nm test wavelength, and since both of the precursor solutions should have provided silica of comparable purity, it was believed that the apparent difference in performance of the two types of coatings was due to an extrinsic effect.

Therefore, we fabricated a third set of coatings on the four substrates that had been used in fabrication of the initial group of coatings. The substrates were etched in dilute HF acid to remove the existing coatings, cleaned in water and ethanol, and recoated using the same ethanol and methanol solutions that had been used in preparation of coatings in sets 1 and 2.

Thresholds for the coatings in set 3 were independent of the type of precursor solution, systematically larger than those obscured in tests of coatings in sets 1 and 2, and they all scaled uniformly with pulse duration. However, for these latter coatings, thresholds for laser-induced light emission were sometimes significantly below the large fluences required to cause detectable permanent physical damage. The fluence for laser-induced emission of light may be the practical upper bound for thresholds in these coatings.

In Fig. 2 we have plotted all the measured thresholds as a function of pulse duration, indicated the median threshold at each pulse duration, and also plotted the function $T = 10.8\tau^{.56}$ which is a best fit for scaling of the median threshold T with pulse duration τ. Note that the median thresholds are generally greater than thresholds for the initial methanol-sol films that may have been limited by substrate cleanliness, but well below the largest thresholds measured for coatings in set 3, and even conservative relative to light emission thresholds for coatings in set 3. Therefore, we believe it is possible by simple attention to preparation to reproducibly prepare coatings with thresholds greater than or equal to the median values.

Table 1. 1064-nm Laser-Damage Thresholds of Sol-Gel AR Coatings on Fused Silica

Laser-Damage Thresholds, J/cm^2

Preparation Sample	Group	Coating Type	1 ns		5.5 ns		9 ns	
			damage	light	damage	light	damage	light
3811	1	Ethanol Sol	10 ± 1.5	< 8	27 ± 4	19 ± 3	36 ± 5	32 ± 11
3815	1	"	13 ± 2	5.8 ± 6	26 ± 4	21 ± 2	41 ± 6	34 ± 5
3810	1	Methanol Sol	9.4 ± 1.4	8.0 ± 2	16 ± 2.4	11 ± 1	17 ± 2.5	15 ± 3
3817	1	"	7.7 ± 2	13 ± 3	16 ± 4.5	> 31	11 ± 2	> 15
3746	2	"	3.4 ± 3	8 ± 2	7.6 ± 1	14 ± 1	6.7 ± 1	> 11
3744	2	Ethanol Sol	7 ± 1.2	7 ± 1.2	19 ± 2.8	18 ± 1.8	28 ± 4	16 ± 1.6
3815	3	Methanol Sol	18 ± 2.7	12 ± 1	46 ± 7	30 ± 1	61 ± 9	37 ± 15
3817	3	"	17 ± 2.6	12 ± 2	42 ± 6	33 ± .6	70 ± 10	50 ± 15
3810	3	Ethanol Sol	11 ± 1.7	11 ± 2	45 ± 7	43 ± 4	62 ± 10	53 ± 6
3811	3	"	13 ± 2	13 ± 1	48 ± 8	32 ± 3	62 ± 4	32 ± 3

215

References:

1. Ian M. Thomas, John G. Wilder, W. Howard Lowdermilk, and M. C. Staggs, "High Damage Threshold Porous Silica Antireflection Coating," elsewhere in these proceedings.

2. David Milam, "1064 nm Laser-Damage Thresholds of Polished Glass Surfaces as a Function of Pulse Duration and Surface Roughness", in Laser Damage in Optical Materials: 1978, NBS Spec. Publ. 541, pp. 164-167, issued Dec. 1978.

3. James E. Swain, W. Howard Lowdermilk, and David Milam, "Raising the Surface Damage Threshold of Neutral Solution Processed BK-7 by Pulse Laser Irradiation," in Laser Induced Damage in Optical Materials: 1982, NBS Spec. Publ. 669, pp. 292-295, issued Jan. 1984.

4. Lee M. Cook, W. Howard Lowdermilk, David Milam, and James E. Swain, "Antireflective Surfaces for High-Energy Laser Optics formed by Neutral-Solution Processing," Appl. Optics, Vol. 21, p. 482-1485, April 15, 1982.
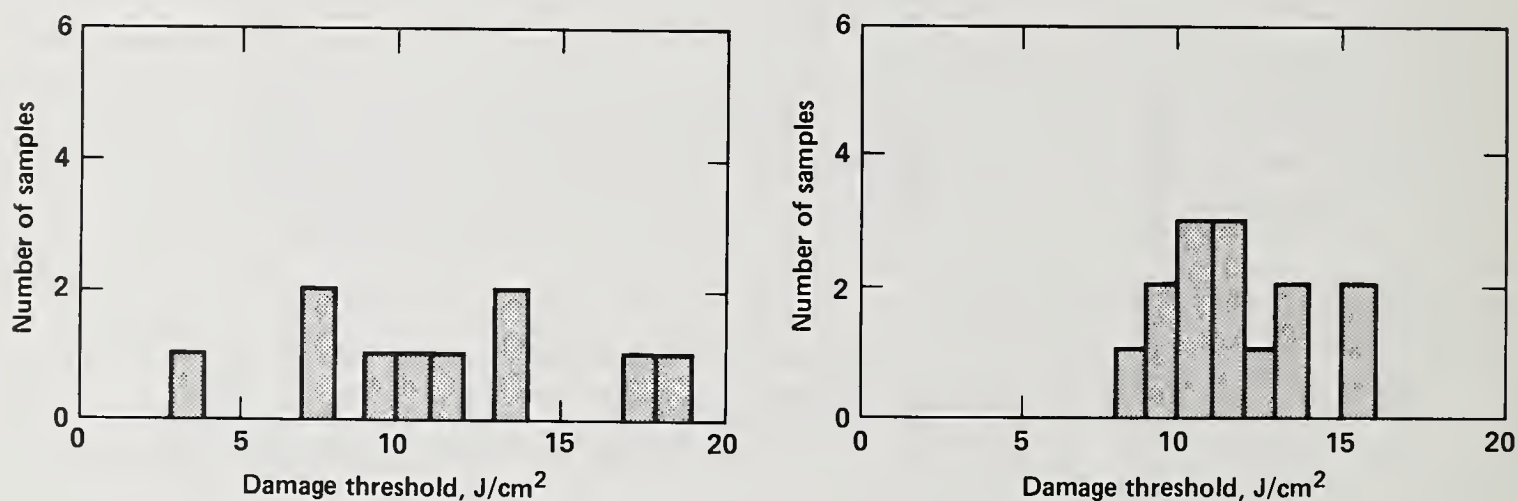
Fig. 3. Laser-damage thresholds measured with 1-ns 1064-nm pulses on sol-gel AR coatings (left) and on surfaces made by neutral solution processing (right).

Variation of Transmittance Spectra of Porous Antireflection
Coatings with Index Profile

David Milam, Giles G. Peterson

Lawrence Livermore National Laboratory
Livermore, CA 94550

Transmittance spectra were calculated for single-layer
coatings with (1) homogeneous refractive index, (2) index profiles
that increase monotonically with distance into the coating, and (3)
index profiles that rise in discrete steps. The calculations
predict that large transmittance at tuned wavelengths can be
obtained using any of these coating designs and known, porous silica
coating materials. The spectral bandwidth of transmittance maxima
increases when the index profile is altered from homogeneous to any
profile whose index increases monotonically with thickness in the
coating. Bandwidth is greatest for the linear-ramp coating whose
index rises linearly from that of air to that of the substrate, but
this design cannot currently be used because we are unable to
fabricate silica coating material with the extremely large porosity
needed to provide a coating index near unity at the air interface.
For currently attainable fractional silica contents, estimated to be
in the range 0.4-0.5, the optimum bandwidth is provided by a coating
with a single discrete step in its index profile.

Key words: transmittance spectra, single-layer coatings, porous
silica, antireflection coatings.

1.   Introduction

Porous silica coatings can be deposited from alcoholic solutions containing either silica
microspheres with diameters of 10-20 nm[1] or smaller polymer silica molecules[2]. A coating made
from a mat of polymer molecules has interconnected pores with an average diameter of 4 nm, but is
spatially homogeneous over any volume containing representative numbers of voids and molecules.
Partial etching of this material can enlarge the pores at the outer surface of the coating and
produce a gradient along the surface normal in both the mass density and the refractive index.

A coating made from microspheres bonded only at points of contact has larger pores, but is
also spatially homogeneous as initially deposited. The refractive index of such coatings is not
easily graded. Etchants readily penetrate the larger pores and produce a spatially homogeneous
reduction of the mass in the film. Further, only slight etching is required to destroy the
coating by breaking the relatively few bonds joining the microspheres.

Coatings of a third class have been fabricated at LLNL from mixtures of the solutions
containing smaller, polymer silica molecules and those containing microspheres. The polymer
material tends to fill the voids between the spheres, so the density of the dried film can be
controlled by the mixing ratio for the two solutions. Antireflection coatings with stepped index
profiles have been made by depositing several layers with progressively lower indices.

The transmittance spectrum of a window bearing coatings made by one of these three techniques is uniquely related to the refractive index profile of the coatings, and our model for computing spectra was initially used only as a technique for determining index profiles in experimental coatings. An assumed profile was adjusted by trial and error to obtain agreement between calculated and measured spectra. Measured spectra could usually be explained by postulating that the index profiles were slight variations of one of three generic profiles: (1) spatially homogeneous index, (2) index increasing monotonically with distance into the coating along a surface normal (linear-ramp or arctangent functions), and (3) index profiles with one or more abrupt steps. In this paper we discuss the basic differences in the spectra for coatings with these index profiles.

Because codes for calculation of transmittance spectra are well known, and because the mathematics describing multilayer coatings is cumbersome, it is tempting to immediately resort to numerical analysis when considering a new type of film. In fact, many of the characteristics of coatings can be estimated through use of much simpler procedures. This is especially true for films such as those described in this paper, films in which the refractive index n_f rises monotonically along a surface normal and spans at most the limited range between the refractive indices of air and the substrate. We have found simple models to be useful in development of intuition and will use them to describe some coatings. Discussions based on intuitive models will be supplemented by presentation of spectra computed by standard numerical techniques and by analysis of closed form equations for transmittance that are known for coatings of some designs.

2.   Calculation of Reflectance and Transmittance

In our calculations of spectra, a coating was described by stating the variation of its fractional silica content, $F(z)$, with distance z into the coating along a surface normal. The physical boundaries of the coating were at $z = 0$ and $z = z_0$. For $z < 0$, the medium was assumed to be air with refractive index $n = 1$. For $z > z_0$ the medium was fused silica with index n_s given by the Sellmeier equation,

$$n_s^2(\lambda) - 1 = \frac{.6961663 \, \lambda^2}{\lambda^2 - (.0684043)^2} + \frac{.4079426 \, \lambda^2}{\lambda^2 - (.1162414)^2} + \frac{.8974794 \, \lambda^2}{\lambda^2 - (9.8916161)^2} \, , \tag{1}$$

where λ is the wavelength in microns. At a position z inside the porous coating, the refractive index of the film was assumed to be a weighted average of the indices of air ($n_a = 1.0$) and silica,

$$n_f(\lambda, F, z) = F(z)n_s(\lambda) + 1 - F(z) \, . \tag{2}$$

This expression incorporates index dispersion through its dependence on $n_s(\lambda)$, is easily understood and provides index values for porous silica that are accurate to within $\sim$ 5% over the whole porosity range, $0 \leq F(z) \leq 100\%$. If desired, indices could be calculated with slightly greater accuracy by use of the Clausius-Mossotti relationship. Finally, note that the silica fraction profile, $F(z)$, is independent of wavelength whereas the index profile $n_f(z)$ varies with wavelength through dispersion. It is advantageous, therefore, to specify the coating by stating $F(z)$ and the physical thickness z_0.

In calculation of single-surface reflectance of a porous coating, the coating was assumed to consist of m (typically 30-50) separate layers with index $n_m(\lambda,z)$ and optical thickness $n_m(\lambda,z)z_o/m$. Reflectance from this stack of coatings was calculated by a standard matrix procedure[3]. Two-surface transmittance, T, of a window with coatings on both its surfaces was calculated from the single-surface reflectance, R, by the equation,

$$T = [1-R]^2 . \tag{3}$$

This neglects the possibility of coherent interaction between waves reflected from the two surfaces of the window and is appropriate for comparison of calculated spectra with those recorded by typical spectrometers, but will not always model spectra measured with narrowband laser sources for coated windows with very parallel surfaces.

3. Spectra of Homogeneous Coatings

In this section transmittance spectra of single-layer homogeneous coatings computed by our model which includes index dispersion are compared with those calculated from the well known analytical expression for transmittance. For a homogeneous film with index n_f and thickness z_o on a substrate with index n_s, the single-surface transmittance t is given by[4],

$$t = \frac{8n_f^2 n_s}{(1 + n_f^2)(n_f^2 + n_s^2) + 4n_f^2 n_s + (1 - n_f^2)(n_f^2 - n_s^2) \cos 2\delta} , \tag{4}$$

$$\delta = \frac{2\pi}{\lambda} n_f z_o \cos \varphi , \tag{5}$$

where φ is the angle of incidence, the index of air was assumed to be unity, and index dispersion was neglected. At normal incidence, $\varphi = 0$, and the transmittance varies between maxima that occur at wavelengths specified by $n_f z_o = m\lambda/4$ with m an odd integer, and minima that occur at $n_f z_o = m\lambda/4$ with m even. At these extrema,

$$t_{max} = \frac{4n_f^2 n_s}{(n_f^2 + n_s)^2} , \quad \text{m odd;} \tag{6}$$

$$t_{min} = \frac{4n_s}{(1 + n_s)^2} , \quad \text{m even.} \tag{7}$$

The second of these equations is simply the transmittance for the surface of the uncoated substrate. Therefore, t_{min} is equal to that of the substrate irrespective of the value of n_f. t_{max} does depend on n_f and has value unity when $n_f = \sqrt{n_s}$.

A calculated two-surface transmittance spectrum for a homogeneous porous coating that was designed to provide maximum transmittance at $\lambda = 1.0$ μm is shown in Fig. 1. This positioning

of the maxima was accomplished by requiring that the optical thickness have the value of $d = \lambda/4$ = 0.25 µm, and setting $n_f = \sqrt{n_s}$ with n_s = 1.4504 at λ = 1.0 µm. The corresponding physical thickness was z_0 = 0.2075 µm, and the silica content, computed from Eq. (2), was F = 0.454. The two-surface transmittance spectrum for the bare polished silica substrate and a plot of silica content vs. physical thickness in the coating are also given in the figure. As expected from Eq. (7), transmittance at spectral minima is equal to that of the uncoated substrate. However, since these spectra were calculated by the computer code that included index dispersion, the substrate transmittance varys with wavelength and the secondary transmittance minima and maxima lie at wavelengths slightly greater than those specified by λ = 4d/m.

At all of the spectral maxima in Fig. 1, peak transmittance is 100%. Although we precisely adjusted n_f and F to obtain best transmittance at maxima, large transmittance would have been obtained over a wide range in those variables. Transmittance exceeds 99% for $1.123 \leq n_f \leq$ 1.295, which corresponds to the range $0.28 \leq F \leq 0.66$, see Fig. 2. Coatings with silica content in the range $0.5 \leq F \leq 0.6$ are readily prepared by known sol-gel coating techniques, so it has been possible to fabricate efficient porous antireflection coatings.

Transmittance at spectral minima is, however, extremely sensitive to the homogeniety of the coating. Figure 3 is a comparison of transmittance spectra for a homogeneous coating with F = 0.454 and for an inhomogeneous coating with F = .445 at the air interface and F = .463 at the substrate. This ±2% ramp in silica content produced a readily apparent change in T_{min}, but no change in T_{max}.
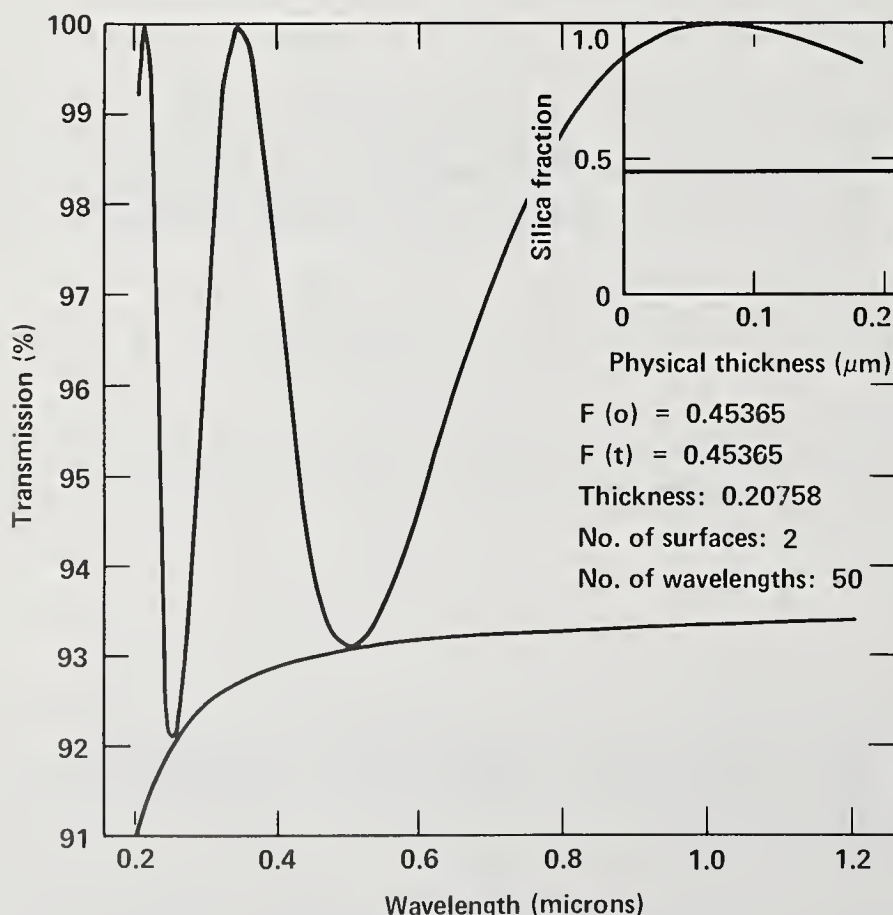

Fig. 1. Calculated two-surface transmittance for a silica window with porous homogeneous coatings. The transmittance for the bare substrate, and a plot of silica content as a function of physical thickness of the coating are also given.
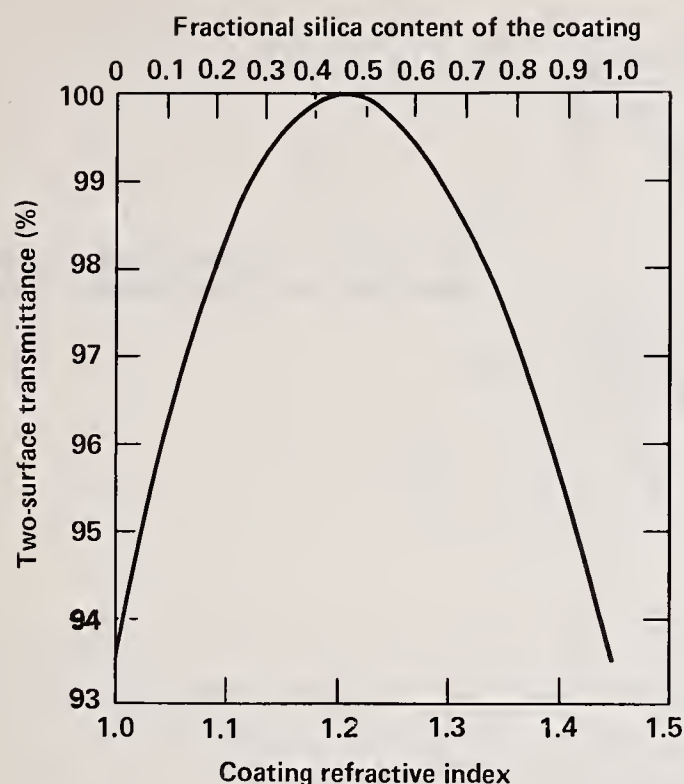
Fig. 2. Two-surface transmittance of porous antireflection coatings as a function of coating index and porosity.
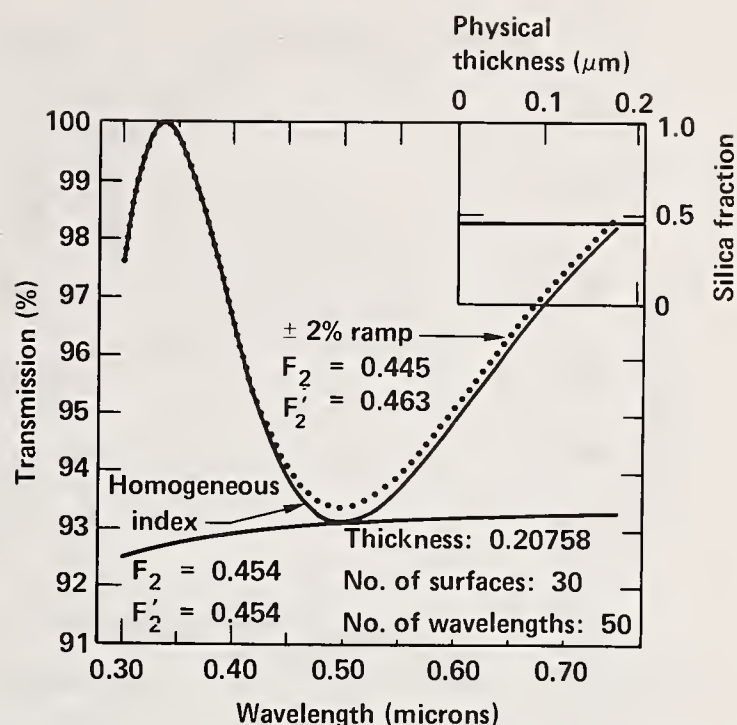
Fig. 3. Variation of two-surface transmittance at spectral minima with coating inhomogeniety.

4. Coatings with Linear-Ramp Profiles

The sensitivity of T_{min} to coating homogeniety illustrates that index gradiation can be used to increase the bandwidth over which transmittance is large. In this section we analyze coatings with linear-ramp silica profiles to illustrate two primary characteristics of graded-index coatings: (1) transmittance at spectral maxima is governed by the average value of the index in the profile and (2) transmittance at minima depends on the slope of the profile.

In an idealized linear-ramp coating, the index increases linearly with distance along a surface normal from the value $n_f = n_2$ at the air interface to a value $n_f = n_2'$ at the substrate. The coating whose index variation spans the entire range $n_2 = 1$ to $n_2' = n_s$ is an excellent tutorial example. The calculated transmittance spectrum for such a coating with physical thickness 0.2075 μm is shown in Fig. 4. Note that the fundamental transmittance maximum for this graded coating with physical thickness 0.2075 μm and optical thickness 0.2542 μm lies at $\lambda = 0.51$ μm, whereas the maximum for a homogeneous coating with the same optical thickness was at $\lambda = 1.0$ μm. In general, graded-index coatings must be about twice as thick as homogeneous coatings when both are designed to function at the same wavelength. The transmittance spectrum of the graded coating is oscillatory, but two-surface transmittance exceeds 99.6% over the entire passband which includes all wavelengths $\lambda < 2d$. Clearly d could be tuned to position the passband to include any desired wavelength for which silica is transparent, or to accommodate incidence angles greater than zero.

221
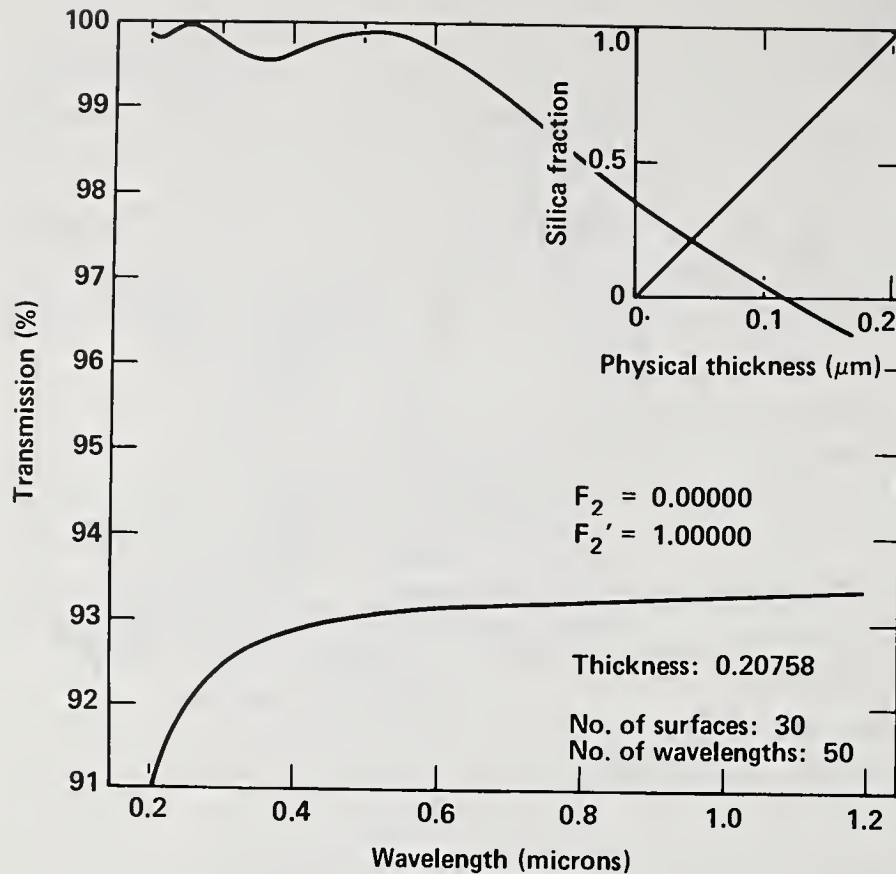
Fig. 4. Calculated transmittance spectrum for linear-ramp coatings.

Considerable insight is gained by examining a very simple model which predicts all the principal features of the spectrum in Fig. 4. The ramp profile of the coating can be approximated by a series of small discrete steps as shown in Fig. 5. To determine the reflectance of this coating at a single wavelength λ_o, we imagine that the coating is irradiated by a plane wave and consider the relative phasing of wavelets reflected from interfaces between the steps. If the optical thickness of the coating, d, is very small relative to λ_o, all reflected waves will be in phase and the surface reflectance will be equal to that of the bare substrate. When d is increased to $\lambda_o/2$, each wave reflected from a step lying in front of the midplane can be paired with an out-of-phase wave reflected from a step lying behind the midplane, and the net reflectance will approach zero. Increase of d from $\lambda_o/2$ to $3\lambda_o/4$ produces a set of partially phased waves and an increase in reflectance, but reflectance will again be small when d is increased to $2\lambda_o/2$.

The coating thickness corresponding to the complete set of reflectance minima (transmittance maxima) are specified by the equation $d = m\lambda_o/2$, with m a positive integer. Reflectance maxima occur for the coating thickness $d = (2m+1)\lambda_o/4$, and the single-surface reflectance at maxima, R_m, decreases as m increases. The reflectance at a particular maximum arises from summation of partially phased waves reflected from steps in the profile lying between $d = m\lambda_o/2$ and $d = (2m+1)\lambda_o/4$. The fraction of the total index discontinuity spanned by steps in that interval, $\Delta n_m = (n_s-1)/(2m+1)$, decreases with m. At the first maximum, m = 1, the greatest possible value for R_m is the reflectance from an interface between index

222
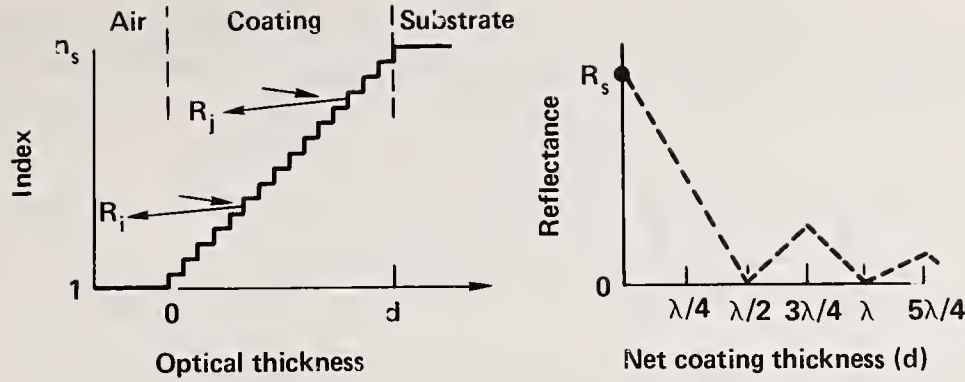
Fig. 5. Approximation of a linear-ramp coating, and its reflectance as a function of coating thickness.

values $n_f = 1.3$ and $n_f = 1.45$; $R_m \sim 003$. Therefore, the amplitudes of secondary reflectance maxima are very small, and the practical requirement for obtaining large transmittance at λ_o is only that $d \geq \lambda_o/2$. This thickness condition would also be met for any wavelength $\lambda < \lambda_o$. Therefore, transmittance is insensitive to wavelength and to incidence angle, provided the coating is sufficiently thick to meet the $d > \lambda/2$ condition for the greatest effective wavelength of interest.

The numerically calculated spectrum shown in Fig. 4 is in remarkable agreement with the predictions of the simple model. The transmissive maxima lie at wavelengths 0.51 and 0.26 µm, very near the predicted positions ($\lambda = 2d/m$) of reflectance minima for a graded coating with $d = 0.254$ µm. A minimum in transmittance is at $\lambda = 0.37$ µm, near the predicted position $\lambda = 4d/(2m+1)$ with $m = 1$. At this minimum, the two-surface transmittance is .996, corresponding to a single-surface reflectance of .002, which is well below the estimated greatest value of reflectance at a secondary maximum, $R_m = .003$.

While the linear ramp spanning the index range $n_2 = 1$ to $n_2' = n_s$ is of tutorial value, currently known procedures do not readily produce coatings with F below 0.4-0.5, which corresponds to refractive indices in the range 1.18 to 1.23, so the value $n_2 = 1$ at the air interface cannot be attained. The impact of this limitation can be understood by examining Schroeder's approximate equations for two-surface transmittance at maxima and minima in the spectrum of a linear-ramp coating;[5]

$$T_{min} = \left[1 - \left(\frac{n_2 n_s - n_2'^2}{n_2 n_s + n_2'^2} \right)^2 \right]^2 \quad , \tag{8}$$

$$T_{max} = \left[1 - \left(\frac{n_2 n_2'^2 - n_s}{n_2 n_2'^2 + n_s} \right)^2 \right]^2 \quad . \tag{9}$$

223

At minima, greatest transmittance occurs for the maximum difference in n_2 and n_2', or for the greatest ramp angle. This is apparent by inspection when T_{min} is written in terms of $\sigma = n_2' - n_2$;

$$T_{min} = \left[1 - \left(\frac{n_2(n_s-1) - \sigma}{n_2(n_s+1) + \sigma}\right)^2\right]^2 . \tag{10}$$

At maxima the transmittance is greatest when n_2 and n_2' are chosen so that $n_2' = n_s/n_2$, and for pairs (n_2, n_2') satisfying this condition, the average value $(n_2 + n_2')/2$ is approximately equal to $\sqrt{n_s}$, the index needed to fabricate efficient homogeneous antireflection coatings. The simultaneous need for $\langle n_f \rangle \sim \sqrt{n_s}$ to optimize T_{max} and for large ramp angle to optimize T_{min} cannot be met with current coating techniques, which do not provide values of $n_2 \ll \sqrt{n_s}$. The design limitation is quantified in Figure 6 which gives plots of T_{min} and of T_{max} as a function of silica fraction and index at the air interface. The curves were plotted from Schroeder's approximate equations and also plotted from values of T_{max} and T_{min} measured from spectra calculated by the matrix technique for coatings with varied n_2 and n_2' all satisfying $(n_2+n_2')/2 = n_s$. To produce linear-ramp coatings with two-surface transmittance even as large as 99%, it will be necessary to produce coatings with $F_2 = 0.15$.

An alternative optimization, allowing $\langle n_f \rangle$ to rise above $\sqrt{n_s}$ so that the ramp angle can be increased without reducing n_2, allows production of some interesting coatings with large bandwidth and moderately large transmittance. An example is given in Fig. 7. Transmittance spectra in that figure were computed under the assumption that the minimum attainable value of silica content at the air interface was $F = 0.3$. Best performance, $T > 98.6\%$ across the passband, occurs when the ramp angle is steepest, i.e., when $n_2' = 1.0$.
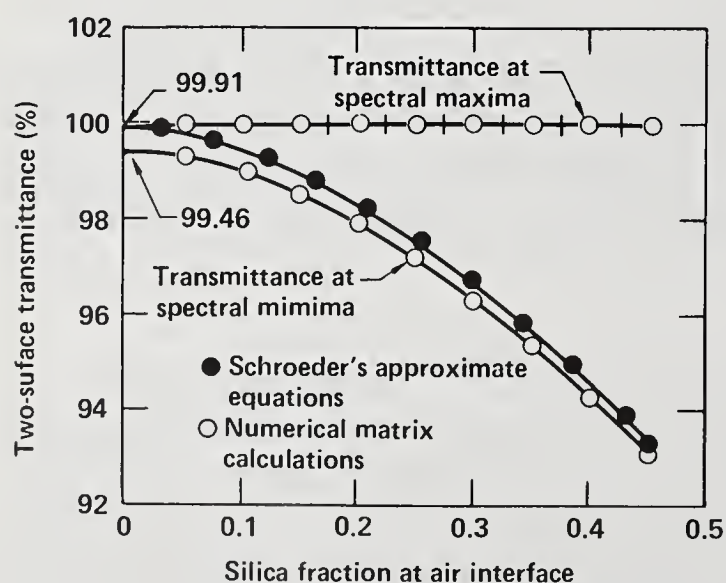

Fig. 6. Two-surface transmittance of a silica window bearing coatings whose average silica content is 0.454, plotted as a function of silica fraction at the air interface.

224
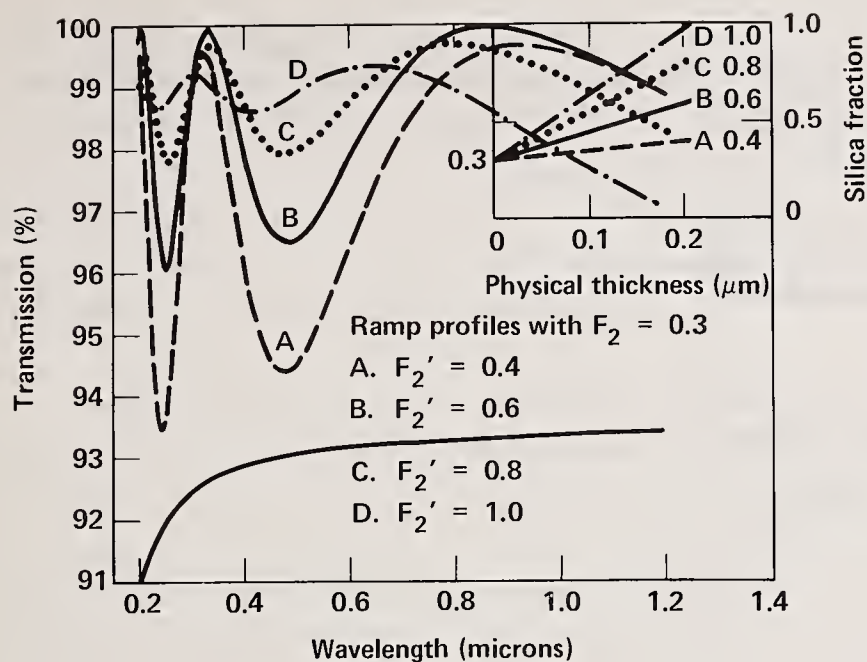
Fig. 7. Two-surface transmittance of linear-ramp coatings with $F_2 = 0.3$.

Ramp profiles with $F_2 = 0.3$
A. $F_2' = 0.4$
B. $F_2' = 0.6$
C. $F_2' = 0.8$
D. $F_2' = 1.0$

5.   Step Function Silica-Content Profiles

Coating with linear-ramp profiles are one of the extreme types of graded-index coatings. The opposite extreme is a coating with a single step ΔF in its silica content profile. The details of spectra of coatings with step-function silica profiles depend on the magnitude of the step, its position in the profile, and the average value of silica content in the coating. Cumbersome exact solutions are known for the reflectance of such a two-layer coating. However, for the purpose at hand, it is easier first to examine a special case which illustrates the influence of a step in silica content on the bandwidth of transmittance maxima, and then to generalize this example, than to attempt a complete discussion of two-layer coatings.

Figure 8 gives spectra for a homogeneous coating with $F = 0.454$ and for a coating with a step, $\Delta F = 0.2$, centered in the coating profile. The primary difference between the two spectra is the improved transmittance at $\lambda = 0.5$ µm for the step-function coating. For both coatings, transmittance at the minimum near $\lambda = .25$ µm is equal to that of the substrate and transmittance at maxima is nearly 100%, although the rudimentary gradiation provided by the step did cause a shift in the positions of the maxima for the step-function coating. Clearly, a properly positioned step can be used to increase transmittance at a selected spectral minimum, thereby broadening the transmittance bandwidth.

The selective increase of transmittance at one minimum can be understood by examining the simple diagram shown in Fig. 9. The homogeneous coating was 0.25 µm in thickness and designed to be antireflective at $\lambda = 1.0$ µm. For an incident wave with wavelength $\lambda = 0.5$ µm, the coating thickness is $\lambda/2$, and according to Eq. (7), the film has no effect on transmittance at 0.5 µm. Stated differently, all waves reflected from the boundaries of the coating are in phase when $\lambda = 0.5$ µm, and the sum of these waves is equal to that of a wave reflected from the bare substrate. Placing a slight step in silica content at the center of the coating, indicated by a dashed line in Fig. 9, generates a new family of reflected waves that are out of phase with the

225
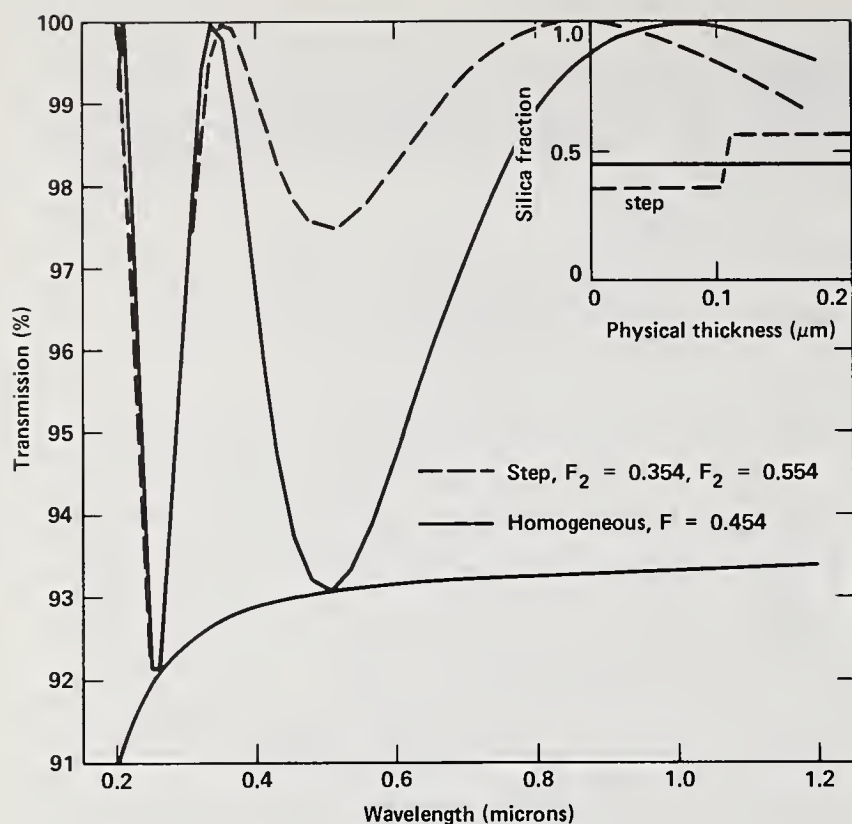
Fig. 8. Two-surface transmittanel for a homogeneous coating with F=0.45 and for a step-function coating with ΔF=0.2.
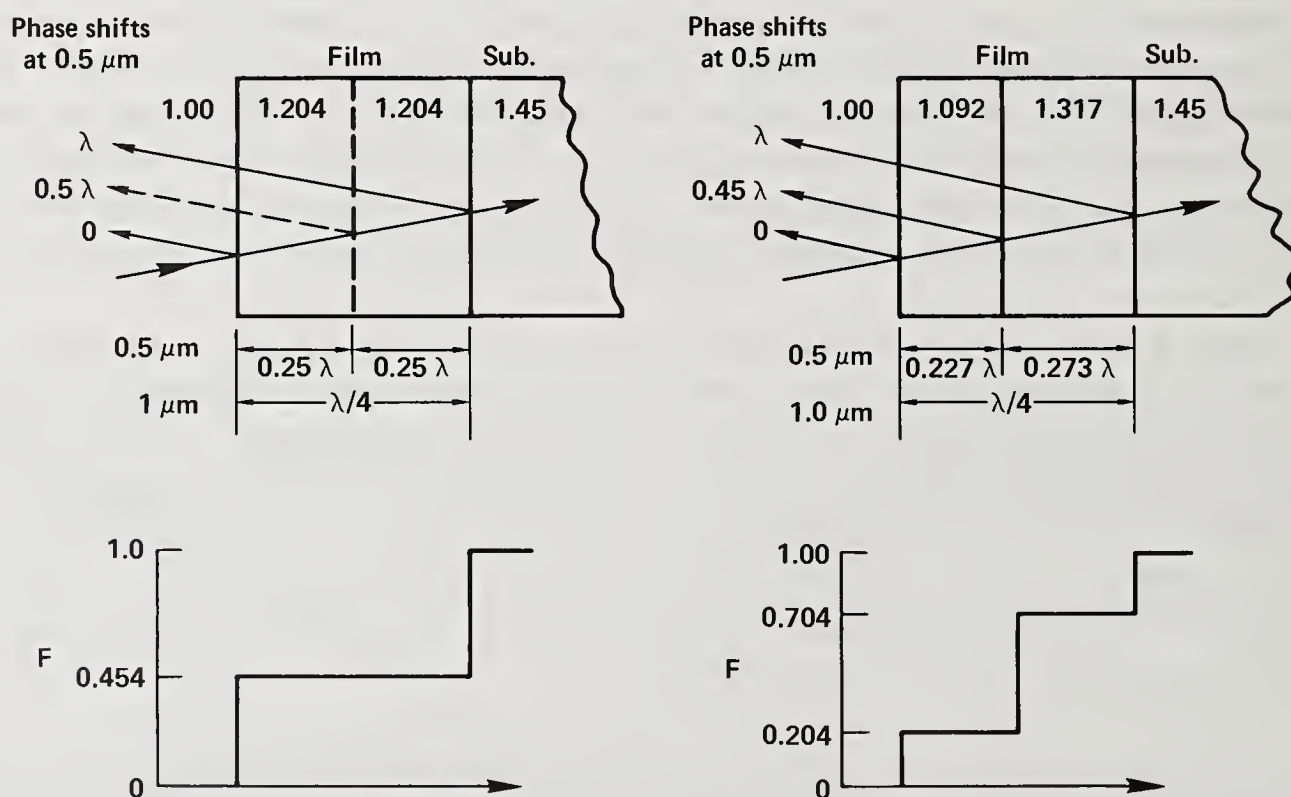
Fig. 9. Relative phase shifts of 0.5-μm wavelength waves reflected from boundaries of a coating and from an index step centered in the coating. Left: for a coating with optical thickness of .25 μm, the wave with .05-μm wavelength that is reflected from a hypothetical index step centered in the coating is out of phase with waves reflected from the coating boundaries. Right: dephasing of the wave reflected from the boundary is only .05 λ when the magnitude of the step is ΔF=0.5.

226

sum of waves reflected from the coating boundaries. If the discontinuity ΔF is sufficiently large, the net sum of all the waves will be zero. While it might seem that placing a large step at the midplane would significantly disturb the relative phasing of the reflected waves, this does not occur because the possible excursion for F, 0 to 1.0, produces an index excursion of only 1.0 to 1.45. The right side of Fig. 9 gives refractive indices and optical thicknesses for the two layers produced by placing a step $\Delta F = 0.5$ at the coating midplane. The dephasing of the wave reflected from the step is only .05 λ and could have been avoided by placing the step slightly more than 50% of the way across the coating.

The sketch in Fig. 9 also shows why a centered step did not influence transmittance at $\lambda = 0.25$ μm in the calculated spectrum shown in Fig. 8. The thicknesses of the homogeneous coating, d = 0.25 μm, and of either half of the coating are multiples of $\lambda/2$ for $\lambda = 0.25$ μm, so all of these films are absentee layers. Note, however, that we could have positioned the step about one-fourth of the way across the coating and made a significant change in transmittance at $\lambda = 0.25$ μm, although it can be shown that this would have provided only a small effect at $\lambda = 0.5$ μm. The step can in fact be thought of as a "transmittance helper" that can be positioned to increase transmittance at a selected minimum, or the step can be divided to provide some increase in transmittance at two or more minima. The linear-ramp coating discussed in the previous section is the limiting case of this process, a discontinuity ΔF that was divided into an infinite set of steps uniformly distributed acrossing the coating. However, nothing is free; as the discontinuity ΔF is distributed its magnitude must be increased if the distributed step is to produce large transmittance over an increased bandwidth. Values of $\Delta F \rightarrow 1$ were needed for the linear ramp; $\Delta F \sim 0.5$ is adequate for the discrete step.

That a smaller value of ΔF is needed for the step-function coating removes some of the practical difficulty in fabrication of such films. In Fig. 10 are shown spectra calculated under the assumption that the minimum achievable value of F is 0.3. A centered step of magnitude $\Delta F = 0.4$, ranging from F = 0.3 to F = 0.7, can provide two-surface transmittance 98.5% for the first three harmonics of the Nd:YAG laser, $\lambda = .355$ μm, 0.532 μm and 1.064 μm, or the coating thickness could be tuned to provide > 99.5% transmittance for two adjacent harmonics.

6. Arctangent-Profile Coatings

In this section we examine spectra of coatings with silica-content profiles described by the functional form F(x) = arctangent x, for $-5.0 \leq x \leq 5.0$. The arctangent function is a better representation of silica content in a coating whose porosity was graded by acid etching than is either the linear ramp or the step function. Since the gradiation in an arctangent coating is intermediate to that in the latter two coatings, the principal characteristics of spectra of arctangent coatings are predictable from results of the previous sections.

As in homogeneous coatings, values of T_{max} in the spectra of an arctangent coating are greatest when <F> = .45, but T_{max} does not vary rapidly with <F>. This is illustrated in Fig. 11. For these calculations, the thickness of the arctangent coating was held at $z_o = 0.2075$ μm, the value used in previous examples, and the arctangent function was "centered" in the coating profile. The resulting spectra have significantly improved transmittance at the minimum near $\lambda = 0.5$ μm, which mimics results obtained with a centered step, and also somewhat
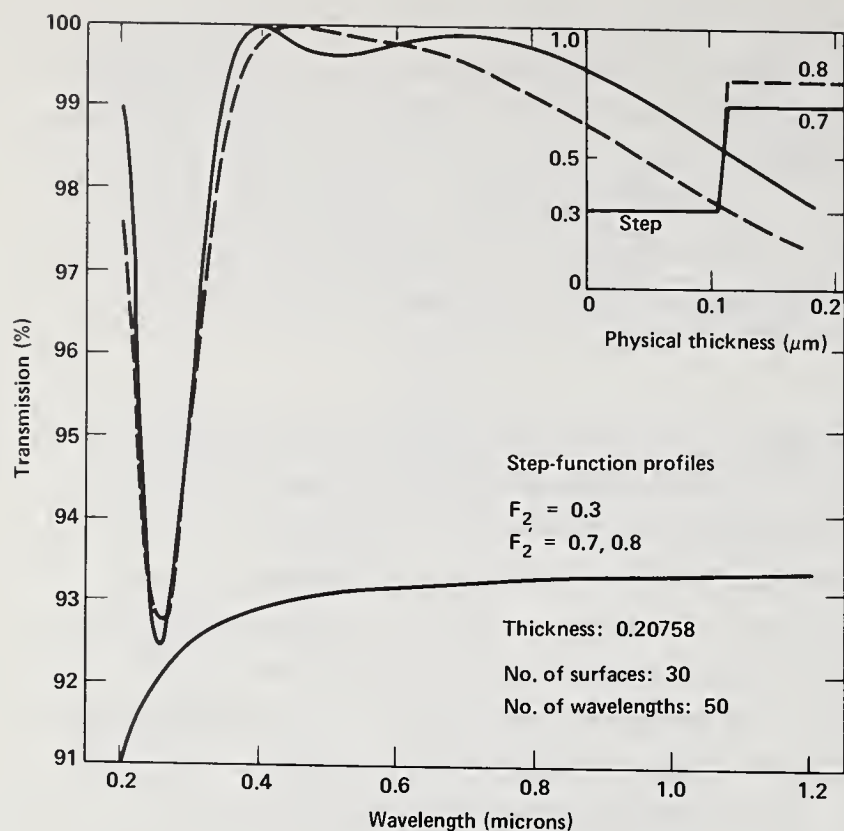
Fig. 10. Optimized spectral bandwidth for step-function coatings.

Step-function profiles

$F_2 = 0.3$

$F_2 = 0.7, 0.8$

Thickness: 0.20758

No. of surfaces: 30

No. of wavelengths: 50

Fig. 11. Variation of transmittance spectra with the average silica content in arctangent-profile coatings.

Arctangent profiles

A. $<F> = 0.354$

B. $<F> = 0.454$

C. $<F> = 0.554$
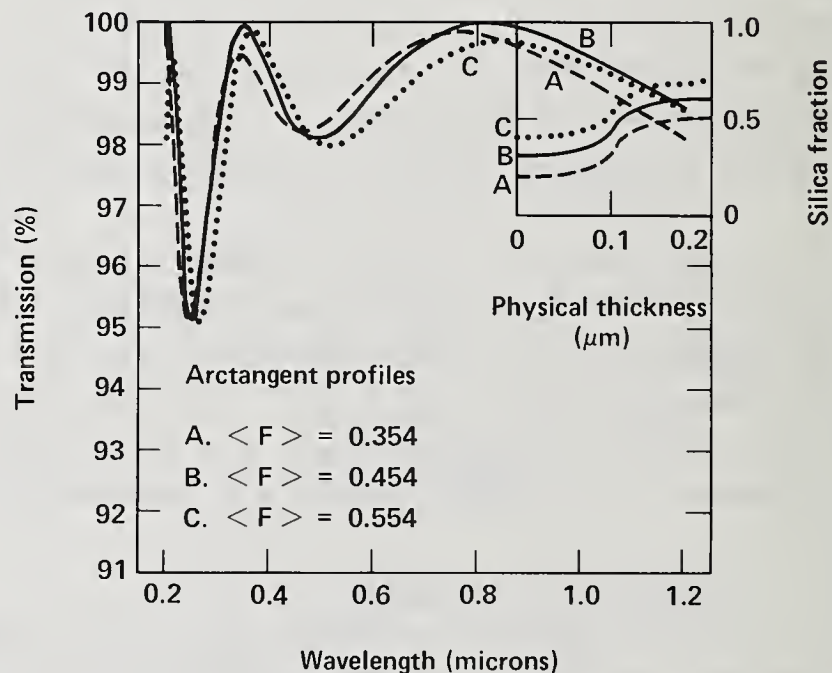
improved transmittance at the minimum near $\lambda = 0.25$ μm, which indicates that the distribution of gradiation in the arctangent function allows the coating to partially replicate the broadband improvement of transmittance that is characteristic of linear-ramp coatings.

Figure 12 gives spectra for four arctangent coatings that have varied excursions in silica content, $\Delta F = 0.2$ to 0.8, but the same average silica content, $<F> = .454$. The bandwidth in the transmittance spectrum is greatest for silica excursions near $\Delta F = 0.6$, but optimization of that coating requires use of a very low value of F at the air interface, $F_2 = 0.15$. In the region of greatest transmittance, $.40 \leq \lambda \leq .65$ μm, transmittance for this optimized arctangent coating is only slightly better than that obtained with a simple step function spanning a smaller range in silica content, $\Delta F = 0.4$.
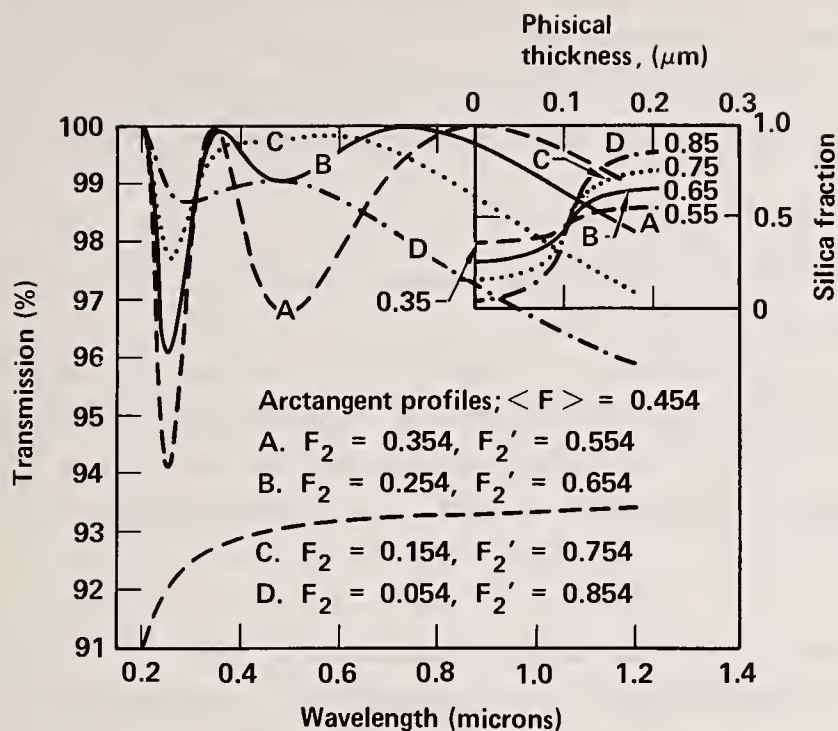
Fig. 12. Variation of transmittance of arctangent-profile coatings with range of silica fraction. The average silica fraction was 0.454 for all coatings.

Arctangent profiles; $<F>$ = 0.454
A. $F_2 = 0.354$, $F_2' = 0.554$
B. $F_2 = 0.254$, $F_2' = 0.654$
C. $F_2 = 0.154$, $F_2' = 0.754$
D. $F_2 = 0.054$, $F_2' = 0.854$

Finally, if we again take $F = 0.3$ as a minimum attainable value, the bandwidth of the arctangent coating is optimized for $\Delta F = 0.5$, with $F = 0.8$ at the substrate interface, see Fig. 13. The optimized coating provides transmittance > 98.5% over the wavelength range from 0.35 μm to 1.064 μm, and > 99.5% transmittance across the visible spectrum.

Fig. 13. Transmittance spectra of arctangent-profile coatings with silica fraction $F=0.3$ at the air interface.

Arctangent profiles; $F_2 = 0.3$
A. $F_2' = 0.4$
B. $F_2' = 0.6$
C. $F_2' = 0.8$
D. $F_2' = 1.0$
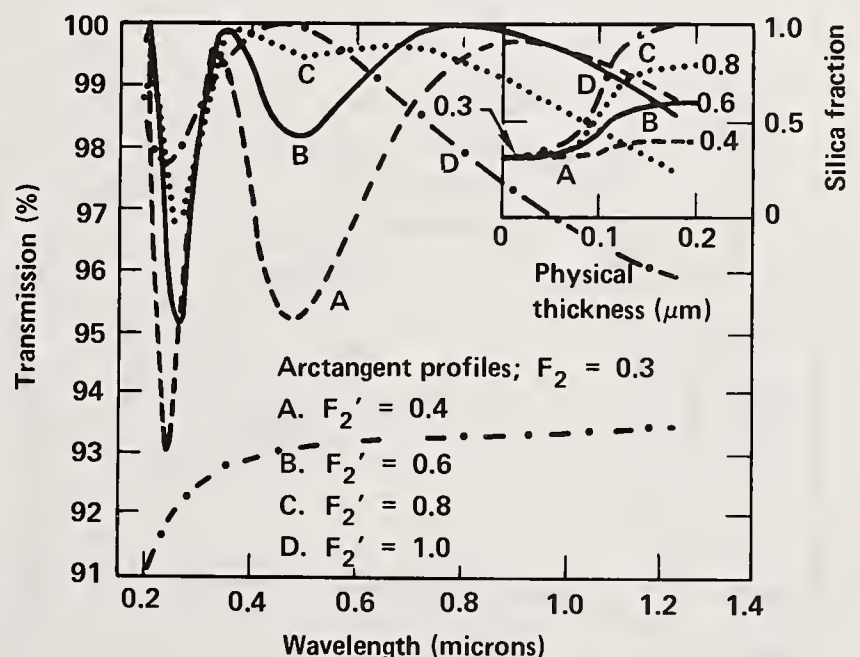
7.   Conclusions

For homogeneous coatings, transmittance oscillates between values T_{max} that depend on n_f and are greatest when $n_f = \sqrt{n_s}$ and $F = 0.454$, and values T_{min} that equal the transmittance of the substrate.

For coatings with a linear-ramp profile, transmittance spectra are also oscillatory, but transmittance at all minima is greater than that of the substrate. The largest values of T_{max}

229

occur when $<F> \sim 0.454$, while largest values for T_{min} occur for the greatest ramp angle. True optimization of the linear-ramp profile requires the attaining of $F \to 0$ ($n_2 \sim 1$) at the air/film interface, which cannot be achieved by currently known sol-gel coating techniques. Partially optimized linear-ramp coatings with $F = 0.3$ at the air/film interface provide $T > 98.6\%$ over the whole passband.

If the gradiation in silica content consists of a single abrupt step, the step can be positioned in the coating to produce a large increase in the value of T_{min} at a selected minimum, but transmittance at other minima may not be improved. Alternatively, the step in silica content can be distributed into several steps to obtain some improvement of transmittance at more than one spectral minima. A single step from $F = 0.3$ to $F = 0.7$ placed near the midplane of the coating with physical thickness 0.2075 μm provides transmittance $> 98.5\%$ for all wavelengths between 355 μm and 1.0 μm.

All other monotonically rising profiles are simply intermediate cases between the linear-ramp profile and the step-function profile, and spectra of such intermediate coatings are a rather predictable mixture of the principal features of spectra of the limiting cases.

To graphically illustrate these conclusions, we show spectra for optimized linear-ramp, centered-step and arctangent coatings with an assumed minimum achievable F of 0.4 (Fig. 14) and with assumed minimum F of 0.3 (Fig. 15). If the lowest silica content attainable is 0.4, and the intent is to fabricate antireflection coatings with good transmittance over the spectrum
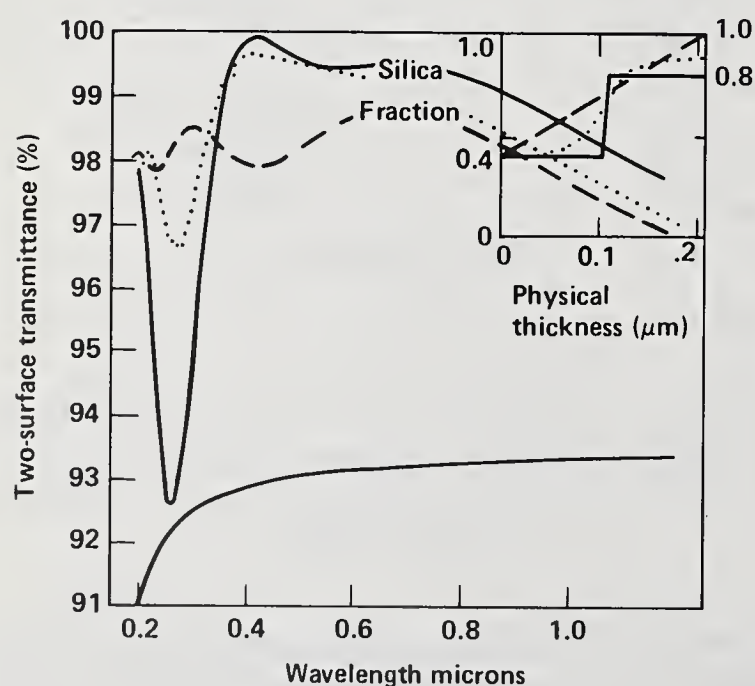
Fig. 14. Spectra for optimized linear-ramp, arctangent and stop-function coatings with F=0.4 at the air interface.
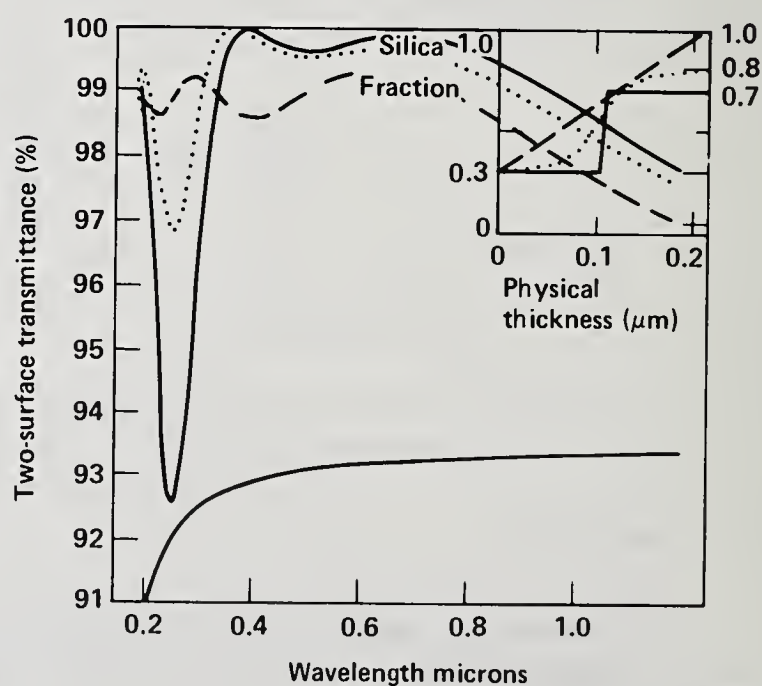
Fig. 15. Spectra for optimized linear-ramp, arctangant and step-function coatings with F=0.3 at the air interface.

encompassing the first three harmonics of the Nd:YAG laser, the step-function is the preferred design. If F can be reduced to 0.3, coatings with some gradation (such as the arctangent) are slightly advantageous. The greater potential of the linear-ramp coating can only be realized when the value of F at the air interface can be reduced to a value approaching zero.

Therefore, mastering the art of fabricating highly porous silica is the key to production of coatings with both large transmittance and large bandwidth.

References

1.   Ian M. Thomas, "Antireflective Coating for KDP Crystals," in the Technical Digest of the Conference on Lasers and Electro-Optics, held June 19-22, 1984 at Anaheim, CA., IEEE catalog number 84CH1965-3, paper THB5, p. 138.

2.   Bulent E. Yoldas, Deborah P. Partlow, and Harry D. Smith, "Polymer Oxide Antireflection Coating for Fused Silica," to be published in the proceedings of Laser Induced Damage in Optical Materials, 1983, held in Boulder, CO., Nov. 14-16, 1983.

3.   M. Born and E. Wolf, Principals of Optics, Pergamon Press, London, 1970 (Fourth Edition), p. 58.

4.   O. S. Heavens, Optical Properties of Thin Solid Films, Butterworths Scientific Publications, London, 1955, p. 58.

5.   H. Schroeder, "Remarks on the Theory of Light Transmission through Inhomogeneous Transparent Layers," (in German), Ann. Phys., Vol. 39, p. 55, 1941.

A question was raised about the form of the function used and a Gaussian was suggested. The author replied that the transmitted spectrum is not strongly affected by the shape that one chooses if it is monotonically rising. There will be some slight redistribution of the transmission at the minimum and you can always choose to put the maximum at 100%. There should thus not be a very strong change if a Gaussian were used in place of the arctan function shown. In response to a question about the antireflectance requirements at Livermore, the author replied that a reflectance less than bare fused silica was an advance. They hoped to get a two surface loss of 1% or less with a two surface loss of ½% at the design wavelength, but they would settle for less if they could find something that didn't blow off.

Characterization of Aluminum Nitride/Aluminum Oxide Reactively Sputtered Antireflection Coatings

L. G. Koshigoe

Michelson Laboratory, Materials Engineering Branch,
Systems Engineering Division

L. F. Johnson, T. M. Donovan, and C. D. Marrs

Michelson Laboratory, Physics Division
Naval Weapons Center, China Lake, California 93555

Aluminum nitride/aluminum oxide multilayer protective antireflection coatings are being developed for use on laser windows. These materials have been shown to be relatively stable and scratch resistant, thus demonstrating their applicability for this use. Both two- and three-layer coatings were designed at the wavelength $0.500\,\mu m$. The design techniques utilized, as well as the resulting transmission spectra, are discussed. Single-layer films have been deposited on fused quartz and calcium fluoride substrates, and a three-layer film has been deposited on a fused quartz substrate. Studies of the resistance of these films to various environmental conditions including laser radiation, fluorine, electron beam irradiation, and humidity are presented. Surface analysis techniques such as scanning Auger microscopy (SAM), scanning electron microscopy (SEM), energy dispersive X-ray microanalysis (EDX), X-ray photoelectron spectroscopy (XPS), and Nomarski microscopy were used to examine coating composition and stoichiometry. Preliminary measurements on the laser resistance of the materials indicate that damage at defects is the predominant failure mode.

Key words: AlN/Al_2O_3 multilayer; antireflection coatings; electron beam irradiation; fluorine exposure; humidity; laser damage.

1. Introduction

New multilayer antireflective coatings are being developed for protective use on laser windows. These coatings consist of alternating layers of aluminum nitride and aluminum oxide, which are stable and scratch resistant. Both materials have large bandgaps and are highly transparent from the ultraviolet to the infrared, thus making them ideal for use with many laser systems.

Both two- and three-layer designs have been developed for use at certain wavelengths. The two-layer design was based upon the work of Cox and Hass [1], and uses aluminum oxide as the outer material. This is particularly desirable since Al_2O_3 is resistant to moisture as well as to fluorine. The three-layer design was developed by applying the works of Baer [2] and Mouchart [3], who have determined techniques which allow for much design flexibility. This flexibility is the result of an extra degree of freedom which may be used to optimize the design with respect to low absorption, large bandwidth, good adherence, or ease of fabrication [4].

Preparations of the films have been achieved by numerous techniques ([5] through [36]), including reactive sputtering and evaporation, chemical vapor deposition, ion plating, activated decomposition of organometallic compound vapors, aluminum anodization, and laser-assisted deposition during electron beam evaporation. In this study, the methods of dc magnetron, ion beam, and rf diode sputtering have been used to deposit single layers and multilayers. Films prepared by these techniques have typically been shown to be stoichiometric and of high packing density.

Studies on the reactions of the multilayer materials with fluorine, electron beam irradiation, and humidity as well as on their damage by laser radiation will be discussed. The main techniques used for analysis and characterization of the films after exposure to the above environments are scanning Auger microscopy (SAM), scanning electron microscopy (SEM), energy dispersive X-ray microanalysis (EDX), X-ray photoelectron spectroscopy (XPS), and Nomarski microscopy.

2. Multilayer Designs

The choice of materials, AlN and Al_2O_3, necessitate the use of multiple-layer design techniques for obtaining zero reflectance. Both materials have high transmittances at the wavelength of interest (i.e., 0.500μm), but by themselves cannot accomplish the reflectance requirement. These materials have been prepared with indices of refraction which allow for production of zero reflectance coatings.

Since quarter-wave designs which produce zero reflectance are not possible, general solutions to the two- and three-layer cases must be used. These solutions allow flexibility in the choices of layer thicknesses, which is very desirable from the standpoints of absorption in the layers and film preparation.

Absorption in the layers is a problem which normally must be accounted for when designing multilayer systems, but the design techniques utilized in this study do not include this factor. Thus, an indirect approach should be used such as optimizing the solution through manipulations of layer thicknesses [2].

2.1 Two-Layer Design

As discussed by Cox and Hass [1], for zero reflectance, when the multilayer consists of two layers whose thicknesses are not related by integral multiples of each other, one obtains:

$$\frac{\tan\phi_1}{\tan\phi_2} = - \frac{r_1-r_3+r_2(1-r_1r_3)}{r_1-r_3-r_2(1-r_1r_3)} \tag{1}$$

and

$$\tan\phi_1\tan\phi_2 = \frac{r_1+r_3+r_2(1+r_1r_3)}{r_1+r_3-r_2(1+r_1r_3)} , \tag{2}$$

where

$$\phi_j = \frac{2\pi n_j l_j}{\lambda} \equiv 2\pi X_j ,$$

and

$$r_j = \frac{n_{j-1}-n_j}{n_{j-1}+n_j} .$$

Note that n_j is the index of refraction of the jth layer, l_j is its thickness, and λ is the design wavelength.

Equations (1) and (2) may be written in the form:

$$X_1 = \frac{1}{2\pi} \tan^{-1} \left[\pm\left(\frac{n_1^2(n_3-n_0)(n_2^2-n_0n_3)}{(n_1^2n_3-n_2^2n_0)(n_0n_3-n_1^2)} \right)^{1/2}\right] + \frac{m_1}{2} \tag{3}$$

and
$$X_2 = \frac{1}{2\pi} \tan^{-1} \left[\pm \left(\frac{n_2^2(n_3-n_0)(n_0n_3-n_1^2)}{(n_1^2n_3-n_2^2n_0)(n_2^2-n_0n_3)} \right)^{1/2} \right] + \frac{m_2}{2} , \tag{4}$$

where
$$m_1 = 0, \pm1, \pm2, \ldots ,$$

and
$$m_2 = 0, \pm1, \pm2, \ldots .$$

Thus, one may obtain a series of X_1's and X_2's and hence a series of physical thicknesses, l_1's and l_2's. Note that eqs (3) and (4) imply four possible pairs of solutions for each m_1 and m_2 set, but in actuality, only two of these pairs will satisfy eqs (1) and (2).

Applying eqs (3) and (4) to the present case of interest, where $n_0=1.00$, $n_1=1.60$, $n_2=2.00$, $n_3=1.46$ (these are the incident medium, outer aluminum oxide layer, inner aluminum nitride layer, and fused quartz substrate indices of refraction, respectively), and $\lambda=0.500\mu m$, a zero reflectance choice of thicknesses is then given by $l_1=0.0631\mu m$ and $l_2=0.0832\mu m$. This configuration is shown in figure 1. From this information, and assuming no absorption in the layers, normal light incidence, and constant indices of refraction for the wavelength region 0.3 to 0.9μm, the transmission spectrum has been determined using a program developed by Loomis [37].

This spectrum is shown in figure 2 as a function of wavelength. As can be seen, there is 100% transmission at 0.500μm and a bandwidth of approximately 0.06μm with a reflectance loss of 0.5% or less. The normalized electric field intensity as a function of depth into the layers is shown in figure 3 and was determined by Elson [38]. It is apparent that the electric field minimum occurs in the thicker aluminum nitride layer. This is advantageous from the standpoint that the aluminum nitride layer is the more absorbing material as shown by preliminary absorption measurements.

2.2 Three-Layer Design

Based upon the works of Baer [2] and Mouchart [3], an analytic solution for a general three-layer antireflective coating has been utilized. According to Baer, Smith's theorem may be used when determining what conditions must be applied to obtain zero reflectance. These conditions indicate that both the real and imaginary components of the Fresnel coefficients must vanish. Then, as discussed by Baer, one obtains:

$$X_1 = \pm \frac{1}{4\pi} \cos^{-1} \left[\frac{r_2^2+r_1^2-|r_b|^2(1+r_2^2r_1^2)}{2r_2r_1(|r_b|^2-1)} \right] + \frac{m_1}{2} , \tag{5}$$

and
$$X_2 = \frac{1}{4\pi} (\delta_a+\delta_b) + \frac{m_2}{2} , \tag{6}$$

where
$$r_a = \frac{r_2+r_1 \exp(-4\pi X_1 i)}{1+r_2r_1 \exp(-4\pi X_1 i)} , \tag{7}$$

$$r_b = \frac{r_3 + r_4 \exp(-4\pi X_3 i)}{1 + r_3 r_4 \exp(-4\pi X_3 i)} \, , \tag{8}$$

and
$$X_j = \frac{n_j l_j}{\lambda} \, , \tag{9}$$

$$m_1 = 0, \pm 1, \pm 2, \ldots \, ,$$

$$m_2 = 0, \pm 1, \pm 2, \ldots \, .$$

Note that δ_a and δ_b refer to the phases of r_a and r_b respectively and that the X_j and r_j are as defined earlier. Hence, for a choice of X_3, and given the indices of refraction of the layers, one may obtain a series of solutions. Note that there are two series of solutions for each X_3.

Figure 4a shows a plot of X_1 and X_2 as functions of X_3 for $\lambda=0.500\mu m$, $n_0=1.00$, $n_1=2.00$, $n_2=1.60$, $n_3=2.00$, and $n_4=1.46$. Figure 4b shows a similar plot with $\lambda=0.500\mu m$, $n_0=1.00$, $n_1=2.00$, $n_2=1.60$, $n_3=2.00$, and $n_4=1.44$. These indices of refraction correspond to the incident medium, aluminum nitride layer, aluminum oxide layer, aluminum nitride layer, and fused quartz substrate (fig. 4a) or calcium fluoride substrate (fig. 4b), respectively. Note that the solid curves correspond to the first solution and the dashed to the second.

A particular solution from the results shown in figure 4a is $X_3=0.250$, $X_1=0.447$, and $X_2=0.326$. Hence, $l_1=0.112\mu m$, $l_2=0.102\mu m$, and $l_3=0.625\mu m$. This configuration is shown in figure 5.

As in the two-layer case, a plot of the transmission spectrum as a function of wavelength is shown in figure 6 (for the particular solution discussed above). Again, there is 100% transmission at $0.500\mu m$ as expected, but the bandwidth at a reflectance loss of 0.5% is reduced to approximately $0.02\mu m$. Hence, from the standpoint of bandwidth, this design is not as desirable. The normalized electric field intensity is shown in figure 7. In this case, the electric field minimum again occurs in one of the aluminum nitride layers, with the maximum occurring in the aluminum oxide layer. Thus, as in the two-layer case, the design appears to be a favorable choice from the standpoint of absorption.

3. Sample Preparation

Several single-layer samples and one three-layer sample were deposited onto substrates of fused quartz, calcium fluoride, or silicon. Substrate diameters were 1 inch and thicknesses were 0.063 inch, 0.058 inch, and 0.023 inch, respectively. Very thin layers of Ag/Cr/Mo, Au/Cr/Mo, or Au/Cr were deposited onto some of the substrates prior to AlN or Al_2O_3 deposition for the purpose of aiding in eliminating charging problems during analysis. Tables 1 and 2 contain lists of the specimens prepared along with any pertinent information relating to their depositions for depositions in the dc magnetron and rf diode sputtering systems, respectively. Approximate deposition temperatures for the two systems were 160°C and 300°C, respectively. Note that samples on Si or on aiding layers were used as witnesses. Sample M-177 of Al_2O_3, prepared in the ion beam sputtering system, was deposited on aiding layers of Au/Cr with a substrate of Si. The approximate gas pressure was 1.5×10^{-4} torr of Ar, deposition was at room temperature, and the estimated film thickness was 2800Å. Table 3 contains information regarding the purities of the materials used (for the various depositions) and their suppliers.

TABLE 1. Information on Samples Prepared in dc Magnetron System.

Sample Number	Film Material	Aiding Layers	Approximate Gas Pressure (torr)	Substrate	Estimated Film Thickness (Å)
T-261S	AlN	-	$3 \times 10^{-3} N_2$	Fused Quartz	2030
T-265S	AlN	-	$1.5 \times 10^{-3} N_2$ $1.5 \times 10^{-3} Ar$	Si	2000
T-266S	AlN	Ag/Cr/Mo	$3 \times 10^{-3} N_2$	Fused Quartz	2000
T-268S	AlN	Ag/Cr/Mo	$1.5 \times 10^{-3} N_2$ $1.5 \times 10^{-3} Ar$	Fused Quartz	2000
T-270S	Al_2O_3	-	$3 \times 10^{-4} O_2$ $2.7 \times 10^{-3} N_2$	Fused Quartz	2000
T-276S	AlN	-	$1.5 \times 10^{-3} N_2$ $1.5 \times 10^{-3} Ar$	CaF_2	2000
T-281S	AlN	-	$3 \times 10^{-3} N_2$	CaF_2	4000
T-289S	(a) AlN (outer)		(a) $3 \times 10^{-3} N_2$	Fused Quartz	(a) 1120
	(b) Al_2O_3 (middle)	-	(b) $3 \times 10^{-4} O_2$ $2.7 \times 10^{-3} N_2$		(b) 1020
	(c) AlN (inside)		(c) $3 \times 10^{-3} N_2$		(c) 625
T-290S	AlN	Ag/Cr/Mo	$3 \times 10^{-3} N_2$	Fused Quartz	2000
T-290S	AlN	Au/Cr/Mo	$3 \times 10^{-3} N_2$	Fused Quartz	2000
T-297S	AlN	Au/Cr	$3 \times 10^{-3} N_2$	Si	2800

TABLE 2. Information on Samples Prepared in rf Diode System.

Sample Number	Film Material	Approximate Gas Pressure (torr)	Substrate	Film Thickness (Å)
S-826	Al_2O_3	$8 \times 10^{-4} O_2$ $7.2 \times 10^{-3} N_2$	Fused Quartz	2100
S-827	AlN	$2 \times 10^{-3} N_2$ $6 \times 10^{-3} Ar$	Fused Quartz	7000
S-833	Al_2O_3	$8 \times 10^{-4} O_2$ $7.2 \times 10^{-3} Ar$	Fused Quartz	2100
S-834	AlN	$2 \times 10^{-3} N_2$ $6 \times 10^{-3} Ar$	Fused Quartz	7000
S-835	AlN	$8 \times 10^{-4} N_2$ $7.2 \times 10^{-3} Ar$	Fused Quartz	7000

TABLE 3. Purities of Materials Used in Sample Depositions.

Material	Purity (%)	Source
Al	99.999	Specialty Metals Division of Varian
Al_2O_3	Unknown	Microelectronics Branch, NAVWPNCEN
Au	99.999	American Smelting Company
Mo	99.999	American Smelting Company
Cr	99.996	Specialty Metals Division of Varian

Most of the samples were deposited using a dc magnetron sputtering system with a 5-inch Varian sputter gun (samples listed with a "T" before their numbers; see table 1). Some samples were prepared in a Randex model 2400 rf diode sputtering system (samples with an "S" before their numbers; see table 2). One sample was prepared by ion beam deposition using an Ion Technology, Inc., 2.5mm ion gun (as indicated by an "M" before the sample number above).

The three-layer sample was prepared according to the 0.500μm design discussed previously (particular solution). Indices were assumed to be 2.00 and 1.60 for AlN and Al_2O_3, respectively, and the materials were deposited until the necessary thicknesses had been obtained. Although the indices of refraction have not been accurately determined in this study, many researchers have previously determined them to range from 1.70-2.15 for AlN and 1.42-1.79 for Al_2O_3 [5], [6], [16], [23], [25], [26], [28], [29], [30], [35], [36], implying that the assumed values are realistic. Furthermore, recent laboratory studies indicate that the assumed indices are more likely.

A transmission spectrum of the three-layer sample coating over the wavelength region of 0.3 to 0.9μm was measured using a Beckman DU-7 UV/VIS spectrophotometer. This spectrum is shown in figure 8. In comparison to the theoretical spectrum shown in figure 6, it is apparent that the two are similar in curve shape, but some additional tuning is necessary in the experimental sample preparation to more closely approximate the theoretical curve. The experimental maximum in transmission of 98.8% occurred at 0.553μm. By the use of a program written by Loomis [37], variations in the thicknesses and indices of the layers were made to attempt to determine what changes would cause a calculated transmission spectrum to approach the appearance of the experimental spectrum. It was found that the differences between the two spectra is a combination of a need to determine the actual film indices and to measure more accurately the deposition rates of the materials. At this time, efforts are being made to accomplish these tasks.

4. Film Structure

Study of the structures of both single and multilayer films were made using a scanning electron microscope. The films were coated with thin layers of Au (approximately 150A) to avoid charging problems.

Shown in figures 9a and 9b are typical top and cross sectional views of an AlN single layer. This film was sample number T-297S prepared in the dc magnetron system. Figures 10a and 10b show top and cross sectional views of an Al_2O_3 single layer prepared in the ion beam system (sample M-177). Figures 11a and 11b show top and cross sectional views of the AlN/Al_2O_3/AlN multilayer (sample T-289S) prepared in the dc magnetron system. In the last case, the three layers can be distinguished.

Many defects are apparent on the surface of the AlN single and multilayer films. It is not known at this time whether the defects are growth defects of a nodular type or whether they are bubbles or splatters on the surfaces only. These defects are typically on the order of 5-10μm in diameter. The Al_2O_3 specimen is of a much finer surface structure, although smaller defects (approximately 1μm in diameter) are apparent on it also. Figures 12a through 12c show magnified views of the AlN, Al_2O_3, and multilayer defects, respectively.

The cross sections or side views of the AlN layers display columnar growth type structures. It has been determined by transmission electron diffraction that these films are polycrystalline. The side views of the Al_2O_3 layers show much smoother textures with no columnar growth structures apparent at the magnifications achieved in these experiments. A pattern was not obtained from the diffraction studies for the Al_2O_3, hence it is probably amorphous. Note that the Al_2O_3 single layer and multilayer specimens were prepared in different sputtering systems, but the texture of the Al_2O_3 still remains similar in the two cases.

From electron spectroscopy for chemical analysis (ESCA) studies, AlN materials have been determined to be 95% stoichiometric with the remainder consisting mostly of Al_2O_3. Al_2O_3 films have been shown to be 99% stoichiometric.

5. Results

Results have been obtained on sample behavior following exposure to laser radiation, fluorine, electron beam irradiation, and humidity. The samples studied were discussed earlier and will be referred to by their designated sample numbers. Not all samples given earlier will be discussed since some were only used for obtaining preliminary spectral information and since experimental difficulties were encountered during analysis with others which were associated with film quality and charging problems.

5.1 Laser Radiation

The effects of laser radiation on the multilayer sample were studied with a Phi 600 scanning Auger microscopy system (after damage). The sample surface was cleaned during analysis by sputtering with Ar ions using an accelerating voltage of 4kV. For SiO_2, an approximate removal rate has been determined to be 40Å/min.

A pulsed dye laser in a triaxial configuration was utilized for damaging the film at a wavelength of 0.497μm. The first step in the laser damage study was to scratch crosshairs onto the film on opposite sides of its center along a sample diagonal. These crosshairs were then used as index marks for locating five equally spaced sites between them. Each site was then irradiated in air with a few laser pulses of increasing energy density. The pulse shape was a 1mm diameter flat top (± 5% flatness) with a duration of 0.55μs. Film breakdown thresholds were roughly determined by observing the beginning of film changes with a video microscopy system (VIMS). Note that no attempts were made in this study to determine actual damage thresholds of the materials. The main purpose of this study was to determine the behavior of the film after exposure to laser radiation.

Table 4 lists the energy density of each shot for the five sites. Shown in figures 13a through 13e are portions of the centers of each of the five sites. These figures in comparison to a typical undamaged site (such as that in fig. 11a), show an increasing number of damage craters with respect to defects for an increasing energy density. Site 1 shows mostly defects plus some small damage craters. Sites 2 and 3 show more and larger damage craters with a reduced number of apparent defects. Site 4 shows the beginning of damage crater agglomeration, and site 5 shows many small pit marks which appear to lay at the centers of what were originally damage craters (the pits are at the centers of circular patterns which resemble agglomerated craters). In addition, for site 5, it is apparent that there is a loss of much of the outer film.

TABLE 4. Laser Energy Densities for the Five Damage Sites.

	Energy Density (J/cm^2)				
	Site 1	Site 2	Site 3	Site 4	Site 5
1st pulse	3.2	9.2	12.	20.	50.
2nd pulse	5.9	9.2	-	-	-
3rd pulse	9.4	-	-	-	-

The approximate number of defects for typical portions of the film where no damage was done is 70 (see the sampling area of fig. 11a for an example). For sites 1 and 2, the number of damage craters plus defects which did not damage are approximately 60 and 70 (in the same size sampling area), respectively. These are similar to that of the undamaged site which implies that damage is initiating at defects. For sites 3 through 5, the number of craters plus undamaged defects is large in comparison to the number of defects on the undamaged site, increasing in number with increasing energy density (assuming the pit marks of site 5 are indeed the centers of what were originally damage craters), although few apparent defects remain on these sites. These results support damage initiating at the defect sites, with some other possible mode(s) of damage (e.g., caused by non-observable defects) also contributing to the cratering.

Auger spectra were obtained for some of the damage sites. Thin layers of gold were deposited on the films prior to the study and then removed by Ar ion sputtering (as discussed earlier) just until Auger peaks corresponding to the underlying film were obtained. Figures 14a and 14b show spectra obtained at site 2. Figure 14a illustrates a portion of the damage site which appeared to be unaffected by the laser radiation (herein referred to as smooth film) and figure 14b was taken within a damage crater. It is apparent that the smooth film consists mostly of AlN and the crater site consists of AlN plus Al_2O_3. Similar spectra were obtained for some of the other sites, where the spectra from the craters always showed an increase in Al_2O_3 with respect to AlN. In addition, when comparing damage sites, it is apparent that the amount of Al_2O_3 with respect to AlN increased with increasing energy density. Figure 15 shows the spectrum obtained on a smooth portion of the film at site 4. A possible explanation for the growth of the oxide peak is the dissociation of some of the surface AlN, and then combination of the Al with oxygen to form Al_2O_3 (recall that these studies were performed in air). Thus, the amount of oxidation of AlN would increase with energy density. In addition, the larger oxide peaks in the craters may be explained by assuming that these are positions on the film where the energy was absorbed more, or not conducted away as quickly, hence resulting in temperature buildup and more oxidation.

5.2 Fluorine Exposure

Single layer samples T-297S and M-177 of AlN and Al_2O_3, respectively, were exposed to 10% HF in Ar for 1 hour, and were then examined for fluorine penetration.

EDX was initially used to detect the fluorine. Since this technique examines the constituents of the materials to a much greater depth (on the order of a micron), than a technique such as AES, any severe fluorine penetration should be detected. Fluorine was not detected in either the AlN or Al_2O_3. Hence, either the fluorine had not penetrated the material to a very great depth, or the fluorine concentration was low (low atomic number materials have low X-ray intensities due to low fluorescence yield and high sample absorption; see [39]).

AES and XPS were then used to analyze the film makeup since the results of the EDX had indicated no great depth penetration of the fluorine in either film. With these techniques fluorine was observed. Figures 16a and 16b display AES profiles of the AlN and Al_2O_3 films, respectively. Note that the AES system used in this case is a Physical Electronics 548 Auger/ESCA system, which employed a 1kV beam of Ar ions for sputter removal. For SiO_2, a removal rate of 15Å/min. is typical. Assuming this rate for AlN and Al_2O_3 yields approximate depth penetrations of 30-45Å for both films, although the fluorine appears to drop off (with depth) at a slightly higher rate in the Al_2O_3 film.

5.3 Electron Beam Irradiation

During surface studies such as SEM and SAM, physical changes of the AlN and Al_2O_3 films were observed. Dark spots indicating changes in electron yields were observed at positions on the films where the electron beams were concentrated. At this time it is uncertain whether these changes were temporary (i.e., caused by contaminants being deposited on or removed from the film surfaces) or permanent. It is important to note that, as discussed earlier, it was necessary to coat the films with thin layers of a conducting material such as Au to avoid charging problems.

5.4 Humidity

Single layer samples T-297S and M-177 of AlN and Al_2O_3, respectively (several sister samples were produced resulting in the availability of a "fresh" sample for each study), were exposed to 95% relative humidity at 60°C for 24 hours. With the use of a Nomarski microscope, no change in the Al_2O_3 sample was observed although the AlN showed signs of degradation.

6. Conclusions

The theoretical aspects of the AlN/Al_2O_3 multilayer designs indicate that perhaps the two-layer case may be more useful because of its bandwidth. At a reflectance loss of 0.5%, it has a bandwidth three times the size of that of the three-layer design. Although it has not been discussed in this study, simple calculations show that a two-layer quarter wave design is possible with a low reflectance (less than 0.005). This may be a more practical design. In this study, a film corresponding to the three-layer design was prepared and transmission results indicated a need to determine more accurately the indices of refraction and deposition rates of the materials.

Film structure studies indicate that defects are apparent on both the AlN, Al_2O_3, and $AlN/Al_2O_3/AlN$ multilayer samples. The defects on the Al_2O_3 appear to be smaller (approximately 1µm in diameter as compared with 5-10µm for the AlN single and multilayer films). The growth structure of the AlN is columnar, whereas that of the Al_2O_3 is much smoother (no structure is observed at the SEM magnifications used in this study).

Laser damage studies indicate that multilayer damage initiates predominately at defect sites. In addition, SAM studies indicate that the AlN outer layer of the multilayer oxidizes upon exposure to laser radiation in air. The amount of oxidation increases with increasing laser energy density and is also greater within damage craters than on portions of the film which appear to be unaffected by the laser radiation.

Fluorine exposure studies show depth penetrations of approximately 30-45A (assuming the same sputter removal rate of AlN and Al_2O_3 as SiO_2) in both films with the fluorine dropping off with depth at a slightly higher rate in the Al_2O_3.

Surface analysis techniques such as SEM and SAM indicate a sensitivity of the films to the electron beams. It is not certain whether the film changes after electron beam exposure are permanent.

After exposure to humidity, a Al_2O_3 single-layer film underwent no observable change, although an AlN single layer film exposed to the same condition degraded.

Most importantly, it is apparent that the use of an AlN/Al_2O_3 multilayer in the environments described above dictates that Al_2O_3 should be the outer material.

Overall, both films appear to be durable and relatively easy to prepare as a multilayer system. These studies are continuing and clean room techniques are being applied to achieve films with fewer defects.

---

7. References

[1] Cox, J. T.; Hass, G. Antireflection coating for optical and infrared optical materials, chapter 5 in Physics of thin films, Vol. 2. Hass, G.; Thun, R. E., ed. New York: Academic Press; 1964. 239-304.

[2] Baer, A. D. Design of three-layer antireflection coatings. Glass, A. J.; Guenther, A. H., ed. Laser induced damage in optical materials: 1976; 1976 July 13-15; Boulder, CO. Nat. Bur. Stand. (U.S.) Spec. Publ. 462; 1976 December. 221-229.

[3] Mouchart, J. Thin film optical coatings. 2: Three-layer antireflection coating theory. Applied Optics 16(10): 2722-2728; 1977 October.

[4] Rudisill, J. E. Exploratory development on antireflective coating for 2 to 6 micrometers for fluorine windows. Hughes Research Laboratories; Malibu, CA. Report No. AFML-TR-78-19; 1978 March. 78 pages.

[5] Duchene, J. Radiofrequency reactive sputtering for deposition of aluminum nitride thin films. Thin Solid Films 8: 69-79; 1971.

[6] Shuskus, A. J.; Quinn, D. J.; Paradis, E. L.; Berak, J. M.; Cullen, D. E. Sputtered thin film research. United Aircraft Corporation Research Laboratories; East Hartford, CT. Report No. M951337-9; AD-769972; 1973 October. 59 pages.

[7] Shuskus, A. J.; Quinn, D. J.; Paradis, E. L.; Berak, J. M.; Cullen, D. E.; Reeder, T. M. Sputtered thin film research. United Aircraft Corporation Research Laboratories; East Hartford, CT. Report No. N921337-15; AD/A-003005; 1974 November. 211 pages.

[8] Lieske, N.; Hezel, R. Formation of Al-nitride films at room temperature by nitrogen ion implantation into aluminum. J. Appl. Phys. 52(9): 5806-5810; 1981 September.

[9] Hantzpergue, J. J.; Pauleau, Y.; Remy, J. C.; Roptin, O.; and Coiller, M. Electrical properties of sputtered AlN films and interface analyses by Auger electron spectroscopy. Thin Solid Films 75: 167-176; 1981.

[10] Murayama, Y.; Kashiwagi, K.; Kikuchi, M. Aluminum nitride films by rf reactive ion plating. J. Vac. Sci. Technol. 17(4): 796-799; 1980 July/August.

[11] Duffy, M. T. ; Wang, C. C. Piezoelectric aluminum nitride films. RCA Laboratories; Princeton, NJ. Report No. PRRL-74-CR-65; AD-A007657; 1974 October. 139 pages.

[12] Liu, J. K.; Lakin, K. M.; Wang, K. L. Growth morphology and surface-acoustic-wave measurements of AlN films on sapphire. J. Appl. Phys. 46(9): 3703-3706; 1975 September.

[13] Lakin, K. M.; Liu, J. K.; Wang, K. L. Abstract: Growth morphology and surface-acoustic-wave measurements of AlN films on sapphire. J. Vac. Sci. Technol. 13(1): 37-38; 1976 January/February.

[14] Lakin, K. M. Aluminum nitride for surface acoustic waves. University of Southern California; Electronic Sciences Laboratory; Los Angeles, CA. AD/A-002138; 1974 August. 37 pages.

[15] Takeda, F.; Mori, T.; Takahashi, T. Effect on hydrogen gas on C-axis oriented AlN films prepared by reactive magnetron sputtering. Japanese J. Appl. Phys. 20(3): L169-L172; 1981 March.

[16] Gerova, E. V.; Ivanov, N. A.; Kirov, K. I. Deposition of AlN thin films by magnetron reactive sputtering. Thin Solid Films 81: 201-206; 1981.

[17] Lakin, K. M.; Wang, J. S.; Landin, A. R. Aluminum nitride thin film and composite bulk wave resonators. 36th Annual Frequency Control Symposium; 1982. AD P001565. 517-524.

[18] Fathimulla, A.; Lakhani, A. A. Reactively rf magnetron sputtered AlN films as gate dielectric. J. Appl. Phys. 54(8): 4586-4589; 1983 August.

[19] Rairden, J. R.; Aluminum nitride thin films deposited by reactive evaporation. Vranty, F., ed. Thin Film Dielectrics Symposium; 1969. Electrochem. Soc., Inc.; New York, NY. 279-285.

[20] Yamashita, H.; Fukui, K.; Misawa, S.; Yoshida, S. Optical properties of AlN epitaxial thin films in the vacuum ultraviolet region. J. Appl. Phys. 50(2): 896-898; 1979 February.

[21] Winsztal, S.; Wnuk, B.; Majewska-Minor, H.; Niemyski, T. Aluminum nitride thin films and their properties. Thin Solid Films 32: 251-254; 1976.

[22] Mirsch, S.; Reimer, H. Preparation and electrical properties of Al-AlN-Si structures. Phys. Stat. Sol. (a) 11: 631-635; 1972.

[23] Puychevrier, N.; Menoret, M. Synthesis of III-V semiconductor nitrides by reactive cathodic sputtering. Thin Solid Films 36: 141-145; 1976.

[24] Noreika, A. J.; Francombe, M. H. Structural, optical, and dielectric properties of reactively sputtered films in the system AlN-BN. J. Vac. Sci. Technol. 6(4): 722-726; 1969 July.

[25] Bauer, J.; Biste, L.; Bolze, D. Optical properties of aluminum nitride prepared by chemical and plasmachemical vapour deposition. Phys. Stat. Sol. (a) 39: 173-181; 1977.

[26] Duffy, M. T.; Kern, W. Chemical vapor deposition of aluminum oxide films from organo-aluminum compounds. RCA Review 31(4): 754-770; 1970 December.

[27] Silvestri, V. J.; Osburn, C. M.; Ormond, D. W. Properties of Al_2O_3 films deposited from the $AlCl_3$, CO_2, and H_2 system.   J. Electrochem. Soc.: Solid-State Science and Technology 125(6): 902-907; 1978 June.

[28] Ferrieu, E.; Pruniaux, B.   Preliminary investigations of reactively evaporated aluminum oxide films on silicon. J. Electrochem. Soc.: Solid State Science 116(7): 1008-1013; 1969 July.

[29] Salama, C. A. T.   RF sputtered aluminum oxide films on silicon. J. Electrochem. Soc.: Solid State Science 117(7): 913-917; 1970 July.

[30] Mier, M. G.; Buvinger, E. A. A comparative study of anodized, evaporated, and sputtered aluminum oxide thin films. J. Vac. Sci. Technol. 6(4): 727-730; 1969.

[31] Kanstad, S. O.; Nordal, P. E.   Infrared photoacoustic spectroscopy of solids and liquids. Infrared Physics 19(3-4): 413-422; 1979 August.

[32] Hart, R. R.; Reuter, F. W. III; Smith, H. P. Jr.; Khan, J. M. Oxygen K-shell X-ray production in thin films of aluminum oxide by 20- to 100- keV photons. Physical Review 179(1): 4-9; 1969 March 5.

[33] Chen, C. H.; Silcox, J.   Surface guided modes in an aluminum oxide thin film. Solid State Communications 17: 273-275; 1975.

[34] Vyatskin, A. Ya.; Trunev, V. V. The interaction of electrons with thin films of dielectrics. Radiotekh. Electron 17(9): 1899-1905; 1972.

[35] Korzo, V. F.   Preparation of thin layers of aluminum oxide by pyroactivated decomposition of organic compounds. Zhurnal Prikladnoi Khimii 49(1): 74-77; 1975 January.

[36] Rowe, J. M.   Laser-assisted deposition coatings. Northrop Research and Technology Center; Palos Verdes Peninsula, CA. Report No. AFWL-TR-83-34; 1983 September. 76 pages.

[37] Loomis, J. S.   Computing the optical properties of multilayer coatings. Air Force Weapons Laboratory; Kirtland Air Force Base, NM. Report No. AFWL-TR-75-202; 1975 September. 30 pages.

[38] The calculation of field dependence was performed by J. M. Elson.

[39] Barbi, N. C.   Electron probe microanalysis using energy dispersive X-ray spectroscopy. Princeton Gamma-Technology, Inc.; Princeton, NJ.
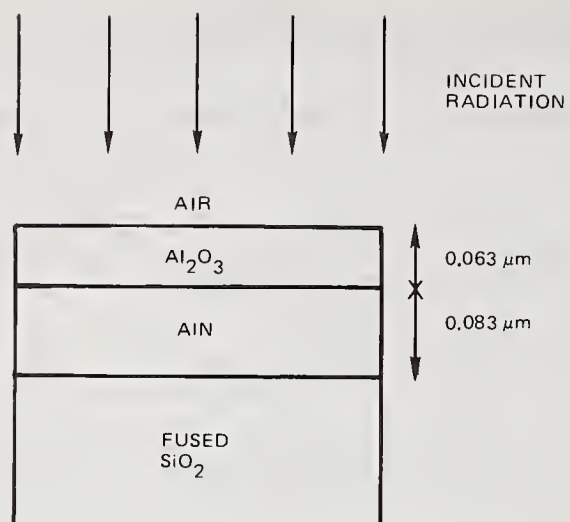
FIGURE 1. Two-layer Design Configuration.
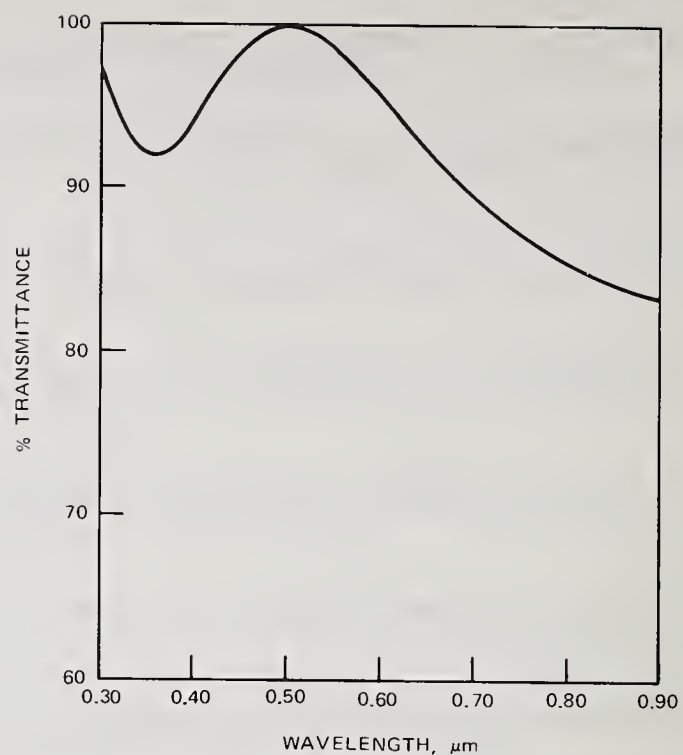
FIGURE 2. Theoretical Transmittance of Two-layer Design.
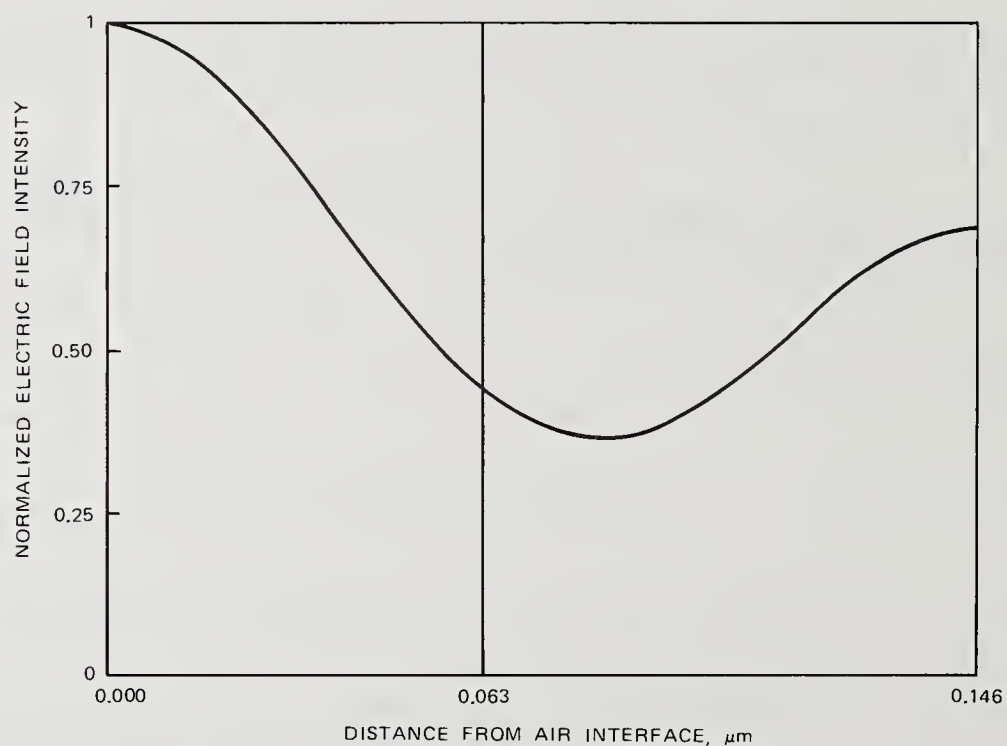
FIGURE 3. Normalized Electric Field Intensity of Two-layer Design.
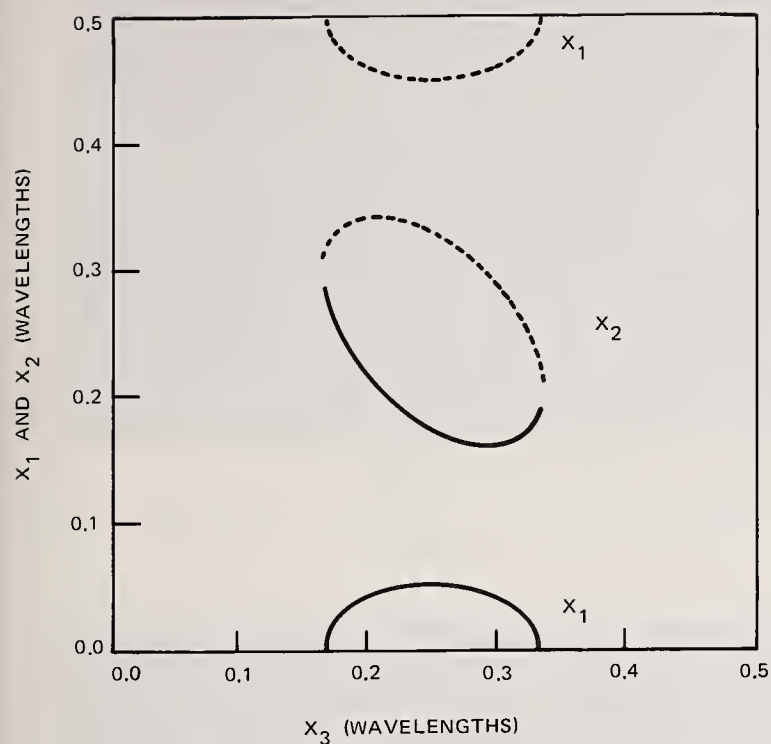
244

FIGURE 4. Antireflection Solutions for a
Three-layer Design with Fused Quartz as Substrate.
(a)
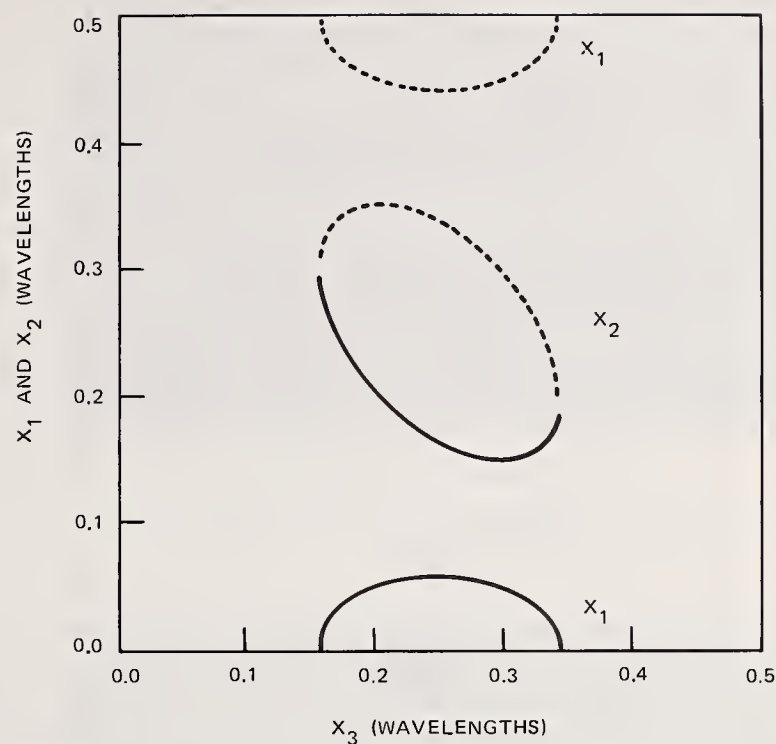
FIGURE 4. Antireflection Solutions for a
Three-layer Design with Calcium Fluoride as Substrate.
(b)
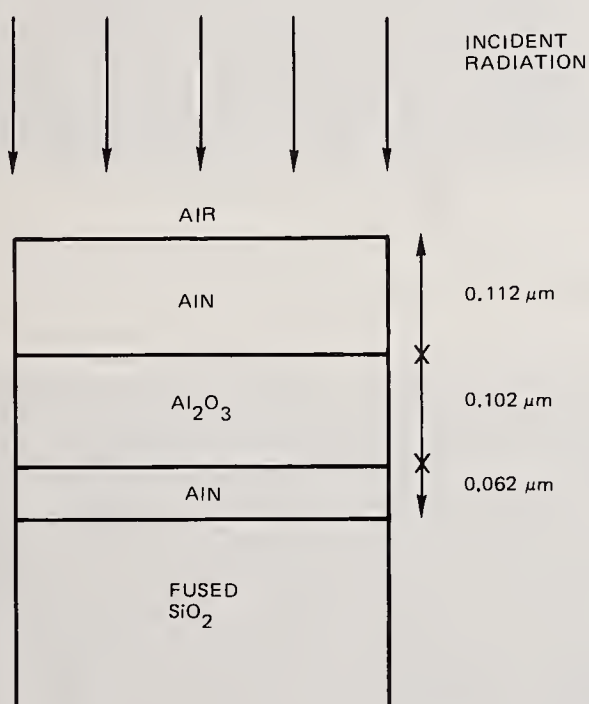
FIGURE 5. Three-layer Design Configuration
with Fused Quartz as Substrate.
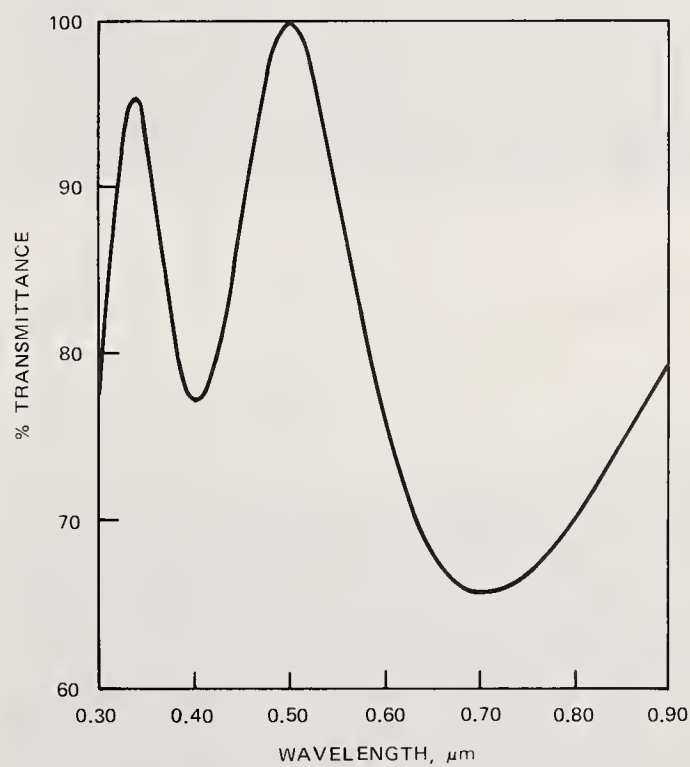
FIGURE 6. Theoretical Transmittance of
Three-layer Design with Fused Quartz as Substrate.

245
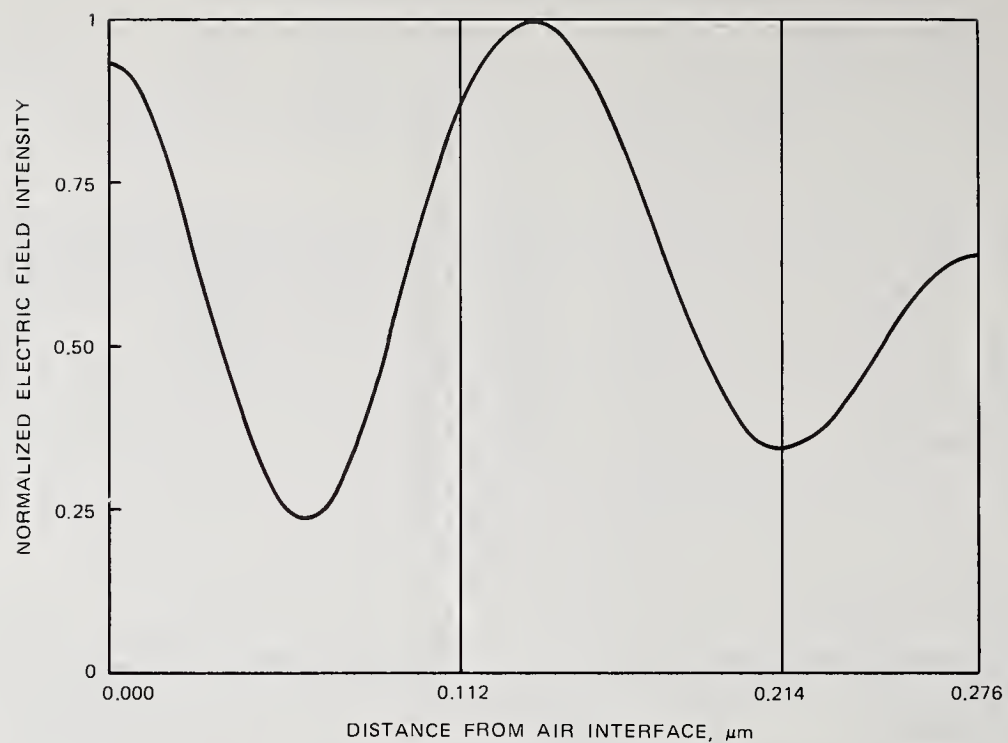
FIGURE 7. Normalized Electric Field Intensity of Three-layer Design with Fused Quartz as Substrate.
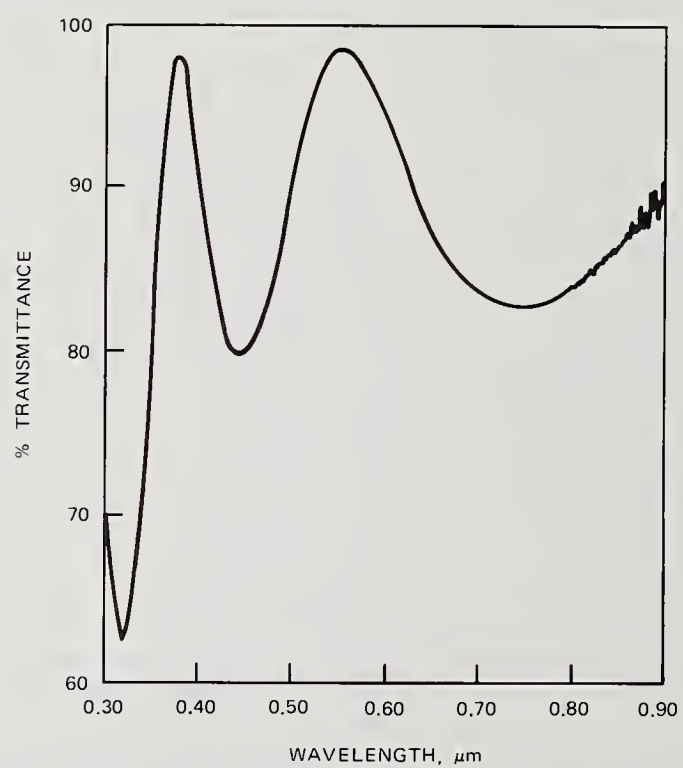
FIGURE 8. Experimental Transmittance of Three-layer Design with Fused Quartz as Substrate.
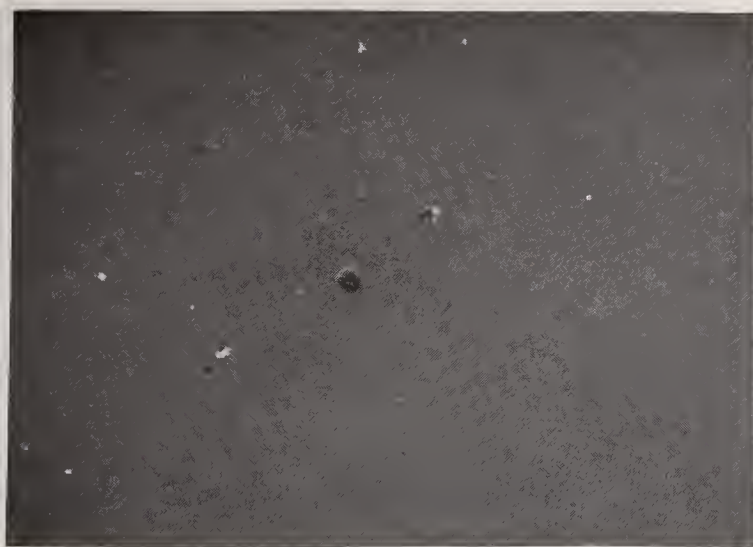
FIGURE 9. Topography of AlN Single Layer.
(a)
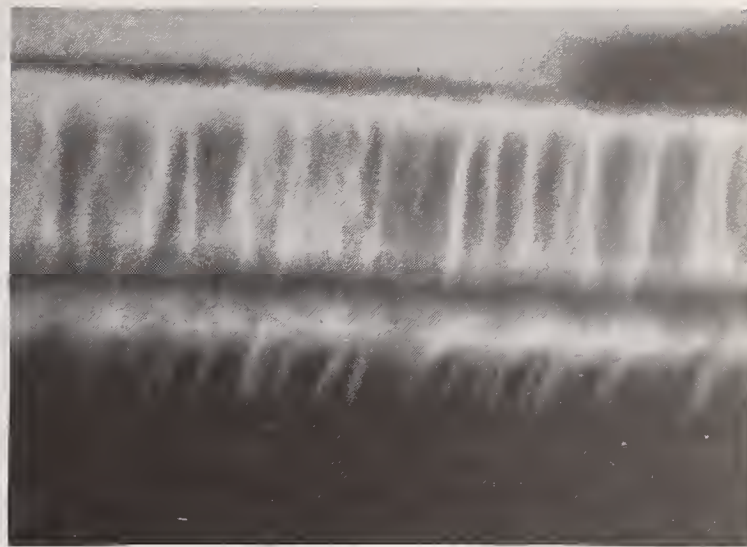
FIGURE 9. Cross Section of AlN Single Layer.
(b)

FIGURE 10. Topography of Al_2O_3 Single Layer.
(a)
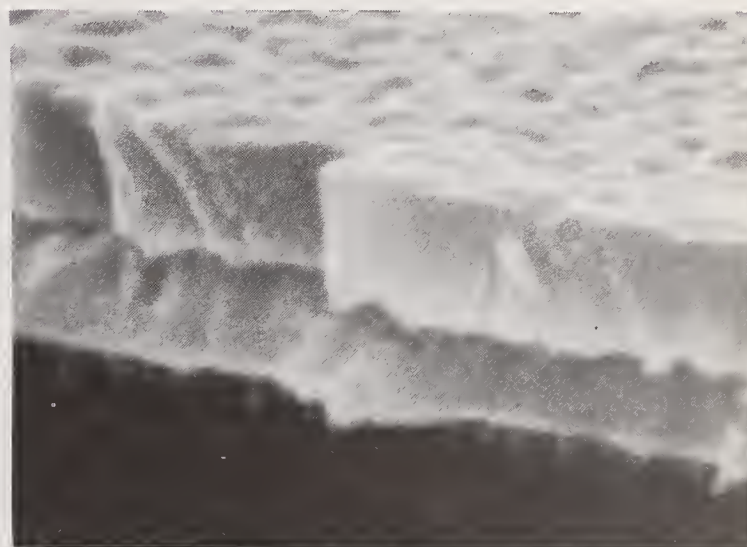
FIGURE 10. Cross Section of Al_2O_3 Single Layer.
(b)
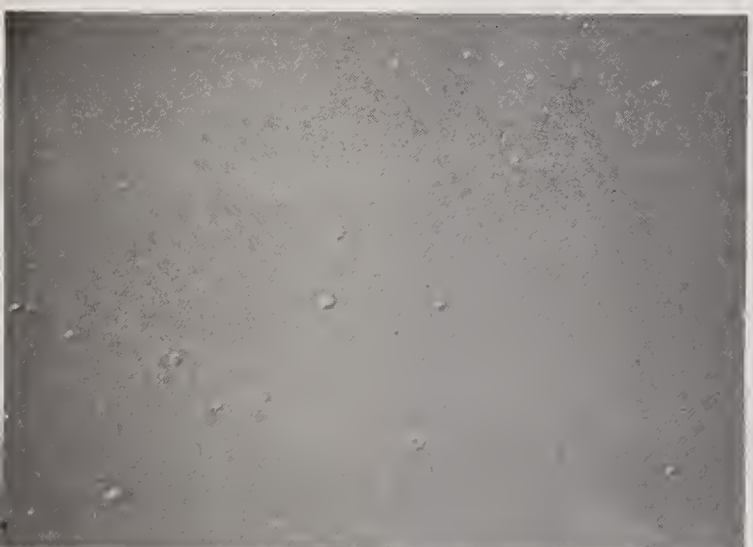
FIGURE 11. Topography of $AlN/Al_2O_3/AlN$ Multilayer.
(a)

FIGURE 11. Cross Section of $AlN/Al_2O_3/AlN$ Multilayer.
(b)
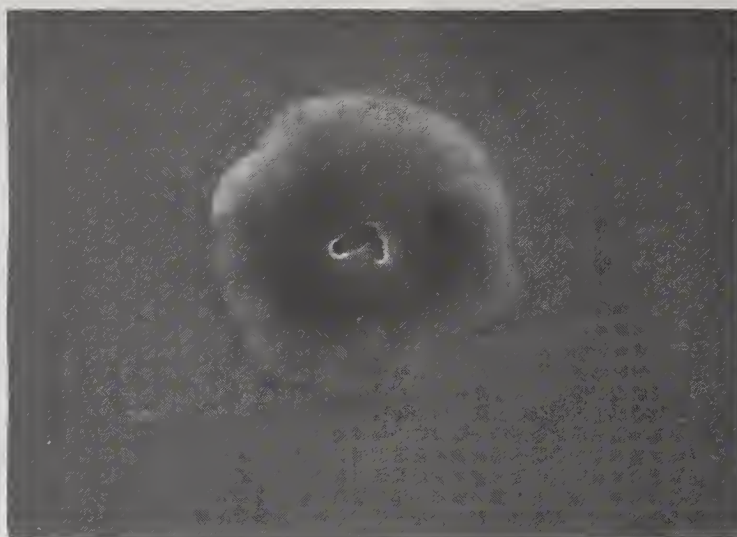
FIGURE 12. Enlargened Top View of AlN Single Layer Defect.
(a)
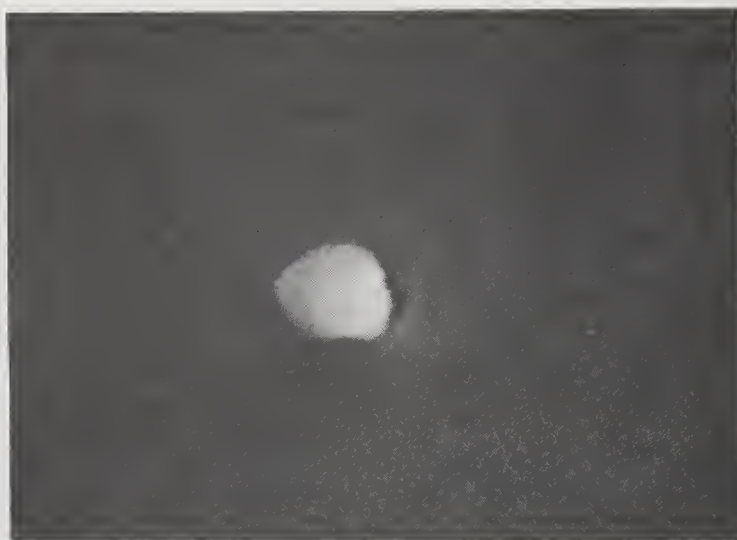
FIGURE 12. Enlargened Top View of Al_2O_3 Single Layer Defect.
(b)
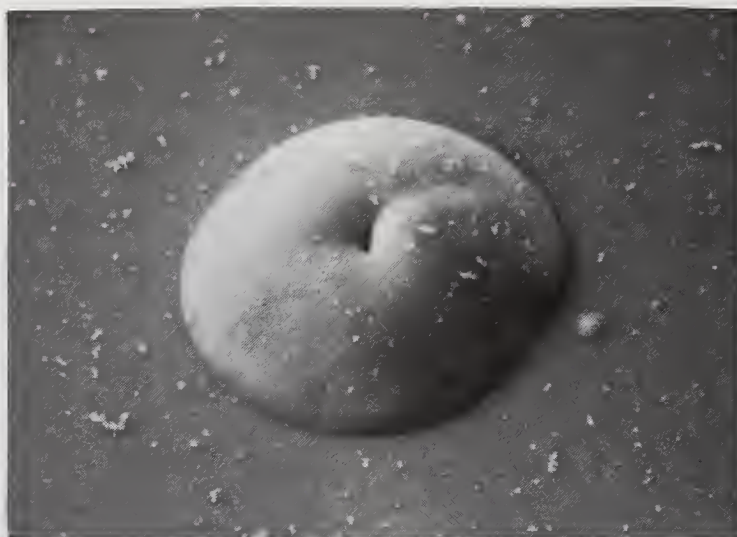
FIGURE 12. Enlargened Top View of AlN/Al_2O_3/AlN Multilayer Defect.
(c)

FIGURE 13. Damage Site 1 Showing Small
Damage Craters Amongst Defects.
(a)
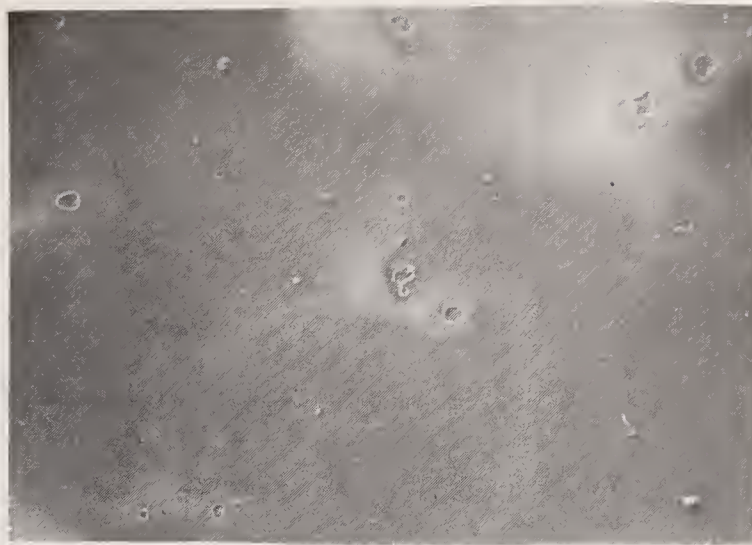
FIGURE 13. Damage Site 2 Showing More and Larger
Damage Craters Amongst Defects (than Site 1).
(b)
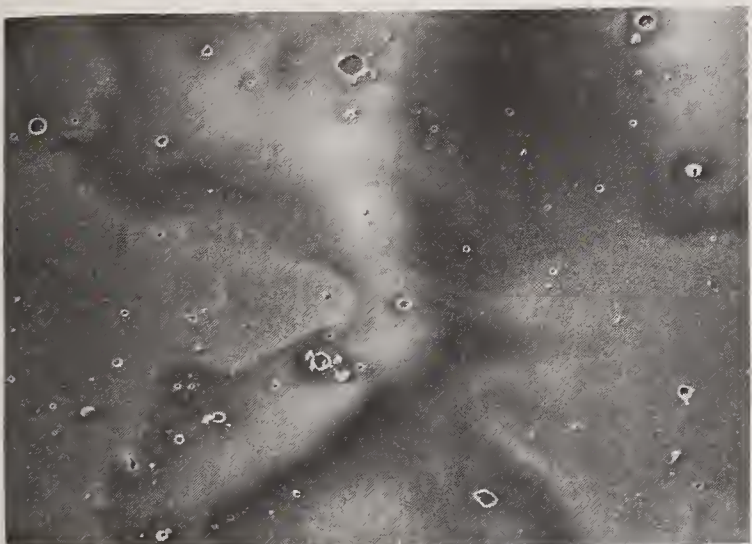
FIGURE 13. Damage Site 3 Showing a Reduced Number of
Apparent Defects and More Damage Craters (than Site 2).
(c)
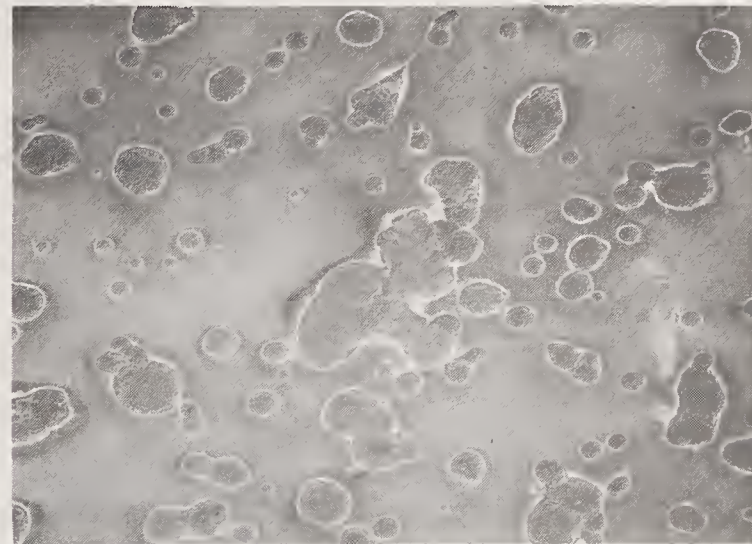
FIGURE 13. Damage Site 4 Showing
Agglomeration of Damage Craters.
(d)
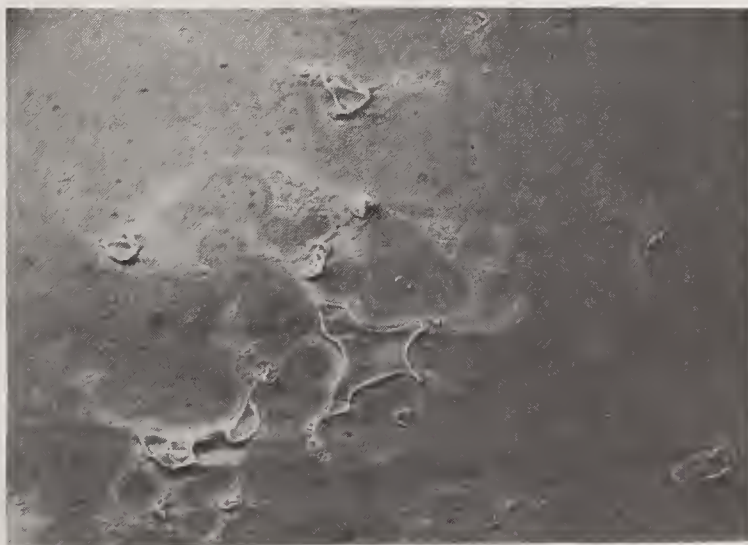
FIGURE 13. Damage Site 5 Showing Small Pitmarks and Loss of Much of Outer Film.
(e)

249
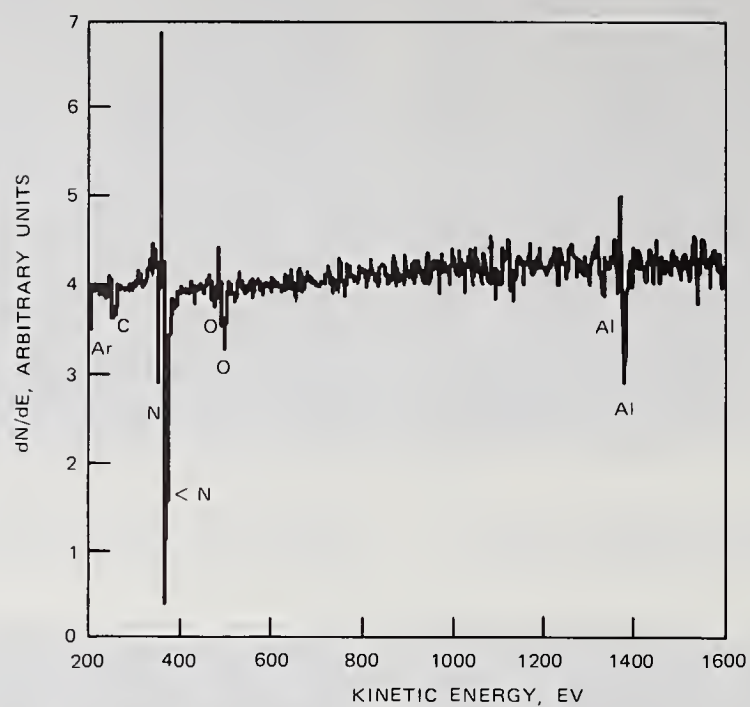
FIGURE 14. AES Spectrum of Smooth Film Portion of Site 2.
(a)
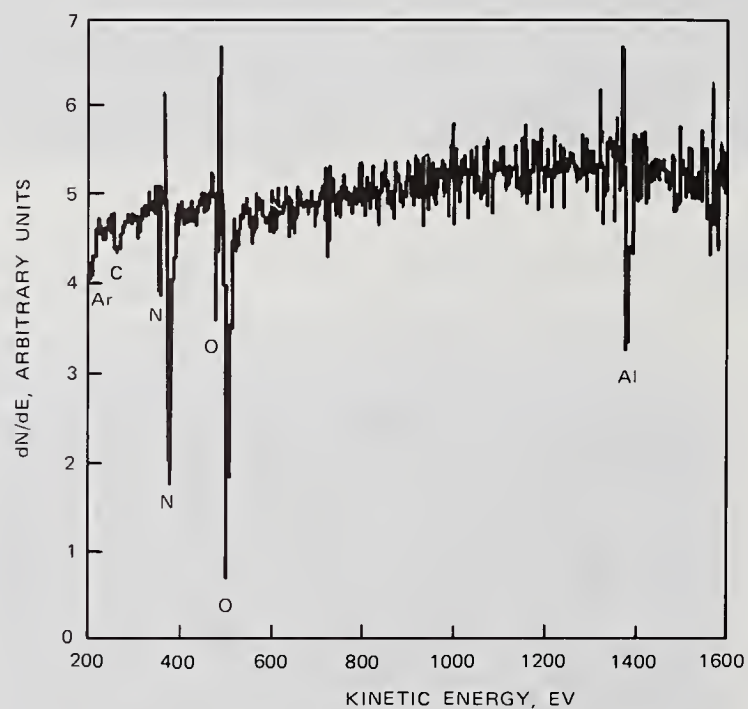
FIGURE 14. AES Spectrum Taken Within Damage Crater of Site 2.
(b)
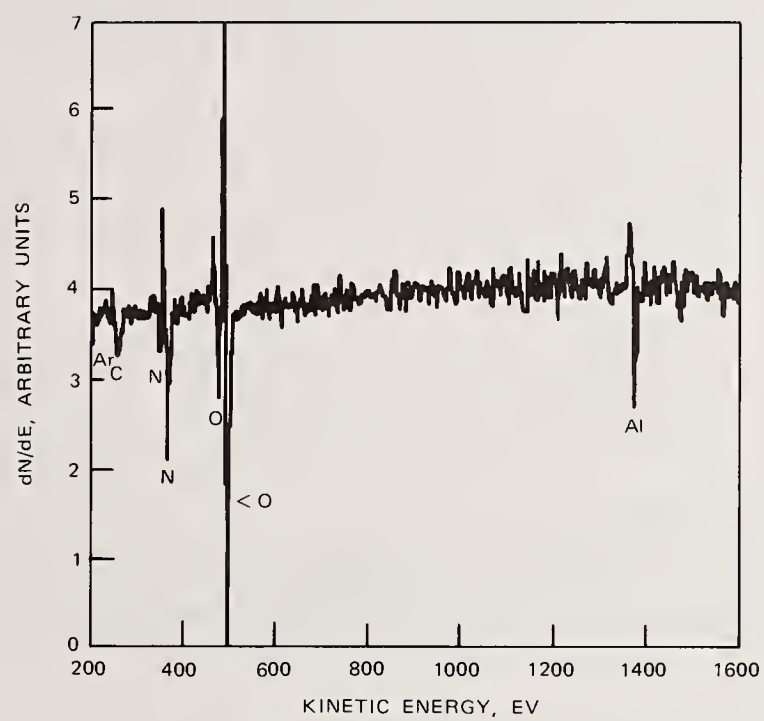
FIGURE 15. AES Spectrum of Smooth Film Portion of Site 4.
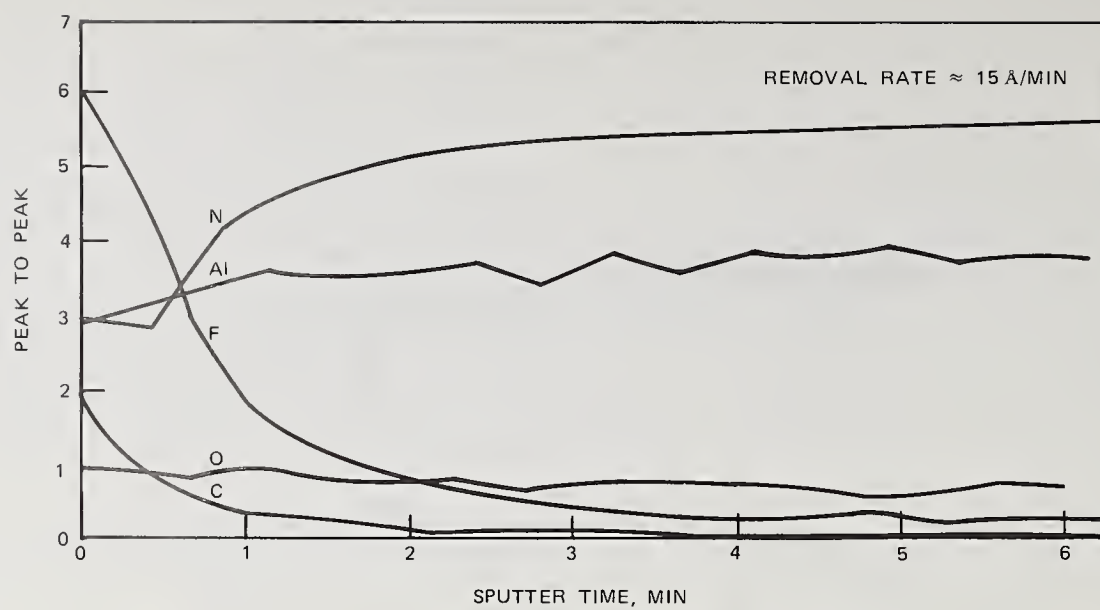
FIGURE 16. AES Profile of AlN Single Layer Exposed to Fluorine.
(a)
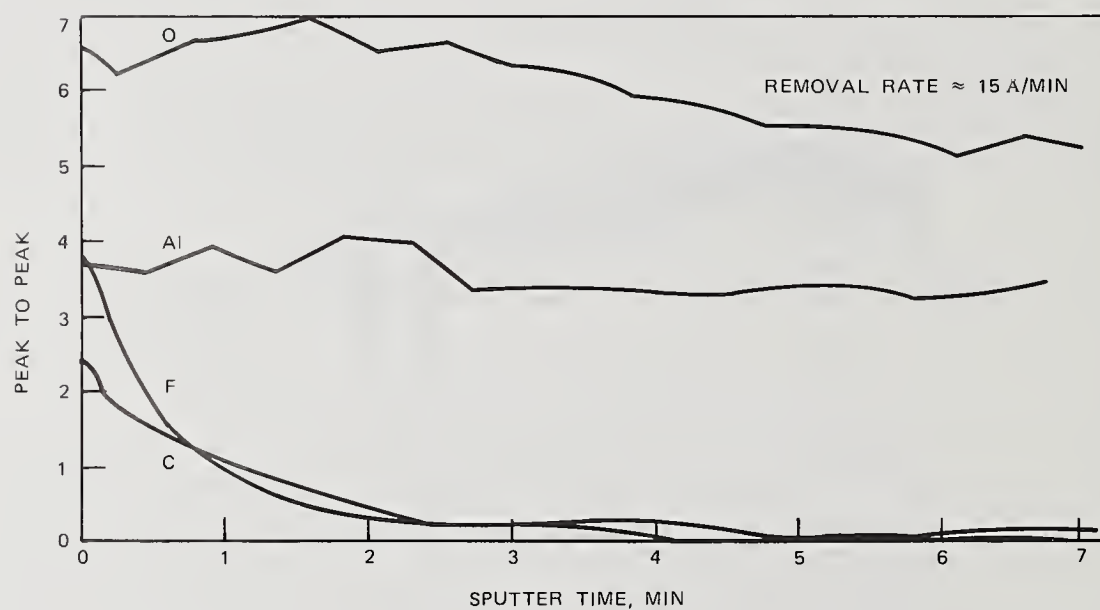
FIGURE 16. AES Profile of Al_2O_3 Single Layer Exposed to Fluorine.
(b)

Crystallization of Titania Films by Thermal Heating

R. Rujkorakarn, L. S. Hsu, and C. Y. She

Physics Department, Colorado State University
Fort Collins, CO 80523

Two types of low-loss, low-scatter submicron thick titania films, deposited by ion-sputtering at room temperature, were thermally annealed in air. Upon heating to about 350°C, these amorphous films show evidence of crystallization. Using a sensitive Raman spectroscopic technique, the crystalline structures are identified as anatase in one case (Type A) and rutile in the other (Type B). This amorphous-crystalline transformation coincides with a decrease in optical transmission and small changes in refractive index and energy gap of the film, along with a dramatic increase ($\sim$100-fold) in elastic light scattering. Further heating of Type A films beyond 900°C shows a second phase transformation to anatase-rutile mixtures.

Key words: absorption; amorphous; anatase; annealing; crystallization; extinction coefficient; ion beam; optical band gap; optical coatings; optical extinction; Raman scattering; refractive index; rutile; titania; titanium dioxide.

1. Introduction

Recent interests in low-loss and low-scatter optical coatings have further promoted studies in deposition and investigation of titania films which have high refractive index and low absorption. Particularly dense titania films can be made by ion-beam sputtering. Sensitive optical diagnostic techniques which are nonintrusive and require a relatively short measurement time are applied here to elucidate the properties of these films.

Ion beam sputter deposition of amorphous titanium dioxide [1] may result in two types of titania films. These films are optically identical but crystallize differently upon annealing to about 350°C. In our study, we investigate the amorphous-polycrystalline transitions and the changes in optical properties of the films upon thermal annealing over a range of temperatures from 200 to 600°C.

Raman spectra [2] show that Type A film crystallizes at $\sim$ 350°C into the anatase phase, where it remains until $\sim$ 900°C, then transforms to anatase-rutile mixtures; Type B film crystallizes directly to rutile phase at 400°C. The crystallization process coincides with a sharp rise in optical extinction, a small increase in refractive index variation, and two orders of magnitude increase in elastic light scattering at visible wavelengths. Film thickness remains constant within experimental error ($\sim$ 5mm), but the optical band gap drops from 3.2 to 3.05 eV.

2. Sample Preparation

TiO_2 films are fabricated by sputtering a metallic Ti target with O_2 and Ar ions from a Kaufman-type ion source [3]. The ion ratio is set to be 1:1 at 7×10^{-5} torr chamber pressure. The primary ion beam energy and the ion flux are 1100 eV and 1.0 mA/cm^2 respectively. Subsequently, the substrate holder can be water cooled if a low substrate temperature is desired.

Recent investigation indicates that Type A films are obtained with low ion beam current (0.4 - 0.8 mA/cm^2) and relatively low substrate temperature, Type B with beam current > 1 mA/cm^2 regardless of substrate temperature.

The titania is sputtered onto three different types of substrate: glass, quartz, and silicon. The coating thickness is determined optically [4], and AES (Auger Electron Spectroscopy) is used to confirm the films' stoichiometry. Two sets of titania films on glass substrates, each set deposited under different deposition conditions, are used for Raman and other optical investigations. The film types and thicknesses are given in table 1.

Table 1.   Sample Characteristics

Sample	Thickness	Substrate	Type
H30905	2233 Å	Corning 7059	A
RAM 11	3117 Å	Corning 7059	B

3.   Experimental Methods

    At each pre-selected temperature (less than 2°C uncertainty) the titania coatings are annealed in an air furnace for 20 minutes. They are slowly cooled to room temperature before the Raman scattering, as well as elastic light scattering and optical transmission measurements are made. After preliminary investigation, the selected set of annealing temperatures are 200, 300, 350, 400, 450, 500 and 600°C. In addition, Raman spectra of the Type A film at 950°C was also taken.

    The Raman spectra from titania coatings are obtained using the technique reported by Hsu, et al. [2] The elastic scattering of laser light integrated over a solid angle of 0.8 sterradian is measured with the same Raman spectrometer. The transmission is measured using a Beckman spectrophotometer with 0.3 to 2.0 μm wavelength range. Optical constants are deduced using the method of Demiryont, et al. [5]

4.   Light Scattering Measurements

    Figure 1 shows the Raman spectra for films deposited on Corning 7059 glass substrates subjected to various annealing temperatures. Raman spectra of the as-deposited films (20°C) are obscured by the broad features of the substrate at 480 cm^{-1} and 790 cm^{-1}; its broad scattering shoulder is indicative of amorphous nature of the film [2]. The spectra of annealed films at 200°C (not shown) and 300°C appear to be identical. For Type A films as shown in figure 1(a). Upon reaching 350°C, there is a small bump at 612 cm^{-1} without any hint of the 144 cm^{-1} feature. This indicates crystallization with some rutile microcrystals, but no anatase. At 400°C, evidence of anatase is quite clear by the appearance of the peaks at 144 cm^{-1} and 635 cm^{-1} and additional shoulders at 400 cm^{-1} and 515 cm^{-1}. The concurrent presence of rutile growth is evident by the weak peaks at 400 cm^{-1} and 612 cm^{-1}. Subsequent annealing at 450°C, 500°C (not shown) and 600°C show that the anatase peaks becoming more prominent while the rutile peaks remain constant. At 600°C and higher temperatures, the Raman intensity tends to be unchanged signifying the completion of the crystallization process.

    If a similar Type A film is heated directly at 600°C, bypassing the relative low temperature steps, it results in anatase crystallization without any detectable rutile as illustrated in figure 2(a). If these Type A anatase films were further heated to 900°C or above, where rutile structure is thermodynamically more favorable [6], the anatase films transform into anatase-rutile structure with rutile dominance, as shown in figure 2(b). The high background above 500 cm^{-1} is due to partial melting of the glass substrate at this temperature. The general behavior of the amorphous-anatase-rutile transformation has been studied recently by laser annealing with titania films on silicon [7].

    As shown in figure 1(b), a Type B film retains its as-deposited amorphous features up to 350°C, where it crystallizes into rutile structure without any anatase. Such evidence again comes from the appearance of the 440 cm^{-1} and 612 cm^{-1} rutile peaks. When the annealing temperature is increased further to 400, and 600°C, the rutile signal intensity increases along with the two-photon Raman modes of rutile at 250 cm^{-1} and 690 cm^{-1}.

    The elastic light scattering of both types of films at various annealing temperatures has also been recorded simultaneously with the Raman spectra of figure 1. Using the scattering from MgO as a calibration, the percentage scattering can be determined and the results are given in figure 3. The dramatic two-order of magnitude increase in elastic scatter accompanying the film crystallization near 400°C has obvious implications for use of these films as coatings for high-power laser mirrors.

254

5. Optical Transmission Measurements

A typical optical transmission scan is shown in figure 4. Using the published technique [5], optical parameters, including film thickness, and energy gap, can be determined in a straightforward manner. These parameters are given for the annealing temperatures used.

The film thickness was determined to be independent of annealing temperature, suggesting negligible porosity in the films as-deposited. The film refractive indices (n) for four different wavelengths are plotted in figure 5(a) and 6(a) as a function of annealing temperatures. The index rises between 300°C and 400°C. Although single crystal rutile (n = 2.71, 2.75) has index higher than that of anatase (n = 2.53, 2.56) [8,9], films of both crystalline phases are found to have similar indices; n = 2.55 (rutile) and n = 2.50 (anatase) at λ = 0.5 μm. Our films appear to be somewhat more dense than those made by Pawlewicz, et al. [10] using RF sputtering (grain size ∿ 20 nm); their titania indices are n = 2.4 to 2.5 (rutile) and 2.30 (anatase). Both Pawlewicz, et al. [10] and Williams and Hess [6] found that RF sputtering at low power densities favors the growth of anatase, consistent with our observations at low ion beam current. Figure 5(b) and figure 6(b) show the annealing temperature dependence of film extinction coefficient (k) at various wavelengths. It increases sharply when the crystallization temperature is reached, due most likely to grain boundary scattering. Comparing the extinction coefficient data of this figure to the scattering data of figure 3, some conjectures are in order. Crystallization and associated grain boundaries cause a two-order of magnitude jump in elastic scattering. In addition, there is an increase in impurities absorption associated with the heating process. This absorption increases further as temperature increases beyond crystallization in contrast to the leveling off of scattering at higher temperatures.

The optical absorption edge data have been plotted to reveal $\alpha \sim (E)^{-1}(E-E_g^o)^2$ dependence [11]. Extrapolation of the absorption beyond the Urbach edge [12] yields the optical band gap E_g^o. As shown in figure 7, E_g^o decreases slightly with annealing temperature. The band gap behavior is consistent with a drop in the conduction band energy minima, during the transition from amorphous to crystalline states.

6. Conclusions

Raman scattering with the complementary optical transmission studies have been shown to be useful in identifying the crystallization of sputtered titania coatings. The amorphous-crystalline transition occurs abruptly at a modest annealing temperature ∿ 350°C.

Crystallization in Type A titania coatings reveals the existence of two competing structures with the rate of anatase growth dominating at higher temperatures (< 900°C). On the other hand, only rutile structure exists in Type B films. The nature of this competing growth mechanisms of Type A films is interesting and is under further study.

Optical constants and optical bandgap are found to be temperature dependent. In particular, both optical extinction and elastic scattering increase drastically at crystallization temperature, suggesting that a moderate amount of heating may degrade the coating performance, and affect the laser damage threshold.

---

7. References

[1] Sites, J. R., Gilstrap, P. Rujkorakarn, R. Ion beam sputter deposition of optical coatings. Optical Engr. 22, 447(1983).

[2] Hsu, L. S., She, C. Y., Exarhos, G. J. Reduction of substrate interference in Raman spectroscopy of submicron titania coatings. Appl. Opt. 23, 3049(1984).

[3] Kaufman, H. R. in Advance in Electronics and Electron Physics (ed. L. Morton, Vol. 36), New York; Academic Press; 1974. 265 pp.

[4] Heaven, O. S. Optical Properties of Thin Solid Films. London; Butterworth; 1950. 158 pp.

[5] Demiryont, H., Kerwin, D. B., Sites, J. R. Optical properties of ion-beam sputtered TiO_2 films. NBS Special Publication, to be published.

[6] Williams, L. M.; Hess, D. W. Structural properties of titanium dioxide films deposited in an rf glow discharge. J. Vac. Technol. 4, 1810(1983).

[7] Hsu, L. S., Solanki, R., Collins, G. J., She, C. Y. Raman study of structural transformations of titantia coatings induced by laser annealing. Appl. Phys. Letts., in press.

[8] Hass, G. Preparation, properties and optical application of thin films of titanium dioxide. Vacuum 2, 331(1952).

[9] Jarzebski, Z. M. Oxide Semiconductors. New York; Pergamon Press; 1973. 224 pp.

[10] Pawlewicz, W. T., Hays, D. D., Martin, P. M., Laegreid, N. Reactively sputtered optical coatings for use at 1064 nm. NBS Special Publication 568: 359-375; 1979.

[11] Tauc, J. Amorphous and Liquid Semiconductors. New York; Plenum Press; 1974. 159 pp.

[12] Urbach, F. The long-wavelength edge of photographic sensitivity and the electronic absorption of solids. Phys. Rev. 92, 1324(1953).
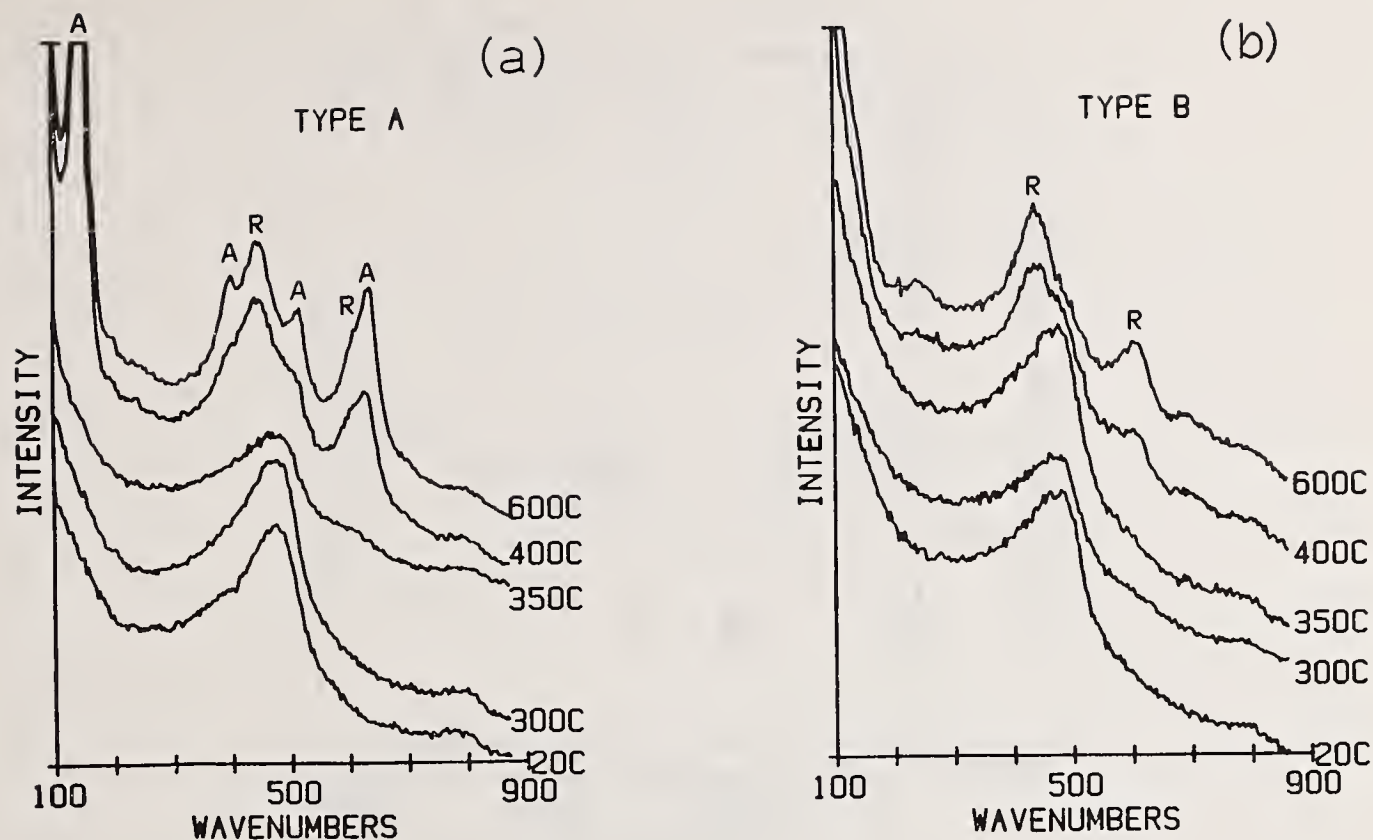
Figure 1. Raman spectra for (a) type A/glass and (b) type B/glass annealed at various temperatures.
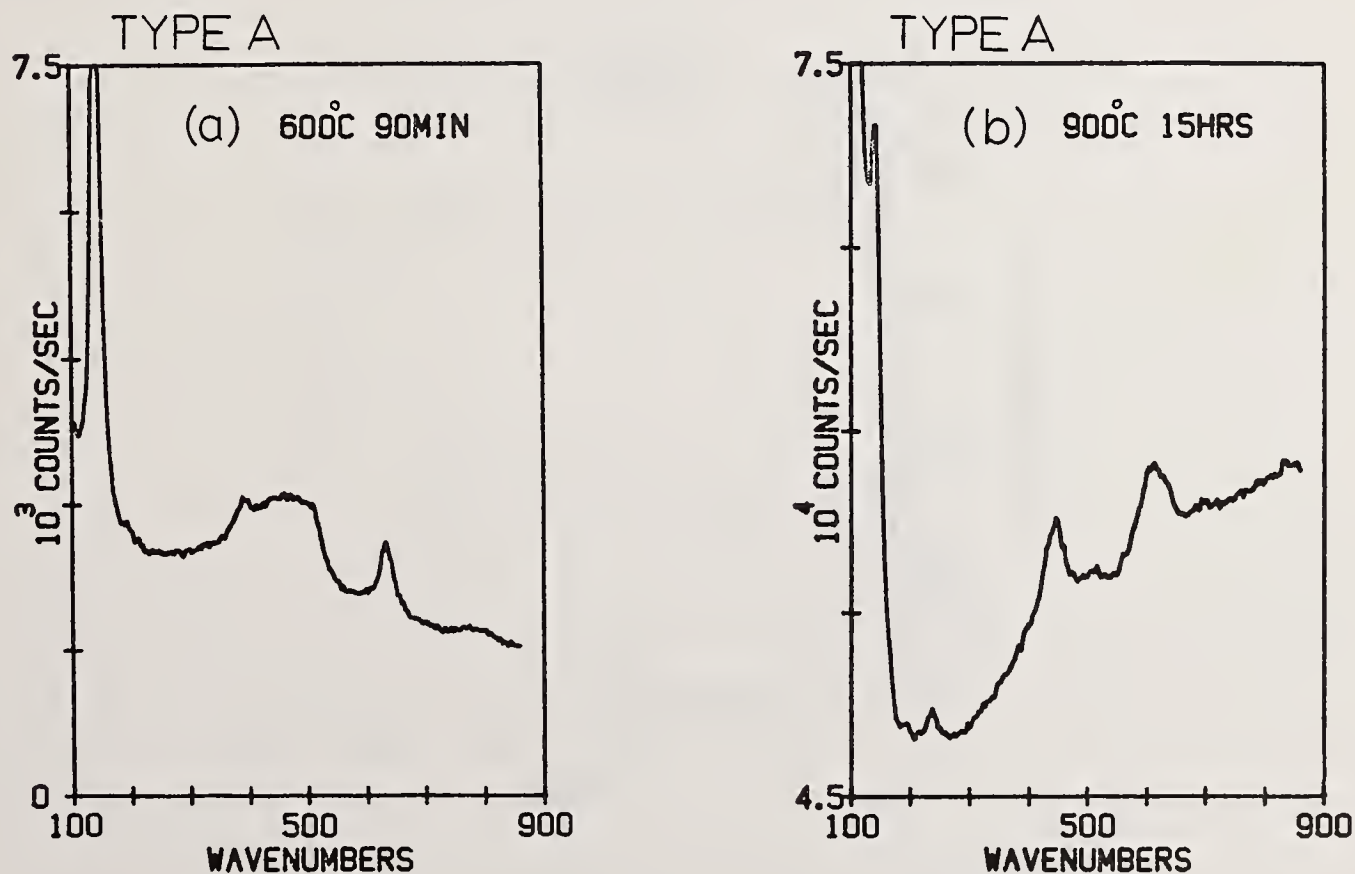
Figure 2. Raman spectrum for type A/glass annealed directly at (a) 600°C to form anatase and (b) 950°C to form anatase-rutile mixture.
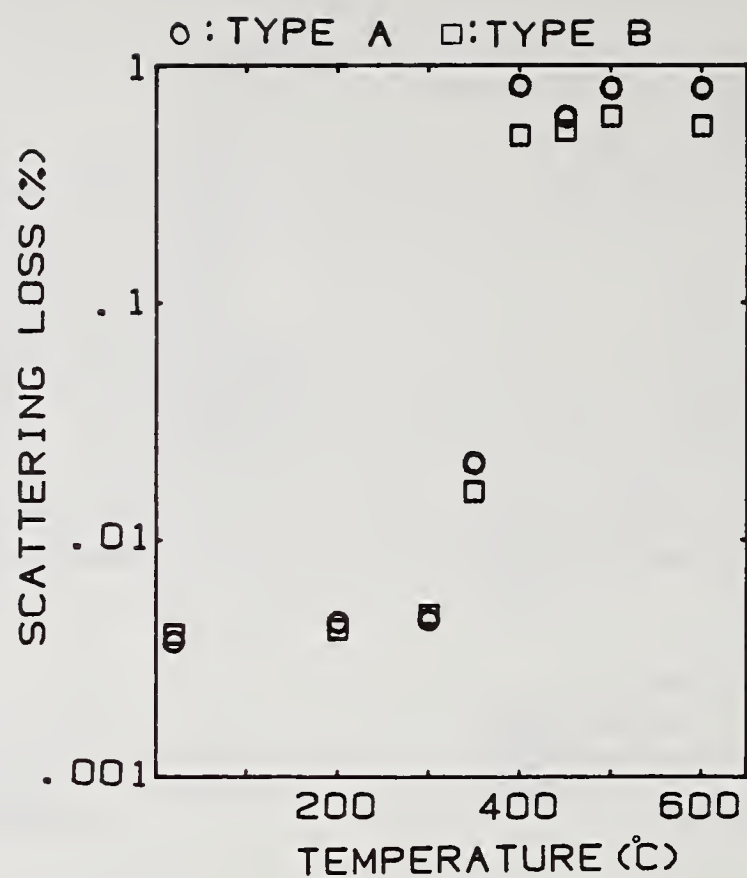
Figure 3. Scattering loss of TiO_2 films as a function of annealing temperature.
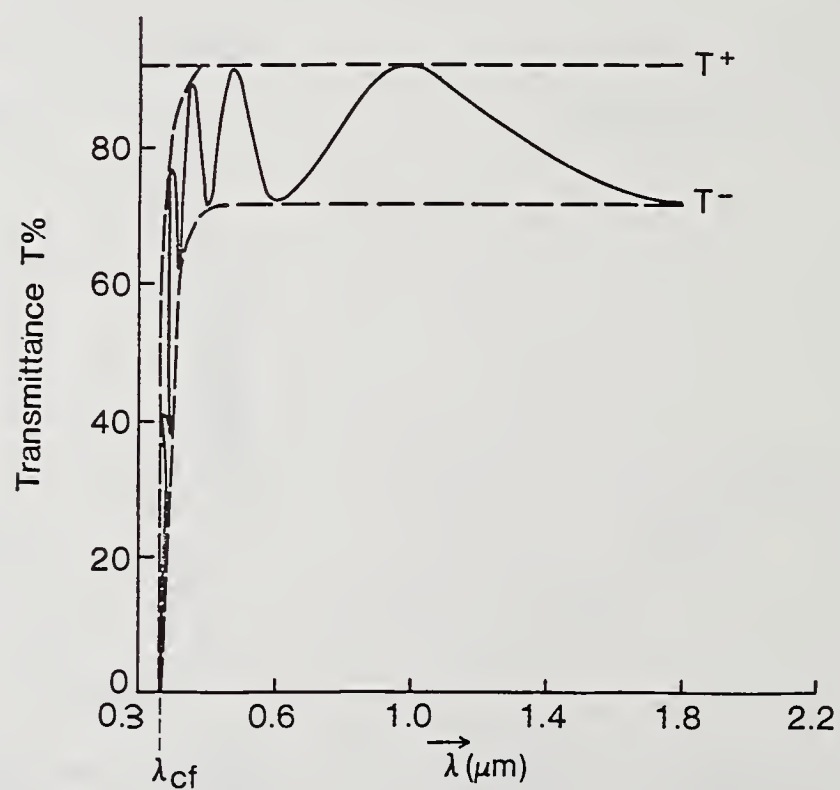
Figure 4. Typical transmission scan for a TiO_2 film where λ_{cf} is the cut off frequency.

258
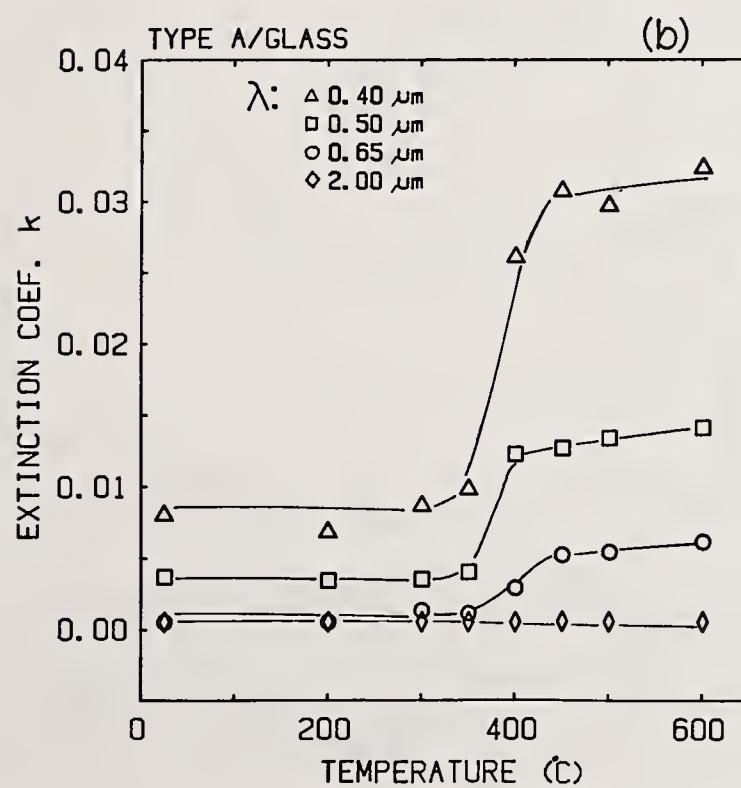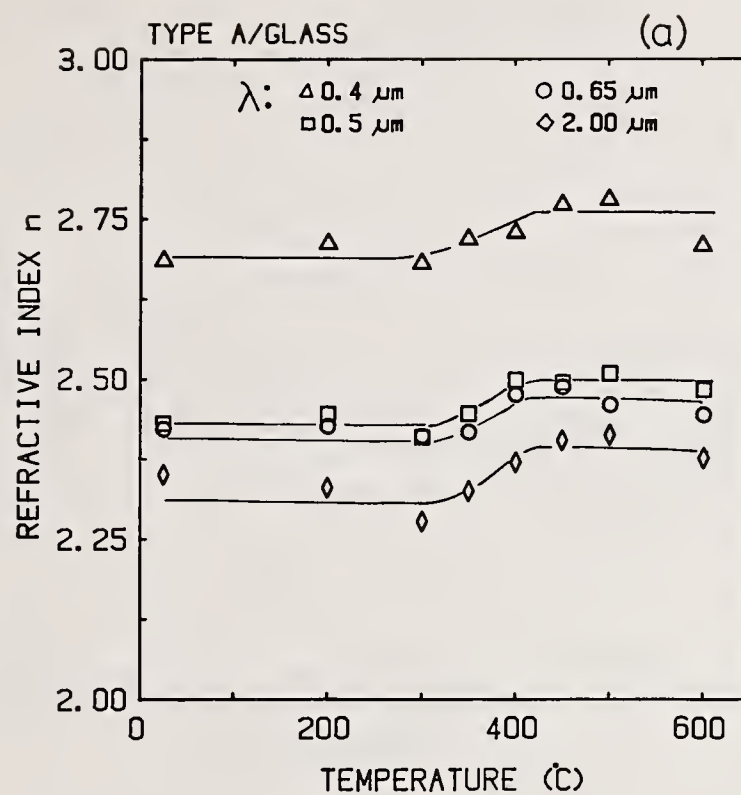
Figure 5. (a) Film refractive index and (b) film extinction coefficient vs. annealing temperature for type A/glass.
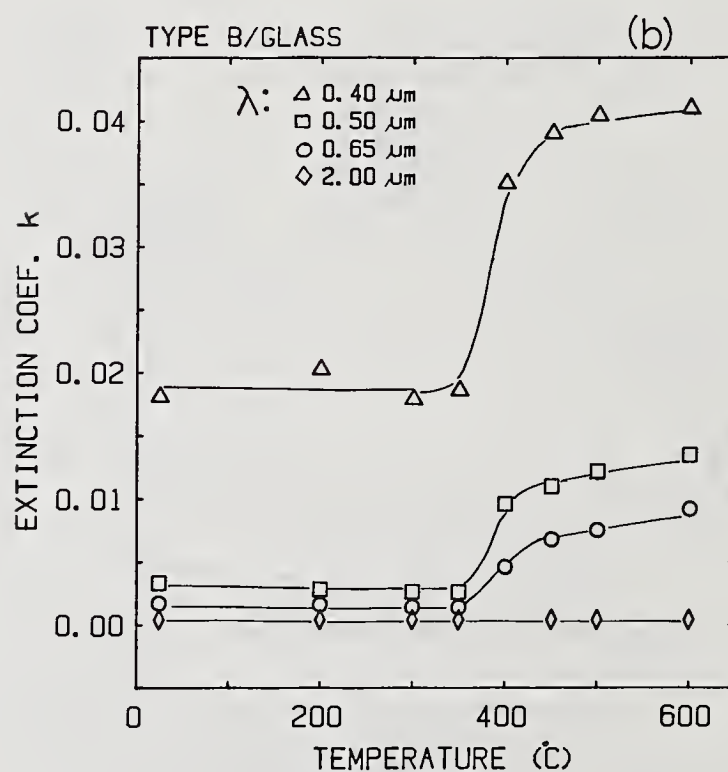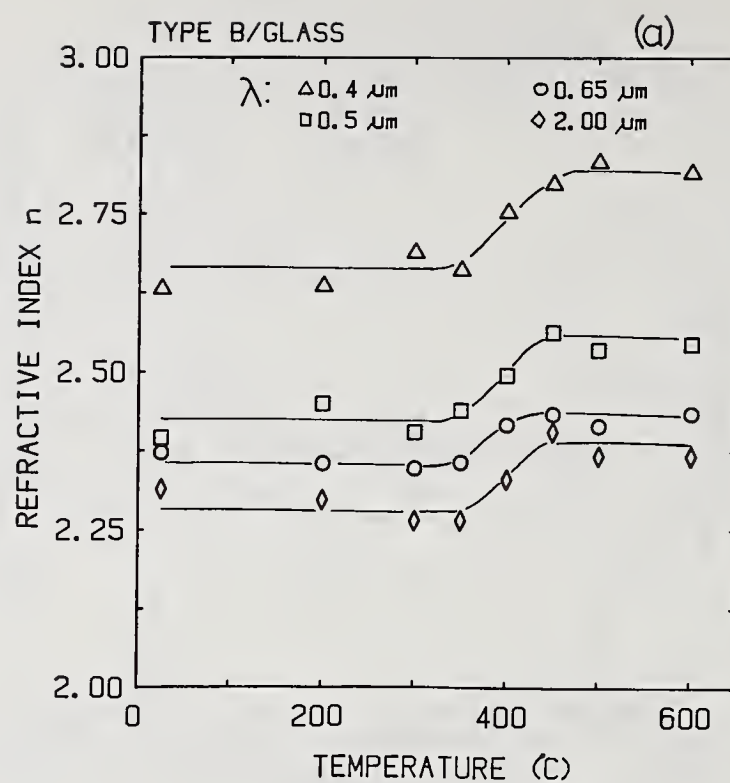
Figure 6. (a) Film refractive index and (b) film extinction coefficient vs. annealing temperature for type B/glass.
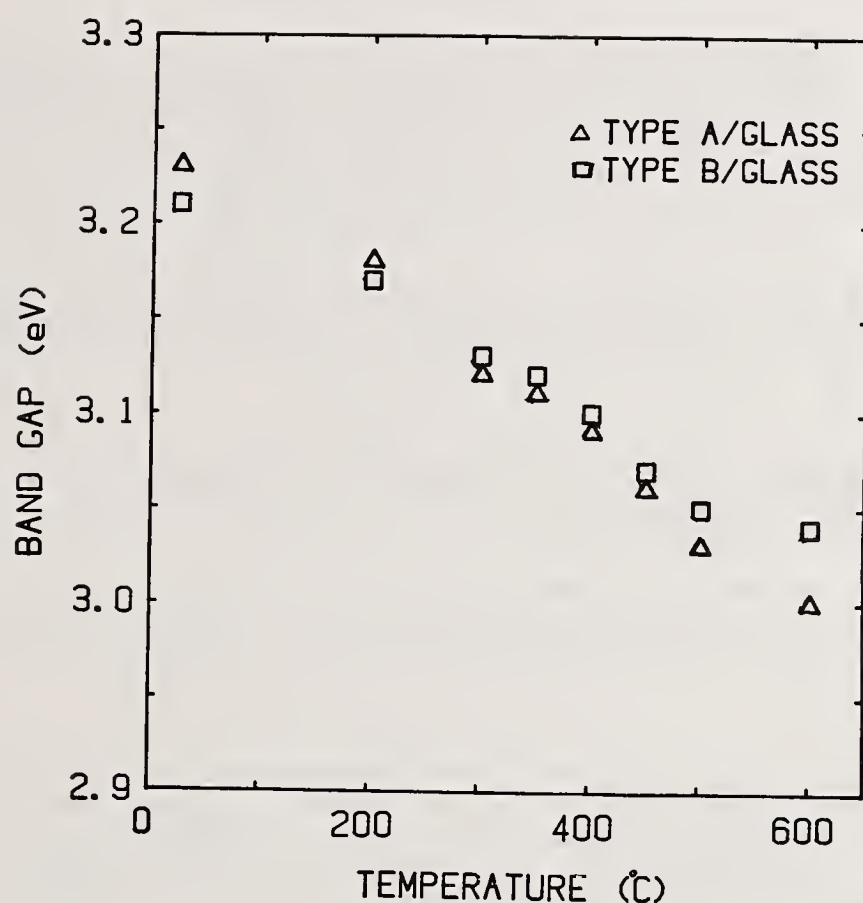
Figure 7. Optical band gap of TiO_2 films as a function of annealing temperature.

Question: Is the light scattering observed coming from the bulk of the film or from the surface? The author had no data on that question. It was pointed out that except for light losses the conventional and the novel optical systems, which are both f/1, should have the same depth of focus. The question of adequate reference data for Raman spectra arose. The author believes that this lack is not a serious limitation to use of this technique. Another member of the audience stated that Raman spectra of both zirconia and tantalum has recently been taken at the Air Force Weapons Lab and is available.

Time Resolved Raman Studies of Laser
Induced Damage in TiO_2 Optical Coatings

G. J. Exarhos and P. L. Morse*

Battelle Pacific Northwest Laboratory**
Richland, Washington 99352

Molecular information available from Raman scattering measurements of sputter deposited TiO_2 on silica substrates has been used to characterize crystalline phases, thickness, and surface homogeneity. A two laser technique is described for investigating transient molecular changes in both coating and substrate which result from pulsed 532 nm laser irradiation. Single layer and multilayer coatings of both anatase and rutile phases of TiO_2 have been probed by Raman spectroscopy immediately following the damage pulse (nanoseconds) and at longer times. Transient measurements are designed to follow surface transformation/relaxation phenomena; measurements at longer times characterize the equilibrium damage state. The anatase coatings were found to be more susceptible to laser damage than rutile coatings and exhibited irreversible changes during the damage process. Rutile coatings exhibited a reversible phase transition to the anatase form followed by recrystallization to the rutile phase (milliseconds). Loss of coating material from all damaged surfaces is inferred from decreased Raman scattering intensity. Substrate damage characterized by laser induced scrambling of polarized light was also observed. Raman results and molecular structural information are used to formulate a possible damage mechanism for TiO_2 coatings.

Key words: laser damage mechanisms; laser heating; molecular vibrational studies; phase transformations; time resolved Raman Spectroscopy; TiO_2 optical coatings.

1.   Introduction

Rapid characterization of thin optical coatings deposited on transparent or opaque substrates is possible through state-of-the-art Raman spectroscopic techniques. This non-destructive optical method which can be adopted for in situ analyses can provide detailed chemical bonding information from measurement of molecular vibrational spectra excited by a low energy probe laser. The technique is particularly well suited to studies concerned with phase identity and homogeneity of thin films, as well as film stability studies under extreme conditions.

Application of Raman spectroscopy to characterization of thin optical coatings has only recently been explored. Conventional measurements of single layer TiO_2 on silica have unequivocally identified the anatase phase in submicron sputter deposited coatings and demonstrated a linear correlation of band intensities with thickness from 0.1μ up to several microns.[1] The technique of interference enhancement has also been developed allowing Raman spectra of extremely thin films to be measured.[2,3] High quality spectra have also been acquired from all-dielectric multilayer SiO_2/TiO_2 coatings of general or arbitrary design with no special specimen preparation required.[4] The Raman technique is also a sensitive probe of microcrystallite grain orientation in sputtered coatings through polarization analysis of the scattered light. Furthermore, suppression of substrate Raman scattering from coatings consisting of unoriented grains can be achieved through measurement of the appropriate polarization component of the scattered light enabling extremely thin coatings to be characterized by this technique.[6]

Raman spectroscopy has been used to evaluate laser damage to single layer TiO_2 coatings on silica and more extensive measurements on multilayer coatings are currently in progress. Conventional measurements are used to characterize the equilibrium damage state where two

colinear laser beams are directed at normal incidence to the sample under investigation. (A low energy CW visible laser serves as the Raman probe while a high energy pulsed laser causes damage to the coatings.) Raman spectra measured before and after the damage pulse provide information on the survivability of the coating and substrate with respect to induced phase transformation and coating decomposition.

A second experiment has been designed to evaluate equilibrium damage in TiO_2 optical coatings caused by changes in sample temperature. Raman spectra are acquired while the sample is heated by an auxilliary CO_2 laser from room temperature to ca. 1500°C. Under these conditions the sample is in thermal equilibrium and the vibrational levels are populated according to the Boltzmann distribution. The Raman experiment probes the ground electronic state. Equilibrium phase transitions (anatase→rutile), should they occur, will be manifested in measured Raman spectra.

To study the dynamics of laser induced damage in optical coatings, Time Resolved Raman Spectroscopy (TRRS) was used. Spectra were acquired at various delay times following the damage pulse. Under these non-equilibrium conditions the Raman experiment probes the excited electronic states of the material. Resonance enhancement of vibrational lines is possible leading to increased intensity of selective Raman modes. Interpretation of measured spectra can yield information concerning structure of the excited state.

The data obtained from these experiments has been used to develop a mechanistic model for laser damage in TiO_2 optical coatings. Both anatase and rutile coatings sputter deposited on silica substrates are the primary materials investigated by Raman spectroscopic methods.

2.   Experimental

All TiO_2 coatings were prepared by reactively sputtering Ti in Ar/O_2 atmospheres in an rf diode system onto fused silica substrates. Deposition details appear in the literature.[6,7] Microcrystalline grain sizes were ca. 50 nm and sample thicknesses varied from 0.1 micron to over 5 microns.

Raman spectra were excited at normal incidence using the 180° backscattering geometry depicted in figure 1. The sample was held in a micropositioning stage having spatial resolution of several microns. Scattered light was collected at f/1.4 and imaged onto the slits of a SPEX
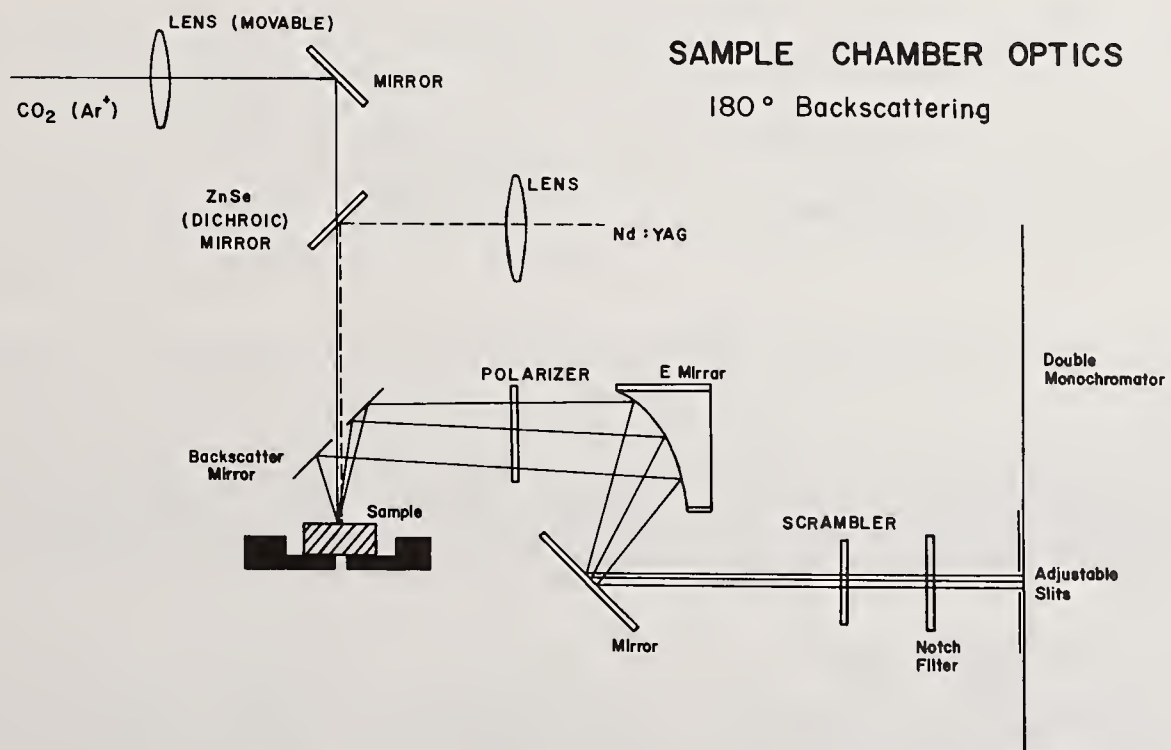
Figure 1. Backscattering geometry for Raman experiment with damage/heating and probe beams colinear.

0.85m double monochromator. Dispersed radiation was detected by an RCA C31034-01 PMT and signals were processed by conventional photon counting electronics. A gated intensified diode array detector was used to record spectra in a time resolved mode. In this instance, only the entrance slits of the monochromator were used; to reject Rayleigh scattered light under these conditions a special notch filter tuned to reject the probe laser wavelength was inserted in front of the entrance slits.

Three different laser beam excitation arrangements were used. Equilibrium laser damage measurements at room temperature required colinear Ar+ Raman probe and Nd:YAG damage beams focused onto the sample surface. The 488 nm CW Ar+ probe beam operating at 200 mW had a 50μ spot size while the 532 nm pulsed Nd:YAG damage beam operating from 1-50 mj/pulse had a 500μ spot size. (Measured pulse widths were 10 nsec.) The second arrangement required combining the 10.6μ CW CO_2 beam used to heat samples appreciably above room temperature with the 532 nm Nd:YAG pulsed beam operated at a low pulse energy as the Raman probe. Sample temperatures were measured by means of a two color optical pyrometer. The final arrangement used the Nd:YAG laser to both create damage and act as the Raman probe as shown in figure 2.

SIGNAL DELAY SCHEMATIC
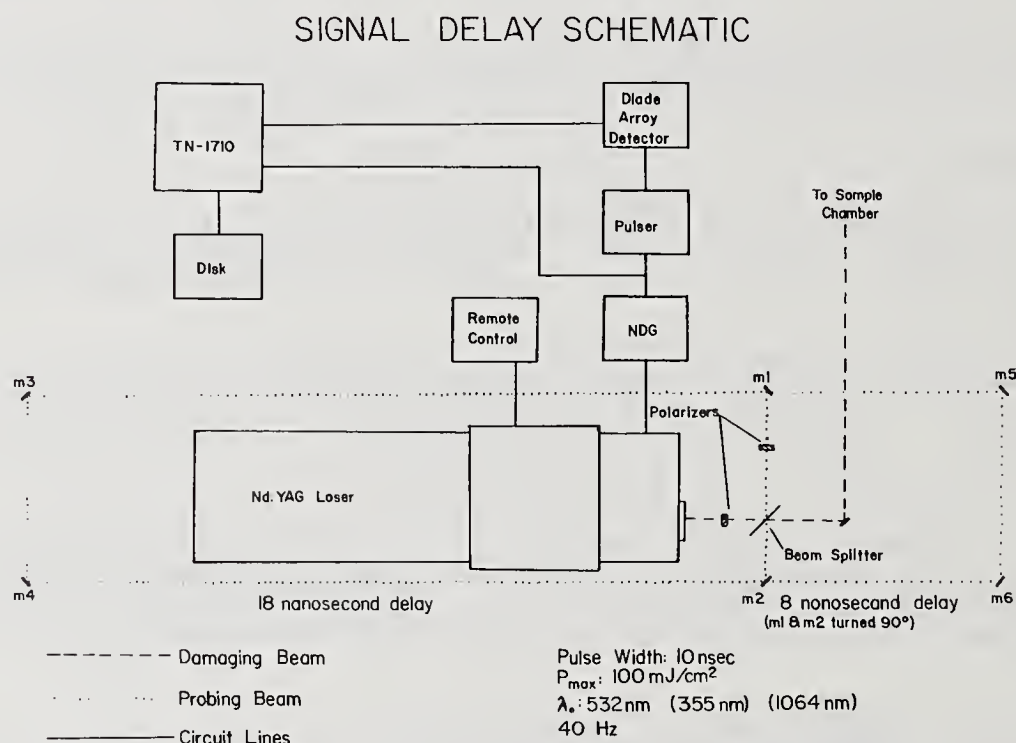
Figure 2. Signal Delay Schematic showing optical delay path. (NDG refers to a nanosecond delay generator.)

A pellicle beamsplitter served to split individual pulses into a primary and secondary pulse which contained ca. 10% of the primary pulse energy. Figure 2 also shows the electronic delay schematic designed to open the array detector at selectable times following arrival of the damage pulse at the sample. The detector bandwidth was maintained at 8 nsec for all measurements.

3. Structural Considerations

Titanium Dioxide occurs mainly in two crystalline phases, anatase and rutile. The general structures of these phases are shown in figure 3. In rutile, the titanium atom is localized in an octahedral oxygen environment, while in the anatase phase, the oxygen atoms in the square plane are puckered forming a tetrahedral-like unit. The puckering of the oxygen atoms results in a much longer bond length in the localized unit. Accordingly, rutile is the denser phase at 4.27 g/cc compared to anatase at 3.90 g/cc.[8] Due to marked structural differences in the phases of TiO_2, individual Raman spectra are rather different and provide unambiguous identification of each phase.

264
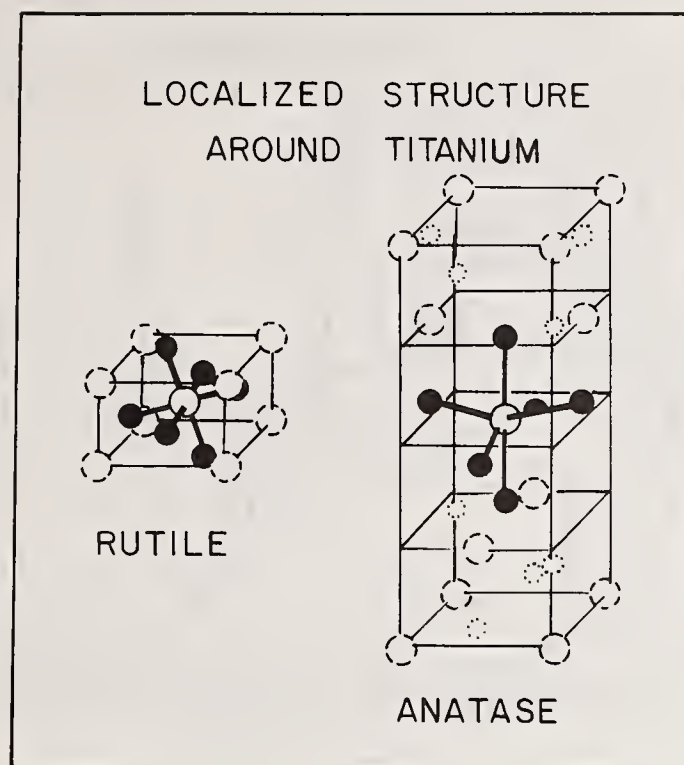
Figure 3. Localized molecular structures of rutile and anatase phases of TiO$_2$.

Thermodynamic data indicates that anatase undergoes a transformation to the rutile phase at ca. 900°C.(9) These structural and thermodynamic considerations are very important in the interpretation of the Raman spectra and subsequent modeling of the damage process.

4. Results

Thin film TiO$_2$ optical coatings have been characterized with regard to phase identity and homogeneity by Raman Spectroscopy. The Raman spectrum of a thin anatase film on silica is depicted in figure 4. By analyzing the Z(X Y)$\bar{Z}$ component of the scattered radiation, Raman scattering from the silica substrate is markedly attenuated at frequencies below 800 cm^{-1}. The broad feature at ca. 800 cm^{-1} is, however, assigned to Raman scattering from the glass substrate. For the other scattering geometry Z(X X)$\bar{Z}$ substrate features overwhelm Raman lines from the thin optical coatings. Therefore, in all subsequent measurements, the Z(X Y)$\bar{Z}$ scattering geometry was used. The major anatase lines at 145, 199, 398, 517, and 639 cm^{-1} and rutile features at 244, 440 and 610 cm^{-1} previously assigned clearly distinguish the two crystalline phases.[10,11]

The equilibrium damage state was characterized by Raman measurements of both anatase and rutile optical coatings subjected to 532 nm pulsed irradiation from a Nd:YAG laser. When the damage threshold for rutile coatings was exceeded, measured Raman spectra at long times following the damage pulse were qualitatively similar to the undamaged coatings; however, band intensities were lower than for the undamaged samples. While no change in crystalline phase was detected, the lower band intensities indicate removal of TiO$_2$ by the damage laser pulse. Since Raman band intensities correlate with coating thickness, depth profiling of the damaged area is possible and has been determined for several samples.

Subtle changes in band positions and bandwidths were observed in Raman spectra of anatase coatings following the damage pulse. As seen in figure 5, all major features are significantly broadened and reduced in intensity. The major 145 cm^{-1} band appears at a higher frequency following damage while features above 300 cm^{-1} appear at slightly lower frequencies. Following damage, the 398 cm^{-1} band shows a weak shoulder at higher frequencies, and the 639 cm^{-1} band appears broadened to the low frequency side. These are regions where Raman scattering attributed to the rutile phase is expected.

Results from such measurements suggest that for a constant laser damage energy and similar coating thickness, rutile coatings appear to have a significantly higher damage threshold than

265
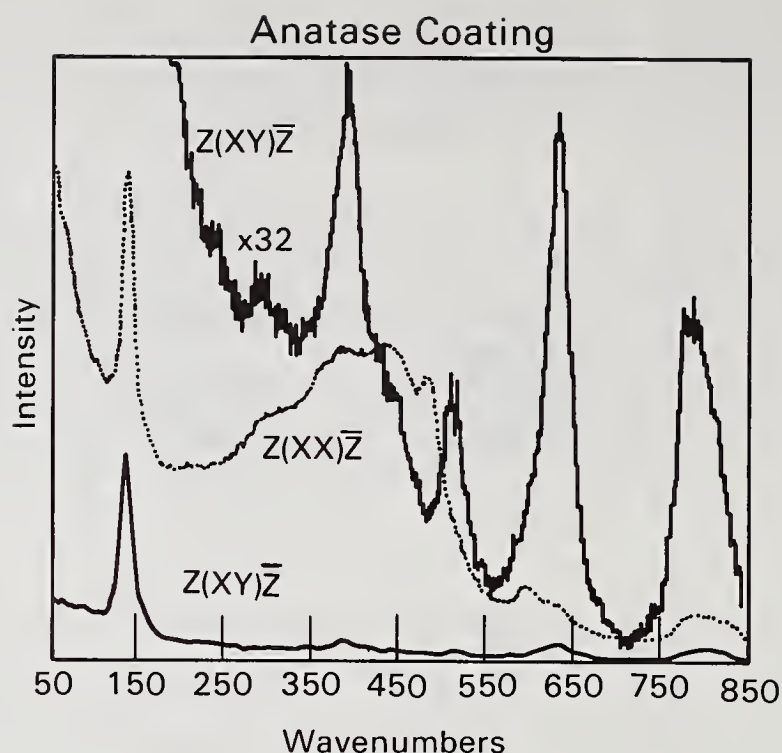
Anatase Coating

Figure 4. Raman spectra of a 1811 Å anatase coating on SiO_2. The standard scattering geometry designation is based upon a coordinate system centered at the sample where Z and Z̄ are the incident and scattered laser directions and X and Y define the particular component of the electric field transmitted by the analyzer.

anatase coatings. In addition, the extent of coating removed depends on the laser pulse energy and coating thickness. Multiple pulses on the same area remove successively less and less coating eventually converging to a limit. The 488 nm Ar+ probe laser (1W CW) was found not to damage these rutile or anatase coatings even when focused to a 50μ spot size at the sample.

The effect of temperature on phase stability of sputtered TiO_2 optical coatings was investigated using 10.6μ radiation from a CW CO_2 laser as a heating source. For this measurement, a colinear pulsed Nd:YAG laser operated at low pulse energy served as a Raman probe. To suppress sample blackbody emission at high temperatures, a gated detection scheme was used and the detector opening was synchronized to the laser pulse. Since the normal Raman effect is a spontaneous process, effective rejection of sample blackbody radiation at high temperatures is achieved.

Rutile coatings exhibited no phase changes during heating to nearly 1500°C. However, significant band shifts to lower frequency were measured. For instance, the a_{1g} mode at 610 cm^{-1} at room temperature shifts to 530 cm^{-1} at ca. 1500°C. Upon cooling to 25°C, the initial room temperature spectrum is recovered.

Anatase coatings exhibited a rather different response to temperature as shown in figure 6. An irreversible phase transition to the rutile crystalline form occurs at a temperature below 910°C. This is consistent with equilibrium thermodynamics which predicts a phase transition in this temperature region. However, when the coating is cooled down to room temperature, the rutile phase persists. The phase change is accompanied by a significant change in density, which leads to swelling and eventual microcrack formation in the coating.

The Raman experiments discussed previously were designed to characterize equilibrium damage to optical coatings induced by pulsed high energy laser irradiation. A second group of experiments was performed in order to characterize the non-equilibrium state immediately following irradiation by a high energy laser pulse in a regime where equilibrium thermodynamics does not apply. The first series of experiments involved measuring Raman spectra separated in time by increments of 10 milliseconds following the Nd:YAG laser damage pulse. The 488 nm CW Ar+ laser line was used as the Raman probe. Below damage threshold for any coating Raman

spectra acquired at 10 msec intervals are identical. When anatase coatings incur damage, a rapid intensity rise near the exciting line is observed, however, the major anatase lines
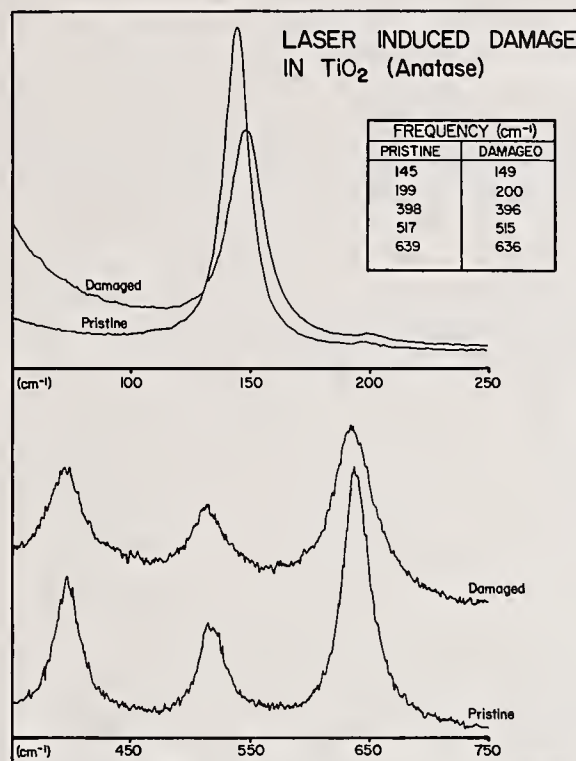
Figure 5. Raman spectra of a 9587 A anatase film on silica before and after exposure to a single 532 nm high energy pulse.
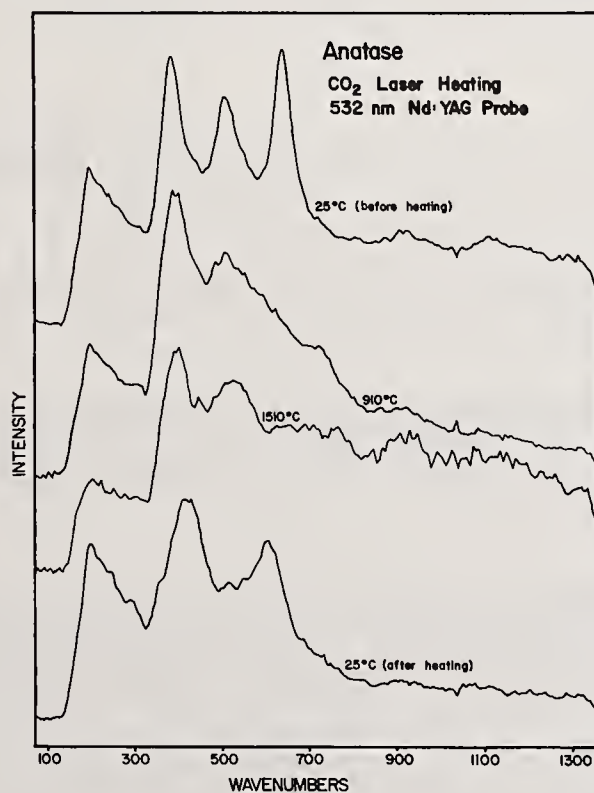
Figure 6. Raman spectra taken during equilibrium CO_2 laser heating experiment showing irreversible transformation of anatase to rutile at ca. 910°C.

267

are still evident albeit at lower intensity in all subsequent spectra. Results for rutile coatings are shown in figure 7. At 10 msec following the damage pulse, the low frequency intensity rise is evident. However, the rutile vibrational lines are not seen. Rather, the 640 cm^{-1} e_g anatase line is observed. At longer times, the rutile spectrum recovers, again at a lower intensity than the undamaged coating. An apparent reversible phase transition to an anatase-like phase has occurred.

The existence of an anatase-like phase at short times following laser damage to rutile coatings is further supported by data depicted in figure 8. Spectra were recorded as a function of detector delay for a single Nd:YAG laser pulse that served to both induce damage and act as the Raman probe. Spectra were acquired for detector delays up to several hundred nanoseconds. Evidence of an anatase-like phase persists even at detector delay times in excess of several hundred nanoseconds. At lower pulse energy below damage threshold conditions only the rutile spectrum is measured at zero detector delay. For longer detector delay times, no Raman signal can be detected. Similar results have been observed using optically delayed laser pulses of high (damage) and low (probe) energy separated in time.
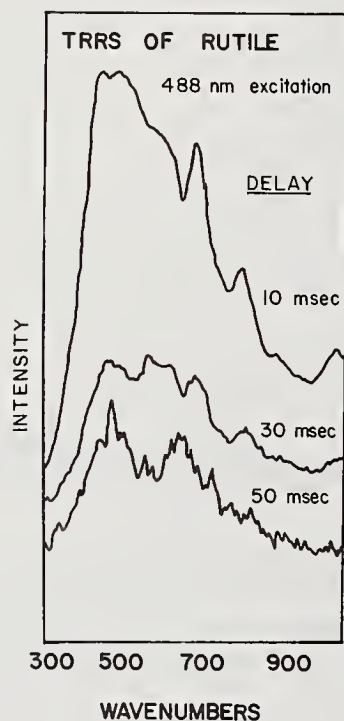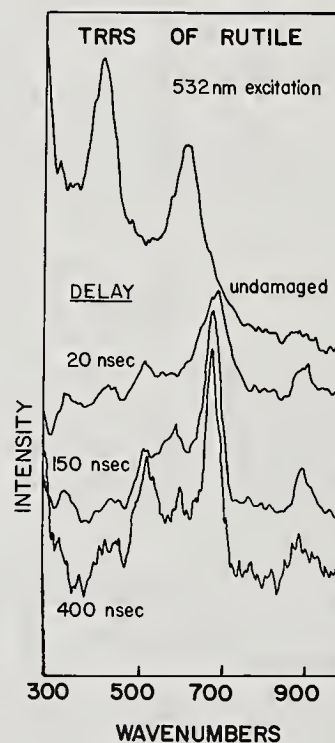
Fig 7   Fig 8

Figure 7. Time resolved Raman spectra of a rutile coating subjected to a high energy laser damage pulse showing reversible transformation to an anatase-like phase. Spectra were acquired under CW Ar+ excitation on a millisecond time scale.

Figure 8. Time resolved Raman spectra of a rutile coating subjected to a single high energy laser pulse acquired under 532 nm Nd:YAG excitation. Vibrational lines characteristic of the anatase lines are seen at short times following the damage pulse.

5. Discussion

Measured Raman spectra under equilibrium and non-equilibrium conditions provide sufficient structural information to formulate a model for the laser damage process in TiO_2 optical coatings. The relative instability of anatase coatings under laser damage conditions results from the observed irreversible phase transformation to the rutile phase at temperatures below 910°C. Localized heating from the laser damage pulse stimulates the phase transition. Induced swelling at the damage spot leads to lattice mismatch and localized fracturing of the surface. Vesitages of the rutile phase are transported away from the damage center. The remaining anatase, not having enough thermal energy to change phases, persists at long times exhibiting lower intensity Raman lines than the undamaged starting material.

A slightly different mechanism is proposed to explain laser damage phenomena in rutile coatings, which exhibit a higher damage threshold than the anatase coatings. The rutile phase

undergoes no detectable phase transition at temperatures below ca. 1500°C. Raman observed band shifts to lower frequencies indicate localized bond length increases which can result in bulk swelling. These changes are reversible, however, and should not contribute to the damage process. However, time resolved Raman measurements reveal features characteristic of the anatase phase for spectra acquired soon after the damage laser pulse has encountered the surface. Since this phase transition (rutile→anatase) does not occur under equilibrium conditions, a non-equilibrium explanation is in order.

High energy laser irradiation of materials can give rise to electronic excitation through multiphoton processes.[12] Vibrational levels may still be populated as in the ground state since the excitation process is rapid. Time resolved measurements will then probe the excited electronic state.

An elementary molecular orbital treatment of titanium localized in an octahedral oxygen environment suggests that the filled sigma bonding molecular orbitals between titanium and oxygen ligands are of a_{1g}, t_{1u}, and e_g symmetry.[13] Theoretical band structure calculations for rutile conclude that the upper valence band has a predominant O-p orbital character whereas the conduction band of TiO_2 is derived mainly from Ti-d states.[14] Therefore, excitation of a bonding electron from the highest occupied e_g state to an antibonding t_{1u}* state which is strongly allowed would tend to weaken the bonding between titanium and oxygen. Electron repulsion effects would act to perturb the octahedral structure forcing the square planar oxygen arrangement to distort. The resulting "puckered" structure in the excited state of rutile is qualitatively similar to the structure of the anatase ground state. Therefore, the Raman spectrum of the excited rutile state should exhibit similar features to the normal Raman spectrum of anatase. When the excited electron relaxes back to the ground state, the rutile structure is recovered. In this non-equilibrium case, the electronic transition causes a "phase change" as opposed to the equilibrium thermally induced phase change for anatase. The higher damage threshold of rutile coatings may result from the fact that a significant amount of the laser damage energy is stored in the excited electronic state, whereas in anatase, the energy may rapidly be thermalized leading to the irreversible phase transformation.

The persistence of the Raman spectrum of laser damaged rutile coatings at times approaching several hundred nanoseconds following the damage pulse may be explained in terms of resonance enhancement of the vibrational band intensities. Rosseau and Williams[15] have demonstrated that under resonance excitation of I_2, Raman spectra can be recorded from a single laser pulse at detector delay times approaching 1 microsecond. A similar mechanism is reasonable when electron excitation is induced in solids by laser irradiation.

6. Conclusion

Raman studies of laser induced damage in TiO_2 optical coatings were undertaken to provide molecular structural information for understanding the damage process. Anatase coatings, determined to have a lower damage threshold than rutile, fail by virtue of an irreversible phase transition to the rutile structure at temperatures below 910°C. Rutile accommodates energy in an excited electronic state resulting in a "non-equilibrium" phase transformation to an "anatase-like" state. Both coatings apparently fail by selective removal of the anatase phase from the coating.

In addition to structural considerations of the coating, substrate effects may also be important in understanding the mechanism responsible for coating failure. Figure 9 shows measureable damage to silica substrates as a function of the number of laser shots. The laser induced polarization intensity changes result from microscopic surface damage (microcracks, density fluctuations) which act to scramble the polarization of the probe laser beam.

Substrate damage could lead to optical coating failure by other mechanisms and suggests another topic for additional work in this area. Raman techniques will be applied to laser damage studies of other coatings such as ZrO_2 and multilayer designs in future work where attention to the coating-substrate interaction will also be focused.
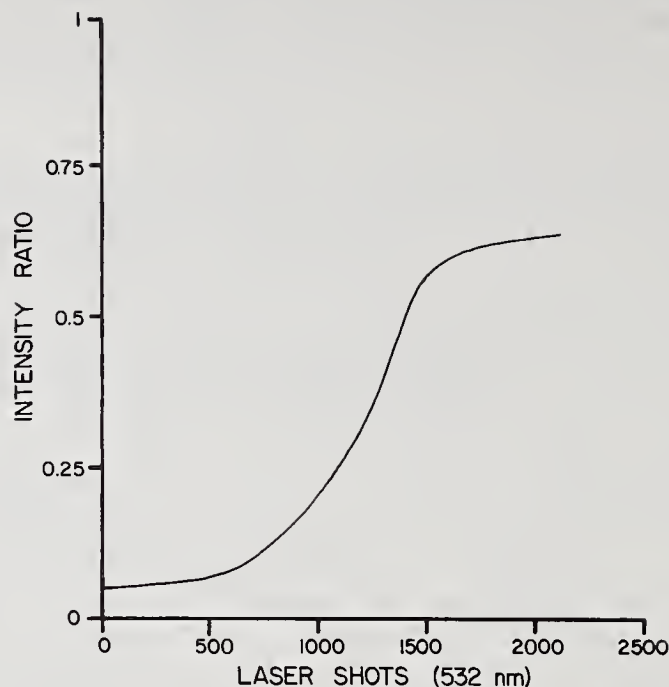
Figure 9. Induced polarization changes in a laser damaged SiO_2 glass substate as a function of number of pulses. The intensity ratio refers to transmitted laser light through crossed polaroid filters relative to the parallel filter orientation.

7. References

[1] Pawlewicz, W. T., Exarhos, G. J., and Conaway, W. E. Structural characterization of TiO_2 optical coatings by Raman spectroscopy. Applied Optics 22(12): 1837-1840; 1983.

[2] Nemanick, R. J. Connell, G. A. N., Hays, T. M., and Street. R. A. Thermally induced effects in evaporated chalcogenide films. Phys. Rev. B. 18: 6900-6914; 1978.

[3] Newmanick, R. J. , Tsai, C. C., and Connell, G. A. N. Interference-enhanced Raman scattering of very thin titanium and titanium oxide films. Phys. Rev. Lett. 44: 273-276; 1980.

[4] Exarhos, G. J. and Pawlewicz, W. T. Raman characterization of all-dielectric multilayer SiO_2/TiO_2 optical coatings. Applied Optics 23(12): 1986-1988; 1984.

[5] Exarhos, G. J. Substrate signal suppression in Raman spectra of sputter deposited TiO_2 films. J. Chem. Phys. 81(10): 000; 1984.

[6] Pawlewicz, W. T., Martin. P. M., Hays, D. D., and Mann, I. B. Recent developments in reactively sputtered optical thin films. Seddon, R. I., Ed. Proceedings of the SPIE conference on optical thin films; 1982 Jan. 26-27; Los Angeles, CA. Proc. Soc. Photo-Opt. Instrum. Eng. 325: 105-116; 1982.

[7] Pawlewicz, W. T., Hays, D. D., and Martin, P. M., High-band-gap oxide optical coatings for 0.25 and 1.06 micron fusion lasers. Thin Solid Films 73: 169-175; 1980.

[8] Clarke, R. J. H., The chemistry of Titanium and Vanadaium, An Introduction to the chemistry of the early transition elements. North Holland; Elsevier Publishing Co.; 1973. 265 p.

[9] Parkes, G. D., Mellor's Modern inorganic chemistry, Revised Edition. London; Longrans Publishing Co.; 1961; 803 p.

[10] Capwell, R. J., Spagnolo, K., and DeSesa, M. A. A rapid determination of low concentrations of anatase in rutile TiO$_2$ pigments by Raman spectroscopy. Appl. Spectrosc. 26: 537-539; 1972.

[11] Beattrie, I. R., and Gilson, T. R. Single crystal laser Raman spectroscopy. Proc. R. Soc. London Sec. A.; 307: 407-429; 1968.

[12] Royce, G. A., and Kay, R. B. Multiphoton interactions in rutile. Applied Optics 23(12): 1975-1979; 1984.

[13] Figgis, B. N. Introduction to Ligand Fields. New York; Interscience Publishers; 1966. 193 p.

[14] Munnix, S and Schmeitz, M. Surface electronic structure of rutile-type semiconductors: SnO$_2$(110) and TiO$_2$(110). Surface Science 126: 20-24; 1983.

[15] Rosseau, D. L. and Williams, P. F. Resonance Raman scattering of light from a diatomic molecule. J. Chem. Phys. 64(9): 3519-3537; 1976.

A questioner wanted to know what temperature change occurred when going from one phase to another. The author had not measured any thermal studies of the phase changes. In answer to the question of how far below damage threshold the laser induced depolarization, presumably caused by laser induced damage, was seen, the author replied that the effect occurred before any damage could be seen under a microscope, but that the laser fluence at which it occurred has not yet been established. Another questioner suggested that the temperature might be measured by determining the ratio of the Stokes to the Anti-Stokes scattering intensity. The author pointed out that this approach would be valid for conventional equilibria Raman scattering. However, if a resonance exists caused by Raman scattering from an excited electronic state, then the ratio may not give the true molecular temperature. Measurement of the surface temperature of bare fused silica should be valid, although the author had not done such measurements. He had used this technique successfully to determine the temperature of the CO$_2$ laser heated material and gotten good agreement with the results of a two color pyrometer. In answer to the question of the magnitude of the peak pressure of the laser induced pressure wave, the author replied that they measured a Raman shift of 4 cm^{-1}. Osaka measured a shift of 18 cm^{-1} for a 43 kbar pressure, which would suggest that at least as a crude approximation the pressure may have been about 10 kbar.

Alan F. Stewart
AFWL/ARBE
Kirtland AFB NM 87117

David J. Gallant
Rockwell International
Rocketdyne Division
P.O. Box 5670
Kirtland AFB NM 87185

ABSTRACT

Multilayer dielectric high reflectance coatings designed for 351nm were fabricated using ion beam sputtering and electron beam deposition on super polished silicon substrates. These optics were evaluated in terms of total integrated scatter levels, absorption, reflectance and laser induced damage thresholds. Ion beam sputtering was found to produce optics with the lowest losses while electron beam deposited coatings demonstrated higher laser damage thresholds.

Key words: Absorption, calorimetry, laser damage, reflectance, roughness, silicon, total integrated scattering, 351nm

1. Introduction.

    Recent advances in the development of high power lasers operating in the visible and ultraviolet have demonstrated that optical thin film coatings for this wavelength regime require considerable study and improvement. The visible free electron laser, operational for the first time in May 1983, required laser cavity optics with extremely low losses.[1] These FEL experiments utilized surfaces and coatings developed by the ring laser gyro industry where "super optics" are commonplace. Higher power applications require the development of different coating materials than those used in the gyro industry as well as the incorporation of silicon substrates for efficient heat removal. To support development programs for the high power excimer laser and the FEL, a program was established at the Air Force Weapons Laboratory to define the state-of-the-art by characterizing low loss substrates and coatings. Our results to date confirm that much additional work needs to be done to develop thin film coatings and surfaces for use in the ultraviolet.

    The objectives of this effort were twofold. The first objective was to design and construct instrumentation for the characterization of low loss optical surfaces and thin film coatings. Evaluation criteria included absorption, reflection, scattering losses and laser induced damage thresholds. The second objective was to determine the performance levels of polished silicon substrates and thin film multilayer high reflectance coatings designed for low total losses. Three different polishing vendors and two deposition techniques from four coating houses formed the sample matrix for this study. Overall, test results were encouraging in the sense that some substrate/coating design combinations performed very well in certain categories. Unfortunately, thin films that had high damage thresholds exhibited higher losses due to scattering, absorption and reflectance.

2. Sample Fabrication.

    To define the state-of-the-art in silicon substrate polishing techniques and low loss optical coatings, vendors were selected with proven past performance. Since the highest quality optical surfaces available are those produced for the ring laser gyro industry, polishing vendors were selected for the study on the basis of their experience with silicon and silica based gyro

optics. Single crystal silicon was specified but the orientation was left to the discretion of the polisher. As indicated in Table 1, polishers "A" and "C" selected the $\overline{111}$ orientation with polisher "B" using the $\overline{100}$ orientation. Polisher "D" had not attempted to polish silicon before but was able to achieve remarkably good surfaces on polycrystalline substrates. Polishers A, B, and C fabricated 38 millimeter diameter substrates for scattering, reflectance and damage threshold measurements. An additional set of 19 millimeter substrates were fabricated for calorimetry measurements.

After Total Integrated Scatter surface roughness measurements had been completed, substrates were placed in sealed containers and distributed to four coating vendors. Electron beam and ion beam coating processes were used to fabricate the high reflectance mirrors characterized in this study.

A variety of coating designs and materials were selected for this study as shown in Table 2. Coater "A" had considerable experience with ion beam sputtering of low loss SiO_2/Ta_2O_5 coatings and success with this combination was easily achieved. With coater "B", we tried to take advantage of the measured high damage threshold of SiO_2/Al_2O_3 coatings[2] while achieving high reflectance with an underlying stack of SiO_2/ZrO_2. One limitation of SiO_2/Al_2O_3 coating stacks is the narrow reflectance bandwidth and this may have affected our subsequent measurements. Coaters "C" and "D" utilized SiO_2/HFO_2, SiO_2/ZrO_2 and SiO_2/Sc_2O_3 multilayer designs which are well presented in the literature.

Before any characterization measurements were performed, substrates and coatings were cleaned carefully. A spinner system was used to dispense low residue electronic grade acetone or methanol on the surface. Collodion was then used for the final cleaning of each part before each set of characterization measurements was performed.

3. Experimental.

Instrumentation was constructed to evaluate optical surfaces and thin film coatings designed for low losses in the mid-visible and ultraviolet. The argon-ion laser was selected as the source for these measurements since it could provide 351nm and 514nm outputs to match the XeF excimer line and possibly a visible FEL. Established and proven instrumentation designs were used to construct a Total Integrated Scatter (TIS) device, a laser calorimeter and a cavity ring-down reflectometer. Adaptation of these instruments for use in the ultraviolet was not a problem except with certain elements of the reflectometer. Cross calibration of these instruments with other laboratories is currently in progress.

Total Integrated Scatter (TIS) is a well known technique used for surface characterization.[3] A schematic layout of the AFWL instrument is shown in Figure 1. The beam is focused to a diameter of approximately 1 millimeter at the sample. Three separate detectors are used in the instrument. The first detector monitors the laser power and this output is used to normalize the outputs of the other two detectors. The second detector monitors both the incident and specular reflected beam with a rotating mirror. The third detector is located at the specimen image plane inside the hemispherical collector to monitor the diffuse reflectance or scatter.

TIS is the ratio of the diffuse reflectance to the total reflectance

or $\qquad TIS \simeq \dfrac{R \text{ diffuse}}{R \text{ diffuse} + R \text{ specular}} \qquad TIS \simeq \dfrac{R \text{ diffuse}}{R \text{ specular}}$

From scalar scattering theory the effective root-mean-square roughness of the surface, σ, is defined by

$$\sigma \simeq \frac{\lambda}{4\pi} (TIS)^{1/2}$$

Because a single wavelength is used to measure the scatter and because of geometrical scatter collector limitations, the device is sensitive to a narrow band of spatial frequency components. The effective bandwidth of this instrument extends from 0.08 to $2.7 \mu m^{-1}$ at 351 nm.

In practice, each sample was measured at three sites on the TIS instrument. Sequential measurements on the same site indicated a measurement precision of ± 0.5 Angstroms RMS. Data obtained on uncoated super polished silicon substrates is summarized in Table 1. This data was taken using an identical TIS device operational at 633nm. The tolerances given are the standard

273

deviation over the set of forty pieces measured from each polisher. The smooth surfaces measured on samples from polisher "D" were a surprise development during this effort. It should be noted that because of bandwidth limitations, TIS is only marginally adequate for the evaluation of such ultrasmooth surfaces. However, it should be pointed out that on our instruments, epitaxial grade silicon wafers consistently measure out at 1 Angstrom RMS, so that the surfaces polished by vendor "D" therefore may be nearly damage free and close to the optimized optical surface.

After coatings had been deposited on this set of super polished silicon substrates, each was again evaluated on the TIS instrument. Measurement data at the design wavelength of 351 nm for each coating vendor and each polishing vendor is summarized in Table 2. The lack of correlation between uncoated surface roughness and subsequent measurements on coated optics should be noted. This is true in all cases except for ion beam sputtered films from vendor "A" which maintain the relative ranking between substrates. These coatings were clearly superior to all others tested in terms of low scatter or surface roughness levels. It is useful for comparison purposes to note that a TIS roughness figure of 7 Angstroms RMS correlates to losses due to scattering of about 650 ppm.

A laser calorimeter was used to measure directly the optical absorption at 351nm. The instrument is designed as described in Figure 2 and can accommodate either reflective or transmissive optics. The calorimeter consists of a vacuum chamber enclosure and an AC thermistor bridge with lock-in detection.[4] The thermistors themselves are unencapsulated ceramic beads 250μm in diameter with 50μm diameter lead wires. Sensitivity was found to vary with chamber pressure and the duration of time the thermistors were under vacuum, perhaps due to the absorption of water vapor into the ceramic beads. Consequently, all measurements were performed with a chamber pressure of 200mTorr. Calibration by electrical substitution indicated a bridge signal output of 1 Volt/°K at this pressure.

Measurements were performed on low thermal mass (approximately 1 gram) super polished silicon and fused silica substrates 19 and 25mm in diameter respectively. The sensitivity of the calorimeter bridge was determined to be about 50 ppm using a laser power of 1 Watt. The beam was "p" polarized with respect to the sample and was incident on the sample at 2.5° off normal.

Absorption measurements for each deposition method and coating design are summarized in Table 2. There was no apparent dependence of coating absorption on substrate polisher and the data is an average value of a number of measurements of each design. Tolerances are indicative of the ±10% estimated accuracy of the instrument. It is important to note that the absorption measured is the sum of absorption in the dielectric stack and that absorbed in the substrate. Measurements on identical coatings on both silicon and fused silica substrates for SiO_2/Ta_2O_5 from polisher "D" indicate that the effect of substrate absorption can be substantial. The fact that the laser was operated broadband with output lines extending from 337 to 363nm may also help to explain the high apparent absorption levels. Even though the coating designs incorporated high index materials and hence, the bandwidth of the coatings was typically 500 Angstroms, spectrophotometer curves of selected mirrors showed ~1% reflectance variations across the bandwidth of the laser. This was unexpected but is unquestionably due to the effect of dispersion in the coating materials used.

A cavity ring-down reflectometer was used to measure the total losses of the test optics.[5] The instrument is shown in Figure 3. The basic elements include the laser source, fast electroptic shutter, mode matching lens and test cavity. When the energy trapped in the cavity reaches a preset level, the detector-amplifier-comparator network shuts off the incident laser light with a 40nsec fall time Pockel's cell. The detector then monitors the decay time of the trapped light in the cavity as it is gradually lost due to cavity mirror transmission, absorption, scattering and diffraction. The reflectivity product of the cavity optics is then determined from the exponential decay time constant (τ)) of the trapped cavity radiation through the relation

$$Rp = \left[\frac{2c\tau}{L + 2c\tau} \right]$$

where L is the round trip cavity length and c is the speed of light.

The detector output is recorded by a digitizing storage oscilloscope and the data is fit to a computer generated exponential curve to determine the cavity decay time. A typical plot appears in Figure 4. The buildup of the trapped cavity energy is plotted on the left side of the figure. The Pockel's cell "fires" at 2.5 microseconds and the cavity energy begins to decay. The solid curve is an exponential curve generated by at least a square's fit to the

digitized data. For the optics tested in this survey at 351nm with "S" polarization, typical decay time constants ranged from 1 to 3 microseconds and total cavity losses ranging from 2,000 to 10,000 ppm. A computer printout for 30 consecutive decay curves for one test optic appears in Figure 5. Lower cavity losses lead to longer decay times and greater precision in the reflectivity product. From the uncertainty in the reflectivity product, the absolute accuracy ranged from 100 ppm to a worst case of 1,000 ppm.

The data obtained on the sample matrix using the reflectometer is summarized in Table 3. The tolerances given in the table are the standard deviation from measurements made on each set of optics and shows the sample-to-sample variation observed in a given coating run. Clearly, ion sputter deposited films deposited by "A" are superior performers with an average reflectance of 0.999. The lowest reflectances were measured on highly scattering SiO_2/ZrO_2 films from coater "D".

Laser damage testing was performed at Los Alamos National Laboratory by Stephen Foltyn, John Jolin and Billie Mauro. A XeF excimer laser was used in N-on-1 testing using standardized test procedures.[2] Damage thresholds were defined as the maximum fluence for which there is zero probability of damage occurring. The results of these measurements appear in Figure 6. Coatings on both fused silica and silicon substrates were tested as indicated in the figure. Clearly, ion beam sputtered films from coaters "A" and "B" have lower damage thresholds by a factor of two or more in comparison to electron beam coatings from the other vendors. There are differences in the materials used by each coater and this prevents a direct comparison between coating technologies. In other test series at LANL, SiO_2/Al_2O_3 coatings have demonstrated superior damage resistance over all other material combinations.[2] However, there have been no iterative coating development and damage testing programs involving ion beam sputtered films to date so there may be considerable room for improvement.

Ion beam sputtered coatings were measured to have lower laser damage thresholds overall and these thresholds appear in Figure 6 to be independent of the substrate type. While electron beam deposited films were superior overall in terms of laser damage thresholds, the measured threshold of coatings on silicon substrates were generally lower than identical coatings on fused silica substrates. The calorimetry data in Table 3 for electron beam deposited films from coater "D" indicates significant transmission through the coating followed by absorption in the substrate. Substrate absorption may therefore account for the lower thresholds observed on silicon substrates with electron beam coatings.

4. Conclusions.

Low loss, high reflectivity, multilayer dielectric mirrors designed for use at 351nm have been evaluated in terms of total losses and laser damage thresholds. Substrates of super polished silicon and fused silica were utilized to minimize coating scatter levels. Our results indicate that fabrication of superior substrate surfaces in terms of figure and roughness can be easily and routinely achieved. Polishing techniques employed by various vendors were capable of producing surfaces with 5 Angstroms RMS roughness. However, it is clear that improvements can be made to produce even better surfaces on silicon approaching the epitaxial grade surfaces used in the semiconductor industry.

Optical coatings pose the most significant development problem for continued advances in the ultraviolet. It was clear from this study that some of the coatings fabricated by the new ion sputtering technology can exhibt very low losses with high reflectivity, low absorption and low scattering losses. However, these films have lower laser damage thresholds than those produced by electron beam technology. While considerable effort has gone into the development of damage resistant electron beam coatings over the past few year, it is hoped that the greater control over deposition parameters achievable with ion technology could result in comparable or superior performance levels after a similar development program. Certainly continued work is necessary for ultraviolet optics, from improvements in characterization methods to advances in polishing and coating techniques.

Table 1. Silicon Crystal Orientation and Average Surface Roughness Determined from TIS Data at 6328 Angstroms.

Table 2. TIS Surface Roughness Data at 351nm on Sample Coating/Substrate Matrix.

Table 3. Laser Calorimetry and Reflectometer Data at 351nm on Sample Matrix.

Figure 1. Total Integrated Scatter Instrument Configurations.

Figure 2.   Laser Calorimeter Optical Configuration and Circuit Layout.

Figure 3.   Cavity Ring-down Reflectometer Instrument Configuration.

Figure 4.   Typical Decay Curve of a Trapped Cavity Mode in the Reflectometer.

Figure 5.   Printout of Reflectometer Data Run Showing Typical Cavity Losses, Decay Times and Reflectivity Products at 351nm.

Figure 6.   Laser Damage Thresholds from N-on-1 Testing at 351nm of High Reflectance Stacks on Super Polished Silicon and Fused Silica.

References.

1.   Billardon, J.M.; Elleaume, P.; Ortega, J.; Bazin, C.; Velghe, M.; Petroff, Y.; Deacon, D.; Robinson, K.; Madey, J.; Phys. Rev. Lett 51, p.1652.

2.   Foltyn, Stephen R.; Jolin, L.J.; "Alumina/Silica Multilayer Coatings for Excimer Lasers"; Nat. Bur. Stand. (US) Spec. Publ. #669, 1983.   Los Alamos Publication LA-UR-84-1831.

3.   Bennett, Jean M. and Stowel, W. Kent; "Round Robin Testing of Low Scatter Optics"; Nat. Bur. of Stand. (US); Spec. Publ. #669, 1983.

4.   Allen, Thomas H., Apfel, Joseph H.; Carniglia, C. K.; "A 1.06μm Laser Absorption Calorimeter for Optical Coatings"; Nat. Bur. Stand. (US); Spec. Publ. 541; 1978 December, pp 33-36.

5.   Anderson, Dana Z.; Frisch, Josef, C.; Masser, Carl S.; "Mirror Reflectometer Based on Optical Cavity Decay Time"; Appl. Opt. 23, p. 1238-1245 (1984).

TOTAL INTEGRATED SCATTER
SUPER POLISHED (UNCOATED) SILICON
6328 Å (HeNe)

	SURFACE ROUGHNESS
POLISHER "A" SINGLE CRYSTAL 1-1-1 ORIENTATION	3.4 Å RMS ± 1.3
POLISHER "B" SINGLE CRYSTAL 1-0-0 ORIENTATION	4.4 Å RMS ± 1.6
POLISHER "C" SINGLE CRYSTAL 1-1-1 ORIENTATION	6.1 Å RMS ± 1.4
POLISHER "D" POLYCRYSTALLINE	1.7 Å RMS ± 0.4

● BEST FUSED SILICA ~ 0.5 Å RMS

Table 1.   Silicon Crystal Orientation and Average Surface Roughness Determined from TIS Data at 6328 Angstroms .

"SURFACE" ROUGHNESS (Å RMS)

COATED SILICON – 351nm

COATER	FILM DESIGN	POLISHER "A" (3.4 Å)	POLISHER "B" (4.4 Å)	POLISHER "C" (6.1 Å)	AVERAGE
"A" (ION BEAM)	SiO_2/Ta_2O_5	6.3 ± 1.0	$6.6 \pm .3$	8.1 ± 1.0	6.9
		5.5 ± 1.0	$6.5 \pm .3$	8.5 ± 1.0	
"B" (ION BEAM)	SiO_2/AL_2O_3 SiO_2/ZrO_2	18.0 ± 5.0	8.7 ± 1.0	10.7 ± 1.0	12.5
"C" (ELECTRON BEAM)	SiO_2/HFO_2	17.6 ± 1.5	20.2	17.3	18.4
"D" (ELECTRON BEAM)	SiO_2/ZrO_2	19.4 ± 5.2	50.3	30.4	33.4
	SiO_2/Sc_2O_3		14.3 ± 1.8	—	14.3

- SCATTER INCREASED FROM 200 – 1100%
- BEST SURFACE PRODUCED BY ION BEAM
- NO CONSISTENT DEPENDENCE ON SUBSTRATE POLISH

Table 2.   TIS Surface Roughness Data at 351 nm on Sample Coating/Substrate Matrix.

278

ABSORPTION/REFLECTION AT 351nm

COATER	FILM DESIGN	ABSORPTION	REFLECTANCE
"A" (I-B)	SiO_2/Ta_2O_5	.0036 ±.0004	.9990 ± 0.0005
		.0038 ±.0004	.9966 ±.0004
"B" (I-B)	SiO_2/AL_2O_3 / SiO_2/ZrO_2	.0075 ±.001	.9980 ±.0004
"C" (E-B)	SiO_2/HFO_2	.0016 ±.0002	.9976 ±.001
"D" (E-B)	SiO_2/ZrO_2	.0021 ±.0002	.9877 ±.001 **
	SiO_2/Sc_2O_3	.011±.001 ON SI .001±.0001 ON SIO_2	.9983 ±.0008

* STD. DEV. FROM 10 MIRRORS

** ABSOLUTE ACCURACY ±.001 PER MIRROR

Table 3. Laser Calorimeter and Reflectometer Data at 351 nm on Sample Matrix.
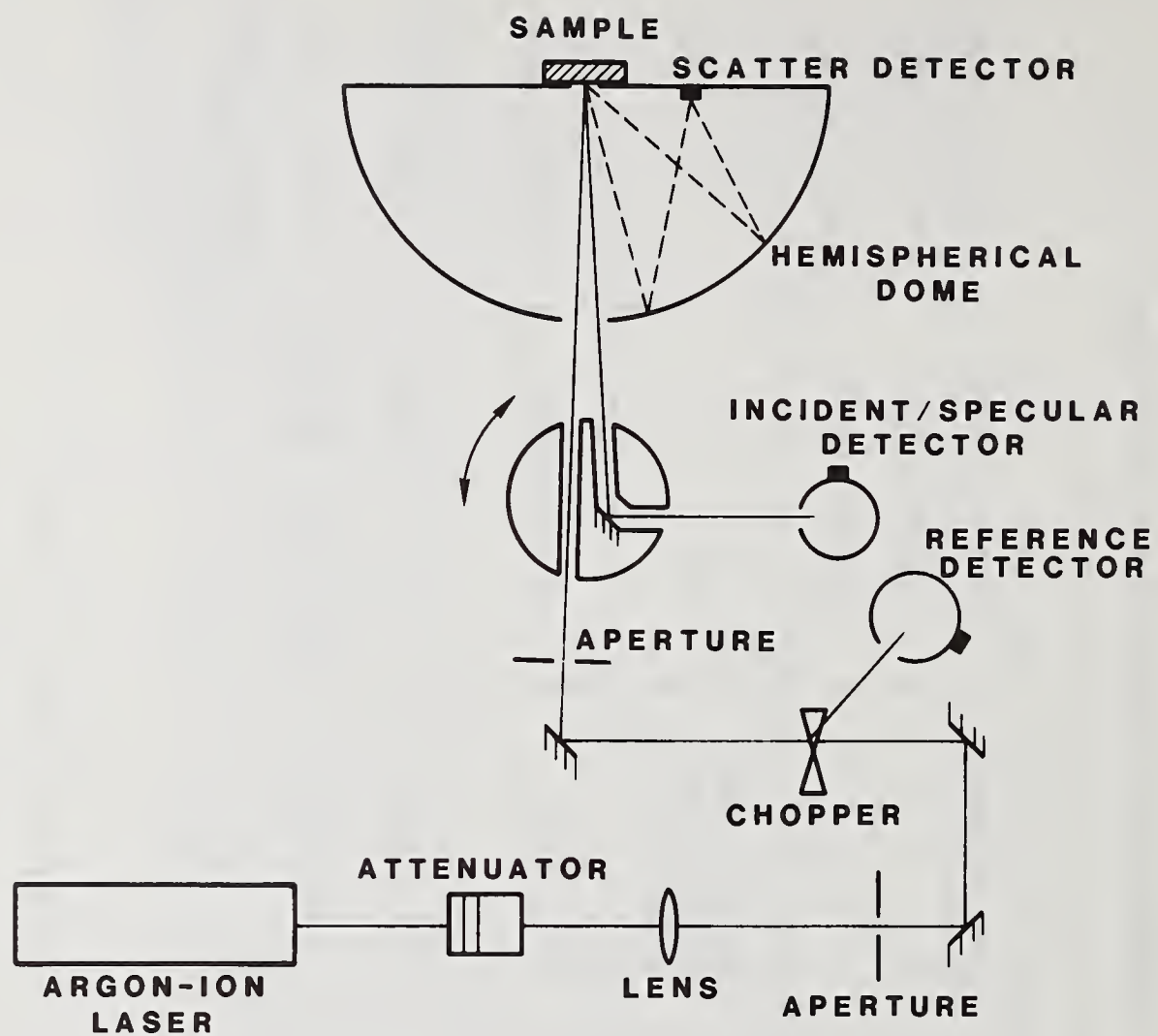
TOTAL INTEGRATED SCATTER (TIS) LAYOUT

$$\sigma(RMS) = \frac{\lambda}{4\pi} (TIS)^{1/2}$$

INSTRUMENT BANDWIDTH : $\lambda = 514.5$nm $f_s \sim .05 - 1.8 \mu m^{-1}$

$\lambda = 351$nm $f_s \sim .08 - 2.7 \mu m^{-1}$

Figure 1.   Total Integrated Scatter Instrument Configurations.
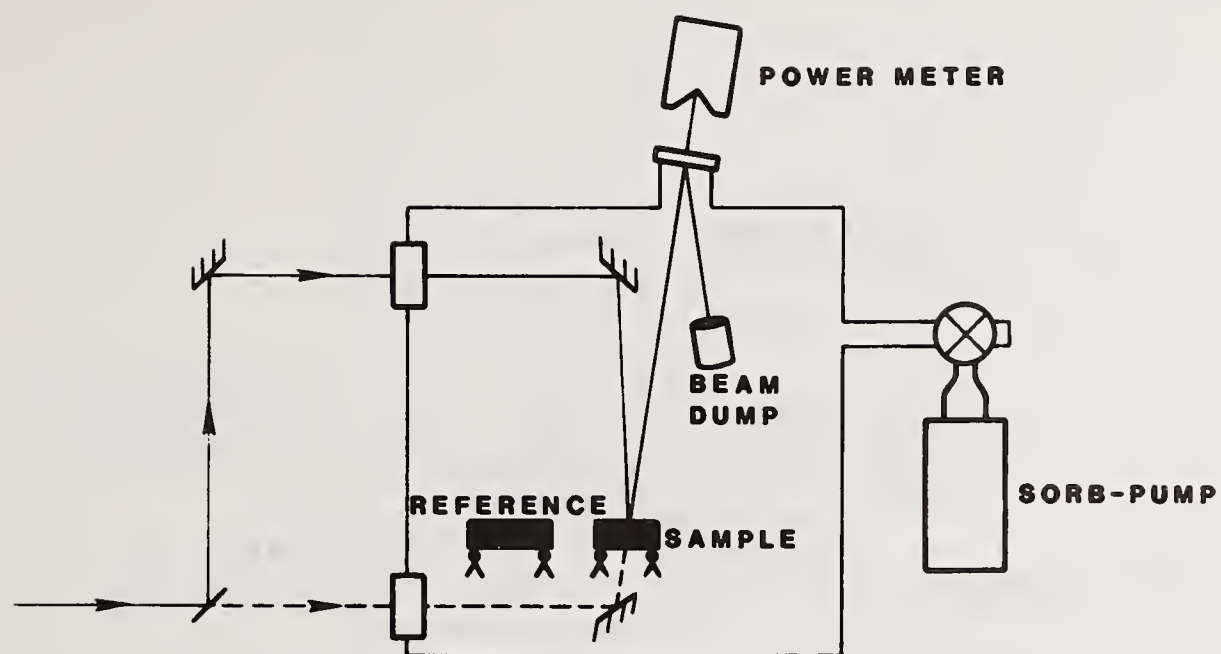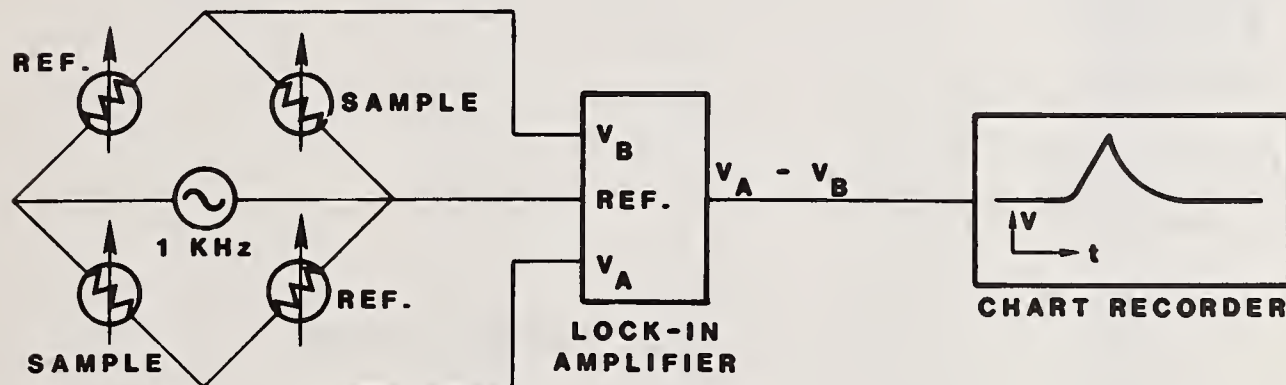
Figure 2. Laser Calorimeter Optical Configuration and Circuit Layout.
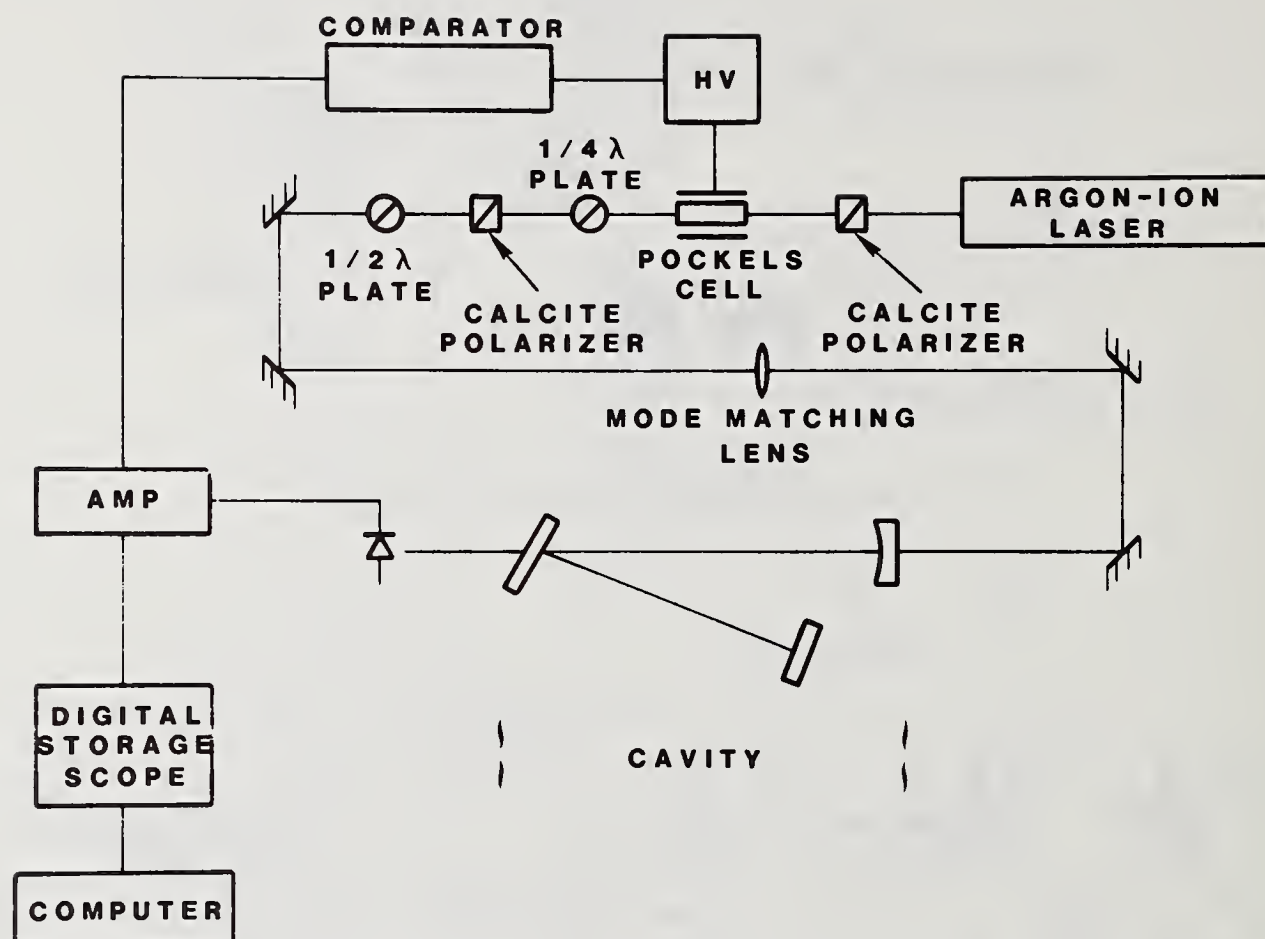
CAVITY REFLECTOMETER LAYOUT

$$\text{LOSSES} = \frac{L}{C\tau}$$

$$R_{PRODUCT} = 1 - \text{LOSSES}$$

Figure 3.   Cavity Ring-down Reflectometer Instrument Configuration.

Figure 4. Typical Decay Curve of a Trapped Cavity Mode in the Reflectometer.

```
OPERATOR:                DAVE GALLANT    26-SEP-84
TEST    MIRROR      ID:             OJAI LOT2 121-5V
CAVITY MIRROR  #1 ID:                      8MTR #1
CAVITY MIRROR  #2 ID:              OJAI 111-13V
WAVELENGTH= 351.0 nM  CAVITY LENGTH= 200.00 CM.
MINIMUM CC = 0.98000                 CUTOFF = 3.50

REFLECTIVITY (PRODUCT) OF CAVITY MIRROR(S): UNKNOWN
```
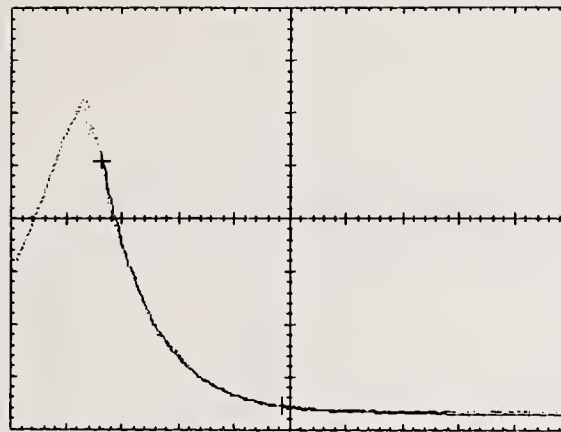
THE DATA POINT NUMBER	CAVITY LOSS IN PARTS PER MILLION (CL)	REFLECTIVITY PRODUCT OF TEST & CAVITY MIRRORS (RP)	DECAY TIME IN SECONDS (DT)	THE CORRELATION COEFFICIENT (CC)
1	7906.60	0.99214	0.16875E-05	-0.99463
2	5699.33	0.99432	0.23411E-05	-0.98035
3	7662.10	0.99238	0.17414E-05	-0.98714
4	8203.46	0.99184	0.16255E-05	-0.98657
5	6403.68	0.99363	0.20936E-05	-0.98880
6	7443.68	0.99250	0.17925E-05	-0.98454
7	7597.34	0.99245	0.17562E-05	-0.98610
8	7523.26	0.99252	0.17735E-05	-0.99489
9	8060.50	0.99199	0.16553E-05	-0.98822
10	8079.52	0.99197	0.16514E-05	-0.98876
11	7280.79	0.99275	0.18326E-05	-0.99438
12	7568.65	0.99247	0.17629E-05	-0.99414
13	8481.56	0.99157	0.15731E-05	-0.98959
14	8142.65	0.99190	0.16374E-05	-0.98669
15	7324.54	0.99272	0.18216E-05	-0.99155
16	8357.63	0.99169	0.15965E-05	-0.99029
17	6010.14	0.99402	0.22200E-05	-0.98456
18	7772.32	0.99227	0.17187E-05	-0.98963
19	6270.74	0.99376	0.21278E-05	-0.99254
20	7903.04	0.99214	0.16883E-05	-0.98806
21	7199.71	0.99284	0.18532E-05	-0.99139
22	7064.47	0.99297	0.18887E-05	-0.98980
23	5897.07	0.99413	0.22626E-05	-0.98183
24	7950.33	0.99210	0.16782E-05	-0.98605
25	7283.84	0.99276	0.18318E-05	-0.99277
26	5640.42	0.99438	0.23655E-05	-0.98288
27	7566.63	0.99248	0.17633E-05	-0.99221
28	5960.55	0.99407	0.22385E-05	-0.98354
29	7996.13	0.99205	0.16686E-05	-0.98847
30	6886.30	0.99315	0.19376E-05	-0.98479

```
AVERAGE CL =     7304.93 PPM        STANDARD DEVIATION = 0.838E+03
AVERAGE RP =      0.99274            STANDARD DEVIATION = 0.830E-03
AVERAGE DT = 0.18524E-05 SEC        STANDARD DEVIATION = 0.235E-06
AVERAGE CC =     -0.98851            STANDARD DEVIATION = 0.394E-02
```

Figure 5. Printout of Reflectometer Data Run Showing Typical Cavity Losses, Decay Times and Reflectivity Products at 351 nm.
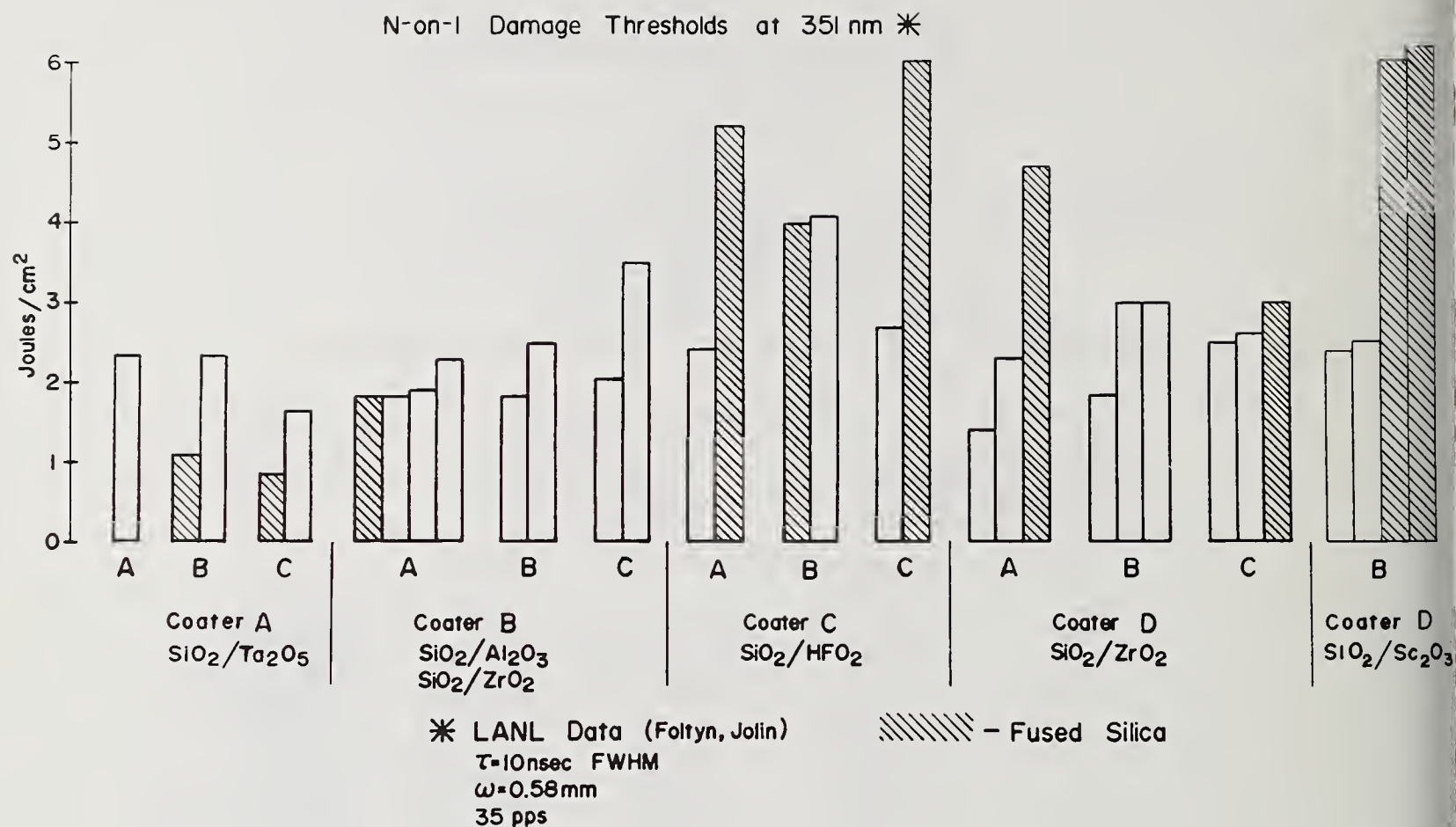
Figure 6. Laser Damage Thresholds from N-on-1 Testing at 351 nm of High Reflectance Stacks on Super Polished Silicon and Fused Silica.

Effect of Overcoats on 355-nm Reflectors

C.K. Carniglia and T. Tuttle Hart

Optical Coating Laboratory, Inc.
2789 Northpoint Parkway
Santa Rosa, CA 95407-7397

M.C. Staggs*

Lawrence Livermore National Laboratory
University of California
P.O. Box 5508, L-470
Livermore, CA 94550

Previous experiments have demonstrated that halfwave overcoats of a low-index coating material are effective in increasing the damage thresholds of dielectric high reflector coatings (HR's) at the wavelengths of 1064 nm and 248 nm. This overcoat layer led to a 50% increase in damage threshold at 1064 nm and to a 100% increase in threshold at 248 nm. This paper presents new results on the effect of halfwave overcoats at an intermediate wavelength: 355 nm.

Results reported at last year's Boulder Damage Symposium indicated that halfwave silica overcoats were detrimental to the damage thresholds of HR's at 355 nm. New results confirm that silica overcoats decrease thresholds and also show that magnesium fluoride overcoats do not improve the thresholds at 355 nm. A series of eight reflectors without overcoats had an average threshold of 2.4 J/sq. cm. The addition of silica overcoats decreased the average threshold by 2%, while magnesium fluoride overcoats decreased the threshold by an average of 7%.

Key words: electric field; high energy laser; laser damage; laser reflector; overcoat; reflector; thin film.

1. Introduction

A high reflector (HR) for use with near infrared (IR), visible, or ultraviolet (UV) lasers typically consists of alternate layers of two dielectric materials which have different refractive indices. The design is such that the optical thickness of each layer (the refractive index times the thickness of the layer) is one quarter of the laser wavelength.

An HR design which has proven to be successful for short-pulse UV lasers [1,2] is illustrated in figure 1a. It consists of 21 quarterwave layers. Scandia (Sc_2O_3) is used for the high-index layers, and silica (SiO_2) and magnesium fluoride (MgF_2) are used for the low-index layers. The design starts and ends with high-index layers to achieve maximum reflectance. The use of two different low-index layers, as illustrated here, has proven useful in reducing the net stress of the coating.

The standing wave electric field pattern for laser light incident on the HR from the left is also shown in figure 1a. It is highest in the outer layers and drops to a negligible value at the substrate. Note that the HR designs shown in both figures 1a and 1b are specifically for use at 355 nm and the refractive indices of the coating materials at this wavelength are given in the figure caption.

The addition of an overcoat of the low-index material is a design trick which has proven useful at wavelengths in the IR and UV [2-5]. The optical thickness of the overcoat is usually half of the design wavelength. Such overcoats have made significant improvements in the damage thresholds of laser reflectors. These results are discussed in section 2. A 355-nm HR with a halfwave magnesium fluoride overcoat is illustrated in figure 1b, together with the resulting electric field distribution. Note that the electric field within the 21-layer HR is unchanged by the addition of

Figure 1a. Design and electric field distribution for a 21-layer, 355-nm laser reflector. The coating design is indicated in the lower part of the figure. The materials and refractive indices are as follows: crosshatched layers - scandia, n = 1.97; unshaded layers - silica, n = 1.47; dotted layers - magnesium fluoride, n = 1.39. The intensity of the incident field is indicated by the arrow at the left, and the curve represents the time average of the square of the electric field within the coating.

Figure 1b. Same as figure 1a for a 21-layer, 355-nm laser reflector with a halfwave magnesium fluoride overcoat.

the halfwave overcoat. The peak electric field within the overcoat itself has a magnitude of $4/n^2$ relative to the incident electric field, where n is the refractive index of the overcoat. Because the overcoat has a low index, the electric field within the overcoat is usually higher than the highest field in the reflector stack itself.

Recent damage results at 355 nm [1] have indicated that the addition of a halfwave overcoat does not improve the damage threshold of 355-nm HR's. It is the purpose of the present study to further investigate this finding. The results of the current work are reported in section 3.

2. Previous results at 1064 and 248 nm

The beneficial effects on laser damage resistance of adding a halfwave silica overcoat to titania/silica quarterwave-stack HR's at 1064 nm has been conclusively demonstrated [3]. Twelve HR's with overcoat had an average threshold of 14.4 J/sq. cm for 1-ns laser pulses. The standard deviation was 3.9 J/sq. cm. Three of the HR's with overcoat had thresholds in excess of 20 J/sq. cm - the highest thresholds observed for conventionally evaporated coatings with 1-ns, 1064-nm laser pulses. The average threshold of 17 HR's without overcoat was 8.8 J/sq. cm, with a standard deviation of 2.8 J/sq. cm. Thus the average threshold was improved by more than 60% by the addition of the silica overcoat.

The reasons for the success of silica overcoats at 1064 nm have not been well understood. As indicated by figures 1a and 1b, electric field considerations do not explain the improvement: the field within the HR is the same with or without the overcoat, and the field within the overcoat is the highest anywhere in the coating. Because of damage morphology differences observed between HR's with and without the overcoat, the improvement in damage threshold for coatings with overcoats has been attributed to an increase in mechanical strength of the coating provided by the overcoat [4]. The titania layers have a columnar structure and are known to fracture easily. The silica layers have a more homogeneous structure and are more fracture resistant. In addition, the compressive stress of the silica layers is thought to be more damage resistant than the tensile stress of the titania layers. Thus the model for the improvement in the thresholds of HR's at 1064 nm due to halfwave overcoats is a mechanical one: the overcoat strengthens the outer surface of the coating, making it more damage resistant.

An extensive study of 45 HR coatings for use at 248 nm [2,5] has demonstrated an even greater improvement in damage threshold due to the addition of a halfwave overcoat. The study involved scandia/silica/magnesium fluoride coatings with designs similar to those shown in figures 1a and 1b. The basic HR stacks had either 19 or 31 layers and were deposited onto either fused silica or BK-7 substrates. Two different coating temperatures were investigated, 150 C and 250 C. The results showed that all films without overcoats had thresholds below 4 J/sq. cm for 20-ns, 248-nm laser pulses, while all coatings with halfwave overcoats had thresholds above 4 J/sq. cm. The median threshold for overcoated HR's was 6.3 J/sq. cm, which was more than double the median threshold of 3.1 J/sq. cm for non-overcoated HR's. [5]

A significant part of this earlier study at 248 nm was that two different low-index materials were used for overcoats: silica and magnesium fluoride. Overall, magnesium fluoride overcoats produced an average threshold 20% greater than silica overcoats. A close inspection of the data [5] reveals that magnesium fluoride gave a greater improvement than silica at the lower coating temperature (150 C). At the higher temperature (250 C), both overcoat materials gave about the same improvement.

The significance of the success of magnesium fluoride as an overcoat material is that it discounts the mechanical model developed to explain the results at 1064 nm. Magnesium fluoride layers have large crystalline structures and high tensile stress. In addition, they are mechanically "soft" at coating temperatures as low as 150 C. Thus, the silica and magnesium fluoride overcoats are mechanical antitheses. The fact that they both lead to large improvements in damage thresholds poses a serious challenge to a mechanical model for explaining the improvement due to the overcoat.

Even without a satisfactory explanation, these previous results make it clear that overcoats are beneficial at two widely different wavelengths: 1064 and 248 nm. While we recognized the necessity to test the effect of overcoats at intermediate wavelengths, there was little doubt that overcoats would lead to an improvement. Surprisingly this was found not to be the case at 355 nm.

3. Results at 355 nm

The first indication that overcoats did not improve the damage thresholds of 355-nm HR's was reported at the 1983 Boulder Damage Symposium [1]. A survey of reflectors made with four different high-index materials produced the following results: the average damage thresholds at 355 nm of

HR's containing zirconia (ZrO_2) and tantala (Ta_2O_5) were 3.0 J/sq. cm and 2.4 J/sq. cm, respectively, without overcoats, and about 20% lower with halfwave silica overcoats. HR's containing hafnia (HfO_2) had a very low average threshold (1 J/sq. cm) with or without silica overcoats. The highest average threshold (3.5 J/sq. cm) was observed for scandia/silica/magnesium fluoride HR's with magnesium fluoride overcoats. No HR's of this type without overcoat were tested, however, since from the earlier work at 248 nm it was assumed that the scandia HR with magnesium fluoride overcoat would have the highest threshold.

The conclusions relative to the effect of overcoats at 355 nm from this early work were unclear. Silica overcoats seemed to be detrimental to the threshold, but the coating with the highest threshold had a magnesium fluoride overcoat. The question remained as to whether the high thresholds observed for the scandia HR were due to the magnesium fluoride overcoat or the differences between scandia and the other high-index coating materials. To answer this question, a set of 24 scandia/silica/magnesium fluoride, 355-nm HR coatings with various overcoat options was made for damage testing. The coatings were made at OCLI in a 1.2 meter box coating machine. All materials were deposited by evaporation using an electron gun source. The substrate for all coatings was BK-7 which had been polished by Zygo Corporation using a continuous-feed polishing technique. Six parts were coated in each of four runs. A 25-layer scandia/silica/magnesium fluoride HR with a design similar to that shown in figure 1a was coated simultaneously onto all six parts. Then, with the help of movable masks, a halfwave silica overcoat was added to two of the HR's and a halfwave magnesium fluoride overcoat was added to two other HR's. The remaining two HR's received no overcoat. Two of these runs were made at 150 C and two were made at 250 C.

The damage testing of these parts was done by LLNL using a frequency tripled Nd-glass laser. The 355-nm, 0.6-ns laser pulses were focused to give a beam with a 1-mm diameter at the coating surface. Each test site was irradiated with one laser pulse and the presence of damage was determined visually using Nomarski microscopy. The precision of the damage threshold determination was ± 10% for each part.

The damage results for the two sets of coatings made at different temperatures are given in figures 2 (T = 150 C) and 3 (T = 250 C). Each open circle indicates the damage threshold measurement for one part. The error bars indicate the precision of the measurement. The four parts for each overcoat option (none, magnesium fluoride, and silica) and each temperature are grouped together in the figures. A horizontal line through the data points indicates the average threshold of the four parts of each type. One immediate observation about the damage results presented in figures 2 and 3 is that the average thresholds of all of the coatings, and especially of those with magnesium fluoride overcoats, are lower than those of the previously reported study. The reasons for this are not understood, but may be due to long-term variations in the coating process. This result emphasizes the importance of making each coating experiment complete by itself, so that it need not rely on earlier work for its validity and significance.

The major conclusion that can be drawn from the data is that neither silica nor magnesium fluoride overcoats improve the damage threshold of these 355-nm HR's. The differences between the average thresholds of the various types of coatings at each temperature are small compared to the overall scatter in the data. However, one cannot help but notice that at both temperatures the average thresholds of the overcoated HR's are lower than the average thresholds for the non-overcoated HR's.

The damage threshold data presented in figures 2 and 3 do demonstrate a clear advantage of coating at the higher temperature. Ignoring overcoat differences, the average threshold of the 12 parts coated at 150 C is 1.85 J/sq. cm with a standard deviation of 0.35 J/sq. cm. The average of the 12 parts coated at 250 C is 2.79 J/sq. cm with a 0.59 J/sq. cm standard deviation. Thus, there is a 50% increase in threshold for coatings made at the higher temperature. This is consistent with results reported previously for zirconia/silica HR's [1].

The reasons for the failure of overcoats at 355 nm are understood to an even lesser degree than the reasons for the success of overcoats at 248 and 1064 nm. There are a number of differences between the coatings that could be related to an explanation. The thickness of the layers is proportional to the wavelength. Thus the layers for the 1064 nm coatings are approximately four times thicker than those for the 248 nm coatings. The thicker layers may have better mechanical integrity, but also higher net stress than the thinner layers. The shorter laser wavelengths are closer to the absorption edges of the coating materials than the longer wavelength is and this may enhance the possibility of multiphoton effects. Also, the absorption of the materials is expected to be higher at the shorter wavelengths. Another, possibly significant, difference in the measurements is the pulse length of the damage test laser. The pulses were on the order of 1 ns for the 1064- and 355-nm lasers (Nd-glass and frequency tripled Nd-glass), but were 20 ns long at 248 nm (KrF). It may be possible that competing mechanisms involving these factors can explain the

Damage Thresholds for 355nm HR's at 150C
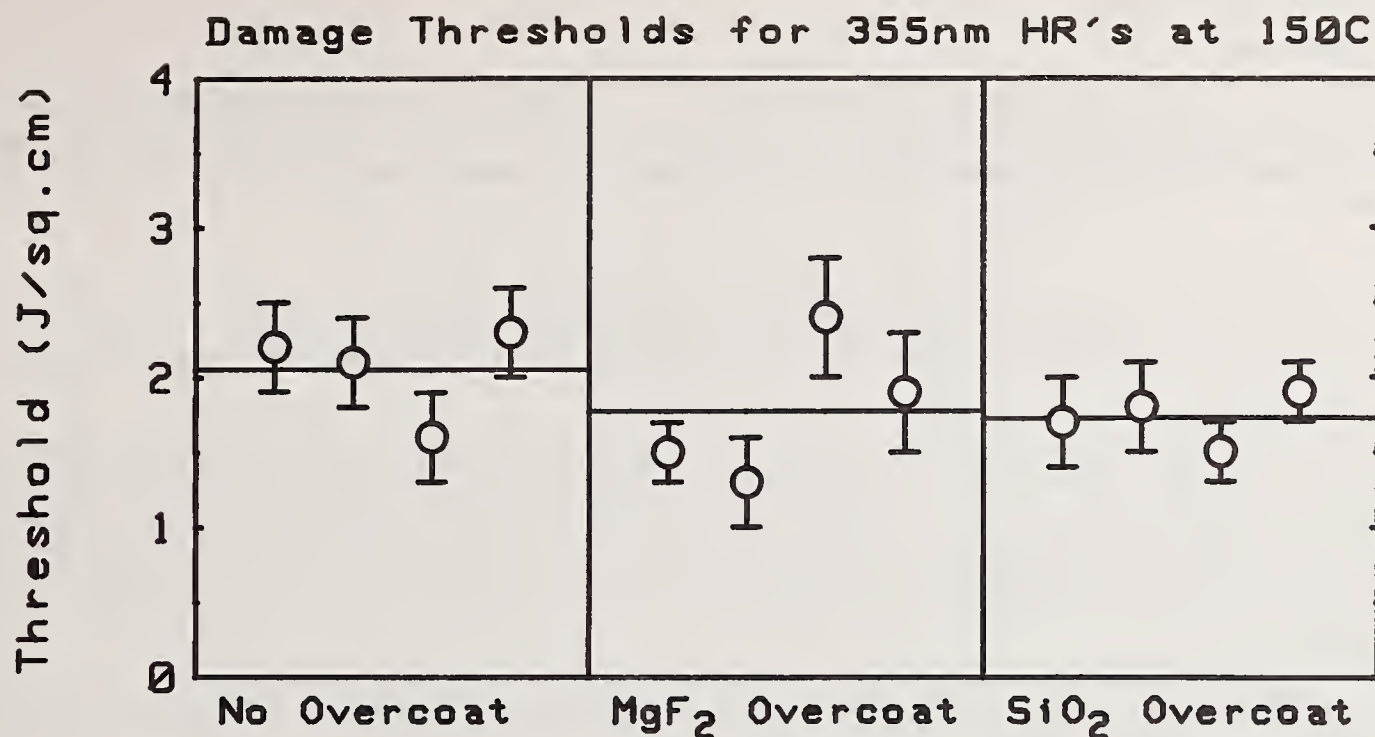
Figure 2. Laser damage thresholds for 355-nm HR's with various overcoat options coated at a temperature of 150 C. Each circle represents the damage threshold of one sample. The error bar for each sample represents the range between the lowest fluence which caused damage and the highest fluence which did not. The average damage threshold for each overcoat option is indicated by a horizontal bar.

Damage Thresholds for 355nm HR's at 250C
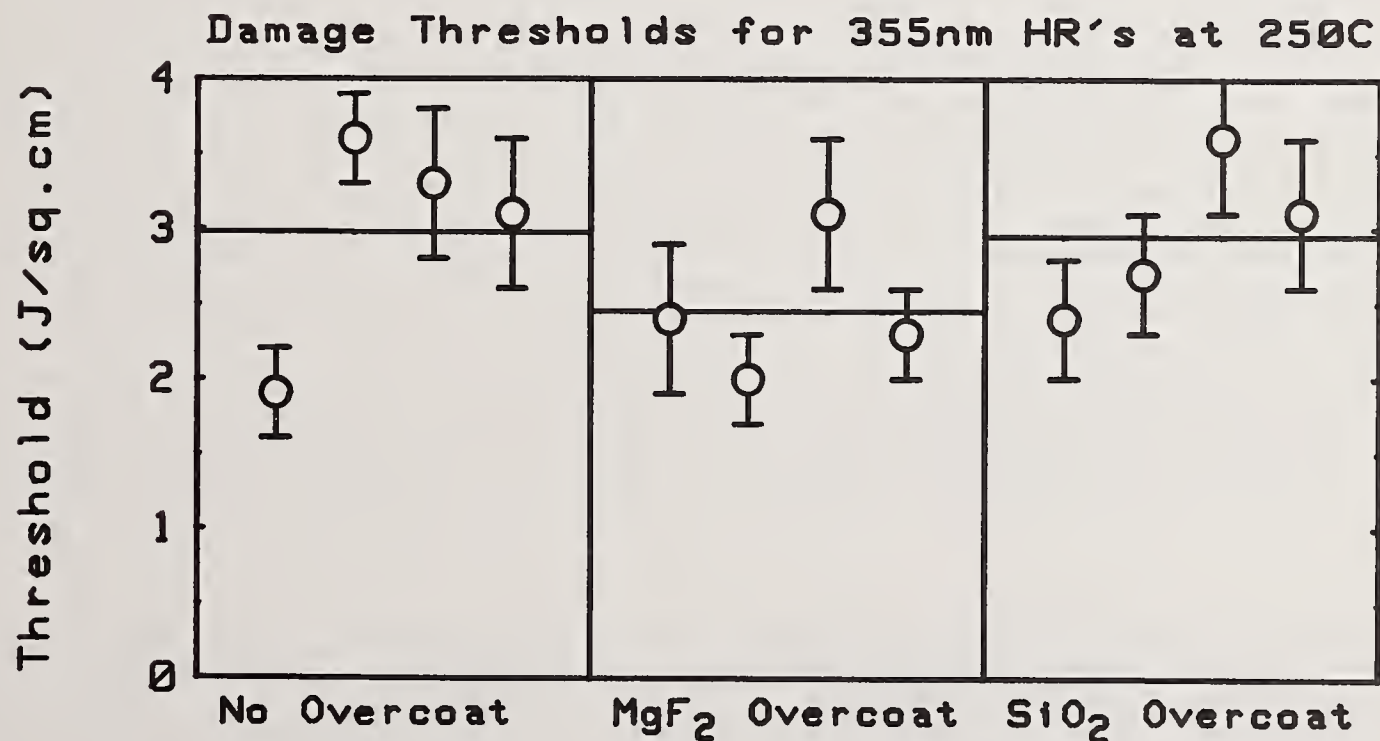
Figure 3. Laser damage thresholds for 355-nm HR's with various overcoat options, coated at a temperature of 250 C. Refer to caption for figure 2.

observed results.

4. Conclusion

    The current results confirm earlier findings that halfwave, low-index overcoats do not improve
the damage thresholds of HR coatings for use at 355 nm. This is an unexpected result in view of
previous damage tests which demonstrate a significant improvement due to overcoats at 1064 nm and
248 nm.

    The authors wish to acknowledge the work of Bill Klapp in preparing the coatings for this study.

8. References

[1] Carniglia, C.K.; Tuttle Hart, T.; Rainer, F.; Staggs, M.C. Recent damage results on high
     reflector coatings at 355 nm. Nat. Bur. Stand. (U.S.) Spec. Publ.; 1983 (to be published).

[2] Tuttle Hart, T.; Lichtenstein, T.L.; Carniglia, C.K.; Rainer, F. Effects of undercoats and
     overcoats on damage thresholds of 248 nm coatings. Nat. Bur. Stand. (U.S.) Spec. Publ. 638;
     1981. 344-349.

[3] Carniglia, C.K.; Apfel, J.H.; Allen, T.H.; Tuttle, T.A.; Lowdermilk, W.H.; Milam, D.;
     Rainer, F. Recent damage results on silica/titania reflectors at 1 micron. Nat. Bur. Stand.
     (U.S.) Spec. Publ. 568; 1979. 377-390.

[4] Carniglia, C.K. Oxide coatings for one micrometer laser fusion systems. Thin Solid Films
     77(3): 225-238; 1981 March 6.

[5] Rainer, F.; Lowdermilk, W.H.; Milam, D; Tuttle Hart, T.; Lichtenstein, T.L.; Carniglia, C.K.
     Scandium oxide coatings for high-power UV laser applications. Appl. Opt. 21(20): 3685-3688;
     1982 October 15.

Thermal Properties of Optical Thin Film Materials*

D. L. Decker, L. G. Koshigoe, and E. J. Ashley

Michelson Laboratory, Physics Division
Naval Weapons Center, China Lake, California 93555-6001

The performance of coatings for high power laser application depends not only on the optical properties of the films, but the thermal properties as well. An examination of the literature indicates that virtually all work has concerned the optical absorptance or reflectance, and that virtually no thermal property data are available for optical materials as thin films. Since it is known that the optical absorptance is often larger by orders of magnitude for a material as a thin film compared to bulk, a similar change (decrease) in thermal diffusivity might be expected. Of additional concern are the interfacial thermal barriers occurring at the boundaries between films. This paper presents experimental data for thin-film materials including Al_2O_3 and SiO_2 deposited in high vacuum. A simple theoretical analysis is also presented as well as recommendation for further work.

Key words: heat capacity; optical materials; optical properties; thermal conductivity; thin films.

Introduction

Much effort has been expended in characterizing and analyzing the optical properties of thin-film materials. It is obvious, however, that an understanding of the thermal properties is also essential to a quantitative description of the laser-induced damage process. Even for heat loading levels below that at which damage occurs, the thermal properties are essential to an engineering analysis of both window and mirror performance. The thermal drop across the dielectric stack of a typical quarter-wave enhanced reflector in the infrared is of the same order as the face sheet drop in a state-of-the-art water-cooled mirror design. Unfortunately, an examination of the literature reveals very little thermal properties data are available for dielectric optical materials as thin films. Direct measurement would be desirable but is very difficult, with potentially serious systematic errors associated with some techniques [1-3].[1] Indirect methods such as photoacoustic spectroscopy can provide thermal data but are subject to potentially large uncertainty. Work has been reported, however, that indicates that with proper analysis and calibration, quantitative results can be obtained by that method [4]. For theoretical reasons to be discussed, it is expected that the disorder typically found in vacuum-deposited thin films will produce a decrease in thermal conductivity of an order of magnitude or more below bulk values. Results presented in this paper corroborate this analysis. Similar results have been reported for a wide variety of thin films deposited for nonoptical application [5,6]. The size effects reported are caused by film thickness, grain size, and crystalline perfection limitations. Results presented in this paper are intended to provide (1) validation of the methods employed and (2) a limited survey of useful optical thin-film materials. Thermal conductivity is shown to be sensitive to deposition technique, so that a full catalogue of thin-film thermal properties data would require a substantial commitment of resources.

Theory

The heat capacity of dielectric materials is a consequence of energy stored in lattice vibrational excitation (phonons). The classical high-temperature molar heat capacity is 3Nk, where k is Boltzman's constant and N is Avogadro's number [7]. This value is closely approached by most materials even at room temperature. The heat capacity at high temperature (i.e., room temperature) is sensitive primarily to short-range order. Hence specific heat C_p/ρ (heat capacity per unit mass) is not sensitive to density ρ or to large-scale imperfection. A measurement of specific heat of thin-film amorphous germanium was performed in support of this paper, which corroborates these

assertions. The density of thin films is usually lower than corresponding bulk material usually by no more than a few percent. Hence, purely density-related effects are not large [8]. Details of these measurements are reported in the experimental section.

Thermal conductivity K, on the other hand, is very sensitive to local order, depending directly on the phonon mean free path $\bar{\ell}$:

$$K \approx \frac{1}{3} C_p v \bar{\ell} \quad , \tag{1}$$

where v is the average phonon velocity. This simple expression is obtained from elementary kinetic theory [7]. The phonon mean free path is limited by scattering from other phonons and from lattice boundaries and imperfections. For an evaporated film, order may exist on a scale no larger than a few lattice units and, hence, may directly limit the conductivity.* As a consequence of the columnar growth morphology, which is evident in many vapor-deposited thin films, it might be anticipated that substantial anisotropy in thermal conductivity might be observed [8]. For such a film, the conductivity would presumably be higher transverse to the film where longer range order would exist in the branching structure of a column. Table 1 gives values of $\bar{\ell}$ computed for various bulk materials and assumes an average phonon velocity of 5×10^5 cm/sec. Very large differences in thin film and bulk thermal conductivity are to be expected.

Table 1. Values of C_p and K taken from the litera-
ture for various bulk crystalline pure materials at
room temperature, together with a value of $\bar{\ell}$ computed
from equation (1) in the text. It is assumed that
values of K for noncubic crystals are for conductivity
parallel to the c axis.

Material	C_p, j/cm^3-°C	K, w/cm-°C	$\bar{\ell}$, Å
SiO$_2$	2.00	0.12	36
Al$_2$O$_3$	3.18	0.25	47
ZnS	1.99	0.26	78
Si	1.81	0.84	278

Other limitations on thermal conductivity of multilayer coatings may arise from interlayer ther-mal resistance of the sort that is observed in mechanically clamped joints even when the fit is essentially an "optical contact" [9,10]. In some coating designs, intimate chemical bonding almost certainly exists, e.g., in a layer pair like Si/SiO. In other cases, the bond is presumably much weaker, and the layers are connected by Van der Waal-type forces, e.g., ZnS/SiO. An additional complication arises in the case of thin films which are transparent in the infrared. At high temperatures, additional heat is transported by radiation. In fact, as has been shown, for very thin, low absorption films, direct radiation transport dominates at temperatures above ~1100K [11]. This is of no direct impact here, as this paper concerns thermal tranport at relatively low temperatures.

Experiment

In this section, sample preparation and experimental measurement techniques will be reported for thin-film specific heat and thermal conductivity. For specific heat measurement, a straightforward technique using microdifferential calorimetry was employed using samples as small as 20 mg. For veri-fication of the prediction made in the Theory section, germanium was chosen because the bulk thermal properties have been so well documented. To obtain a suitable sample, 99.999% pure amorphous german-ium was sputter-deposited using a commercial rf diode system on a polished sodium chloride substrate [12]. Upon cooling, the germanium film would show negligible adhesion to the substrate and could be easily removed mechanically. A 1-μm-thick film of approximately 40-cm^2 coating area was required to obtain the necessary 20 mg. A straightforward but very carefully executed measurement with a commer-cial differential scanning calorimeter [13] yielded an average value 0.082 cal/gm-°C. Over a temperature range of 50 to 150°C, no variation in specific heat was observed for the thin-film sample. A 100-mg mass sample of 99.999% pure bulk amorphous germanium was also prepared and examined

_____
* On such a scale, the very concept of lattice waves may be called to question, but this simple model can serve the purposes of this paper.

in the differential calorimeter. The measured value of specific heat was temperature dependent, with a value at 50°C of 0.0775 cal/gm rising linearly to 0.0825 at 225°C. The small discrepancy between bulk and thin-film values was thus as expected [14].

To obtain insight into thin-film thermal transport, it was decided that for a first attempt, a straightforward measurement of thermal conductivity would be appropriate. Figure 1 schematically shows the apparatus used. The thin-film sample is suitably vapor deposited on a 0.020-in.- (0.50-mm) thick, 0.75-in.- (19-mm) diameter, single-crystal, polished sapphire disk. This disk in turn is thermally contacted to source and sink blocks, which have an interface diameter of 0.444 in. (area A = 1.00 cm^2). The heater in the source block can dissipate a maximum of 100 W, so the maximum heat flux through the sample can approach 100 W/cm^2. Because the source and sink areas are identical and the thickness of the substrate is small by comparison to their diameter, negligible radial flow occurs in the substrate and the heat flow in the thin film or in the substrate is accurately one dimensional. The source and sink surfaces are finished by lapping. Thermal connection to the sample is typically enhanced with a thermal grease containing a high concentration of Al_2O_3 particles. The entire assembly was then clamped with a force of about 700 gm.

Type-K thermocouples (chromel/alumel) were used for temperature measurement, since they have high sensitivity but low thermal conductivity. Fine-wire thermocouples (0.003-in. diameter), TC_1 and TC_4, were placed in 0.006-in.-diameter holes drilled just under the interface surface of both source and sink blocks. The configuration just described permits the simple calculation of thermal conductivity:

$$K = (P_h/A)(dT/dx)^{-1} \quad , \tag{2}$$

where the heater power P_h is measured electrically by measuring the voltage drop across the heater and across a known series resistor to obtain the current flow (see fig. 2). The thermal gradient dT/dx can be directly obtained from the temperature drop TC_1-TC_4 and the known sample thickness. If the sample were homogeneous and if negligible temperature drop existed across the thermal grease connections to the sample, a satisfactory measurement of K would be obtained. However, unless great care in construction and assembly is used, larger thermal drops occur across the grease interfaces than across the sample. Also, the thermal drop across the substrate is typically significantly larger than the film drop. To eliminate these error sources, a modification to the procedure described above was employed in which thin-film thermocouples were directly deposited on the sapphire substrate and on top of the dielectric thin films. The dielectric thin film provided electrical isolation of the thin-film thermocouples (TC_2 and TC_3), and an additional 0.020-in.-thick sapphire disk provided electrical isolation for TC_2 from the source block. TC_2-TC_3 now provides a direct measurement of the thermal drop across the thin film and is thus independent of the substrate or thermal grease drop. The thin-film thermocouples were deposited by direct e-gun evaporation of heavy (10 ga) thermocouple wire segments. Sequential deposition of the chromel and alumel elements was made through suitable masks. The actual thermocouple was formed in the center of the sample by crossing the 1-mm-wide × 1000-Å-thick deposited elements. Electrical connection was made to the external switches and microvoltmeter by soft soldering 0.003-in. chromel or alumel wire to thin-film pads deposited for the purpose on the substrate. This scheme is similar to a thin-film thermocouple device reported by Goldsmid and Paul [15]. Figure 3 shows the calibration of a thin-film thermocouple so constructed with the temperature determined by a calibrated mercury-in-glass thermometer. Interestingly, the measured sensitivity differs from published bulk-wire, type-K thermocouple results by less than 3% over the 20 to 160°C range [16].

Table 2 gives a summary of results for measurements made on a nominal 1-μm-thick SiO_2 e-gun evaporated film [17]. The physical thickness was measured by a Talystep stylus instrument [18]. All

Table 2. Measured values of source heater power and thermocouple potentials for an e-gun evaporated 1.05-μm-thick thin film. Data are given as an example.

P_h, W	TC_1, μV	TC_2, μV	TC_3, μV	TC_4, μV	$(TC_2-TC_3)/P_h$, μV/W
19.9	970	660	620	390	2.30
39.8	1770	1050	980	580	2.41
62.1	2660	1520	1350	800	2.35

293

thermocouple measurements are referred to junctions held at ambient temperature. The thermocouple potential $\Delta = TC_2 - TC_3$ is caused by the thin-film temperature drop. The thermocouple electromotive force per watt Δ/P_h is given in the last column. The average value of Δ/P_h can be obtained, 2.35 μV/W. The thermal conductivity is simply

$$K = S(t/A)(\Delta/P_h)^{-1} \quad . \tag{3}$$

The appropriate sensitivity S, for type-K thermocouples, is 39 μV/°C; substituting the appropriate thickness t, area A, and value of Δ/P_h, one obtains a value $K = 1.74 \times 10^{-3}$ W/cm-°C. The thermocouple difference $TC_1 - TC_2$ is produced by the total temperature drop across 0.50 mm of sapphire and two thermal grease joints. $TC_3 - TC_4$ is produced similarly, except that only one grease interface is involved. These values are consistent with a sapphire bulk conductivity (parallel to the c-axis) of 0.25-W/cm-K average grease interfacial drop of 0.1°C/W.

For direct comparison, table 3 summarizes thin-film measurements made on this and other samples and appropriate bulk values. Note that significantly higher conductivity was measured on an rf diode

Table 3. Summary of thin-film thermal conductivity values computed from experimental data such as is summarized in table 2. Bulk handbook values are also given for reference.

Material	Deposition method	Thickness, μm	K, W/cm-°C
SiO_2	e-gun evaporated	1.05	1.7×10^{-3}
	sputtered	0.50	2.8×10^{-3}
	bulk (amorphous)	----	1.4×10^{-2}
Al_2O_3	sputtered[a]	1.00	3.6×10^{-4}
	sputtered	1.00	2.5×10^{-3}
	bulk (polycrystalline)	----	2.0×10^{-1}

[a]High visible absorption

reactively sputtered SiO_2 film [19] than on the e-gun evaporated film just discussed in detail. This value is, however, a half-order of magnitude lower than reported in the literature for fused silica, which was chosen to have a bulk structure most like the disordered structure of the thin film [20]. Similarly, data were obtained for a 1-μm-thick film of reactively ion-beam-sputtered Al_2O_3 [21]. A surprisingly low conductivity was measured, a half-order of magnitude lower even than the thin-film SiO_2 result. However, this film showed considerable absorption in the visible caused by contamination or lack of stoichiometry ($\alpha \sim 10^3$ cm^{-1}). Accordingly, a second sample was prepared in a nominally identical manner and measured. The value obtained, 2.5×10^{-3} W/cm-°C, is also shown in table 3. This film displayed very low visible absorption and was in all respects a high-quality film. This value is essentially identical to that obtained on sputtered SiO_2 but is a factor of 80 lower than reported on sintered bulk (crystalline) Al_2O_3. No bulk Al_2O_3 material with greater disorder was found for comparison [22]. The estimated uncertainty in these measured results is ±5% based upon the reproducibility of the necessary thermocouple potentials and from an estimate of heat lost unavoidably from the source block down thermocouple and heater leads and otherwise not strictly accounted for.[*]

Table 4 is a summary of known potential sources of systematic error. Of the potential errors listed, all have been carefully addressed in the design of the experiment and discussed in some detail in this paper. The last listed is the most difficult to address. A simple experimental approach to directly assessing the effect would consist of measurement on nominally identical films of differing thickness. A solution to the resulting linear equations would yield values of thin-film and interfacial resistances. However, resources precluded such measurements for this paper. It can be seen, however, in comparing results for the two SiO_2 films reported, that the effect (if it exists) must be small. If it were present in the measurements reported but not separately accounted for, the effective thin-film conductivity value would be lower for the thinner film. In fact, a larger value is inferred, presumably the result of real material property differences.

---

[*]The entire apparatus was effectively insulated with glass fiber wool, and both thermocouple and heater leads were 0.003-in. diameter. To directly verify that the losses were small, a simple calorimeter experiment was performed in which a fixed volume of water was continuously recirculated through the sink block and the rate of rise in temperature measured and compared with the known electrical input power. No heat loss was detectable at the 0.5-W level for an input power of 40 W.

Table 4. List of known sources of systematic error that apply to the thermal conductivity measurements reported in this paper.

1. Thermocouple calibration errors
2. Error in measurement of P_h
3. Unknown heat loss or gain to source
4. Sample thickness error
5. Unknown thermal resistance between thin film thermocouples and thin dielectric film

Discussion

For some time, it has been suggested that defects leading to localized laser damage can be thermal in origin as well as optical [23,24]. The thermal properties measured by the techniques described in this paper yield values averaged over a significant area (1 cm^2). To obtain thermal conductivity values as low as those reported here has very important implications, especially upon realizing that at some defect sites even lower effective conductivity may prevail. It is instructive to consider a simple example. A typical multilayer enhanced reflector in the mid-infrared has a total coating thickness of perhaps 4 μm. If we assume an overall effective conductivity of 2×10^{-3} W/cm-°C and at a nominal steady-state heat flux of 100 W/cm^2, a total temperature drop of about 20°C would occur if all of the heat were to flow through the entire stack. The obvious significance is that, for severe thermal loading in high-power CW applications, the coating temperature rise is much larger than estimated from bulk thermal conductivity values and, in fact, can easily approach damaging levels on average. For the analysis of transient thermal effects, similar conclusions can be reached since the diffusivity, which is the appropriate thermal variable in that case, is just the ratio $K/\rho c_p$. Since thin-film densities are typically very nearly equal to bulk values, large reductions in thin-film-vs-bulk-diffusivity values are to be expected. It is tempting to conclude that proportionately higher peak temperatures during pulsed irradiation will result. However, caution must be used in attempting to apply these results to the analysis of pulsed laser-induced damage. In this case, very high peak temperatures may occur, with additional heat transport by radiation [11]. This case is further complicated by the necessity to take into account the temperature dependence of the transport and optical properties. It is likely that only numerical solutions to the appropriate heat flow equation will be possible.

Summary and Conclusions

The experimental results and predictions of the simple theory presented here are in qualitative agreement. It is to be expected that the specific heat of a material is largely independent of structural perfection and density. Measurements of thin-film and bulk Ge corroborate this assertion: The thin-film and bulk specific heat values are in agreement. However, the thermal conductivity of thin films has been argued to be significantly lower than bulk values as a result of thin-film disorder. Measured values of SiO$_2$ thin-film conductivity are lower than bulk fused silica by a factor of 5 to 8. In comparing a high-quality amorphous Al$_2$O$_3$ film with bulk crystalline material, a reduction of ~80 was observed. It has been predicted and corroborated to a limited extent with SiO$_2$ films produced by thermal and sputter deposition that the thermal conductivity will depend strongly on deposition technique. A major area yet to be explored concerns the effect of interfacial discontinuities on thermal resistance and the closely related problem of interlayer bonding and adhesion. The data presented here are clearly to be regarded as tentative, and additional corroborative data for the same and different materials must be obtained. However, these results and predictions for dielectric thin-film materials are in agreement with a rather massive body of similar data in the literature primarily relating to thin metallic and semiconducting films. Although disturbing, the results disclosed in this paper are not surprising.

References

[1] Boiko, B. T.; Pugachev, A. T.; Bratsychin, V. M. Thin Solid Films 17; 157-161; 1973.
[2] Kelemen, F. Thin Solid Films 36; 199-203; 1976.
[3] Nath, P.; Chopra, K. L. Thin Solid Films 18; 29-37; 1973.
[4] Swimm, R. T. Appl. Phys. Lett. 42; 11; 955-957; 1983.
[5] Nath, P.; Chopra, K. L. Thin Solid Films 20; 53-62; 1974.
[6] Boikov, Yu. A.; Gol'tsman, B. M.; Kutasov, V. A. Sov. Phys. Solid State 20; 894-895; 1978.
[7] Kittel, C. Solid state physics, 5th ed. New York: Wiley; 1976.
[8] Macleod, V. A. In Proceedings of the SPIE Int. Soc. Opt. Eng. 325; 21-28; 1983.
[9] Clemens, P. G. Thermal conductivity, Chapter 1, Vol. 1. R. P. Tye, ed: New York: Academic Press; 1969. 51-58.

[10] Fried, E. Thermal conductivity, Chapter 5, Vol. 2. R. P. Tye, ed: New York: Academic Press; 1969.

[11] Howlett, S. P.; Taylor, R. Thermal conductivity, Session TC-11B. J. G. Hust, ed: New York: Plenum; 1982. 447-457.

[12] The r.f. diode sputtering system used was manufactured by the Perkin-Elmer Corporation, Randex Model 2400.

[13] The differential scanning calorimeter, Model DSC-2, manufactured by the Perkin-Elmer Corporation was employed.

[14] Chen, H. S.; Turnbull, D. Harvard University Division of Engineering and Applied Physics Technical Report No. L2, 1969.

[15] Goldsmid, H. J.; Paul, G. L. Thin Solid Films 103; L47-L48; 1983.

[16] Manual on the Use of Thermocouples in Temperature Measurement. Philadelphia, PA: American Society for Testing and Materials, 1974. ASTM STP470A.

[17] The SiO_2 films were deposited using a Varian e-gun at a deposition rate of about 10 Å/sec at a background pressure of 5×10^{-6} Torr in a diffusion pumped vacuum system.

[18] Bennett, J. M.; Dancy, J. H. J. Appl. Opt. 20; 1785; 1981.

[19] Reactive sputter deposition was performed in the Randex system (reference 12) at an O_2 partial pressure of 8×10^{-4} Torr.

[20] Wray, W. L.; Connolly, T. J. J. Appl. Phys. 30; 1702; 1959.

[21] The ion beam system used was custom made at Naval Weapons Center but employed an Ion Tech 2.5-cm ion gun source.

[22] Kingery, W. C. J. Am. Ceram. Soc. 44; 302; 1961.

[23] Decker, D. L.; Franck, J. B.; Faith, W. N.; Porteus, J. O. In Proceedings of the 14th annual symposium on optical materials for high power lasers, Bennett, H. E.; Guenther, A. H.; Milam, D.; Newnam, B. E., ed. 1982 November 15-17; Boulder CO. Nat. Bur. Stand. (U.S.) Spec. Publ. 669; 1984 January. Pp. 178-185.

[24] Walker, T. W.; Guenther, A. H.; Nielsen, P. IEEE J. Quantum Electron QE-17; 2053-2065; 1981.
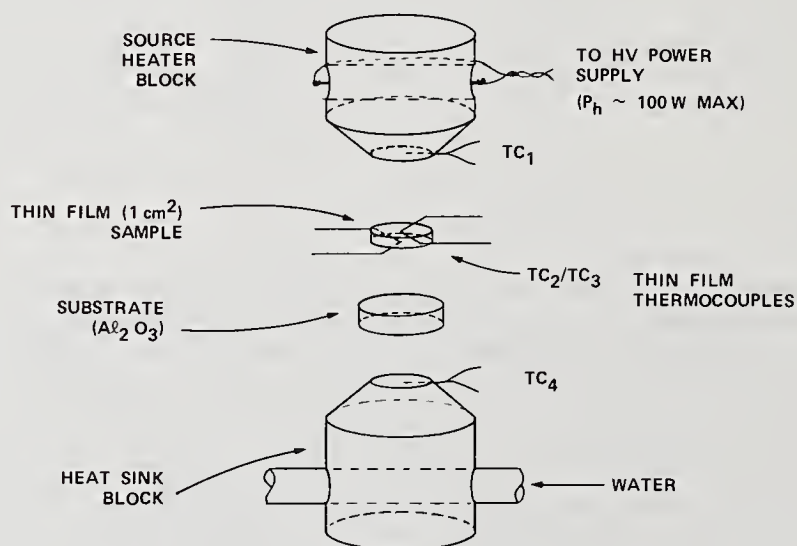
Figure 1. Mechanical schematic of thermal source, sample, and thermal sink together with thermocouple placement. Additional construction and operation details are furnished in the text.
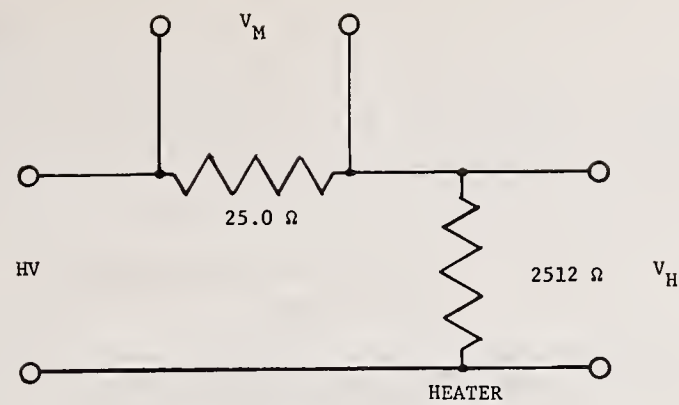
$$P_H = V_M V_H / (25.0) \quad \text{(watts)}$$

Figure 2. Schematic diagram of electrical measurement of heater power. High voltage heater minimizes lead size and hence heat loss.
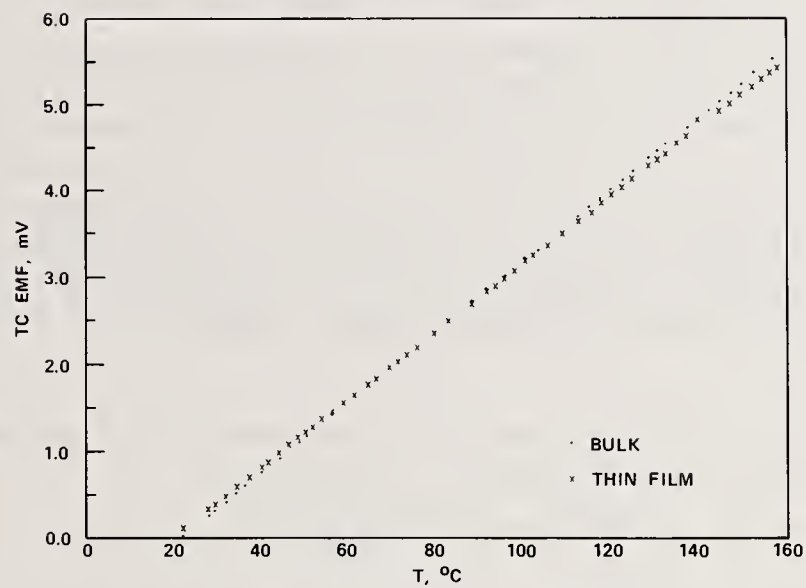
Figure 3. Intercomparison of thin-film and bulk-wire type-K thermocouple calibration over the temperature range from 20 to 160°C.

297

Interface and Bulk Absorption of Oxide Layers and Correlation to Damage Threshold
at 1.06 μm

D. Ristau, X.C. Dang* and J. Ebert

Institut für Quantenoptik
Universität Hannover
Federal Republic of Germany

We describe an infrared line scanning technique for measuring the temporal and spatial
development of a temperature field which is generated by a high power cw Nd-laser on
the surface of a coated sample. A theoretical model based on the solution of the dif-
ferential equation of heat transport for an instantaneos point source is discussed.
In this theory the optical and thermal properties of a laser heated single layer
are related to its temperature field. Investigations on a temperature calibration
technique are made in order to rule out the effect of different emissivities of the
coating materials under test. In the present study interface and bulk absorption of
single layers and multilayer stacks are measured and related to the laser damage
threshold attained from 15 ns pulses at 1.064 μm. The layers are produced by e-beam
evaporation and by ion-beam assisted deposition. Results will be given on TiO_2, Ta_2O_5,
HfO_2, Al_2O_3 and SiO_2.

Key words: Bulk absorption measurement; infrared temperature field measurement; interface
absorption; Nd-YAG-laser; oxide layers ; Pb-Se detector

1. Introduction

Oxides are still of current interest for the production of high power coatings in the range
of .2 to 3.5 microns [1]. As those materials improved interface and surface absorption have
become increasingly the dominant parts of the total absorption in a multilayer-stack. Since
there is a strong correlation between the absorption and the damage thresholds of oxide coatings
interface and surface absorption have to be regarded as an important cause for laser induced
damage [2].

We apply a pyrometric temperature recording technique in order to determine the absorption
in a thin film coating. Temperature profiles of laser-heated In_2O_3-layers were measured and
compared to a theory describing the temporal and spatial behavior of the generated temperature
field. The interface absorption of oxide-materials in conjunction with SiO_2 was measured
indirectly. Damage tests were carried out with a pulsed Nd-YAG laser.

---

* X.C. Dang is a Humboldt fellow from the Institute of Physics,
  Academie of Sciences of Vietnam, Hanoi- S.R. Vietnam

2 Absorption measurement

Our absorption measurement facility consists of a high power cw laser and an infrared line scanning device. If the laser beam is focussed on the coated sample a temperature field is built up in the layers due to absorption. Thus it is possible to determine the total absorption by recording this temperature profile with the use of an infrared line scanning device.

2.1 Generation of the temperature field

In order to determine thin film absorption by temperature measurement one has to know how the absorption is related to the spatial und temporal development of the laser generated temperature profile. The actual problem is illustrated in figure 1. The laser beam with a gaussian intensity distribution hits an absorbing layer coated on a substrate with thermal properties distinct from thin film properties. Having a small spotsize 2s compared to the dimensions of the substrate and the thin film area the substrate can be assumed as infinite. As long as the thin film absorption is low the temperature dependence of the absorption coefficient and the other parameters, like the thermal conductivity K and the heat capacity c, can be neglected. The differential equation of heat transport for our problem

$$\rho c \dot{T}(r,t) = K \Delta T(r,t) + A(r,t) \tag{1}$$

contains the additional source term $A(r,t)$ which describes the heat generation in the layer due to absorption. It has a gaussian radial distribution and it is uniform inside the layer along the z-direction. Instead of integrating eq (1) [3,4,5] we start with the solution of the transport equation for an instantaneos point source located in an infinite medium with thermal diffusivity k_m [6].

$$T_0(r,t) = \frac{Q}{8\pi\sqrt{k_m t}} \exp(r^2/4k_m t) \tag{2}$$

This equation describes how the heat quantity Q which is produced at time t=0 propagates into the medium for t>0. A set of these point sources, radiating with different intensities and at locations distributed like the incoming heat flux, can be superposed for solving the heat transport equation (1) under consideration. Since the layer's surface is in contact to the surrounding air and there is a film substrate interface two optional boundaries have to be considered. Like for the corresponding optical model a reflection coefficient for thermal waves can be attached to every interface. The coefficients are functions of the specific weights ρ, the heat capacities c and the thermal diffusivities k of the two materials as long as the thermal contact is ideal. They are derived from the condition that the temperature field must be continous at the boundary. (Subscript 1 depicts the coefficients of the air, subscript s depicts the substrate's coefficients and the layer's coefficients have no subscript)

$$R_1 = \frac{k_1\rho_1 c_1\sqrt{k} - k\rho c\sqrt{k_1}}{k_1\rho_1 c_1\sqrt{k} + k\rho c\sqrt{k_1}} \tag{3}$$

$$R_2 = \frac{k\rho c\sqrt{k_s} - k_s\rho_s c_s\sqrt{k}}{k\rho c\sqrt{k_s} + k_s\rho_s c_s\sqrt{k}} \tag{4}$$

R_1 is the thermal reflection coefficient for the film air interface and R_2 describes the film substrate interface.

With all the assumptions made above the final expression for the temperature field in the layer can be found by adding the effects of all reflected point source fields in the beam area along the z-diretion.

$$T(r,z,t) = \int_0^t dt \; \frac{\exp(-r^2/p(t))}{p(t)} \left[\sum_{i=0}^{n_o} (R_1 R_2)^i \cdot \right. \tag{5}$$

$$\left. \cdot \{ I(z_o^+, z_o^+ - d) + I(z_o^-, z_o^- - d) + R_1 I(z_1^+, z_1^+ - d) + R_2 I(z_1^-, z_1^- - d) \} - I(z, z+d) \right] F$$

$$z_o^+ = z + 2id \qquad z_o^- = z - 2id \qquad z_1^+ = z + (2i+1)d \qquad z_1^- = z - (2i+1)d \tag{6}$$

$$I(a,b) = \int_{b/2\sqrt{kt}}^{a/2\sqrt{kt}} dv \; \exp(-v^2) \tag{7}$$

$$p(t) = 4kt + 2s^2 \tag{8}$$

$$F = \frac{2\alpha I_o s^2}{\pi \rho c} \tag{9}$$

Where I_o is the incoming intensity and d is the film thickness. α is the absorption coefficient of the layer, R_1 and R_2 are the thermal reflection coefficients and s is the beam radius as stated before. The sum regarding to the reflected parts of the heat flux is extended to a value n_o representing a number of reflections for which the reflected heat fluxes become negligable. n_c is directly correlated to the exposure time.

$$n_o = 2\sqrt{kt}/d \tag{10}$$

Cw-operation is allowed for by a time integration over the exposure time t. The radial integration is already carried out, but the z as well as the time integration must be performed numerically. A seperation of bulk and interface absorption can be made by inserting a z-dependend absorption factor $\alpha(z)$, but for the real situation the thickness of the layer is small compared to the thermal diffusion length leading to a non detectable difference in the temperature profiles. For sligthly different thermal properties of substrate and coating materials the temperature rise on the surface in the beam centre can be described by a simple atn-function.

$$T(0,0,t) = L \cdot atn(\sqrt{2kt}/s) \tag{11}$$

$$L = \frac{\sqrt{2}}{\pi} \frac{\alpha I_o s d}{\rho c k} (2 + R_1 + R_2') \tag{12}$$

300

If the beam size is known the thermal diffusivity of the layer can be determined by this dependence. If there is more than one layer the expression becomes more complex because more interfaces are to be considered, so that we restricted ourselves to single layer calculations. But having long exposure times the multilayer structure can be considered as a single layer with an average absorption because diffusion length is big compared to the scale of the film structure.

2.2 Experimental setup

The temperature profile recording set up is shown in figure 2. The pump beam is produced by a 200 Watts cw Nd-YAG-laser consisting of two arc lamp pumped 1/4 3" Nd-YAG rods. The resonator is fit to the thermal lenses of the rods so that the output beam profile is nearly gaussian. The deviation of the diode array recorded spatial profile in the focus of the lens from the ideal profile is less than 5% for the entire range. A gold coated curved mirror images the heated sample on a lead selenide detector. Scanning is performed by a plane mirror which is driven with the aid of a galvanometer scanner. The window in front of the detector is an antireflection coated germanium plate with high transmittance in the range of 2.2 to 6.5 microns. Thus the low wavelength sensitivity limit for temperature radiation is 2.2 microns ruling out the effect of scattered 1.064 micron pump radiation. The upper limit of 6.5 microns is given by the detector characteristic. The cooling device of the PbSe-detector is not shown. It consists of a liquid nitrogen dewar and a temperature regulation system with a peltier element.

The detector signal is amplified by a low noise preamplifier and then fed via an analog to digital converter into a CBM 3032 minicomputer. The computer is synchronized to the sine wave motion of the scanner with the aid of the nonmaskable interrupt input of the 6502 micro-processor, so that the temperature profile can be displayed on the screen and stored away on a floppy disc for calculating the thermal diffusivity and the absorption.

Table 1 Scanning system data	
PbSe detector	cooled with liquid nitrogen, temperature regulated
	wavelength-response: 1 - 6.5 µm, with window: 2.2 - 6.5 µm
Scanning range	line of 25 mm length
Scanning rate	60 lines per second
Spatial resolution	256 points/line according to .1 mm
Temperature resolution	temperature 20 - 70 °C smaller than 1 °C
	temperature higher than 70 °C smaller than .5 °C

2.3 Calibration

A severe problem related to the temperature measurement by radiation detection lies in the different emittances of the coating and substrate materials. Since emittance is a function of wavelength and temperature, and the surrounding atmosphere affects the measurement also the

apparatus has to be calibrated to every sample separately. Calibration is performed in two steps: First a blackened substrate with defined temperature is measured. This gives a calibration curve of the detector voltage vs. "blackened substrate"-temperature if the used paint is selected so that the detector voltage is the same for all other substrates and coatings with equal temperature. For the second step the sample under test is one half black painted and again heated up to a defined temperature . Now the temperature record shows a step according to the difference of emittance of the coated and the blackened part of the sample. Since the calibration curve exists for the blackened part the detector is now calibrated to the specific sample under test.

In figure 3 calibration curves for BK 7 glass, some coating materials and the painted substrate are shown. They are nearly linear in the depicted temperature range, but for temperatures above 50 °C detector voltages are increasing faster with temperature due to the nonlinear wavelength response of the detector and the increase of temperature radiation.. The detector noise voltage is also indicated, it limits the smallest detectable black body temperature to 13 °C.

2.4 Measurement of moderately absorbing films

Temperature profile recordings of BK 7 samples coated with $In_2 O_3$ have been performed and compared to the theoretically predicted behavior. $In_2 O_3$ was choosen because it has a considerable absorption at 1.064 micron, so that clear temperature profiles are produced in the films. The computer calculated data are in good agreement with the temperature distribution measured (fig. 4). This can only be achieved by assuming the thermal conductivity of the $In_2 O_3$ -films being orders of magnitude smaller than that of the bulk. This effect of reduced thin film thermal conductivity for oxide materials is also reported by D.L. DECKER et al. in this publication. In this paper thin film thermal data were directly measured with the aid of thermocouples giving very low conductivies for SiO_2 and $Al_2 O_3$ layers. In figure 5 the temperature rise in the beam centre is shown for the aforementioned sample. The curve for a film of the same thickness produced with ion beam assistance is also depicted. The temperature rise is in accordance with the predicted atn-function for either sample, although the thermal conductivities of the substrates and the films are totally different. The superior properties of the ion beam processed sample can be clearly seen: The e-beam deposited film has the higher absorption and the lower thermal conductivity in both samples.

2.5 Measurement of slightly absorbing films

The absorption of e-beam deposited high power oxide coatings is too small for recording a temperature profile with the line scanning method. Even with films thicker than 15 quarterwaves and a laser power of 200 Watts the maximum temperature in the beam centre amounts to less than 1 °C. Therefore the apparatus was changed to an absorption measurement facility.

The optical path of the new setup is the same as in the linescanning device, but the output signal is now ac-coupled to a lock in amplifier. Since the temperature rise in the coating is small, the second harmonic of the detector voltage is a direct measure for the heat quantity deposited in the film by the pump laser. Thus the reading of the lock in amplifier can be interpreted as the thin film absorption if the reference signal has the doubled frequency of the scanning sine wave voltage. The sensitivity of this measurement is limited by the scattered laser light as in the laser calorimeter, but since the sensitive element is located at a long distance from the irradiated area sensitivity is much higher. By comparing the device with a laser calorimeter the sensitivity was found to be 2 ppm. The output voltage of the lock in amplifier is only nonzero if there is a temperature gradient on the sample or on the imaging

components. Thus a change of room temperature does not affect the measurement. Scattered light might be a source for errors because it leads to an inhomogenous heating of the imaging mirror. Depending on the substrate material also temperature gradients in the back area can be detected and influence the measurement. For shielding the backgroud we used a plate cooled down to a temperature well below the detection limit of the device. A hole is provided for the beam outlet.

Suggestions for improving the sensitivity may be the use of a mercury-cadmium-telluride detector with a doping ratio aligned to a wavelength range of 8 to 12 microns. Although those detectors have a lower detectivity they are superior to lead selenide detectors for temperature recording due to the fact, that the temperature radiation maximum for room temperature falls into their wavelength range. A resolution of .1 °C is common for infrared cameras using this detector type. Sensitivity might be also increased with an optional in phase Q-switching technique of the pumplaser. A big step towards better performance can be achieved by keeping the sample under vacuum because convection losses are avoided leading to higher temperature and a better accuracy [7]. With all these improvements the sensitivity for this absorption measurement technique may be far below 1 ppm.

3. Samples

All layers are deposited in a high vacuum evaporation plant using electron beam evaporation in a reactive oxygen atmosphere. The film thickness is monitored optically while the deposition rate is controlled by a quartz crystal monitor.

In order to distinguish bulk and interface absorption two stacks for each material were produced (fig. 6). One system consists of a four halfwaves block of high index material and a four halfwaves block of SiO_2. The second stack with alternating halfwave layers was produced by keeping all cleaning and evaporation parameters constant. Compared to the block sample it has six additional interfaces but the same optical thickness and the same distribution of the electric field strength for both materials. Assuming equal surface and bulk absorption for corresponding samples it is now possible to calculate the interface absorption. Especially for TiO_2 other samples with gradual interfaces were produced by controlling the shutter position during simultaneous operation of both electron beam sources. In order to determine bulk absorption for each material a single layer of eight halfwaves was used.

Table 2	Evaporation process data
Substrate	Suprasil I, 25mm diameter, 1mm thick
Substrate cleaning	lens tissue rub with isopropanol, draw off with solidified collodium
Reactive evaporation	oxygen into electron beam, partial pressure: $2 - 4 \cdot 10^{-4}$mbar
	substrate temperature 200 - 350 °C, evaporation rate: 5 - 20 Å/s
Ion-assisted evaporation	Argon-ion arc discharge gun, substrates exposed to high current ion flux during e-beam deposition
Electron gun	8 kV, rotating targets 60 mm diameter

4.Results

For high index materials, we tested Al_2O_3 ,HfO_2 ,Ta_2O_5 and TiO_2 in conjunction with SiO_2 because of the widespread use of these materials for high power coatings (fig. 9). In all cases

total absorption of the stacks is higher than that of the blocks. HfO_2 has the smallest absorption among those four materials followed by Ta_2O_5 and Al_2O_3. The absorption of the TiO_2 films was found to be the highest. With the exception of HfO_2 the contribution of the interface absorption to the total absorption is small. But testing the single film for each material we found a very considerable increase of absorption when passing from the single films to the stack designs with SiO_2. HfO_2, known as a good high power material with small bulk absorpion, has in conjuntion with SiO_2 an interface absorption that dominates the other absorption sources. In order to rule out the effect of contamination at the interfaces we deposited an optional HfO_2 stack consisting only of five halfwave layers , whereby the evaporation source was shut down for five minutes after the completion of every halfwave layer before depositing the next one. The absorption of this sample was only 20% higher than that of the bulk sample. The TiO_2/SiO_2 stack with coevaporated boundaries has a total absorption value which is higher than that of the block sample but lower than that of the sample with abrupt index transitions. In order to compare our results for the blocks to the single film absorption we produced for every material optional single layers with eight quarterwaves of optical thickness. The absorption data of these samples are illustrated in the backplane of figure 8 which also shows the absorption per interface for the corresponding stacks in conjunction with SiO_2. The extinction coefficients (losses due to scattering are not included) in table 3 are also calculated from these single film samples.

Table 3 Absorption of oxide materials in conjunction with SiO_2
8 QWOT at 1.064 µm central wavelength

material	total absorption	absorption per interface	extinction coefficient of bulk
HfO_2	194 ppm	32 ppm	2.5 E-6
Ta_2O_5	274 ppm	5 ppm	2.0 E-5
Al_2O_3	316 ppm	5 ppm	1.9 E-5
TiO_2	812 ppm	42 ppm	5.0 E-5
SiO_2			9.0 E-7

4.2 Damage thresholds

Measurements are made with a single stage passivily Q-switched Nd-YAG-laser (fig. 7). TEM_{00} operation is guarenteed by the use of a convex-concave resonator in conjunction with two apertures and is controlled with a diode array. The spot size for damage tests is adjusted to approximately 90 µm with the aid of a convex lens with a focal length of 160 mm. Q-switching is achieved by two sheets of KODAK-dye No. 14015 in celloluse-acetate as a saturable absorber giving ripple-free pulses of 15 ns duration with energies up to 90 mJ. For every shot the energy is measured by a diode (BPX 65) and an integrating amplifier, while the temporal profile is monitored with a fast photodiode and a transient digitizer (Tektronix model R 7912). Damage is detected by recording the scattered light of a HeNe-laser and by an optional plasma-detector. After the tests every sample is visually inspected with a Nomarski-microscope. All damage data in figure 10 refer to one on one experiments.

We tested the same set of specimens as for the absorption measurements (table 4). With the exception of the HfO_2 samples and the coevaporated TiO_2 layers there is a strong correlation

304

between damage thresholds and absorption data. Materials with high absorption have a low damage resistivity, and apart from TiO_2 the stacks are damaged always with less energy than the blocks. The experimental findings are the best for HfO_2, but they indicate a discrepancy because the damage thresholds for the stacks are, in contradiction to the absorption data, only slightly smaller than those for the blocks. Looking at the damage morphology there is evidence of inclusion dominated breakdown of these samples leading to thresholds not according to the interface absorption of HfO_2. Damage thresholds of the Ta_2O_5 and Al_2O_3 films are nearly equal like the corresponding absorption data. Most damage sites of the blocks reveal inclusion and defect dominated damage while there is a totally different breakdown mechanism for the stacks. Therefore interface absorption has to be regarded as one of the most important parameters for increasing the damage thresholds of Ta_2O_5 and Al_2O_3 layer designs. TiO_2 blocks have the lowest damage thresholds among all the tested samples. This may occur due to the high stress formation in thick TiO_2 layers. An interesting result is, that the damage thresholds of the TiO_2 stacks can be doubled by coevaporation. By switching from abrupt to graduel interfaces there is a drastic change in breakdown mechanism. The damage of coevaporated stacks is inclusion dominated, but the stacks with abrupt interfaces are mainly destroyed due to melting of the deposited material.

Table 4 Damage thresholds of oxide materials in conjunction with SiO_2
pulselength: 15 ns; spotsize: 90 µm; wavelength: 1.064 µm

materials	design		threshold (J/cm^2)
HfO_2/SiO_2	HHHHHHHHLLLLLLLL	block	192
HfO_2/SiO_2	HHLLHHLLHHLLHHLL	stack	166
Al_2O_3/SiO_2	HHHHHHHHLLLLLLLL	block	119
Al_2O_3/SiO_2	HHLLHHLLHHLLHHLL	stack	78
Ta_2O_5/SiO_2	HHHHHHHHLLLLLLLL	block	114
Ta_2O_5/SiO_2	HHLLHHLLHHLLHHLL	stack	72
TiO_2/SiO_2	HHHHHHHHLLLLLLLL	block	44
TiO_2/SiO_2	HHLLHHLLHHLLHHLL	stack	35
TiO_2/SiO_2	HHLLHHLLHHLLHHLL	stack coevaporated	75

5. Conclusions

In this paper we have presented a new high sensitive absorption measurement technique and the corresponding theoretical model on the temperature field in a single layer structure. For In_2O_3 the calculated results are in good agreement with recorded profiles. The interface absorption and bulk absorption of HfO_2, Al_2O_3, Ta_2O_5 and TiO_2 in conjunction with SiO_2 was measured and compared to the damage thresholds at 1.064 um. In all cases but TiO_2 blocks damage thresholds can be related to the total absorption and stacks have lower radiation resistivity than blocks due to interface absorption. Regarding thresholds and absorption HfO_2 appears to be the best material among the tested samples. All HfO_2 specimens show inclusion dominated breakdown. The damage threshold of TiO_2 stacks can be doubled by the use of a coevaporation technique. These results show that interface absorption is an important parameter for high power laser coatings.

6 References

1 Bennett, H.E.; Guenther, A.H.; Milam, D.; Newnam, B.E.; Laser induced damamge in optical materieals: fourteenth ASTM symposium. J. Appl. Opt. 23(20): 3782-3795; 1984 November

2 Küster, H,; Ebert, J.; Laser induced damage in optical materials. Nat. Bur. Stand. (U.S.) Spec. Publ. 568; 1979. 269p

3 Lax, M.; Temperature rise induced by a laser beam. J. Appl. Phys. 48(9): 3919-3924; 1977 September

4 Calder, I.D.; Sue, R.; Modeling of cw laser annealing multilayer structures. J. Appl. Phys. 53(11): 7545-7550; 1982 November

5 Mansuripur, M.; Cornell, G. A. N.; Laserinduced local heating of moving multilayer media. Appl. Opt. 22(5): 66-670; 1983 March

6 Carslaw, H.S.; Jaeger J.C.; Conduction of heat in solids, Oxford, Great Britain: Clarendon Press; 1959

7 Bernal,B.G.; Heat flow analysis of laser absorption calorimetry. Appl. Opt. 14(2): 314-321; 1975 Februar

figure 1: Statement of the situation described by the theoretical model: A beam with gaussian intensity distribution hits an arrangement consisting of an absorbing single layer with thermal diffusivity K_1 on an infinite nonabsorbing substrate with thermal diffusivity K_2. R_1 and R_2 are the reflection coefficients of the heat flux.

incident laser beam

R_1
reflected heat flux

absorbing layer

R_2

nonabsorbing substrate

transmitted heat flux

200 W cw Nd-YAG laser

f=26 mm

sample

imaging mirror

scanning mirror

interface   amplifier

Ge-window aperture

PbSe-detector
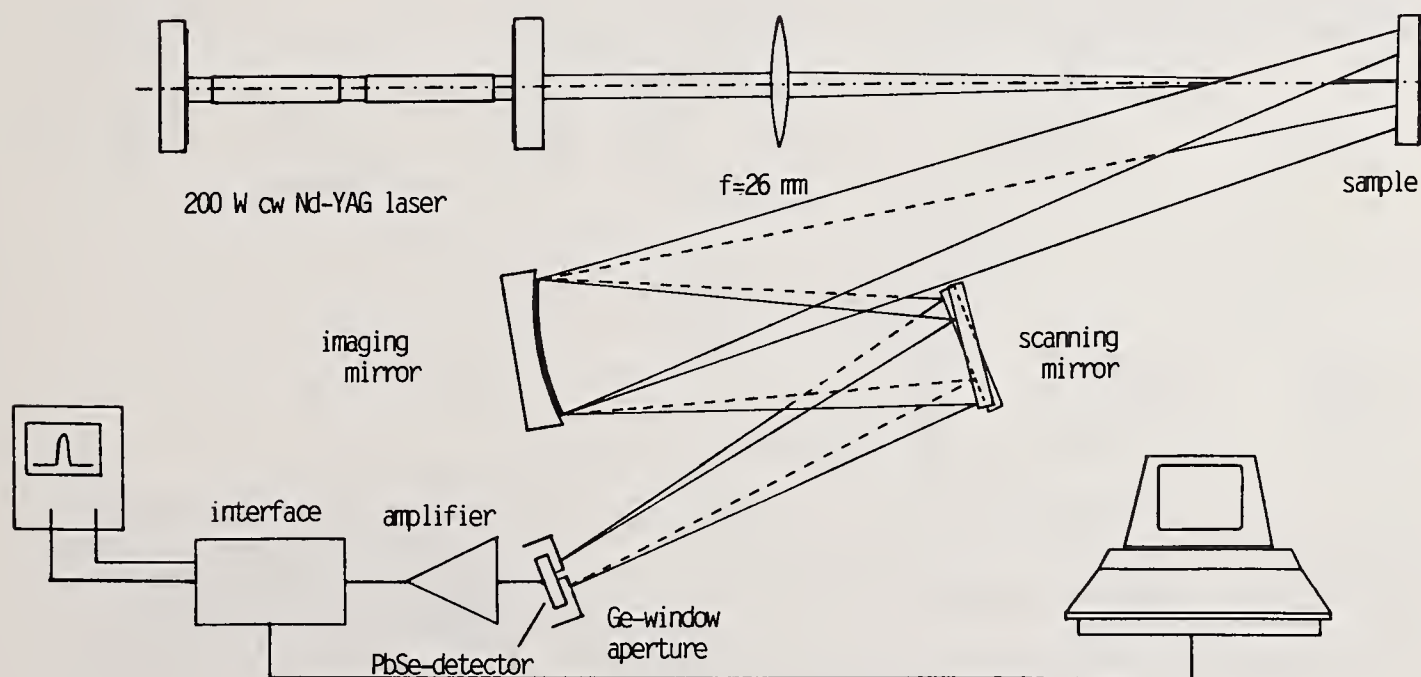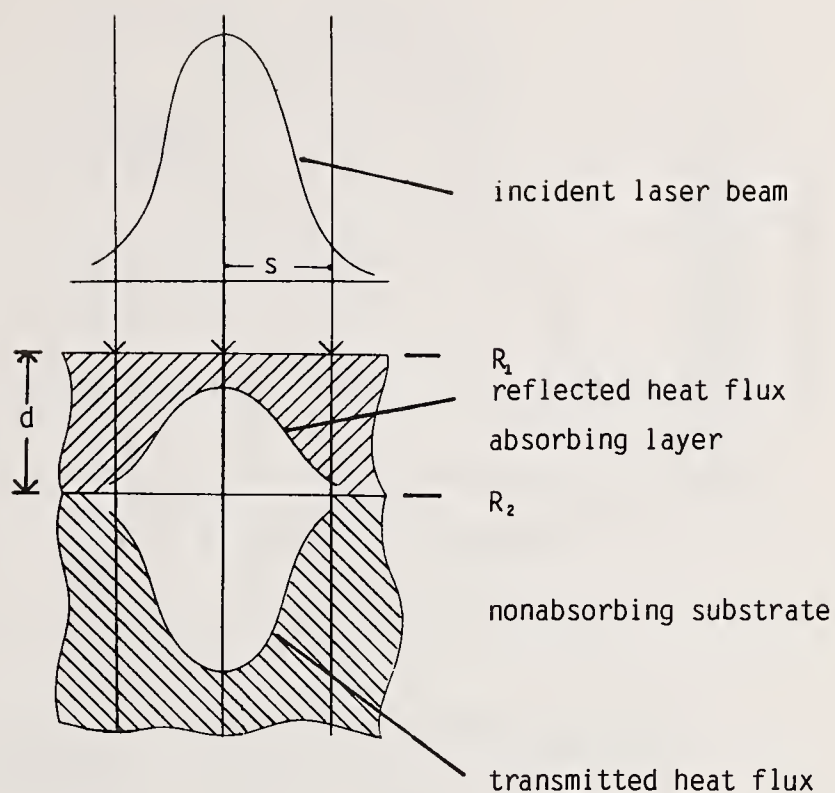
figure 2: Experimental arrangement of the temperature line scanning device
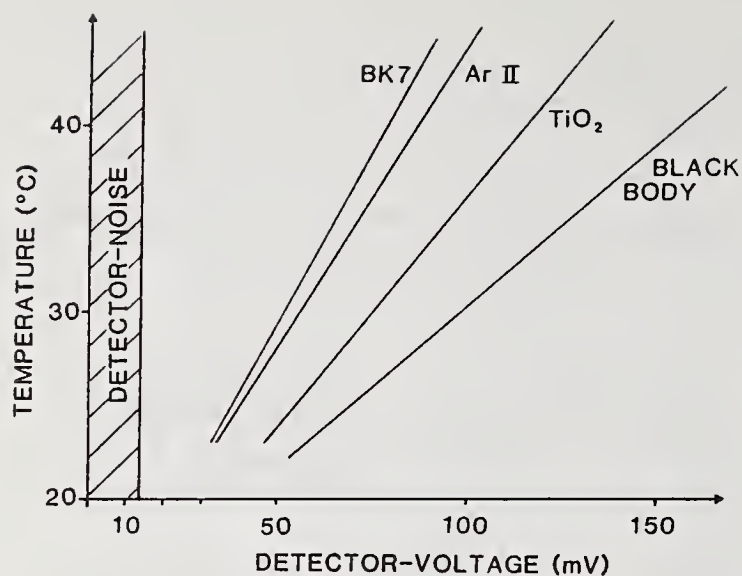
figure 3: Temperature calibration curves for several materials coated on BK 7. The antireflection coating AR II consists of ThF₄ ZnS. The depicted detector noise allows for temperature measurements below room temperature. The calibration curve for the blackened substrate is the same as that for the black body.

figure 4: The radial temperature profile of a laser heated In₂O₃ layer post an exposure time of 32 seconds. The calculated temperature distribution is indicated by the solid line. Parameters are: k=4.5 E-5; s=150 μm
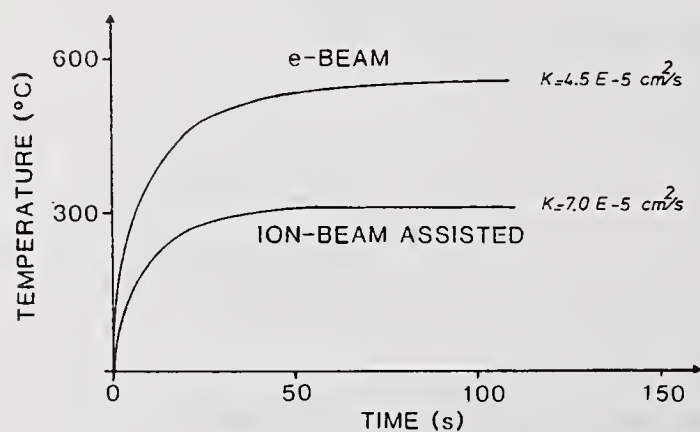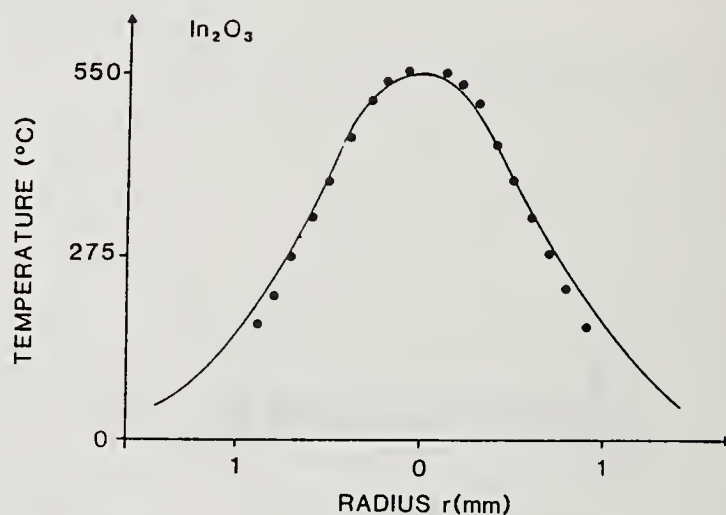
figure 5: Measured temperature in the beam centre as a function of time. The temperature rise of both samples is nearly ideally according to an atn-function.
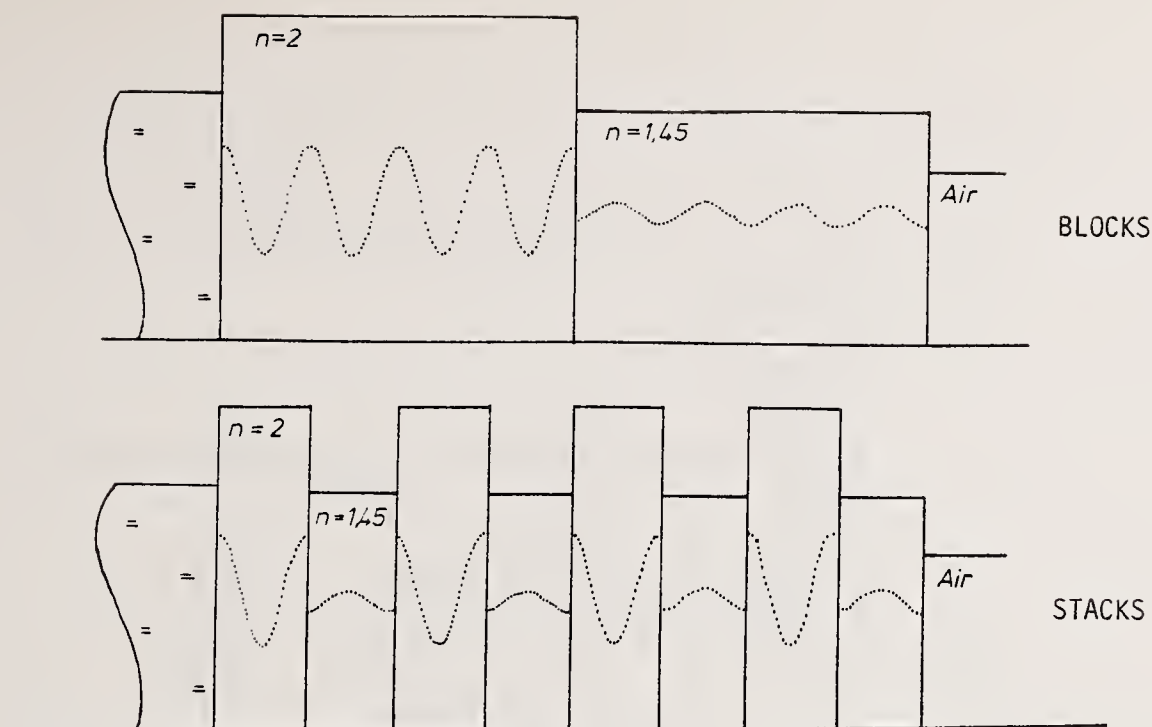
figure 6: 'Layouts of the samples. Both samples have the same optical thickness but the stack has six additional interfaces. The distribution of the electric field strength is illustrated by the dotted curves. For each material the distribution in the stack is equal to that in the corresponding block.
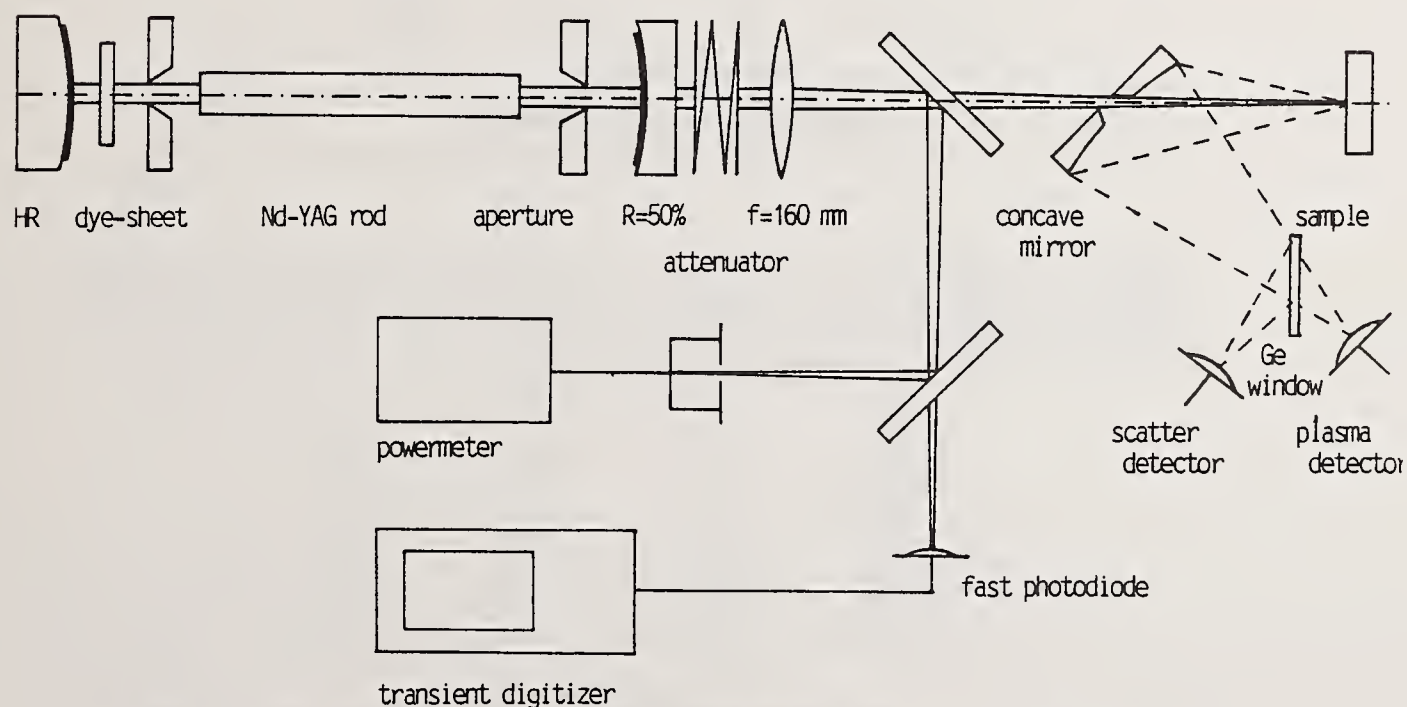
figure 7: Experimental set up of the damage test facility. Damage detection is achieved by a plasma detector and a detector for the scattered light of a HeNe-laser beam which is superposed with the test beam of the Nd-YAG-laser. The Ge-window reflects the scattered light of the HeNe-laser onto the scatter-detector meanwhile the infrared radiation for the plasma and temperature detector passes the window.
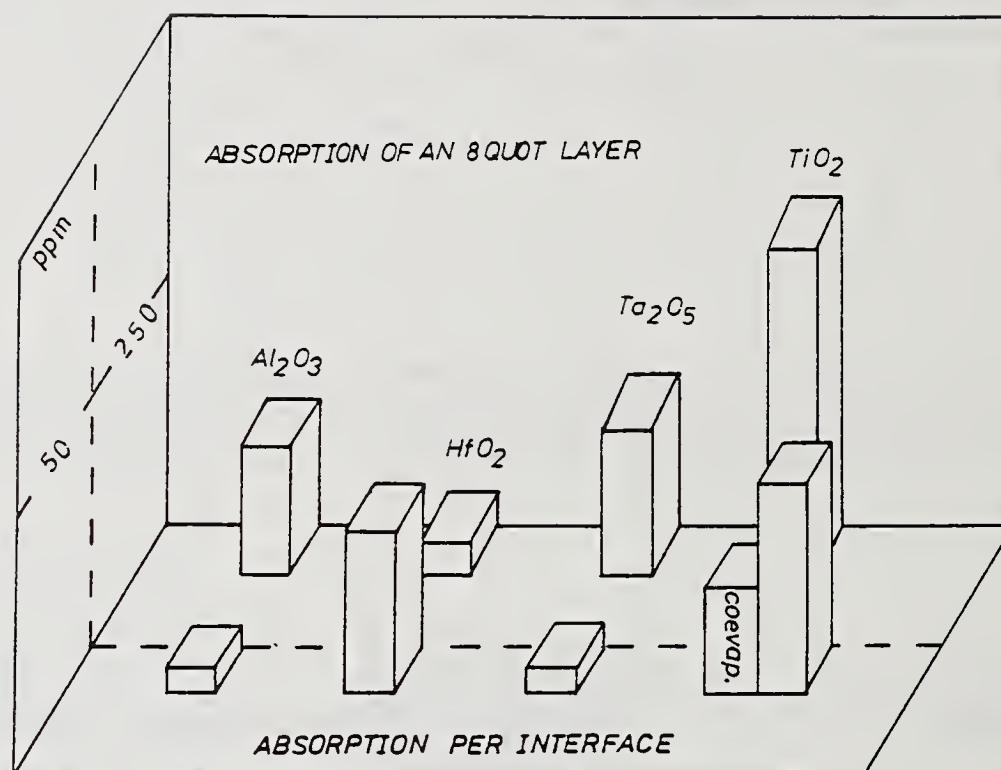
figure 8: The absorption of single layers of eight quarterwaves optical
thickness compared to the absorption per interface for the corresponding
stacks. The interface absorption for the TiO_2-stacks can be decreased
with the aid of a coevaporation technique.
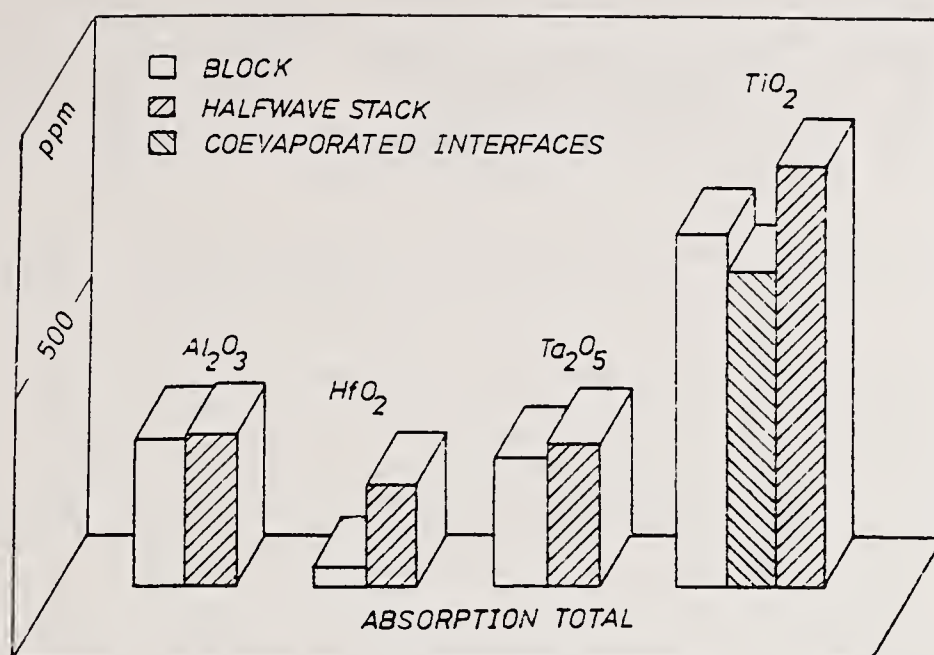
figure 9: The absorption data of the block and stack samples. The blocks have lower absorption than the corresponding stacks. All blocks consist of a HHHHHHHHHLLLLLLLLL-design. The stacks have the same optical thickness as the blocks for each material but the design is HHLLHHLLHHLLHHLL.
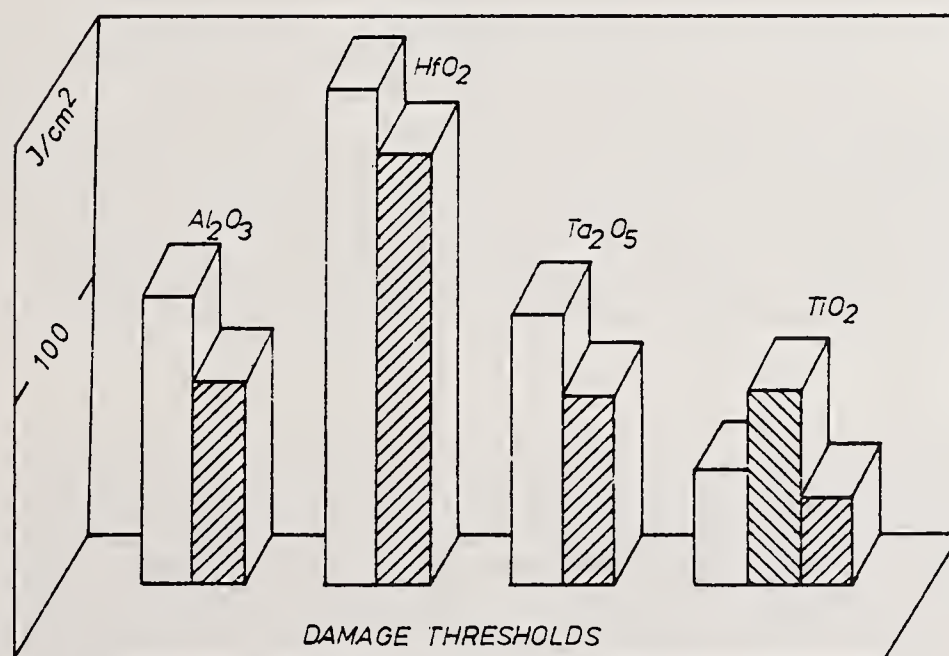
figure 10: Damage thresholds of the same set of samples as above. Pulse length is 15 ns, beam diameter is 90 μm at a wavelength of 1.064 μm.

It was pointed out that a necessary assumption in the paper was that the surface absorption for the thin films and for the thick films was the same. The author agreed, but felt that this assumption was reasonable in this case, because the same chambers and techniques were used for both and the chamber was not used for anything else. However, it was pointed out that the stresses in a film are very thickness dependent. To the extent that the surface absorption is caused by these stresses, the equality assumption may be questioned. The author agreed and stated he would investigate this question in the next series of experiments.

Effect of Anisotropic Stress on Thin Flim Damage Thresholds

A.J. Heiney*, J. Eastman, and C.W. Gabel

The Institute of Optics and Laboratory for Laser Energetics
University of Rochester
Rochester, NY 14627

Damage thresholds for silica/titania multilayer reflectors are measured using single, 30 ps, Nd:YAG laser pulses to study the effect of anisotropic stress on thin film performance. Damage testing sites near the edges of coatings were used to spatially correlate damage with reproducible anisotropic stress profiles taken parallel to the edge.

Anisotropic stress in a coating is stress which has a directional dependence in the plane of the film. A microscope based modulated ellipsometer is used to measure anisotropic stress via induced birefringence. The damage testing system centers around a vertical illumination microscope. The damage pulse is directed by a 45° high reflector in the microscope tube section through a low power objective. The sample surface is viewed through the same objective used to focus the laser to 8 μm FWHM in the center of the viewing field. The goal is to spatially relate this data with microscopic stress measurements.

In most cases, negative anisotropic stress areas are found to have lower damage thresholds while positive anisotropic stress correlates well with high damage threshold. Damage thresholds for uniform striplike areas of film are found to change dramatically compared to adjacent strips. In one case average damage threshold changed from 1.3 to 6.9 J/cm^2 within 100 μm. The width of measured threshold bands in this work ranged from 0.5 to 2.5 J/cm^2.

Key words: Anisotropic Stress; Ellipsometry; Microscope-laser integration; Picosecond laser induced damage; Thin films.

1. Introduction

Optical coatings have spatial variations in damage resistance, either due to inclusions or other effects. Here we attempt to show a relationship between the spatially resolved damage resistance of a coating and its anisotropic stress. Damage test areas were chosen near the edge of two multilayer SiO_2/TiO_2 high reflectors designed for normal incidence and 1.06 μm. These areas were chosen because reproducible stress measurements over a wide area were possible. Anisotropic stress will occurr in the center of films that were coated at a high angle of incidence but not rotated, or highly stressed films which have or are about to craze. Bloom and Costitch[1] have indicated that the passage of picosecond laser pulse in SiO_2/TiO_2 films causes compressive stresses in the film structure due to linear absorption and heating. Therefore, the stress integral of a film having compressive ambient stress will increase with the passage of a picosecond pulse and therefore will damage sooner. Tensile areas, however, have more "headroom" to absorb induced compressive stress and will have a higher damage threshold. A calculation based on this premise is presented in Section 3.

2. Apparatus

Single pulse damage thresholds were obtained with the damage testing system shown in figure 1. It consists of a passively mode-locked/Q-switched Nd:YAG laser, a single pass amplifier when needed, a microscope, and beam diagnostics. The oscillator, similar to those used for short pulse fusion experiments, uses a flowing dye cell at the HR end and incorporates a single pulse switchout system. This yields 20-50 picosecond pulses at 100 μJ. The laser is operated near threshold where repeatability is good and double pulsing is minimized. The beam waist is located at the output coupler and is ~850 μm in radius.

Pulses are incident on a modified metallurgical microscope as shown in figure 2. Viewing with vertical illumination is possible through the permanently mounted 1.06 μm reflector so the surface of the film could be examined using the same microscope objective used to focus the beam onto the film surface. The Bausch & Lamb 4x doublet has a focal length of 32.75 mm at 1.06 μm. With a laser beam spot the size of 3.3 mm at the objective, the system is ~f/5.

---

* Present address: Allied Corporation, Corporate Technology, 7 Powder Horn Drive, Mt. Bethel, NJ
                    07060

Beam spatial profile was examined extensively with this stable output and energy density ratios were obtained. A separate beam profile for each damage shot was not obtained. We used an aluminized mirror as very high contrast film by damaging it. By varying the incident energy, we were able to map the focal energy distribution. A peak energy density factor of 1.3 $J/cm^2/\mu J$ was obtained. This number transforms the damage thresholds which were obtained in total energy to energy densities. Since we are looking for a relative connection between stress and damage, the accuracy of this number is not critical. Even so, some astigmatism was measured and we modeled the expected beam spatial profile at the circle of least confusion on a beam propagation code and obtained a peak energy density factor of 1.5 $J/cm^2/\mu J$.

A streak camera was used to measure pulsewidth and a photodiode was used to measure total energy. The photodiode was calibrated using a Laser Precision ratiometer. Figure 9 shows a sample shot on the streak camera as well as a calibration curve in picoseconds per OMA channel. The pulse is bounced through an etalon having 70% reflective surfaces thereby giving successive pulses reduced in intensity by a factor of two. Pulsewidth data was also used to test for peak power damage dependence. No power dependence was found, as expected.

To measure anisotropic stress, a modulated ellipsometer[2] was adapted for microscopic measurement and visual inspection/indexing. The system is shown in figure 3. A 45° polarized HeNe laser beam is incident on a natural quartz wedge mounted on a common audio driver. An identical wedge is rigidly mounted in compensation for the wedge angle. The beam is then focused onto the sample surface and recollimated by a pair of microscope objectives. A microscope cover slide directs incoherent illumination in the opposite direction using the collimating objective as a condenser. An eyepeice views the image reflected by the first cover slide. A sample has anisotropic stress proportional to its birefringence which can be measured accurately using the lock-in amplifier:

$$\sigma = \frac{\Delta \cdot \lambda}{360 \, C_o h} \times 10^7 \, \frac{nm}{cm}$$

where C_o is the stress-optic coefficient and h is the film thickness. Δ is related to the birefringence and is derrived from Lichtenstein's[2] application of the generalized ellipsometry equations[3]:

$$\frac{I_\omega}{I_{dc}} = \frac{2 \, Sin \, \Delta \, J_1(B)}{Cos \, \Delta \, J_0(B) - 1}$$

where I_ω is the signal at the fundamental lock-in frequency and I_{dc} is measured independently. B is the modulation phase retardance range covered and was set to be 360°. Therefore,

$$\frac{I_\omega}{I_{dc}} = \frac{0.43 \, Sin \, \Delta}{1 - 0.22 \, Cos \, \Delta}$$

and Δ must be solved for analytically.

It should be pointed out that a uniform stress level in the plane of the film would not give rise to birefringence and is therefore unmeasureable by this method.

3. Experimental Results

Two stress scans were made perpendicular to the edge of a film on either side of the damage testing region and these regions were in narrow strips parallel to the edge spanning a large distance. The damage testing conditions used closely follow those of Newnam, Gill, and Faulkner[4]:

- $\lambda = 1.064 \, \mu m$
- single pulse, 30 picoseconds
- single irradiation per site

- normal incidence irradiation
- energy controlled with optical density filters
- 40-50 shots to establish a threshold

A threshold as taken in film area A of figure 5 is shown in figure 4. Damage was detected by microscopic inspection at 200x. Damage thresholds are given in total energy which can be related to energy density by the data obtained on beam spatial profile (section 2.). Figures 5 & 6 shows the relationship between an anisotropic film scan in two paths perpendicular to the film edge and the same damage thresholds measured near those scan regions. There is a good relationship between positive values of σ and high damage thresholds and between negative values of σ and low damage thresholds for areas A - D. Regions E and F show an apparent lack of correlation. This could be due to less spatial selectivity exercised when damage threshold measurements (which were completed before stress measurements) were made. Notice that within <50 µm between areas A and B, threshold changes by more than a factor of four. The damage threshold increases again in area C. Another reflector was tested showing a similar result (figure 7). In this case, however, damage thresholds were obtained by extrapolating from damage site diameter data. This was done with the methods used to measure beam spatial profile at the focus of the mircroscope objective.

A scanning electron micrograph of a damage site occurring well above damage threshold in a low threshold area in figure 8. The layers of the film peeled away cleanly and the deformation of the substrate appears to have been caused by melting. Considering that the film/substrate interface is particularly susceptible in a stressed coating because that is where the net stress changes sign, a thermal event at the interface is likely to be catastrophic for the film.

We will now calculate the stress induced by the passage of a picosecond pulse. The induced stress caused by heating is compressive and is given by:

$$\sigma = -Y \alpha \Delta T$$

where Y is Young's modulus, α is the expansion coefficient of the film, and ΔT is the temperature rise. Note that these quantities are always positive so σ is always negative. Table 1 shows the ambient anisotropic stress from figure 5 for areas B, C, and D. The average damage threshold for those areas are given in the next line (an energy density factor of 1.3 $J/cm^2/\mu J$ was used).

Table 1. Calculations of the Stress Induced by a Short Laser Pulse

Damage Area in Sample #1	B	C	D
Ambient Anisotropic $\times 10^3$ kg/cm^2 Stress	-8.4	+7.0	-2.4
Average Damage J/cm^2 Threshold	1.3	7.1	2.5
Temperature rise (°C) Assuming: $\frac{15°}{J/cm^2}$ / $\frac{95°}{J/cm^2}$	19.0 / 120	106.5 / 670	37.5 / 240
Induced Stress $\times 10^3$ kg/cm^2	-0.47 / -3.0	-2.7 / -16.8	-0.94 / -6.0
Total Stress $\times 10^3$ kg/cm^2	-8.9 / -11.4	+4.3 / -9.8	-3.3 / -8.4

Bloom & Costitch[1] assumed a temperature rise in the film of 15°C for a 1 J/cm^2 pulse. In addition we chose to calculate the induced stress arbitrarily assuming 95°C/ J/cm^2. By multiplying the energy density at damage threshold by these factors we get the temperature rise ΔT. We then calculate the induced stress from the above equation and finally add the induced stress to the ambient anistropic stress to get the total stress at threshold. We see that for the 95°C/ J/cm^2 case, the total stress in the three areas are within ±16% when damage occurs indicating that this is the point at which the mechanical strength of the film is exceeded. This supports the assertions of Bloom & Costitch.

4. Conclusions

We have spatially resolved the varying damage thresholds of two samples and related them to the measured anisotropic stress in those areas. We found that nominally compressive anisotropic stress areas have a lower damage threshold than tensile anisotropic stress areas. We also made a quantitative comparison based on a temperature rise assumption. In most cases we obtained reasonably narrow threshold bands indicating good distinction between adjacent stress areas, good damage detection sensitivity, and a stable focal energy distribution. The microscope based damage testing facility was extremely useful for this work. It is particularly suitable for integration of the ellipsometer and perhaps other measurement/detection schemes into a single unit.

---

5. References

[1] Bloom, A.L.; Costitch, V.R., Design for High Power Resistance. Nat. Bur. Stand. (U.S.) Special Publication 435; 1975. 248 p.

[2] Lichtenstein, T.L., M.S. Thesis, Institute of Optics, University of Rochester, 1980.

[3] Azzam, R.M.A.; Bashara, N.M., Ellipsometry and Polarized Light. New York: North-Holland; 1977.

[4] Newnam, B.E.; Gill, D.H.; Faulkner, G., Influence of Standing-Wave Fields on the Laser Damage Resistance of Dielectric Film. Nat. Bus. Stand. (U.S.) Special Publication 435; 1975. 254 p.

[5] Agostinelli, J.A., Ph.D. Dissertation, Institute of Optics, University of Rochester, 1980.

6. Figures
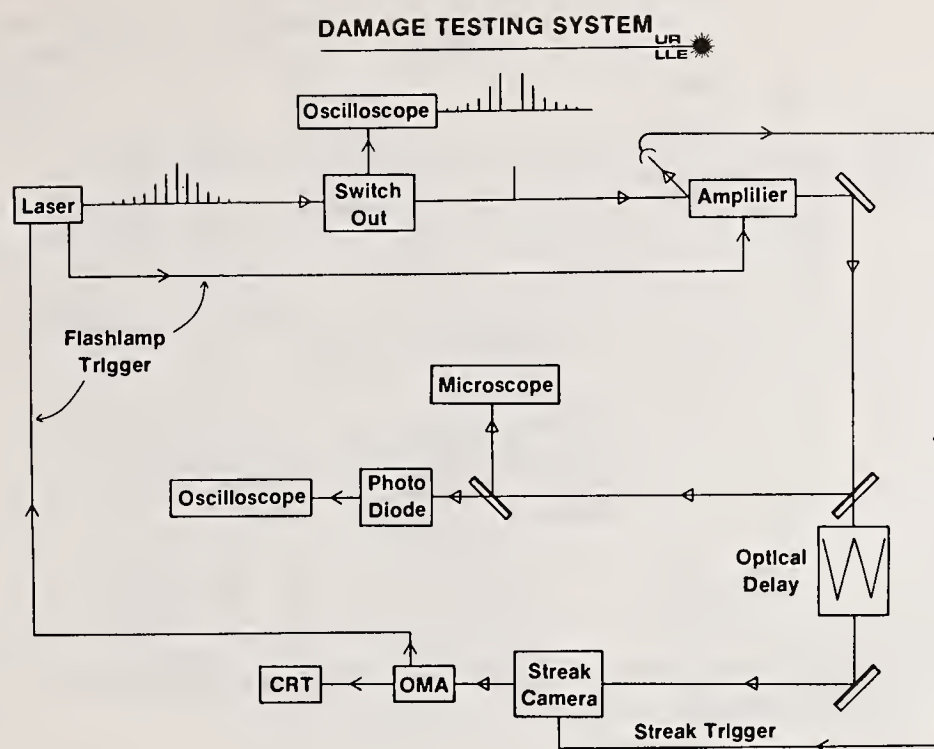
Figure 1. Schematic of Nd:YAG laser damage testing facility.
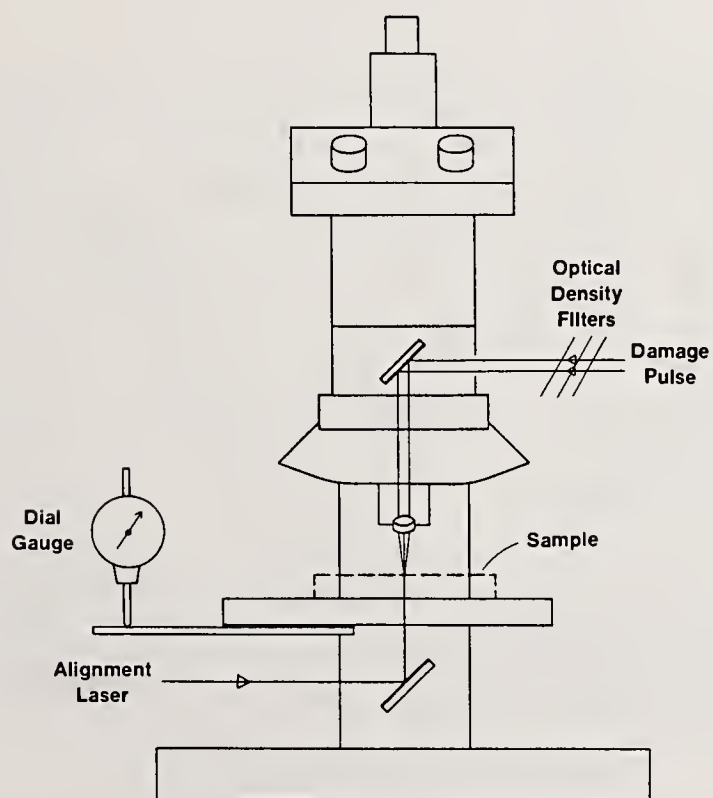
Figure 2. Microscope used for irradiation and examination of samples. Dial guage is used to return to IR focus.

MODULATED ELLIPSOMETER SYSTEM
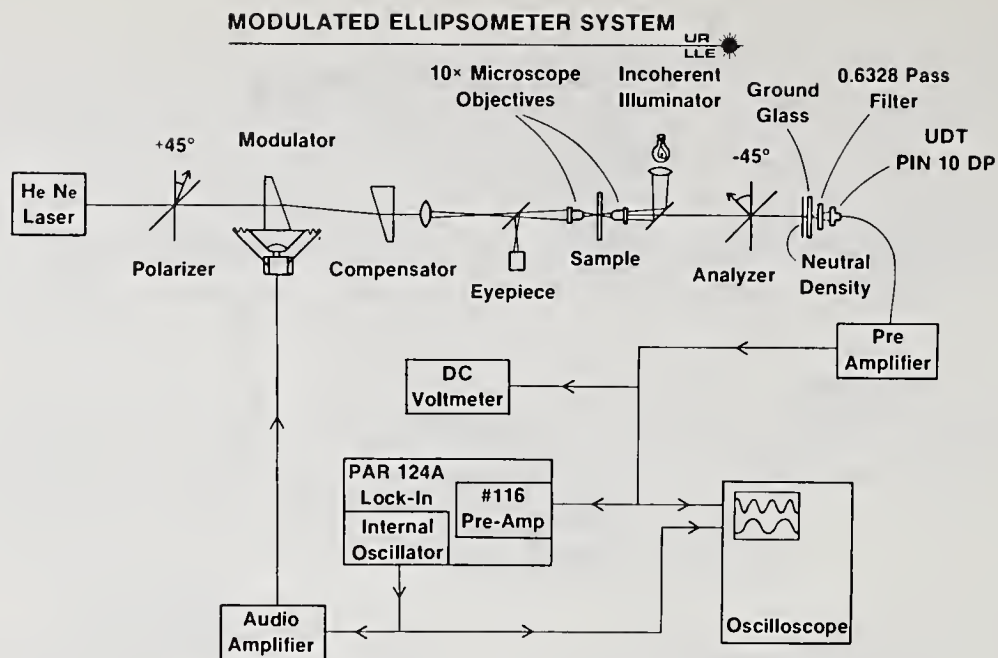
Figure 3. Birefringence measuring AC modulated ellipsometer showing quartz wedge modulator.
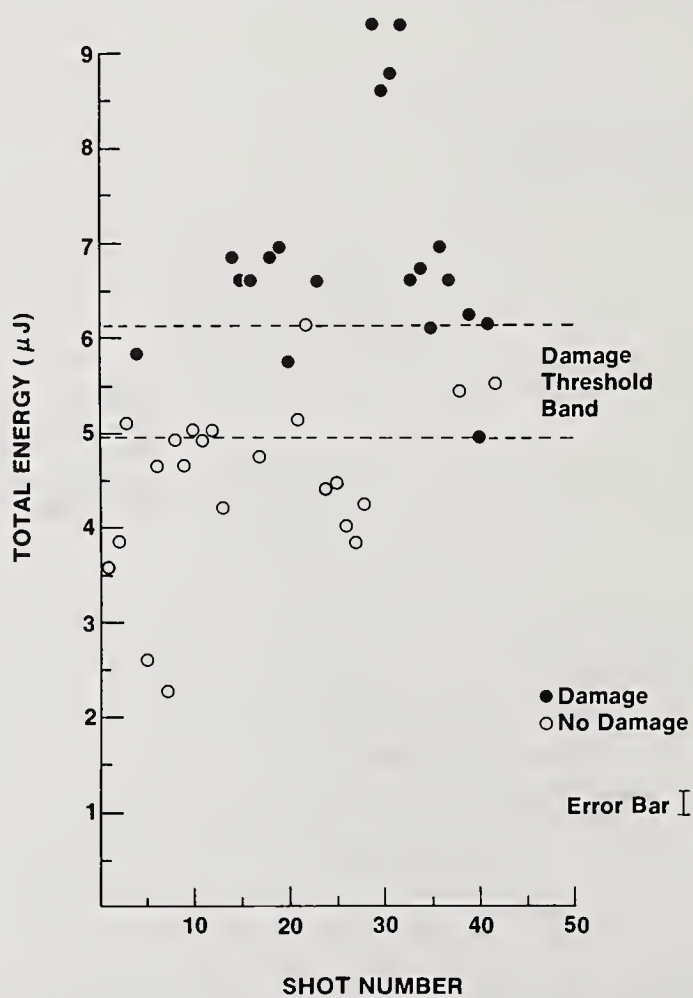
Figure 4. Damage threshold of area A as shown in figure 5.
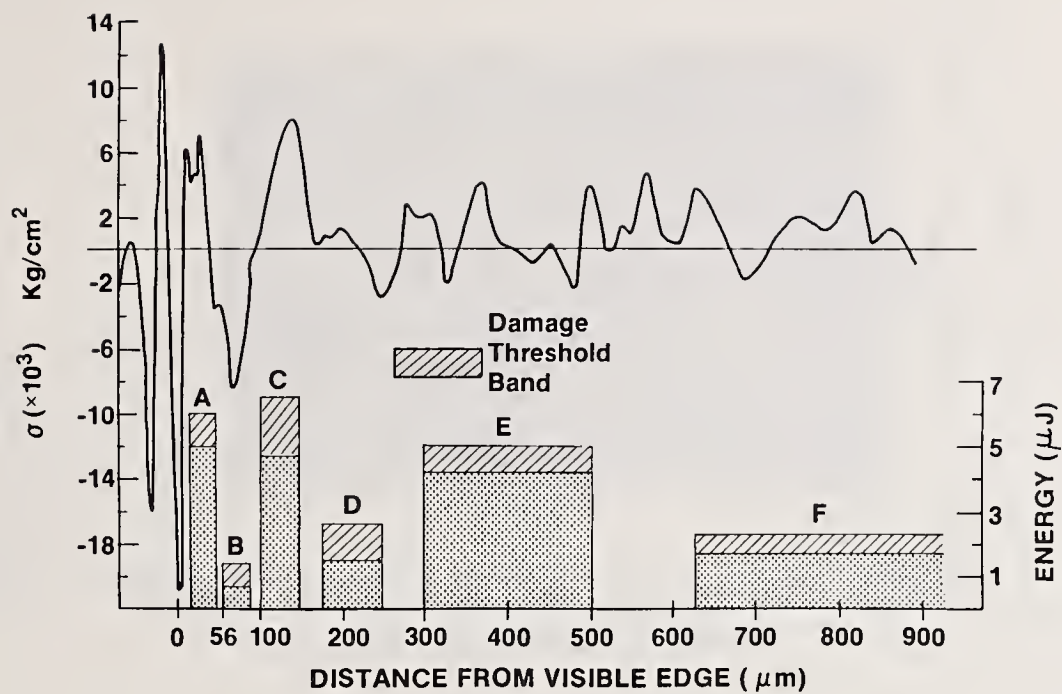
Figure 5. Anisotropic stress scan spatially aligned with damage thresholds relative to the edge of the uniform film region. Energy threshold scale on right.
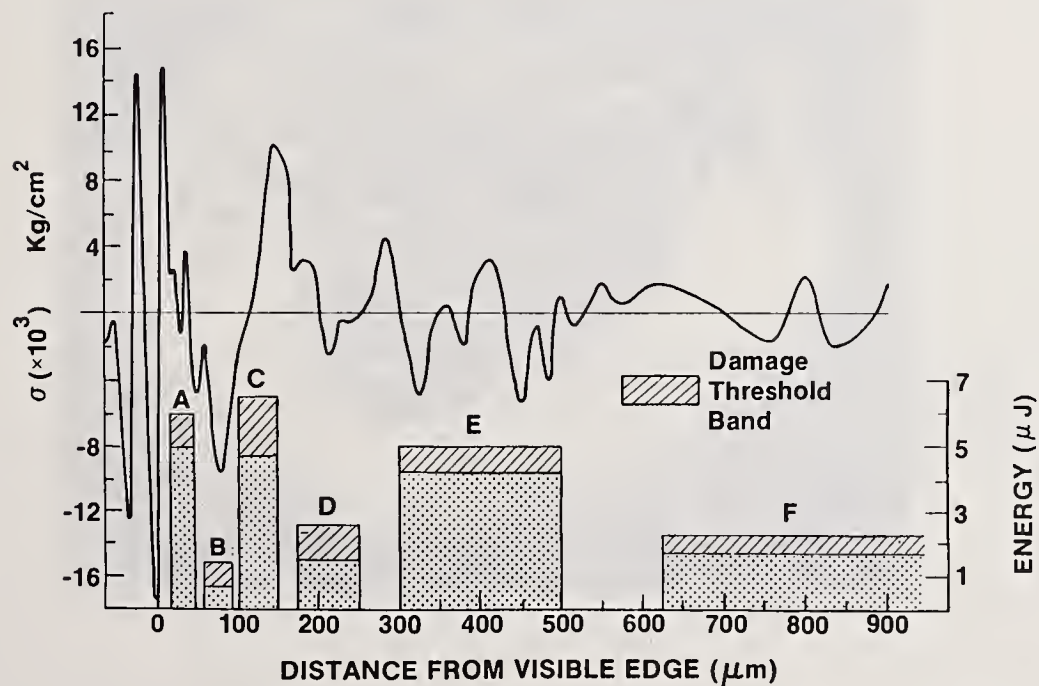
Figure 6. Scan made on the other side of the damage testing region shown with the same thresholds.

319
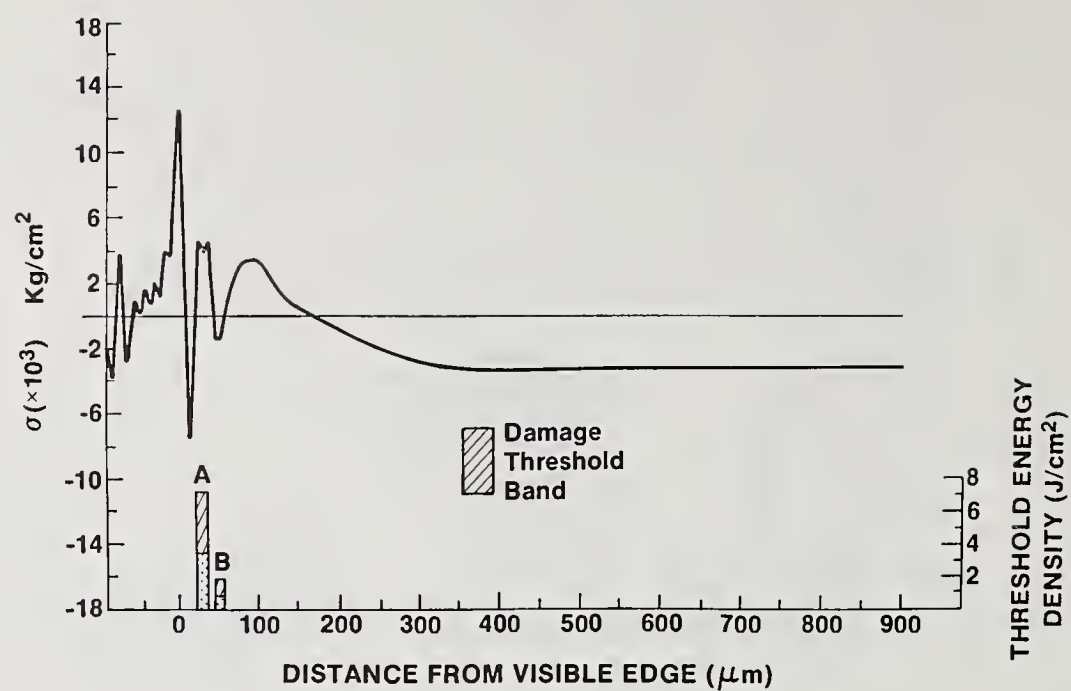
Figure 7. Anisotropic stress scan of the second sample.

1 μm

Figure 8. Scanning electron micrograph of a damage site
occurring well above threshold.

320
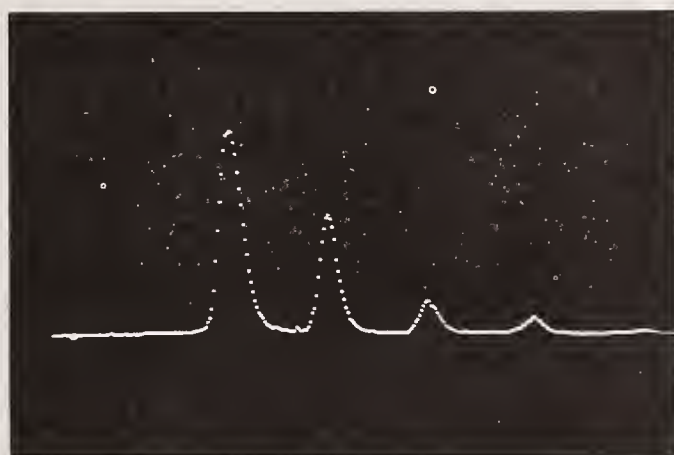
(a)
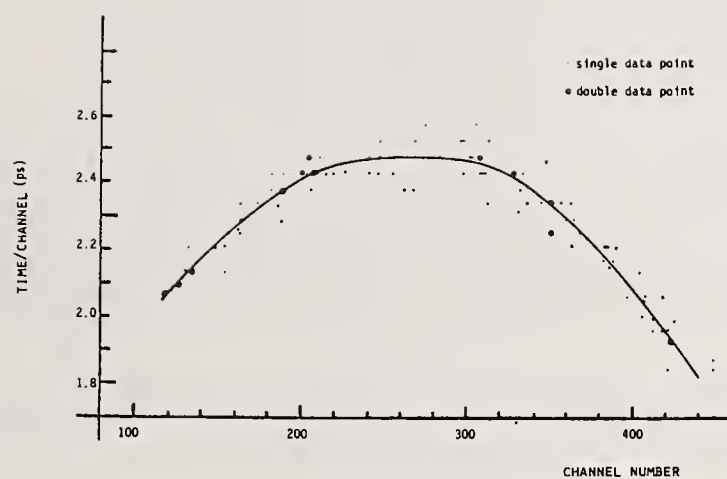
(b)

Figure 9. a) Streak camera/Optical Multichannel Analyzer (OMA)
output of a 30 ps pulse bounced through a thick etalon having a
125 ps round trip time; b) Calibration curve for the streak cam-
era obtained using the 125 ps bounce time vs. channel # midway
between peaks [5].

Design of High Power Laser Coatings for
Grazing Incidence Mirrors

W.H. Southwell

Rockwell International Science Center
Thousand Oaks, California 91360

Several interesting features occur for high reflectance (HR) coatings at near-grazing incidence: the existence of a Brewster's angle, a double-valued effective index for the p-polarization (enabling a MacNeille-type polarizer to be constructed in air), and a half-wave retarder. It is shown that HR coatings can be designed which have high reflectance and, as compared to normal-incidence designs, extremely low internal E-field standing waves for both s- and p-polarization components. Such mirrors should exhibit considerably less thermal distortion due to decreased laser absorption.

Key words: coatings; damage thresholds; electric fields; grazing incidence; mirrors.

1. Introduction

The use of grazing incidence mirrors has been proposed for high power free electron lasers. Mani and Hammond[1] cite the advantage of grazing incidence mirrors as being their decreased absorption due to grazing incidence, resulting in higher damage thresholds. They also cite a disadvantage, however, which is that only one polarization component allows this decreased absorption which necessitates the use of a linear, rather than helical, wriggler configuration. Woodberry[2] has recently shown that multilayer enhanced reflectors at grazing incidence can have internal standing wave E-field patterns which are over two orders of magnitude less than enhanced mirrors at normal incidence. This E-field suppression is accompanied by high reflectance for s-polarized beams. Such multilayer designs show no such suppression for p-polarized incident light, nor are they highly reflective for the p-component. The coating design presented by Woodberry should have high damage thresholds, although one must guard against any p-polarization. This also places a constraint on the amount of curvature on the grazing mirror and in the incident beam.

In this paper we present a new dielectric multilayer design which has high reflectance for both s- and p-polarization components and in addition has low internal standing wave E-fields, which gives it the potential for high damage thresholds for any polarization.

We begin the discussion with a comparison of high reflectance coating performance at normal incidence, 45° and 86° in order to illustrate some interesting features of grazing incidence reflection. Throughout the paper we emphasize the role of the internal standing wave E-fields.

2. Tuned Quarter-Wave Stacks

The standard high reflectance coating consists of a quarter-wave stack alternating between a high index and a low index layer. In standard notation, an example is Air (HL)^{10} H Sub, where H and L represent a quarter-wave thick layer of high or low index material. Tuning the stack for a particular angle of incidence means that the layer thickness, t, has the value,

$$t = \frac{\lambda}{4(n^2 - n_0^2 \sin^2 \theta_0)^{1/2}} \quad , \tag{1}$$

where λ is the wavelength, n is the layer index, n_0 is the incident medium index (usually 1.0), and θ_0 is the angle of incidence in air. This thickness provides a quarter-wave optical thickness for both s- and p-polarization components.

Figure 1 shows the reflectance for HR (high reflectance) coatings at normal incidence, 45° and 86°. In each case the thicknesses are "tuned," that is, determined by eq. (1) so as to be quarter-wave at each angle of incidence. (In these examples we chose 2 and 1.38 as the high and low index values for the layers and a substrate index of 1.45.) At normal incidence s- and p-components coincide. At 45° the reflectance zone broadens and increases for the s-component and

narrows and decreases for the p-component. This is consistent with the concept of effective index, which states that the layer index for s-polarization at an angle of incidence, θ_0, behaves as though it were at normal incidence with the same optical thickness but with an index

$$n_s = n \cos \theta \quad . \tag{2}$$

Likewise for p-polarization the layers have an effective index

$$n_p = n/\cos \theta \quad , \tag{3}$$

where θ is the incident angle in that layer. The angle, θ, is also a function of the layer index, n, and the angle of incidence in air, θ_0, through Snell's law,

$$\cos \theta = \frac{(n^2 - n_0^2 \sin^2 \theta_0)^{1/2}}{n} \quad . \tag{4}$$

Using these equations one can show that the high/low index ratio increases with angle of incidence for s-polarization and decreases for p-polarization. Generally, it is this ratio that determines the reflectivity and bandwidth of the high reflectance zone. However, we may apply the effective indices (including the incident medium and substrate) to a normal incidence expression[3] for reflectance

$$R = \left[\frac{n_0 n_s - n_A^2 (n_A/n_B)^{\ell-1}}{n_0 n_s + n_A^2 (n_A/n_B)^{\ell-1}} \right]^2 \quad , \tag{5}$$

where ℓ is the number of layers (odd), n_A is the index of the outside layer (next to air), and n_B is the index of the other layer material, and obtain the reflectance as a function of the angle of incidence for tuned HR coatings. It turns out that for some combinations of materials the numerator in eq. (5) vanishes at a particular angle. This angle represents the Brewster's angle for the HR coating substrate. For the materials chosen in figure 1 this angle is about 88°, which explains the low p-reflectance at 86°.
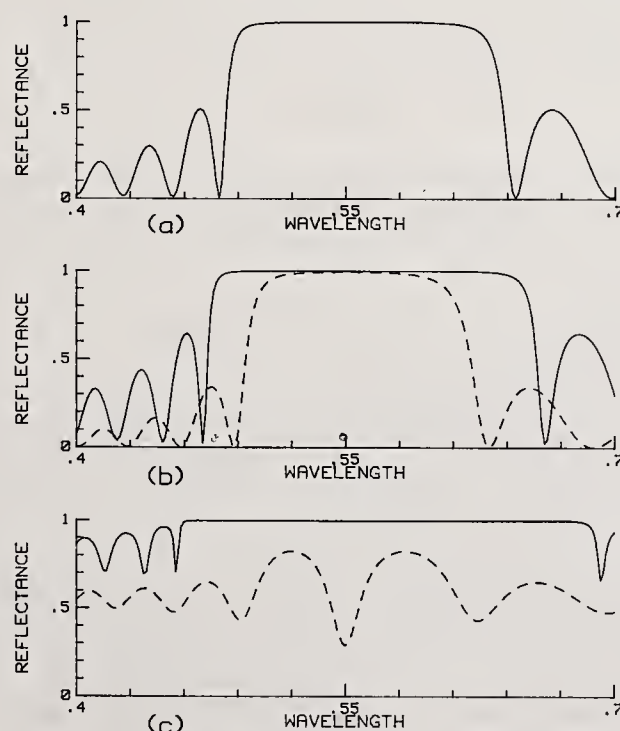
Figure 1. Reflectance versus wavelength for the coating design Air (HL)[10] H Sub tuned for (a) normal incidence, (b) 45°, and (c) 86° angle of incidence. Dashed curves, in all figures in this paper, are the p-polarization components.

323

In addition to the existence of a Brewster's angle, tuned HR coatings at high angles of inci-
dence may also be used as a basis for a MacNeille polarizer[4] in air. That is, one not requiring
the coating to be placed on the back side of a prism. This becomes evident when the effective in-
dices are plotted versus n, the material index, as is shown in figure 2. At 86° angle of inci-
dence, we note that the effective index for p-polarized light is double valued. This means we may
pick a high and a low index material that has the same effective index for p-polarized light and
yet good contrast for s-polarized light. Each quarter-wave pair becomes a half-wave layer and,
hence, absentee for p-polarization. For an even number of layers, the reflectance becomes that of
the substrate for the p-component. If the appropriate antireflection layer (or layers) is
applied, then the p-component is transmitted and the s-component reflected. Previously, it had
been supposed that this could only occur for values of $n_0 \sin \theta_0$ greater than unity, hence, the
requirement to have the incident medium be a prism.
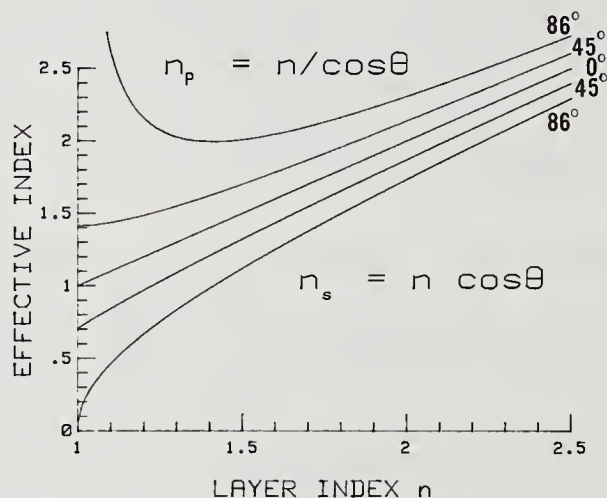
Figure 2. Effective index n_p (upper curves) and n_s (lower curves) as a
function of actual index n.

3. Internal Standing Wave E-fields

Shown in figure 3 are the internal E-field standing wave patterns for the tuned quarter-wave
coatings described in figure 1. Also plotted are the E-field patterns outside the stack in a
half-wave air "layer." A striking feature of this figure is the large width of the half-wave air
layer at 86°. Additional half-waves of the incident medium would show more fringes identical to
the one shown. In fact, that pattern represents the fringe pattern for a Lloyd's mirror experi-
ment.[5] At near grazing incidence, the reflected beam interferes with the incident beam producing
a fringe spacing which increases as the angular separation of the two beams decreases.

We also note that at 45° angle of incidence the s field inside the stack is less than the p
field and has a desirable null at the air-coating interface. At 86° the s field is too small to
be seen on the scale of figure 3. It is shown on an expanded scale in figure 4. As observed by
Woodberry,[2] we note that the peak value of the standing wave (calculated as $|E|^2$) is over 160
times smaller than at normal incidence. This is a dramatic result and should lead to increased
damage thresholds over whatever is observed at normal incidence.

The above prediction is based on the assumption that the damage mechanism involved has an
associated E-field threshold. Such an assumption is a straightforward consequence of the
existence of an incident laser beam power threshold. The internal E-fields in the coating are
directly proportional to the incident beam intensity. Since there is an E-field null at the
coating surface, the damage can only be due to the internal E-field.

Of course, we have assumed that we have infinite plane waves and perfectly plane layers of
homogeneous, nonabsorbing material. Although this won't occur in practice, we should expect,
through careful coating procedures, that the layer surface roughness and the size of the imperfec-
tions be small compared to the wavelength so as not to perturb the gross features of the standing
wave E-fields. It has been shown[6] that local fields near micropores and cracks could be enhanced
by as much as n^4 (if the size and shape were just right), which is a factor of 16 in our case.
However, these effects are also present at normal incidence, so the improvement over normal inci-
dence damage thresholds should still be observed. Even so, 16 is still small compared to the
theoretical 160.
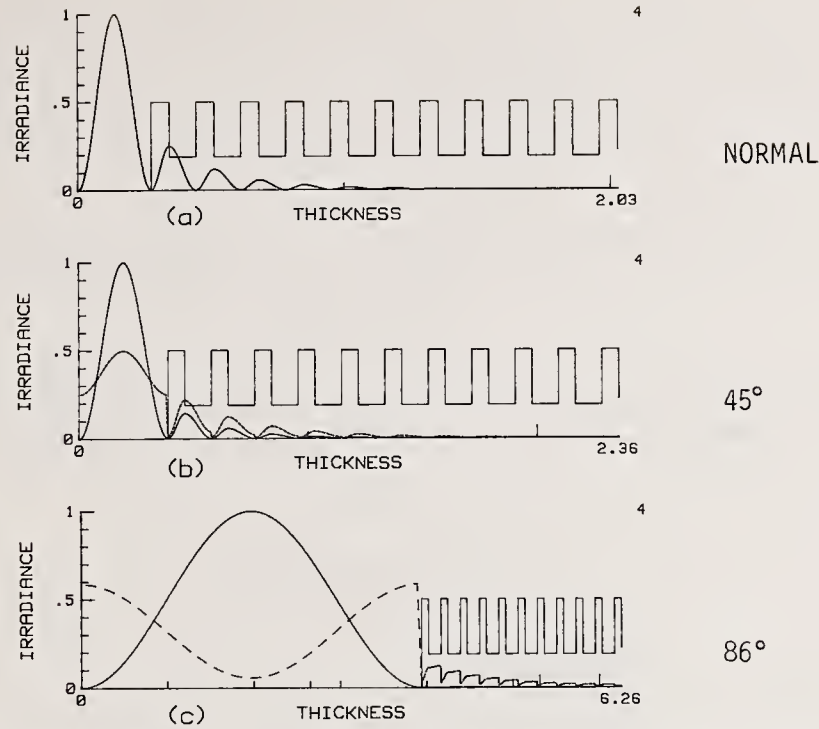
Figure 3. Standing wave E-fields, $|E|^2$, for the configurations shown in figure 1. Also shown are the standing waves in a half-wave air layer just outside the coating surface.
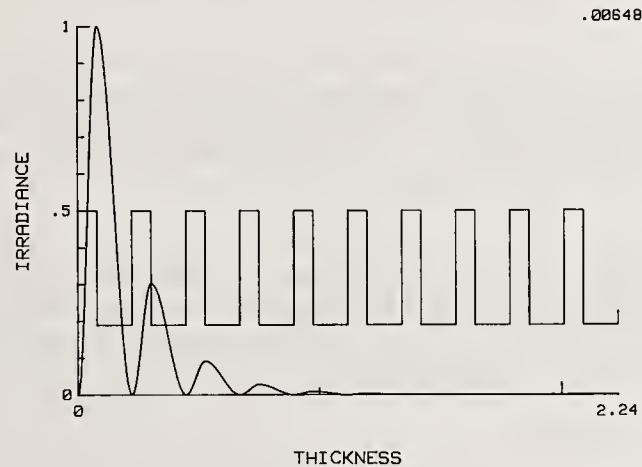
Figure 4. Standing waves for the s-polarized component inside the coating of figure 1 at 86° of incidence. The number at the upper right, 0.00648, is the peak value relative to an incident beam of unity amplitude.

So far, we have only discussed the decrease in the E-fields. Another factor which should also improve damage thresholds is the decrease in energy density due to the large beam cross section inside the layers due to the large angle of incidence. The geometry of the situation is shown in figure 5. As seen there, this effect is equal to $\cos \theta_0/\cos \theta$, where θ is the refracted angle of the beam in the layer, and is given in eq. (4). A plot of this factor for a layer of index 2 is shown in the upper curve in figure 6. It should be noted that this factor is related to the width of the beam in the layer and not related to the width or footprint of the beam at the coating surface. It is a smaller effect than would be predicted on the basis of the size of the beam footprint. The middle curve in figure 6 is the peak value of $|E_s|^2$ for tuned high-low HR coatings. The E-field reduction is much more dominant than the geometrical effect shown in the upper curve.

Absorption or heating at any point in the coating is proportional to the quantity,

$$kn|E|^2 \frac{\cos \theta_0}{\cos \theta} \quad , \tag{6}$$

325
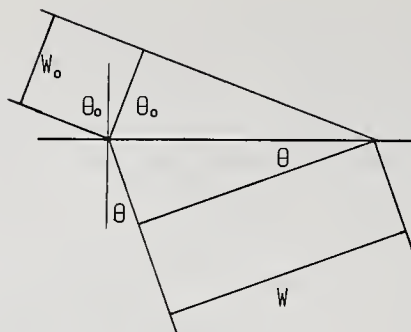
Figure 5. Geometry of a beam entering a layer of index n. The energy
density of the beam decreases by the ratio $W_0/W = \cos \theta_0/\cos \theta$.
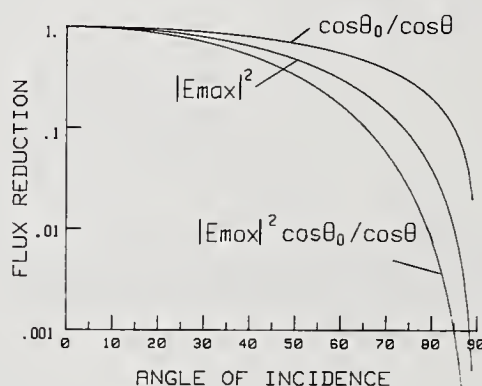
Figure 6. Internal coating flux reduction factors for s-polarized
light for tuned HR coatings of the type shown in figure 1.
The upper curve is the geometrical angle of incidence factor.
The middle curve is the peak value of $|E_p|^2$, and the lower
curve is the product of the upper two.

where k is the extinction coefficient. The lower curve in figure 6 is a plot of the peak value of
$|E_s|^2 \cos \theta_0/\cos \theta$ as a function of angle of incidence for a tuned HR stack. This plot should be
a predictor of laser damage thresholds. We note three orders of magnitude less heating at 85°
than at normal incidence for the s-component for the incident beam.

4. High Reflectance Criteria Coatings

We have shown the extremely good performance that can be expected for the s-component of an
HR coating near grazing incidence. We have also shown its poor performance for the p-polarization
component. Before addressing the problem of finding an HR coating with improved p-performance, we
ask: what configuration gives the highest reflectance for both s- and p-components, regardless of
the internal field strengths?

From an examinaton of eq. (5), we see that by placing a low index layer next to air, the
numerator will not vanish. Such a configuration will not exhibit a Brewster's angle and we can
expect good reflectance for both s- and p-polarizations.

Figure 7 shows the reflectance of such a low-high quarter-wave stack. Also shown in figure 7
are the standing wave E-field patterns for the same coating. Several interesting features of this
design are worthy of comment. First of all, the design is probably optimum for high reflectivity
for both s- and p-polarizations. The p-component now has a standing wave null at the coating
surface and low levels inside the coating. The s-component, on the other hand, has a standing
wave peak at the coating surface and rather high levels in the stack. Since the coating surface
can pick up dust or other contaminants, the high E-field at the surface seems undesirable for high
power laser applications where damage is likely. However, for other applications, this HR coating
may be well suited. For example, unpolarized light would not exhibit fringes in the region above
the surface (near grazing incidence). This is because the s- and p-fringe patterns are out of
phase and produce a uniform sum.

326

The above observation, as seen in figure 7, means that if one were to perform a Lloyd's mirror experiment[5] with this mirror, fringes would not be seen. Furthermore, if incident s-polarized light were used, the opposite result would be obtained. This means that there is no pi phase change on reflection for the s-component as would be expected for both p- and s-reflection from dielectric substrates and metals. This means that this HR coating produces a pi retardation in the reflected beam. Thus, it acts as a half-wave plate. This feature may be of interest in some applications.

We would not expect this design, however, to have high damage thresholds because of the high internal fields for the s-polarization.
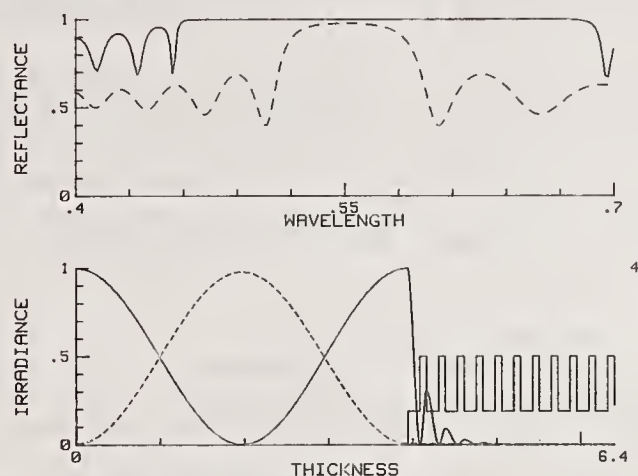
Figure 7. Reflectance and standing wave patterns for a low-high quarter-wave stack Air (LH)[11] Sub tuned for 86° angle of incidence. The dashed curve is the p-component.

5. High Reflectance and Low E-field Criteria Coatings

Our goal is to obtain high reflectance for both s- and p-components and, in addition, have low standing-wave E-fields internal to the coating and at the coating surface for near grazing incidence radiation.

After a numerical optimization study, we have discovered that such objectives can be achieved. A design using the example index values and number of layers used previously in this paper is shown in figure 8. The standing wave patterns are also shown in figure 8. We note that there is not a strong field at the coating surface for either polarization. This is a consequence of adjusting the phase shift of the p-reflection. We note that there is now only a small phase shift between the s- and p-components.
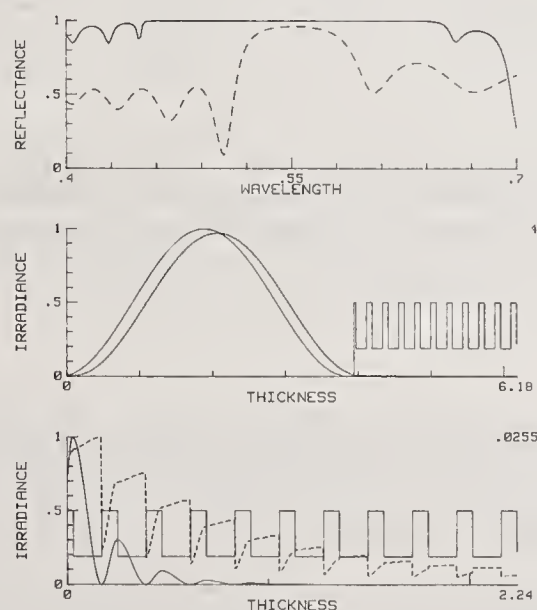
Figure 8. 21 layer HR coating Air 0.35 H 0.988 (LH)[10] Sub tuned for 86° angle of incidence with the high and low index being 2 and 1.38.

327

The lower plot in figure 8 shows that the peak internal standing wave is the same for both components. Furthermore, this peak value is almost a factor of 40 less than the normal incidence value. Although this is 4 times worse than the high-low quarter-wave stack for the s-component, it is 40 times better for the p-component. When coupled with the cosine ratio effect, heating losses show a theoretical reduction by a factor of 100 over normal incidence HR coatings for both polarizations.

The design feature that predominates in achieving this performance is the reduced thickness of the outer high index layer. In the design shown in figure 8, the outer high index layer is 0.35 of a quarter-wave in thickness. The rest of the stack is slightly detuned to account for the small shift in peak reflectivity produced by the nonquarter-wave outer layer.

Finally, two things can be done to boost the p-reflectance; use a higher high index material and increase the number of layers. This is illustrated in the design shown in figure 9.
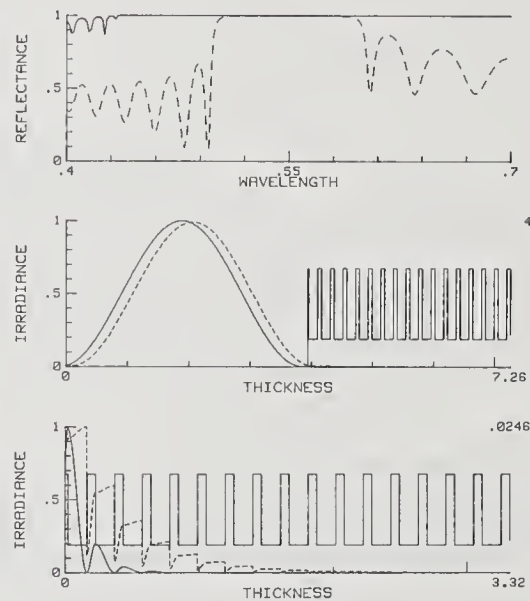
Figure 9.   33 layer HR coating Air 0.285 H 0.988 (LH)[16] Sub tuned for 86° angle of incidence with the high and low index being 2.35 and 1.38.

6. Comments

We have shown that HR coatings can be designed for grazing incidence applications. Such coatings can also be designed to sustain very low E-field standing waves for both polarization components as compared to HR coatings for normal incidence. These dramatic decreases in E-field strengths should result in higher damage thresholds according to current damage mechanism theories. Perhaps more important is the decrease in thermal distortion that these mirrors should provide when used in laser cavities.

We are aware of some experimental results which failed to show the predicted angular dependence on damage thresholds of coatings at 351 nm. Our only comment at this point is that the assumptions regarding the standing waves and laser damage are better satisfied at longer wavelengths, since optical tolerances become tighter at ultraviolet wavelengths and electric fields are more sensitive to coating imperfections and surface roughness.

7. References

[1] S.A. Mani and J.H. Hammond, "Optics and resonator design issues for high-power free electron layers," Proceedings of the International Conference on Lasers (1981) p. 586.

[2] F.J. Woodberry, "Electric fields in grazing incidence laser mirror coatings," Appl. Opt. 23, 3493 (1984).

[3] P.H. Berning, "Theory and Calculatins of Optical Thin Films," in Physics of Thin Films, vol. 1, G. Hass, editor, Academic Press, New York (1963) p. 96.

[4] S.M. MacNeille, "Beam Splitter," U.S. Patent no. 2,403,731, July 9, 1946.

[5] F.A. Jenkins and H.E. White, <u>Fundamentals of Optics</u>, McGraw Hill, New York (1957) p. 243.

[6] N. Bloembergen, "Role of Cracks, Pores, and Absorbing Inclusions on Laser Damage Threshold at Surfaces of Transparent Dielectrics," Appl. Opt. <u>12</u>, 661-664 (1973).

[7] B.E. Newnam, S.R. Foltyn and D.H. Gill, "Angular Dependence of Multilayer Reflector Damage Thresholds," Sixteenth Annual Symposium on Optical Materials for High Power Lasers, National Bureau of Standards, 17 Oct. 1984.

The question was asked "How critical is your design to layer thickness control?" The author replied that the outer layer was going to be sensitive because it changes the coating from a high-low stack to a low-high stack as one varies that outer layer. He has not yet calculated the exact tolerances. Concern was expressed as to the number of layers. The author replied that the limiting number of layers depends on the absorption per layer and 33 layer coatings have been made successfully.

The Design of Optimum High Reflectivity Coatings
for Grazing Angles of Incidence

Jeffrey B. Shellan

W. J. Schafer Assoc., 22222 Sherman Way, #205
Canoga Park, CA 91303
(Material was actually presented at the classified session)

Abstract

Although quarter-wave multilayer dielectric coatings (QW MLDCs) usually offer the highest reflectivity possible at a single wavelength, this may not be the case at grazing angles of incidence. For incident angles greater than the Brewster angle, the p polarization absorption can easily be several orders of magnitude higher than the s polarization absorption due to the destructive interference between the reflection from the superstrate - top layer interface and the rest of the coating. An analytic approach is developed for designing optimum reflectivity coatings at grazing angles of incidence, once the fraction of s and p polarized light is given. These coatings can give at least an order of magnitude reduction over QW MLDCs in total coating absorption, even for the case where less than 0.1% of the incident radiation is p polarized. The absorption of the designs found from the analytic results compare favorably with designs generated using numerical methods of non-linear optimization.

Key words: FEL optics; grazing angle of incidence coatings; optical coatings

1. Introduction

The purpose of this paper is to present analytic results that can be used to design multilayer dielectric coatings (MLDCs) with maximum reflectivity at grazing angles of incidence. The designs found can have absorptions orders of magnitude less than quarter-wave stack designs, since the p polarzation reflectivity of quarter-wave stacks can be quite low at grazing angles. The closed form solutions found compare quite favorably with designs generated using numerical non-linear optimization procedures.

Grazing angle of incidence optics are used in numerous applications where ultra-high reflectivity, high damage thresholds, or reflectors in the far ultra-violet and soft x-ray are needed. For example, the high flux levels needed in the gain region of a free electron laser (FEL) are several orders of magnitude greater than can be handled by conventional optics. A possible solution to this problem is to use a grazing incident angle mirror (GIAM) to expand the beam geometrically before it strikes a mirror normally. If α is the grazing angle, defined as $\pi/2$ minus the incident angle, then the beam foot print will be increased by a factor $1/\alpha$ (for small α). In addition, the absorption will be shown to vary as α, giving an absorbed flux per area proportional to α^2, and damage threshold proportional to $1/\alpha^2$. It has been shown by S. A. Mani and J. H. Hammond[1] that the optimum value of α, for minimizing the resonator length, is on the order of one to two degrees for high power FELs invisioned for the near future.

Another area where grazing incident optics are needed is for the reflection of very short wavelengths where the index of refraction of most dielectrics approaches 1 and reflection from bare metal at normal incidence is quite low.

For most applications where maximum reflectivity at a single wavelength is desired a quarter-wave MLDC is used, since it usually allows the coherent addition of the reflections from each dielectric interface. The advantages of deviating from a quarter-wave stack have been discussed for the case of slightly absorbing dielectric layers,[2,3] as an attempt to increase the damage threshold by reducing the internal flux,[4] and as a means of controlling the difference in s and p polarization phase shifts.[5]

Figure 1 illustrates the phase shifts experienced by a beam reflection from each of a number of dielectric interfaces. The 0 superstrate is usually air, the S layer represents the substrate, and H and L represent high and low index layers, respectively. In most cases the phase is shifted by π when radiation incident from a low index medium is reflected from a high

index medium. There is no phase shift when the light incident from a high index material is reflected by a low index material. Thus if the layer thicknesses in figure 1 are all quarter wave at the incident wavelength, maximum reflectivity will result for both s and p polarized light. The phase shifts shown in figure 1 hold for all incident angles ϕ in the case of s polarized light. They also hold for p polarized light if ϕ is less than the Brewster angle, ($\tan \phi_B \equiv n_H/n_o$, where n_H and n_o are the indices of the high index layer and the superstrate respectively). For ϕ greater than ϕ_B, the superstrate - high index layer phase shift is 0 for p polarized light as shown in figure 2. Thus the quarter-wave stack will give poor p polarization reflectivity at grazing angles $\phi > \phi_B$.

From figures 1 and 2 it is clear that if only s polarization is present, then the quarter-wave design is best, while if only p polarization is present the top layer should be half-wave and the remaining layers quarter-wave thick ($\phi > \phi_B$). The purpose of this paper is to develop expressions for the coating design that will give the minimum total absorption as a function of the fraction of s and p light incident on the MLDC.

Section 2 will develop the theory used to find the optimum coating. A review will be given of work by Shellan[6] in which simple expressions were found for the reflectivity of quarter-wave stacks at oblique angles of incidence. This analysis technique is then extended to the case of one layer being non-quarter wave thickness. Section 3 uses these results to find the coating with maximum reflectivity. Section 4 compares the results of sections 2 and 3 with exact computer results based on the matrix method. Numerical non-linear optimization solutions are compared with the analytic solutions and the reflectivities in the two cases are found to agree closely.

2. Analysis Approach

M. Sparks[7], H. E. Bennett and D. K. Burge[8], and Jeffrey B. Shellan[6] have found simple but powerful techniques for calculating the optical properties of quarter-wave reflectors. The approach by Shellan[6] is the most general since it is valid for arbitrary angle of incidence. The techniques will be reviewed and then extended to the case of a quarter-wave stack containing one layer of arbitrary thickness. Expressions can be developed to include the effects of substrate, volume, and interface absorption, as was done in references 6, 7, and 8, but only substrate absorption will be considered here. For high quality coatings, especially ones deposited with advanced deposition techniques such as ion beam sputtering, the substrate absorption will usually dominate unless many layers are used. For the grazing angles of primary interest in this paper, designs with 1, 2, or 3 layer pairs are probably sufficient.

Figure 3 illustrates the E field distribution and B field distribution for s and p polarized light, respectively, within a quarter-wave stack. The quantities O, H, L, and S designate the superstrate with index n_o, high-index layer with index n_H, low-index layer of index n_L, and the substrate with index n_s. The E field with incident amplitude E_o (normal to the plane of incidence) is shown by the solid line and the amplitude attenuation factor S_{ij} was shown[6] to be given by

$$S_{ij} = n_i/n_j \qquad (1)$$

$$\text{where} \qquad n_i \equiv (n_i^2 - n_o^2 \sin^2 \phi)^{1/2} \qquad (2)$$

ϕ = angle of incidence from superstrate

The B field distribution, used to find the properties of p polarized light, is given by the dashed curve in figure 3 and its attenuation factor P_{ij} was shown to be equal to

$$P_{ij} = (n_i^2 n_j)/(n_j^2 n_i) \qquad (3)$$

The fields are sinusoidal in each layer, and the thickness of layer i in the quarter-wave stack is

$$\ell_i = \lambda/(4n_i) \tag{4}$$

where λ is the wavelength in free space.

From figure 3, the electric field penetrating into the substrate for the S polarization is given by $S_{OH}S_{LH}{}^{N-1}S_{LS}2E_o$, where 2N is the total number of layers and E_o is the incident field. The incident flux is proportional to $n_o E_o{}^2 \cos^2\phi$, whereas the flux penetrating into the substrate is proportional to $n_S(S_{OH}S_{LH}{}^{N-1}S_{LS}2E_o)^2 \cdot \cos\phi_S$, where ϕ and ϕ_S are the angle of incidence and the propagation angle in the substrate, respectively. The fraction of energy penetrating into the substrate, the absorption of the substrate, for 2N layers and S-polarized light is

$$A_S(2N)$$
$$= n_S(S_{OH}S_{LH}{}^{N-1}S_{LS}2E_o)^2\cos\phi_S/(n_o E_o{}^2\cos\phi) \tag{5}$$
$$= 4S_{OS}S_{LH}{}^{2N}.$$

From the form of the B-field distribution for the P-polarized light in figure 3, the B field penetrating into the substrate is equal to $P_{LH}{}^N 2B_o$. The flux is proportional to $(1/n)B^2 \cos\phi$, and the P-polarization substrate absorption for a coating with 2N layers is found to be

$$A_p(2N) = 4P_{OS}P_{LH}{}^{2N}. \tag{6}$$

If we consider the case of grazing incident angle mirrors (GIAMs) and neglect second order terms in the grazing angle α ($\alpha=\pi/2-\phi$), then equations 5 and 6 can be rewritten as

$$A_S(2N)$$
$$\approx 4 \ (S_{LH}^o)^{2N} \ S_{LS}^o \ \frac{n_o}{n_L^o} \ \alpha \tag{7}$$

$$A_p(2N)$$
$$\approx 4 \ (P_{LH}^o)^{2N} \cdot P_{LS}^o \ \frac{n_o n_L^o}{n_L^2} \ \frac{1}{\alpha} \tag{8}$$

where S_{ij}^o, n_L^o, P_{ij}^o are equal to S_{ij}, n_L, and P_{ij} evaluated at $\phi = \pi/2(\alpha=0)$.

Equations 7 and 8 indicate that for a quarter-wave stack the s and p polarization are proportional to α and $1/\alpha$, respectively, for GIAMs. In deriving equations 5 and 6 it was assumed that the absorption is small and thus equation 8 will breakdown as α approaches zero.

Up to this point we have implicitly assumed that the substrate is a dielectric since we have taken n_i, η_i, S_{ij}, and P_{ij} to be real quantities. For a metal, these quantities are complex, but we can effectively make S_{ij}, and P_{ij} real by covering the metal substrate with a thin dielectric layer. The details of this are covered in Reference 6.

Although the s and p absorptions for bare metal can differ by almost two orders of magnitude in the visible, the difference in the two absorptions is even more pronounced for MLDCs at grazing angles. The ratio of the MLDC absorptions can be 3 to 5 orders of magnitude at $\alpha \sim 1°2°$. For this reason it is desirable to alter the quarter-wave stack slightly to improve the p polarization reflectivity. Expressions will now be derived for the s and p absorption for a modified quarter wave stack.

Figure 4 illustrates the effects on the internal electric field of including one layer, the nth low index layer, of arbitrary thickness. The tangential component of the electric field is fixed at zero at the substrate interface, for most high reflectivity coatings containing a metal substrate. This has been verified by exact computer runs based on the matrix method[9,10]. The field distribution is the same as for a perfect quarter-wave stack between the substrate interface and the perturbed layer.

The thickness of the nth low index layer (n is measured from the superstrate) is $\frac{\pi}{2} + \Delta_L^{(n)}$, measured in phase units. The actual thickness of the perturbed layer is thus

$$\ell_L^{(n)} = (1+2\Delta_L^{(n)}/\pi)\ell_{1/4} \tag{9}$$

where $\ell_{1/4}$ is the quarter wave thickness.

The perturbed layer has been expanded in the drawing for clarity, but its unperturbed width, from the LH interface to the vertically dashed line (of phase width $\pi/2$), is the same width as all the other unperturbed L layers. The distance $\Delta_L^{(n)}$ from the vertically dashed line to the HL interface is the perturbation. If we start from the substrate where the penetrating field has amplitude $2E_S$ and work backward to the nth L layer, the amplitude of the sine wave in the perturbed layer is $2E_S S_{SL} S_{HL}^{N-n}(-1)^{N-n+1}$ for S-polarized light.

The equation for the field in the nth L layer in a coordinate system whose origin is at the front surface of the layer (see fig. 4) is

$$D \cos[x - \Delta_L^{(n)}] = D \cos\Delta_L^{(n)}\cos x + D \sin\Delta_L^{(n)}\sin x, \tag{10}$$

where

$$D \equiv 2E_S S_{SL} S_{HL}^{N-n}(-1)^{N-n+1} \tag{11}$$

333

The cos x and sin x field components of $\cos[x-\Delta_L^{(n)}]$ have been drawn in dashed lines in figure 4. Equation (1) indicates that when the null of a sinusoidal wave is at an ij interface, the ratio of the wave amplitude on the i side to the j side is S_{ij}. On the other hand, if the peak of the sinusoidal wave is at the interface, the amplitude is the same in the i and j regions. Using this fact, we can easily find the amplitude of the sin x and cos x components at the mirror surface. At a y-coordinate system whose origin is at the mirror surface (see fig. 4), the field is

$$E(y) = (-1)^n D [S_{HL}^{n-1} S_{HO} \cos \Delta_L^{(n)} \sin y$$

$$+ S_{LH}^n \sin \Delta_L^{(n)} \cos y]. \tag{12}$$

This can be expressed as the sum of a forward-propagating wave and backward-propagating wave

$$C[e^{-iy} + (G-iF)/(G+iF)e^{iy}], \tag{13}$$

where

$$C = \frac{(-1)^n D}{2} [i \, S_{HL}^{n-1} S_{HO} \cos \Delta_L^{(n)} + S_{LH}^n \sin \Delta_L^{(n)}] \tag{14}$$

and F and G are defined as the coefficients of sin y and cos y, respectively, in equation 12.

Since the incident intensity is equal to $|C|^2$, the absorption is proportional to $|E_s/C|^2$, with the constant of proportionality quickly found by comparing equation 5 with $|E_s/C|^2$ for the case $\Delta_L^{(n)} = 0$. The s polarization absorption for the case of quarter-wave stack where the nth low index layer is perturbed by $\Delta_L^{(n)}$ is found to be

$$A_S(2N, \Delta_L^{(n)}) = \frac{4 \, S_{OS} \, S_{LH}^{2N}}{\cos^2 \Delta_L^{(n)} + [S_{LH}^{2n-1} \, S_{OH} \sin \Delta_L^{(n)}]^2} \tag{15}$$

In a similar manner, an expression can be found for the s polarization absorption, $A_S(2N, \Delta_H^{(n)})$, a quarter-wave stack with the nth high index layer shifted by $\Delta_H^{(n)}$ phase units.

$$A_S(2N, \Delta_H^{(n)}) = \frac{4 \, S_{OS} \, S_{LH}^{2N}}{\cos^2 \Delta_H^{(n)} + [S_{LH}^{2(n-1)} S_{OH} \sin \Delta_H^{(n)}]^2} \tag{16}$$

The corresponding expressions for p polarization are

$$A_p(2N, \Delta_L^{(n)}) = \frac{4 \, P_{OS} \, P_{LH}^{2N}}{\cos^2 \Delta_L^{(n)} + [P_{LH}^{2(n-1)} P_{OH} \sin \Delta_L^{(n)}]^2} \qquad (17)$$

$$A_p(2N, \Delta_H^{(n)}) = \frac{4 \, P_{OS} \, P_{LH}^{2N}}{\cos^2 \Delta_H^{(n)} + [P_{LH}^{2(n-1)} P_{OH} \sin \Delta_H^{(n)}]^2} \qquad (18)$$

Equation 8 indicated that the p polarization absorption varies as $1/\alpha$ for small grazing angles and quarter-wave stacks. Since P_{OS} as well as P_{OH} vary as $1/\alpha$, equations 17 and 18 indicate that $A_p(2N, \Delta_L^{(n)})$ and $A_p(2N, \Delta_H^{(n)})$ will vary as α, not $1/\alpha$, for sufficiently small α, as long as $\sin\Delta^{(n)} \neq 0$. Equations 15 through 18 also indicate that the absorption is periodic in $\Delta^{(n)}$ with period equal to π (half wave thicknesses), as expected.

Equations 15 through 18 will now be used to find optimum GIAM reflectors.

3. Optimum Grazing Incidence Coatings

If we let A_t be the total substrate absorption due to both s and p absorption, and f_s be the fraction of s polarized light incident on the MLDC, then

$$A_t = f_s A_s(2N) + (1-f_s) A_p(2N) \qquad (19)$$

where equation 15 or 16 is used for $A_s(2N)$ and equation 17 or 18 is used for $A_p(2N)$, depending on where a high or low index layer is perturbed.

If we differentiate equation 19 with respect to $\sin\Delta^{(n)}$, we find two solutions for the coating design giving lowest total absorption, $A_t(min)$. The result is

$$\sin^2\Delta_i^{(n)} = 0 \qquad (20)$$

or

$$\sin^2\Delta_i^{(n)} = \frac{[(1-f_s) \, P_{OS} \, P_{LH}^{2N} \, (p_{OH}^{(in)^2}-1)]^{1/2} - [f_s S_{OS} \, S_{LH}^{2N} \, (1-s_{OH}^{(in)^2})]^{1/2}}{(1-s_{OH}^{(in)^2})[(1-f_s) P_{OS} P_{LH}^{2N}(P_{OH}^{(in)^2}-1)]^{1/2} + (p_{OH}^{(in)^2}-1)[f_s S_{OS} S_{LH}^{2N}(1-s_{OH}^{(in)^2})]^{1/2}} \qquad (21)$$

335

where

$$i = L \text{ or } H, \quad n = 1, 2, \ldots N$$

and

$$s_{OH}^{(Hn)} \equiv S_{LH}^{2(n-1)} S_{OH} \tag{22}$$

$$p_{OH}^{(Hn)} \equiv P_{LH}^{2(n-1)} P_{OH} \tag{23}$$

$$s_{OH}^{(Ln)} \equiv S_{LH}^{2n-1} S_{OH} \tag{24}$$

$$p_{OH}^{(Ln)} \equiv P_{LH}^{2n-1} P_{OH} \tag{25}$$

Equation 21 will give the minimum absorption design if two conditions are met. Otherwise equation 20, which refines the standard quarter-wave stack, will give the optimum coating. The first of these two conditions is that

$$p_{OH}^{(in)2} > 1 \tag{26}$$

For the case of thickness adjustments to the outermost high-index layer, $p_{OH}^{(in)}$ = P_{OH} and the condition $P_{OH}=1$ defines the Brewster angle discussed in the introduction. The second condition that must hold for equation 21 to give the best coating is that the numerator be positive. This in effect defines a critical value for $f_p \equiv (1-f_s)$, the fraction of p polarized light.

If equations 15 through 19 and 21 are combined, the absorption can be found for the optimum MLDC for GIAMs, $A_t^{(min)}$. The result is

$$A_t^{(min)} = 4 \left\{ \left[\frac{f_s S_{OS} S_{LH}^{2N}}{1 - s_{OH}^{(in)2}} \right]^{1/2} + \left[\frac{(1-f_s) P_{OS} P_{LH}^{2N}}{p_{OH}^{(in)2} - 1} \right]^{1/2} \right\} \cdot$$

$$\cdot \left\{ \frac{(1-s_{OH}^{(in)2}) \left[(1-f_s) P_{OS} P_{LH}^{2N} (p_{OH}^{(in)2} - 1) \right]^{1/2} + (p_{OH}^{(in)2} - 1) \left[f_s S_{OS} S_{LH}^{2N} (1-s_{OH}^{(in)2}) \right]^{1/2}}{p_{OH}^{(in)2} - s_{OH}^{(in)2}} \right\} \quad (27)$$

$$i = L \text{ or } H, \quad n = 1, 2, \ldots N$$

It can be shown that the best layer to adjust to achieve the lowest absorption is the outermost high index layer. Thus $s_{OH}^{(in)}$ and $p_{OH}^{(in)}$ should be replaced with S_{OH} and P_{OH} in equations 21 and 27.

Section 4. will compare the predictions of equations 15, 16, 17, 18, and 27 with numerical results. The $A_t^{(min)}$ given in equation 27, which is based on a quarter-wave stack with only the outer layer adjusted, will be shown to compare quite favorably with that obtained using a numerical non-linear optimization procedure in which all layers can be adjusted.

4. Comparison Of Analytic And Exact Results

The accuracies of equations 15 through 19 can be verified by comparing them with numerical results. The computer results were obtained by using 2 x 2 matrices to represent the effects of dielectric discontinuities and propagation in a uniform dielectric layer.[9,10] The relationship between left-and right-traveling light is established at each side of the dielectric discontinuities and at each end of uniform layers. The product of these matrices then gives a relationship between incident, reflected, and transmitted light for the entire system.

Figure 5 is a plot of A_s and A_p versus outer-layer thickness for the coating $Si(Al_2O_3/ZnS)^9$ comparing the analytic results (equations 16 and 18) with exact results. The curves are indistinguishable for A_s and only differ for A_p in regions of high absorption. All layers, other than the top ZnS layer, are quarter-wave thick at the incident angle of 88°. There is almost a four order of magnitude change in the s absorption and more than a two order of magnitude variation in A_p as $\Delta_H^{(1)}$ is varied from 0 to π.

In order to assess the optimum MLDC design given in equation 21, the absorption given in equation 27 was compared with that of a quarter-wave stack ("substrate compensated design") as well as that generated using a numerical non-linear optimization procedure.

A Ag $(SiO_2/ZrO_2)^N$ "substrate compensated" quarter-wave stack at incident angle 89° with one adjustable layer was used ($\lambda=1.06\mu m$, $n_H=2.1$, $n_L=1.4$, $n_S=0.18+7.05i$). The absorption was calculated using equation 27 for N = 1, 2, 3, 4, 5 and n = 1, 2,...N for f_s = 0.990 to $f_s=0.999$. It was found in all cases that varying the thickness of the top layer gave the lowest absorptions and that the absorption was 6 to 100 times less than for the quarter-wave reflector, depending on the number of layers used.

There are many techniques of non-linear optimization used in coating synthesis.[11,12,13,14] The one first suggested by Dobrowolski was used with the merit function equal to the total absorption, and compared with the analytic results.

Figure 6 compares the absorption for a quarter-wave design, the ideal coating found from equations 21 and 27, and the numerically generated design. In all cases the absorption of the analytic result is within 10% of that found using the non-linear optimziation computer program.

5. Summary and Conclusion

Equations were derived for the reflectivity of quarter-wave stacks containing one layer of arbitrary thickness. The expressions were compared with exact numerical results and found to agree quite closely as long as the total absorption was small. These results were then used to find the MLDC with highest reflectivity at angles of incidence greater than the Brewster angle, once the fraction of s and p polarized light was specified. The designs found can have absorptions at least an order of magnitude less than QW designs, even if only 0.1% of the incident flux is p polarized. Good agreement was found between the absorptions of the analytically generated designs and that of coatings found using numerical methods.

References

[1] S. A. Mani and J. H. Hammond, "Optics and resonator design issues for high-power free electron lasers," Proceedings of The International Conference on Lasers, New Orleans, La., December, 1981.

[2] C. K. Carniglia and Joseph H. Apfel, "Maximum reflectance of multilayer dielectric mirrors in the presence of slight absorption," J. Opt. Soc. Am. 70, 523-534 (1980).

[3] P. H. Lissberger, "The ultimate reflectance of multilayer dielectric mirrors, "Opt. Acta 25, 291-298 (1978).

[4] Joseph H. Apfel, "Optical coating design with reduced electric field intensity," Appl. Opt. 16, 1880-1885 (1977).

[5] W. H. Southwell, "Multilayer coatings producing 90° phase change," Appl. Opt. 18, 1875 (1979).

[6] Jeffrey B. Shellan, "Simple expressions for predicting substrate, volume, and interface absorption and reflective phase shifts in high-reflectance quarter-wave stacks at oblique angles of incidence," J. Opt. Soc. Am. 73, 1272-1281 (1983).

[7] M. Sparks, "A simple method for calculating the optical properties of multilayer-dielectric reflectors," J. Opt. Soc. Am. 67, 1590-1594 (1977).

[8] H. E. Bennett and D. K. Burge, "Simple expressions for predicting the effect of volume and interface absorption and of scattering in high-reflectance or anti-reflectance multilayer coatings," J. Opt. Soc. Am. 70, 268-276 (1980).

[9] P. Yeh, A. Yariv, and Chi-Shain Hong, "Electromagnetic propagation in periodic stratified media. I. General Theory," J. Opt. Soc. Am. 67, 423-438 (1977).

[10] M. Born and E. Wolf, Principles of Optics (MacMillan, New York, 1964).

[11] Arnold L. Bloom, "Refining and optimization in multilayers," Appl. Opt. 20, 66-73 (1981).

[12] William E. Case, "New systhesis method for optical thin-film coatings," Appl. Opt. 22, 4111-4117 (1983).

[13] J. A. Dobrowolski, "Completely automatic synthesis of optical thin-film systems," Appl. Opt. 4, 937-946 (1965).

[14] J. F. Tang and Q. Zheng, "Automatic design of optical thin-film systems - merit function and numerical optimization method," J. Opt. Soc. Am. 72, 1522-1528 (1982).
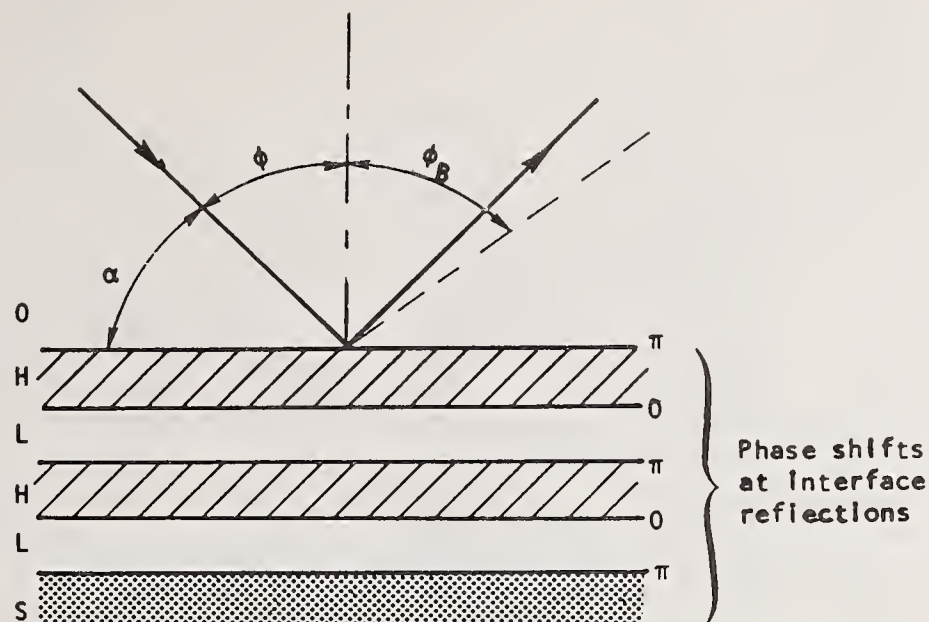
Figure 1. Phase shifts at each dielectric interface
for s polarized light for all incident
angles and for p polarized light if
$\phi < \phi_B$, where ϕ_B is the Brewster angle.

(H and L designate the high and low index
layers, O represents a low index superstrate,
and S is a high index substrate.)
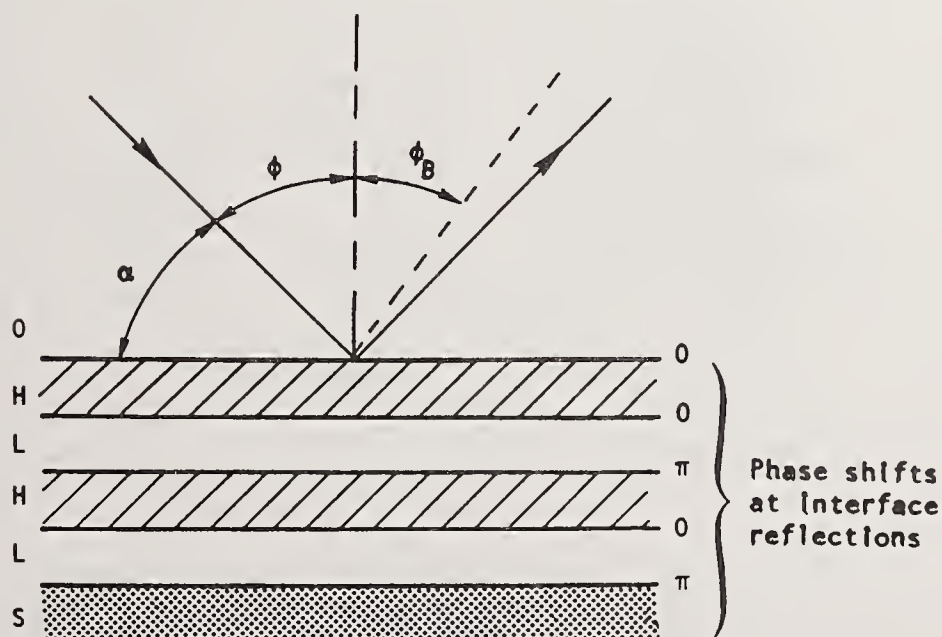
Figure 2. Phase shifts at each dielectric interface
for p polarized light incident at $\phi > \phi_B$.

Figure 3. E-field distribution for S-polarized light and B-field distribution for P-polarized light in a high-reflectivity quarter-wave stack.
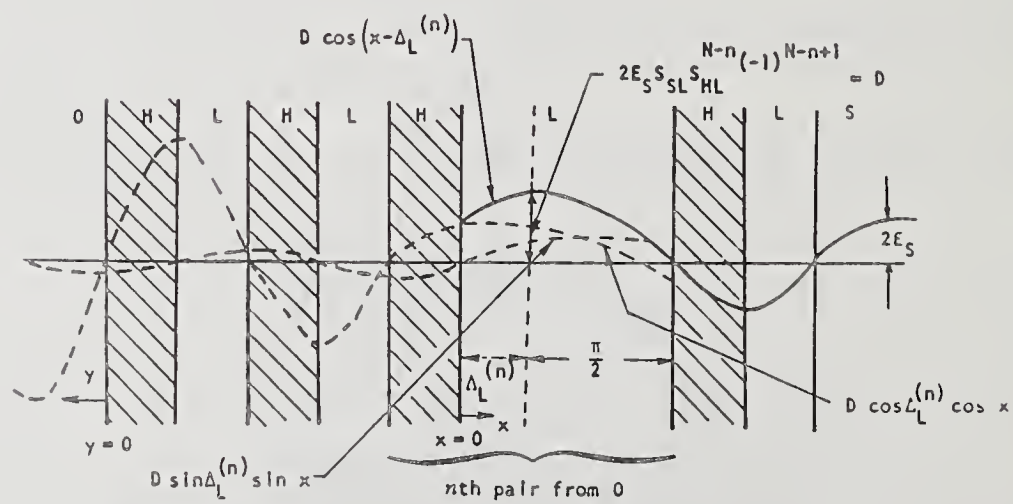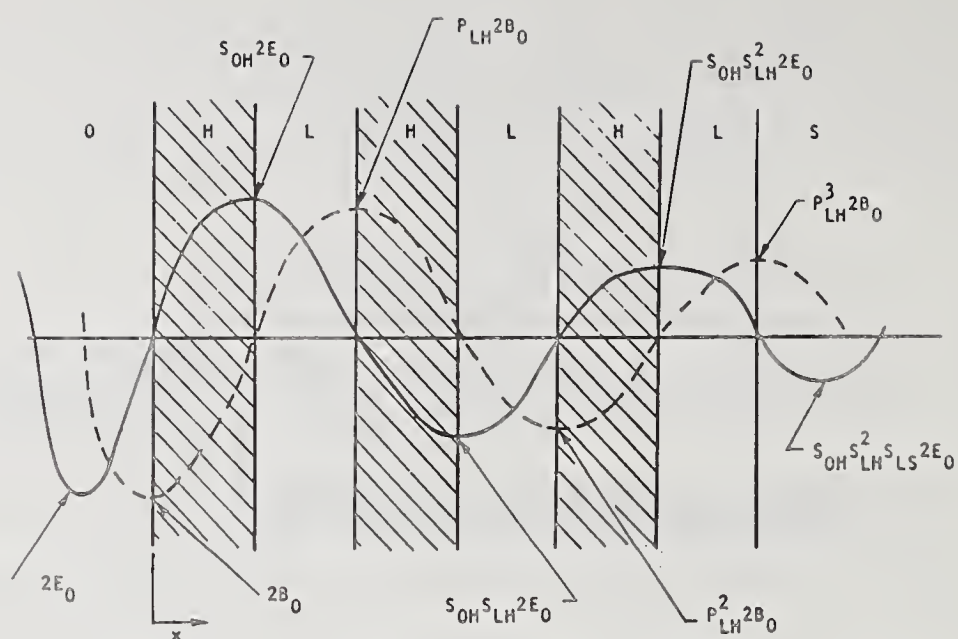
Figure 4. Geometry and field distribution for calculating the reflectivity of a quarter-wave stack with one layer of arbitrary thickness.
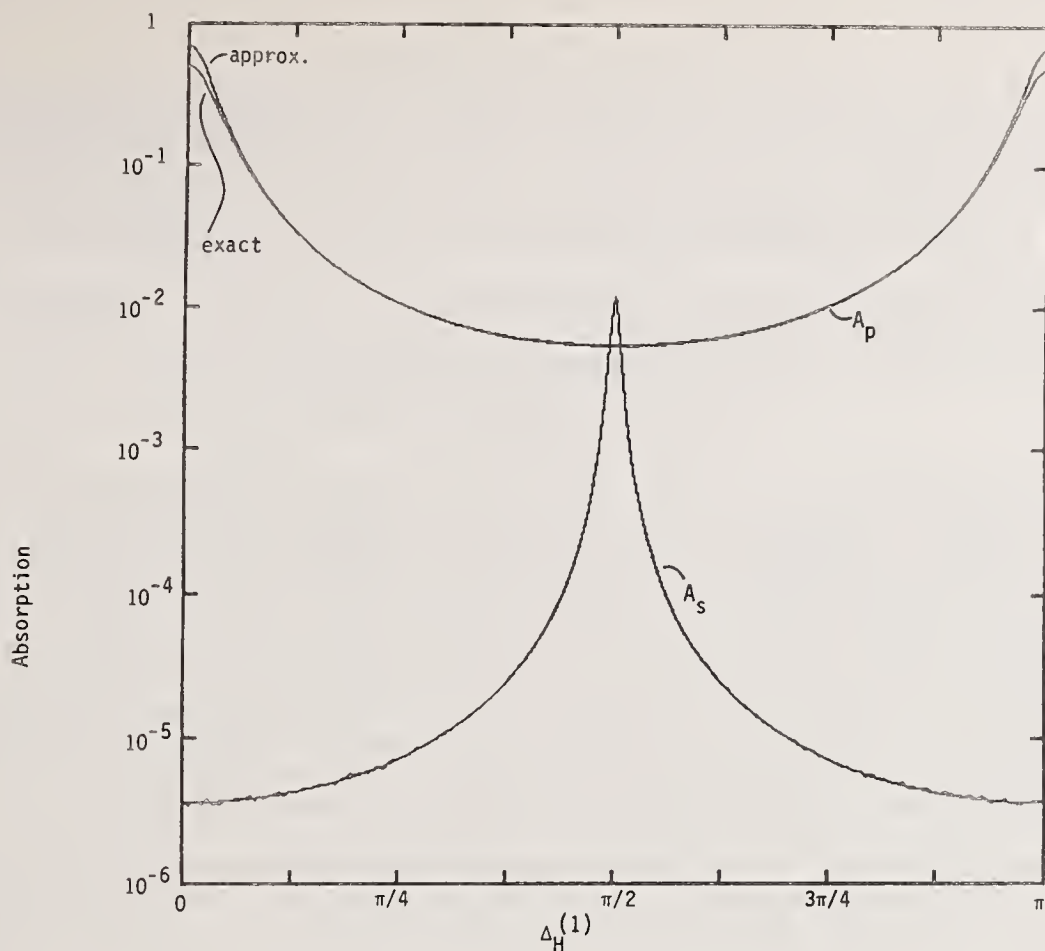
Figure 5. S and P polarization absorption as a function of top layer thickness $\Delta_H^{(1)}$ as calculated exactly and in the standing wave approximation for $Si(Al_2O_3/ZnS)^9$. All layers, other than the top one, are quarter-wave thick at the incident angle of 88°. ($\lambda = 2.8\mu m$)
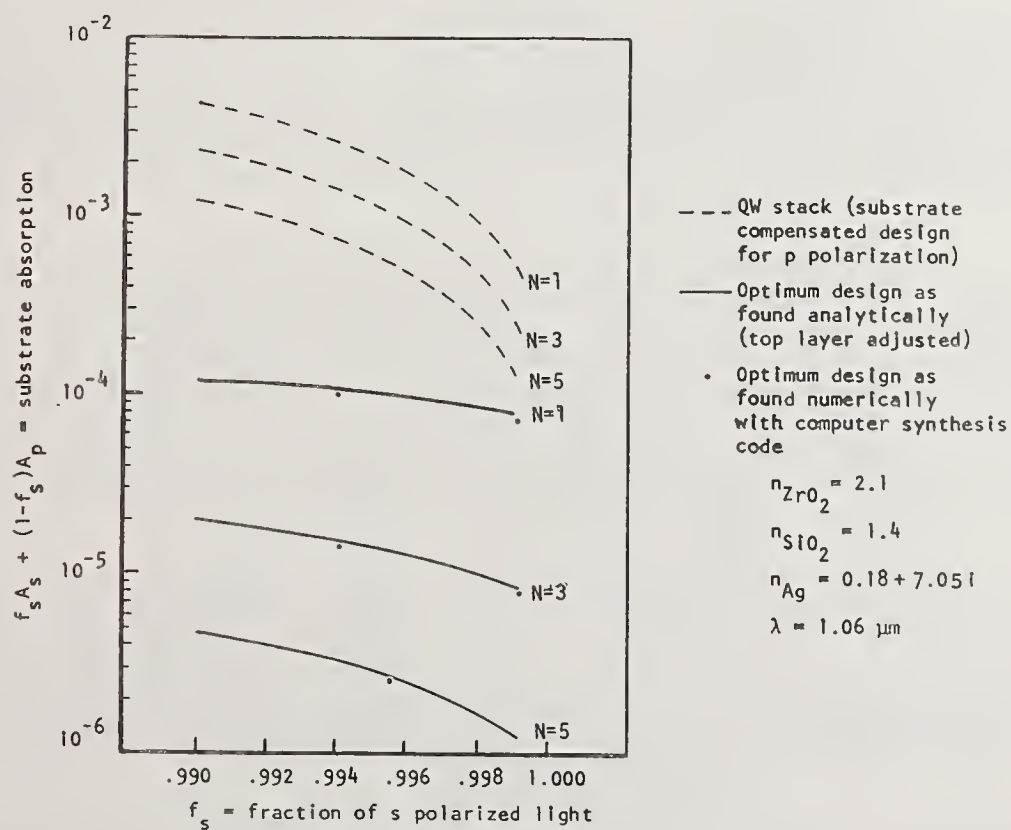
Figure 6. $Ag(SiO_2/ZrO_2)$ absorption as a function of the amount of s polarized light incident at 89°.

341

ANGULAR DEPENDENCE OF MULTILAYER-REFLECTOR DAMAGE THRESHOLDS*

Brian E. Newnam, Stephen R. Foltyn, Dennis H. Gill, and L. John Jolin

Los Alamos National Laboratory
Chemistry Division
Los Alamos, New Mexico 87545

The damage resistance of HfO_2/SiO_2 multilayer dielectric reflectors was measured as a function of angle of incidence with 351-nm XeF-laser irradiation. The laser produced nominal 10-ns pulses at a repetition rate of 35 pps. A series of reflectors designed for 0°, 30°, 45°, 60°, 75°, and 85° was tested with an S-plane polarized beam. To account for variations in the separate coating depositions, some of the coating designs were tested at two angles of incidence. At large angles of incidence, we did not observe the anticipated large increases in damage threshold predicted theoretically on the basis of spatial dilution ($1/cos\theta$) of the intensity at the reflector surface and standing-wave electric fields. For example, the threshold for a reflector designed and tested at 85° was only a factor of 2.5 larger than that of normal-incidence reflectors tested at 0°. Several possible mechanisms to explain this discrepancy were considered.

Key words: coating defects; free-electron lasers; grazing-incidence reflection; hafnium oxide, laser damage thresholds; multilayer reflectors; multiple-shot laser damage; silicon dioxide; standing-wave electric fields; thin films; ultraviolet reflectors; xenon fluoride lasers.

1. Introduction

Free-electron laser (FEL) oscillators, driven by rf linear accelerators, are being designed for high-average power applications in the ultraviolet to the near infrared from 400 to 1000 nm. The pulse format of these oscillators requires mirrors that will not damage or degrade under high peak intensities and high repetition rates ranging from 10^7 to 10^8 Hz. To function without significant distortion, the resonator mirrors must not be subjected to excessive average-power loading. Thus, very high mirror reflectance is required as well as low optical absorption to minimize the heat flow into the water-cooled mirror substrates. Multilayer dielectric (MLD) reflectors are the logical choice for the resonator mirrors since they have demonstrated the highest reflectance values, e.g. $\geq 99.99\%$ for small-diameter, ion-beam deposited reflectors for 633-nm laser gyro cavities.

It is necessary to include FEL physics in establishing the resonator mirror design. Specifically, high intracavity intensity is required within the magnetic-undulator gain region to obtain efficient conversion of the electron energy to coherent radiation. With undulator lengths ranging from 1 to 10 meters, the optical beam should have both a small waist and low divergence i.e., a long Rayleigh range. FEL beams have exhibited the desirable characteristic of near-diffraction-limited quality [1]. As a result, very long distances are required between resonator end mirrors to attain an acceptable intensity loading. However, if the mirror separation becomes too long, the cavity becomes less stable and unavoidable mirror jitter can seriously decrease the overlap of the optical and electron beams and thereby reduce the FEL efficiency.

Restriction of the FEL resonator length to minimize the effect of mirror jitter opposes the need for large distances to allow diffraction to dilute the intensity on the mirrors. A solution to this problem is to add a set of slightly curved intracavity mirrors oriented at large angles, e.g. 85°, to diverge the optical beam to an acceptable intensity level on the end mirrors. Because the FEL radiation is linearly polarized, these intracavity mirrors are oriented for S-polarized reflection only. Theoretically, use at large angles should result in very high damage resistance and less thermal distortion for a given beam intensity.

Since FEL oscillators are a relatively new development, we have given special attention to their mirror needs in the above discussion. However, both excimer laser and FEL oscillator and amplifier systems have the common additional requirement for beam directing mirrors used at non-normal incidence, and mirror damage data is urgently needed to permit realistic design of these external systems.

For metal mirrors, there have been a few measurements of laser damage resistance and optical absorption at large incidence angles. These demonstrated the theoretically predicted $[1/\cos\theta]^2$ threshold dependence for metals for S-polarization [2-4]. This quadratic dependence derives from (1) the increased beam area on the surface as $1/\cos\theta$, and (2) the angular dependence of S-plane absorptance $\alpha_s(\theta) = \alpha(0°)\cos\theta$. However, data regarding the angular dependence of MLD reflectors are sparse and have been limited to incidence angles of 0° and 45°.

The present set of experiments was motivated to determine the angular dependence of multiple-shot damage resistance of MLD reflectors for incidence angles from 0° to 85° and S-polarized beams. Conducted at the low repetition rate of 35 pps, these tests did not address the issues of average-power damage threshold or thermal distortion of mirrors both of which must be evaluated in further test series with cw or long-pulse (>10 μs) lasers.

Special consideration was given to the possible role of the standing-wave (SW) electric field as a function of angle of incidence because of previous correlations with damage thresholds. From multiple-shot tests using ~10-ns pulses at ultraviolet wavelengths of 248 nm [5], 308 nm [6], and 355 nm [7], we identified the peak SW electric field in the outermost high-index layer as setting the threshold of damage. On this basis, our calculations of the SW fields led us to predict mono-tonically increasingly higher damage thresholds with angle of incidence, but only for S-polarized laser beams. The results of these calculations for the specific reflectors tested in the present experiments are shown in figure 1 for incidence angles of 0° and 85° for both S- and P-polarized beams. The cosine intensity-dilution factor is inherently accounted for in the SW field calcula-tions. The SW fields for angles less than 85° are intermediate to the curves shown. If optical damage is correlated with the peak value of $[E/E_o^+]^2$ in the first high-index layer, as would be the case with linear absorption, figure 1 indicates that we might expect the damage threshold at 85° to be a factor of 102× larger than that at normal incidence.

2. Test Specimens

The test specimens were coated by Broomer Labs by electron-beam evaporation with ordinary conditions as used in their commercial production. In addition to the general features listed in table 1, particular details of the coating depositions included the following: 300°C substrate temperature, deposition rate of 5 min/QW, 8×10^{-5} Torr background pressure with O_2 bleed, and 5×10^{-6} Torr initial vacuum. The reflectors were not post baked. For purposes of computing the film thicknesses, Broomer used the refractive indices of 1.51 for SiO_2 and 2.08 for HfO_2, which are typical values at 351 nm.

Because the magnitudes of the SW fields can be strongly affected by film thickness errors, we evaluated the spectral transmittance curves from spectrometer measurements at normal incidence. Comparisons of the design and measured center wavelengths are provided in table 2. We think that the measured thickness discrepancies should not have influenced the damage thresholds to any great degree.
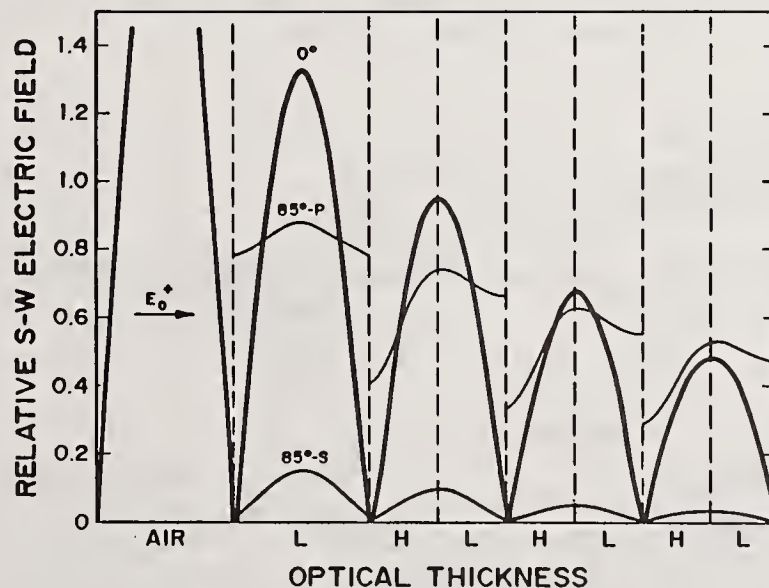
Figure 1. Standing-wave electric-field distributions in HfO_2/SiO_2 reflectors designed for 0°- and 85°-incidence. Fields are plotted normalized to E_o^+, the incident electric field in air. At large angles such as 85°, the internal fields for S-polarized radiation are much lower than for normal incidence; modest advantage is attained with P-polarization. For angles smaller than 85°, intermediate field distributions are calculated.

Table 1. Test samples

Coating materials:	HfO_2 and SiO_2
Design:	$S/(HL)^{11}HL^2/A$ for S-polarization
Deposition process:	Electron gun
Coating vendor:	Broomer Labs
Substrates:	Fused silica (5.1-cm diam)
	BK-7 glass (6.4 × 12.7 cm)

Table 2.   Coating thickness errors

Design Angle	Center Wavelength for Design (nm)	Normal Incidence Measured (nm)[a]	Deviation[b]
0°	351	354	+1%
30°	367	384	+5%
45°	386	403	+4.5%
60°	407	405	-0.5%
75°	426	420	-1.5%
85°	434	425	-2%

[a]Wavelength corresponding to the center frequency midway between 1% transmittance points of the reflection band.

[b]For 0° incidence on a reflector designed for 0°, a 3% thickness error results in ≦1% increase in the SW electric-field peaks. For 85° incidence (S-polarized light) on a reflector designed for 85°, a 10% thickness error results in a 25% increase of the field peak in the uppermost high-index layer and a 20% increase in the uppermost (HW overcoat) low-index layer.

3.   Laser Damage Test Conditions

The laser damage test facility depicted in figure 2 and our standard multiple-shot measurement procedures have been described previously [5,6]. One modification, not shown, was inclusion of multilayer polarizers which we aligned very carefully to obtain a polarization purity of I_s/I_p ≥ 1000 on the samples. In addition, the beam dimensions in the sample plane, which varied with incidence angle, were measured directly with a Reticon silicon-diode linear array. As shown in table 4, the measured diameters of the near-Gaussian beam did not deviate significantly from the predictions. Naturally, the measured beam sizes were used in calculations of the damage thresholds.
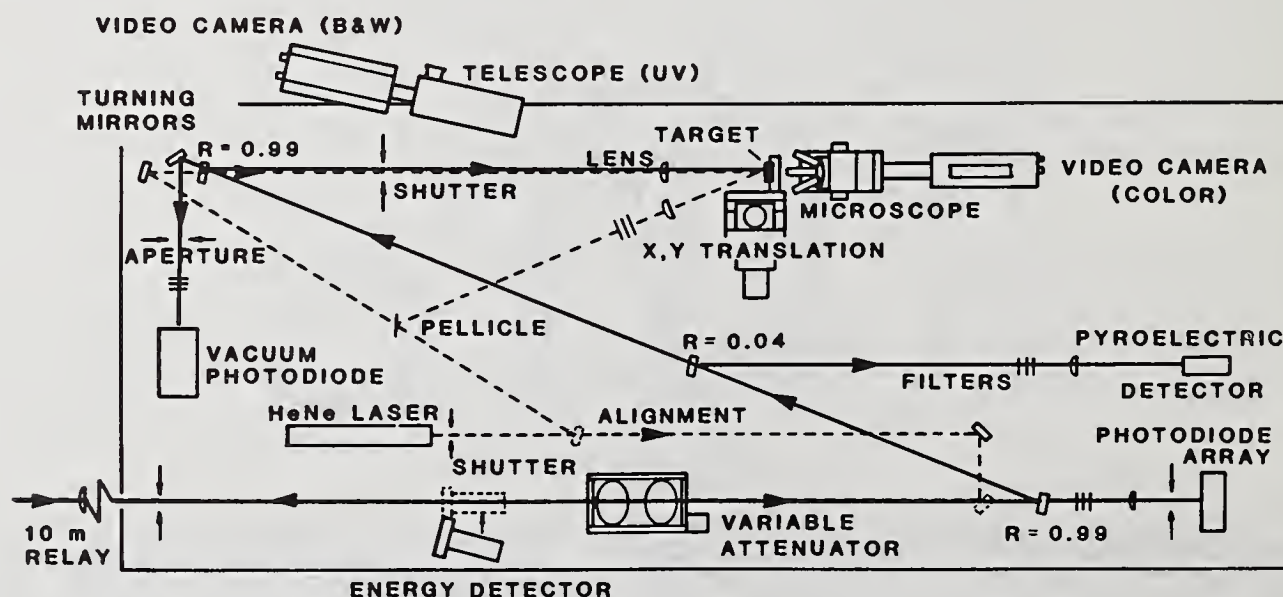
Figure 2. Schematic of the Los Alamos excimer-laser, multiple-shot, laser damage test facility.

Table 3. Laser test parameters

Wavelength:	351 nm (XeF)
Polarization:	S-plane with purity $I_s/I_p \geq 1000$
Pulsewidth:	10 ns (FWHM)
Spot-size diameter $(1/e^2)$:	0.4 mm, mean value normal to the beam 0.4 mm/$\cos\theta$, mean value on sample
Repetition rate:	35 pps
Shots per site:	140 if no damage detected, or $\leq$140 if damage

Table 4. Angular dependence of the laser beam diameter (vertical plane) at the reflector surface

Angle of Incidence	Predicted Diameter $2w_o/\cos\theta$, (mm)	Measured Diameter (mm)	Deviation from $1/\cos\theta$
0°	0.128	0.128	---
30°	0.148	0.142	-4%
45°	0.181	0.173	-4%
60°	0.256	0.235	-8%
75°	0.495	0.470	-5%
85°	1.47	---	---

4. Experimental Results

Preliminary to damage tests over the entire range of angles of incidence, the possible threshold variations within a given coating run were determined for the 0° and 30° designs. These threshold values, given in table 5, indicate a range of ±10 to ±15%. Also, the 4 to 5 J/cm^2 magnitude was about the same as our previous measurements of other reflectors composed of these same coating materials. Since each angle of incidence required a separate coating deposition, we attempted to account for run-to-run variations by testing some of the reflectors at two angles of incidence. We intended to obtain this two-angle registration for each coating design, but only 0° and 30° designs were so evaluated due to decreased coating target area available at the larger angles. For these two designs, the variations were within 10% as shown in table 6. Predicted differences on the basis of the peak SW electric fields also were small.

Table 5. Comparison of damage thresholds of HfO$_2$/SiO$_2$ reflectors fabricated in the same coating run.

Design and Test Angle	Sample Identification	Damage Threshold J/cm^2
0°	0-1	4.1
	0-2	4.7
	0-3	5.2
30° (S-polar)	30-1	4.0
	30-2	4.5

The results as a function of the full range of incidence angles are listed in table 7, and the supporting data from which the threshold values were obtained are presented in the series of figures 3. This extensive display of test data is given because of (1) the significance that might be given these results in optical designs of FEL resonators and other beam directing elements, and (2) to allow the reader the opportunity for a thorough examination of these results with the possibility that other interpretations might become evident. We note that the available laser energy was insufficient to reach the saturation fluence (damage at 10 out of 10 test sites) for the 85° case. Figure 4 allows direct comparison of the experimental results for all of the angles of incidence used.

345

Table 6. Comparison of damage thresholds for HfO_2/SiO_2 reflectors tested at two angles of incidence.

Sample Number	Design Angle	Test Angle	Damage Threshold J/cm^2	Peak SW Electric Field[a]
0-1	0°	0°	4.1	0.95
		30°	4.5	0.89
30-1	30°	30°	4.5	0.85
		45°	4.6	0.76

[a]Calculated in the HfO_2 films (for reflectors centered at 351 nm) and normalized to the S-polarized incident field E_o^+.

Table 7. Damage thresholds versus angle of incidence for HfO_2/SiO_2 reflectors tested at the design angle.

Design and Test Angle	Damage Threshold J/cm^2	Peak SW Electric Field[a]
0°	4.6 ± 0.5	0.95
30°	4.3 ± 0.4	0.85
45°	5.2	0.72
60°	6.6	0.52
75°	6.9	0.28
85°	11.5 ± 0.5	0.094

[a]Calculated in the HfO_2 films (for reflectors centered at 351 nm) and normalized to the S-polarized incident field E_o^+.

We observed that the damage morphology at high angles of incidence differed from that for near-normal incidence. At the large angles, the damage sites had an elongated triangular pattern, different from the elliptical beam footprint, with the long dimension aligned along the direction of the incident beam.
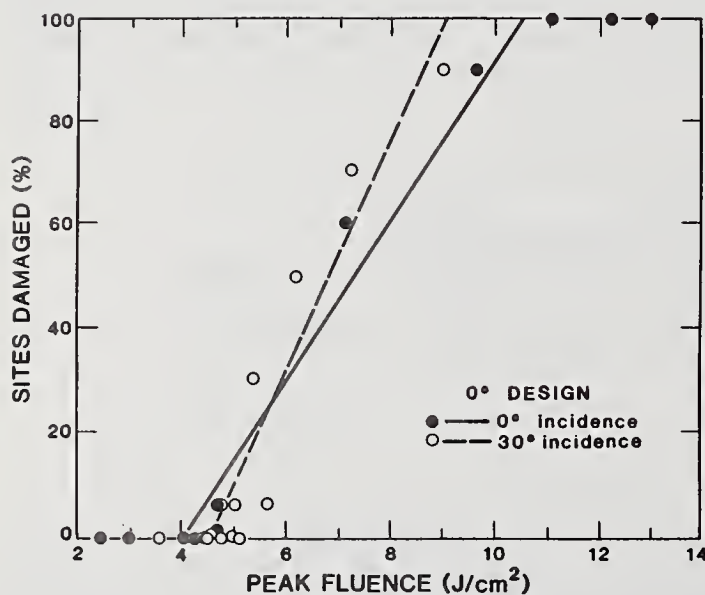
Figure 3a.
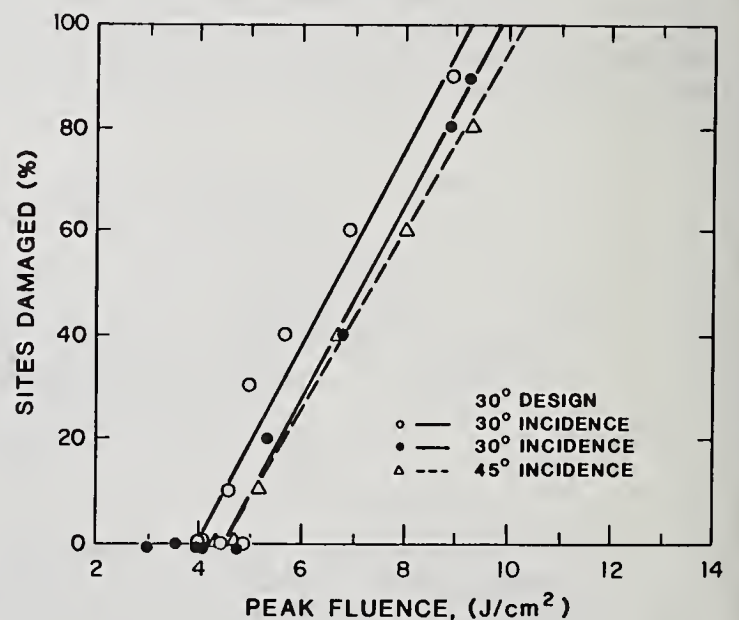
Figure 3b.
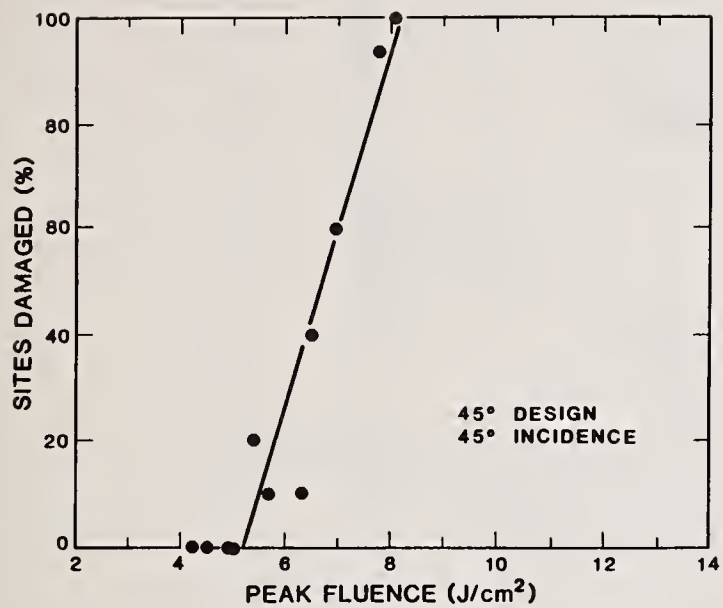
Figure 3c
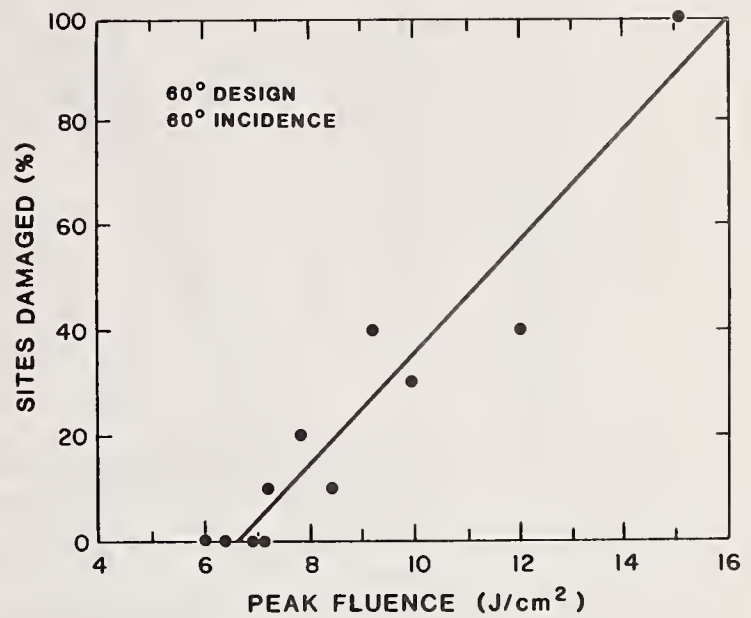
Figure 3d
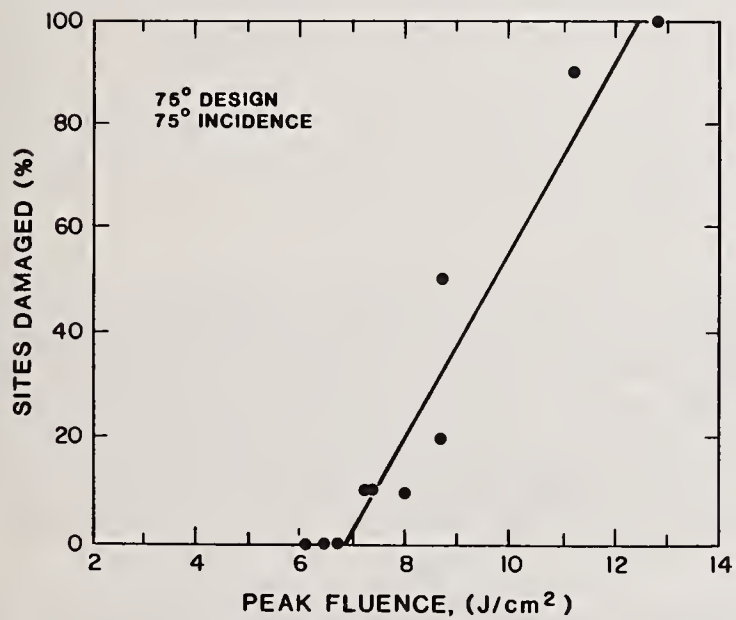
Figure 3e
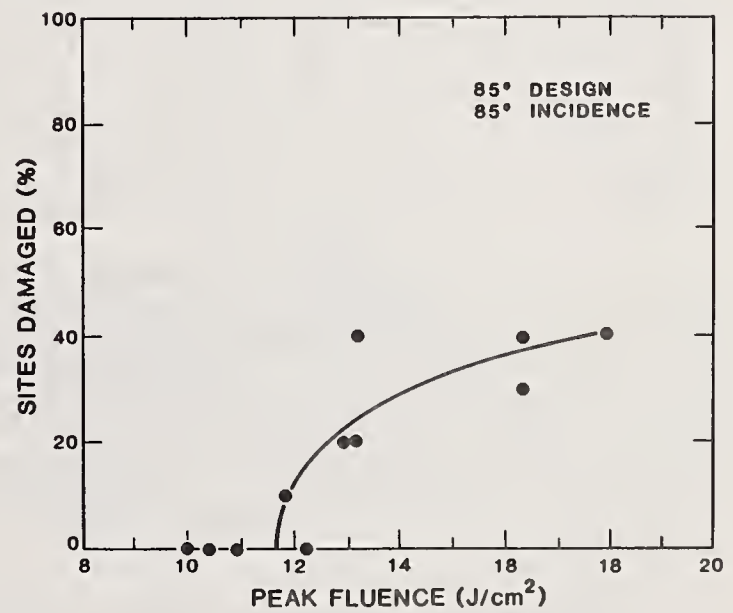
Figure 3f

Figures 3a-f. Multiple-shot laser damage test results for 351-nm HfO_2/SiO_2 multilayer reflectors as a function of angle of incidence with S-polarization.
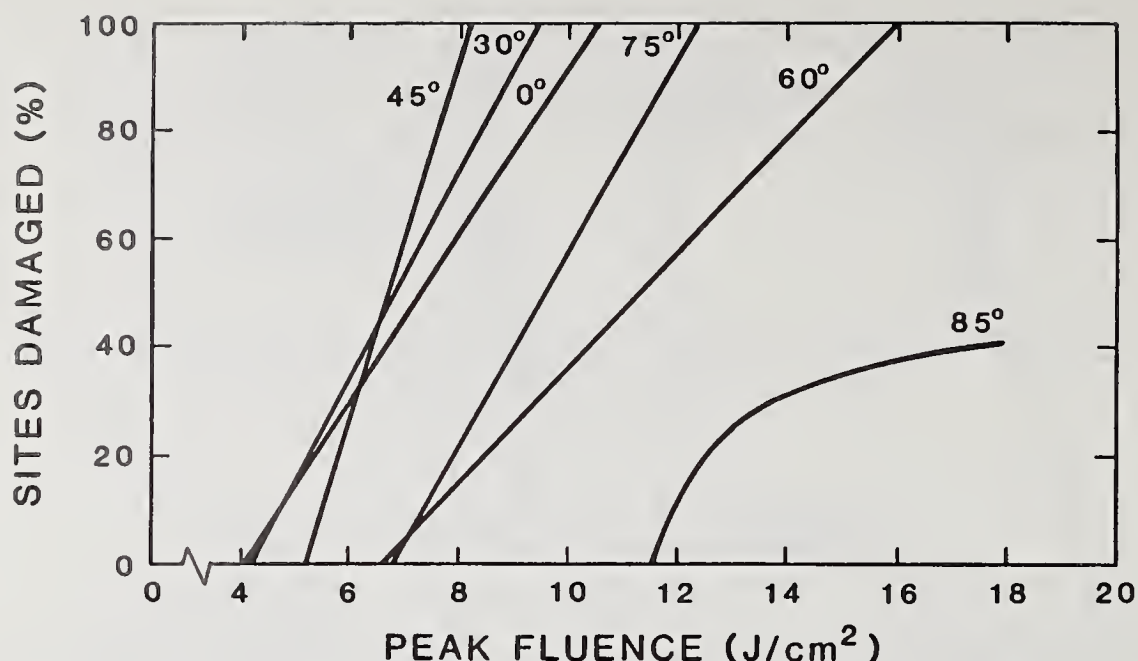
Figure 4. Angle dependence of multiple-shot damage thresholds summarized from test results given in figure 3.

5.   Discussion

It is informative to compare the angular dependence of the damage thresholds against the predictions of several possible physical models. One obvious model is that the threshold is determined by the laser fluence incident on the outer surface of the reflector. Because the beam footprint becomes elongated as $1/\cos\theta$, the fluence at the surface is diluted by the same $1/\cos\theta$ factor. Therefore, in terms of the laser fluence measured normal to the incident beam, which is the value cited when measuring damage thresholds, this model would predict that the threshold should increase as $1/\cos\theta$. The second and third models predict that damage resistance is inversely proportional to some power of the peak SW electric fields in the high-index layers. In one case, the fields were computed for the case of a 100% S-plane polarized incident beam. In the other, the fields were computed as if there were a 100% conversion of the beam to P-polarization.

In figure 5, the angular dependence of the measured damage thresholds, normalized to the average result for 0° incidence, is compared to the predictions of the three models considered. Clearly, at large angles the measured damage thresholds fell far below the model predictions for both the $1/\cos\theta$ dilution and the S-polarized peak field-squared which assumes linear absorption. For 85° incidence, for example, the damage threshold was only 2.5 times larger than at normal incidence. However, the P-polarized peak-field-squared model underestimated the thresholds. It is worth citing a similar result obtained at the U.K. Rutherford Appleton Laboratories for reflectors designed for S-polarized laser radiation at 248 nm using ThF_4/cryolite films [8]. In that case, the single-shot (15-20 ns pulses) threshold of ~15 J/cm^2 at 86° exceeded that for 0° incidence, ~3 J/cm^2, by only a factor of five.

Unfortunately, we have insufficient data by which to uniquely determine the cause of the unexpectedly low damage thresholds at angles of incidence greater than 30°. We have, however, speculated on a number of possible mechanisms. We list the most plausible ones for further consideration.

1.   Larger surface areas exposed at large angles result in more coating defects being irradiated, thereby increasing the probability of damage.

2.   Reflectors designed for large angles of incidence are composed of thicker films which have lower thresholds (more defects).

3.   Nonuniform SW electric fields may occur near coating defects, and the near-field diffraction field maxima directly behind opaque coating defects could be very large.

4.   Scattered light trapped within the layers by total internal reflection could either increase the effective film absorption or be channeled to absorbing coating defects. See figure 6.
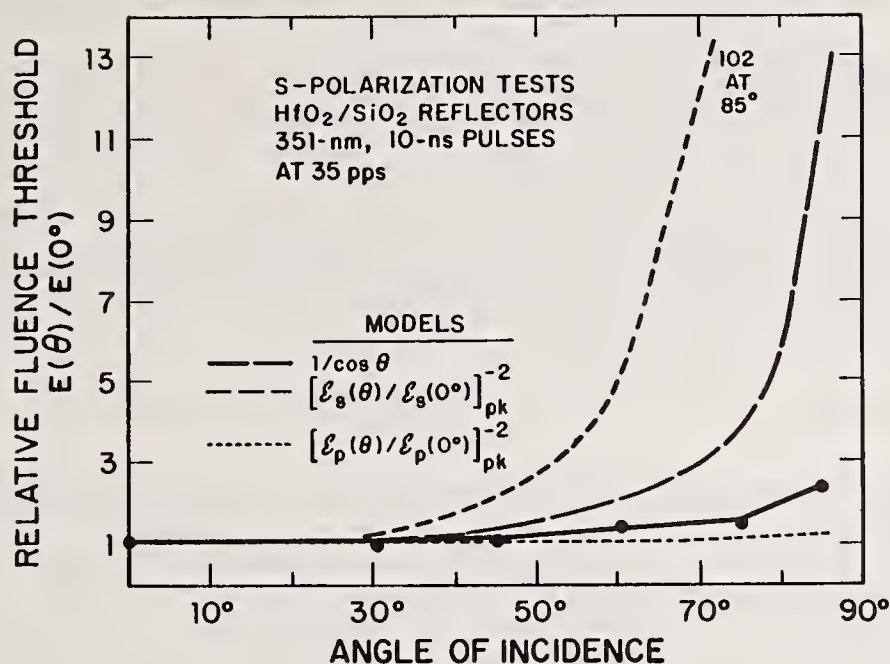
Figure 5. Measured damage thresholds normalized to the average result for normal incidence are compared to the predictions of three models: (1) $1/\cos\theta$ dilution of the fluence at the reflector surface, (2) inverse of the normalized peak electric-field-squared in the top HfO_2 layer for S-polarized light, and (3) for P-polarization.
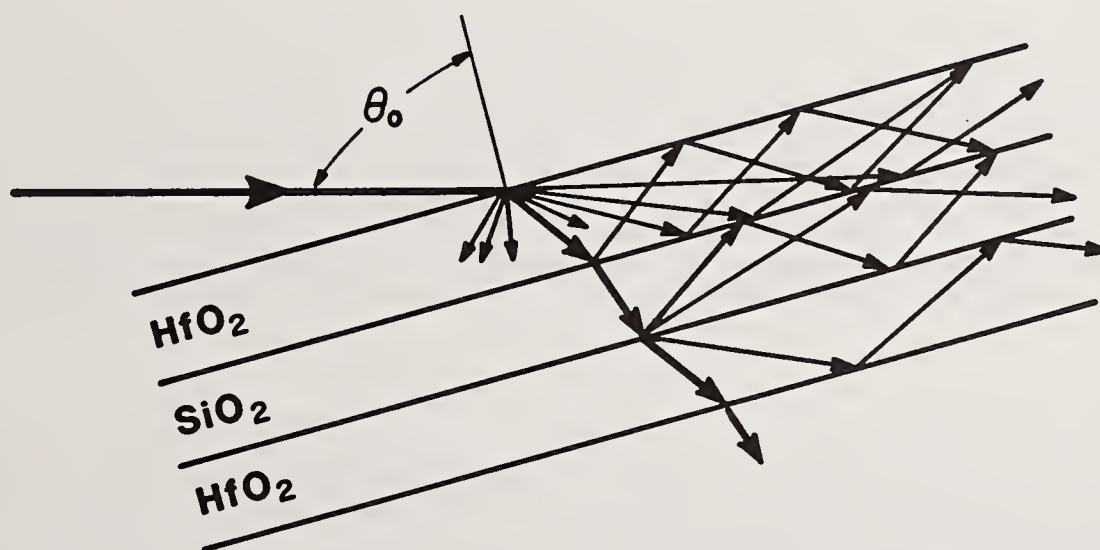
Figure 6. One physical model that may explain the anomalously low damage thresholds at large incidence angles: Scattered light, trapped in the layers by total internal reflection, could either sufficiently raise the effective absorption or channel radiation to absorbing defects.

349

5. Pinholes in the coatings could act like light tunnels. At large angles, incident radiation could be funneled into the interior more or less independent of the angle of incidence.

6. The angular dependence of damage may have been only a measure of film defects at the air-film interface. Protruding defects could have interacted with the SW electric field maxima in air, $2E_o$, which are much larger than those in the interior of the multilayer [9]. With increasing angle, the location of the SW peaks moves away from the air-film interface.

7. The polarization purity of the incident beam ($I_S/I_p \geqq 1000$) might have been degraded upon scattering within the multilayers or rotated by coating birefringence. Depolarization of scattered light from multilayers has been observed previously [10]. (Almost total depolarization ($I_S/I_p = 1$) of the entire beam would have been necessary to have produced the unexpectedly low thresholds.)

8. The coating depositions for the 60°-, 75°-, and 85°-reflectors may have produced more absorbing films.

Although we have no supporting evidence to absolutely distinguish between the above speculations, we suspect that items 1 to 5 are more plausible than items 6 to 8. Further clarification will require auxiliary tests, e.g., calorimetric measurements of absorption which could detect any unexpected (spatially averaged) increases in reflector absorption at large angles due, for example, to trapped scattered light. If film scatter is responsible for restricted thresholds at large angles, reflectors produced by coating deposition processes that produce films with less scatter should be tested. These processes include rf sputtering, ion-beam sputtering, and ion-assisted electron-beam deposition. According to S. Lu, however, the measured absorption of ion-beam-deposited reflectors for an S-polarized 633-nm beam was the same at 0° and 45° [11].

The experimental data as shown in figures 3 and 4 exhibited a second feature that is not understood. For angles of incidence from 0° to 45°, the slopes (% damage/energy fluence) increased as expected, since the spot area was increasing and more defects were irradiated. As first revealed by Foltyn [12], increased irradiation area should result in steeper slopes, but the threshold (0/10 sites damage) should remain essentially the same. However, for incidence angles from 45° to 85°, the present experimental data produced slopes which declined with increasing angle. There is an opportunity for some clever detective work to explain this.

6. Conclusions

The damage resistance of HfO_2/SiO_2 multilayer dielectric reflectors was measured as a function of angle of incidence from 0° to 85° using S-polarized, 10-ns, 351-nm XeF laser pulses at 35 pps. At large angles of incidence, we did not observe the anticipated large increases in damage threshold predicted theoretically on the basis of either spatial dilution ($1/\cos\theta$) of the intensity at the reflector surface or SW electric fields. For example, the threshold for a reflector designed and tested at 85° was only a factor of 2.5 larger than that of normal-incidence reflectors tested at 0°. The absence of correlation with the peak SW fields is contrary to previous experience with non-quarter-wave reflector designs at UV wavelengths. We considered several possible mechanisms to explain this discrepancy, but further testing is necessary to prove whether any of these are responsible.

7. References

[1] Newnam, B. E. Capabilities of broadly tunable free-electron lasers. New Lasers for Analytical and Industrial Chemistry, Proc. SPIE 461; 1984. 90-97.

[2] Goldstein, I.; Bua, D.; Horrigan, F. A. Pulsed laser damage to uncoated metallic reflectors. Nat. Bur. Stand. (U. S.) Spec. Publ. 435; 1976. 41-48.

[3] Figueira, J. F.; Thomas, S. J.; Harrison, R. F. Damage thresholds to metal mirrors by short-pulse CO_2 laser radiation. Nat. Bur. Stand. (U.S.) Spec. Publ. 638; 1983. 229-238; also, IEEE J. Quantum Electron. QE-18, 1381-1386 (1982).

[4] Decker, D. L.; Porteus, J. O. Laser damage to metal mirrors at nonnormal incidence. ibid. 239-245.

[5] Newnam, B. E.; Foltyn, S. R.; Jolin, L. J.; Carniglia, C. K. Multiple-shot ultraviolet laser damage resistance of nonquarterwave reflector designs for 248 nm. Nat. Bur. Stand. (U.S.) Spec. Publ. 638; 1983. 363-371.

[6]   Foltyn, S. R.; Jolin, L. J.; Newnam, B. E.   Progress in ultraviolet damage testing at Los Alamos.   Nat. Bur. Stand. (U.S.) Spec. Publ. 669; 1984.   266-273.

[7]   Carniglia, C. K.; Hart, T. T.; Rainer, F.; Staggs, M. C.   Recent damage results on high reflector coatings at 355 nm.   Nat. Bur. Stand. (U.S.) Spec. Publ. 688; 1985.   347-353.

[8]   M. Lunt, Technical Optics, Ltd., private communication on damage test results of their reflectors as reported to him by F. O'Neill of Rutherford Appleton Laboratory, United Kingdom.

[9]   P. A. Temple, Naval Weapons Laboratory, private communication; also Total internal reflection microscopy: a surface inspection technique.   Appl. Opt. 20, 2656 (1981).

[10]   J. O. Porteus, Naval Weapons Laboratory, private communication.

[11]   S. Lu, Litton Industries, private communication.

[12]   Foltyn, S. R.   Spotsize effects in laser damage testing.   Nat. Bur. Stand. (U.S.) Spec. Publ. 669; 1984.   368-379.

SURVEY OF LASER DAMAGE THRESHOLDS FOR HIGH REFLECTOR

FILMS AT 1.315 MICRONS

Terrence F. Deaton
Frank J. Seiler Research Laboratory
United States Air Force Academy
Colorado Springs, CO 80840-6528

ABSTRACT

We present the results of a survey of laser-induced damage measurements for high-reflector films at 1.315 microns. A pulsed atomic iodine laser with a maximum output energy of 5 Joules in a pulsewidth of approximately 8 microseconds was used, with a spot diameter at the sample of about 2.8 mm. All the thresholds reported are for single shot per site illumination. The pulse energy, temporal profile, and spatial profile information were monitored for each shot.

The samples tested are part of an extensive survey of currently available coatings from several vendors and represent a wide variety of materials and designs. Each coating was prepared on both silicon and molydbenum substrates. Damage thresholds were defined by the presence of surface pitting visible under Nomarski microscopy. Threshold fluence levels ranged from 10 J/cm^2 to 150 J/cm^2 with uncertainties of typically $\pm$ 15%.

1. Introduction

Recent interest in the applicability of high energy chemically driven atomic iodine lasers for weapons applications has led to a survey of the current state of the art of optical coatings for the laser wavelength of 1315 nm (ref. 1). This survey was performed by the Air Force Weapons Laboratory and encompasses a wide variety of materials and designs. In this paper I will present damage data for several high reflector coatings from this survey.

2. Laser Damage Experiment

The laser source used for this work is a pulsed photodissociation atomic iodine laser currently on loan to the Frank J. Seiler Research Laboratory from Sandia National Laboratories in Albuquerque. It has been significantly modified from its original configuration at Sandia (refs. 2,3) by the conversion of one of the original preamplifier stages into a long-pulse oscillator. The laser head is a quartz tube of 22 mm ID and 1.22 meters length. The tube is filled to a pressure of approximately 50 Torr with n-heptafluoropropyl iodide (C_3F_7I) with no broadening gas being used. The gas tube is surrounded by four linear high-pressure Xenon flashlamps connected in two parallel circuits. Each pair of lamps is driven by a capacitance of 4 Mfd charged to a maximum voltage of 38 KV. In the experiment the output energy of the laser is controlled by varying the voltage and/or the fill pressure.

The laser is operated as a single-shot device, with the gas tube evacuated after each shot, and in a gain-switched mode, with the pulse length determined by the flashlamp pulse-forming network. For this work the pulse length (FWHM) is approximately 8 microseconds. A sample temporal profile obtained with an ITT vacuum photodiode is shown in figure 1. The optical resonator consists of a total reflector with 20 m radius of curvature and a flat, 30% reflective output coupler. This geometry results in highly multimode beam, which is ultimately focussed to a waist diameter many times the diffraction limit. The spatial profile at the waist proved to be a relatively smoothly varying "blur," however.

The optical layout for the measurements is shown in figure 2. The output beam from the laser is focussed onto the sample with lens of focal length 50 cm. A fused silica beamsplitter after the lens diverts some of the energy to a photodiode for temporal profile measurements and to an aperture plate for spatial profile characterization. The spatial profile of the beam at the sample was determined by measuring the transmission through a series of apertures ranging in size
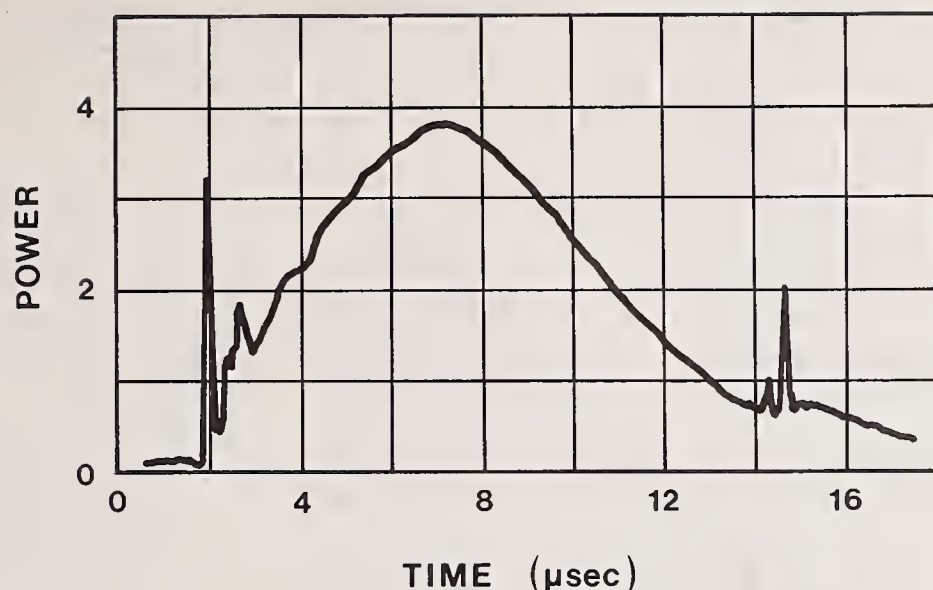
Figure 1. Temporal profile of atomic iodine laser
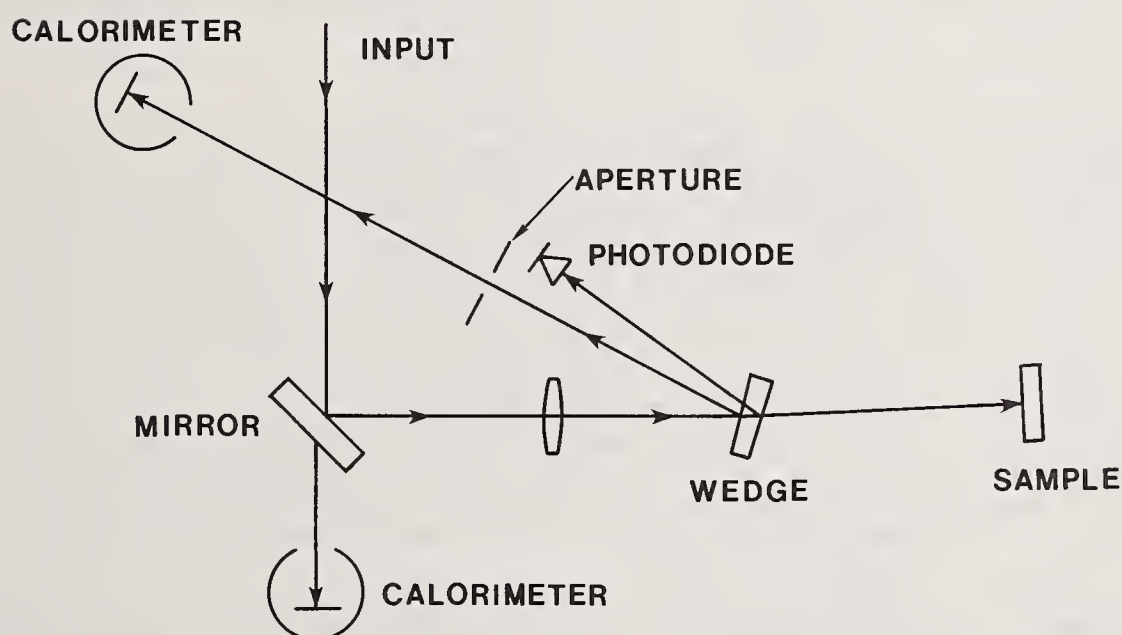
Figure 2. Optical layout for laser damage experiment

down to 0.25 mm diameter. The transmission is plotted against aperture diameter in figure 3. The solid line in the figure represents the expected results for a gaussian profile with a $1/e^2$ diameter of 2.8 mm, and it provides a reasonably good fit to the actual transmission data.

3. Results and Discussion

All the thresholds reported are for single shot per site illumination. Typically five shots at a given fluence were done. The occurrence of damage was determined by either white light light scattering or Nomarski microscopy. The microscopy was necessarily performed after a series of shots and thus was employed only for those sites which were apparently near the threshold level. The reported threshold is the average of the lowest fluence at which damage always occurred and the highest at which damage never occurred in the five-shot sequence. The uncertainty values reported in the table approximate the range between those two levels plus the uncertainty of the peak fluence for a given shot as described above.
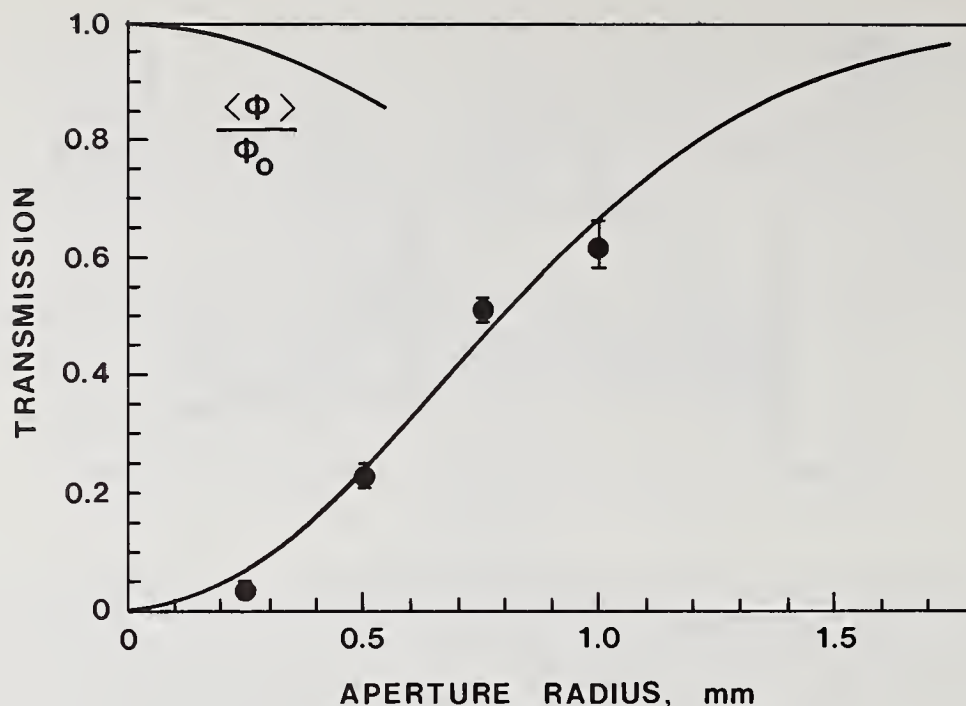
Figure 3. Aperture transmission for beam, taken at waist produced by lens of 50 cm focal length

The samples tested are all high-reflector film designs prepared by various vendors on substrates provided by the Air Force Weapons Laboratory, and they represent a small portion of an extensive industry-wide survey effort undertaken a few years ago. Each coating was prepared on both molybdenum and silicon substrates. The substrates as well as the finished samples were characterized at the University of Dayton Research Institute facility at AFWL (ref. 1). The fractional power absorbed at a wavelength of 1.319 microns was determined for each mirror in the set, and the values ranged from a low of 1.7×10^{-4} for the OCLI $(SiO_2/TiO_2)^8$ coating on silicon to a high of 4.4×10^{-3} for a $(PbF_2/ZnSe)^4$ coating prepared by Laser Power Optics on a molybdenum substrate. The rms roughness of the surfaces were determined by a total integrated scattering measurement at 633 nm both before and after coating (ref. 4). The silicon substrates were determined to have an rms roughness of approximately 10 Angstroms, with the coated mirrors having roughness values ranging up to 50 Angstroms. The molybdenum substrates typically had an rms roughness of approximately 35 Angstroms, with the coating rms roughness varying 40 and 70 Angstroms (ref. 1). The complete tabulation of data is not reproduced in this report.

As shown in table 1, the observed damage thresholds for this set vary over quite a wide range, with the titania/silica coatings typically at the highest values and the various lead fluoride designs, the lowest. The films prepared on silicon substrates systematically showed higher thresholds than those on molybdenum substrates, although the difference is most cases slight. In virtually all cases the threshold level damage consisted of a few randomly distributed micro-pits apparently originating in the first few layers of the coating.

4. Acknowledgements

I would like to thank Captain Mickey MacLin and Lieutenant Patricia Morse of the Air Force Weapons Laboratory for supplying the samples as well as financial support for this work. I would also like to thank Mr. Lee Burton for his assistance with the measurements.

Table 1. Iodine Laser Damage Survey

VENDOR	COATING DESIGN	SUBSTRATE	THRESHOLD (J/cm^2)
Laser Power Optics	$(PbF_2/ZnS)^4$	Molybdenum	27 ± 7
Laser Power Optics	$(PbF_2/ZnS)^4$	Silicon	17 ± 3
Laser Power Optics	$(ThF_4/ZnS)^4$	Molybdenum	74 ± 10
Laser Power Optics	$(ThF_4/ZnS)^4$	Silicon	85 ± 12
Laser Power Optics	$(PbF_2/ZnSe)^4$	Molybdenum	5 ± 2
Laser Power Optics	$(PbF_2/ZnSe)^4$	Silicon	11 ± 3
Laser Power Optics	$(ThF_4/ZnSe)^4$	Molybdenum	9 ± 2
Laser Power Optics	$(ThF_4/ZnSe)^4$	Silicon	13 ± 3
OCLI	$(SiO_2/TiO_2)^8$	Molybdenum	18 ± 3
OCLI	$(SiO_2/TiO_2)^8$	Silicon	24 ± 7
OCLI	$(ZnS/ThF_4)^8$	Molybdenum	117 ± 23
OCLI	$(ZnS/ThF_4)^8$	Silicon	54 ± 8
Spectra Physics	$(ZrO_2/SiO_2)28$ layers	Molybdenum	47 ± 10
Spectra Physics	$(ZrO_2/SiO_2)28$ layers	Silicon	55 ± 8
Spectra Physics	$(TiO_2/SiO_2)16$ layers	Molybdenum	117 ± 17
Spectra Physics	$(TiO_2/SiO_2)16$ layers	Silicon	32 ± 5
Northrop	$(ThF_4/ZnS)^4$	Molybdenum	92 ± 14
Northrop	$(ThF_4/ZnS)^4$	Silicon	70 ± 10
Northrop	$(Al_2O_3/HfO_2)^5$	Molybdenum	35 ± 7
Northrop	$(Al_2O_3/HfO_2)^5$	Silicon	35 ± 5
Litton	$Al(LH)^7LL$ Run #2	Molybdenum	117 ± 17
Litton	$Al(LH)^7LL$ Run #2	Silicon	80 ± 12
Litton	$Ti(LH)^{10}LL$ Run #1	Molybdenum	50 ± 8
Litton	$Ti(LH)^{10}LL$ Run #1	Silicon	50 ± 8
Coherent	(G1777)	Molybdenum	95 ± 15
Coherent	(G1777)	Silicon	144 ± 20
Coherent	(G1752)	Molybdenum	40 ± 8
Coherent	(G1752)	Silicon	44 ± 6

5. References

1. Detrio, J.A.; Fernelius, N. C.; Harris, R. J.; Walsh, D. A. Optical Characterization of IR Transmitting and Laser Window Materials. Semiannual Report No. 2, UDR-TR-81-76, University of Dayton Research Institute; Sep 1981.

2. Fisk, G. A.; Gusinow, M. A.; Hays, A. K.; Padrick, T. D.; Palmer, R. E.; Rice, J. K.; Riley, M. E.; Truby, F. K. The Atomic Iodine Laser. Technical Report SAND78-1071, Sandia National Laboratories; May 1978.

3. Jones, E. D.; Palmer, M. A.; Franklin, F. R. Subnanosecond high-pressure Iodine Photodissociation Laser Oscillator. Opt. Quant. Electron. 8:231; 1976.

4. Detrio, J. A. Proceedings SPIE, 276:136-9; 1981.

Scanning Electron Microscopy Studies of Laser Damage Initiating
Defects in ZnSe/ThF$_4$ and SiH/SiO$_2$ Multilayer Coatings*

L. F. Johnson, E. J. Ashley, T. M. Donovan, J. B. Franck
R. W. Woolever, and R. Z. Dalbey

Michelson Laboratory, Physics Division
Naval Weapons Center, China Lake, California 93555

Scanning electron microscopy (SEM) was used to identify four distinct laser damage morphologies in ZnSe/ThF$_4$ multilayer mirrors. There were three types of defect-initiated damage morphologies. Oblong-shaped damage sites oriented perpendicular to the electric field vector of the laser were associated with particulates on or near the surface of the ZnSe/ThF$_4$ multilayers. Circular-shaped damage sites were initiated by particulates embedded beneath the top ZnSe layer. Selective laser damage at pinholes was identified as the third defect-initiated damage morphology. In addition to defect-initiated damage, stress-related damage was indicated by cracks near or within laser damage craters and erosion sites. Selective laser damage at nodular growth defects in SiH/SiO$_2$ multilayers was also observed using SEM. Samples with different numbers of nodules were prepared in-house using RF-diode, reactive sputtering. The low-defect mirror had the highest laser damage onset, and the mirror with the highest number of nodules had the lowest laser damage onset.

Key words: defect-initiated laser damage; laser damage; nodular growth defects; optical thin films; particulate impurities; pinholes; scanning Auger microscopy; scanning electron microscopy; SiH/SiO$_2$ multilayer mirrors; ZnSe/ThF$_4$ multilayer mirrors.

1. Introduction

One of the first steps toward the fabrication of laser-damage-resistant optical coatings is to identify the defects which initiate the damage. In addition, film properties which contribute to the damage susceptibility can be inferred from the laser damage morphologies. One unwanted property which can lead to inferior damage resistance is a high level of stress. Cracks in the coating near or within damage craters or within erosion patterns are an indication that high levels of stress existed in the film at those sites before laser damage. In all of the laser damage sites shown here, the laser was operated just above the fluence at which damage begins to occur. In other words, the laser was operated just above the onset of damage for each of the multilayers. When the laser is operated just above onset, selective sites associated with defects and sites associated with high levels of stress begin to fail. These sites show nonuniform, irregular damage morphologies. By performing careful beam scans, the spatial profiles of the lasers used in this study were determined to be Gaussian. The irregular, nonuniform shapes of the damage sites are the result of defects in the coatings, not irregularities in the spatial profiles of the laser beams.

Scanning electron microscopy (SEM) has been used to identify five laser damage morphologies in two different optical coatings. Summaries of each of the five damage morphologies are outlined here as an introduction.

1.1 (ZnSe/ThF$_4$)^5 Multilayers

Orientation effects: Oblong-shaped, selective damage sites inside a larger erosion pattern. The oblong sites are oriented perpendicular to the electric field vector of the laser and are initiated by particulates at the film surface.

Embedded particulates: Selective erosion around particulate impurities located under the outer ZnSe layer.

Pinhole defects: Selective laser damage initiated at pinhole defects.

Stress and thermal effects: Selective crater formation inside a larger erosion pattern. The craters exhibit stress-related cracking. Temperatures high enough to melt gold (1064°C) illustrate the extreme thermal conditions that the multilayer experiences during laser damage.

1.2 $(SiH/SiO_2)^5$ Multilayers

Nodular growth defects: Selective laser damage at nodular growth defects.

2. $(ZnSe/ThF_4)^5$ Multilayers

2.1 Fabrication of the ZnSe/ThF$_4$ Multilayer Mirrors

The ZnSe/ThF$_4$ multilayer mirrors are experimental coatings and were provided by Perkin-Elmer. The multilayers were evaporated onto molybdenum substrates overcoated with gold. The vapor stream was electrostatically filtered during the deposition in two of the three mirrors studied. Filtering the vapor stream reduced the number of particulates in the coatings.

2.2 Experimental Parameters for Laser Damage Studies

The ZnSe/ThF$_4$ multilayers were tuned for enhanced reflectivity at 3.8 µm. The HF/DF laser operating in the DF mode (3.8 µm) did not produce sufficiently high fluences to consistently damage each sample. For this reason, laser damage morphologies were produced using both the DF and the stronger HF (2.7 µm) lasing modes. The HF/DF laser had a $1/e^2$ spot size of 150 µm in almost all of these experiments. For one of the damage sites, the $1/e^2$ spot size was 500 µm. The pulse length is nominally 1 µs.

2.3 Orientation Effects

The most dramatic damage morphology in the ZnSe/ThF$_4$ films is the selective, oblong damage sites oriented perpendicular to the electric field of the laser. The oblong damage sites occur within a larger erosion pattern which is somewhat larger than the $1/e^2$ laser spot size of 150 µm. Figure 1 shows the results of rotating the sample in the laser beam. In all three orientations, the oblong sites are oriented perpendicular to the electric field of the laser.

The occurrence of these oblong sites was modulated by the density of particulates on the surfaces of the mirrors. In areas where a high density of particulates existed, this damage morphology frequently occurred. In areas where no particulates existed within the damage spot, this orientation effect did not occur.

The undamaged surfaces of three ZnSe/ThF$_4$ mirrors were examined using SEM (fig. 2). For samples A and B, the vapor stream was filtered during the coating process. Consequently, a low number of particulates appeared on the surfaces of samples A and B; sample C, unfiltered, produced many more particulates.

Fewer oblong damage sites were obtained on samples A and B than on sample C. On sample A, oblong sites were obtained only when two or more particulates were located within the laser spot. No oblong damage sites were obtained in particulate-free areas of sample A.

Different damage sites exhibit varying numbers of oblong sites within the larger erosion pattern (fig. 3). Again, the number of oblong craters that occur within a single erosion pattern may be modulated by the density of particulates.

Scanning Auger maps of the first damage site in figure 3 are shown in figure 4. The elongated shape of the erosion pattern is due to the tilt of the sample in the microscope. Light areas indicate regions of higher counts. The zinc and selenium maps show that the entire first layer of ZnSe was removed during the damage pulse. The thorium and fluorine maps confirm that the laser has eroded the top layer of ZnSe and exposed the underlying ThF$_4$ layer.

The oxygen map indicates that oxygen is associated with the ThF$_4$ layer. Knowing that ThF$_4$ is very hygroscopic and considering the oxygen map, the presence of water in the ThF$_4$ layer may be deduced.

The depth of the oblong crater is revealed in close-up scanning electron micrographs (fig. 5). The cratering has exposed at least an additional six layers (or three pair) of the ZnSe/ThF$_4$ stack.

The oblong-shaped craters may be due to an interference effect between the incident laser beam and the scattered waves from the surface particulates. All of the sites shown here were obtained with the incident laser beam at normal incidence. If the orientation effect is an interference phenomenon,

the shape of the craters should change as the angle of incidence of the laser beam is changed [1].[1] Similar orientation or ripple effects have been seen in bulk silicon [2-5] and other semiconductors [6].

2.4 Embedded Particulates

Selective erosion at embedded particulates is shown in the scanning electron micrographs on the left in figure 6. The laser spot for the damage site had a $1/e^2$ diameter of 500 µm. A micrograph of an embedded particulate appears on the right. An Auger depth profile, not shown here, indicates that the particulate is embedded beneath the ZnSe layer and is composed of calcium, carbon, and oxygen. This combination suggests that it is calcium carbonate ($CaCO_3$). The bulk ThF_4 may have been stored with a desiccant containing calcium carbonate.

2.5 Pinhole Defects

Pinhole defects were found to initiate selective laser damage (fig. 7). Figure 8 shows a pinhole before irradiation and another pinhole after laser damage. Pinholes are growth defects often associated with adherence problems. The melt pattern seen in figure 8 is caused by the poor thermal contact of the jagged pinhole edges.

2.6 Stress and Thermal Effects

The preceding laser damage morphologies dealt with defect-initiated damage. The fourth type of laser damage morphology in these ZnSe/ThF_4 multilayers shows effects of a high level of stress in the films. Figure 9 shows selective crater formation within a larger erosion pattern. The cracking at the edges of the crater indicates that the film was highly stressed at this site. The irregular shape of the erosion pattern also suggests a high level of stress.

An Auger line scan across the crater mid-line indicates that the 3-µm-size particle at the center of the crater is gold (fig. 10). A probable explanation is that the underlying gold layer melted and flowed up through the cracks in the ZnSe/ThF_4 stack. To melt the gold, the multilayer temperature had to reach 1064°C, illustrating the intense thermal conditions produced during the laser damage pulse.

3. (SiH/SiO$_2$)^5 Multilayers

3.1 Fabrication of the SiH/SiO$_2$ Multilayer Mirrors

The SiH/SiO_2 multilayers are in-house coatings made at the Naval Weapons Center. The multilayers were deposited using RF diode, reactive sputtering. A Randex Model 2400-6J sputter system with a 6-in. high-purity silicon target was used for both the SiO_2 and SiH layers. The target-to-substrate distance is 3.8 cm.

The SiH and SiO_2 in these multilayers are amorphous. Table 1 lists the deposition parameters for the multilayers shown in the cross sections. Table 1 also summarizes the deposition parameters for the mirrors in the laser damage tests.

The substrates in the cross sections of figures 11 and 12 are glass cover slips which are easily fractured. The partial pressure of H_2 during the deposition of the multilayer showing the nodular growth defect (fig. 11) was lower than the partial pressure of H_2 during the deposition of the nodule-free multilayer (fig. 12). For both cross sections, the deposition parameters for the SiO_2 layers were identical.

Mirror substrates for the laser damage tests were 1-inch-diameter 0.020-inch-thick silicon wafers with a standard polish on both sides. Mirror A had a low density of nodular growth defects and mirror B had a high density. The deposition parameters for the SiO_2 layers in both mirrors again were identical, whereas the forward powers for the SiH layers were changed. The forward power for the SiH layers was 500 W in the low-defect mirror and 250 W in the high-defect mirror.

3.2 Experimental Parameters for Laser Damage Studies

The (SiH/SiO_2)^5 multilayers were tuned for enhanced reflectivity at 2.7 µm. The in-band laser damage onset data were obtained with an HF/DF laser operating in the HF mode (2.7 µm). Out-of-band damage was obtained using a Nd:YAG laser at 1.06 µm. Selective laser damage at nodules was produced by operating the Nd:YAG just above onset. The Nd:YAG laser had a $1/e^2$ spot size of 50 µm and a pulse length of 10 ns.

---

[1]Numbers in brackets indicate the literature references at the end of the paper.

3.3 Nodular Growth Defects

A nodular growth defect in a SiH/SiO$_2$ multilayer is shown in figure 11. The SiH layers show columnar structure at this magnification (20,000X), whereas the SiO$_2$ layers do not. The nodule appears to originate at the third SiH layer and not at the substrate. This indicates that the nodules are not a result of particulates on the substrate and are not caused by improper cleaning of the substrate. Other cross sections, not shown here, of different multilayers clearly show the nodules originating in the SiH layers and not in the SiO$_2$ layers.

The top surface and a cross section of a "nodule-free" film are shown in figure 12. The film may not be entirely free of nodules but can be considered nodule-free in this discussion. As previously stated, the SiH layers for the nodule-free film were deposited using a higher partial pressure of H$_2$ than for the nodular film in figure 11. As can be seen in figures 11 and 12, the SiH layers have less columnar structure in the nodule-free film, whereas the SiH layers have more columnar structure in the nodular growth film. A possible conclusion is that the conditions which lead to increased columnar structure may also contribute to the occurrence of nodular growth defects. Table 2 lists some possible causes for nodular growth defects [7].

Unequal growth competition, the result of inadequate adatom mobility, can be relieved by heating the substrate during the film deposition. Careful attention must be paid to the possible loss of hydrogen from the SiH layers at elevated substrate temperatures [8,9]. Similarly, it is possible that the growing film will incorporate less hydrogen at elevated temperatures. In either case, loss of hydrogen due to excessive substrate heating during the deposition could cause the optical properties of the SiH films to change and ultimately deteriorate [10].

Table 1 indicates that the substrate bias was floating. According to Messier [11], a negative substrate bias is induced by using low total pressures of reactive gas mixtures (Ar + H$_2$ and Ar + O$_2$). The substrate bias was not measured in these depositions, but it is assumed that the pressures were low enough to induce a negative bias on the substrate. A negative substrate bias means that the substrate and growing film are bombarded by positive Ar ions. In principle, small defects are sputtered from the surface of the growing film by positive Ar-ion bombardment. The small defects are eliminated before growing into large growth defects.

Although further work needs to be done on the SiH to eliminate the nodular growth defects, the SiO$_2$ film has superior properties. The lack of columnar structure in the SiO$_2$ was previously noted (figs. 11 and 12). The x-ray photoemission spectroscopy data shown in figure 13 indicate that the SiO$_2$ is fully oxidized. The water band is absent in the Fourier transform infrared transmission spectrum shown in figure 14, indicating that very little water is present in the SiO$_2$ film. The position of the Si-O-Si stretching frequency at 1075 cm^{-1} is another indication that the SiO$_2$ is fully oxidized [12].

Out-of-band laser damage at a fluence just above onset was obtained on the SiH/SiO$_2$ multilayers using a Nd:YAG laser operating at 1.06 μm. SEM showed that selective laser damage occurred at nodular growth defects (fig. 15).

Two SiH/SiO$_2$ multilayers with different numbers of nodules were prepared as described in Table 1. SEM was used to determine the number of nodules per unit area using several fields of view. Figure 16 shows representative fields of view for the two mirrors. No nodules were found in the fields observed for the first multilayer, whereas about 5×10^7/cm^2 were observed for the second mirror. Although no nodules were observed in the fields for the first sample, the sample may not have been strictly nodule-free and should be considered a low-defect sample.

In-band laser damage using an HF laser was performed according to the method of Porteus and Seitel [13]. The onset data for the low- and high-defect mirrors are shown in figures 17 and 18, respectively. The HF laser at 2.7 μm had a pulse length of 1 μs. The spatial profile was near Gaussian with a 1/e^2 diameter of 150 μm. The test was performed using 1 pulse per site with a site separation of 0.5 mm. The site array was rectangular. A parameter which is a function of the uncertainty in the damage frequency is used to determine when an adequate number of pulses at a particular fluence has been taken. At low fluences and low damage frequencies, many more pulses are necessary than at high fluences and high damage frequencies. A total of 738 pulses were taken for the curves shown in figure 17, and a total of 1010 pulses were taken for the curves shown in figure 18.

At onset, the fluence was 0.27 arbitrary units for the low-defect mirror and 0.07 arbitrary units for the high-defect mirror. In other words, the low-defect mirror has superior damage resistance.

4. Conclusion

This study has identified two categories of failure of optical coatings under pulsed laser radiation. One mode of failure is defect-initiated damage caused by particulates, pinholes, and nodular-growth defects. The second category of failure involves local areas of high stress. Improvements in the laser damage resistance of optical coatings depend upon reducing the defects and the stress, while at the same time maintaining the desired optical properties.

Two examples were described in which the deposition processes were modified and the resulting defect densities were changed. The first example showed that electrostatically filtering the vapor stream lowered the density of particulates in the evaporated ZnSe/ThF$_4$ multilayers. In the second example, the density of nodules increased in the RF-diode-sputtered SiH/SiO$_2$ multilayers when the forward power for the SiH layers was decreased from 500 to 250 W. When low forward powers are used, the temperature of the growing film does not increase as rapidly as when high forward powers are used. This suggests that the increase in nodular growth was actually caused by a decrease in the temperature of the growing film. It may be possible to eliminate the nodular growth which occurs at low forward powers by using a substrate heater. Clearly, further work needs to be done to understand the relationship between the deposition parameters and the nodular growth in RF-diode-sputtered SiH films.

Table 1. Deposition Parameters for SiH/SiO$_2$ Multilayers.

SiH layers	Partial pressure of H$_2$, mTorr	Total pressure of H$_2$+Ar, mTorr	Forward power applied to target, W	Reflected power, W	Target bias, V	Substrate bias, V	Rate, Å/sec
Cross section A "nodule free"	1	7	250	4	1100	floating	1.8
Cross section B nodular growth defect	0.1	7	250	4	1100	floating	2.0
Mirror A low defect	0.15	11	500	4	1600	floating	4.8
Mirror B high defect	0.15	11	250	4	1100	floating	2.3

SiO$_2$ layers	Partial pressure of O$_2$, mTorr	Total pressure of O$_2$+Ar, mTorr	Forward power applied to target, W	Reflected power, W	Target bias, V	Substrate bias, V	Rate, Å/sec
Cross section A "nodule free"	0.2	11	500	4	1300	floating	1.6
Cross section B nodular growth defect	0.2	11	500	4	1300	floating	1.6
Mirror A low defect	0.2	11	500	4	1300	floating	1.6
Mirror B high defect	0.2	11	500	4	1300	floating	1.6

Table 2. Possible Causes of Nodular Growth Defects.

1. Unequal growth competition
   a. Low adatom mobility - the surface temperature of the growing film is too low to provide a narrow, highly peaked thermal distribution.
   b. Low substrate bombardment - insufficient local resputtering of small growth defects.
2. Coating material spatters
   a. Fluctuations in the power supply.
   b. Arcing due to the buildup of material between the target and the insulated target holder.
3. Microscopic dust particles sputtered from the inside of the coating chamber.
4. Substrate defects such as cleaning residues and polishing marks.

5. References

[1] Ledger, T. Private communication.

[2] Bordelon, M.; Walser, R. M.; Becker, M. F.; Jhee, Y-K. "A study of the prf dependence of the accumulation effect in multiple pulse laser damage of silicon," in Laser induced damage in optical materials: 1982, Bennett, H. E.; Guenther, A. H; Milam, D.; Newnam, B. E., ed. 1982 November 16-17; Boulder, CO. Nat. Bur. Stand. (U.S.) Spec. Publ. 669; 1984 January. Pp. 427-435.

[3] Becker, M. F.; Jhee, Y-K; Bordelon, M.; Walser, R. M. "Charged particle exoemission from silicon during multi-pulse laser induced damage," ibid. Pp. 415-426.

[4] Soileau, M. J.; Van Stryland, Eric W. "Ripple structures and enhanced absorption associated with ordered surface defects," ibid. Pp. 406-414.

[5] Walser, R. M.; Becker, M. F.; Sheng, D. Y. "Laser damage of crystalline silicon by multiple 1.06 μm picosecond pulses," in Laser induced damage in optical materials: 1981, Bennett, H. E.; Guenther, A. H.; Milam, D.; Newnam, B. E., ed. 1981 November 17-18; Boulder, CO. Nat. Bur. Stand. (U.S.) Spec. Publ. 638; 1983 September. Pp. 103-113.

[6] Mansour, N.; Reali, G.; Soileau, M. J. "Laser generated ripple patterns on intermediate band gap semiconductors," in Laser induced damage in optical materials: 1984, Bennett, H. E.; Guenther, A. H.; Milam, D.; Newnam, B. E., ed. 1984 October 15-17; Boulder, CO. Nat. Bur. Stand. (U.S.) in process.

[7] Guenther, Karl H. "Columnar and nodular growth of thin films," in Proceedings of SPIE: thin film technologies and special applications, Hunter, William R., ed. 1982 May 6-7, Arlington, VA. Proc. SPIE Vol 346; 1982. Pp. 9-18.

[8] Oguz, S.; Collins, R. W.; Paesler, M. A.; Paul, W. "Effects of partial evolution of H from a-Si:H on the infrared vibrational spectra and the photoluminescence," J. Non-Cryst. Solids 35 and 36; 231-236; 1980 January and February.

[9] Zanzucchi, P. J.; Wronski, C. R.; Carlson, D. E. "Optical and photoconductive properties of discharge-produced amorphous silicon," J. Appl. Phys. 48(12); 5227-5236; 1977 December.

[10] Ghosh, A. K.; McMahon, T.; Rock, E.; Wiesmann, H. "Optical and electrical properties of evaporated amorphous silicon with hydrogen," J. Appl. Phys. 50(5); 3407-3413; 1979 May.

[11] Ross, R. C.; Messier, R. "Microstructure and properties of rf-sputtered amorphous hydrogenated silicon films," J. Appl. Phys. 52(8); 5329-5339; 1981 August.

[12] Lehman, A.; Schumann, L.; Hübner, K. "Optical phonons in amorphous silicon oxides (II)," Phys. Status Solidi B 121(2); 505-511; 1984 February.

[13] Porteus, J. O.; Seitel, S. C. "Absolute onset of optical surface damage using distributed defect ensembles," Appl. Opt. 23(21); 3796-3805; 1984 November 1.

L_____J 100 um
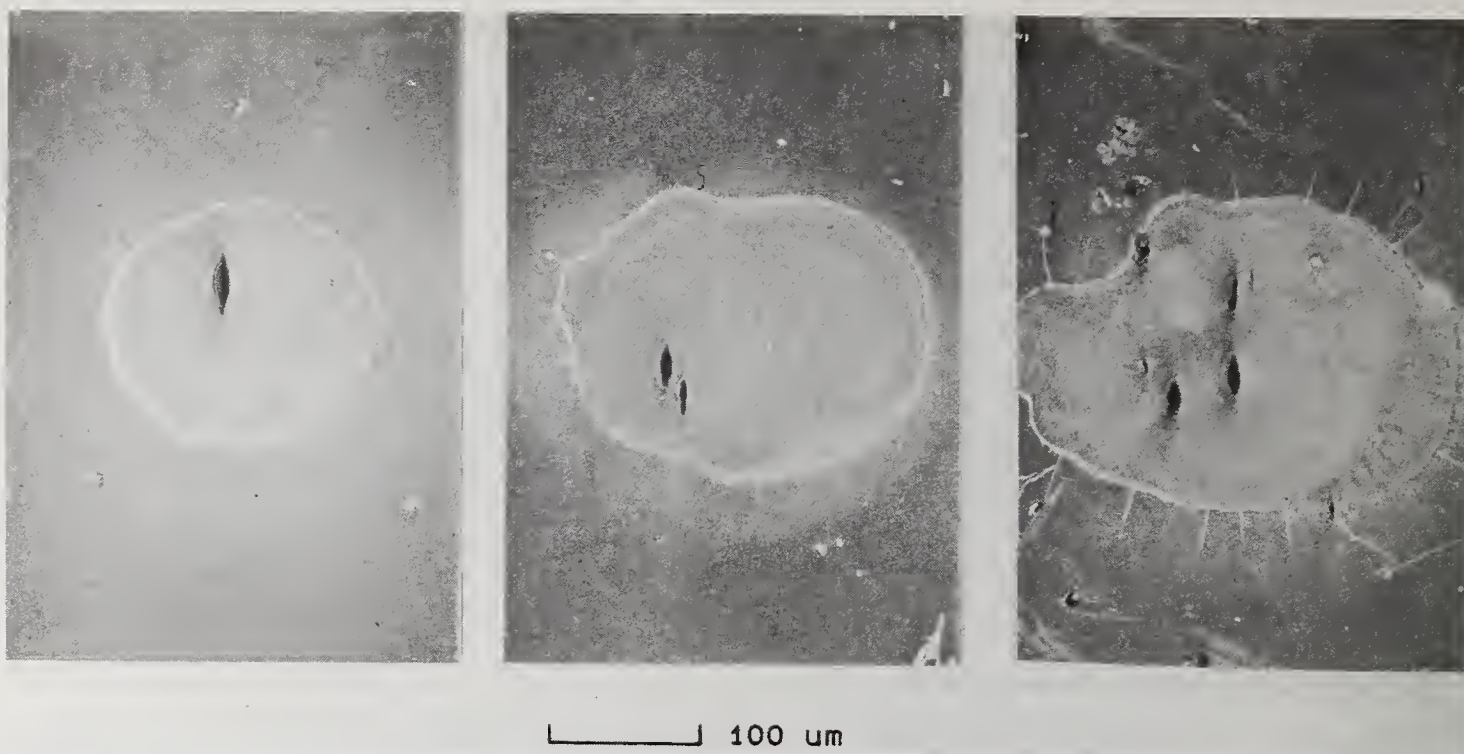
Figure 3.   Scanning electron micrographs (250X) of three laser damage sites.   The different
numbers of oblong craters within the larger erosion pattern suggest that the occurrence of
oblong craters is modulated by the density of particulates.

(a)   (b)

Figure 4.   Scanning electron micrograph (a) and scanning Auger maps (b) zinc, (c) selenium, (d)
thorium, (e) fluorine, and (f) oxygen (570X) of the first damage site shown in figure 3.
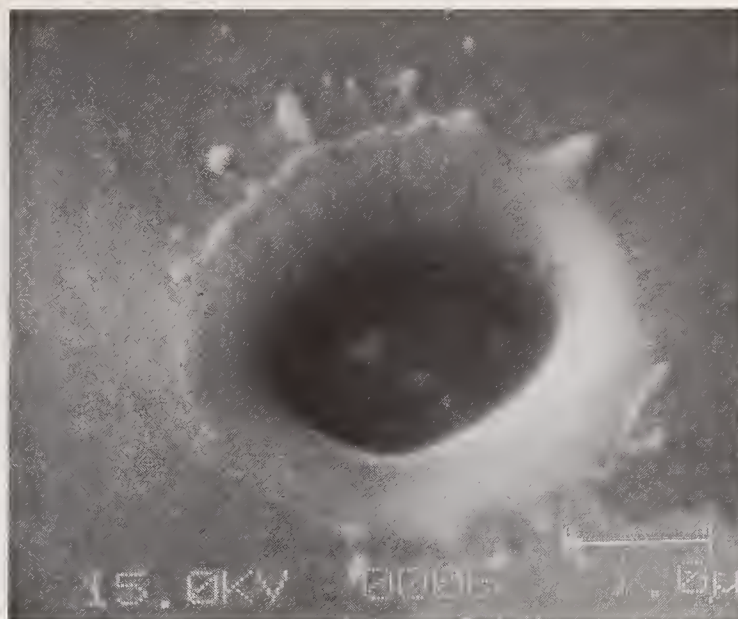
(a)   (b)

Figure 8.   (a) Scanning electron micrograph showing a pinhole before laser irradiation (24000X) and (b) another pinhole after laser damage (20000X).

⊢————————⊣ 100 um
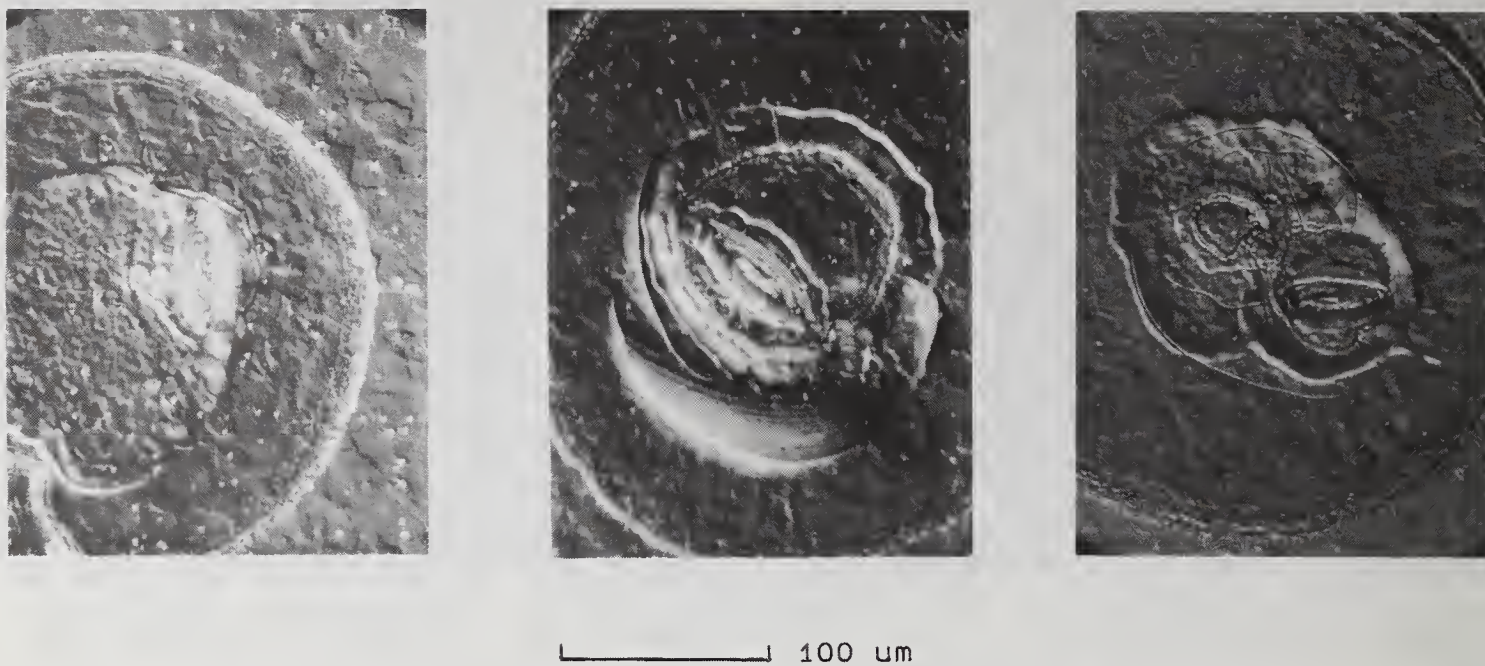
Figure 1. Normarski micrographs (360X) showing selective, oblong damage sites within a larger erosion pattern. The sample was rotated in the laser beam. In all three orientations, the oblong damage craters were oriented perpendicular to the electric field vector of the laser.

(a)   (b)   (c)

⊢————————⊣ 100 um
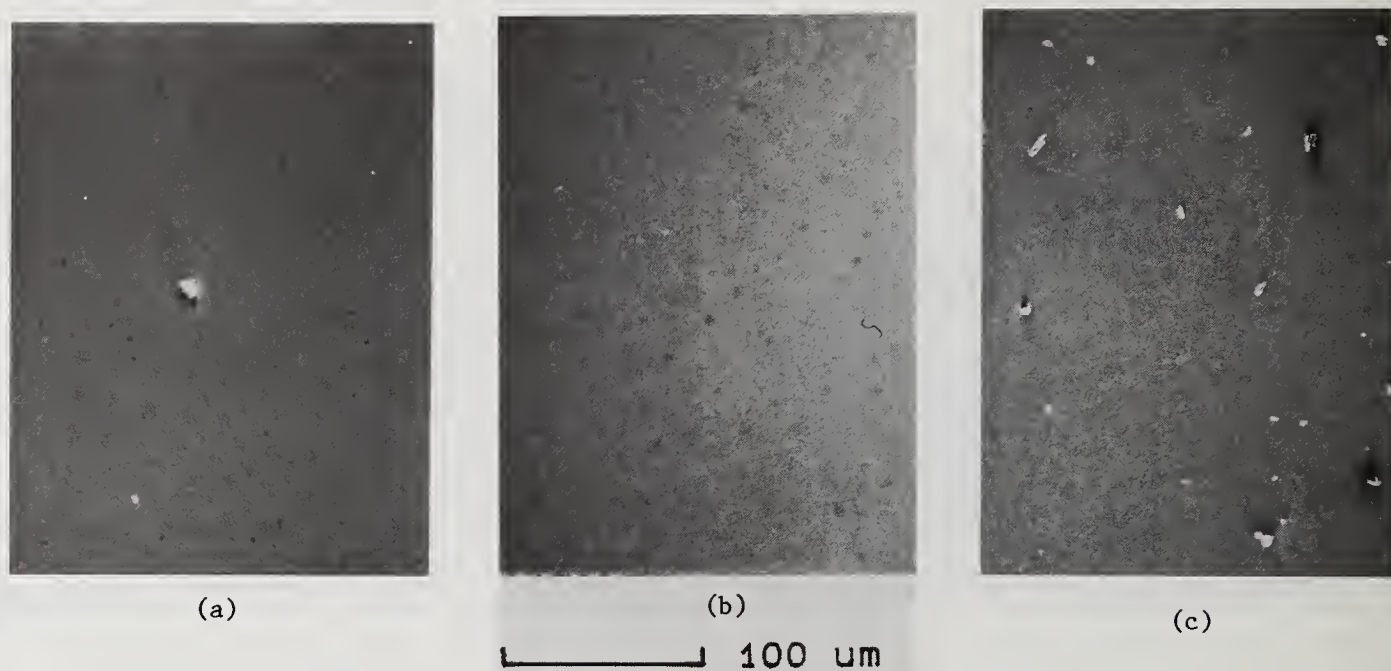
Figure 2. Scanning electron micrographs (250X) showing a low density of particulates on the filtered samples (a and b) and a high density of particulates on the unfiltered sample (c).

(c)
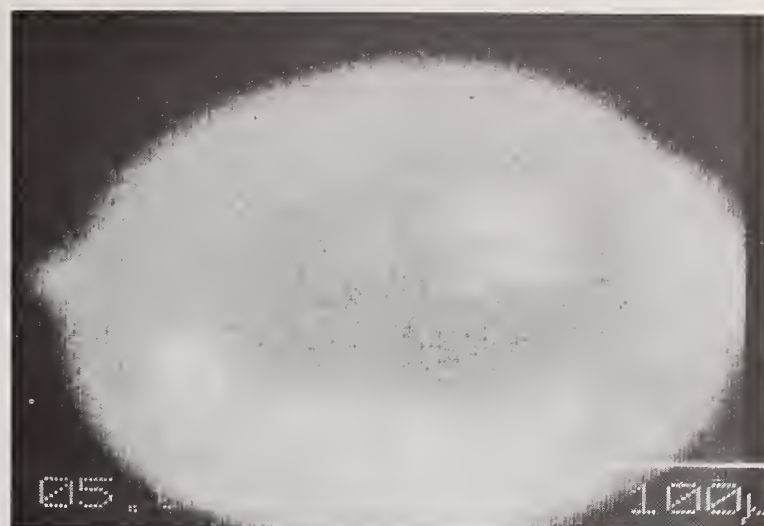
(d)
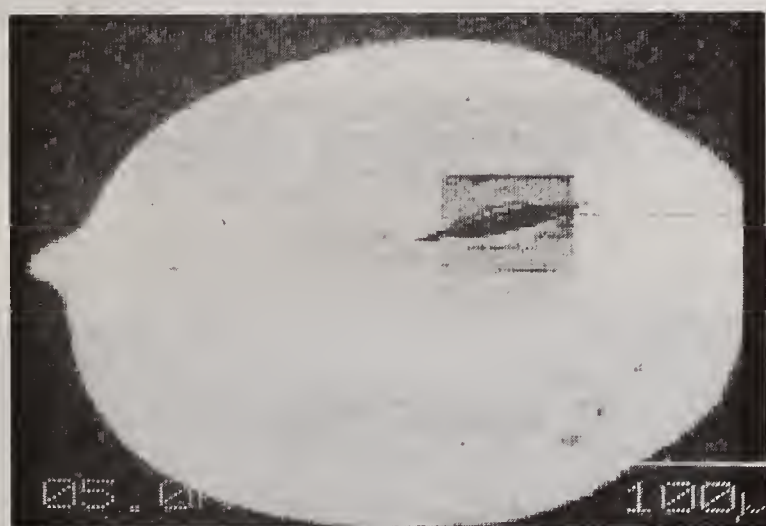
(e)
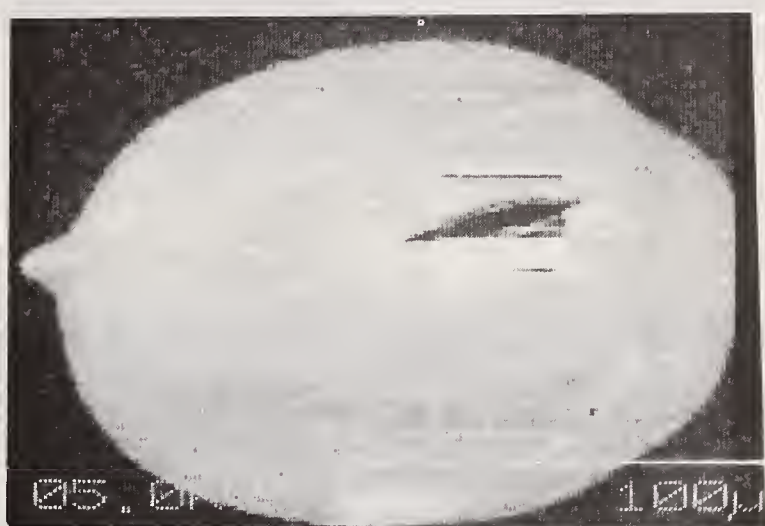
(f)

Figure 4. Contd.

(a)
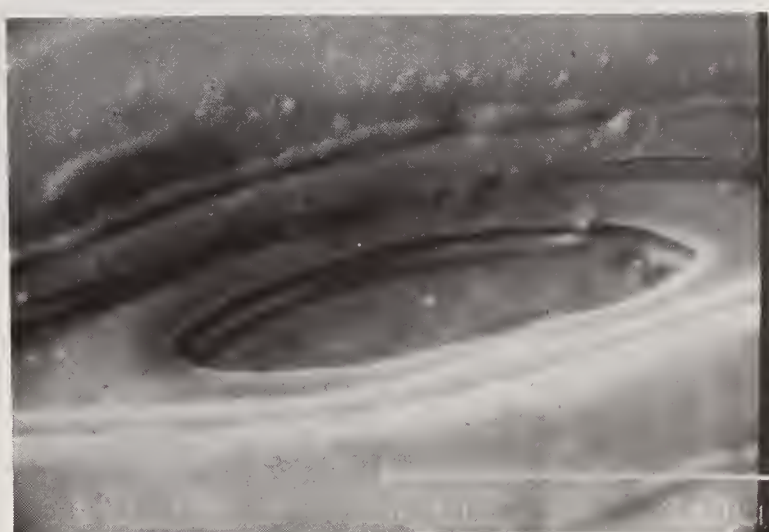
(b)

Figure 5. Scanning electron micrographs showing close-ups of the oblong damage crater in figure 4 (a) 2100X and (b)5300X.

(a)
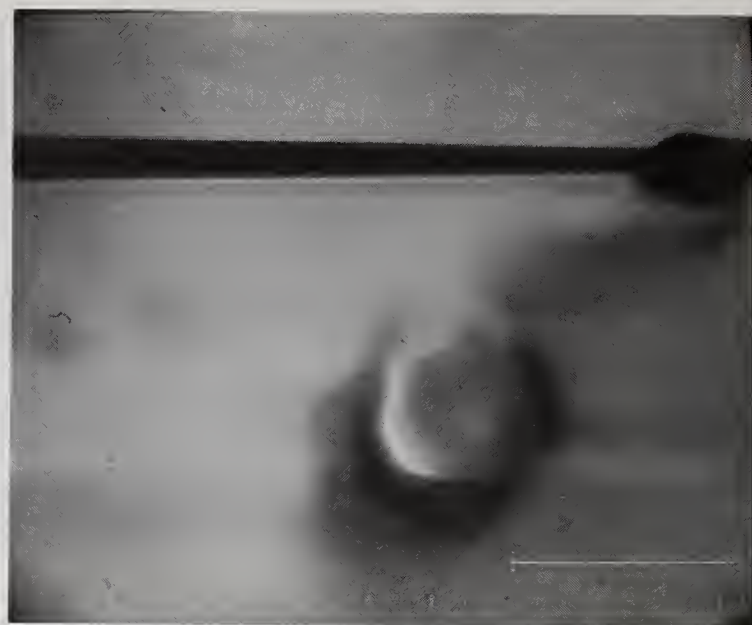
(b)

Figure 6.   (a) Scanning electron micrograph (120X) showing selective erosion around embedded particulates and (b) scanning electron micrograph (3100X) showing an embedded particulate that has not been damaged.

(a)
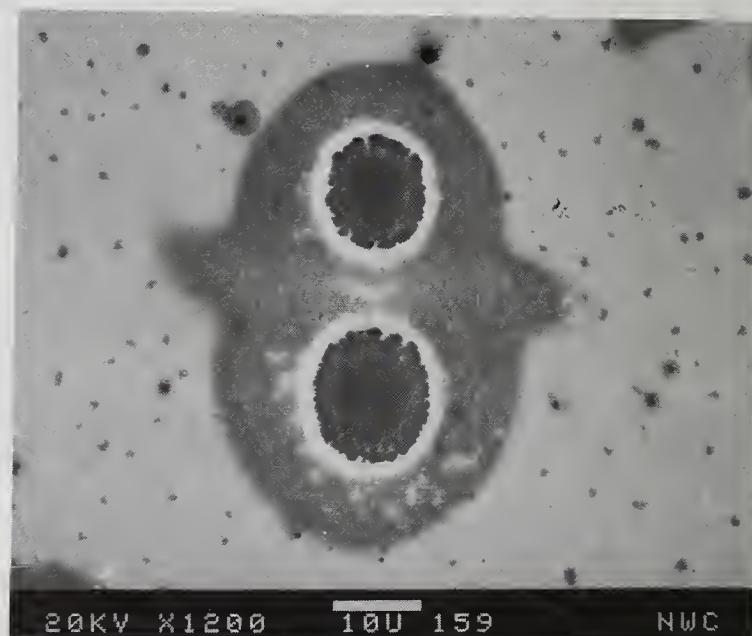
(b)

Figure 7.   Scanning electron micrographs of laser damage initiated by pinhole defects at (a) 250X and (b) 1200X.
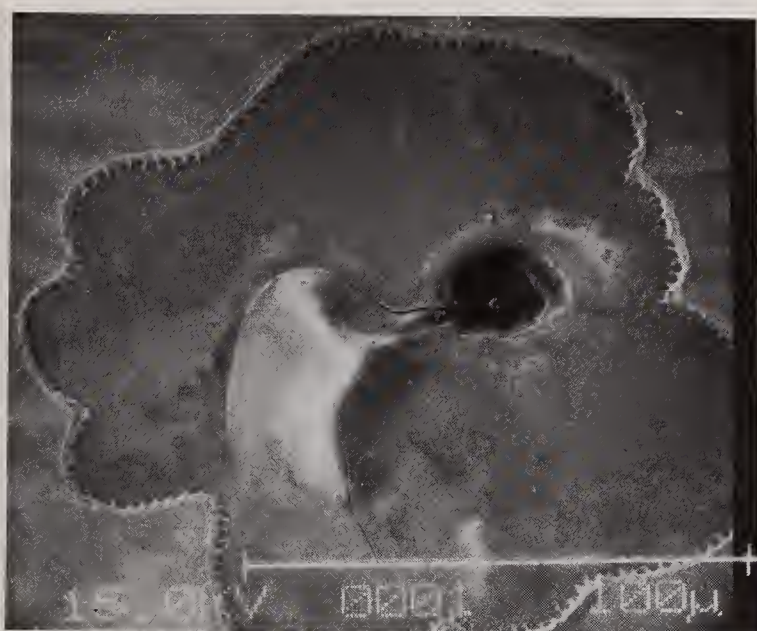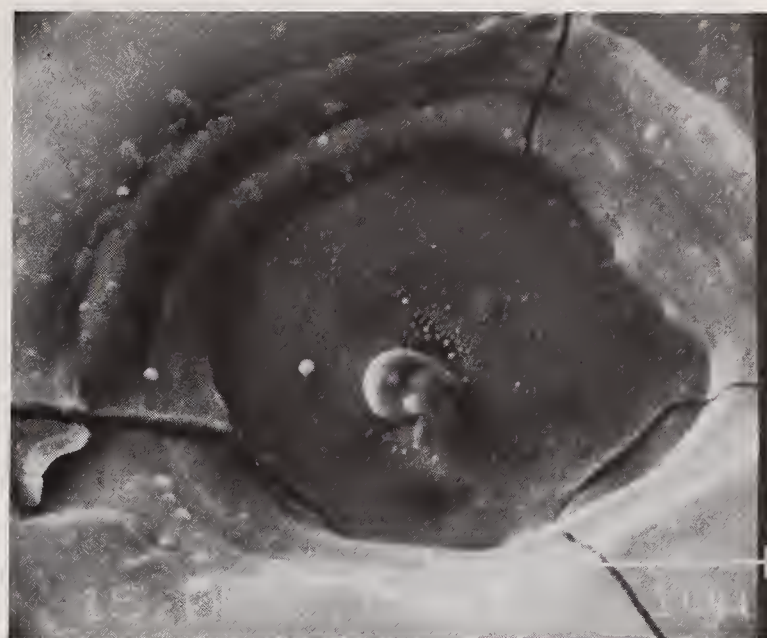
(a)   (b)

Figure 9. Scanning electron micrographs (a) 680X and (b) 4500X of a laser damage site showing selective crater formation within a larger erosion pattern. The site shows stress-related cracking and loss of adherence within the erosion pattern.
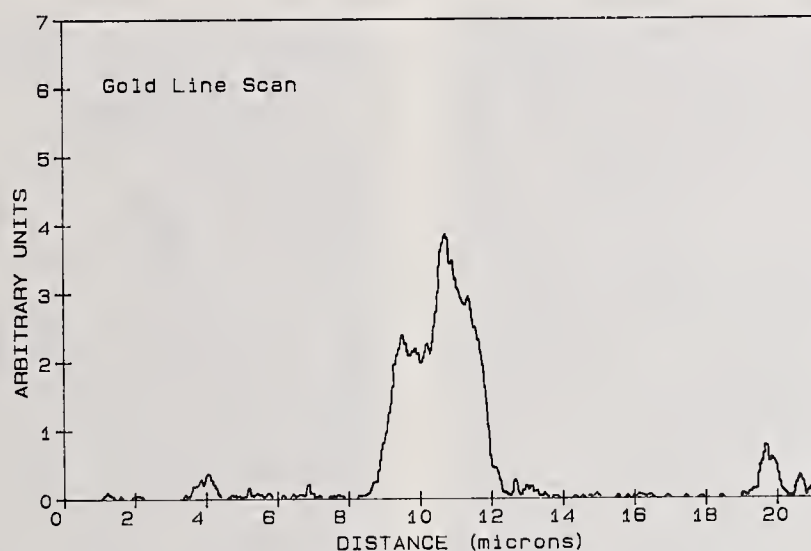
Figure 10. An Auger scan across the crater mid-line indicating that the 3-µm-size particle at the center of the crater in figure 9(b) is gold.

367

(a)
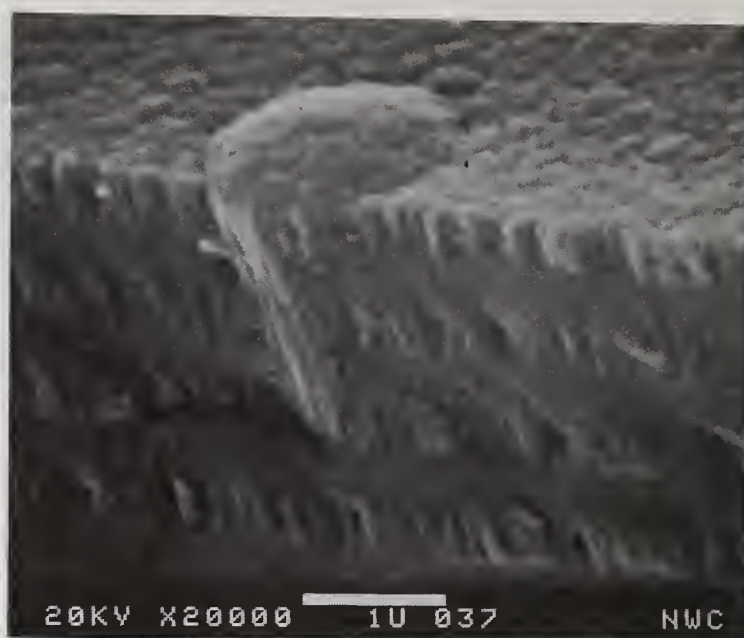
(b)

Figure 11. Scanning electron micrographs (a) 10000X and (b) 20000X showing a cross section of a nodular growth defect in a SiH/SiO$_2$ multilayer. The SiH layers show columnar structure whereas the SiO$_2$ layers do not.
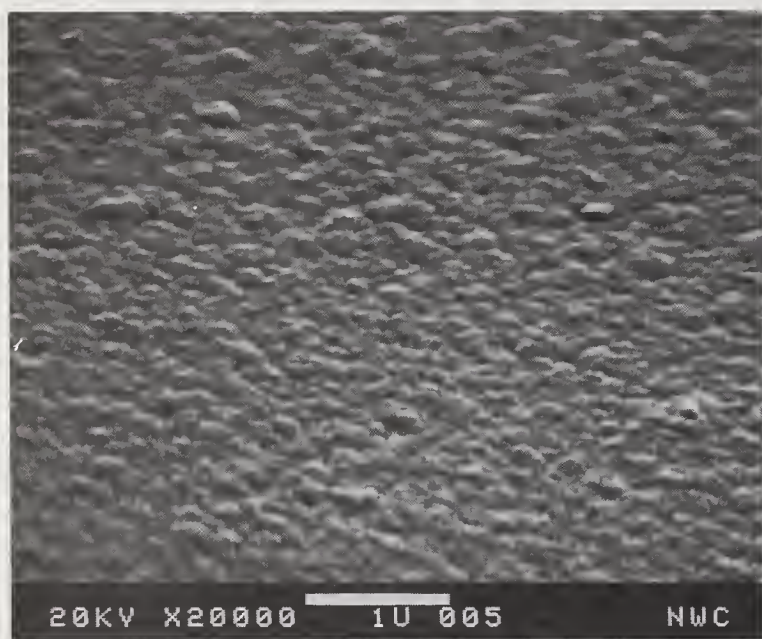
(a)
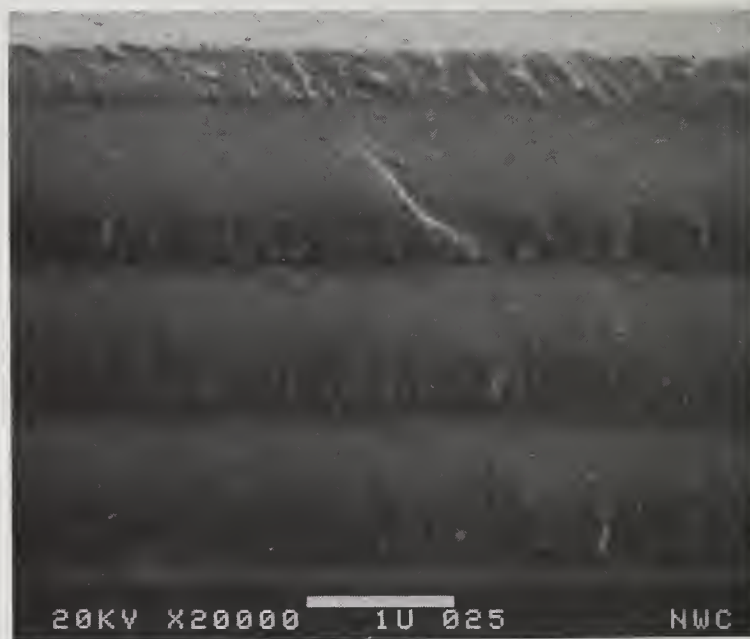
(b)

Figure 12. Scanning electron micrographs (20000X) showing (a) the surface and (b) a cross section of a nodule-free multilayer. The SiH layers have less columnar structure in this figure than in figure 11.
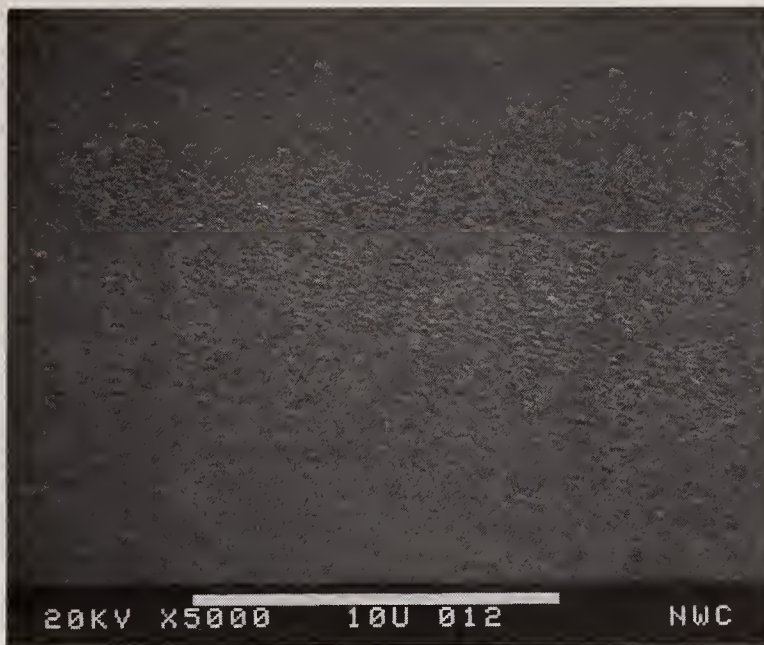
(a)

(b)

Figure 16. Scanning electron micrographs (5000X) showing representative fields of view of two different multilayers. (a) No nodules were observed in the multilayer and (b) $5 \times 10^{7}/cm^{2}$ were observed in the multilayer.
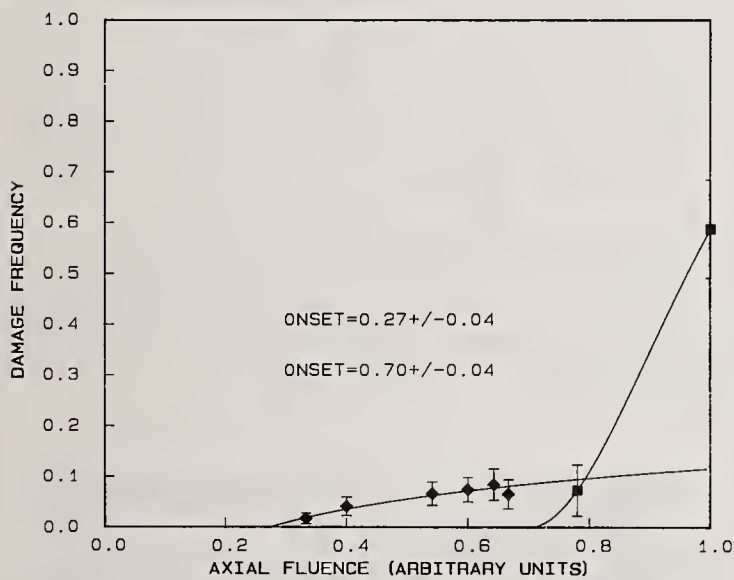
Figure 17. Single-shot laser damage frequency data for the low-defect mirror shown in figure 16.
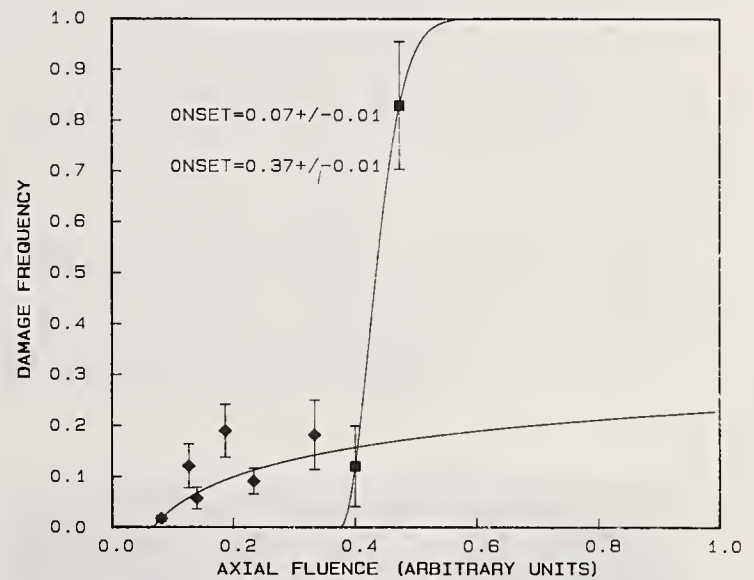
Figure 18. Single-shot laser damage frequency data for the high-defect mirror shown in figure 16.

369
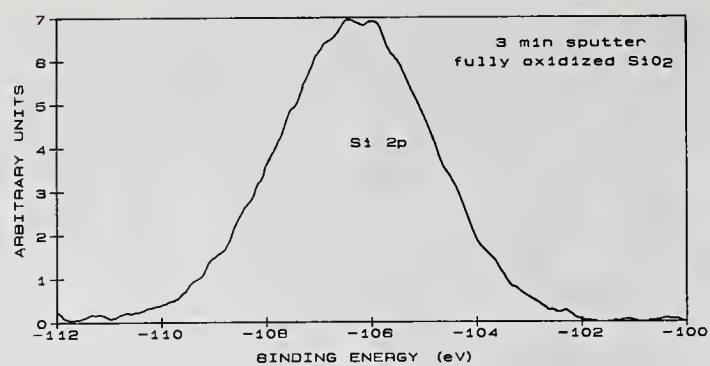
(a)
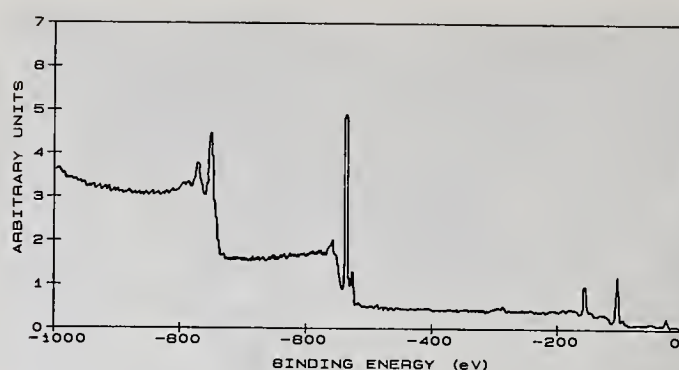
(b)

Figure 13. The x-ray photoelectron spectrum taken after a 3-minute sputter indicates that the SiO$_2$ is fully oxidized and shows no detectable impurities.
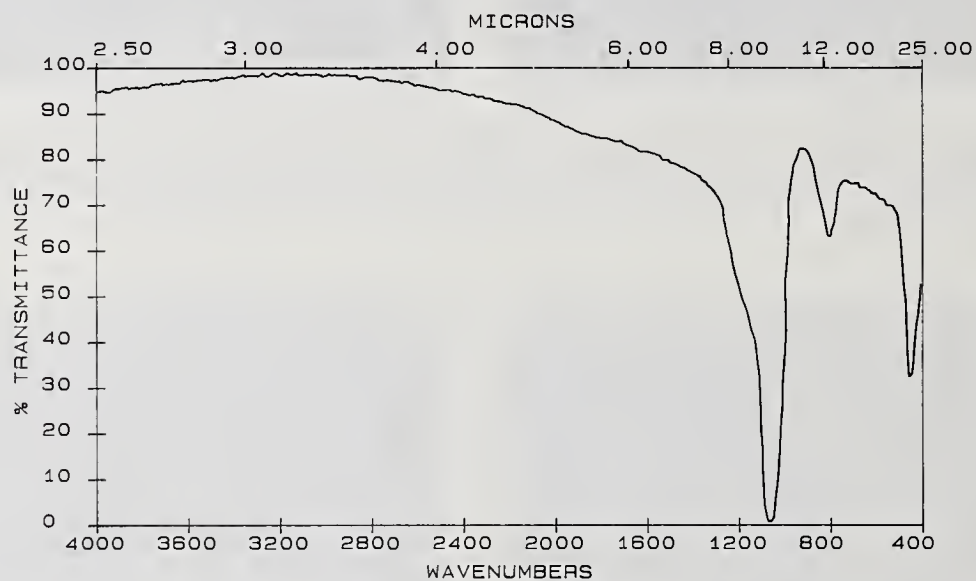
Figure 14. The Fourier transform infrared transmission spectrum shows no water band near 3 μm. The strong Si-O-Si stretching frequency at 1075 cm^{-1} indicates that the SiO$_2$ is fully oxidized.

10 um

(a)

1 um
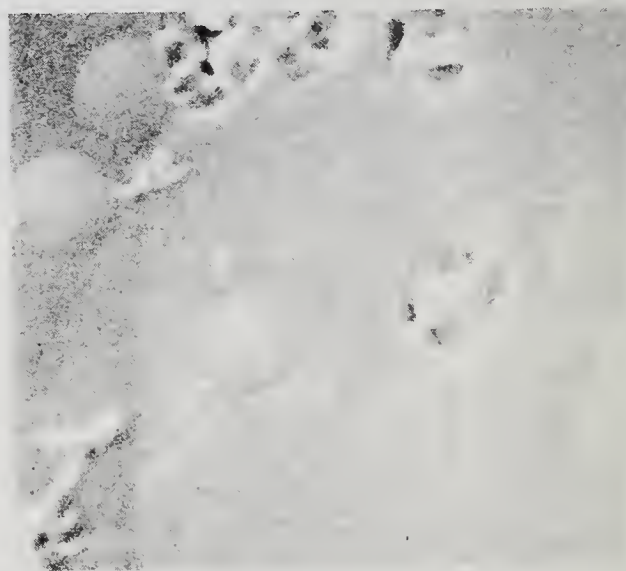
(b)

Figure 15. Scanning electron micrographs showing selective laser damage at nodular growth defects at (a) 5000X and (b) 20000X.

370

Single Pulse Laser Induced Damage in IR Coatings at 10.6 μm

H. Deng, M. Bass and N. Koumvakalis

Center for Laser Studies, University of Southern California
University Park,   Los Angeles, California 990089-1112

Results on single pulse laser damage to several reflective and anti-reflective coatings designed for use at 10.6 μm are reported. Samples from two different manufacturers were studied. Nomarski microscopy and TV vidicon detection were used for the characterization of the samples before and after damage. Suggestions about the future use of an improved TV system for the detection of scattering centers in the visible are made.

Key words: damage thresholds; electric field; micrographs; reflective coatings; scattering centers; substrate.

1. Introduction

Optical coatings, although studied for some time are still the weak points in high power laser systems operating in the UV, visible or IR spectral ranges. In this paper experimental results are reported on the single pulse laser induced damage properties of several coatings designed for use at 10.6 μm. The coatings were reflective (100%, 85% and 65%) and anti-reflective designs involving layers of ZnSe and ThF placed on Si, Ge and ZnSe substrates. No significant differences were found in the damage thresholds of the reflective coatings. For the beam diameter used, the thresholds, ~90J/cm^2, were independent of the reflectance, substrate and the defect density of coatings as determined by examination of Nomarski micrographs. The damage threshold of the anti-reflection coatings was significantly lower than the threshold of the reflective coatings with an average value of ~40 J/cm^2. This result may be related to the design of the AR coatings.

The damage thresholds were measured by using well established techniques of beam characterization and damage detection [1]. The samples were examined with Nomarski optical microscopy before and after irradiation. In addition, initial studies of visible light scattering using Ar ion laser illumination and TV vidicon detection were performed to explore the possibility that scattering centers could be detected whose presence would be correlated with the damage data.

2. Experiments

2.1 Damage Experiments

The laser damage experiments were carried out using the apparatus shown in Fig. 1. The CO_2 laser was restricted to operate in the TEM_{00} mode by the intracavity cw discharge. The light energy incident upon the samples was controlled by one fixed and one rotatable wire grid polarizer. This energy was monitored for each pulse by the beam splitter-detector combination shown. The beam was focused on the sample with a ZnSe lens to a spot with beam radius at the 1/e point of intensity of 60 μm. The pulse duration was 230 nsec.

The damage threshold, as conventionally defined is the value of the incident energy or intensity lying midway between the lowest value at which damage always occur and the highest at which damage never occurs. Table 1 lists the damage thresholds of all the coatings studied. The damage thresholds for the reflective coatings are essentially independent of the reflectance, substrate and the defect density. Due to the paucity of anti-reflective coated samples we could not examine their damage threshold as a function of such a range of parameters. The average value of threshold for the reflective coating is 90J/cm^2 or 370 MW/cm^2 whereas the average value for the anti-reflection coatings is 40J/cm^2 or 150 MW/cm^2.

2.2 Coating Design

The variety of optics that were tested for laser damage included AR, partial reflectors and high or total reflectors. These optics used the same material pair combination for all designs, ZnSe/ThF, differing however in the number of pairs or the layer thickness. The AR design consists of a standard two layer "V" coat with a relatively thin outer (air interface) layer thickness.

Table 1. Damage Thresholds of 10.6 μm Coatings

Substrate	Reflectance	Nomarski Defect Density (mm^{-2})	Energy Density (J/cm^2)	Intensity (MW/cm^2)
Si	100%	37	91 ± 18	371 ± 74
Si	100%	54	84 ± 22	359 ± 100
Si	100%	--	80 ± 31	342 ± 132
Si	100%	39	100 ± 21	410 ± 86
Ge	99.3%	23	99 ± 19	404 ± 76
Ge	99.3%	18	96 ± 21	392 ± 84
ZnSe	60%	18	86 ± 58	345 ± 58
ZnSe	85%	25	88 ± 12	361 ± 49
ZnSe	AR	27	41 ± 12	169 ± 48
ZnSe	AR	32	30 ± 9	123 ± 37

Analysis of the electric field distribution in each layer for the various designs shows a twenty five percent increase in the peak electric field at the air interface for the AR coating relative to the other designs [2]. This electric field value remains high through the next interface between layer 1 and layer 2. It is well known that all interfaces in thin film coating structures have high potential for gathering contaminants, creating nucleation defects and material mixing via diffusion across the interface. As a result, coating designs having the peak electric field at the air interface and maintaining a high value at the film/film interface is not optimum for high damage threshold designs. Changing the electric field distribution by innovative coating design is called for and may be an approach to increasing the damage threshold for the AR coatings.

3. Morphology

Nomarski micrographs were taken before and after the damage experiments. Figure 2 shows a characteristic picture for the undamaged surface of a 100% reflective coating on Si. One can see that there are rises or pits in the coating. These are 100 μm apart and could be encountered by the small area beam used in the damage studies. The before damage morphology of all reflective coatings was quite similar. The data of table 1 indicate that the defects seen by Nomarski microscopy could be responsible for the failure of the reflective coatings and consequently this failure would then be independent of coating design, substrate and manufacturer. Figures 3 and 4 show Nomarksi micrographs of various damage sites in different coatings. The damage site at threshold is often smaller than the irradiated area. The role of the distributed defects in the damage process can be demonstrated by those micrographs where a normally incident circular TEM_{00} beam produces an asymmetric damage site.

4. Visible Light Scattering

The use of a TV vidicon system and a pulsed dye laser as a means of detection of scattering from defects has been demonstrated recently [3]. A similar system shown in figure 5 was used by the present authors to explore for the presence of scatterers in the coatings of interest. The 0.5145 μm, 0.200 W output of an Ar ion laser was used as the probe beam for this work. The output of the Vidicon was displayed on a monitor adjusted in combination with the iris in the focusing lens so that scatterers such as seen in figure 6 were observed against a black background. Figure 6 is a photograph of the monitor screen showing scatterers in or on a 100% R coating on a Si substrate before the damage tests. The magnification is about 10x. The important point is the presence of discrete scattering sites spaced by about 0.5mm. The majority of the samples examined display the same behavior. Table 2 compares the scattering with the threshold damage. There is no correlation but the scattering centers were not necessarily present in the small sites tested for laser damage, so the measured low end of the damage range could not properly account for them. Obviously experi-

Table 2. Comparison of 0.5145 µm Scatter and 10.6 µm Damage Threshold

Type & Manufacturer	Scatter	Threshold
AR on ZnSe:		
II-VI	Low	Comparable ($30J/cm/cm^2$)
L.P.O	High	Comparable ($34J/cm^2$)
Partial Reflectors:		
II-VI	Low	Comparable ($86J/cm^2$)
L.P.O.	Low	Comparable ($86J/cm^2$)
100% R Coatings on Si:		
II-VI	Average	Comparable ($91J/cm^2$)
L.P.O.	Average	Comparable ($100J/cm^2$)

ments must be performed in which the irradiated area is likely to include the discrete scatterers and their role, if any, in determining the "onset" [4,5] of damage must be determined. In addition, higher resolution TV vidicon-monitor combinations should be used to improve the sensitivity of this technique to small, closely spaced scatterers.

5. Conclusion

The laser damage threshold of reflective and anti-reflective coatings on a variety of substances was examined. It was found that anti-reflective coatings of the design studied would represent the weak link in a high power optical system. The damage thresholds of reflective coatings on the other hand, for the beam sizes employed, are independent of the coating reflectance, substrate material and defect density.

6. References

[1] Tang, C. C., Bass, M., Soileau, M. J., and Van Stryland, E. W., "10.6 µm Laser Damage in Coatings Containing As_2Se_3", Laser Induced Damage in Optical Materials: 1977, NBS Special Pub. 509, 316 (1977).

[2] Rudisill, J. E., Laser Power Optics, Private Communications

[3] Marrs, C. D., Porteus, J. O., and Palmer, J. R., "Defect Damage Precursors in Visible-Wavelength Mirrors" presented at the 1983 Symposium on Laser Induced Damage in Optical Materials, Boulder, Colo., Nov. 1983 and to be published in the Proceedings of that meeting.

[4] Porteus, J. O., "Determination of the Onset-Driven Pulsed Laser Damage in 2.7 µm Optical Coatings", High Power Laser Optical Components Topical Meeting, Boulder, Colo., 18-19 November 1982. (Proceedings in process).

[5] Seitel, S. C., and Porteus, J. O., "Toward Improved Accuracy in Limited-Scale Pulse Laser Damage Testing Via the Onset Method", 15th Annual Sympsoium on Optical Materials for High Power Lasers, Boulder, Colo., November 14-16, 1983. (Proceedings in process.)
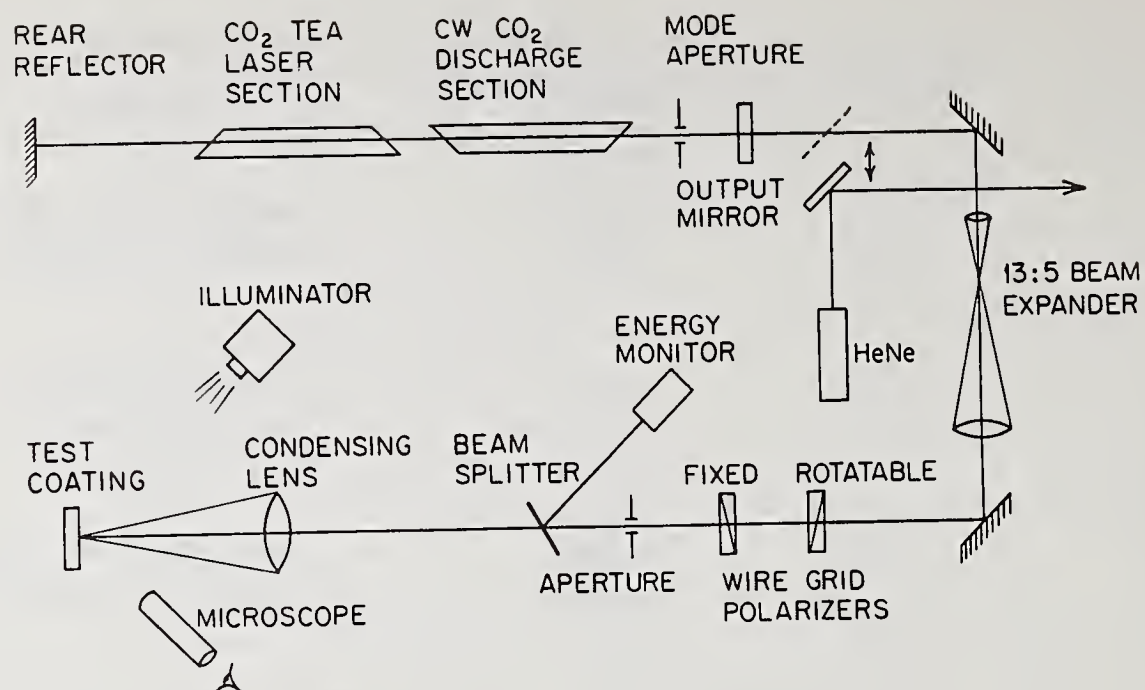
Figure 1. Laser Damage Experiment.

Nomarski Micrographs
100 % R on Si
Undamaged Region

(L.P.O.)

(L.P.O.)

(II - VI)

156 μm
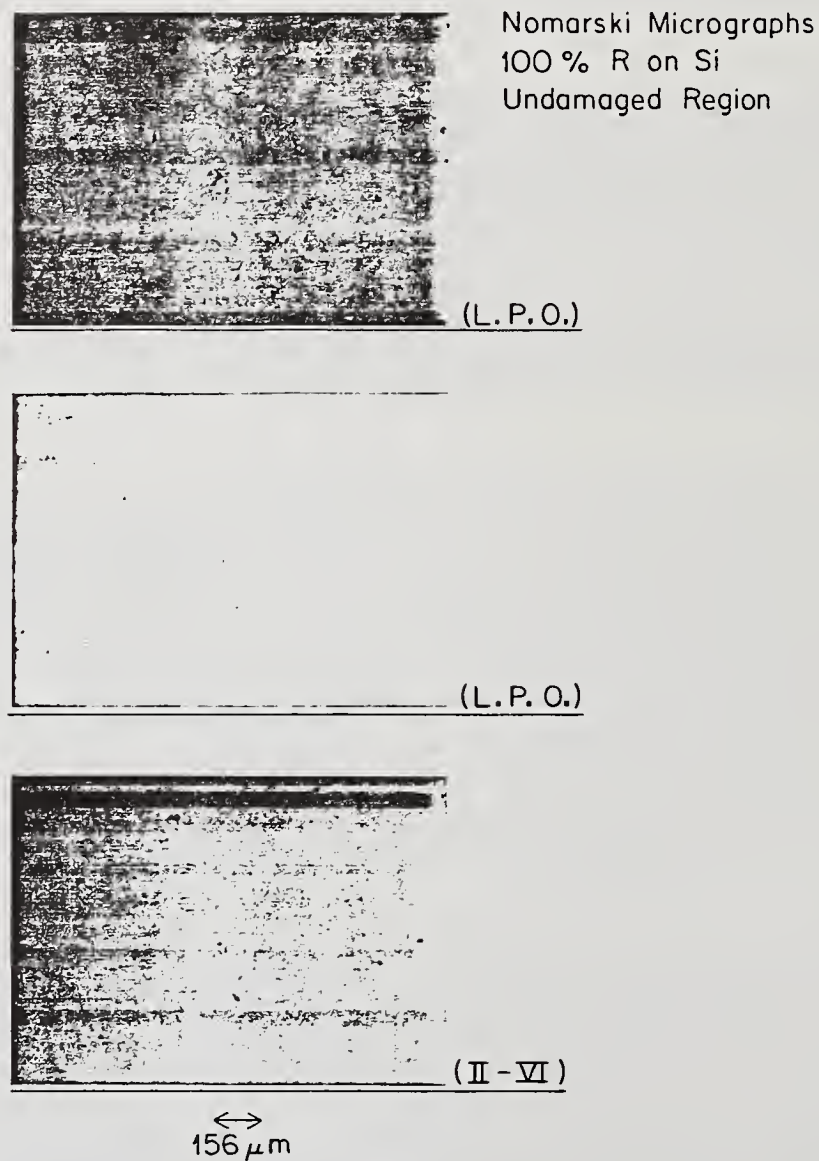
Figure 2. Nomarski micrographs of undamaged regions of 100% R, 10.6 μm, coatings on Si substrates. The coater is indicated.

Nomarski Micrographs
Threshold Laser Damage
to 100% R on Si
$(85J/cm^2)$

(L. P. O.)

$\longleftrightarrow$
$100\mu m$
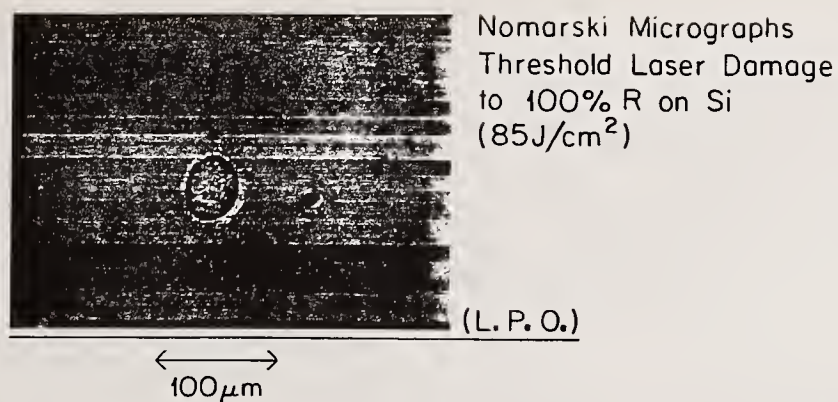
Figure 3. Nomarski micrograph of thereshold 10.6 µm laser damage to a 100% R, 10.6 µm, coating on Si.

Nomarski Micrographs
Threshold Laser Damage
to:
60% R on ZnSe
$(85J/cm^2)$

(II – VI)

85% R on ZnSe
$(85J/cm^2)$

(L. P. O.)

$\longleftrightarrow$
$100\mu m$
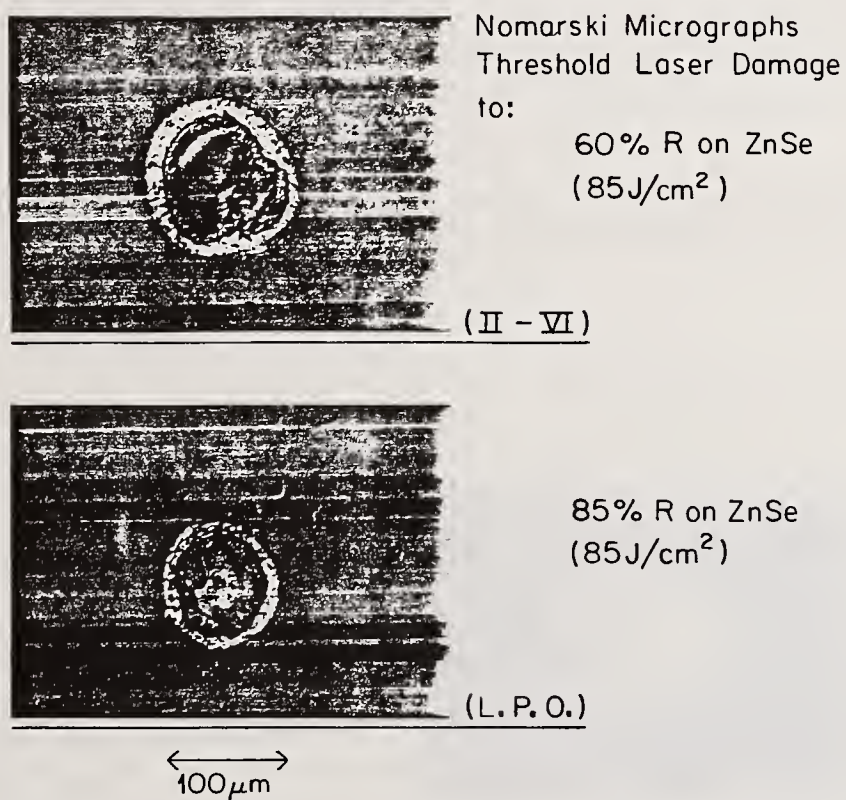
Figure 4. Nomarski micrographs of threshold 10.6 µm laser damage to transmissive coatings on ZnSe.

SCATTERING EXPERIMENT
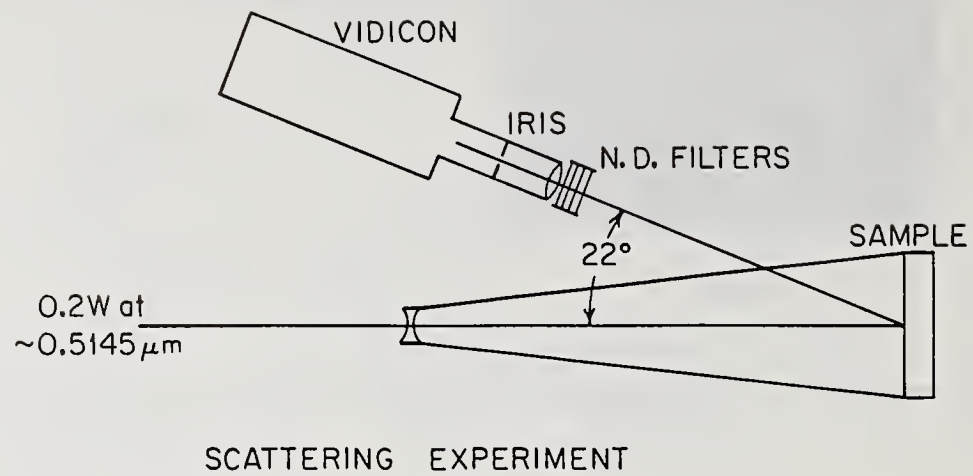
Figure 5. Visible scattering centers experiments.

0.5145 μm Scattering
from 100% R on Si
(~10×)

Figure 6. 0.5145 μm scattering centers in an undamaged 100% R, 10.6 μm coating on Si.

376

Light Stripping of UV Dielectric Coatings

John F. Asmus and Jerry R. Oldenettel

Maxwell Laboratories, Inc.
San Diego, CA 92123

High-performance ultraviolet lasers require optics with a tighter tolerance on surface figure than comparable visible and infrared systems. Consequently, the costs of large-aperture figured substrates can be quite high. When ultraviolet coatings become damaged through exposure to photons and/or halogen radicals, recoating is often performed in order to salvage such substrates. If the coating is not strippable, this entails the expense of regrinding and repolishing. We have found that the remains of damaged coatings of SiO_2, LaF_3, MgF_2, and HfO_2 can be removed with pulsed xenon flashlamp radiation. A train of shots at 30 J/cm^2 is sufficient to dislodge a coating without damaging fused silica and Zerodur substrates. A pulselength of 600 microseconds was employed. Frequently, photochemical damage involves only the coating and not the substrate. In these instances flashlamp stripping may be employed to salvage the substrate without reworking the surface.

Key words: coating removal; coating stripping; dielectric coating; laser mirror; mirror damage; xenon flashlamp

1.   Introduction

The harnessing of light energy for industrial and commercial cleaning applications has grown in importance during the last decade. A recently developed industrial flashlamp cleaning system has been undergoing evaluation for a number of applications [1]. Such systems have their origin in the pioneering work of laser cleaning [2]. Use of the unique properties of laser radiation -- extremely fine focusing, directionality, high brightness, monochromaticity -- has allowed solutions to surface preparation problems once considered untenable by conventional cleaning methods. The optimism that has met these impressive successes, however, has been tempered by the fact that laser photons are expensive photons. Consequently, surface cleaning with lasers is presently warranted for rare and costly items, or as a solution to "when all else fails" scenarios.

The use of flashlamp systems presents a cost effective alternative to laser light cleaning. While lacking the sophisticated aspects of laser radiation, a flashlamp will emit very intense, broad-band, short pulses of light. This radiation is of sufficient energy to physically and chemically alter and/or remove a variety of surface deposits. Additionally, the flashlamp cleaning process is often self-limiting in that once the unwanted surface layer has been removed, the exposed substrate will be immune to further radiation treatment. Flashlamp induced divestment is thus an effective technique particularly amenable to large surface areas. The uncollimated, diffuse characteristics of the radiation, however, diminish its usefulness on surfaces which are not flat.

Experimental studies of flashlamp cleaning effectiveness have involved a variety of materials. Successful applications include divestment of polyurethane and epoxy paints from metal, removal of paint overcoats without destruction of the underlying primer, and etching of polymer surfaces for coating purposes (Figure 1). The potential application presented here involves the use of intense flashlamp radiation for the stripping of damaged large-area ultraviolet coatings from laser optics. This opportunity is of particular interest as the figuring costs of larger ultraviolet optical surfaces are especially high due to the short wavelength. Thus, there is a strong economic incentive in developing a method of stripping damaged "hard" coatings without altering the substrate. This would facilitate the reuse of such substrates.

377
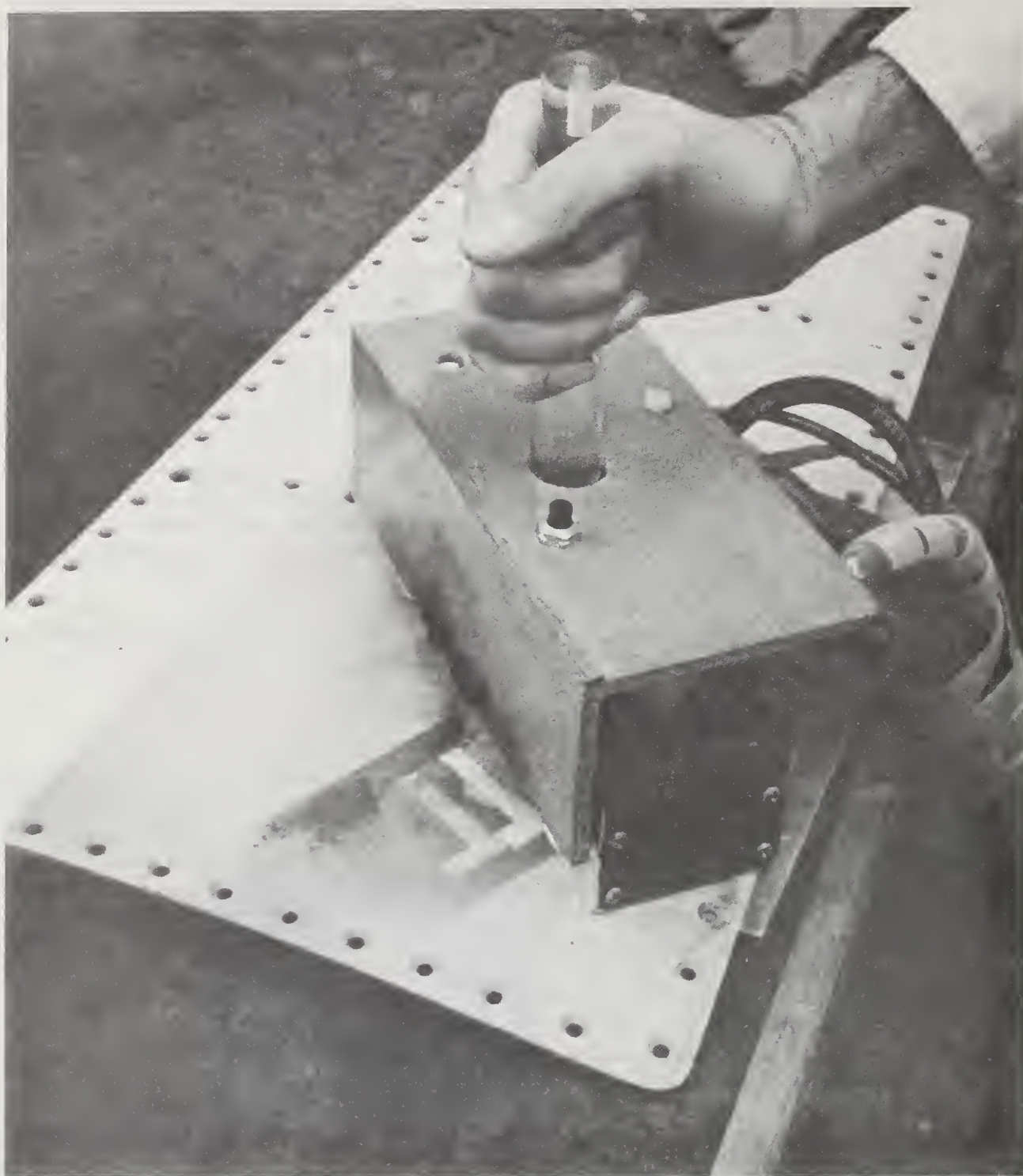
Figure 1.   Xenon flashlamp head positioned above aircraft panel
for radiation-induced paint-stripping test.

2.   Background

In most instances of intense xenon flashlamp radiation, stripping the surface film is absorbing and the temperature rise is substantial (500-1000 °C). Several divestment mechanisms come into play in such instances. First, there is the possibility of superficial evaporation and sublimation of substances. Second, if the heating is sufficiently rapid, the expanding vapors are able to scour the surrounding areas much like hydro or air blasting. Any surfaces that are coated with water during the irradiation will produce a steam cleaning effect. Third, depending on the absorption properties of the material, a given layer may be broken down photochemically or photolytically. Fourth, differential thermal expansion of substances may lead to delamination of surface deposits. Finally, for short laser pulses of a few tens of nanoseconds, a shockwave is generated causing material removal by ablation and spallation. Which of these mechanisms, or combination of mechanisms, is of predominant importance depends on the substance and conditions under treatment.

The materials employed in ultraviolet dielectric coatings are generally oxides and fluorides. They are of course very low in optical absorption and have moderately high sublimation and decomposition temperatures. Consequently, light-induced divestment by the mechanisms cited above would not seem particularly plausible. However, it is known that the thermal conductivities of thin film materials are lower than those of bulk materials [3]. Consequently, it may be possible to induce mechanism four mentioned above. As many thin film materials cutoff in either the ultraviolet or the infrared before reaching the fused silica cutoff limits of a flashlamp, it may be possible to produce some differential heating via the wings of the xenon radiation.

3.   Results

By operating a linear xenon flashlamp at the upper end of its useful range we have been able to illuminate surfaces at 30 J/cm^2. The lamp employed in these tests had an 8 mm bore, a 5-inch arc length, and a Suprasil envelop. The radiation output had a 600 μs FWHM and the input electrical energy was 4.5 kJ.

The coating stripping tests were performed by placing the lamp and its reflector housing above the coated surfaces much as indicated by Figure 1. Two damaged ultraviolet reflectors were obtained from a 40 liter e-beam excited excimer laser employing unstable resonator internal optics. The thin film layers on these two Zerodur substrates employed SiO_2/LaF_3 and MgF_2/HfO_2. Figure 2 shows the output coupler after one end of it had been exposed to five shots of the xenon flashlamp at 30 J/cm^2. About 99% of the coating was removed from the exposed end. The substrate was free of observable damage.

The unstable resonator primary reflector was then scanned by the flashlamp and about 100 shots were applied sequentially by displacing the lamp laterally by a few mm after each five shots. Whereas most of the thin film material has been ejected, a residue remains over about one half of the surface. It appears that the low intensity fringes of the radiation footprint precondition the coating so that complete ejection is not obtained when the high-intensity portion of the profile reaches that zone. This radiation-stripped primary reflector is shown in Figure 3.

4.   Conclusions

It appears that it may be technically feasible to employ intense xenon flashlamp radiation to cleanly strip damaged hard ultraviolet coatings from substrates. However, it will probably be necessary to employ a large array of lamps for total illumination of the surface. A fluence of 30 J/cm^2 in a 600 μs pulse is marginal for state of the art coatings. The utilization of a lamp array may permit the attainment of a higher fluence which may yield better results. The results reported here employed a low 0.1 Hz pulse rate. Higher pulse repetition rates may also be more favorable.
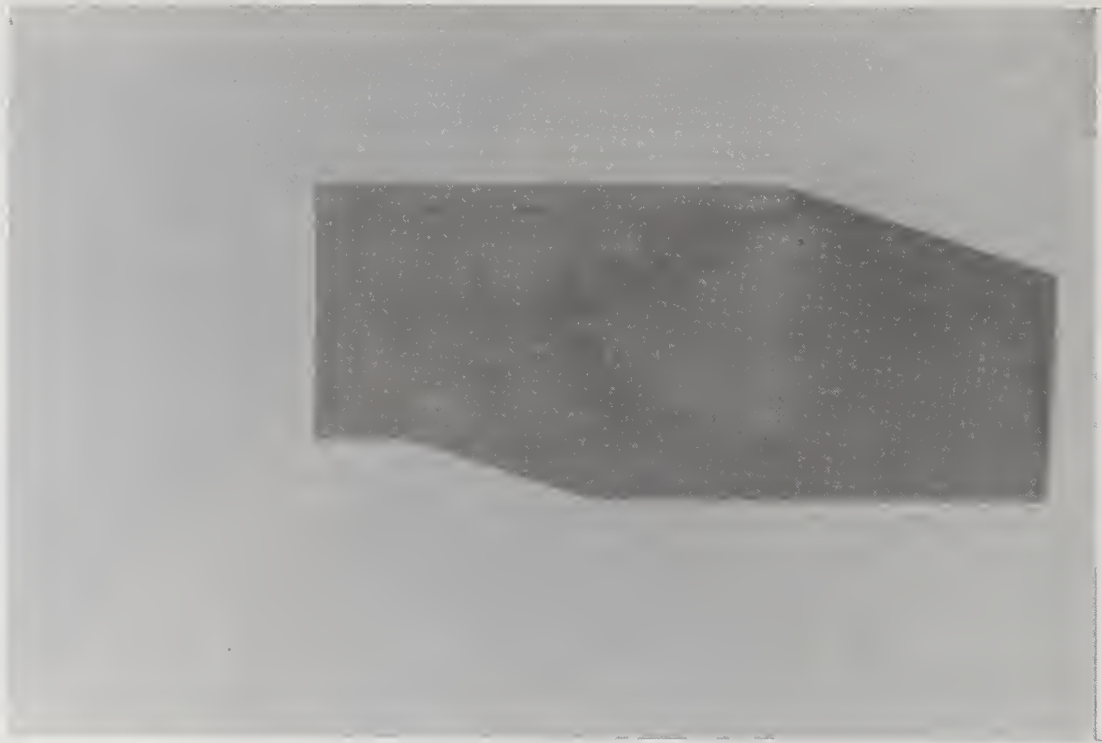
Figure 2. Partially stripped output coupler.
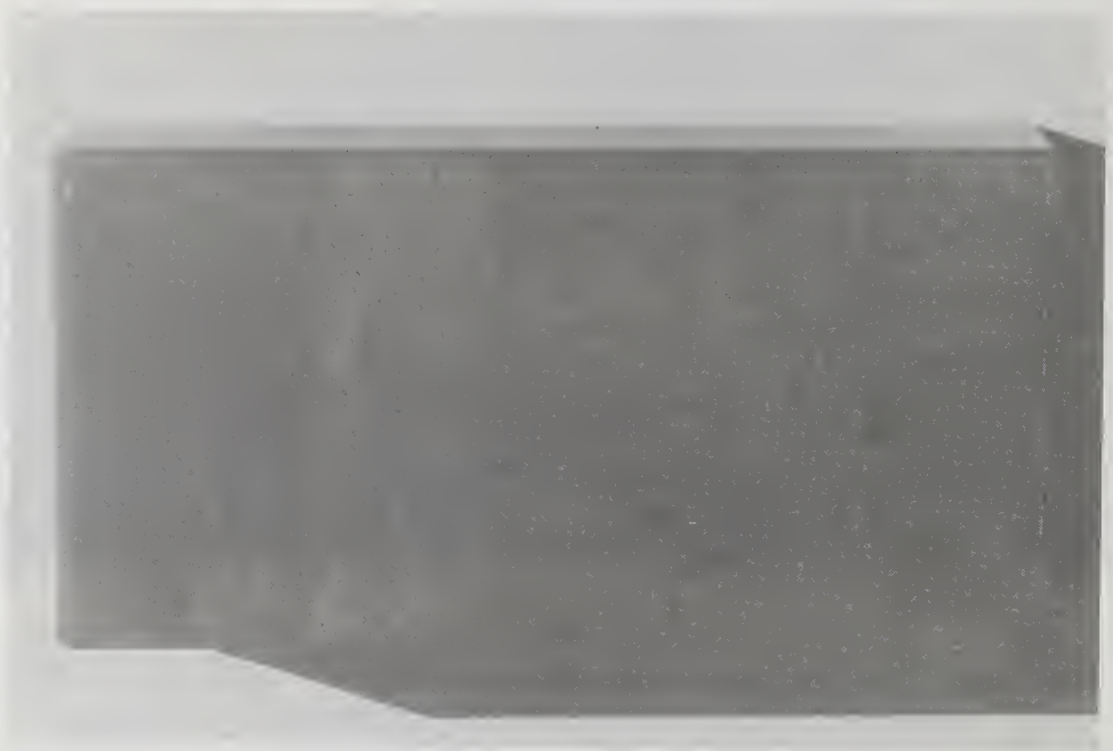
Figure 3. Flashlamp scanned primary reflector.

References

[1]   "Light Cleaning," <u>Science Digest</u> 89(3): 27; 1981 April.

[2]   Asmus, John F.   "Technology and Conservation," <u>3</u> (3); 14-18; 1978 Fall.

[3]   Decker, D. L.; Ashley, E. J.; Koshigoe, L. G.   "Thermal Properties of Thin Film Materials," in Program of the Sixteenth Annual Symposium Optical Materials for High Power Lasers; 1984 October 15-17; Boulder, CO, 34.

An Initial Study of: *Manuscript Received*
The Inclusion Model for Repetitively Pulsed Laser Damage   *1-9-84*   *SAR*

M.R. Lange* and J.K. McIver

Institute of Modern Optics, University of New Mexico, Albuquerque NM 87131

Arthur H. Guenther

Air Force Weapons Laboratory, Kirtland AFB, NM 87117

The inclusion model of laser initiated damage is extended to include an arbitrary but repetitive and reproducible variation of the laser irradiation in time. The controlling influence of the thermal properties of the film/substrate system and inclusion, together with the duty cycle of the laser, i.e., the duration and energy of a single pulse and of the repetition rate, on the damage threshold is discussed. The predictions of this model are then compared to the results of the single-shot model of inclusion dominated damage. Suggestions for experimental tests of this model are given.

Key words: Absorbing inclusion, laser induced damage, repetitively pulsed, thermal properties.

1. Introduction

The problem of multiple pulse laser induced damage in optical components is a very important and general one. It is the real situation that we wish to address when considering the durability of optical components. This stems from the fact that multiple pulsed damage concerns the use of optical elements that are subjected to more than one cycle regardless of the time delay between pulses.

In a review of experimental results relating to this area, one encounters a large array of seemingly contradictory data. For example in some instances there is no apparent effect of prior pulses [1] (i.e., no memory), while in other cases there is unmistakable evidence of a build-up or accumulation of damage.[2] Some situations demonstrate clear evidence of thermal build-up effects [3,4] while others [5] show no discernable evidence of this effect. A pulse repetition frequency dependence in some cases [3,4,6] exhibits reversible effects in some materials while others [5] show no such evidence. It is also known that low level irradiation can condition elements such that they can ultimately withstand higher fluences without damage.[7,8] A possible clue to an understanding of this wide diversity of responses is the fact that damage is dependent upon the configuration of the material (i.e. bulk, film, surface, crystalline, amorphous, metallic, polymer, etc.)

The morphology of multi-pulsed damage is, as one might expect, just as varied, not only between different materials, but between different configurations of the same material (i.e., anti-reflecting films and high-reflecting films).[9] One mode of damage for films, both with and without some sort of accumulation mechanism, is for a small pit to form and no subsequent damage to occur.[9] Another mode is for damage to grow with subsequent pulses to a diameter that is consistent with points in the incident field that are ~ 25% of the single pulse damage threshold.[9] Clearly there is no simple universal multipulse laser induced damage scenario. There are many classes of multipulse damage morphology.

What we do herein is to once again exploit the thermal model of laser induced damage and apply it to multipulsed laser irradiation The justification for this course of action is as follows. Absorption and diffusion must occur in all cases of laser damage. There is very

strong evidence that at least some cases of laser induced damage (certain optical films) are thermally dominated for the single pulse case.[10] There is, in addition, evidence that the mechanism for certain cases of laser induced damage is the same for the first pulse as for subsequent pulses [6,11,12] (though, for other cases [3,13] this is evidently not true). Even situations where damage is not thermally dominated a change of state necessarily accompanies a change in temperature (e.g. a change in band gap) and thus, it is desirable to know the temperature field. Finally, evidence of absorbing microinclusions [7] as damage initiators gives further support for this model. One should note that beyond requiring a microinclusion or some localized initiating mechanism, the physics involved is not restricted by this model, nor is it determined. It simply implies that an isolated region absorbs energy in some manner and subsequently diffuses the absorbed energy throughout the surrounding matrix. It is also not required that this absorbing region remain fixed with time, pulse number, pulse repetition frequency or any other experimental variable.

The model is generalized to handle any sort of general absorption that may occur in various materials. However, at this stage of the model development the absorption function must be determined for each different situation. The determination of the temporal and spatial dependence of the absorption function for each situation, as for the single pulse case, is the primary difficulty. For certain single pulse situations [10] a very simple absorption function can prove adequate. However, due to irreversible changes (i.e. memory) of some sort, this is not true for most multiple pulse interactions.

In the section that follows we derive the general theory of arbitrary multi-pulse absorption for both a spherical inclusion in an infinite medium and a cylindrical inclusion in a thin film. The arbitrary form of the absorption allows application to laser windows with macroscopic gaussian beam absorption.[4] In addition, it allows application to an opaque material with absorption of any general form (Eg. Ref. 3). The problem is then simplified to the case of a uniform, non-expanding absorption, without irreversible processes as an illustration of the effects purely due to thermal build-up.

The results are as expected, in that thermal build-up in itself can not be responsible for the observed decrease in damage threshold in most cases of isolated absorbing inclusion. Other mechanisms must couple with the diffusion process to provide the observed behavior. The key to understanding the many observations and mechanisms involved is to determine specific pulse to pulse behavior of the absorption function. Any correct theory of the interaction involved must predict the spatial, temporal pulse repetition frequency and pulse number dependence of the absorption term in the heat diffusion equations.

2. Theory

In previous works we have described models of absorbing regions which subsequently diffuse their energy through the surrounding matrix. Both a spherical model [10], valid for the region where the pulse length is not larger than the diffusion time to the boundaries of the film, and a cylindrical model [14], valid for much longer times, have been derived.

In general we use the diffusion equation to describe the distribution of temperature within the system. In the absorbing region (the subscript i denotes the absorbing impurity),

$$\frac{1}{D_i} \frac{\partial T}{\partial t} = \nabla^2 T + \frac{A(\vec{r},t)}{K} \tag{1}$$

and T, D, K are temperature, diffusivity (cm^2/s) and conductivity
(J/°K-s-cm) respectively while A is the volume absorption function in (J/cm^3-s).

$$\frac{1}{D_h} \frac{\partial T}{\partial t} = \nabla^2 T \tag{2}$$

corresponds to the heat material (subscript h) outside of the absorbing region. Here, perfect thermal contact is assumed at the boundaries of the absorbing region and r and t are the radius and time respectively. The two geometries give specific solutions within the impurity of

$$T_i = \frac{1}{r} \int_o^\infty \frac{d\alpha}{N(\alpha)} \sin(\alpha r) \, \hat{\bar{A}}(\alpha,t) \tag{3}$$

for the spherical case [10]

and

$$T_i = \int_o^\infty \frac{d\alpha}{N(\alpha)} \alpha \, J_o(\alpha r) \sum_{j=0}^\infty \cos(\frac{j\pi z}{\ell}) \, \hat{\bar{A}}(\alpha,t) \tag{4}$$

for the cylindrical case. [14]

Here $\hat{\bar{A}}$ is the transformed absorption function (defined below), $N(\alpha)$ is a normalization factor, α the radial eigenvalue and ℓ is the length of the cylinder (i.e., the thickness of the film). The expression for the source term in the above equations is

$$\bar{\hat{A}} = \exp\left[-\xi t\right] \, \int_o^t dt' \, \exp\left[\xi t'\right] \, \int_{Vol} dr^3 \, \psi_j(\vec{r},\alpha) \, A(\vec{r},t') \quad (5)$$

Here ξ is the composite eigenvalue of the system, $\psi_j(\vec{r},\alpha)$ is the eigenfunction of the composite region and $A(\vec{r},t)$ is the general absorption function with "Vol" refering to the volume of the absorbing region. The subscript j on ψ applies to axial modes of the cylindrical geometry. Expressions for these parameters are given in table 1 for specific geometries. The absorption function written in the form

$$A(\vec{r},t) = \sum_{n=1}^{N} A_n(\vec{r},t) \quad (6)$$

contains the complete evolution of the absorption including irreversible or long lived changes to the material with each pulse from 1 to N. There is data [5] indicating that in some cases the change in absorption occurs within a time that is small compared to the delay time 't_d' between pulses. In some cases it may occur within a time that is small compared to the pulse length 't_p' itself. For an idealized case where the absorption evolves early into the pulse and the absorption that follows is proportional to the field, or the case where the evolution transient occurs completely in between the pulses, we may write

$$A(\vec{r},t) = \sum_{n=1}^{N} A_n(\vec{r}) \left\{ \Theta(t-[(n-1)t_p + (n-1)t_d]) - \Theta(t-[nt_p+(n-1)t_d]) \right\}. \quad (7)$$

Here the nth pulse turns on at $t = (n-1)t_p + (n-1)t_d$ and turns off at $t = nt_p + (n-1)t_d$ with t_p being the pulse length and t_d being the delay time between pulses and Θ being the step function.

Thus, we need only concern ourselves with the spatial dependence of absorption from pulse to pulse. In other cases [9] multipulse damage has been observed to occur after some number of pulses, but not grow spatially. In fact, no further damage is observed after the initial pitting. One may have totally vaporized the impurity. In this case

$$A(\vec{r},t) = f(\vec{r}) \sum_{n=1}^{N} A_n \left\{ \Theta(t-[(n-1)t_p + (n-1)t_d]) - \Theta(t-[nt_p + (n-1)t_d]) \right\} \quad (8)$$

so that only the magnitude of absorption varies with the pulse number.

In all of these cases the absorption evolution is unknown and is observed to be strongly material and laser parameter dependent with an unspecified physical mechanism.

In at least one case [15] there is evidence, or at least it has been suggested that for the

385

material polymethylmethacrylate the absorption evolution is governed by irreversible mechano-chemical processes driven by a temperature gradient induced stress. Whatever the driving source, a measured empirical or theoretically derived form of A_n must be found before any specific situation can be treated adequately.

Example case

An illuminating exercise as a first step, is to assume 'A_n' is constant and develop the solution. There are some cases where this seems to apply. This exercise also serves to demonstrate purely thermal effects for repetitively pulsed lasers. It may be used to study temperature profiles within optical windows and in absorbing inclusions at fluences below those at which nonlinear absorption effects become important. For this case

$$A(\vec{r},t) = f(\vec{r}) \, A_o \sum_{n=1}^{N} \{ \Theta(t-[(n-1)t_p + (n-1)t_d]) - \Theta(t-[nt_p + (n-1)t_d]) \} \quad (9)$$

so that

$$\hat{\bar{A}} = Exp[-\xi t] \int_o^t dt' \, Exp[\xi t'] F(\alpha) \, A(t') \quad (10)$$

where

$$A(t') = A_o \sum_{n=1}^{N} \{ \theta(t,(n-1)t_p,(n-1)t_d) - \theta(t,nt_p,(n-1)t_d) \}$$

$$F(\alpha) = \int_{vol} d^3r \, \Psi(\vec{r},\alpha) \, f(\vec{r}). \quad (11)$$

Various $F(\alpha)$'s are listed in Table 2 for different geometries and situations. The time integration in equation (10) is carried out term by term and the resulting series is summed to a result of

$$\hat{\bar{A}} = A_o \frac{F(\alpha)}{\xi} (1-e^{-\xi t_p}) \frac{(1-e^{-N\tau\xi})}{(1-e^{-\xi\tau})} \quad (12)$$

where $\tau = t_p + t_d$. This is a particularly simple and elegant result first realized by Walker [16] in connection with the Goldenberg and Tranter [17] solution using the Laplace transform and now proven here for that case and any general related case. Though this solution does not apply in general to catastrophic repetitively pulsed laser induced damage, it is likely that it does apply to some cases and may be informative for others for which it is not valid.

Results

Numbers are applied to the previous expression providing a sense of the effect of thermal build-up in optical materials subjected to repetitive laser pulses. For example, for a one-half micron thick thorium fluoride film using the isolated spherical absorbing impurity model with a 0.1 nanosecond pulse, if no growth of the absorbing region occurs we would need a repetition frequency of greater than 10^8 hz to see any significant decrease in damage threshold due to thermal build-up. The criterion that we use for damage here is for the edge of the absorbing region to reach the film melting temperature. Note on figure 1 the increase in radius most likely to damage with increased number of pulses. So, if no growth of the inclusion occurs (i.e. disc like growth into the film) and we are limited by the film thickness then the effect of thermal build-up is even less. Note also in Figure 2, of pulse repetition frequency equal to 10^8 Hz, that essentially no thermal build-up occurs. Thus thermal build-up could not be a factor in damage for this idealized case. This does not take into account a possibly dense distribution of particles so that the diffused heat of nearby absorbing regions could build-up in the surrounded region. Detailed experimental determination of the distribution and strength of absorbers would be required for this calculation.

The largest possible effect of thermal build-up for a single isolated absorber would be for a free standing film (allowing only two dimensional heat diffusion) of very low thermal conductivity with a large strongly absorbing inclusion and a long pulse length. So, assume we have a free standing film of SiO_2 (k=0.014 J/cm-°K-s) ten microns thick with a 10 microsecond incident pulse repeated at 1000 hz. The largest inclusion that could intially be embedded in the film would be one with a diameter equal to the film thickness. Again, assuming no growth of the absorbing region we find a decrease in damage threshold of only ten percent for 10^3 pulses due to thermal build-up compared to the single exposure threshold. For a substrate of greater than zero conductivity this value would be further decreased. These extreme conditions should indicate that thermal build-up by itself should not be a major factor in this case. However, there are conditions with and without the assistance of additional mechanisms where it is imaginable that thermal build-up would be a factor in decreasing the damage threshold.

Suffice it to say, a dense distribution of absorbing impurities, irreversible changes or temperature dependent absorption that is initiated at an absorbing inclusion are a few such cases. The latter suggestion is not new. Komolov [18] has analyzed non-linear temperature dependent absorption of the form

$$X(T) = X_i + X_o e^{-u/T} \qquad\qquad (14)$$

Where X_i is the impurity absorption and $X_o e^{-u/T}$ is an intrinsic film absorption, and u is a constant.

Also Manenkov et. al. [15] has suggested irreversible mechano-chemical reactions with a rate

constant of

$$K_{mch} \alpha \; e^{-(E_a - \gamma \sigma)/k_b T} \qquad\qquad (15)$$

where E_a is an activation energy and $\gamma \sigma$ is the stress proportional factor driven by temperature gradients assisting in the damage.

With one of these mechanisms the region that is absorbing expands into the film from its origin at an inclusion or impurity. This inclusion may be as small as 100 A according to some theoretical work of Babadzhan et. al. [19]. Under these conditions a model, either theoretical or empirical, of the absorbing function must be incorporated. This expansion to macroscopic dimensions then necessarily involves thermal build-up. In fact according to the theories mentioned above, the expansion in turn is driven by the thermal build-up.

Another situation involving thermal build-up is the case where absorption occurs on a macroscopic scale (on the order of the diffusion length between pulses). This occurs, for example, in semiconductor grade windows [4] and on intrinsic absorbing metallic mirrors [3]. Table 2 lists the spatial part of the solutions for some of these cases. In particular the case of a weakly absorbing window such that absorption is uniform with depth into the window and the case of a standing wave in a thin film are shown. Many other similar solutions are possible (surface absorption or absorption which has essentially any arbitrary depth dependence). These are just mentioned to point out the tremendous generality of the integral transform technique.

As with microscopic absorption, most cases of observed macroscopic absorption are also dependent on the number of pulses and/or the pulse repetition frequency. So once again a function versus time, temperature, pulse number and pulse repetition frequency must be known or assumed to properly model this situation.

Some work by Nathan et. al. [20] has indicated that a multi-pulse damage decrease can occur by thermal build-up and various relations involving multipulse parameters were realized. Together these lead to

$$E_d \sim \left(\frac{t_p}{N_{min}}\right)^{1/2} \qquad\qquad (16)$$

The terms above are defined as follows: E_d is the damage threshold in (J/cm^2) and N_{min} is the number of pulses at which damage is most likely to occur given some pulse length and frequency. Like our previous works [10,21] this was found based upon the fact that the heat balance gives some particle radius a_{min} most likely to damage. Here a_{min} is the radius of the particle most likely to damage at this pulse length and pulse repetition frequency. These authors mention that relation 16 also applies to uniformly absorbing semi-infinite surfaces.

The numerical work of Nathan et. al. [20] was verified and the basic trends are shown in figure 1. In addition, approximate relations for E_d $(K, \rho, C_p, t_p, t_d, N)$ and a_{min} $(K, \rho, C_p, t_p, t_d, N)$ were derived exactly as done in a previous work [21] further verifying the numerics. Unfortunately, as also indicated in figure 1, the minimum radius for damage to occur quickly becomes very large. In fact it becomes several orders of magnitude larger than most thin films for reasonable laser parameters. Nathan's relations therefore primarily apply to bulk materials with extremely large inclusions, or more reasonably to surface absorption on a semi-infinite absorber.

The derived relations mentioned above are not given because of their extreme complexity yielding little additional insight into the problem. However, as with most real lasers, if one assumes that $t_d \gg t_p$ and that impurity radii are small (limited to a thin film thickness) the relations simplify to the ones given in reference [21] for the single pulse case. This simply indicates that no thermal build-up can occur (i.e. in thin films, if inclusions damage thermally, it must be on the first shot instead of the Nth). It also indicates that multipulse thermal damage scales against the thermal parameters in a similar manner to the single pulse case. This has not as yet been investigated for pulse dependent absorption.

The results of this work are certainly not conclusive. The problem as initially stated is that there is no simple universal effect in multipulse damage. The aim of this work is more the beginnings of an effort to isolate and classify multipulse damage, a baseline study, as it were. It is believed that an understanding of the variation of the absorption function from pulse to pulse will provide essential knowledge for understanding the mechanisms involved for both single and multi-pulsed damage. Also, any theory of multi-pulse damage must predict the appropriate behavior of this function. The primary direction of the research to follow will be in the development of theories to predict this function. It is hoped that this summary of our efforts has stressed the importance of real time pulse to pulse observation of damage evolution in all cases of multi-pulse laser induced damage. Along with this, pulse repetition rate dependence, damage morphologies and laser hardening [7,8] or its inverse need to be studied for all materials and classes of materials used in high energy laser optical components. The statistics of damage along with the collection of data points above will provide essential information for the isolation of the particular mechanisms involved in both single and multipulse damage.

TABLE 1

	Sphere	Cylinder in a Film
	$= \dfrac{Y^2 D_i}{a^2}, \; Y = \alpha a$	$= D_i \left(\alpha^2 + \left(\dfrac{j\pi}{\ell}\right)^2 \right)$
$\Psi \, (\bar{r},\alpha)$	$= \dfrac{\sin (\alpha r)}{r}$	$= J_0 \, (\alpha r) \, \cos \left(\dfrac{j\pi z}{\ell}\right)$
$N(\alpha)$	$= 2\pi^2 \dfrac{K_i}{bY^2 D_i} \left((C\sin Y - Y\cos Y)^2 + b^2 Y^2 \sin^2 Y \right)$	$= \dfrac{\ell}{2} \, (A^2 + B^2) \dfrac{K_h}{D_i}$
	$b = \dfrac{K_h}{K_i} \dfrac{\sqrt{D_i}}{\sqrt{D_h}}$	$A = \dfrac{\pi a}{2K_h} \{ K_i \alpha J_1(\alpha a) Y_0(\beta a) - K_h \beta J_0(\alpha a) Y_1(\beta a) \}$
	$C = 1 - \dfrac{K_h}{K_i}$	$\beta = \alpha \sqrt{\dfrac{D_i}{D_h}}$
		$B = \dfrac{\pi a}{2K_h} \{ K_h \beta J_1(\beta a) J_0(\alpha a) - K_i \alpha J_1(\alpha a) J_0(\beta a) \}$
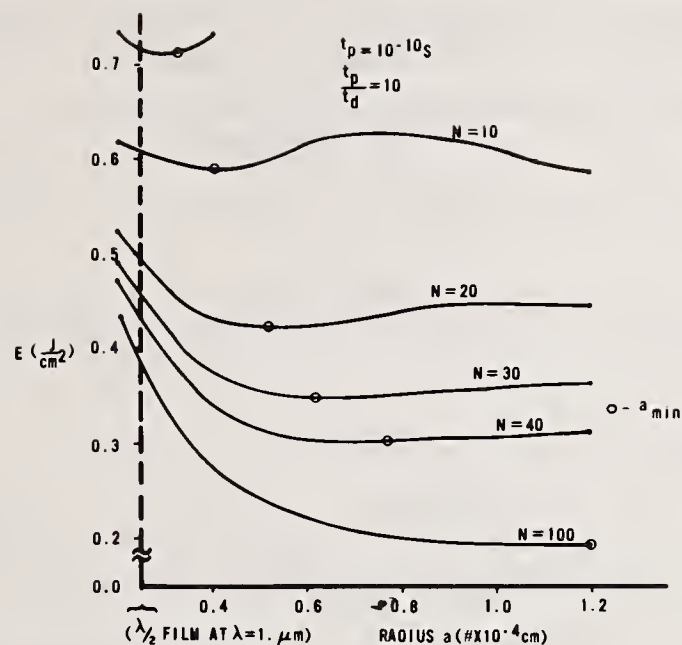
Figure 1. This is a plot of one example of computed damage threshold in (J/cm^2) versus radius of the absorbing inclusion for various numbers of pulses. The pulse repetition frequency is 10^9 Hz.
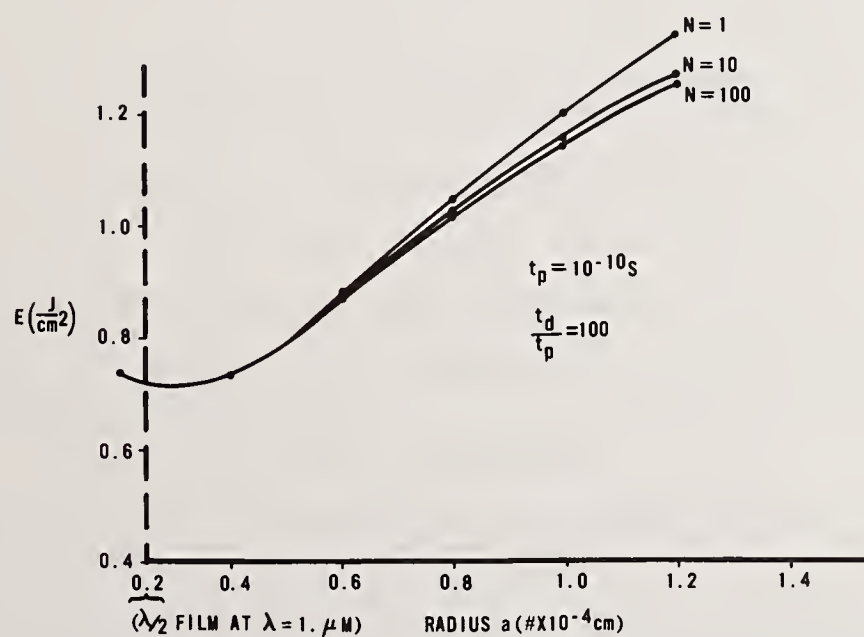
Figure 2. This is a plot of computed damage threshold in (J/cm^2) versus radius of the absorbing inclusion similar to Figure 1, but with a pulse repetition frequency of 10^8 Hz.

TABLE 2. $F_j(\alpha)$

	Sperical Absorption	Cylindrical Absorption
Uniform Absorption	$4\,\dfrac{\pi a^2}{Y^2}(\sin Y - Y\cos Y)$ $Y = \alpha a$	$J_1\,\dfrac{(\alpha a)\,\ell a}{\alpha}$
Standing Wave $p\lambda/2$		$J_1\dfrac{(\alpha a)a}{\alpha}\;\dfrac{\ell}{2}\{\delta_{j,o} - \dfrac{\delta_{j,2p}}{2}\}$
Uniform Depth Gaussian Beam Cross Section (Weakly absorbing window)		$\dfrac{\sqrt{\pi}\;\alpha e^{-\alpha^2 a^2/16}}{(16/a^2)^{3/2}}\;[I_{-1/2}(\alpha^2\dfrac{a^2}{16}) - I_{1/2}(\alpha^2\dfrac{a^2}{16})]\ell\delta_{j,o}$ where a is the Gaussian spot size radius and $I\pm_{1/2}$ is the exponentially increasing modified Bessel function
Gaussian Cross Section Standing Wave (Weakly absorbing thin film)		$\dfrac{\sqrt{\pi}\;\alpha e^{-\alpha^2 a^2/16}}{(16/a^2)^{3/2}}\;[I_{-1/2}(\alpha^2\dfrac{a^2}{16}) - I_{1/2}(\alpha^2\dfrac{a^2}{16})]\;\dfrac{\ell}{2}\{\delta_{j,o} - \dfrac{\delta_{j,2p}}{2}\}$

REFERENCES

[1] M. Bass, H.H. Barrett, eds, A.J. Glass and A.H. Guenther, NBS Spec. Publ. 372: 58; 1972.

[2] L.D. Merkle, M. Bass, R.T. Swimm, eds., H.E. Bennett, A.H. Guenther, D. Milam, and B. Newnam, NBS Special Publication 669: 50; 1982.

[3] N. Koumvakalis, E.S. Lee, M. Bass, eds., H.E. Bennett, A.H. Guenther, D. Milam, and B. Newnam, NBS Special Publication 669: 186; 1982.

[4] R.M. Wood, S.K. Sharma, P. Wate, eds., H.E. Bennett, A.H. Guenther, D. Milam, and B. Newnam, NBS Special Publication 669: 44; 1982.

[5] M. Bordelon, R.M. Walser, M.F. Becker, Y-K. Jhee, eds., H.E. Bennett, A.H. Guenther, D. Milam, and B. Newnam, NBS Special Publication 669: 427; 1982.

[6] S.K. Balitskas and E.K. Maldutis, Sov. J. Quant. Elect. 11 (4): 541; 1981.

[7] B.G. Gorshkov, Yu. K. Danieliko, U.N. Nikolaev and A.V. Sidorin, Sov. J. Quant. Elect. 13 (3): 388; 1983.

[8] M.F. Becker, F.E. Domann, A.F. Stewart, A.H. Guenther, eds., H.E. Bennett, D. Milam A.H. Guenther, and B. Newnam, NBS Special Publication (Boulder Proc.); 1983.

[9] S.R. Foltyn and L.J. Jolin, eds., H.E. Bennett, D. Milam, A.H. Guenther, and B. Newnam, NBS Spec. Publ. (Boulder Proc.); 1983.

[10] M.R. Lange, J.K. McIver, and A.H. Guenther, J. Thin Solid Films, Proc. ICTF-6 (to be published); 1984.

[11] M. Bass and H.H. Barret, Appl Opt. 12: 690; 1973.

[12] A.A. Kovalev, B.I. Makshantsev, N.F. Dilipetskii, Tu V. Sidorin and O.G. Stonik, Sov. J. Quant. Elect. 10: 736; 1980.

[13] E.K. Maldutis, Izvestiya Akademii Navk SSSR, Seriya Fizicheskaya, 41 (1): 196; 1983.

[14] M.R. Lange, J.K. McIver and A.H. Guenther, J. Thin Solid Films, 118 (1):47; 1984.

[15] A.A. Manenkov, G.A. Matylshin, V.S. Nechitailo, A.M. Prokhorov, and A.A. Tsaprikov, eds., H.E. Bennett, A.H. Guenther, D. Milam, and B. Newnam, NBS Spec. Publ. 669: 436; 1982.

[16] T.W. Walker, Air Force Weapons Laboratory, Private communication

[17] H. Goldenberg and J.C. Tranter, Brit. J. Appl. Phys., 3: 296; 1952.

[18] V.L. Komolov, Sov. Phys. Tech. Phys. 27 (3): 307; 1982.

[19] E.I. Babadzhan, V.V. Kosachev, Yu. N. Lokhov and M.I. Ryazanov, Fizika i Khimiya Obrabotki Materialov, 17 (1): 12; 1983.

[20] V. Nathan, T.W. Walker, A.H. Guenther, unpublished

[21] M.R. Lange, J.K. McIver, A.H. Guenther and T.W. Walker, eds., H.E. Bennett, A.H. Guenther, D. Milam, and B. Newnam, NBS Spec. Publ. 669: 1982.

Diffusion barriers were suggested by Raj of Martin Marietta as a possible way to increase damage threshold. Barriers as thin as 50 Å have been tried in the semiconductor industry and are reasonably effective; 50 to 200 Å are commonly tried for semiconductor coatings where diffusion has been a problem.

Self-Focusing in Damage Experiments Revisited

M. J. Soileau, William E. Williams,* and Eric W. Van Stryland

Center for Applied Quantum Electronics
Department of Physics
North Texas State University
Denton, Texas 76203

Last year we reported that the power of importance in self-focusing experiments is the second critical power, P_2, defined by $P_2 = 3.77\,P_1$ rather than the often quoted $P_1 = c\lambda^2/(32\pi^2 n_2)$. Here n_2 is the nonlinear refractive index, c the speed of light and λ the wavelength (both in vacuum). The factor of 3.77 is a numerical factor coming from computer calculations as discussed by Marburger [1]. We also presented a method by which we could obtain n_2 at irradiances very near to damage. In addition, we showed the experimental conditions under which self-focusing is unimportant in damage experiments. We have now extended these results so that in damage experiments where self-focusing is important we can estimate the reduced spot size within the bulk at damage and, thus, obtain the damaging electric field magnitude. This we do by observing the far field time integrated spatial irradiance distribution. We present data for SiO_2, NaCl, BK-7, and CS_2.

Key Words: critical power; laser damage; picosecond pulses; self-focusing.

1. Introduction

The role of self-focusing in laser-induced breakdown was examined in detail in a paper presented at the 1983 Boulder Damage Symposium [2]. In this paper we address questions raised in response to that paper and present additional data that support the conclusions reached in reference 2. The conclusion of reference 2 is that the critical power of importance for laser-induced damage experiments employing tightly focused Gaussian beams is the second critical power P_2, where

$$P_2 = 3.77\,P_1 \tag{1}$$

and

$$P_1 = \frac{c\lambda^2}{32\pi^2 n_2} \tag{2}$$

where λ is the wavelength, c is the speed of light, and n_2 is the nonlinear refractive index. (Equations (1) and (2) are taken from the classic work of Marburger [1].) We based this conclusion upon measurements of the polarization dependence of picosecond laser-induced breakdown and upon measurements of beam distortions in the time-integrated spatial profile of beams transmitted through the samples. In a related paper we reported the results of n_2 in NaCl and SiO_2 at 1064 nm and 532 nm [3].

Much of the past bulk laser-induced damage research assumed that self-focusing corrections to damage data are required for data taken with input power a fraction of P_1 [4]. On the other hand, we have published work for which no self-focusing corrections were made even though the measured breakdown power was a substantial fraction of P_1 [5,6]. In references 5 and 6 we used the lack of polarization dependence and lack of observable beam distortions to justify neglecting self-focusing in computing the laser-induced breakdown electric fields. It is critical that researchers interested in this problem take into account these differences in interpretation and data reduction when comparing the results and conclusions of the various bulk laser-induced

*Present Address: Texas Instruments, Inc., 8505 Forest Lane, P.O. Box 660246, M/S 3123, Dallas, Texas 75266

breakdown experiments. One can question the sensitivity of the null test used in references 5 and 6 in ruling out self-focusing. For example, the beam distortion measurements involve the time integrated spatial profile and are only sensitive to about $\lambda/4$ peak distortion in the transmitted beam. This problem emphasizes the importance of direct measurements of n_2 in a manner independent of the damage test.

In the sections that follow we will review the theoretical treatment of self-focusing in bulk damage experiments and present results of extensive studies we have conducted to verify several key features of the theory. We then discuss in more detail the relevance of the results in reference 2 to prior experiments.

2.   Self-Focusing Theory

Marburger has addressed the problem of self-focusing for "pre-focused" beams in great detail (see reference 1, pp. 66-67). By "pre-focused" we mean a beam focused into the medium by an external lens. The approximate expression for the irradiance, $I(z)$, as a function of propagation distance (z) in the nonlinear medium is given by:

$$I(z)/I(o) \cong \frac{1}{(1-z/R)^2 + (1-P/P_2)(z^2/k^2a^4)} \tag{3}$$

$$\text{where } P_2 = \frac{3.77c\,\lambda^2}{32\pi^2 n_2} \tag{4}$$

P = power in the beam

$k = 2\pi/\lambda$

a = beam waist at the entrance of the sample

R = radius of curvature of the beam phase front due to the external lens

λ = laser wavelength

n_2 = nonlinear refractive index

At the beam waist (focus) eq. (3) reduces to

$$I_{SF} \cong I_o \left[\frac{1}{1-P/P_2}\right] \tag{5}$$

where I_{SF} = peak irradiance in the presence of self-focusing

I_o = peak irradiance without self-focusing

Equations (3) and (5) are approximations (sometimes referred to as the constant shape approximation) and are valid for

$$P < P_2/4 \qquad\qquad\qquad (6)$$

When the input power is significantly greater than $P_2/4$ one must use the more complete numerical solution to compute the enhanced irradiance due to self-focusing. Table 1 is a comparison of the approximation given by eq. (5) and the exact numerical solution given by Marburger (see reference 1, p. 66).

The factor of 3.77 in eqs. (1) and (4) comes from numerical solutions of the nonlinear wave equation for an input beam with a Gaussian spatial profile. The power P_2 is the least power for a singular self-focus to occur within the Rayleigh range, i.e., the beam confocal parameter, for both pre-focused and unfocused geometries. This means that for samples thicker than the Rayleigh range (as is the case for bulk laser-induced damage experiments) singular self-focus will occur within the sample and laser-induced damage will occur for input power equal to P_2. Note that for tightly focused beams, i.e., very small spot sizes, the breakdown field will be reached before P approaches P_2. If that is the case, then the results will be independent of self-focusing effects. The focal spot size needed will depend on the material P_2 and the material breakdown threshold.

Equation (4) can be verified by arranging an experiment in which the breakdown threshold is very high and P_2 is very low. A classic example of such a material is CS_2. This material is an excellent choice for model system studies since its nonlinear behavior has been studied for years and is relatively well understood. The first step is to measure the n_2 in a manner independent of the laser-induced breakdown measurements. Table 2 is a summary of such measurements for CS_2 and other materials of interest using the technique described in reference [3]. Values obtained by other workers using various techniques are listed for comparison [7-10]. With one exception the agreement with other work is excellent. Note that as expected there is no dispersion in n_2 for CS_2 over the 532 to 1064 nm wavelength range and little or no dispersion in n_2 for SiO_2 and NaCl-- contrary to the predictions of widely used theory for this phenomena [11]. BK-7 exhibits a negative dispersion in n_2 over this wavelength range.

We set up a bulk breakdown experiment in CS_2, i.e., arranged the sample length to be much longer than the beam confocal parameter, and measured the breakdown power [12,13]. We then used eq. (4) to calculate n_2 and compared this n_2 to values obtained by beam distortion measurements [3,7]. The results of this comparison are shown in figure 1. In this experiment laser-induced breakdown is totally dominated by self-focusing and the breakdown power is independent of the focusing conditions [12]. Note the excellent agreement between the n_2 determined from the breakdown measurements and eq. (4) and those determined by beam distortion measurements. This verifies that to the factor of 3.77 predicted by theory in reference 2 is correct to within the error bars shown.

Note the lack of dispersion in n_2 in CS_2 for the 532 nm and 1064 nm breakdown measurements. The n_2 values are computed from P_2 measurements using eq. (4). The beam distortion measurements confirm that there is no dispersion in n_2 (the nonlinearity is due to nonresonant reorientation of the CS_2 molecules). This implies that the λ^2 dependence of P_2 in eq. (4) is correct. This λ^2 dependence is a well known consequence of self-focusing theory, however, to our knowledge this is the first direct confirmation of this wavelength dependence.

These results and those in reference 2 confirm is that P_2 is the critical power of importance in laser-induced breakdown experiments. For input powers much smaller than P_2 self-focusing effects will be minimal. As P approaches P_2 self-focusing effects will dominate. For $P < P_2/4$ one may use eq. (5) to correct for self-focusing effects and for $P_2 > P > P_2/4$ one must use the full numerical solution to the nonlinear wave equation to calculate the irradiance at the focal position.

3. Relevance to Past Work

One conclusion of reference 2 was that past work in laser-induced breakdown needs to be re-examined in light of the new results regarding the role of self-focusing. This is what we attempt in this section. Much of the early experimental work [14-16] used the scaling law proposed by Zverev and Pashkov [17] in 1970. Fundamental to that technique is the assumption that the damage threshold irradiance for highly transparent materials is an intrinsic [18] property of the material and that any apparent dependence of the breakdown irradiance on focal spot radius is, w_0, in the material is due to self-focusing. The breakdown power for a given material was then measured as a function of focal spot radius and the results were fit to the equation [15]:

$$\frac{1}{P_B} = \frac{2}{I_B \pi w_0^2} + \frac{1}{P_1} \qquad . \qquad\qquad\qquad (7)$$

where P_B is the power required for breakdown, I_B is the so-called intrinsic damage irradiance and P_1 is the first critical power for self-focusing as defined by eq. (2). [Note that eq. (7) can be derived from eq. (5) if P_2 is replaced by P_1 and the assumptions regarding intrinsic damage are made [15]. Such plots of $1/P_B$ as a function of $1/area$ were assumed to yield I_B as a slope and $1/P_1$ as the y-intercept. Figure 2 is an example of such a plot for two samples of NaCl from the same vendor (Harshaw Chemical Co.). Note that the two plots yield values of P_1 that differ by about a factor of 4 and the I_B is approximately an order of magnitude larger than commonly measured for this material. A similar plot of the results for sample 6 at 1064 nm yields $P_1=0.70$ MW. This result is unreasonable in that n_2 for NaCl has little if any dispersion in the wavelength region and therefore P_1 at 1064 nm should be about 4 times larger than that at 530 nm (not equal as this result implies).

The data shown in figure 2 were taken in recent measurements in our laboratory and are presented in this manner simply to illustrate the problems associated with using the procedure discussed above. The main problems with the procedure are the assumption that I_B is intrinsic and the use of P_1 in eq. (7).

Our conclusion in reference 2 was that prior damage results be reexamined. Unfortunately, much of the work using the Zverev and Pashkov [17] scaling is not recoverable from the literature since the uncorrected thresholds are not reported and cannot be extracted due to insufficient information. However Fradin [14], in anticipation of some problem with the Zverev and Pashkov method did not scale the data reported in 1973 for self-focusing. Smith et al. [16] in 1977 also found some problem in using P_1 to correct their 532 nm and 355 nm picosecond damage thresholds for self-focusing. In most cases their 355 nm thresholds were higher than P_1. A scaling factor, $\phi(P)$, was proposed such that the equation for the beam intensification as a function of input power is given by

$$I = \frac{I_0}{[1 - (P/\phi(P)P_1)]} \qquad . \qquad\qquad\qquad (8)$$

Numerical values for $\phi(P)$ were proposed such that $\phi(P)=1$ for $P \ll P_1$ and $\phi(P)=3.7$ for $P \rightarrow P_2$. However, since the exact functional dependence of $\phi(P)$ was unknown at the time the thresholds reported, reference 16 included the breakdown power and the uncorrected focal area so that future workers could reexamine the data in the light of new measurements.

The results of this work indicate that $\phi(P)$ is a constant with a numerical value probably close to 3.77, the numerical value predicted by Marburger [1] for Gaussian beams. If $\phi(P)$ exhibited the functional dependence predicted by Smith et al. [16] then our experimental data should have indicated the presence of strong self-focusing for input powers below P_1. For example, if we take $\phi(P)=1$ and let our input power equal $0.9 P_1$ then eq. (8) would predict a factor of 10 increase in the peak-on-axis irradiance. This increase in the peak-on-axis irradiance in the material would result in an easily detectable change in the far-field transmitted beam profile. The fact that beam distortions and a polarization dependence are only seen in our test materials for beam powers approaching P_2 indicate that $\phi(P)$ is independent of power.

We will now use eq. 8 with $\phi(P)=3.77$ to reexamine the 532 nm breakdown data of Smith et al. [16]. In that work, the breakdown powers are all below P_1 so the irradiance increase predicted by eq. (8) with $\phi(P)=3.77$ should be valid. In Table 3 we reproduce the 532 nm breakdown thresholds reported in reference 16. Six materials were studied including fused quartz and NaCl. The second and third columns contain the damage threshold power and the uncorrected focal area. The fourth column contains the ratio of the breakdown power to the P_1 critical power for the material. The P_1 values were calculated using n_2 values measured by techniques other than interferometry [15]. The fifth column contains the ratio of the breakdown power to the critical power P_2 calculated using the interferometric measurements of n_2 of Weber et al. [18]. We use the n_2 values of Weber et al. [18] to calculate P_2 rather than scaling column four by the factor of 3.77, since the measurements in reference 18 are more accurate and are conducted using picosecond pulses. Thus the n_2 values should be a reflection of the electronic nonlinear polarizability only. In the sixth column we list the R. M. S. breakdown fields in MV/cm uncorrected for self-focusing. Column

seven contains the data corrected for self-focusing using P_1 as the critical power. These are the breakdown thresholds for 532 nm light published in reference 16. The number in parentheses represents the percentage increase of the corrected threshold over the uncorrected threshold. Finally in column eight we list the R. M. S. breakdown threshold fields corrected for self-focusing using the ratio P/P_2 in column five. Again the numbers in parenthesis represent the percentage increase over the uncorrected threshold.

In examining the data in column seven we see that the breakdown threshold fields increased as much as 50-60 percent using P_1. However, when the thresholds are properly corrected using the second critical power P_2 we see on the average only a 5 percent increase. This is well within the ±15 percent absolute uncertainty in the uncorrected breakdown fields reported by Smith et al. [16] at 532 nm. In addition, the percentage increases in the breakdown threshold field for SiO_2 could well be smaller (assuming the fused quartz sample of Smith et al. [16] (Suprasil I) has the same n_2 value at high irradiance as our own Corning 7940 fused quartz).

Smith et al. [16] also reported breakdown thresholds at 355 nm laser wavelength in thee materials listed in Table 3. The results for this near uv study indicate that, in most cases, the breakdown threshold powers for these materials were substantially higher than the P_1 critical powers at this wavelength. The only exception was CaF_2 where P_B was found to be 0.7 P_1. The P_1 critical powers were calculated using the n_2 values measured at 1064 nm under the assumption that the dispersion in n_2 over this wavelength range was small [16]. In an attempt to correct their data for the presence of self-focusing they scaled their breakdown threshold irradiance levels in KH_2PO_4, NaF, and LiF using eq. (8) and $\phi(P)=2.5 \rightarrow 3.7$. The fused quartz data was scaled using the same equation and $\phi(P)=2.0 \rightarrow 3.0$.

While they were on the right track, meaningful comparison of the 355 nm data with results at other wavelengths is difficult due to the very poor spatial quality of the 355 nm beam used in the measurements. The uncertainty in the 355 nm focal area and the uncertainty in the energy distribution within the focal area lead Smith et al. [16] to assign a factor of two range for the scaled breakdown threshold fields at this wavelength. The actual breakdown thresholds fields may or may not be within this range. A further complicating factor for interpreting Smith et al. [16] 355 nm work is the recent result that the effective n_2 for a material may not be constant as a function of wavelength for photon energies approaching a substantial fraction of the band gap energy. Based on our measurements in BK-7 at 532 nm and those of White et al. [19] in BK-10 at 355 nm the n_2 values for these materials may well be substantially lower at the third harmonic wavelength when compared to the values at 1064 nm. This points to the need for accurate measurements of n_2 in these materials in the regime where multiphoton effects may be coming into play. As such we will not attempt at this time to reexamine the 355 nm thresholds.

In our reevaluation of the breakdown results of other workers we have concentrated on the work of Smith et al. [16] primarily for two reasons. The first reason is that the breakdown measurements in that work were conducted for pulse durations comparable to our own. Therefore, the self-focusing mechanisms in the test materials will be the same. The second reason is that, of the workers who scaled their breakdown thresholds for the presumed presence of self-focusing, Smith et al. [16] is the only work that contains sufficient data to deconvolve the true breakdown thresholds. Other workers merely reported the scaled breakdown threshold irradiance levels without including the focal spot radii used in the measurements [14,15,17]. This makes it impossible to recalculate the breakdown thresholds.

Several other breakdown studies have been conducted in these materials in which no self-focusing corrections were made. For example, Manenkov [20] reported breakdown measurements in the alkali halides (including NaCl) for nanosecond pulse durations at 10.6, 1.06, 0.69, and 0.53 μm laser wavelengths. There is some uncertainty in the focal spot radius used in the measurements since two values are reported without specifying which correspond to the breakdown irradiance levels listed in Manenkov's [20] work. Therefore, we will examine both cases. First, we must include the effects of electrostriction in our value for n_2 since this mechanism is believed to play a strong role in the alkali halides for nanosecond pulse durations. We will use the value of $n_2=4.0 \times 10^{-13}$ esu calculated from nanosecond three wave mixing experiments [21]. With this in mind we find that P_B in NaCl is 0.5 P_2 at 532 nm and P_B is 0.14 P_2 at 1064 nm if we use the larger of the two focal radii cited in reference 20. If we use the smaller focal radius we find that P_B for NaCl is 0.07 P_2 at 532 nm and 0.02 P_2 for 1064 nm. Thus self-focusing effects in Manenkov's [20] work for NaCl are negligible except for the combination of largest spot size and shortest wavelength.

In a similar nanosecond study, Merkle et al. [22] reported single shot damage thresholds for Corning 7940 fused quartz for laser wavelengths ranging from 1064 nm to 355 nm. In fused quartz electrostriction has been shown to play a small role in self-focusing effects for pulse durations

around 30 nsec [23]. Therefore, we will use the n_2 value of 0.95×10^{-13} esu reported by Feldman et al. [23] for nanosecond pulse durations which includes contributions from electrostriction, thermal and electronic effects. We find that the breakdown powers, P_B, reported by Merkle et al. [22] for Corning 7940 are ≤ 0.08 P_2 at 1064 nm and equal to 0.07 P_2 at 532 nm. Therefore, self-focusing effects in the work of Merkle et al. [22] are negligible.

We have also reexamined [10] our own results published in references 5 and 6. In that work we used beam distortion and polarization dependence to verify that self-focusing was not the dominant breakdown effect. However, these tests (i.e., polarization dependence and beam distortions) were not conducted for each experimental condition used. In addition, there is a limit in the sensitivity of these techniques in detecting the presence of self-focusing, e.g., the time integrated beam distortion measurements can only detect a quarter-wave peak distortion. For the most part, little or no adjustment of the originally published numbers is needed. For the ultra-short pulse data (pulsewidth less than 5 psec) and largest spot sizes (14 micron $1/e^2$ half-width) for SiO_2 at 1054 nm adjustments as high as a factor of two were needed. However, for most of the SiO_2 data only small adjustments were required. The corrected data showed essentially the same general dependences on pulsewidth and wavelength reported in references 5 and 6. For SiO_2 and NaCl the pulsewidth dependence was consistent with the predictions of electron avalanche breakdown theory, while the wavelength dependence was not. The conclusion that bulk damage in these materials at 532 nm and 1064 nm is due to multiphoton initiated, electron avalanche breakdown is consistent with the corrected data. Even with self-focusing absent, a spot size dependence remains and sample to sample differences are observed. The latter results indicate the laser-induced breakdown is an extrinsic effect initiated by material defects.

4.   Summary

The key conclusions of this paper and reference 2 is that P_2 is the critical power of importance in laser-induced damage experiments. Equation (5) can be used to correct for self-focusing if $P < 0.25$ P_2, otherwise the full numerical solution to the nonlinear wave equation must be used. Beam distortion and polarization dependence of laser-induced breakdown can be used to avoid experimental conditions for which self-focusing dominates the results.

The data reviewed in the last section of this paper is but a small sample of the laser-induced breakdown measurements available in the literature. We have examined a few specific examples for the purpose of illustrating the importance of using P_2 instead of P_1 in scaling breakdown results for self-focusing effects. It is important to note in Marburger's landmark review paper [1] he noted that Akhmanov's [24] constant shape approximation (which uses P_1 and is the basis of the Zverev and Pashkov procedure) gives correct results only if P_1 is replaced with P_2 and $P < P_2/4$. Our work simply confirms this early theoretical conclusion.

---

5.   References

[1]   Marburger, J. H., in Progress in Quantum Electronics, J. H. Sanders and S. Stenholm, eds., New York, Pergamon Press, pp. 35-110, 1974.

[2]   Williams, William E., M. J. Soileau, and Eric W. Van Stryland, "The Effects of Self-Focusing on Laser-Induced Breakdown," Proceedings of the 1983 Boulder Damage Symposium, to be published.

[3]   Williams, William E., M. J. Soileau, Eric W. Van Stryland, "Simple Direct Measurements of n_2," Proceedings of the 1983 Boulder Damage Symposium, to be published.

[4]   Smith, W. L., Opt. Eng. 17, 489 (1978).

[5]   Soileau, M. J., William E. Williams, Eric W. Van Stryland, Thomas F. Boggess, and Arthur L. Smirl, National Bureau of Standards (U.S.), Special Publication #669, 387 (1982).

[6]   Soileau, M. J., William E. Williams, Eric W. Van Stryland, Thomas F. Boggess, and Arthur L. Smirl, Opt. Eng. 22(4), 424 (1983).

[7]   Witte, K. J., M. Galanti, and R. Volk, Opt. Commun. 34(2), 278 (1980).

[8] Weber, M. J., D. Milam, and W. L. Smith, Opt. Eng. 17(5), 463 (1978).

[9] Owyoung, A., R. W. Hellwarth, and N. George, Phys. Rev. B 5, 628 (1972).

[10] Williams, William E., Ph.D Thesis, North Texas State University, 1984.

[11] Boling, Norman L., Alexander J. Glass, and Adelbert Owyoung, IEEE J. Quantum Electron. QE-14, 601 (1978).

[12] Soileau, M. J., William E. Williams, and Eric W. Van Stryland, IEEE J. Quantum Electron. QE-19, 731 (1983).

[13] Williams, William E., M. J. Soileau, and Eric W. Van Stryland, Opt. Commun. 50, 256 (1984).

[14] Fradin, D. W., IEEE J. Quantum Electron. QE-9, 954 (1973).

[15] Smith, W. L., J. H. Bechtel, and N. Bloembergen, Phys. Rev. B 12(2), 706 (1975).

[16] Smith, W. L., J. H. Bechtel, and N. Bloembergen, Phys. Rev. B 15(8), 4039 (1977).

[17] Zverev, G. M. and V. A. Pashkov, Sov. Phys. JETP 30(4), 616 (1970).

[18] Bloembergen, N., IEEE J. Quantum Electron. QE-10(3), 375 (1974).

[19] White, W. T., III, W. L. Smith, and D. Milam, Appl. Opt. Lett. 9(1), 10 (1984).

[20] Manenkov, A. A., National Bureau of Standards (U.S.), Special Publication #509, 455 (1977).

[21] Levenson, M. D. and N. Bloembergen, Phys. Rev. B 10, 4447 (1974).

[22] Merkle, L. D., N. Koumvakalis, and M. Bass, J. Appl. Phys. 55(3), 772 (1984).

[23] Feldman, A., D. Horowitz, and R. M. Waxler, IEEE J. Quantum Electron. QE-9, 1054 (1973).

[24] Akhmanov, S. A., A. P. Sukhorukov, and R. V. Khokhlov, Zn. Tekh. Fiz., 51, 296 (1966); JETP 24, 198 (1966).

Table 1. Comparison of Constant Shape Approximation to
Numerical Solutions for Focused Gaussian Beams

P/P_2	(I/I_0) Constant Shape Approximation	(I/I_0) Numerical Solution	Numerical Solution/ Constant Shape Approximation
0.27	1.37	1.30	0.95
0.60	2.50	2.08	0.83
0.80	5.00	3.94	0.79
0.90	10.00	7.15	0.72
0.95	20.00	16.45	0.82
0.96	25.00	28.60	1.14
0.97	33.30	63.40	1.92
0.98	50.00	100.00	2.00
0.99	100.00	192.00	1.92

Table 2. n_2 Measurements in Liquids and Solids

Material	Wavelength (μm)	n_2 (x 10^{-13} esu) This Work	n_2 (x 10^{-13} esu) Other Workers
CS_2	1.06	128 ± 10	125 ± 30[a]
	0.53	123 ± 10	
NaCl	1.06	1.37 ± 0.15	1.22 ± 0.21[b]
	0.53	1.38 ± 0.13	
SiO_2	1.06	0.62 ± 0.03	0.95 ± 0.10[b]
	0.53	0.60 ± 0.04	
BK-7	1.06	1.45 ± 0.15	
	0.53	1.01 ± 0.08	

[a] K. J. Witte, M. Galanti, and R. Volk, Opt. Commun. 34, 278-282 (1980); Time Integrated Interferometry at 1.32 μm.

[b] M. J. Weber, D. Milam, and W. L. Smith, Opt. Eng. 17(5), 463-469 (1978); Time Resolved Interferometry at 1.06 μm.

Table 3. 532 nm Breakdown Thresholds of Smith et al. [16]

Material	P_B (KW)	A (μm)^2 (unscaled)	P/P_1	P/P_2	E_0 (MV/cm) (unscaled)	E_{P_1} (scaled)	E_{P_2} (scaled)
KH_2PO_4	151.0	16.0	0.57	0.15	15.3	23.4(53%)	16.6(8%)
SiO_2	129.0	15.9	0.46	0.12	14.5	19.0(31%)	15.4(6%)
NaCl	38.4	15.1	0.60	0.05	7.9	12.4(57%)	8.1(3%)
CaF_2	146.0	15.9	0.62	0.09	15.5	25.2(63%)	16.3(5%)
NaF	126.0	15.8	0.45	0.05	15.0	19.4(30%)	15.4(3%)
LiF	171.0	16.1	0.59	0.06	16.9	26.5(57%)	17.5(4%)

The last three columns contain the uncorrected breakdown fields and the values corrected for the presence of self-focusing. Column seven (E_{P_1}) represents the data reported in reference 16. Column eight (E_{P_2}) contains the data scaled using the correct critical power.
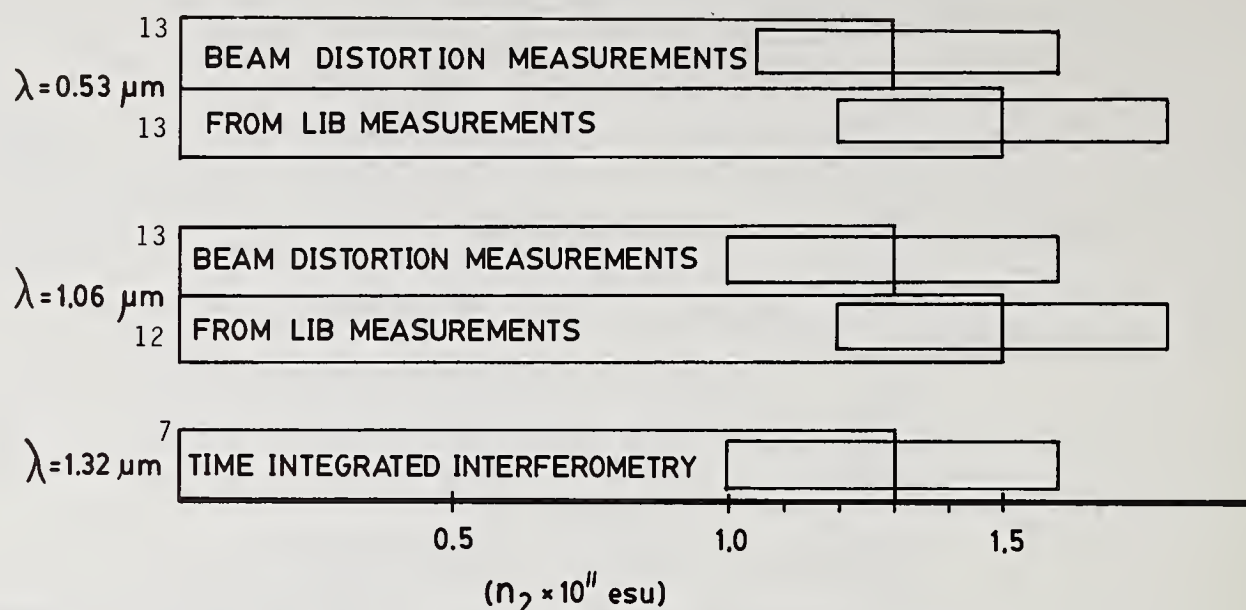
[13] WILLIAMS, ET AL., OPTICS COMM., 50, 256, 1984.
[12] SOILEAU, ET AL., QUANT. ELECT. QE-19, 731, 1983.
[7] WITTE, ET AL., OPTICS COMM. 34, 278, 1980.

Figure 1. n_2 from laser-induced breakdown (LIB) measurements. The LIB results were conducted by measuring the power required for breakdown for a sample of CS_2 thick compared to the beam confocal parameter.   Equation (2) was then used to calculate n_2.
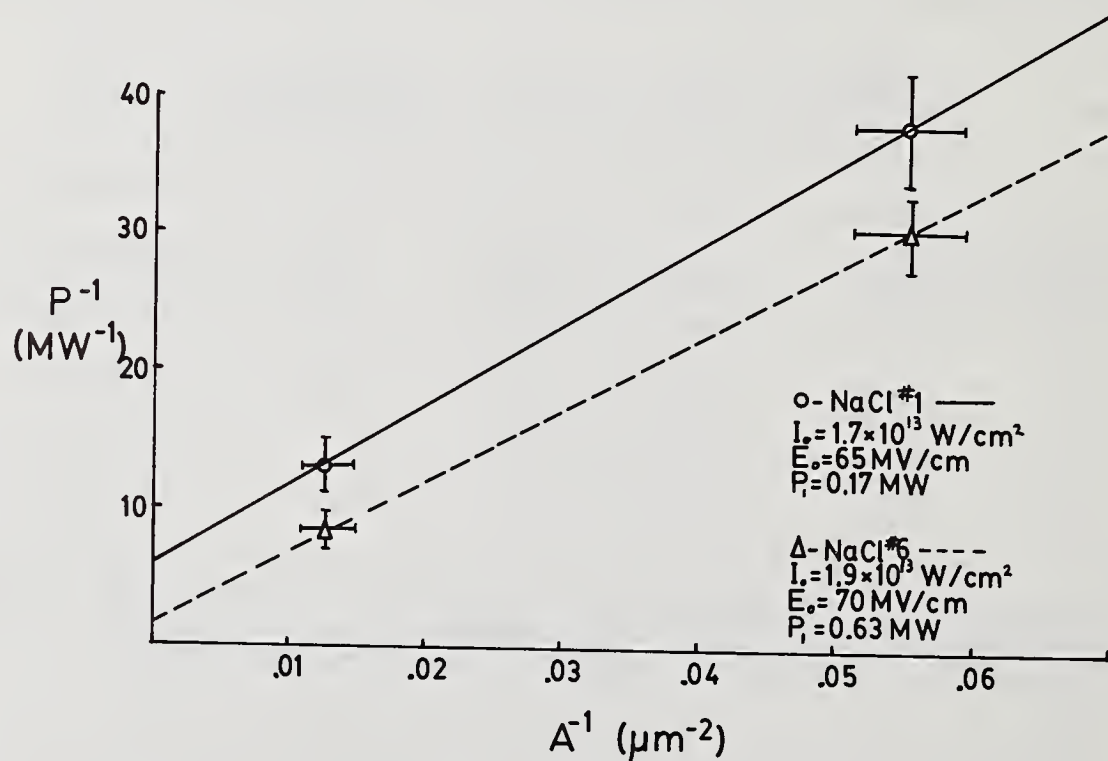
Figure 2. P^{-1} vs. (Area)$^{-1}$ for NaCl. These data are for linear polarized, 532 nm, 35 ± 10 psec pulses. Note that these data are plotted in this manner to show that the procedure on which eq. (7) is based does not work! The I_B thusly determined are too large by an order of magnitude and the P_1's for the two samples of the same material differ by a factor of 4.

In response to the question as to theoretical predictions of whether n_2 should go up with optical frequency, the author replied that the change in dispersion for picosec pulses is entirely because of electronic contributions and should go up with frequency, but only because of local field considerations, which would be expected to be minor. Experimentally it goes up significantly and the theory needs to be reexamined.

Two-Photon Absorption, Nonlinear Refraction and
Optical Limiting in Semiconductors

Eric W. Van Stryland, H. Vanherzeele, M. A. Woodall, M. J. Soileau,
Arthur L. Smirl, Shekhar Guha, and Thomas F. Boggess

Center for Applied Quantum Electronics
Department of Physics
North Texas State University
Denton, Texas 76203

Two-photon absorption coefficients β_2 of eight different semiconductors with band-gap energy E_g varying between 1.4 and 3.7 eV are measured using 1.06 μm and 0.53 μm picosecond pulses. β_2 is found to scale as E_g^{-3} as predicted by theory for the samples measured. Extension of the empirical relationship between β_2 and E_g to InSb with E_g=0.2 eV also provides agreement between previously measured values and the predicted β_2. In addition the absolute values of β_2 are in excellent agreement (the average difference being <26%) with recent theory which includes the effects of nonparabolic bands. The nonlinear refraction induced in these materials is monitored and found to agree well with the assumption that the self-refraction originates from the two-photon generated free carriers. The observed self-defocusing yields an effective nonlinear index as much as two orders of magnitude larger than CS_2 for comparable irradiances. This self-defocusing in conjunction with two-photon absorption is used to construct a simple, effective optical limiter that has high transmission at low input irradiance and low transmission at high input irradiance. The device is the optical analog of a Zener diode.

Key Words: nonlinear absorption; nonlinear refraction; n_2; optical limiting; semiconductors; two-photon absorption; CdTe; GaAs; CdS; CdSe; ZnTe; ZnSe; ZnO.

1.   Introduction

The ever increasing role of semiconductors in light-wave technology has created a pressing demand for the characterization of the nonlinear optical properties of these materials. Semiconductors are attractive as elements in nonlinear-optical devices because of their large and potentially extremely fast optical nonlinearities. A careful study of these <u>macroscopic</u> non-linearities should allow one to determine the dependence of these nonlinearities on fundamental <u>microscopic</u> mechanical and electronic material properties (e.g., band gap, carrier lifetime, carrier effective mass, etc.). The data base formed by this information would then allow one to not only tabulate the materials that exhibit large nonlinearities but also to predict the specific material parameters that give rise to these high nonlinearities. This predictive capability is extremely important from the standpoint of searching for materials with large non-linearities.

A study of the nonlinear optical properties of several semiconductors is presented here, and a relationship between the two-photon absorption coefficient (β_2) and other material properties is verified. Eight different materials were experimentally studied for which the incident photon energy $\hbar\omega$ is less than the band-gap energy E_g but greater than $E_g/2$ so that two-photon absorption (2PA) is allowed [1]. Both 1.06 and 0.53 μm picosecond pulses are used in transmission experiments using semiconductors with E_g ranging from 1.4 to 3.7 eV. We find that the 2PA coefficient β_2 is given by

$$\beta_2 = K \sqrt{E_p}\ f(2\hbar\omega/E_g)/n^2 E_g^3 \tag{1}$$

where K is a material independent constant, n is the linear refractive index, and E_p is nearly material independent for a wide variety of semiconductors [2]. The function f, whose exact form depends on the assumed band structure, is a function only of the ratio of the photon energy $\hbar\omega$ to E_g which determines the states that are optically coupled. The scaling given by eq (1) agrees with the most recent theories for two-photon absorption [3-5] and allows for predictions of 2PA

coefficients for other materials at other wavelengths given minimal materials parameters. For example, extension of this scaling to InSb (300°K) at 10.6 μm predicts a β_2 of 6.8 cm/MW which is in excellent agreement with recent experiments. Specifically, Miller et al. [6] obtain a value of 8 cm/MW. Equation 1, is therefore valid over a range of 20 in band-gap energy from the infrared to the visible. In addition we find that the proportionality constant K as calculated by Weiler [4] for nonparabolic bands agrees with our experimentally determined K to within better than 26%.

We use the experimentally determined 2PA coefficients along with a modified Drude theory (modified to include effects of interband transitions and band filling) to model the nonlinear refraction in these semiconductors. We quantitatively fit the predictions of this theory to beam propagation data obtained for CdSe and obtain excellent agreement when all of the nonlinear refraction is assumed to arise from the carrier generation [7]. That is, the contributions proportional to the photogenerated carrier density dominate the usual bound electron nonlinear refractive index changes. This has been previously shown to be the case for one-photon absorption in materials such as InSb at 5 μm [8] and Si at 1 μm [9]. We find that the effective nonlinear refraction can be two orders of magnitude larger than that for CS_2 at comparable irradiances.

Finally we utilize the combined effects of two-photon absorption and nonlinear refraction in GaAs to make an irradiance (fluence) limiting device [10]. This device has high linear transmission at low irradiance (fluence) and low transmission at high irradiance (fluence). At very high irradiances, laser induced melting is also involved in the limiting action. This device is passive, has picosecond turn on time and is the optical equivalent of a Zener diode.

In Section 2 we describe the model used and derive the equations needed to describe both the nonlinear transmission and nonlinear refraction observed in the semiconductors studied. In Section 3 we outline the experimental procedure used to determine the two-photon absorption coefficients and present the experimentally determined 2PA coefficients. Section 4 presents a comparison of the two-photon absorption data to theory for parabolic and nonparabolic bands with and without exciton corrections. In Section 5 we present the experiments and fits to the beam propagation data using the results of Section 2. We describe a semiconductor optical limiter, based on 2PA, its design, operation, and uses in Section 6.

2. Theory

The experimental configuration used throughout this work is one in which the sample was very thin compared to the confocal beam parameter, and moreover, any self-induced beam phase changes were small enough that beam propagation effects in the sample were negligible (i.e., self action was "external" as described by Kaplan [11]). In this case the Maxwell wave equation for the propagation of the electric field E can be written as

$$2ik\ \partial E/\partial z = i\omega\sigma\mu_o\ E - (\omega^2/2c^2)\ \chi^{(3)}\ |E|^2 E \tag{2}$$

where $\chi^{(3)}$ denotes the third order nonlinear susceptibility, and

$$\sigma = (\alpha + \sigma_{ex} N)\ n\ \sqrt{\varepsilon_o/\mu_o} + i\ Ne^2/(m_{eh}\omega) \tag{3}$$

denotes the conductivity. Here, we have explicitly included the possibility of photogenerated carrier absorption through the term $\sigma_{ex} N$, where σ_{ex} is the total carrier cross section (holes + electrons) and N is the density of these carriers. Also α is the usual residual linear absorption (e.g., band tail absorption, impurity absorption, etc.), and m_{eh} is the reduced electron-hole effective mass. Writing the electric field as

$$E = Ae^{i\Phi} \tag{4}$$

with the irradiance given by $\quad I = (n\varepsilon_o C/2)A^2\quad,$

405

equation 2 can be separated giving

$$\frac{dI}{dz} = -\alpha I - \beta_2 I^2 - \sigma_{ex} N I \tag{5}$$

and

$$\frac{d\Phi}{dz} = \beta_1 I - \gamma_1 N \quad , \tag{6}$$

where β_2, the two-photon absorption coefficient, is proportional to the imaginary part of $\chi^{(3)}$ and $\beta_1 = \omega\gamma/c$ is proportional to the real part of $\chi^{(3)}$. γ is related to the more usual n_2 by $n_2(esu) = cn\gamma/40\pi$ where the right hand side of the equation is in MKS units. γ_1 in equation 6 is given by

$$\gamma_1 = \mu_0 e^2 CP/(2nm_{eh}\omega) \quad . \tag{7}$$

The parameter P is introduced here to account for contributions to the nonlinear refraction proportional to N_{ex} but not explained by the Drude model. An example of such a contribution is that arising from interband transitions [12].

The equation governing the carrier generation is

$$dN/dt = \beta_2 I^2/(2\hbar\omega) \quad , \tag{8}$$

showing that for every two absorbed photons one electron-hole pair is generated. This equation is valid only for pulses short enough that recombination and diffusion can be neglected during the pulse. We assume this to be the case for our picosecond pulses [13].

We note that eq (5) for the irradiance is independent of the phase eq (6). This is due to our assumption of a thin sample (i.e., no irradiance changes due to nonlinear refraction within the material). We can, therefore, solve eq (5) simultaneously with eq (8) for the beam attenuation in a sample of thickness L. These equations must be solved numerically unless the contribution to the absorption from the photogenerated carriers is negligible. We can estimate under what conditions this is true by finding the irradiance, denoted as I_{cr}, for which the carrier absorption is equal to the multiphoton absorption. An approximate relation is found in the limit of small total absorption as

$$I_{cr} \sim 2\sqrt{2}\,\hbar\omega/[\sigma_{ex}t_0(1-R)] \quad , \tag{9}$$

where R is the surface reflectivity and t_0 is the HW 1/e M (half-width at 1/e of the maximum in irradiance) of the assumed Gaussian temporal profile pulses. This result was first given by Bechtel and Smith [13]. Note that this critical irradiance is independent of β_2 since both the transmission change and the photogenerated carriers result from 2PA. Thus, materials with small β_2, which require high incident irradiance to observe a transmission change, will be the most likely materials to be affected by photogenerated carrier absorption.

The contribution to the change in transmission from these carriers is proportional to t_0^{-1}. Longer pulses of the same irradiance contain more energy and, therefore, produce more carriers. We can determine if these carriers are contributing to the nonlinear absorption by measuring the change in transmission for different pulsewidths. We show in Section 3 that the irradiances used are well below I_{cr} and that we can ignore photogenerated carrier absorption. This is the reason for using picosecond pulses as discussed in ref. 13. While we find the carrier absorption to be negligible, the refractive index change proportional to the carrier density eq (6) is

406

definitely not negligible as discussed in Section 5.

The solution to eq (5) with this assumption is

$$I(z,r,t) = (1-R)^j \ I(o,r,t) \ e^{-\alpha z}/[1+q(z,r,t)] \quad . \tag{10}$$

where $q(z,r,t) = \beta_2 \ I(o,r,t)(1-R)(1-e^{-\alpha z})/\alpha$.

Inside the sample j=1, and behind the sample j=2, since there are two surface reflections. Also z is equal to L, the length of the sample. The effect of the rear surface reflection on the absorption has been ignored but is not expected to lead to significant errors in the determination of β_2 for the samples used [14]. Equation 10 can be rearranged to give the instantaneous transmission T' at each radial position of a sample of length L as

$$T'^{-1} = [1+q(L,r,t)] \ e^{\alpha L}/(1-R)^2 \quad . \tag{11}$$

Since $q(z,r,t)$ is directly proportional to $I(o,r,t)$ a plot of T'^{-1} versus incident irradiance should yield a straight line whose intercept determines α and whose slope determines β_2. Experimentally, pulses of Gaussian spatial and temporal profiles are used, which requires spatial and temporal integration of eq (10). The resulting plot of T^{-1} versus I has a slight downward curvature caused by these integrations, since at the higher irradiances both the spatial and temporal profiles are broadened toward the rear of the sample (i.e., there is more 2PA at the middle, brightest part of the beam). Taking account of the temporal and spatial integrals we find for the pulse transmission

$$T = 2\alpha(1-R)/[I_0 \ \sqrt{\pi} \beta_2(e^{\alpha L}-1)] \int_0^\infty dx \ \ln \ [1+q(L,o,o) \ e^{-x^2}] \tag{12}$$

where we have taken

$$I(o,r,t) = I_0 \exp \ [-(r/r_0)^2 \ -(t/t_0)^2] \tag{13}$$

Examples of plots of T^{-1} from eq (12) as a function of I_0 are shown in figures 5a and b of Section 3.

In order to model the beam profile of the pulse and its propagation, we now integrate eq (6) using eq (8) for N and eq (10) (j=1), for the irradiance to obtain an expression for the phase:

$$\Phi(L,r,t) = \Phi(o,r,t) + \frac{\beta_1}{\beta_2} \ (1-R) \ \ln \ [1 + q(L,r,t)]$$

$$+ \frac{(1-R)^2 \gamma_1}{2\hbar\omega \ \beta_2} \int_{-\infty}^t dt' \ F_1(t') \quad , \tag{14}$$

where

$$F_1(t) = \alpha\ln \ [1 + q(L,r,t)] - \frac{q(L,r,t)\alpha}{1-e^{-\alpha L}} \left[1 - \frac{e^{-\alpha L}}{1 + q(L,r,t)} \right]$$

407

Equations 10 (j=2) and 14 together, completely describe the electric field at the exit plane of the sample. From these solutions for I(L,r,t) and Φ(L,r,t), the field at any position outside the sample (L+z,r,t) can then be determined using the Huygens-Fresnel propagation formalism as [15]

$$E(L+z,r,t) = \frac{2\pi}{i\lambda z} \exp\left(\frac{i\pi r^2}{\lambda z}\right)\int_0^\infty r'dr' \; E(L,r',t-\frac{z}{c}) \exp\left(\frac{i\pi r'^2}{\lambda z}\right) J_0\left(\frac{2\pi rr'}{\lambda z}\right) . \tag{15}$$

What we measure in our experiments, using short pulses, is the fluence given by

$$F(L+z,r) = \frac{c\epsilon_0}{2}\int_{-\infty}^\infty |E(L+z,r,t)|^2 \, dt \tag{16}$$

Experimental results are compared with numerical evaluations of eq (16) and/or spatial integrals of eq (16) as described in Section 5.

3. Experiment and Data

3.1 Experiment

In the first set of experiments we measured the transmission of several semiconductors as a function of incident irradiance to determine their nonlinear absorption coefficients. The experimental arrangement is shown in figure 1. The laser source used was a microprocessor controlled, passively mode-locked, Nd:Yag laser that produced single amplified pulses of energy up to 7 mJ per pulse at 1.06 μm when operated in the TEM_{00} mode [16]. The pulsewidth could be varied between 40 and 150 psec (FWHM) by selecting etalons of varying thickness as the output coupler. The width of each pulse was monitored by measuring the ratio, R, of the square of the energy of the fundamental (1.06 μm) pulse to the energy of the second harmonic (0.53 μm), pulse that was produced in a $LiIO_3$ crystal [17]. This ratio is directly proportional to the laser pulsewidth provided that the spatial profile remains unchanged. This ratio was calibrated by measuring the pulsewidth using nearly background free second-harmonic autocorrelation scans while accepting only pulses having a fixed ratio R within 15% of a preset value. To ensure that the ratio, R, was proportional to the pulsewidth autocorrelation, scans were performed for three output coupler etalons, and indeed, the ratio scaled properly. An example of such an autocorrelation scan is shown in figure 2 along with the best Gaussian fit. The autocorrelation width of 54 psec (FWHM) corresponds to a Gaussian pulsewidth of 38 psec (FWHM).

When 0.53 μm light was required, a temperature tuned CDA crystal was placed in the beam at the position indicated by the arrow in figure 1. Light at 1.06 μm was blocked with a polarizer and two 100% dielectric reflecting mirrors. Autocorrelation scans of the second harmonic beam performed with an angle tuned KDP crystal showed that these pulses scaled as the 1.06 μm pulsewidth divided by $\sqrt{2}$ to within 10%, as expected for Gaussian shaped pulses. Again the ratio R was held fixed, and the autocorrelation data was as clean as that shown for 1.06 μm in figure 2.

Two different pulsewidths of 40 and 150 psec were used in the transmission experiments on each sample at 1.06 μm. Since the output coupler etalons used to change the pulsewidth were optically contacted to a flat rotatable quartz plate, the beam line as well as the measured beam parameters remained fixed. (A few percent change in the beam spatial width probably caused by slight self-focusing in the amplifier was taken into account.) The relative error bars between one transmission experiment and the next, where only the pulsewidth was changed, were very small. While at high irradiances (a few GW/cm^2) we did see a small pulsewidth dependence of the transmission in some samples, this difference was consistent with values for the free carrier cross sections (10^{-17} to $10^{-18}cm^2$). No pulsewidth dependence was observed at the low irradiance levels (0.5 GW/cm^2 at 1 μm) used to extract values of the 2PA coefficient. A calculation of I_{cr} from Section 2 for typical samples at 1 μm gives $I_{cr} \sim 5$ GW/cm^2 for $\sigma_{ex}=5\times10^{-18}cm^2$. In fact, eq (9), considerably underestimates I_{cr}. From computer calculations, we find that I_{cr} is several times larger, the difference arising mainly from the fact that the spatial irradiance averaging was ignored in the approximate expression. In addition, at 0.5 μm the contribution of photogenerated carrier absorption will be less than at 1 μm since $\hbar\omega$ increases and σ_{ex} decreases, both leading to an increase in I_{cr}. The maximum experimental irradiance used to extract β_2 from the 0.53 μm data was, therefore, increased to 2 GW/cm^2. The above experimental considerations justify

408

ignoring free carrier absorption in calculating the transmitted irradiance eq (5) [13].

The spatial beam profiles in both the horizontal and vertical direction were determined by scanning a 25 μm pinhole at the position of the sample. The beam size was adjusted at the sample by using pairs of collimating lenses. In all, four different spot sizes were used for the 1.06 μm data from 0.5 mm to 1.5 mm (FWHM). At 0.53 μm the beam size used was 0.5 mm. In addition the beam profiles were monitored on a vidicon to ensure that there were no hot spots, spurious reflections, or shot-to-shot beam width fluctuations. Figure 3 shows a representative pinhole scan for a 1.06 μm beam of FWHM 1.50 mm (FWHM).

The incident energy was continuously varied using a stepping motor controlled rotating half-wave plate in combination with a fixed polarizer. This apparatus kept the polarization on the sample fixed and introduced no measurable beam walk with rotation angle. Previous experience indicates that other alternatives, for example, rotating calcite polarizers, may cause the beam to walk across the sample and across the energy monitoring detectors.

The choice of detectors, as well as the detection geometry, was also determined to be critical. As discussed in Section 5 the phase aberrations introduced on the beam by the two-photon generated free carriers cause considerable defocusing so that the beam profile at the detector varies with incident irradiance. Figure 4 shows an example of this defocusing as observed in the near field behind a sample of CdTe. As the irradiance is increased the beam broadens and breaks up as is characteristic for self-defocusing [18]. Thus, any spatial nonuniformities in the detector response can lead to errors. Indeed care must be exercised to ensure that "external" self action [19] does not result in overfilling the transmission detector--an occurrence that could result in an overestimate of β_2 [20] or result in optical limiting as discussed in Section 6. We found, however, that by using large area detectors (1 cm^2) with a measured spatial uniformity of better than 10% and placing them as close as possible to the sample (3 cm) that these effects were eliminated. The detectors were also determined to be linear over their range of use and were absolutely calibrated with respect to a pyroelectric energy monitor [21] which was in turn checked against two others. In addition, absorbing type neutral density filters placed in front of these detectors were checked to have linear trasmission over a range at least a factor of ten greater than the range used in these experiments. Filters were never used to attenuate the beam prior to the sample. In addition, spike filters transmitting only 1.06 μm (0.53 μm) were placed directly in front of the detectors to reduce optical noise from the flashlamps.

3.2 Data

Table I lists the 10 samples used in these experiments. In all, eight different materials having either a zincblende or wurtzite structure were investigated. All of the samples were II-VI materials except for GaAs which is a III-V material. The thickest sample used (0.5 cm) was over 100 times thinner than the confocal beam parameter (the Rayleigh distance) used for this study. Experiments were performed on each single crystal sample for two orthogonal directions of linear polarization. Within our experimental accuracy, no anisotropy in the measured values for β_2 was observed. A 15 percent variation was reported in ref. 34 for room temperature CdTe; however, the optical pulsewidth was not given. In addition the absolute values of the 2PA coefficients reported there were an order of magnitude larger than we measure. This may indicate the dominance of carrier absorption for long pulses. In ZnTe and the single crystal CdTe, the light propagation direction k was in the (110) direction and in GaAs, $\underset{\sim}{k}$ was in the (111) direction. In CdSe, CdS$_{.5}$Se$_{.5}$ and CdS$_{.25}$Se$_{.75}$, $\underset{\sim}{k}$ was parallel to the c axis; while in CdS and ZnO, k was perpendicular to the c axis. Examples of data used to extract the 2PA coefficient are shown in figures 5a and 5b for 1.06 μm and 0.53 μm respectively. Each data point is the average of five laser firings. The solid line in figure 5a is a fit for CdSe using α=0 and β_2=18 cm/GW in eq (12) of Section 2. The solid line in figure 5b is a similar fit for ZnSe using α=0.5 cm^{-1} and β_2=5.5 cm/GW at 0.53 μm. In all samples the linear absorption was small, and its value was unimportant in the determination of β_2. In both samples of ZnS the scattering was significant and this loss mechanism was included in the model as linear absorption. In the latter case, the effect of the choice of σ on β_2 was less than 10%.

The results of these measurements of the two-photon absorption coefficients are given in the next to the last column of Table I. The absolute error bars on the values of β_2 are estimated to be ±40%. The relative error bars of β_2 determined from one sample to the next, are considerably better as observed by measuring all the samples in sequence for each spot size and each pulsewidth. For example, ZnS(y) listed in Table I always had a larger β_2 than ZnS(c). We conservatively estimate these relative error bars which are important in determining the parametric dependence of β_2 as discussed in the next section, to be ±25%.

409

In the second set of experiments (to be discussed in Section 5) we replaced the transmission detector in figure 1 by either a vidicon tube interfaced with an optical multichannel analyzer (PARC 1215) or by a a 25 μm pinhole placed at various radial positions and longitudinal distances from the sample. We then monitored the spatial beam profile of the transmitted beam using the vidicon, or we monitored the pinhole transmission as a function of incident irradiance. In Section 5, we describe the use of eq (16) to theoretically fit both of these results.

4. Comparison of β_2's to Theory

4.1 2PA Theory

We make three separate comparisons in this section. We first compare our experimentally determined β_2's with the theory of refs. 3, 4, and 5 using parabolic band structure. Excellent agreement is found for all materials except ZnTe. We then use the nonparabolic theory and again find good agreement for all materials except ZnTe. As shown by Weiler, [4] the differences between the parabolic and nonparabolic theories are minor so that this fit is expected. We then include exciton correction factors, as given by Lee and Fan [35] and as calculated by Weiler, [4] and we find that when these are included, ZnTe nearly fits the dependencies shown by the other materials.

As stated in ref. 5, the parametric dependence of β_2 on n, E_g and E_p was first explicitly pointed out by Pidgeon et al., [3] although it was present in the calculations of Basov et al. [36] The band structure and transition scheme used by Pidgeon et al. [3] is shown in figure 6. Calculations using this scheme have been performed for parabolic and nonparabolic bands. They found

$$\beta_2 = \frac{4\pi e^4}{\sqrt{2m}\; c^2} \frac{\sqrt{E_p}}{n^2 E_g^3} f\left(\frac{2\hbar\omega}{E_g}\right) = 53.8 \frac{\sqrt{E_p}}{n^2 E_g^3} f\left(\frac{2\hbar\omega}{E_g}\right) \tag{17}$$

where E_p and E_g are in eV and β_2 in cm/GW in the last expression. Here, m is the electron mass, e the electron charge, c the speed of light in vacuum, and n the refractive index. The values for E_g, E_p and n for each material are listed in Table I. It is important to note that for both parabolic and nonparabolic bands the parametric dependences on n, E_g, and E_p predicted by the theories are the same. The differences lie in the function f and the ratio of $\hbar\omega$ to E_g (i.e., which states are optically coupled). Weiler [4] corrected an error in the calculation of f in ref. 3 and obtained the following expression using parabolic bands.

$$f(x) = \frac{2^5}{\sqrt{6}} \left(4 + \frac{29\sqrt{2}}{12}\right) \left\{ \frac{(x-1)^{3/2}}{x^5} \right\} = 96.9 \left\{F_2(x)\right\} \tag{18}$$

where $F_2(x)$ is the same function defined in ref. 5. For nonparabolic bands, Weiler [4] finds

$$f_{np}(x) \overset{\Delta \ll E_g}{=} \frac{32}{5} \frac{(x-1)^{3/2}}{x^3} \left\{ \frac{3\sqrt{x}}{\left(\frac{3}{2}x-1\right)^2} + \frac{(x+1)^{3/2}}{3x^5} (x^4 + 2x^2 + 6) \right\} \;. \tag{19}$$

As shown in ref. 4 the differences between f_{np} for $\Delta \ll E_g$ and $\Delta \gg E_g$, where Δ is the split-off energy shown in figure 6 are small. The expression for $\Delta \gg E_g$ is

$$f_{np}(x) \overset{\Delta \gg E_g}{=} 16\sqrt{\frac{2}{3}} \frac{(x-1)^{3/2}}{x^3} \left\{ \frac{\sqrt{x}}{\left(\frac{3}{2}x-1\right)^2} + \frac{6}{45} \frac{(x+1)^{3/2}}{x^5} \left(\frac{9}{16}x^4 + \frac{5}{2}x^2 + 6\right) \right\} \tag{20}$$

Exciton corrections to values of β_2 have been predicted by Lee and Fan [35]. Weiler [4] has evaluated these corrections in terms of the ratio ε of the exciton binding energy E_b to the band-gap energy E_g. These ratios are listed in Table I. We reproduce the results of these calcula-

410

tions at the excitonic enhancement g_{ex}, of β_2, as a function of $\hbar\omega/E_g$ in figure 7 for various values of [4].

4.2 Comparison to Theory

Figure 8 shows a log-log plot of β_2 scaled by $n^2/(\sqrt{E_p}F_2)$ (see eq (10) for F_2) as a function of E_g. The solid line is a least squares fit to the data (excluding ZnTe) for a line having a slope of -3 to account for the E_g^{-3} dependence of β_2. Clearly the parametric dependences using this parabolic theory fit the data very well except for ZnTe. This single parameter fit yields a two-photon absorption coefficient given by the following equation:

$$\beta_2 = (3.1 \pm 0.5)10^3 \; \frac{\sqrt{E_p}F_2(\frac{2\hbar\omega}{E_g})}{n^2 E_g^3} \tag{21}$$

where again E_p and E_g are in eV and β_2 is in cm/GW. The values predicted from eq (21) are listed in the last column of Table I for each material. The value of the constant (3.1×10^3 in eq (21) predicted by theory from eqs. (17 and 18) is 5.21×10^3, so that the absolute values of the experimentally determined β_2's are, on the average, low by a factor of 1.7.

If we now compare the experimentally determined β_2's with the nonparabolic theory ($\Delta \ll E_g$, eq (19) we obtain the results shown in figure 9. While the overall fit to the parametric dependence is not quite as good as for the parabolic case (again the solid line is a least squares fit to a line of slope -3 excluding ZnTe), the absolute values are, on average, only 26% lower than predicted by this theory. The dotted line is the curve predicted by eqs. (17 and 19).

A similar plot (not shown) using eq (20) for $\Delta \gg E_g$ gives an almost identical fit except in this case the difference between theory and a least squares fit of the data is reduced to only 3.5%. The actual case for these materials lies in between these two theories, although closer to $\Delta \ll E_g$, and may be partially responsible for scatter in the data (up to 23% change in β_2).

If we now include corrections to β_2 due to excitons as given in figure 7 we obtain the curve of figure 10. Here, we have used the parabolic theory (i.e., F_2) except for the additional scaling with g_{ex}. This correction factor has only been calculated for parabolic bands.[35] What we see in figure 10 is that most of the discrepancy between theory and experiment observed for ZnTe (g_{ex}=4.3)[4] has been removed by including excitonic enhancement. However, the overall fit to the parametric dependence (again the straight line is a least squares fit) is somewhat worse. This may be attributed to our lack of accuracy in calculating g_{ex}. Note that for most materials g_{ex} is of the order of 2 even when the coupled states are well above the gap (see fig. 7). Consequently, when excitonic enhancement is included for parabolic bands, the absolute β_2 values predicted by theory are a factor of 3.3 larger than those measured.

The reason that the exciton enhancement for ZnTe is considerably larger than for the other materials is that at 1.06 μm, two photons couple states only 3.5% above the gap, where excitonic effects should be greatest as shown in figure 7. We should point out, however, that we have only one material where the coupling is this close to the gap, and the error bars for this material are larger than for the other materials. ZnTe damaged easily allowing us to use a small spot size, only and limited the range of irradiances for fitting β_2. On the other hand (as shown in fig. 8), where there is overlap between the data taken here and data taken by Bechtel and Smith, [13] the agreement is excellent. They also obtained a large β_2 for ZnTe.

Two other data points listed in Table I and shown in figures 8, 9, and 10 require comment. The polycrystalline CdTe sample gave an experimental β_2 lower than the single crystal CdTe sample. It is designed as a 10.6 μm optical window and is doped with 10^{17}cm^{-3} indium [24]. It is not understood at present if or how these impurities lower the measured β_2. The ZnS(y) sample is a chemical-vapor-desposition grown sample that has a yellow appearance caused by crystal lattice imperfections that can be annealed out by a special heat treatment process [26]. The ZnS(c) is the same starting material that has undergone this heat treatment. It appears water clear, and its linear transmission cutoff is shifted into the UV. The indication from the data presented here is that not only has the linear absorption in the visible and near UV been reduced, but that the two-photon absorption at 0.5 μm has also been reduced by this heat treatment. That is, defects may be contributing to β_2. This may also be true for the ZnTe sample at 1 μm since it damaged easily.

5. Self-Refraction

In this section we present results for the beam propagation behind the sample given the irradiance and phase distributions of equations 10 (j=2) and 14. Equation 16 (Section II) describes the fluence at any point z,r behind the sample. We present data here using a beam of width 1.70 mm (FWHM) incident on the CdSe sample listed in Table I, that is placed near the beam waist. Thus $\Phi(o,r,t)$ is taken to be zero in eq (14). The transmitted signal was monitored at distances of 0.5 m and 2 m behind the sample which are both near field regions. Figure 11 illustrates the change in the beam profile with irradiance at z=0.5 m (using 92 psec FWHM pulses) as displayed on the vidicon. This scan is a narrow slice through the center of the beam equivalent to a pinhole scan. The dotted line is a fit to eq (16) as a function of r for β_2=18 cm/GW, P=3, and γ=0(i.e., n_2=0). We find that if present, the effects of bound electronic contributions to the nonlinear refractive index are overshadowed by the photogenerated carrier effects. This is confirmed by our other measurements which monitored the fluence transmitted by a pinhole as a function of irradiance.

Using a 25 μm diameter pinhole in front of a photodetector we measured the on-axis (r=0) fluence of the transmitted signal as a function of the peak on axis input irradiance for two pulsewidths and two distances. The results are shown in figures 12 and 13. To further verify the validity of the theory, the irradiance dependence of the transmitted fluence at an off-axis point was also measured. This is shown in figure 14.

The theoretical fits in figures 12, 13, and 14 were obtained from the numerical evaluation of F given in eq (16). Other parameters (see Table I) used in the calculation are α =.2 cm^{-1}, m_{eh}=.104 m [30]. The total density N of charge carriers generated by two-photon absorption on axis can be calculated by integration of eq (8). At a peak input irradiance of 1 GW/cm^2, we obtain a peak value of N evaluated at the input plane of the sample to be 2 x 10^{18}cm^{-3}. We find that the best agreement between the theory and the experiments is obtained for P=3.5. The fits shown in figures 12, 13, and 14, are for values of P=3.5 ± 1, with the exact value of P adjusted between 4.5 and 2.5 to obtain the best fit. Using a two-level model, P has been calculated to be $E_g^2/(E_g^2-h^2\omega^2)$ [37]. For CdSe, E_g=1.74 eV at room temperature, and this formula predicts P=2 at 1 μm. The peak phase change undergone by the beam, calculated from eq (14) of Section II is (for I_0=1 GW/cm^2) $\Delta\Phi$ =-8.1, which is 1.3 wavelengths distortion. We have ignored the n_2 due to bound electronic effects in these calculations. Even if this nonlinearity for CdSe were as high as the n_2 of CS$_2$ (i.e., 10^{-11} esu), the maximum contribution to the phase change would be 40πLIωn_2/n_0 which is 0.2 for I_0=1 GW/cm^2. This index change also would be a self-focusing effect and not a defocusing effect as observed. Thus the nonlinear refraction observed in CdSe is approximately 40 times larger than in CS$_2$ at this irradiance. Higher irradiances give rapidly increasing values of defocusing since the nonlinearity is induced by 2PA (i.e., a factor of two increase in irradiance gives nearly a factor of four larger phase distortion).

6. Optical Limiter

In this section we describe a nonlinear optical device (an optical power limiter) [10] which utilizes both two-photon absorption, as discussed in Sections III and IV, and the associated nonlinear refraction discussed in Section V. This completely passive device has a high transmission for low input irradiance (fluence) but it clamps the output at a constant irradiance (fluence) above a predetermined input. Such a device can be used as a protective element to restrict the irradiance (fluence) of a pulse incident upon sensitive optical components or as a regulator to smooth optical transients. This device is the optical analog of a Zener diode.

Optical limiting by nonlinear absorption in semiconductors was proposed and demonstrated in the late 1960's [38-40]. Moreover, nonlinear refraction combined with spatial filtering has been used to demonstrate optical limiting in liquid [41,42] and gas filled cells [43]. Here we demonstrate optical limiting in GaAs. Below the melting threshold, what we have done differently is to use not only nonlinear absorption (2PA) in GaAs but nonlinear refraction together with spatial filtering to construct a more effective device. Above the melting threshold, we also take advantage of a solid-to-liquid phase transition, which affects the reflectivity and transmission.

The geometry we used for optical limiting is shown in figure 15. A single 40 ps (FWHM) 1.06 μm pulse was focused to a 100 μm (FWHM) spot at the surface of the GaAs with a 465-mm-focal-length lens L_1. The transmitted beam was collected and collimated by a 381-mm-focal lens L_2 placed one focal length behind the sample. The recollimated beam then passed through a 2-mm-diameter aperture placed one focal length beyond L_2 and directly in front of a photodiode. The sample used was nearly identical to the sample listed in Table I. The limiting capabilities of the device are shown by the triangles in figure 16. At low input energies (< 0.5 μJ), the device

412

response was linear and was consistent with the 45% linear transmission of the GaAs and the 73% transmission of the pinhole. Above 10 μJ input, the output energy was essentially clamped at 1 μJ. The device continued to limit for input energies greater than 1 mJ. Over the full range of operation, the system transmission was reduced from 33% to 0.1%. Notice that regulation continued for input energies far above the GaAs single shot melting threshold of 0.9 J/cm² (indicated by the arrow in fig. 16). Above the melting threshold, the GaAs was translated before each firing so that each pulse irradiated virgin material.

Below the irradiance required for melting, as the input energy was increased, the transmission of the GaAs was reduced by 2PA. In this regime, the amplitude of the spatial beam profile transmitted by the GaAs was distorted solely by 2PA, and the phase distorted by index changes associated with the 2PA-generated free carriers as discussed in Sections II and IV. The self-diffraction associated with this phase and amplitude distortion reduced the effective pinhole transmission. Above the melting threshold, the increase in the reflectivity and absorptivity of the molten region further reduced the GaAs transmission and further distorted the amplitude profile of the transmitted beam.

The contribution of 2PA and nonlinear reflection to the limiting action can be separated from the contribution of nonlinear refraction by carefully collecting all of the transmitted energy with the pinhole removed as shown in figure 16. These results are shown by the circles in figure 16. Below E_{TH}, the nonlinear transmission is dominated by 2PA and can be fit by a 2PA coefficient of 26 cm/GW [10]. The value of 26 cm/GW reported in ref. 10 for the 2PA coefficient β_2 of GaAs is nearly identical to the value of 23 cm/GW shown in Table I and indicates the confidence in the values of β_2. These measurements of β_2 on GaAs were made independently with a nearly identical laser system. Above E_{TH}, the problem becomes much more complicated and is outside the scope of this paper. In this regime, the central region of the pulse that arrives after melting is initiated is heavily attenuated and reflected by the molten layer of GaAs. In addition, there is considerable evaporation of material for fluences more than ~10% above the melting threshold. It is clear, however, that the transition from below to above threshold is a smooth one. That is, there is no discontinuity in limiter response at threshold.

It is interesting to compare the contributions of TPA and self-diffraction just below the melting threshold. At an input energy of 80 μJ, 2PA acting alone has reduced the transmission by a factor of 5. On the other hand, the combined effects of TPA and self-diffraction have reduced the transmission by a factor of 30. Thus, the present configuration is a considerable improvement over limiters that utilize 2PA exclusively.

We should also like to contrast the present switch with the Si device demonstrated in ref. 44 that utilizes indirect absorption, free-carrier absorption, self-diffraction and a solid-to-liquid phase change to limit energetic pulses at 1 μm. The nonlinear absorption in Si at 1 μm is strictly fluence dependent, and the device operation is independent of pulsewidth for pulsewidths shorter than the carrier recombination time. The present device is considerably more complicated. The nonlinear absorption, which is dominated by 2PA, is irradiance dependent, while the nonlinear refractive index that arises from the 2PA-generated free-carriers is a time integrated effect that persists for the duration of the carrier lifetime. Nevertheless, the carriers cannot be generated without a sufficiently intense pulse, which in practice restricts this device to operation with short pulses. However, the limiting pulse energy can be varied considerably by changing the geometry (e.g., using a very short focal length lens L_1 in figure 15 will lower the limiting energy). An advantage of the present device (and 2PA-based optical limiters in general) over the Si device is its higher linear transmission at 1 m. Another more important advantage of 2PA-based limiters is the broader band-pass that they offer. For example, the GaAs device should function for wavelengths between approximately 0.9 and 1.7 μm where 2PA is the dominant absorption process.

7. Conclusion

The material parameter dependence found for a wide variety of semiconductors as discussed in Section III allows us to predict, with reasonable confidence, the two-photon absorption coefficient of other materials at other wavelengths. This includes, for example, mixed ternary compounds. Thus the 2PA at a particular wavelength can be tailored for a specific application.

The fact that this scaling fits the data so well implies that all of the important materials parameters have been included in the theory and that other contributions to β_2 (e.g., higher bands) cause small effects. One possible deviation from the predicted scaling is the effect of excitons. We have one material (ZnTe) which indicates that such effects may be important. If we attempt to extend this theory into the UV, we find that the predictions are in general considerably lower than experiments; however, a general trend can be found. If the coupled states

are well above the gap the deviations are relatively small, on the order of a factor of 4 or 5. As the coupled states get close to the gap, however, the deviation increases rapidly. For example, in RbI at 266 nm where $2\hbar\omega/E_g=1.47$ the experimentally measured 2PA coefficient of 2.49 cm/GW [45] is 3.7 times larger than predicted by eq (21). At a wavelength of 355 nm where $2\hbar\omega/E_g=1.10$, however, the measured 2PA coefficient of 5.08 cm/GW [45] is 14 times larger than predicted. This trend is maintained for the limited data available [45]. Considering color centers as excitons with large binding energies, such large correction factors may be accounted for. The role of excitons and color centers in 2PA needs further study. A study of the wavelength dependence of 2PA near the gap using a continuously tunable laser should help clarify the role of excitons.

It is interesting to look at the history of the measurement of 2PA coefficients. Figure 17 shows experimental values of β_2 reported for GaAs and CdSe for years beginning with 1966. This figure illustrates the fairly steady decrease in reported values as both the lasers and the experimental technique were refined. Much of the earlier data was obtained with nanosecond pulsed lasers where photogenerated carrier absorption is expected to dominate. Additionally in some instances multimode lasers were used. An additional experimental problem not previously recognized that can lead to an overestimate of β_2 is that the extreme defocusing present may allow some of the transmitted light to go undetected.

While this defocusing may be an experimental difficulty in determining β_2 it can be extremely useful for nonlinear optical devices such as the limiter discussed in Section VI. We found that this defocusing was quantitatively explained by attributing all of the nonlinear refraction to the build-up of excited carriers although the simple Drude theory had to be modified to allow for interband transitions. These fits indicate that interband transitions may actually dominate the refractive index change in these two-photon absorbers. In addition, we demonstrated a simple but effective optical limiter based on two-photon absorption, the associated self-defocusing, and spatial filtering. By choosing a substance with the proper materials parameters and a specific geometry, this limiting can be tailored to suit a specific need. Clearly further applications of the combined action of 2PA and self-refraction in nonlinear optical devices have and will be made.

---

8. References

[1] E. W. Van Stryland, H. Vanherzeele, M. A. Woodall, and M. J. Soileau, in "Laser Induced Damage in Optical Materials," NBS Special Publication, to be published in 1985.

[2] $E_p=2P^2m/\hbar^2$ where P is the Kane momentum parameter and m is the electron mass, E. O. Kane, J. Chem. Phys. Solids 1, 249, 1957.

[3] C. R. Pidgeon, B. S. Wherrett, A. M. Johnston, J. Dempsey, and A. Miller, Phys. Rev. Lett. 42, 1785, 1979.

[4] M. Weiler, Solid State Commun. 39, 937, 1981.

[5] B. S. Wherrett, JOSA B 1, 67, 1984.

[6] A. Miller, A. Johnston, J. Dempsey, J. Smith, C. R. Pidgeon, and G. D. Holah, J. Phys. C Solid State Phys. 12, 4839, 1979.

[7] Shekhar Guha, E. W. Van Stryland, and M. J. Soileau, to be published, 1985.

[8] D. A. B. Miller, S. D. Smith, and B. S. Wherrett, Opt. Commun. 35, 221, 1980.

[9] H. J. Eichler, Opt. Commun. 45, 62, 1983.

[10] T. F. Boggess, A. L. Smirl, S. C. Moss, I. W. Boyd, and E. W. Van Stryland, to be published in IEEE JQE, 1985.

[11] S. A. Akhmanov, R. V. Khokhlov, and A. P. Subhorukov, "Laser Handbook," ed. by F. T. Arecci

and E. O. Scholz-Duboie, North Holland Pub. Co., Amsterdam, 1972.

[12] B. S. Wherrett and N. A. Higgins, Proc. R. Soc. Land. A379, 67, 1982.

[13] J. H. Bechtel and W. L. Smith, Phys. Rev. B 13, 3515, 1976.

[14] A. F. Stewart, "Intensity Dependent Absorption in Semiconductors," dissertation, University of Southern California, unpublished, 1980.

[15] M. Born and E. Wolf, "Principles of Optics," 5th edition, page 383, Pergamon Press, Oxford, U.K., 1975.

[16] Quantel Model YG40, Quantel International, Inc., 385 Reed Street, Santa Clara, California 95050.

[17] W. H. Glenn and M. J. Brienza, Appl. Phys. Lett. 10, 221, 1967.

[18] D. Weaire, B. S. Wherrett, D. A. B. Miller, and S. D. Smith, Opt. Lett. 4, 331, 1979.

[19] A. E. Kaplan, Radiophys. Quantum Electron. 12, 692, 1969.

[20] E. W. Van Stryland, M. A. Woodall, W. E. Williams, and M. J. Soileau, in "Laser Induced Damage in Optical Materials," NBS Special Publication #638, 589, 1981.

[21] Gentec ED-100, Gentec Inc., 2625 Dalton Street, Ste-Foy, Quebec, Canada G1P3S9.

[22] Values taken from E. O. Kane "Band Structure of Narrow Gap Semiconductors," in Narrow Gap Semiconductors Physics and Applications, ed. W. Zawadzki, Springer Verlag, New York, 1980, p. 13, for values not listed in this reference the value of 21 eV was assumed.

[23] Cleveland Crystals, P.O. Box 17157, Euclid, Ohio 44117.

[24] II-VI, Inc., Saxonburg Blvd., Saxonburg, PA 16056.

[25] Morgan Semiconductors, 2623 National Circle, Garland, Texas 75041.

[26] CVD Inc., 35 Industrial Parkway, Woburn, MA 01801.

[27] Raytheon Co., Missile Systems Div., Hartwell Rd., Bedford, MA 01730.

[28] Atomergic Chemetals, 100 Fairchild Ave., Plainview, NY 11803.

[29] Landolt-Bornstein Numerical Data and Functional Relationships in Science and Technology, Vol. 17, Semiconductors, Subvolumes (a) and (b), editor in chief, K. H. Helelwege, Springer-Verlag, New York, 1982.

[30] M. Neuberger, "II-VI Semiconducting Compound Tables," Electronic Properties Information Center, Hughes Aircraft Co., Culver City, CA, 1969.

[31] Y. S. Park and D. C. Reynolds, Phys. Rev. 132(6), 2450, 1963.

[32] These values obtained by linear extrapolation as a function of composition between the known values for CdS and CdSe. Y. S. Park and D. C. Reynolds, Phys. Rev. 132, 2450, 1963.

[33] Richard H. Bube, Photoconductivity of Solids, John Wiley & Sons, New York, New York, 1960.

[34] Stephen J. Bepko, Phys. Rev. B 12, 669, 1975.

[35] C. C. Lee and H. Y. Fan, Phys. Rev. B 9, 3502, 1974.

[36] N. G. Basov, A. Z. Grasyuk, I. G. Zubarev, V. A. Katulin, and O. N. Krokhin, Sov. Phys. JETP 23, 366, 1966.

[37] R. K. Jain and M. B. Klein, in "Optical Phase Conjugation," ed. R. A. Fisher, Academic Press, New York, 1983.

[38] J. E. Geusic, S. Singh, D. W. Tipping, and T. C. Rich, Phys. Rev. Lett. 19, 1126, 1967.

[39] J. M. Ralston and R. K. Chang, Appl. Phys. Lett. 15, 164, 1969.

[40] V. V. Arsen'ev, V. S. Dneprovskii, D. N. Klyshke, and A. N. Penin, Sov. Phys. JETP 29, 413, 1969.

[41] R. C. C. Leite, S. P. S. Porto, and T. C. Damen, Appl. Phys. Lett. 10, 100, 1967.

[42] M. J. Soileau, W. E. Williams, and E. W. Van Stryland, IEEE J. Quantum Electron. QE-19, 731, 1983.

[43] J. E. Bjorkholm, P. W. Smith, W. J. Tomlinson, and A. E. Kaplan, Opt. Lett. 6, 345, 1981.

[44] T. F. Boggess, S. C. Moss, I. W. Boyd, and A. L. Smirl, Opt. Lett. 9, 291, 1984.

[45] P. Liu, W. L. Smith, H. Lotem, J. H. Bechtel, and N. Bloembergen, Phys. Rev. B 17, 4620, 1978.

[46] S. Jayaraman and C. H. Lee, Appl. Phys. Lett. 20, 392, 1972.

[47] Ya. A. Oksman, A. A. Semenov, V. N. Smirnov, and O. M. Smirnov, Sov. Phys. Semicond. 6, 629, 1972.

[48] A. Z. Grasyuk, I. G. Zubarev, V. V. Lobko, Yu. A. Matreets, A. B. Mirnov, and O. B. Fhatberashvili, Sov. Phys. JETP Lett. 17, 416, 1973.

[49] D. A. Kleinman, Robert C. Miller, and W. A. Nordland, Appl. Phys. Lett. 23 243, 1973.

[50] Haim Lotem, J. H. Bechtel, and W. L. Smith, Appl. Phys. Lett. 28, 389, 1976.

[51] A. Saissy, A. Azema, J. Botineau, and F. Gires, Appl. Phys. 15, 99, 1978.

[52] B. Bosacchi, J. S. Bessey, and F. C. Jain, J. Appl. Phys. 49, 4609, 1978.

[53] F. Bryuknar, V. S. Vneprovskii, and V. U. Khattatov, Sov. JQE 4, 749, 1974.

[54] Michael Bass, E. W. Van Stryland, and A. F. Stewart, Appl. Phys. Lett. 34, 142, 1979.

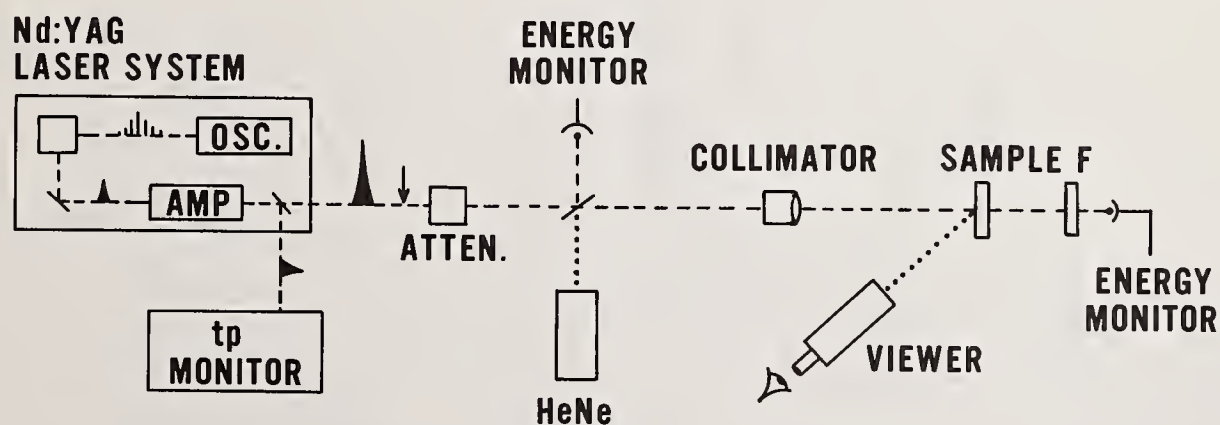Two-photon Absorption: $\lambda = 1.06\mu m$ $2\hbar\omega = 2.34$ eV

Material	form[a]	$n(\lambda)$	$E_g(eV)$	$E_p^{(b)}(eV)$	E_b/E_g	$\beta_2^{exp}(\frac{cm}{GW})$	$\beta_2^{theor.}(\frac{cm}{GW})$
ZnTe[c]	Z	2.79[c]	2.26[i]	19.1	0.004[o]	4.5	0.89
CdSe[c]	W	2.56[c]	1.74[j]	21	0.007[i]	18	18.6
CdTe[d]	Z	2.84[c]	1.44[c]	20.7	0.003[o]	22	25.1
CdTe[d]	Zp	2.84[c]	1.44[c]	20.7	0.003[o]	15	25.1
CdS$_{.5}$Se$_{.5}$[c]	W	2.45[l]	1.93[k]	21	0.010[l]	10	12.1
CdS$_{.25}$Se$_{.75}$[c]	W	2.51[l]	1.78[k]	21	0.008[l]	15	17.7
GaAs[e]	Z	3.43[i]	1.42[i]	25.7	0.003[o]	23	19.7

Two-photon Absorption: $\lambda = 0.53\mu m$ $2\hbar\omega = 4.68$ eV

Material	form	$n(\lambda)$	$E_g(eV)$	$E_p(eV)$	E_b/E_g	$\beta_2^{exp}(\frac{cm}{Gw})$	$\beta_2^{theor.}(\frac{cm}{GW})$
ZnS[f]	Zp(c)	2.40[i]	3.66[i]	20.4	0.010[i]	2.0	2.10
ZnS[f]	Zp(y)	2.40[i]	3.66[i]	20.4	0.010[i]	3.5	2.10
ZnSe[g]	Zp	2.70[i]	2.67[i]	24.2	0.008[o]	5.5	4.27
CdS[c]	W	2.60[i]	2.42[c]	21	0.012[i]	5.5	4.87
ZnO[h]	Ẇ	2.05[i]	3.20[n]	21	0.020[i]	5.0	4.77

Table 1. Material parameters and two-photon absorption coefficients of the materials studied.

(a) z=zincblende, w=wurtzite p=polycrystalline (h) ref. 28
(b) ref. 22   (i) ref. 29
(c) ref. 23   (j) ref. 30
(d) ref. 24   (k) ref. 31
(e) ref. 25   (l) ref. 32
(f) ref. 26   (m) ref. 33
(g) ref. 27   (n) ref. 4

Figure 1. Experimental setup for measuring the two-photon absorption coefficients β_2 at 1.06 µm. The arrow before the beam splitter indicates the position of the second harmonic crystal when 0.53 µm pulses were used.
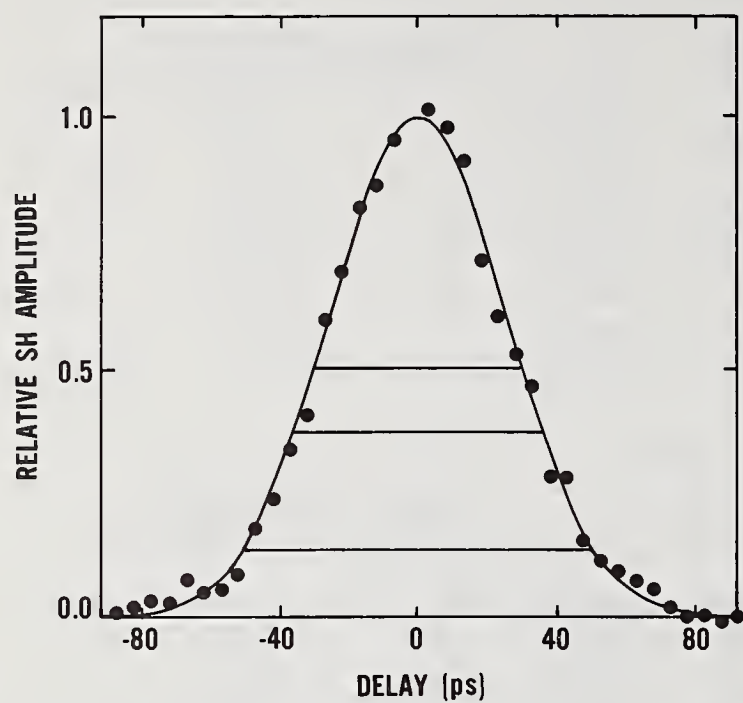
Figure 2. An autocorrelation scan of pulses having a FWHM of 38 psec as calculated from the best fit Gaussian (solid line) autocorrelation.
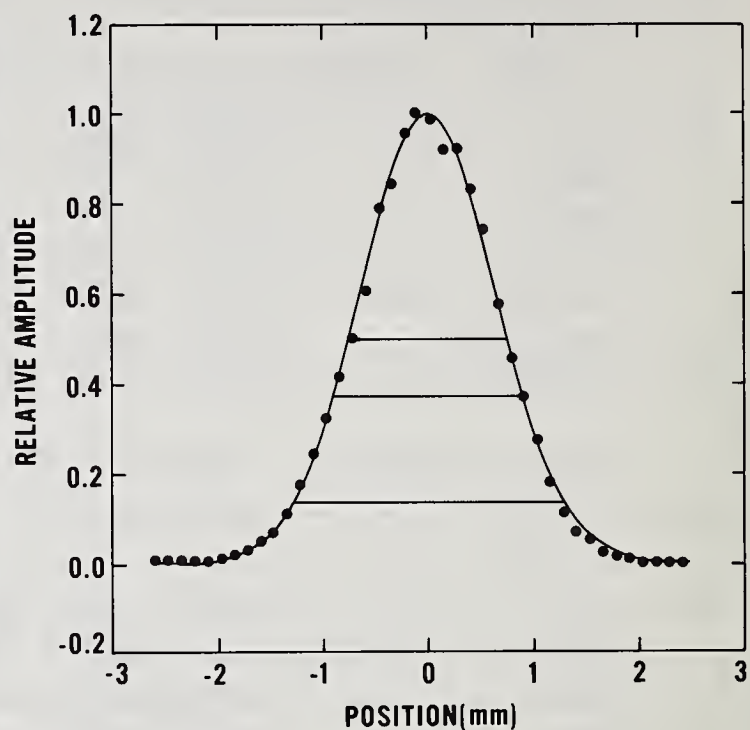
Figure 3. A pinhole beam scan showing a best fit Gaussian (solid line) of FWHM 1.50 mm.
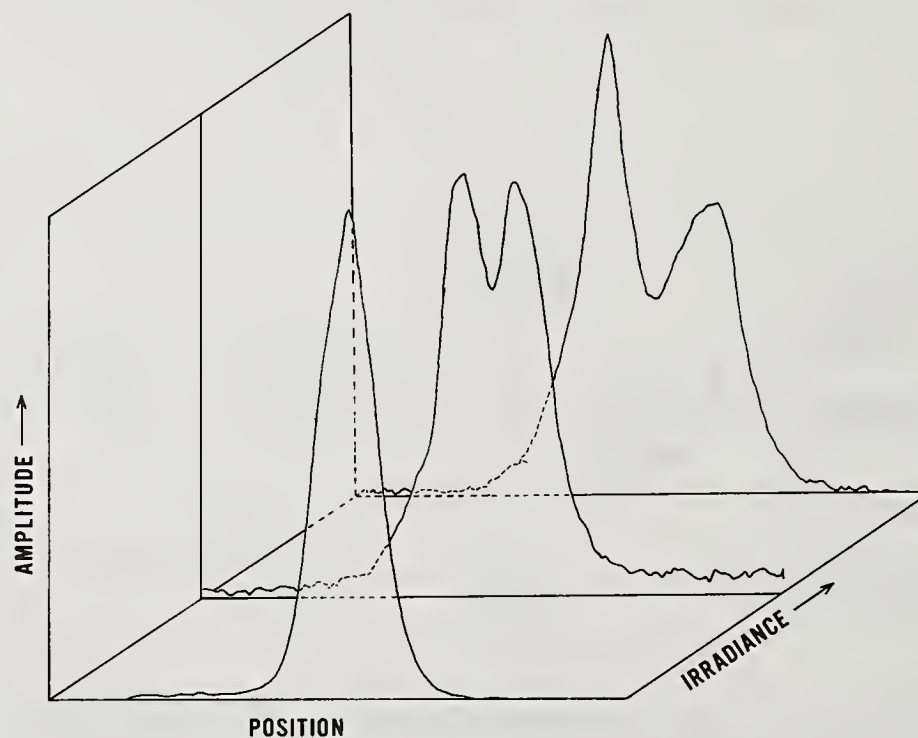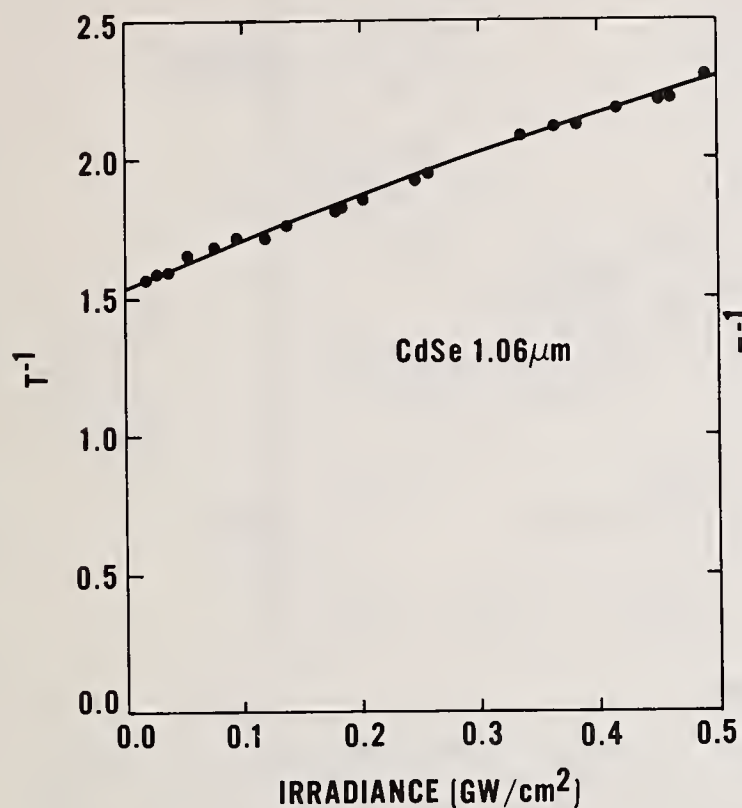

Figure 4. Vidicon scans (equivalent to a pinhole scan) in the near field of the 1.06 μm beam transmitted through a polycrystalline sample of CdTe showing the defocusing for increasing irradiance.
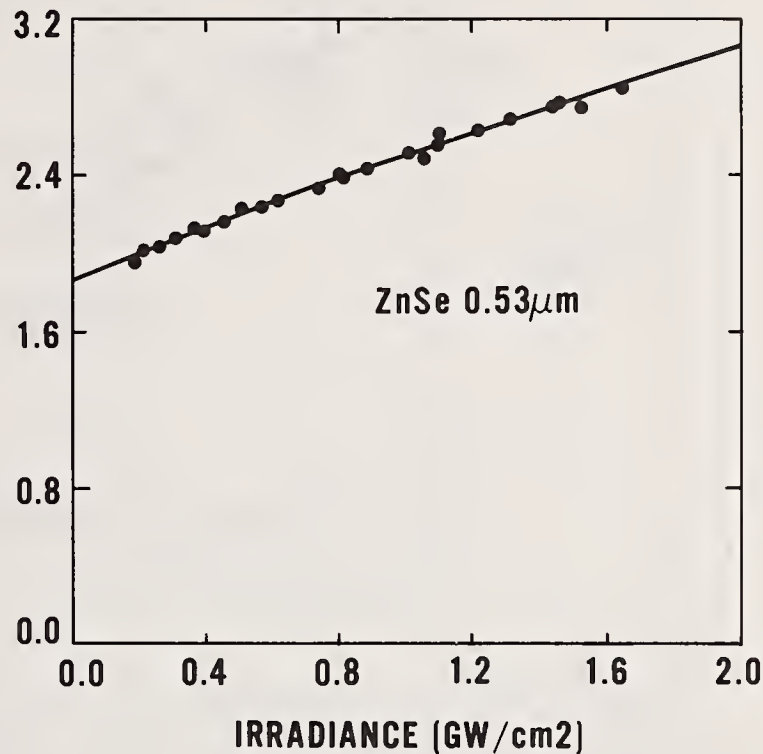
(a)

(b)

CdSe 1.06μm

ZnSe 0.53μm

Figure 5. Inverse transmission versus incident irradiance for (a) CdSe at 1.06 μm and (b) ZnSe at 0.53 μm. The solid lines are fits using eq (12) of Section II.
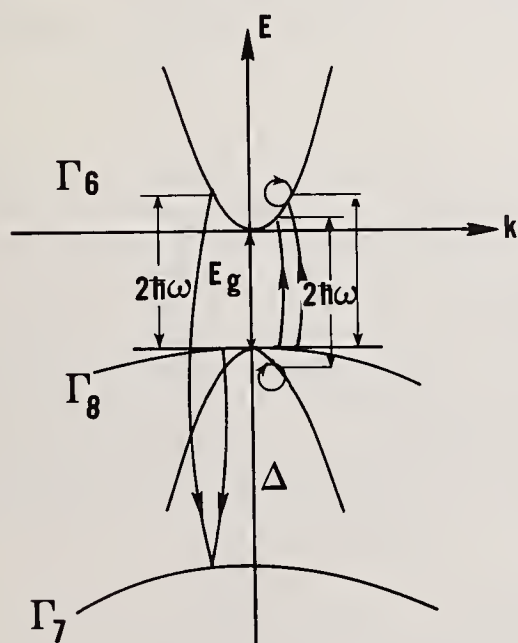

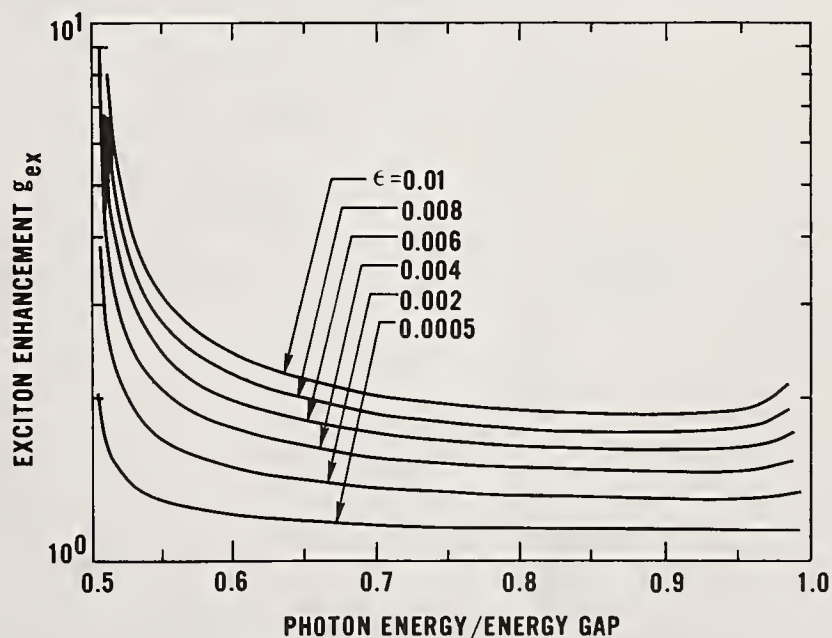Figure 6. Band structure used in refs. 3 and 4 calculate two-photon absorption coefficients.

Figure 7. Exciton enhancement factor g_{ex} as a function of $\hbar\omega/E_g$ for various values of the excition binding energy E_b to the band-gap energy E_g (reproduced with permission from ref. 4).
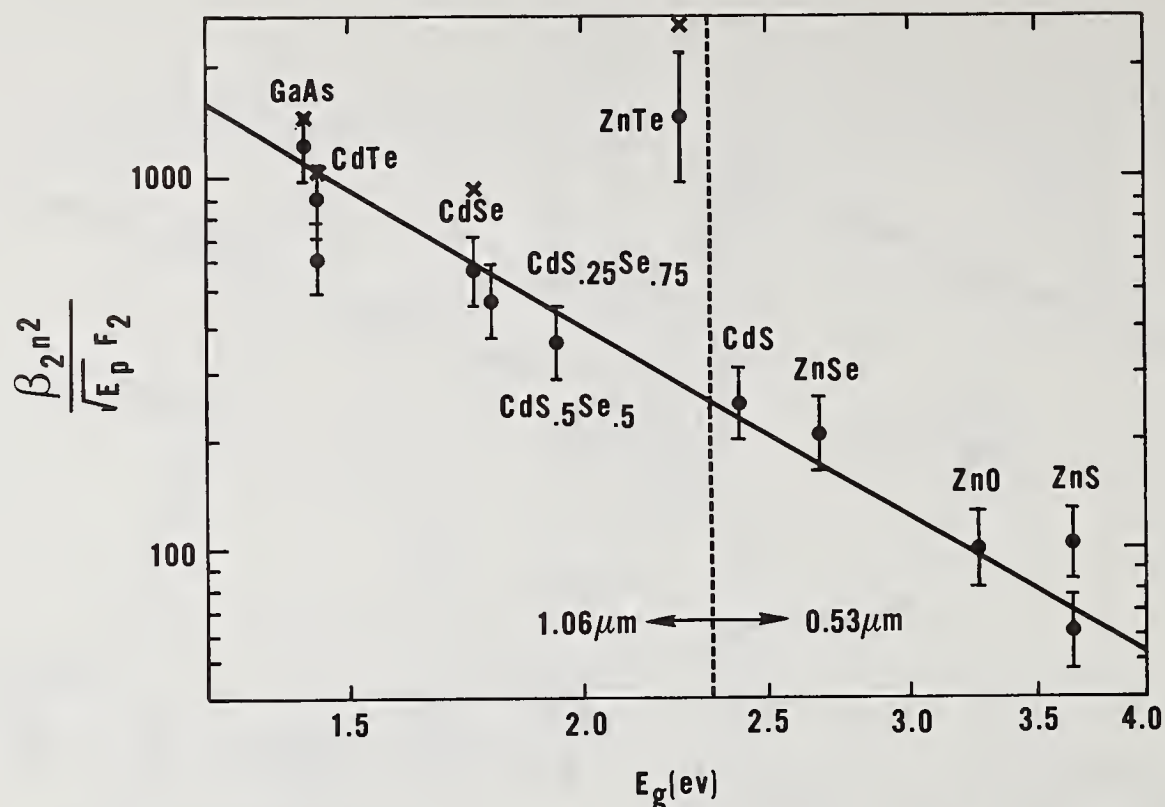
419

Figure 8. A log-log plot of the scaled two-photon absorption coefficient versus energy gap assuming parabolic band structure. The solid line is a least squares fit of the data to a line of slope -3 (omitting ZnTe). The x's shown for GaAs, CdTe, CdSe and ZnTe are data from ref. 13. Data to the left of the vertical dotted line was taken with 1 μm light, and to the right with 0.5 μm light.
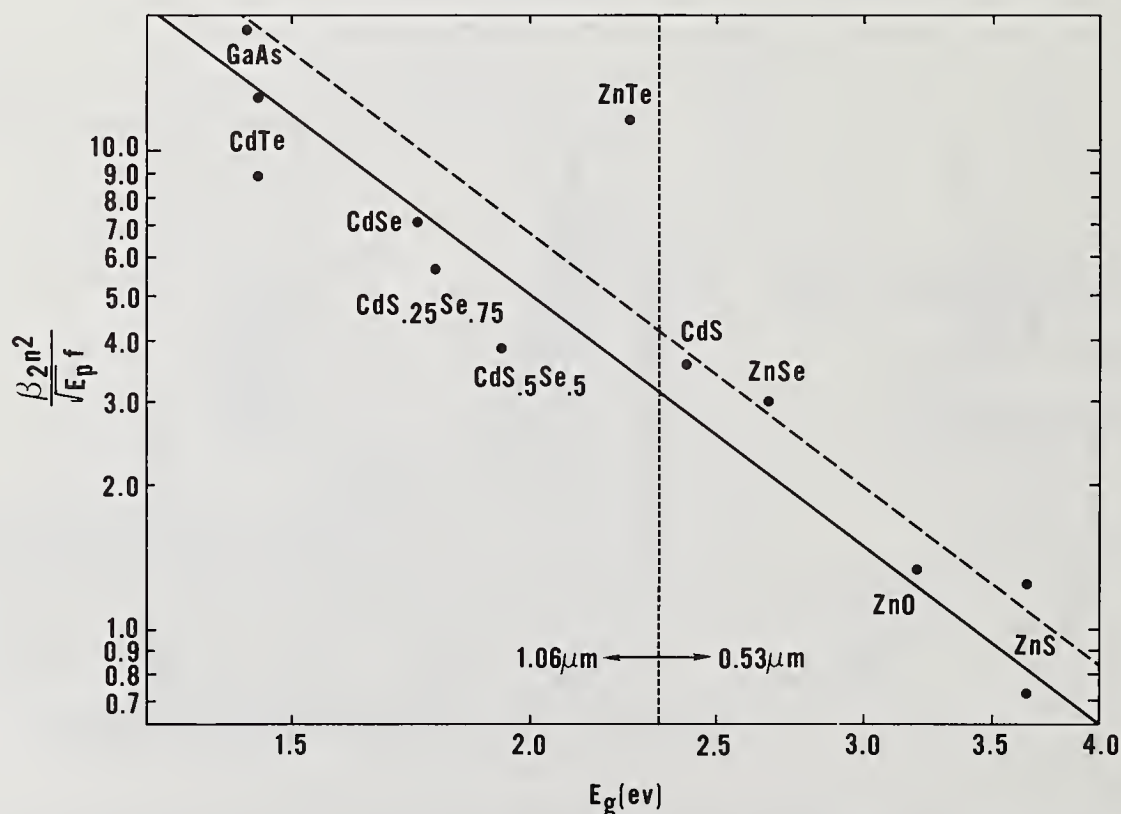

Figure 9. A log-log plot of the scaled two-photon absorption coefficients for nonparabolic band structure ($\Delta \ll E_g$) versus energy gap. The solid is a least squares fit of the data to a line of slope -3 (omitting ZnTe). The dashed line is the theory of ref. 4.
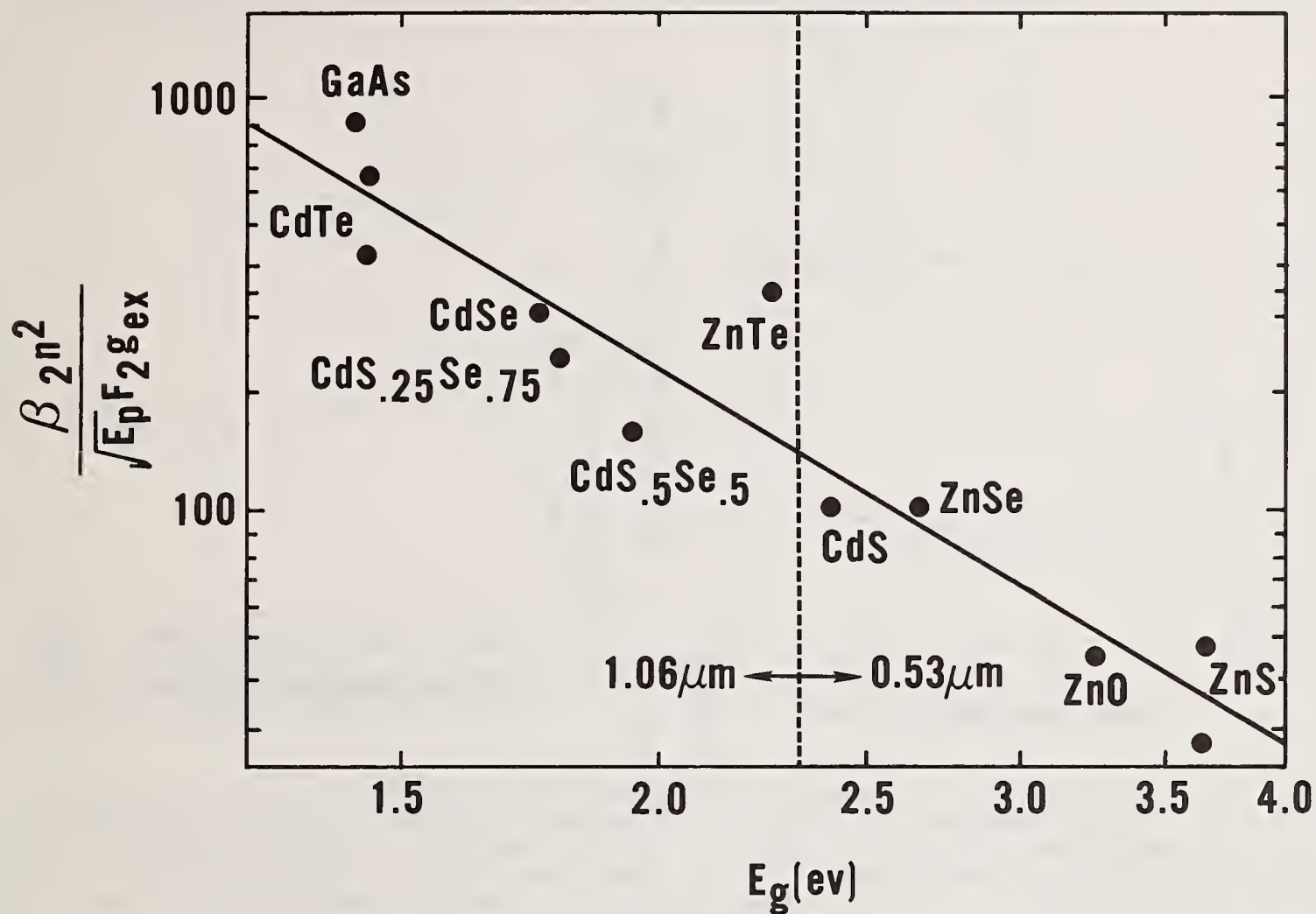
Figure 10. A log-log plot of the scaled two-photon absorption coefficients including exciton enhancement (g_{ex}) for parabolic band structure versus energy gap.

Figure 11. Vidicon scan of the beam transmitted through the polycrystalline sample of CdSe at (a) high irradiance (1 GW/cm^2) and (b) low irradiance (0.3 GW/cm^2) at a distance of 0.5 m behind the sample (near field). The pulsewidth used was 92 psec FWHM. The beam profiles are normalized to have the same on axis fluence. The dashed line is experimental and the solid line is a theoretical fit using eq (16) of Section II.
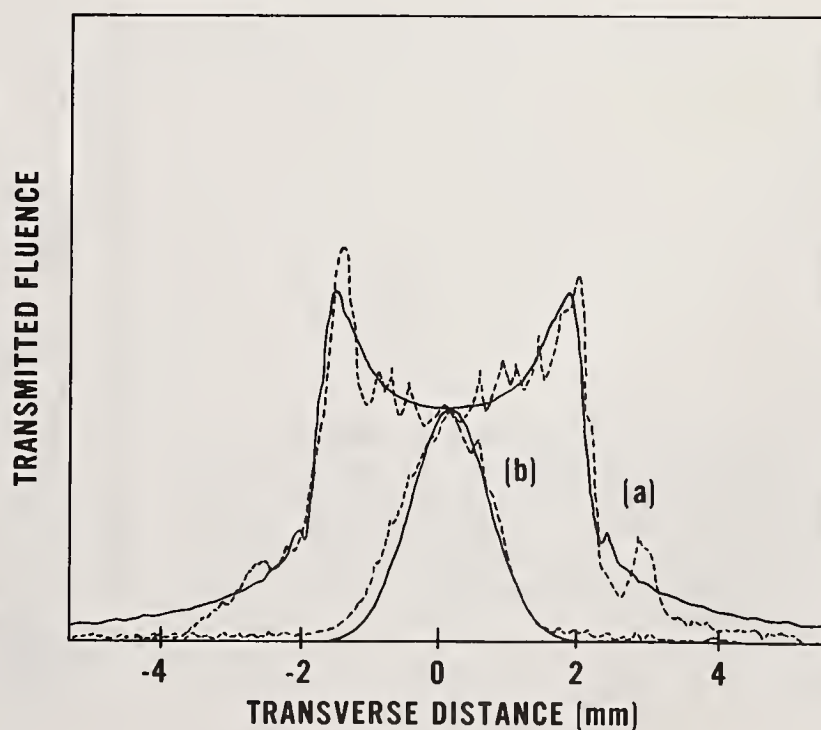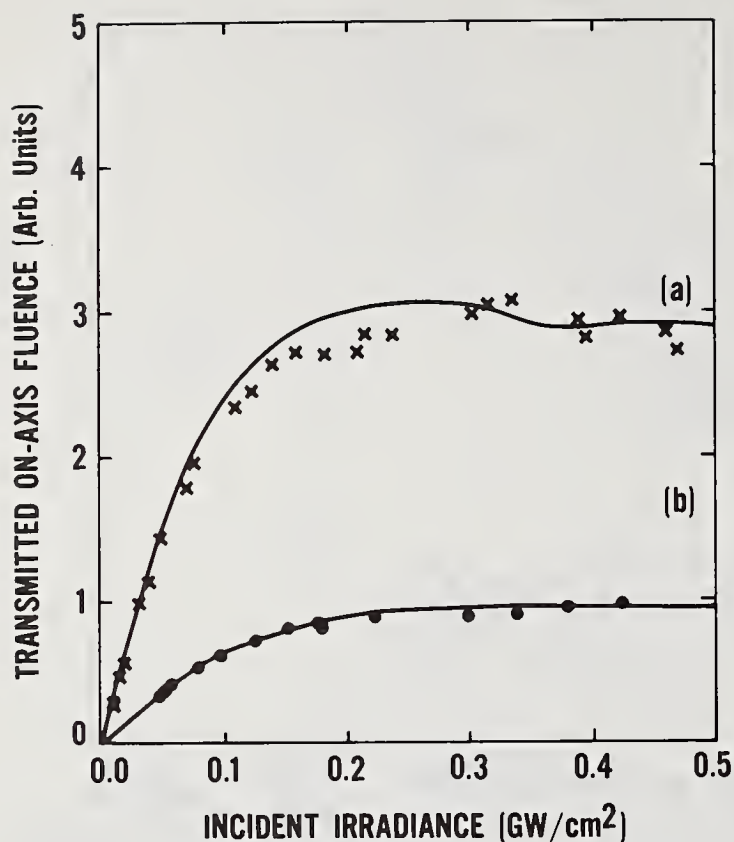
Figure 12. Transmitted on axis fluence as a function of incident irradiance at a distance of 0.5 m behind the sample. (a) 92 psec FWHM pulses and (b) 43 psec FWHM pulses. The solid lines are numerically calculated from eq (16) of Section II.

Figure 13. Transmitted on axis fluence as a function of incident irradiance at a distance of 2.0 m behind the sample. (a) 92 psec FWHM pulses and (b) 43 psec FWHM pulses. The solid lines are numerically calculated from eq (16) of Section II.

Figure 14. Transmitted fluence measured at a point 1.1 mm off-axis as a function of incident irradiance at a distance of 0.5 m behind the sample. (a) 92 psec FWHM pulses and (b) 43 psec FWHM pulses. The solid lines are numerically calculated from eq (16) of Section II.
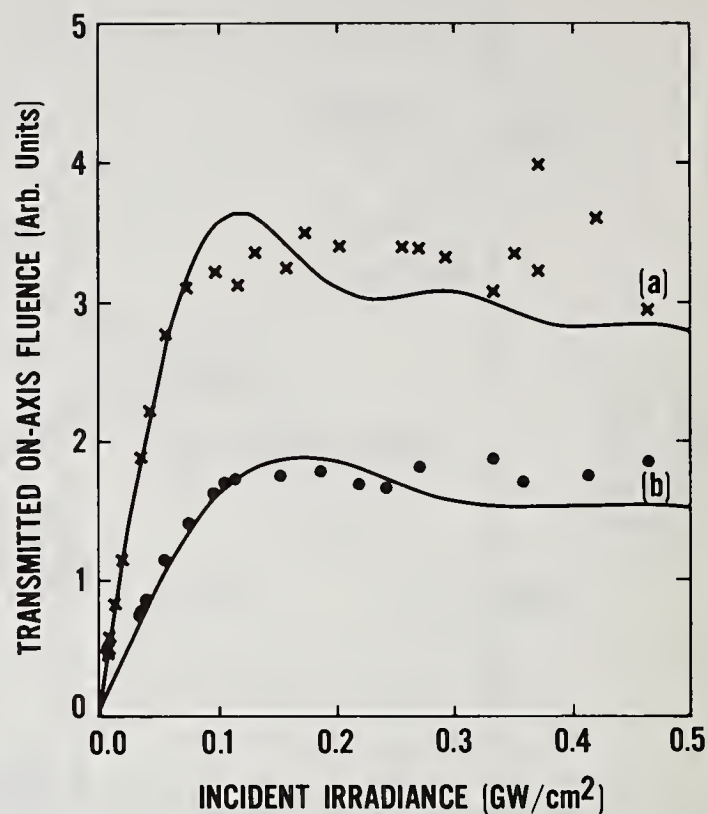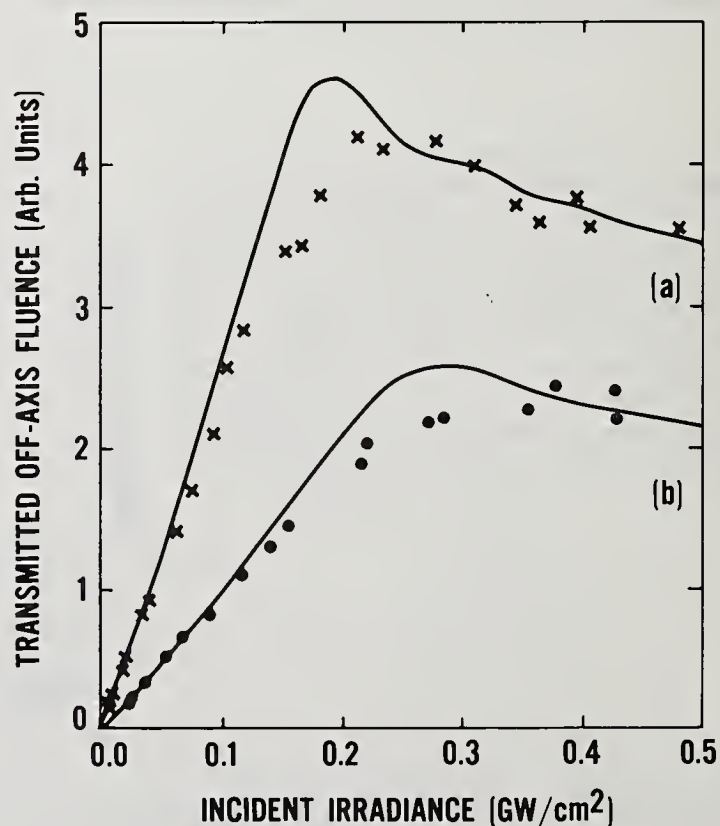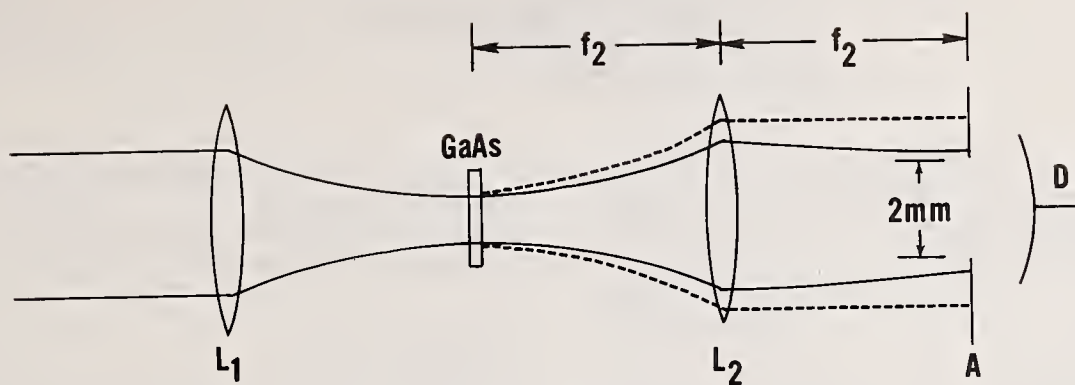
Figure 15. Schematic of GaAs optical limiter.

Figure 16. Device response with (triangles) and without (circles) the 2 mm aperture in place. E_{th} represents the single-shot melting threshold.
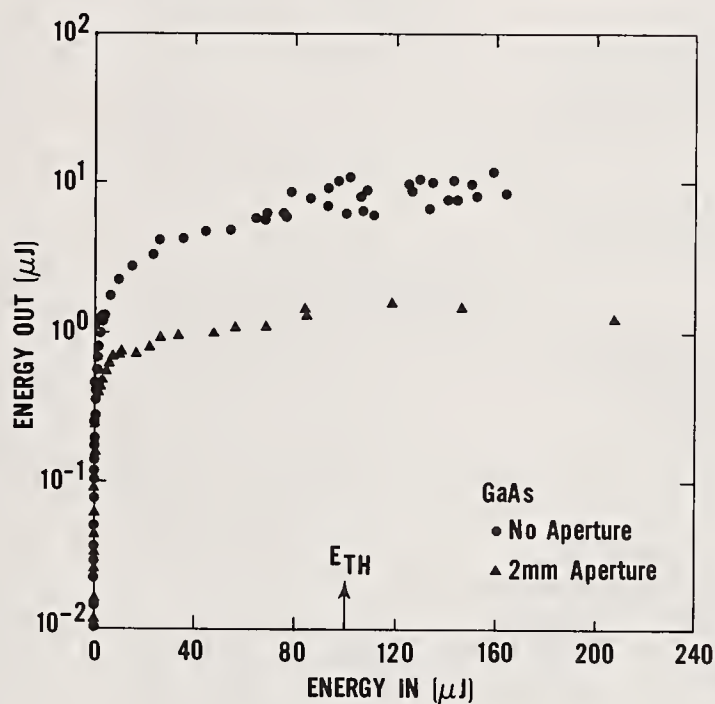
Figure 17. A semilogarithmic plot of the reported two-photon absorption coefficients for GaAs (lower case letters) and CdSe (upper case letters) versus year.

(a)   ref. 36   (A)   ref. 36
(b)   ref. 40   (B)   ref. 39
(c)   ref. 39   (C)   ref. 53
(d)   ref. 46   (D)   ref. 13
(e)   ref. 47   (E)   ref. 54
(f)   ref. 48   (F)   this work
(g)   ref. 49
(h)   ref. 35
(i)   ref. 34
(k)   ref. 13
(l)   ref. 51
(m)   ref. 52
(n)   this work
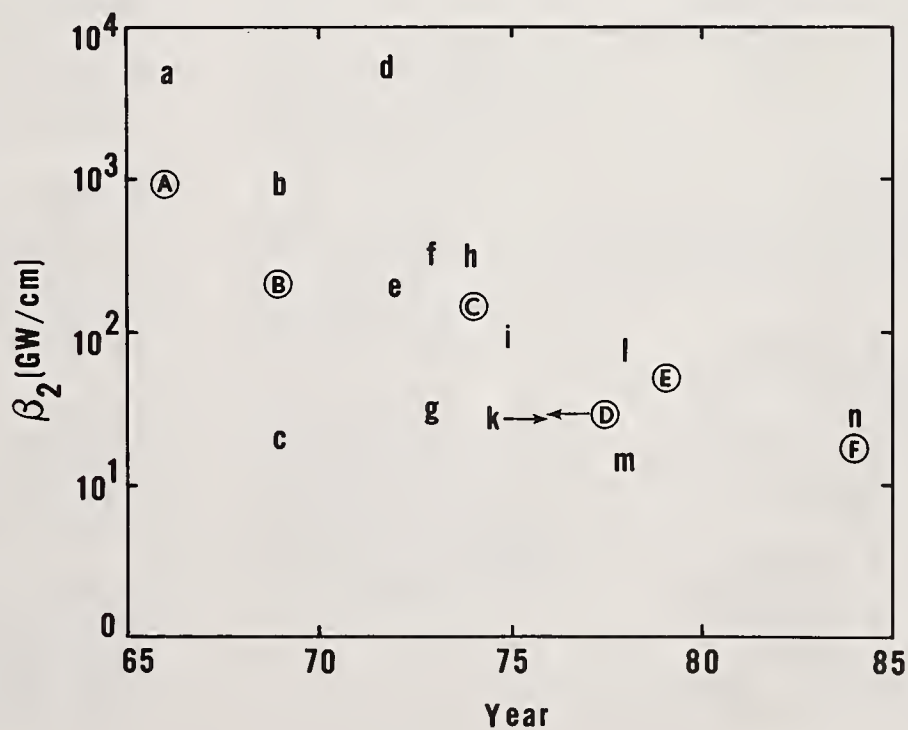
M. A. Acharekar
International Lasers Systems
3404 N. Orange Blossom Trail
Orlando, FL 32804
(305) 295-4010

Dennis P. Arndt
Naval Weapons Center
China Lake, CA 93555
(619) 939-3247

John F. Asmus
Maxwell Laboratories
9244 Balboa Avenue
San Diego, CA 92123
(619) 279-5100, ext 178

David S. Atlas
Eastman Kodak Company
Rochester, NY

William P. Barnes, Jr.
ITEK Optical Systems
Litton Industries
10 Maquire Road
Lexington, MA 02173
(617) 276-2246

W. T. Beauchamp
Optical Coating Laboratory, Inc.
2789 Northpoint Parkway
Santa Rosa, CA 95401-7397
(707) 525-7649

Michael F. Becker
University of Texas
Electrical Engineering Dept.
Austin, TX 78712
(512) 471-3628

Bernard Bendow
BDM Company
1801 Randolph Road, SE.
Albuquerque, NM 87106
(505) 848-5129

Harold E. Bennett
Naval Weapons Center
Code 38101
Michelson Laboratory
China Lake, CA   93555
(619) 939-2869

Steven L. Bernasek
Princeton University
Dept. of Chemistry
Erick Laboratory
Princeton, NJ 08544
(609) 452-4986

Lt. Col. Jerry R. Bettis
U.S. Air Force
Air Force Weapons Laboratory/CA
Kirtland AFB, NM 87117

Leonard Bordzol
Perkin Elmer
M/S 843
100 Wooster Heights Road
Danbury, CT 06810

Gordon Boultee
Optical Coating laboratory, Inc.
Dept. 441-2
2789 Northpoint Parkway
Santa Rosa, CA 95407-7397
(707) 525-7110

Ernie Braunschweig
Research & Developemnt Associates
P. O. Box 9377
Albuquerque, NM 87119
(505) 243-5609

Morris Braunstein
Laser Power Corp.
4746 N. LaVilla Marina
Marina del Rey, CA 90292

Ronald Braustein
Corion Corporation
73 Jeffrey Avenue
Holliston, MA 01746
(617) 429-5065

George Brost
FJ Seiler Reserach Lab.
U.S. Air Force Academy
Colorado Springs, CO 80840
(303) 472-3122

Richard R. Brown
The Boeing Company
Mail Stop 8C-23
P.O. Box 3999
Seattle, WA 98124
(206) 746-4672

Dennis Burge
Naval Weapons Center
Code 3816
China Lake, CA 93555
(619) 939-3049

Charles K. Carniglia
Optical Coating Laboratory, Inc.
2789 Northpoint Parkway
Santa Rosa, CA 95401-7397
(707) 525-7191

Lloyd L. Chase
Indiana University
Physics Department
Bloomington, IN 47405
(812) 335-1485

Rod Clark
Teledyne Brown Engineering
Cummings Research Park
M/S 19
Huntsville, AL 35808
(205) 532-2355

Charles Cockrum
Laser Power Optics
11211-U Sorrento Valley Road
San Diego, CA 92121
(619) 455-0751

Edward L. Courtright
Battelle, Pacific Northwest Labs
Metallurgy & Coatings
2955 George Washington Way
Richland, WA 99352
(509) 375-6926

Terrence F. Deaton
Frank J. Seiler Research Lab.
U.S. Air Force Academy
Colorado Springs, CO 80840
(303) 472-3502

Hulya Demiryont
Colorado State University
Dept. of Physics
Fort Collins, CO 80523
(303) 491-7272

He Deng
Center for Laser Studies
Univ. of Southern California
University park
Los Angeles, CA 90089-1112

Hermann J. Donnert
Kansas State University &
Frank J. Seiler Research Lab.
Ward Hall
Manhattan, KS 66506-7039
(913) 532-5960

Fred W. Doss
Spectra Physics
Optics Division
1250 W. Middlefield Road
Mountain View, CA 94039
(415) 961-2550, ext 2145

Richard Dyer
W. J. Schafer Assoc.
Corporate Place 128
Wakefield, MA 01880
(617) 246-0450

Anne Easton
Optical Components Group
Ferranti PLC.
Dunsinane Ave.
Dundee, SCOTLAND

Dr. J. Ebert
Institut fur Quantenoptik
Universitat Hannover
Welfengarten 1
D 3 Hannover 1
Federal Republic of Germany
0511-762-4894

David F. Edwards
Lawrence Livermore Natl. Labs.
L-432
Livermore, CA 94550

Osama H. El-Bayoumi
U.S. Air Force
RADC/ESM
Hanscom Field AFB, MA 01731
(617) 861-5832

Edward A. Enemark
Optical Coating Laboratory, Inc.
2789 Northpoint Parkway
Santa Rosa, CA 95401-7397
(707) 525-7108

Gregory J. Exarhos
Pacific Northwest Laboratory
P.O. Box 999
Richland, WA 99352
(509) 375-2440

Philip M. Fauchet
Princeton University
Dept. of Electrical Engineering
  and Computer Science
Princeton, NJ 08544

Herbert W. Feinstein
MIT Lincoln Laboratory
244 Wood Street
Lexington, MA 02173
(617) 863-5500, ext 3671

Joseph Figueira
Los Alamos National Laboratory
P.O. Box 1663
Los Alamos, NM 87544
(505) 667-6448

Paul Filbert
Lockheed Palo Alto
  Research Laboratory
0191-10, B/203
3251 Hanover Street
Palo Alto, CA 94304
(415) 424-2043

Dennis Fischer
Coherent Inc.
2301 Lindbergh Street
Auburn, CA
(916) 823-9550

Diane M. Fischer
Air Force Weapons Lab./ARBE
Kirtland AFB, NM   87117
(505) 844-0226

Steven E. Fisher
Rockwell International/
  Rocketdyne Division
P.O. Box 5670
Kirtland AFB, NM   87108
(505) 846-7845

Steven Foltyn
Los Alamos National Laboratory
CHM-5, MS J566
Los Alamos, NM   87545
(505) 667-1123

Jerome Franck
Naval Weapons Center
China Lake, CA   93555
(619) 939-2470

Daniel Friart
Commissariat a'lEnergie Atomique
Centred'Etudes de Limeil-Valenton
B.P.n 27
g4190 Villeneuve-Saint-George
FRANCE
1-590-96 60 POSTE 6473

David Gallant
Rockwell International
Rocketdyne Division
P.O. Box 5670
Kirtland AFB, NM   87185
(505) 844-2052

Gerald A. Gallager
Los Alamos National Labs.
Los Lamos, NM   87544
(505) 667-9926

Dennis H. Gill
Los Alamos National Labs.
Chemistry Division, J563
P.O. Box 1663
Los Alamos, NM   87544
(505) 667-6250

George A. Graves
University of Dayton
RM165 Kettering Labs.
300 College Parkway
Dayton, OH   45469
(513) 229-4341

Jeffrey W. Griffin
Batelle Pacific Northwest Labs
P.O. Box 999
Richland, WA   99352
(509) 375-2081

Ed Griggs
Los Alamos National Labs.
P.O. Box 1663
Los Alamos, NM   87544
(505) 667-6712

Arthur H. Guenther
U.S. Air Force
AFWL/CA
Kirtland AFB
New Mexico   87117

William J. Gunning
Rockwell International Science Center
1049 Camino Dos Rios
Thousand Oaks, CA   91360
(805) 498-4545

Lt. Michael Hackett, Jr.
AFWL/ARBE
Kirtland AFB, NM   87117-6008
(505) 844-1776

Steven G. Hadley
CVI Laser Corporation
P.O. Box 11308
Albuquerque, NM   87192
(505) 296-9541

James Harris
IITRI
1495 Bimini Drive
Dayton, OH   45459
(513) 435-6717

John S. Hartman
Pacific Northwest Laboratory
MS/2400 Bldg.
P.O. Box 999
Richland, WA   99352
(509) 375-2101

Allan Heiney
Allied Corporation
7 Powderhorn Drive
Mt. Bethel, NJ   07060
(201) 560-1750, ext 222

Paul D. Hillman
USAF
AFWL/ARBE
Kirtland AFB, NM   87117-6008
(505) 844-1776

Van A. Hodgkin
Naval Weapons Center
China Lake, CA   93555
(619) 939-3247

Samuel J. Holmes
Northrop Research & Technology Center
One Research Park
Palos Verdes Peninsula, CA 90274
(213) 377-4811

Alan K. Hopkins
AFWAL Materials Laboratory
   (AFWAL/MLPJ)
WPAFB, OH 45433
(513) 255-6652

Marshall N. Huberman
TRW, Bldg 01, Rm 1051
One Space Park
Redondo Beach, CA 90278
(213) 536-4413

Thomas L. Hursman
TRW
One Space Park
Redondo Beach, CA 90278
(213) 535-8252

Hugh Hurt
Naval Weapons Center
Code 3816
China Lake, CA 93555
(619) 939-3049

Long S. Hsu
Colorado State University
Physics Dept.
Ft. Collins, CO 80521
(303) 491-5524

Thomas Hynes
Army Materials & Mechanics
   Research Center
AMXMR-MCS
Watertown, MA 02172

Mark Imus
Optical Coating Laboratory, Inc.
2789 Northpoint Parkway
Santa Rosa, CA 95401-7397
(707) 525-7742

Stephen D. Jacobs
University of Rochester
Laboratory for Laser Energetics
250 East River Road
Rochester, NY 14623
(716) 275-4837

Linda Johnson
Naval Weapons Center
Physics Division, Code 3818
China Lake, CA 93555
(619) 939-2977

George T. Johnston
Optical Coating Laboratory, Inc.
2789 Northpoint Parkway
Santa Rosa, CA 95401-7397
(707) 525-7148

L. John Jolin
Los Alamos National Lab.
P.O. Box 1663
CHM-5 MS-J566
Los Lamos, NM 87544
(505) 667-7314

John A. Kardach
U.S. Air Force
AFWL/CA
Kirtland AFB, New Mexico 87109
(505) 844-7368

David Keaton
Los Alamos National Lab.
CHM-6, MS J564
Los Alamos, NM 87545
(505) 667-1123

Kent Kogler
ITT Research Institute
4130 Linden Avenue
Dayton, OH 45432
(513) 252-9969

W. M. Koldewyn
Scientech Inc.
5649 Arapahoe
Boulder, CO 80303
(303) 444-1361

Leslie G. Koshigoe
Naval Weapons Center
Code 3941
China Lake, CA 93555
(619) 939-3364

Munson Kwok
Aerospace Corporation
P.O. Box 92957
MS/747
Los Angeles, CA 90009
(213) 648-5441

Nessim Lagnado
Hughes Aircraft Company
Mail Station ED El D160)
2000 E. El Segundo Blvd.
El Segundo, CA 90245
(213) 616-6237

Michael R. Lange
Univ. of New Mexico
Albuquerque, NM 87131
(505) 277-6317

Joseph R. Latore
Airtron Div. of Litton Systems Inc.
200 E. Hanover Avenue
Morris Plains, NJ 07950
(201) 539-5500

Paul S. Laybourne
W. J. Schafer Associates, Inc.
303 San Mateo, NE Rte 103
Albuquerque, NM 87108
(505) 266-7701

R. J. L. Lerou
Physics Laboratory TNO
P.O. Box 96864
2509 JG The Hague
NETHERLANDS
970-264221 or 070-972925

Keith L. Lewis
Royal Signals & Radar Establishment
St. Andrews Road
Malvern
Worcss WR14 3PS
UNITED KINGDOM
06845 2733, ext 3062

Tony Lowderback
Ojai Research Corp.
11554 Ventura Ave.
Ojai, CA 93023
(805) 646-7198

W. Howard Lowdermilk
Lawrence Livermore Natl. Laboratory
P.O. Box 5508, L-490
Livermore, CA 94550
(415) 422-5498

Samuel Lu
Litton Industries
GCS
5500 Canoga Avenue
Woodland Hills, CA 91365
(213) 715-3180

David L. J. Lunt
Lunt & Co.
P.O. Box 368
Richland, WA 99352
(509) 375-4792

Michael Lunt
Technical Optics Ltd.
Second Avenue
Onchan, Isle of Man
BRITISH ISLES
44 624 4443

Capt. Myron T. Maclin
USAF
AFWL/ARBE
Kirtland AFB, NM 87117-6008
(505) 844-1776

Jeffrey J. Malanify
USAF
AFWL/ARBE
Kirtland AFB, NM 87117-6008
(505) 844-7360

Tarro Mandre
TRW
One Space Park
Redondo Beach, CA 90278

Nastaran Mansour
North Texas State Univ.
Physics Dept., Box 77
Denton, TX 76203
(817) 565-3307

Frane Marcelja
Corion Corporation
73 Jeffrey Avenue
Holliston, MA 01746
(617) 429-5065

C. Denton Marrs
Naval Weapons Center
Code 3817
China Lake, CA 93555
(619) 939-2470

Diane J. Martin
USAF
AFWL/ARBE
Kirtland AFB, NM 87117-6008
(505) 844-1776

Robert L. Martin, Jr.
Optical Coating Laboratory, Inc.
2789 Northpoint Parkway
Santa Rosa, CA 95407-7397
(707) 525-7647

Billie R. Mauro
Los Alamos National Lab.
CHM-5
P.O. Box 1663, MS J566
Los Alamos, NM 87545
(505) 667-9679

James W. Mayo III
USAF
AFWL/ARB
Kirtland AFB, NM 87117-6008
(505) 844-0721

Fred J. McClung
Hughes Aircraft Company
2650 Yale Blvd. SE.
Albuquerque, NM 87106
(505) 242-9818

Michael McGuirk
Perkin-Elmer
Main Ave., MS 420
Norwalk, CT 06856
(203) 834-4921

J. K. McIver
Univ. of New Mexico
Dept. of Physics & Astron.
Albuquerque, NM 87131
(505) 277-8484

Jim McNally
U.S.A.F.
Univ. of New Mexico
9608 Avenida de La Luna
Albuquerque, NM 87111
(505) 822-8143

John R. McNeil
Elect. Eng. Dept.
Univ. of New Mexico
Albuquerque, NM 87131
(505) 277-5502

Charles Mellor
GTE Lighting Products
60 Boston St.
Salem, MA 01970
(617) 777-1900

Jean Francois Mengue
Commissariat a l'Energie Atomique
Centre d_Etudes de Limeil-Valenton
B.P. no 27
94190 Villeneuve-Saint-Georges
FRANCE
-1-590 96 60 poste 6473

David Milam
Lawrence Livermore Lab.
7000 E. Ave.
Livermore, CA 94550
(415) 422-5499

Michael J. Monsler
KMS Fusion Inc.
P.O. Box 1567
3621 S. State Road
Ann Arbor, MI 48106
(313) 769-8500

David Mordaunt
Hughes Aircraft Company
Bldg E1, Mail Station E142
P.O. Box 902
El Segundo, CA 90245

Dennis Morelli
Optical Coating Laboratory, Inc.
2789 Northpoint Parkway
Dept. 428-1
Santa Rosa, CA 95407-7397
(707 525-7011

Patricia L. Morse
AFWL/ARBE
Optical Components Branch
Kirtland AFB, NM 87117
(505) 844-0226

Bill W. Mullins
USAF Academy
Dept. of Physics
USAFA/Dep
USAF Academy, CO 80840-5821
(303) 472-4158

George F. Nado
Texas Instruments
Box 226015, M/S 3196
Dallas, Texas 75231
(214) 995-6412

Elizabeth Anne Nevis
Coherent Inc.
3270 W. Rayshore Rd.
Palo Alto, CA 94303
(415) 858-2250

Davis B. Nichols
Boeing Aerospace Co.
Physics Tech. Dept.
P.O. Box 3999, MS 8H-18
Seattle, WA 98124
(206) 773-8938

Andy Nowak
Los Alamos National Lab.
M/S J564
Group Chm 6
Los Alamos, NM 87545

Robert M. O'Connell
Univ. of Missouri - Columbia
Elect. Eng. Dept.
Columbia, MO 65201
(314) 882-8373

James R. Palmer
Comarco, Inc.
1201 N. China Lake Blvd.
Ridgecrest, CA 93555
(619) 446-7671, ext 295

Roger A. Paquin
The Perkin Elmer Corp.
Electro-Optical Division
100 Wooster Heights Road
M/S 955
Danbury, CT 06810
(203) 797-6130

Charles Edgar Patty, Jr.
Teledyne Brown Engineering
Cummings Research Park
Mail Stop 19
Huntsville, AL 35807
(205) 532-1000, ext 3210

Walter T. Pawlewicz
Battelle, Pacific Northwest Labs
Metallurgy & Coatings Section
2955 George Washington Way
Richland, WA 99352
(509) 375-2074

Robert D. Poirier
Perkin Elmer Corporation
77 Danbury Road
M/S 420
Wilton, CT 06897

Dave Pollock
Teledyne Brown Engineering
Cummings Research Park
MS 19
Huntsville, AL 35807
(205) 532-1605

Jim Porteus
Naval Weapons Center
Code 3817
China Lake, CA 93555
(619) 939-3827

Scott Price
Martin Marietta Denver Aerospace
P.O. Box 9316
International Airport
Albuquerque, NM 87119
(505) 844-1064

Diane Quinn
Optical Coating Laboratory, Inc.
2789 Northpoint Parkway
Santa Rosa, CA 95401-7397
(707) 525-7652

John Rahn, MS-12
Litton Guidance & Control
5500 Canoga Ave.
Woodland Hills, CA 91365
(818) 888-3415

Tilak Raj
Martin Marietta Denver Aerospace
P.O. Box 9316
International Airport
Albuquerque, NM 87119
(505) 844-1064

Herman E. Reedy
II-VI Inc.
Saxonburg Blvd.
Saxonburg, PA 16056
(412) 352-4455

David Reicher
Herron Optical Division
Laser Power Corp.
2035 E. 223rd Street
Long Beach, CA 90810
(213) 830-5404

David H. Rester
Texas Instruments
P.O. Box 660246
Dallas, TX 75266
(214) 995-1805

Detleu Ristau
Universitat Hannover
Weleengarten 1
Hannover 1
GERMANY
0511 762 4834

Andrew B. Romberger
Pennsylvania State Univ.
Berks Campus
P.O. Box 2150
Reading, PA 19608
(215) 375-4211

Carlos Roundy
Spiricon, Inc.
2600 N. Main
Logan, UT 84321
(801) 753-3729

J. Earl Rudisill
Laser Power Optics
11211-U Sorrento Valley Road
San Diego, CA 92121
(619) 455-0751

Rong Rujkorakarn
Dept. of Physics
Colo. State Univ.
Ft. Collins, CO 80523
(303) 491-1105

Joseph Sanchez
Optical Coating Laboratory, Inc.
2789 Northpoint Parkway
Santa Rosa, CA 95407-7397

Haluk Sankur
Rockwell Int. Science Center
1049 Camino Dos Rios
Thousand Oaks, CA 91360
(805) 498-4545, ext 263

Paul Schall
The Aerospace Corporation
M2/321
P.O. Box 92957
Los Angeles, CA 90009
(213) 648-7502

Gary L. Scheidegger
Martin Marietta Aerospace
Mail Point 185
P.O. Box 5837
Orlando, FL 32855

Erik A. Schwendeman
Corion Corporation
73 Jeffrey Avenue
Holliston, MA 01746
(617) 429-5065

Marion L. Scott
Research & Development Assoc.
P.O. Box 9377
Albuquerque, NM 87119
(505) 844-0434

S. C. Seitel
Naval Weapons Center
Code 3817
China Lake, CA 93555
(619) 939-3827

Robert R. Shannon
Optical Sciences Center
University of Arizona
Tucson, AZ 85721
(602) 621-6997

Chiao-Yao She
Colorado State University
Physics Dept.
Fort Collins, CO 80523
(303) 491-5524

Dennis R. Sigler
Burleigh Northwest Optical, Inc.
Burleigh Park
Fishers, NY 14453
(716) 924-9350

Robert M. Silva
VIT Inc.
4032 Linden Avenue
Dayton, OH 45432
(513) 254-6201

Meyer Silver
TRW
01/1240
One Space Park
Redondo Beach, CA 90278
(213) 535-8252

James R. Sites
Dept. of Physics
Colorado State University
Fort Collins, CO 80523
(303) 491-5850

Robert Soales
CVI Laser, Inc.
200 Dorado Place SE.
Albuquerque, NM 87123
(505) 296-9541

M. J. Soileau
North Texas State Univ.
Dept. of Physics
Denton, TX 76303
(817) 565-3263

William H. Southwell
Rockwell International Science Center
1049 Camino Dos Rios
Thousand Oaks, CA 91360
(805) 498-4545

Michael C. Staggs
Lawrence Livermore Labs.
East Ave.
Livermore, CA 94550
(415) 422-6060

James L. Stanford
Naval Weapons Center
Code 3818
China Lake, CA 93555
(619) 939-2443

James L. Stapp
Rocketdyne Div.
Rockwell Int.
P.O. Box 5670
Kirtland AFB, NM 87185
(505) 846-0204

Lawrence A. Stelmack
M/S 87
Litton Industries
Guidance and Control Divison
5500 Canoga Avenue
Woodland Hills, CA 91365
(818) 715-5184

Alan F. Stewart
Air Force Weapons Lab.
AFWL/ARBE
Kirtland AFB, NM 87117
(505) 844-7368

W. Kent Stowell
USAF
AFWAL/AADO-2
Wright-Patterson AFB, OH 45433
(513) 255-5147

Joseph Tajani
Hewlett Packard
640 Page Mill Rd.
Palo Alto, CA 94304

Steven M. Teare
Spiricon, Inc.
2600 N. Main
Logan, UT 84321
(801) 753-3729

Paul A. Temple
Naval Weapons Center
Code 3816
China Lake, CA 93555
(619) 939-3247

Ian Thomas
Lawrence Livermore National Lab.
P.O. Box 5808
Livermore, CA 94550

Scott J. Thomas
Los Alamos National Laboratory
P. O. Box 1663 /MSJ566
Los Alamos, NM 87545
(505) 667-6952

Gary Thompson
Optical Coating Laboratory, Inc.
2789 Northpoint Parkway
Santa Rosa, CA 95407-7397

Stephen Tuenge
Martin Marietta Denver Aerospace
P.O. Box 9316
International Airport
Albuquerque, NM 87119
(505) 844-1064

Lt. John F. Turner
USAF
AFWL/ARBE
Kirtland AFB, NM 87117-6008
(505) 844-1776

Trudy Tuttle Hart
Optical Coating Laboratory, Inc.
2789 Northpoint Parkway
Santa Rosa, CA 95401-7397
(707) 525-7192

Eric W. Van Stryland
Center for Appl. Quantum Electronics
North Texas State Univ.
Dept. of Physics
P.O. Box 5368, NT Station
Denton, TX 76203
(817) 565-3263

Marc Von Gunten
Mail Stn. 4-30
Spectra-Physics Inc.
Optics Division
1250 W. Middlefield Road
Mountain View, CA 94039-7013
(415) 961-2550, ext 3008

Willard R. Wadt
Los Alamos National Laboratory
MS J569
P.O. Box 1663
Los Alamos, NM 87545
(505) 667-7763

Lawrence Weaver
Martin Marietta Denver Aerospace
P.O. Box 9316
International Airport
Albuquerque, NM 87119
(505) 844-1064

Annetta J. Weber
USAF
AFWL/ARBE
Kirtland AFB, NM 87117-6008
(505) 844-1776

Carolyn Weinzapfel
Lawrence Livermore National Lab.
East Ave.
Livermore, CA 94550
(415) 422-6060

James A. Wells
Teledyne Brown Engineering
Mailstop 19
300 Sparkman Dr.
Huntsville, AL 35807
(205) 532-1592

Keith Wier
Scientech Inc.
5649 Arapahoe
Boulder, Co 80303
(303) 444-1361

John Wilder
Bendix Field Engineering Corp.
Mail Stop L483
P.O. Box 5508
Livermore, CA 94550
(415) 423-3896, 422-0790

Ronald Willey
Mail Point 185
Martin Marietta
P.O. Box 5837
Orlando, FL 32855
(305) 356-2427

A. D. Wilson
Barr & Stroud Ltd.
Caxton Street
Anniesland
Glasgow, 9131HZ
SCOTLAND, UK
(041) 954-9601, ext 111

G. Richard Wirtenson
Lawrence Livermore Natl. Lab.
P.O. Box 5508
7000 East Avenue L-491
Livermore, CA 94550
(415) 422-1332

Frank J. Wodarczyk
Rockwell International Corp.
Science Center
1049 Camino Dos Rios
Thousand Oaks, CA 91360
(805) 498-4545, ext 195

John Wollam
Dept. of Electrical Engineering
University of Nebraska
Lincoln, NB 68588
(402) 472-1964

Roger M. Wood
GEC Research Laboratories
Wirst Research Centre
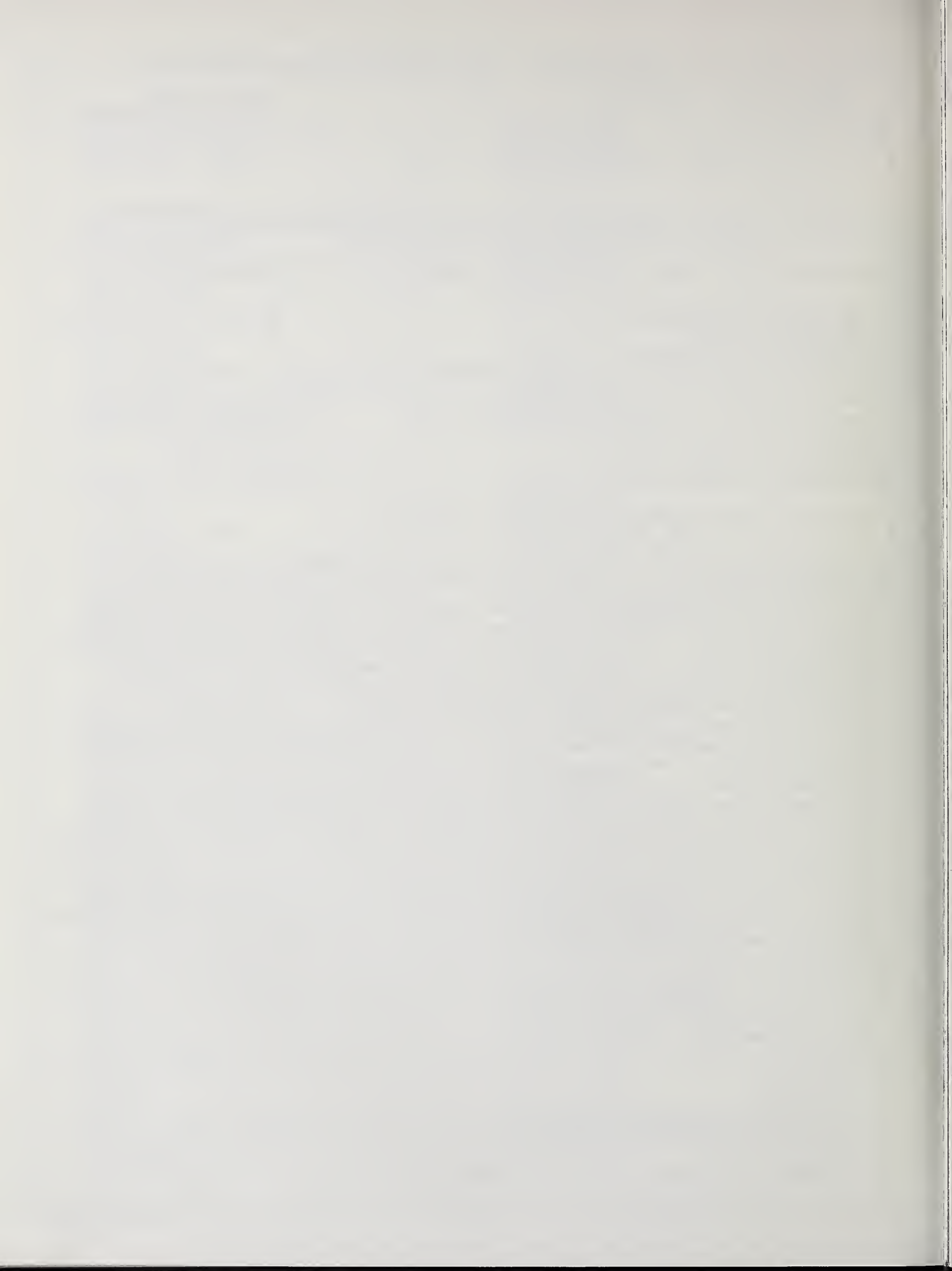East Lane
Wembley, UNITED KINGDOM

Frank Woodberry
Rockwell Int.
6633 Canoga Ave., FA-42
Canoga Park, CA 91304
(818) 700-4931

Guy T. Worth
Rockwell International
Rocketydyne Division
P.O. Box 5670
Kirtland AFB, NM 87185
(505) 846-7824

Shin-Tson Wu
Hughes Research Laboratory
3011 Malibu Canyon Road
Malibu, CA 90265
(213) 317-5901

Rick Zoborowski
OCLI
2789 Northpoint Parkway, Dept. 428-1
Santa Rosa, CA 95407-7397
(707) 525-7011

432

U.S. DEPT. OF COMM. **BIBLIOGRAPHIC DATA SHEET** *(See instructions)*	1. PUBLICATION OR REPORT NO. NBS/SP-727	2. Performing Organ. Report No.	3. Publication Date October 1986

4. TITLE AND SUBTITLE

Laser Induced Damage in Optical Materials: 1984

5. AUTHOR(S)   Harold E. Bennett (NWC), Arthur H. Guenther (AFWL)
David Milam (LLNL) and Brian E. Newnam (LANL)

6. PERFORMING ORGANIZATION *(If joint or other than NBS, see instructions)* **NATIONAL BUREAU OF STANDARDS** **DEPARTMENT OF COMMERCE** ~~WASHINGTON, D.C. 20234~~ Gaithersburg, MD 20899	7. Contract/Grant No. 8. Type of Report & Period Covered Final

9. SPONSORING ORGANIZATION NAME AND COMPLETE ADDRESS *(Street, City, State, ZIP)*

National Bureau of Standards (NBS)
American Society for Testing and Materials (ASTM)
Office of Naval Research (ONR)
Department of Energy (DOE)

Defense Advanced Research
 Project Agency (DARPA)
Air Force Office of Scientific
 Research (AFOSR)

10. SUPPLEMENTARY NOTES

Library of Congress Catalog Card Number: 86-600587

☐ Document describes a computer program; SF-185, FIPS Software Summary, is attached.

11. ABSTRACT *(A 200-word or less factual summary of most significant information. If document includes a significant bibliography or literature survey, mention it here)*

The Sixteenth Annual Symposium on Optical Materials for High Power Lasers (Boulder Damage Symposium) was held at the National Bureau of Standards in Boulder, Colorado, October 15-17, 1984. The Symposium was held under the auspices of ASTM Committee F-1, Subcommittee on Laser Standards, with the joint sponsorship of NBS, the Defense Advanced Research Project Agency, the Department of Energy, the Office of Naval Research, and the Air Force Office of Scientific Research. Approximately 200 scientists attended the Symposium, including representatives of the United Kingdom, France, West Germany, and the Netherlands. The Symposium was divided into sessions concerning Materials and Measurements, Mirrors and Surfaces, Thin Films, and Fundamental Mechanisms. As in previous years, the emphasis of the papers presented at the Symposium was directed toward new frontiers and new developments. Particular emphasis was given to materials for high power apparatus. The wavelength range of prime interest was from 10.6 μm to the uv region. Highlights included surface characterization, thin film-substrate boundaries, and advances in fundamental laser-matter threshold interactions and damage mechanisms. Harold E. Bennett of the Naval Weapons Center, Arthur H. Guenther of the Air Force Weapons Laboratory, David Milam of the Lawrence Livermore National Laboratory, and Brian E. Newnam of the Los Alamos National Laboratory were co-chairmen of the Symposium. The Seventeenth Annual Symposium is scheduled for October 28-30, 1985, at the National Bureau of Standards, Boulder, CO.

12. KEY WORDS *(Six to twelve entries; alphabetical order; capitalize only proper names; and separate key words by semicolons)*

laser damage; laser interactions; optical fabrication; optical materials; properties; thin film coatings.

13. AVAILABILITY ☒ Unlimited ☐ For Official Distribution. Do Not Release to NTIS ☒ Order From Superintendent of Documents, U.S. Government Printing Office, Washington, D.C. 20402. ☐ Order From National Technical Information Service (NTIS), Springfield, VA. 22161	14. NO. OF PRINTED PAGES 444 15. Price

NBS Technical Publications

Periodical

Journal of Research—The Journal of Research of the National Bureau of Standards reports NBS research and development in those disciplines of the physical and engineering sciences in which the Bureau is active. These include physics, chemistry, engineering, mathematics, and computer sciences. Papers cover a broad range of subjects, with major emphasis on measurement methodology and the basic technology underlying standardization. Also included from time to time are survey articles on topics closely related to the Bureau's technical and scientific programs. Issued six times a year.

Nonperiodicals

Monographs—Major contributions to the technical literature on various subjects related to the Bureau's scientific and technical activities.

Handbooks—Recommended codes of engineering and industrial practice (including safety codes) developed in cooperation with interested industries, professional organizations, and regulatory bodies.

Special Publications—Include proceedings of conferences sponsored by NBS, NBS annual reports, and other special publications appropriate to this grouping such as wall charts, pocket cards, and bibliographies.

Applied Mathematics Series—Mathematical tables, manuals, and studies of special interest to physicists, engineers, chemists, biologists, mathematicians, computer programmers, and others engaged in scientific and technical work.

National Standard Reference Data Series—Provides quantitative data on the physical and chemical properties of materials, compiled from the world's literature and critically evaluated. Developed under a worldwide program coordinated by NBS under the authority of the National Standard Data Act (Public Law 90-396).
NOTE: The Journal of Physical and Chemical Reference Data (JPCRD) is published quarterly for NBS by the American Chemical Society (ACS) and the American Institute of Physics (AIP). Subscriptions, reprints, and supplements are available from ACS, 1155 Sixteenth St., NW, Washington, DC 20056.

Building Science Series—Disseminates technical information developed at the Bureau on building materials, components, systems, and whole structures. The series presents research results, test methods, and performance criteria related to the structural and environmental functions and the durability and safety characteristics of building elements and systems.

Technical Notes—Studies or reports which are complete in themselves but restrictive in their treatment of a subject. Analogous to monographs but not so comprehensive in scope or definitive in treatment of the subject area. Often serve as a vehicle for final reports of work performed at NBS under the sponsorship of other government agencies.

Voluntary Product Standards—Developed under procedures published by the Department of Commerce in Part 10, Title 15, of the Code of Federal Regulations. The standards establish nationally recognized requirements for products, and provide all concerned interests with a basis for common understanding of the characteristics of the products. NBS administers this program as a supplement to the activities of the private sector standardizing organizations.

Consumer Information Series—Practical information, based on NBS research and experience, covering areas of interest to the consumer. Easily understandable language and illustrations provide useful background knowledge for shopping in today's technological marketplace.
Order the above NBS publications from: Superintendent of Documents, Government Printing Office, Washington, DC 20402.
Order the following NBS publications—FIPS and NBSIR's—from the National Technical Information Service, Springfield, VA 22161.

Federal Information Processing Standards Publications (FIPS PUB)—Publications in this series collectively constitute the Federal Information Processing Standards Register. The Register serves as the official source of information in the Federal Government regarding standards issued by NBS pursuant to the Federal Property and Administrative Services Act of 1949 as amended, Public Law 89-306 (79 Stat. 1127), and as implemented by Executive Order 11717 (38 FR 12315, dated May 11, 1973) and Part 6 of Title 15 CFR (Code of Federal Regulations).

NBS Interagency Reports (NBSIR)—A special series of interim or final reports on work performed by NBS for outside sponsors (both government and non-government). In general, initial distribution is handled by the sponsor; public distribution is by the National Technical Information Service, Springfield, VA 22161, in paper copy or microfiche form.